Geodynamic Evolution and Genesis of the Cannington Broken Hill-type Ag-Pb-Zn deposit, Mount Isa Inlier, Queensland

By

Stephen B. Bodon
(B.App.Sc., M.Sc.)

(Stephen Bruce)

UNIVERSITY OF TASMANIA

Submitted in fulfilment of the requirements for the degree of
Doctor of Philosophy

March 2002

Centre for Ore Deposit Research
University of Tasmania

For my sons, Matt and Andy

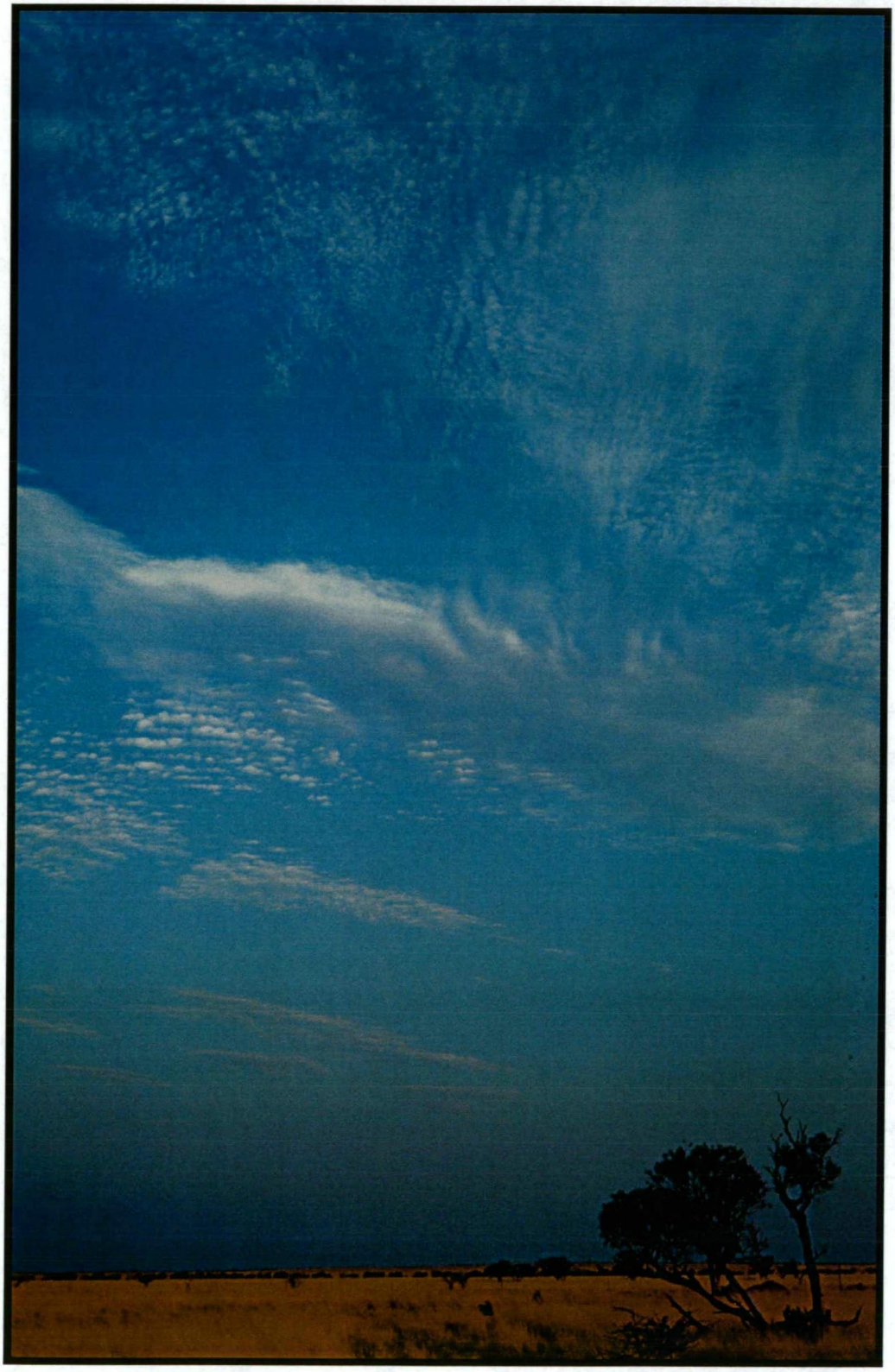

Twilight at Cannington.

Looking west from the first established exploration camp.
(Oct '94)

This thesis contains no material which has been accepted for the award of any other higher degree or graduate diploma in any tertiary institution and, to the best of the author's knowledge and belief, the thesis contains no material previously published or written by another person, except where due reference is made in the text of the thesis.

Stephen B. Bodon

Date: 27/3/02

This thesis is not to be made available for loan or copying for 18 months following the date this statement was signed. Following that time, the thesis may be made available for loan and limited copying in accordance with the Copyright Act 1968.

Stephen B. Bodon

Date: 27/3/02

Abstract

The Cannington Ag-Pb-Zn deposit is located in the southeastern area of the Palaeo- to Mesoproterozoic Mount Isa Inlier, northwest Queensland. The orebody is totally concealed beneath 10-60m of flat-lying, semi-lithified Cretaceous to Recent sediments of the Eromanga Basin. The deposit constitutes an economic resource of 43.8 million tonnes (Mt) at 11.6% Pb, 4.4% Zn and 538g/t Ag, and currently the mine is the world's largest Pb and Ag producer.

The deposit has been classified as a classic Broken Hill-type (BHT) Pb-Zn deposit based on remarkably similar geochemical, mineralogical and host rock affinities to the giant ~280Mt Broken Hill deposit in New South Wales, Australia; the holotype of the BHT classification. Conjecture over the genesis of the Cannington deposit has arisen because of two disparate lines of thought. Metamorphogenic models assume that ore textures, mineralogies and chemistries are a record of the primary ore formation process, whereas syngenetic models consider that the same characteristics have been extensively modified by post-depositional deformation and metamorphism. As a result, premetamorphic and metamorphic-metasomatic models have been proposed. This thesis contributes to this debate by integrating geological, paragenetic, geochemical and isotopic constraints to identify the most plausible genetic model.

Cannington is hosted by migmatitic gneiss with intercalated pegmatites, amphibolites, minor quartzites and rare Fe-Mn silicate (± sulphide) units. Various lines of evidence indicate that the gneiss represents metamorphosed, immature, siliciclastic sediments that were deposited during the early stages of intracontinental rifting ca. 1675 Ma. The migmatitic gneiss grades into a 250m-wide sillimanite-garnet schist and garnetiferous quartzite ore envelope that is interpreted to be a metamorphosed hydrothermal alteration halo genetically related to ore formation. Gahnite-bearing schists are a less common, but important component of the envelope.

The host succession was subjected to polydeformation and high-P/low-T metamorphism related to dominantly west-vergent folding and thrusting during the Isan Orogeny between ca. 1600-1480 Ma. Using a combination of mineral equilibria and cation exchange thermobarometers, M_1-M_2 metamorphism is characterised by an anti-clockwise P-T-t path, with peak metamorphic conditions (M_1) of ~730-750°C and 5-6kbar; consistent with upper amphibolite to transitional granulite facies conditions. It was during M_1 that substantial anatectic partial melting of the host metasedimentary succession occurred ca. 1580 Ma. This was followed by a retrograde M_2 event that involved the ingress of metamorphically-derived, acidic fluids and the development of characteristic secondary sillimanite shear fabrics (S_2). Third generation recumbent folding and thrusting resulted in the development of the Cannington Synform and Footwall Shear; an interpreted fold-thrust pair. The Cannington Synform controls the gross geometry of the deposit, resulting in repetition of ore lenses in the structural hanging wall and footwall. The Footwall Shear truncated ore lenses in the lower, attenuated limb of the Cannington Synform. A fourth generation of deformation (D_4) appears to be related to a transient thermal perturbation (M_3) initiated by the intrusion of voluminous granitic melts of the Williams-Naraku Batholith ca. 1520 Ma. D_4 has a moderate effect on the geometry of the deposit, and is manifested by an open, upright synform. D_5 represents a change in deformation style to a brittle regime. Two generations of subvertical faults overprint the orebody and locally offset ore lenses by up to 50m. The youngest of these generations comprises a conjugate fault set.

Mineralised rocks can be divided into graphitic, Fe-Mn silicate and siliceous types, based on differing mineralogies, metal zonation and Fe, Mn, Pb and Zn concentrations. Textures are extremely variable depending on the ore type, and include: i) laterally continuous, millimetre to centimetre-scale compositional banding; ii) granoblastic sulphide-silicate textures with spheroidal sulphide inclusions in silicate minerals; iii) durchbewegt textures; iv) anastomosing mylonitic zones in fluorite-magnetite-rich ores, and; v) quartz-sulphide breccias. The paragenesis of the deposit has been divided into three principal stages based on mineralogical assemblages and temporal relationships to deformation and metamorphic events recorded in the host metasediments and proximal garnetiferous alteration halo. *Stage I:* peak metamorphic assemblages comprise anhydrous minerals in sulphide-bearing graphitic, olivine and hedenbergite ores; *Stage IIa:* retrograde syn- to post-D_2 metasomatism associated with

anhydrous alteration assemblages (hedenbergite-garnet-quartz-pyroxferroite) and silicification; *Stage IIb:* amphibole veining and alteration, and minor sulphide deposition; and *Stage IIc:* syn- to post-M_3 pyrosmalite-magnetite alteration associated with abundant secondary sulphides, sulphosalts and antimonides; *Stage III:* syn to post-D_5 quartz-carbonate-chlorite alteration, temporally and spatially associated with two generations of subvertical faulting. The Stage IIa hedenbergite-garnet-quartz metasomatism and silicification produced a range of protolith-dependent metasomatic ore types such as siliceous Pb-Zn-Ag and siliceous Zn ore breccias. Overall, syn- to post-D_2 metasomatism resulted in reworking and zone-refining of the deposit via localised solution-associated remobilisation of sulphides. Granoblastic sulphide-silicate textures and spheroidal sulphide inclusions in Stage I olivines and magnetite are consistent with the presence of sulphides prior to peak metamorphism. The presence of pseudomorphic bow-tie textures and relic inclusion trials (S_i) in garnet porphyroblasts in graphitic ores, indicate that the timing for ore formation can be traced back through prograde metamorphism to pre- Isan Orogeny times. This is supported by cation exchange thermometric estimations that record the prograde evolution of the ores.

Compared to migmatitic gneiss, sillimanite-garnet and gahnite-bearing schists have higher K/Na ratios and anomalous Mn, Pb and Zn concentrations. The most significant mass changes associated with alteration of gneissic protolith to sillimanite-garnet and gahnite-bearing schist involved mass gains in K, Mn, Pb, Zn and Rb, and losses in Si, Fe, Mg, Na, Sr and Ba, with average, absolute net mass gains of 0.8g/100g and 5.9g/100g respectively. On the basis of immobile elements (Ti, Zr, Al) graphitic ores contain a pelitic detrital component. Mass balance calculations between an average pelitic gneiss precursor composition and graphitic ores indicate absolute net mass gains between 25.0g/100g for samples that contain the highest proportion of pelitic detritus, to >1000g/100g that contain the least. Such large net mass changes can be explained by the presence of hydrothermal components in the ores, in addition to pelitic detritus. Chondrite-normalised REE signatures are characterised by LREE-enrichment and strong positive Eu anomalies, similar to hydrothermal fluids and chemical sediments proximal to mid-ocean ridge hot springs. Calculated hydrothermal REE signatures are characterised by strong positive Eu anomalies when normalised to the local host gneiss. The data are consistent with the interpretation that graphitic ores are metamorphosed chemogenic sediments. $\delta^{13}C$ signatures of graphite in graphitic ores range between –27‰ to –25‰, consistent with a biogenic origin. The preservation of carbon is best accounted for by an anoxic environment if a synsedimentary origin is assumed. The data do not support a retrograde metasomatic model for ore formation.

Paragenetically constrained Pb isotope signatures were determined on various ore types, and host rocks. Stage I and II galenas plot as a distinct linear cluster oriented along the machine fractionation trend, but within the limits of the precision ellipse. Most of the data plot just below the average crustal growth curve, and compared to other Proterozoic sediment-hosted Pb-Zn deposits in northern Australia (e.g. McArthur River and Mount Isa), have more primitive μ values similar to other BHT deposits, such as Pegmont (30km west of Cannington) and Broken Hill in New South Wales. A strong correlation between Pb isotope signatures from Stage I and II galenas indicates that syn- to post-D_3 metasomatic fluids sourced Pb from pre-existing Stage I ores and that significant exotic Pb was not introduced. Stage III galena and amazonite in lode pegmatites inherited their Pb isotopic signatures from pre-existing galena, as well as from radiogenic Pb in gneissic and garnetiferous rocks. The Pb isotope data also reveals that Stage I Pb was not sourced from the nearby granites, or the host metasediments. The available evidence suggests a more primitive, exotic source that is not exposed in the region. Development of a terrain-specific Pb isotope model for the Mount Isa region suggests that mineralisation was deposited at ~1675 Ma. This age coincides with maximum depositional ages of ca. 1680 Ma (zircon U-Pb SHRIMP date). It provides further evidence that the orebody formed in a synsedimentary environment.

Ore textures, thermobarometric estimates, $\delta^{13}C$, Pb isotope systematics and geochemical affiliations, combined with U-Pb zircon ages, provide firm evidence for a synsedimentary timing for ore formation. This is further supported by the fine-scale laterally continuous and compositionally diverse banding in graphitic ores that are interpreted to represent chemogenic sediments with a variable detrital pelitic component. Precursor authigenic hydrothermal assemblages are likely to have been dominated

by variable proportions of Fe-Mn carbonates (manganoan siderite and ankerite), fluorapatite, fluorite, magnetite, Fe-Mn chlorites (chamosite, greenalite) and clays, quartz, biogenic matter (kerogens) galena, sphalerite, pyrrhotite, antimonides, arsenopyrite and minor chalcopyrite. These assemblages are consistent with a reduced, anoxic environment where $\Sigma H_2S >> \Sigma SO_4^{2-}$ was maintained during ore deposition in an otherwise oxidised basin. Metal solubility data and interpreted precursor mineralogies suggest that the weakly acidic to neutral (pH ~5.5), hypersaline (~15-25 wt% equiv. NaCl), hot (250-300°C) ore-forming fluid contained low ΣS (10^{-3}-10^{-4}*m*) high ΣCO_2 (~1*m*), Σmetals>>ΣS. In consideration of these aspects and the chemogenic nature of graphitic ores, a fluid of this composition would, upon discharge into oxidised seawater, form a dense brine pool in topographic depressions on the seafloor. A brine pool model provides the best explanation for the existence and long-term maintenance of an anoxic, reduced environment that was insulated from the surrounding oxidised seawater. It also provides an explanation for the lack of barite and/or anhydrite in the ores. Pb isotopes suggest that metals were sourced from exotic rocks that are presently unexposed. This aspect leaves scope for a speculative model involving the generation of hydrothermal fluids via partial melting and concomitant metasomatism of mantle derived mafic melts related to underplating in the middle to lower crust during intracontinental rifting. This implies that deep-seated extensional structures facilitated the rapid advection of ore-forming fluid to the ocean floor.

Acknowledgements

There are a large number of people that I have had the pleasure of meeting and working with over my time at CODES. First and foremost, I am indebted to my supervisor, Garry Davidson, for his support and encouragement throughout the period of my PhD. Garry's patience, understanding and exuberance were unrivalled. I must also thank Mike Solomon who took time out to review drafts of chapters and afforded many hours of thought provoking discussions. Mike's prompt reviewing of chapters was greatly appreciated. My gratitude is extended to Ron Berry who helped me understand some of the finer points of metamorphic petrology in discussions and reviewing of my "metamorphic chapter." Dave Cooke not only managed to instil confidence through good and bad times, but also did a great job reviewing my last chapter in an exceptionally short period of time when it really mattered. Thank you to Dave Steele from the Central Science Laboratory for his assistance on the microprobe. Nilar Hlaing is thanked for generously donating her time helping with the REE analyses in the wet chemistry lab. Thanks also to the administrative staff including Chris, Di, Lynn, Peter, June and Simon. I must also extend my thanks to the staff at the CSIRO Pb isotope facility.

BHP Minerals are thanked for the supporting this study. In particular, I would like to extend my gratitude to current and former BHP geologists for their valuable geological discussions. Thanks to Andy Bailey, Mark Dugmore, Steve Walters, Paul Fell, Brentan Grant, Steve Konecny and Kath McGuckin. Pat Williams (James Cook University) is thanked for his stimulating discussions on Broken Hill-type deposits.

My postgrad. peers have made my time at CODES an enjoyable one to say the least. The sharing of friendships, geological discussions and the occasional Friday night beer has made my stay a memorable one. Thanks to Mike Roache, Stu Smith, Mark Doyle, Karin Orth, Owen Hatton, Chris Muller, Darryl Clark, Andrew Stewart, Rohan Wolfe, Andrew Dacey, Mike Buchanan, Mawson Croaker, James Cannell, Mike Agnew, Andrew Wurst, Dave Rawlings, Catherine Reid, Robin Cantrill, and many others. In addition, the generosity and enthusiasm of those who helped me in the final stages of putting my thesis together was enormously appreciated. Thank you Mawson, Chris, James, Rohan and Sarah. A very special thank you to Vanessa in more ways than one.

A special thanks to my family for providing the kind of moral, and at times financial, support that one needs. Thanks Mum and Dad, Mark and Peter. Thanks to my sons, Matt and Andy, for the inspiration and reminding me that it's all worth it.

Table of Contents

List of Figures

List of Tables

Chapter 1

Introduction

1.1 FOREWORD

The Cannington Ag-Pb-Zn deposit is located in the southeastern area of the Palaeo- to Mesoproterozoic Mount Isa Inlier, northwest Queensland, at latitude 21°52'9"S and longitude 140°55'10"E, approximately 135km south-southeast of the township of Cloncurry (Fig. 1.1). The orebody is totally concealed beneath 10-60m of flat-lying, semi-lithified Cretaceous to Recent mudstones, sandstones and gravels of the Eromanga Basin. The mine is 100% owned and operated by BHP Billiton and presently is the world's largest producer of Pb and Ag

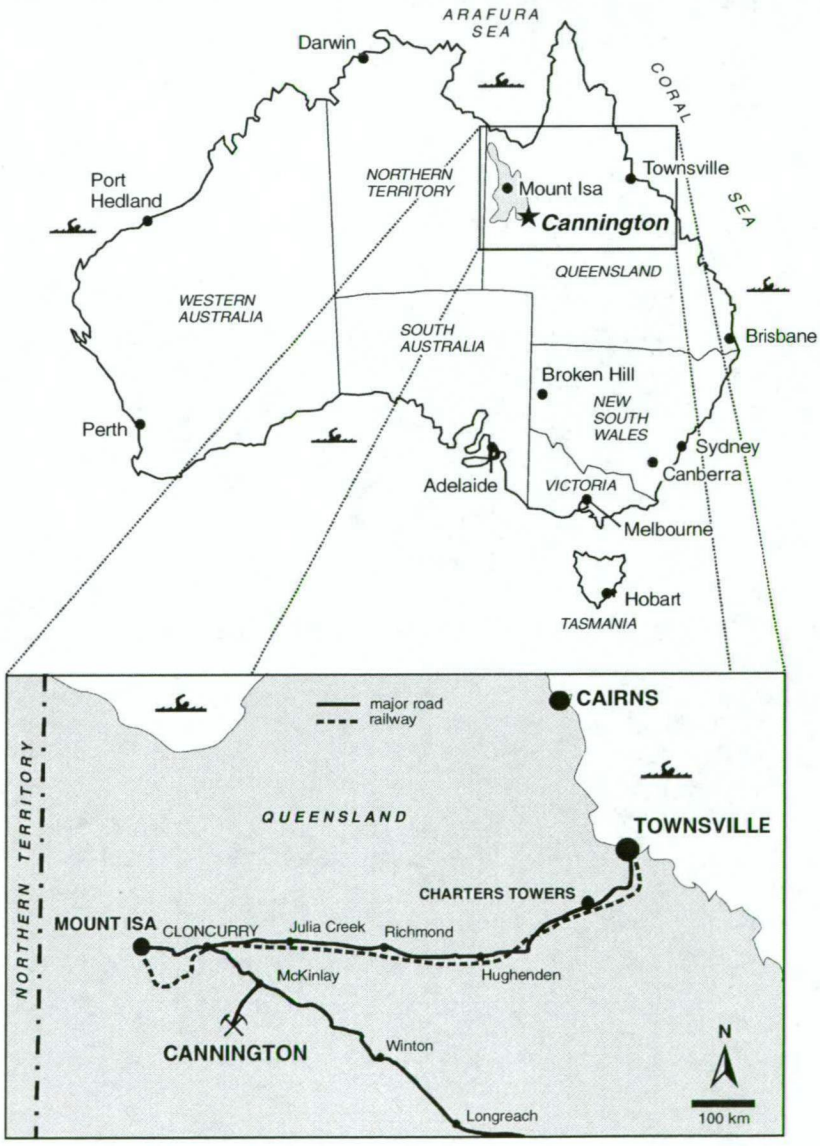

Figure 1.1 Location of the Cannington Ag-Pb-Zn deposit and the Mount Isa Inlier.

with an annual output for the financial year ending 30th June 2000 quoted at:

- 323,756 wet metric tonnes of Pb concentrate
- 145,345 wet metric tonnes of Zn concentrate
- 31.7 million ounces of Ag (contained in concentrates)

It is also one of the richest Ag resources of its class (Walters, 1994a, 2000; Bodon, 1998; Walters and Bailey, 1998; Dugmore, 1998) with grades up to 2,000g/t Ag not unusual. From a historical perspective, *in situ* Ag reserves of ~750 million ounces make it the 6th largest resource behind the likes of Broken Hill, Australia (~950 million ounces) and Potosí, Bolivia (~5,500 million ounces; Dugmore, 1998). Reserves as at May 1997 were estimated at 43.8 million metric tonnes (Mt) grading at 11.6% Pb, 4.4% Zn and 538g/t Ag (Bailey, 1998), with the resource occurring in two discrete zones, viz.:

- the Southern Zone comprising the bulk of the reserves at 34.7Mt grading 12.4% Pb, 4.9% Zn, 582g/t Ag (op. cit.);
- and the lower grade and tonnage Northern Zone containing 9.1Mt at 8.9% Pb, 3.0% Zn, 371g/t Ag (op. cit.).

The entire mineralised system is an order of magnitude larger than the economic resource and there is strong potential for additional reserves. A minimum mine life of 20 years is anticipated based on the latter reserve estimates and planned processing of 1.5Mt of ore annually (see below).

1.1.1 Discovery, development and production

The discovery of Cannington by BHP Minerals in 1990 was the culmination of some 10 years of systematic research and exploration for Broken Hill-type (BHT) deposits in Australia (section 1.2). The company was drawn to the Eastern Succession of the Mount Isa Inlier after regional appraisals highlighted strong lithostratigraphic similarities to the Willyama Supergroup in the Broken Hill Block, New South Wales, which hosts the giant Broken Hill Pb-Zn-Ag deposit. Complex polydeformation and high grade metamorphism were also important key similarities between the two terranes.

The presence of stratiform ironstones and unusual Fe-Mn silicate rocks in the Eastern Succession with geochemical and mineralogical affinities indicative of BHT systems provided a clear indication of the potential for economic BHT deposits within the region. These smaller occurrences include the Fairmile, Cowie, Black Rock and Dingo prospects (Alcock, et al., 1973), as well as the Pegmont Pb-Zn-Ag deposit, discovered in 1971 (Locsei, 1977). In 1985 BHP drilled an intense magnetic feature intersecting sub-economic BHT Pb-Ag mineralisation under 10-30m of Cretaceous cover at the Altia prospect (Skrzeczynski, 1993). Three years later the Maronan Pb-Ag deposit was discovered by Billiton confirming the fertility of the terrane for BHT deposits (Randell, 1993). These encouraging results ignited BHP's exploration effort and in June 1990 drilling of a discrete 1000nT aeromagnetic bulls-eye anomaly at the Cannington prospect (Fig. 1.2) yielded a 20m intersection of sulphide

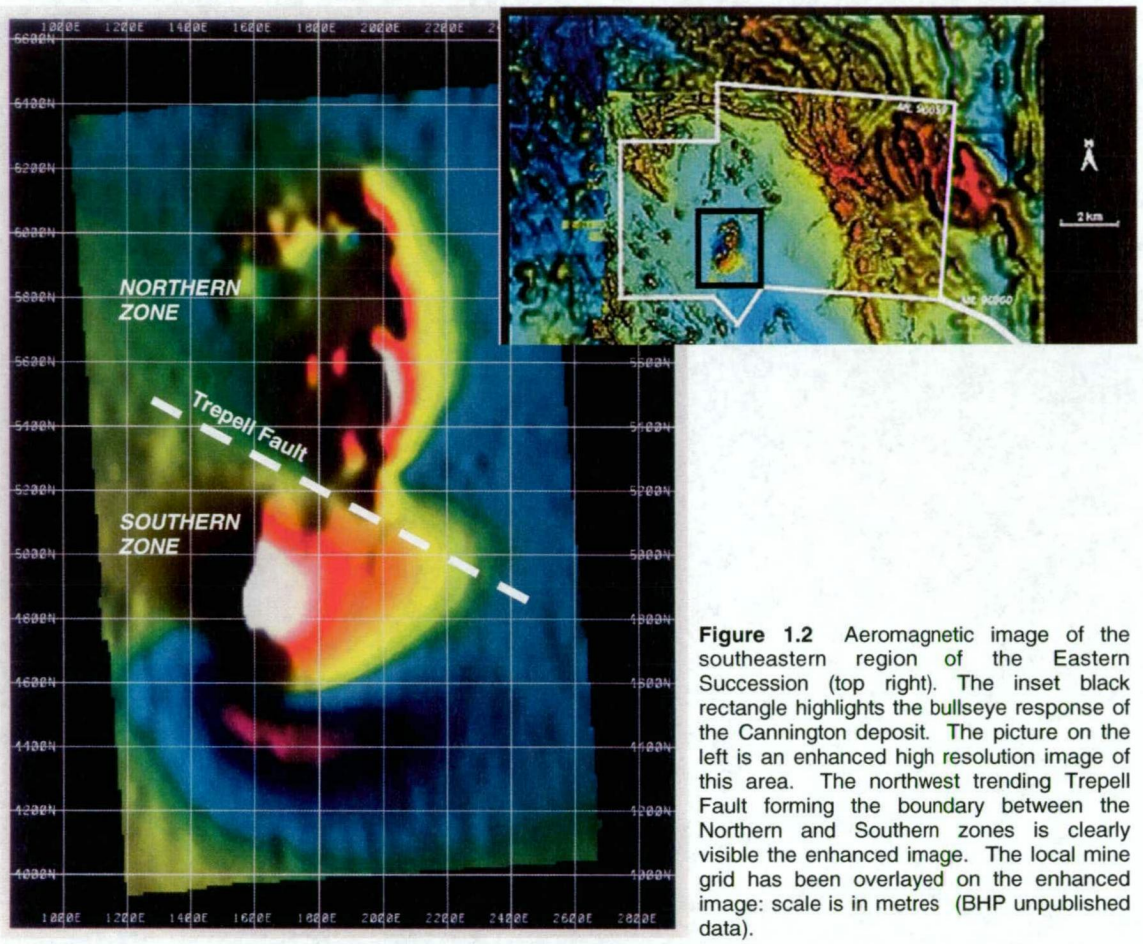

Figure 1.2 Aeromagnetic image of the southeastern region of the Eastern Succession (top right). The inset black rectangle highlights the bullseye response of the Cannington deposit. The picture on the left is an enhanced high resolution image of this area. The northwest trending Trepell Fault forming the boundary between the Northern and Southern zones is clearly visible the enhanced image. The local mine grid has been overlayed on the enhanced image: scale is in metres (BHP unpublished data).

mineralisation that averaged 12.1% Pb, 0.6% Zn and 870g/t Ag in Proterozoic rocks concealed beneath approximately 40m of Cretaceous cover (Skrzeczynski, 1993). Subsequent drilling showed that this hole intersected the footwall Pb lode in the Southern Zone, a relatively narrow fluorite-magnetite-rich, high grade lens (op. cit.).

A full feasibility study, which included the construction of a 1-in-8 exploration decline and some 100km of diamond drilling, was completed in 1995. In 1996 the decision was made to commence development of an underground mine in the Southern Zone. Construction was completed by the end of 1997 and the mine went into production (Fig. 1.3).

Today, extraction of ore is by means of long-hole open stoping and paste backfill that consists of a mixture of tailings and 5% cement. The ore treatment plant is designed to process 1.5Mt of ore per annum with an anticipated annual output of 750 tonnes of Ag contained within 265,000 tonnes of Pb concentrate and 110,000 tonnes of Zn concentrate. A blend of ore types is required for the mill feed in order to dilute contaminants such F and Sb that are concentrated in some ore types but not in others. Concentrates are trucked and then railed to the storage and loading facility at the Port of Townsville before being shipped to various smelters around the world and within Australia (Fig. 1.1). Further information about the mine infrastructure, mining methods, minerals processing plant and product marketing is available on the BHP Billiton website at *www.bhpbilliton.com*.

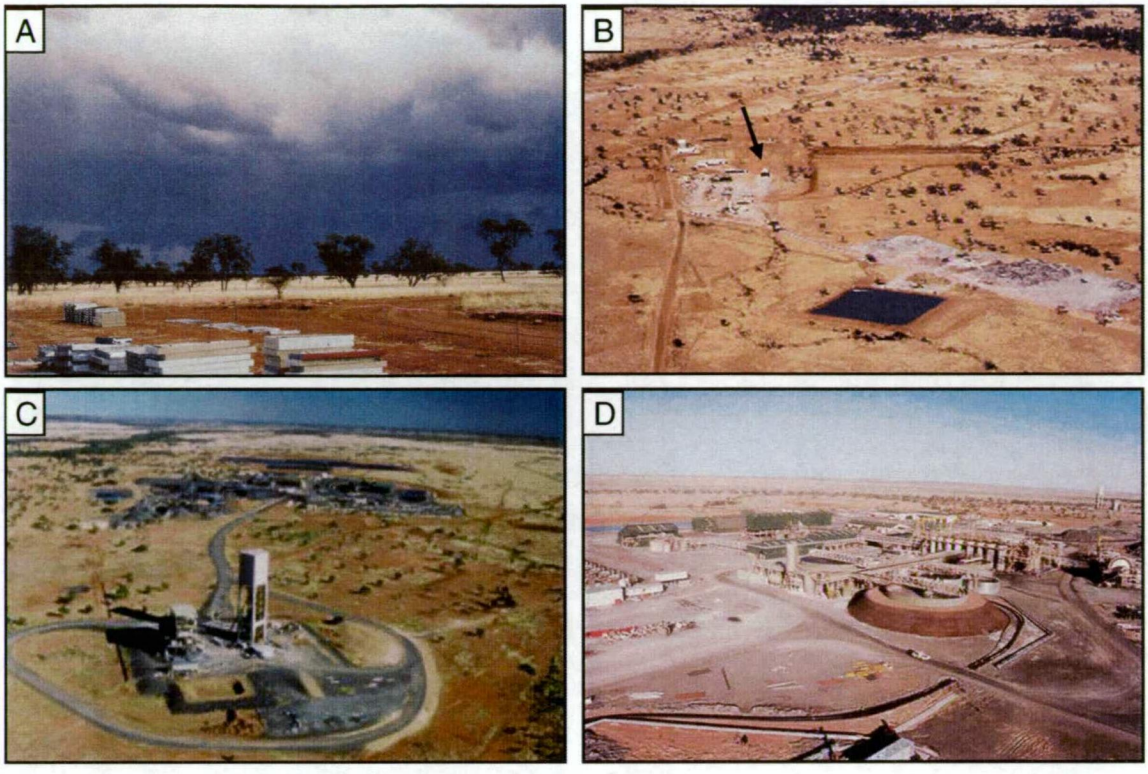

Figure 1.3 The Cannington mine site. **A.** view from the core yard looking southwest to the area where the air strip now lies, circa 1994. **B.** aerial view of the mine site looking south showing the entrance to the development decline (arrow), circa 1995 (photo courtesy of BHP) **C.** aerial view of the shaft and mill in the background looking northwest, circa 1999 (photo courtesy of BHP). **D.** aerial view of the ore treatment plant looking southeast, circa 1999 (photo courtesy of BHP).

1.1.2 Physiography and climate

The countryside at the Cannington mine is dominated by flat grassland with gentle low rises and occasional low-lying black-soil plains (Fig. 1.3). It is locally referred to as "downs country". The climate is semi-arid with a relatively short and unreliable wet season between December and March. The vast majority of the 250mm of average annual rainfall occurs between these months, with pan evaporation averaging 3,000mm per annum. Dry, tree-lined sandy creeks only flow during torrential rainfall in the summer months and the area is particularly susceptible to flooding. Average daily maximum air temperatures range between 35-40°C in December to February with minimum temperatures averaging 25°C. Maximum temperatures from June to August range between 18-25°C with minimum temperatures averaging 10°C.

1.2 OVERVIEW OF THE BROKEN HILL-TYPE CLASSIFICATION

The Cannington deposit was formally classified as a Broken Hill-type deposit by Walters (1994a) based on remarkably similar geochemical, mineralogical and host rock affinities to the giant ~280Mt Broken Hill deposit in New South Wales; the holotype of the BHT classification. Cannington represents the most significant example of the class since the discovery of the Broken Hill deposit itself in 1883 (Dugmore, 1998). BHT deposits are traditionally much valued exploration targets due to their potential for hosting large, high grade reserves of chiefly Pb, Zn and Ag, and lesser Au and Cu. The most significant BHT deposits on a global-scale, including variants with BHT-like affinities are summarised in Table 1.

Table 1 Tonnages and grades for significant BHT deposits around the world (collated from Parr and Plimer, 1993; Höller et al., 1996; Dugmore, 1998; Walters, 1998).

Location	Deposit	Size (Mt)	Pb (%)	Zn (%)	Ag (g/t)	Cu (%)	Fe (%)
Classic BHT deposits							
Broken Hill Block, Australia	Broken Hill	280	10	8.5	148	0.14	~8
ca. 1690-1670 Ma	Pinnacles	0.8	10	2.5	420	-	-
Mt Isa Inlier, Australia	Cannington	43.8	11.6	4.4	538	0.05	~15
ca. 1680 Ma	Pegmont	11	8.4	3.7	12	0.05	~20
Namaqua Belt, South Africa	Gamsberg	150	0.55	7.1	6	0.02	~30
ca. 1600 Ma	Broken Hill	38	6.35	2.9	82	0.45	~35
	Black Mountain	82	2.67	0.59	30	0.75	~30
	Big Syncline	101	1.01	2.45	13	0.09	~35
Bergslagen, Sweden	Zinkgruvan	40	5.5	10	100	-	-
ca. 1890-1870 Ma	Garpenberg	21.5	3.3	5.3	98	-	-
BHT-like variants							
Purcell Basin, Canada *ca. 1400 Ma*	Sullivan	155	6.1	5.9	68	-	28
Aravalli-Dehli Belt, India *ca. 1800 Ma*	Rampura Agucha	63.7	1.9	13.6	45	-	-

Reviews of the BHT classification and deposit examples can be found in Beeson (1990), Parr and Plimer (1993) and Walters (1996, 1998, 2000). Occurrences are restricted to Early to Middle Proterozoic, immature, quartzofeldspathic, oxidised sedimentary to volcanosedimentary sequences that were deposited in active intracontinental rift settings characterised by high heat-flows. Extensional tectonics ceased before the production of oceanic crust. Amphibolites, interpreted as shallow level intrusive sills, and banded iron-formations are also often spatially associated with BHT occurrences. In instances, the iron-formations may host BHT mineralisation. Shallow level felsic intrusive and extrusive rocks also form a component of the succession. The host terranes record a complex post-depositional orogenic history manifested by polydeformation and high-T/low-P metamorphism. Anticlockwise P-T-t paths are an intrinsic feature of the regional metamorphism. Crustal-scale fluid-flow during retrogression is exemplified by structurally controlled zones of metasomatised rock, the degree of which varies between terranes.

Sulphide minerals are hosted in stratiform to stratabound Fe-Mn-Ca-Si-P(-F)-rich rocks that are comprised of a diverse range of 'skarnoid' Fe-Mn-Ca silicate and carbonate minerals. These rocks typically occur within conformable 'ore-equivalent' horizons, which are characterised by distinct quartz-gahnite and garnetiferous rocks that can be regionally correlated over several tens of kilometres. Such BHT 'horizons' are anomalous in Pb, Zn and Mn, and have been used as regional stratigraphic markers for exploration. Generally, BHT deposits can be subdivided into Fe-rich and Mn-rich end-members based on gangue mineralogies (Parr and Plimer, 1993; Walters, 1998, 2000). Large deposits that show extremes of these end-members include the Fe-rich Gamsberg deposit in South Africa (~30% Fe_{total}) and the Mn-rich Broken Hill deposit in Australia (~8% Fe_{total}; Table 1). Cannington falls

between these two end-members (~20% Fe_{total}) with the majority of Fe occurring as magnetite. In contrast, magnetite is sparse at Broken Hill. These variations are most likely artefacts of differing fluid chemistries and depositional processes involved in ore formation.

In general, BHT deposits can be distinguished from contemporary sediment-hosted Pb-Zn deposits (SEDEX) based on distinct differences in geochemistry, mineralogy, metal zonation, host rock affiliation, tectonic environment, and basin and fluid chemistry (Plimer, 1986, 1991; Beeson, 1990; Parr and Plimer, 1993; Large et al., 1996; Walters, 1996, 1998). These differences imply that chemical processes involved in the formation of BHT deposits were significantly different from classic SEDEX deposits (Cooke and Large, 1996; Large et al., 1996; Cooke et al., 1999).

The genesis of BHT deposits has been controversial for over a century. This is chiefly due to the complex polydeformation and metamorphic histories of the host terranes. The Broken Hill deposit in Australia is the most renowned example with a spectrum of genetic models proposed, spanning synsedimentary exhalative to inhalative models at one extreme, to epigenetic-replacive models at the other, despite the large amount of research carried out on the deposit since its discovery. Genetic models proposed for other classic BHT deposits found around the world such as the South African deposits of the Namaqua Belt (e.g. Gamsberg; Table 1), appear to be less contentious in comparison.

The conjecture has arisen because of two disparate lines of thought. Metamorphogenic models presume that ore textures, mineralogies and chemistries are a record of the primary ore formation process frozen in time, whereas syngenetic models consider that ore textures, mineralogies and chemistries have been extensively modified by post-depositional deformation and metamorphism. It is well established that deformation, high grade metamorphism and retrogression, including metasomatism, have the potential to cause severe modification or total obliteration of primary ore features (Lawrence, 1973; Mookherjee, 1976; Plimer, 1979; Marshall and Gilligan, 1987; Gilligan and Marshall, 1987; Stanton, 1989; Parr and Plimer, 1993; Webster, 1994; Bodon and Valenta, 1995; Walters, 1996; Marshall et al., 2000; Marshall and Spry, 2000 and many others). In extreme cases syn-metamorphic partial melting of sulphide ores is theoretically possible, as was proposed during granulite facies metamorphism of the Broken Hill deposit (Brett and Kullerud, 1967; Lawrence, 1967; Mavrogenes et al., 2001). As a result, ore textures record the last event with little relict evidence for earlier events (Marshall et al., 2000). Deciphering the geodynamic evolution of BHT deposits can therefore be extremely difficult and complex.

Even though the camouflaging effects of subsequent orogenesis greatly hinder attempts to reconstruct pre-metamorphic histories, the characterisation and formulation of the geodynamic evolution into a workable framework is fundamental for the development of constrained genetic models that can be used as predictive tools for successful exploration. In fact, at Broken Hill in Australia, the difficulty of the challenge is exacerbated by the overwhelming size of the deposit

and shear diversity of mineral assemblages and ore textures that occur throughout this giant hydrothermal system (e.g. Worner and Mitchell (1982) including papers and references therein). The Cannington deposit is no exception and like Broken Hill, its genesis remains controversial.

1.3 CHIEF OBJECTIVES OF THE STUDY

Cannington is unique amongst large BHT deposits because it represents a near complete and 'pristine' BHT system that at the commencement of this study, had not lost any of its genetic secrets to mining. This study was initiated by BHP Minerals in collaboration with the Centre for Deposit Research, University of Tasmania, with the aim of documenting the geology, and unravelling the geodynamic evolution and genesis of the deposit. It represents a component of a co-ordinated effort at the time by BHP Minerals into the origin and exploration for BHT deposits, and is one of two PhD projects carried out on Cannington to date (section 1.6). The chief objectives of this project were to:

- document the geology, ore types, metal zonation and geochemical features of the deposit;
- decipher the geodynamic evolution of the deposit in the form of a deposit-wide paragenetic framework and resolve the timing of ore formation;
- propose a possible genetic model constrained by the paragenetic framework, metal zonation, geochemistry, and the structural and metamorphic history of the surrounding host rocks.

On a broader scale, this thesis contributes to the ongoing effort to understand the geodynamic evolution and genesis of BHT systems; an extremely complex and enigmatic deposit type.

1.4 METHODS

Research carried out was based upon observations gathered from detailed logging of ~30-35km of diamond drill core and limited underground exposures collectively spanning the entire deposit. Surface drilling completed between 1991 to 1995 make up the majority of drill holes logged, while the remainder comprise underground holes completed up to early 1996. Additional BHP core logs from surface holes drilled in the Northern Zone during 1996-1997 were kindly provided by K. McGuckin (BHP Cannington) upon request. Over 1,000 hand specimen samples were collected from drill core and slabbed for subsequent textural and geochemical studies. Microtextural investigations were carried out on over 180 polished thin and thick sections. Overall, the sample database constitutes the most complete record of the deposit to date that is located outside of the mine itself.

This study commenced at an early stage in the history of the Cannington deposit when much of the resource was being proven by exploration drilling. Geochemical characterisation and subsequent ore type nomenclature, in addition to structural models, were being developed in conjunction with BHP geologists at the time. Logging codes used today at Cannington were developed from this study by modification of existing BHP logging codes and introduction of

additional codes to more accurately define the large diversity of mineralogically and geochemically distinct ore types comprising the orebody (e.g. Bodon, 1995).

Techniques used to constrain the initial timing of ore formation and the geodynamic evolution of the deposit included a combination of metamorphic textural interpretations and more traditional low temperature overprinting-type textural criterion. A multidisciplinary geochemical approach was undertaken to augment, test and further constrain the paragenetic framework developed from the textural studies and ultimately, the genetic aspects of the deposit. This included paragenetically constrained:

- Pb isotope modelling to determine Pb sources and quantify the age of ore formation;
- electron microprobe data used for cation exchange thermobarometry and characterisation of mineral compositions;
- carbon isotope signatures of graphite to determine carbon sources;
- wholerock major, trace and rare-earth element (REE) determinations for mass balance studies used to constrain various genetic hypotheses including the physicochemical nature of the ore-forming environment.

1.5 THESIS LAYOUT

An appreciation of the geodynamic evolution of the terrane that hosts the Cannington deposit is crucial for the development of an integrated genetic model that can assist exploration strategies. Chapter 2 presents the most current paradigms for the Eastern Succession, host to the Cannington deposit and other BHT prospects. Rather than presenting a stoic account of the stratigraphy, structure and metamorphism of the terrane, it presents the most current geodynamic framework from the initial tectonic setting and depositional environment within which the stratigraphy accumulated, to the subsequent development of a complex fold-thrust terrane commensurate with high grade metamorphism, plutonism and exceptional crustal-scale fluid-flow exemplified by regionally extensive metasomatism. From this basis the metallogeny of the terrane is presented.

The mine-scale geology and deposit geometry is addressed in detail in Chapter 3, which includes descriptions of the local host rocks and the interpreted alteration halo surrounding the deposit. It also presents the most current structural and metamorphic framework for local area. Chapter 4 documents the ore types that comprise the deposit, specifically the distribution, mineralogy, geochemistry and paragenesis. The chapter also documents metal zonation features and concludes by presenting a deposit-wide paragenesis based on macro- and micro-textural and structural criteria. It is important to note that throughout this thesis the term "ore" refers to mineralised rock and is not used in the strict economic definition of the term.

The metamorphic history of the deposit is detailed in Chapter 5. The chapter aims to evaluate the metamorphic history of the ores relative to that of the host rocks by using various cation exchange thermobarometers with corrections that cater for elevated concentrations of Mn, Ca,

F and Cl in the gangue minerals concerned. The origin of finely banded graphite-bearing ore that comprises the majority of the Northern Zone is the subject of Chapter 6. Techniques used here include carbon isotopes, mass balance calculations and REE geochemistry. The geochemistry of the interpreted alteration halo cocooning the orebody is also investigated and a modified terrane-specific BHT alteration 'index' is proposed to augment current exploration techniques used in the region.

The source of the metals is tackled in Chapter 7 using Pb isotope tracing. In addition, a terrane-specific Pb isotope model is proposed and a Pb-model age calculated for the formation of the deposit. Chapter 8 integrates all the evidence and conclusions drawn in preceding chapters. It presents a model for the geodynamic evolution of the deposit, constrained by the structural and metamorphic history and geochronology of the host rocks, and the terrane as a whole. A preferred genetic model is proposed and the main conclusions of the study outlined.

1.6 OVERVIEW OF PREVIOUS RESEARCH

Research on the deposit commenced in 1993 and has chiefly focussed on geological documentation of the deposit, the timing of ore formation and genetic issues. Studies include those conducted internally by BHP Minerals (e.g. Walters, 1994a), the CSIRO Division of Exploration and Mining (e.g. French et al., 1994) and a range of projects undertaken at 3 Australian universities in collaboration with BHP. The majority of university research was carried out at the:

- Economic Geology Research Unit (EGRU), James Cook University.
- Centre for Ore Deposit Research (CODES SRC), University of Tasmania.
- Department of Earth Sciences and the Australian Crustal Research Centre, Monash University.

EGRU have undertaken the most research on the Cannington deposit to present, encompassing 7 Honours projects (Chapman, 1993; Mark, 1993; Strain, 1993; Jenkins, 1994; Richmond, 1994; Pringle, 1999; Smith, 1999), 1 MSc project (Dugmore, 1998) and studies associated with the Australian Mineral Industry Research Association (AMIRA) P438 Cloncurry Base Metals and Gold project (see Pollard (1997) for an executive summary). CODES SRC and Monash have each hosted a PhD (this study and Giles (2000) respectively) and an Honours project (McCarthy (1996) and Sheehan (1994) respectively). The deposit was also included in a Masters study at CODES SRC on the magnetic properties of BHT systems (Kerr, 1994). The majority of this research, including internal BHP investigations, remains unpublished (e.g. French et al., 1994; Walters 1994a and b; Pringle, 1999; Giles, 2000; this study and many more). However, significant seminal works are reported in mainstream publications such as Economic Geology (e.g. Bodon, 1998; Chapman and Williams, 1998; Walters and Bailey, 1998), the Australian Journal of Earth Sciences (e.g. Mark et al., 1998) and the Geology of Australian and Papua New Guinean Mineral Deposits (e.g. Bailey, 1998), as well as other less widely distributed conference publications (e.g. Roche, 1994; Bodon, 1996a and b; Carr and Sun, 1996; Richmond et al., 1996a and b; Walters and Bailey, 1996;

Walters and Bailey, 1998), the Australian Journal of Earth Sciences (e.g. Mark et al., 1998) and the Geology of Australian and Papua New Guinean Mineral Deposits (e.g. Bailey, 1998), as well as other less widely distributed conference publications (e.g. Roche, 1994; Bodon, 1996a and b; Carr and Sun, 1996; Richmond et al., 1996a and b; Walters and Bailey, 1996; Williams et al., 1996, 1997, 1998b).

The scale of research has varied from focussed studies on particular areas of the orebody and host rocks (e.g. EGRU research; Chapman and Williams, 1998), to deposit-wide studies (this study; Sheehan, 1994; Bodon, 1998; Walters and Bailey, 1998; Giles, 2000), up to regional-scale perspectives (Giles, 2000 and in press). Due to the diversity of mineralised rock types, large size of the hydrothermal system and complex structural and metamorphic history, this approach has culminated in a range of genetic interpretations for particular ore types and their temporal relationships to the host rocks, deformation and metamorphism.

From 1993 to 1998 there was much debate over the timing of ore formation, with two disparate models proposed, viz.:

- the "metamorphosed model" that involved the modification of a synsedimentary to diagenetic deposit by later polydeformation, metamorphism and metasomatism (e.g. French et al., 1994; Walters, 1994a; Sheehan, 1994; Bodon, 1995, 1996a and b, 1998; Bailey, 1998; Dugmore, 1998; Walters and Bailey, 1996, 1998; Pringle, 1999);
- the "metamorphogenic model" involving metasomatism and stratabound replacement of a pre-existing chemically reactive stratigraphic unit via interaction with an exotic post-peak metamorphic hypersaline fluid (e.g. Chapman, 1993; Mark, 1993; Williams and Baker, 1995; Richmond et al., 1996a and b; Williams et al., 1996, 1997, 1998b; Dong et al., 1997; Pollard et al., 1997; Williams, 1995a and b, 1998b; Chapman and Williams, 1998).

Much of the paragenetic and geochemical interpretations in the seminal Honours project of Chapman (1993), now published by Chapman and Williams (1998), was augmented by other early EGRU Honours theses (e.g. Mark, 1993; Strain, 1993; Jenkins, 1994; Richmond, 1994) and subsequent publications (e.g. Williams and Baker, 1995; Richmond et al., 1996; Williams et al., 1996). The interpretations also propagated through later EGRU studies, especially the AMIRA P438 project. In particular, the interpreted paragenetic framework was adopted for the stable isotope and fluid inclusion work undertaken by the AMIRA P438 project (Dong et al., 1997b), which in turn, had a compounding effect on the proposed regional-scale metallogenic model that evolved from the project (Pollard et al., 1997). Overall, the early EGRU work and the AMIRA P438 project supported a post-peak metamorphic, metasomatic model for the timing of ore formation (i.e. the metamorphogenic model) and this was bolstered by results from $^{40}Ar/^{39}Ar$ (Pollard and Perkins, 1997) and interpreted Pb-model ages (McNaughton, 1997b). However, as pointed out by Bodon (1998), Chapman (1993) and Chapman and Williams (1998) focussed on a particular area in the Southern Zone and whilst the interpreted

structural and metamorphic framework for the host sequence. The initial framework proposed by Gray (1993, 1994) and Sheehan (1994) suffered from some fundamental geometrical problems (Bodon, 1995; Giles, 2000). Deficiencies were overcome by the subsequent PhD study of Giles (2000) that provided a well defined and regionally constrained geodynamic framework which could be used for past and future genetic paradigms for the deposit.

Chapter 2

Regional Geology and Tectonostratigraphic Evolution of the Eastern Succession

2.1 INTRODUCTION

The Mount Isa Inlier is an extensively eroded Early to Middle Proterozoic mobile belt that outcrops over an area of approximately 50,000km^2 in northwest Queensland. It forms one of several terrains that represent structural relics of the Northern Australian Craton (Plumb et al., 1980; Etheridge and Wall, 1994; O'Dea et al., 1997a) and is subdivided into three major tectonostratigraphic domains corresponding to the Western and Eastern Successions, and the intervening Kalkadoon-Leichhardt Belt (Carter et al., 1961; Blake, 1987; Blake and Stewart, 1992; Fig. 2.1 inset). The Cannington deposit is hosted within the Eastern Succession. Each domain has unique geophysical trends, stratigraphic packages and structural styles, and is separated by regional north-south striking transcurrent fault zones. These fault zones are the Quilalar and Pilgrim Fault Zones, forming the western and eastern boundaries of the Kalkadoon-Leichhardt Belt respectively (Blake and Stewart, 1992; Wellman, 1992; O'Dea et al., 1997a). The Western Succession is further subdivided into the Leichhardt River Fault Trough and the Lawn Hill Platform, which are separated by the north-south trending Mount Isa Fault (Blake and Stewart, 1992).

The central Kalkadoon-Leichhardt Belt consists of; 1) metasedimentary basement rocks that were deformed and metamorphosed during the Barramundi Orogeny ca. 1870-1840 Ma; and 2) late-orogenic granite intrusions and contemporaneous felsic volcanic rocks (Etheridge et al., 1987; Page, 1988; Blake et al., 1990; Blake and Stewart, 1992). The adjacent Western and Eastern Successions comprise volcanosedimentary and plutonic rocks that formed during an extended period of episodic intracontinental rifting and associated basin subsidence, without intervening compressional events, between ca. 1800-1600 Ma (Carter et al., 1961; Derrick, 1982; Blake, 1987; Page, 1988; Blake et al., 1990; Blake and Stewart, 1992). The onset of compressional tectonics during the ca. 1590-1500 Ma Isan Orogeny interrupted the extensional evolution of the inlier and resulted in polydeformation, metamorphism and basin inversion, culminating in regional-scale wrenching (Lister et al., 1986; Blake and Stewart, 1992; O'Dea et al., 1997a). In comparison to the Western Succession, the Eastern Succession underwent more intense polydeformation and metamorphism during the Isan Orogeny (Betts et al., 1997a; O'Dea et al., 1997a; Giles, 2000).

Syn- to post-peak metamorphic metasomatism is a noteworthy feature of the Mount Isa Inlier, the intensity and extent of which surpasses other Proterozoic terrains on a global-scale (O'Dea et al., 1997a; Williams, 1998). The Eastern Succession in particular, preserves an extensive history of metasomatism that occurred between ca. 1740 Ma and 1500 Ma reflecting the

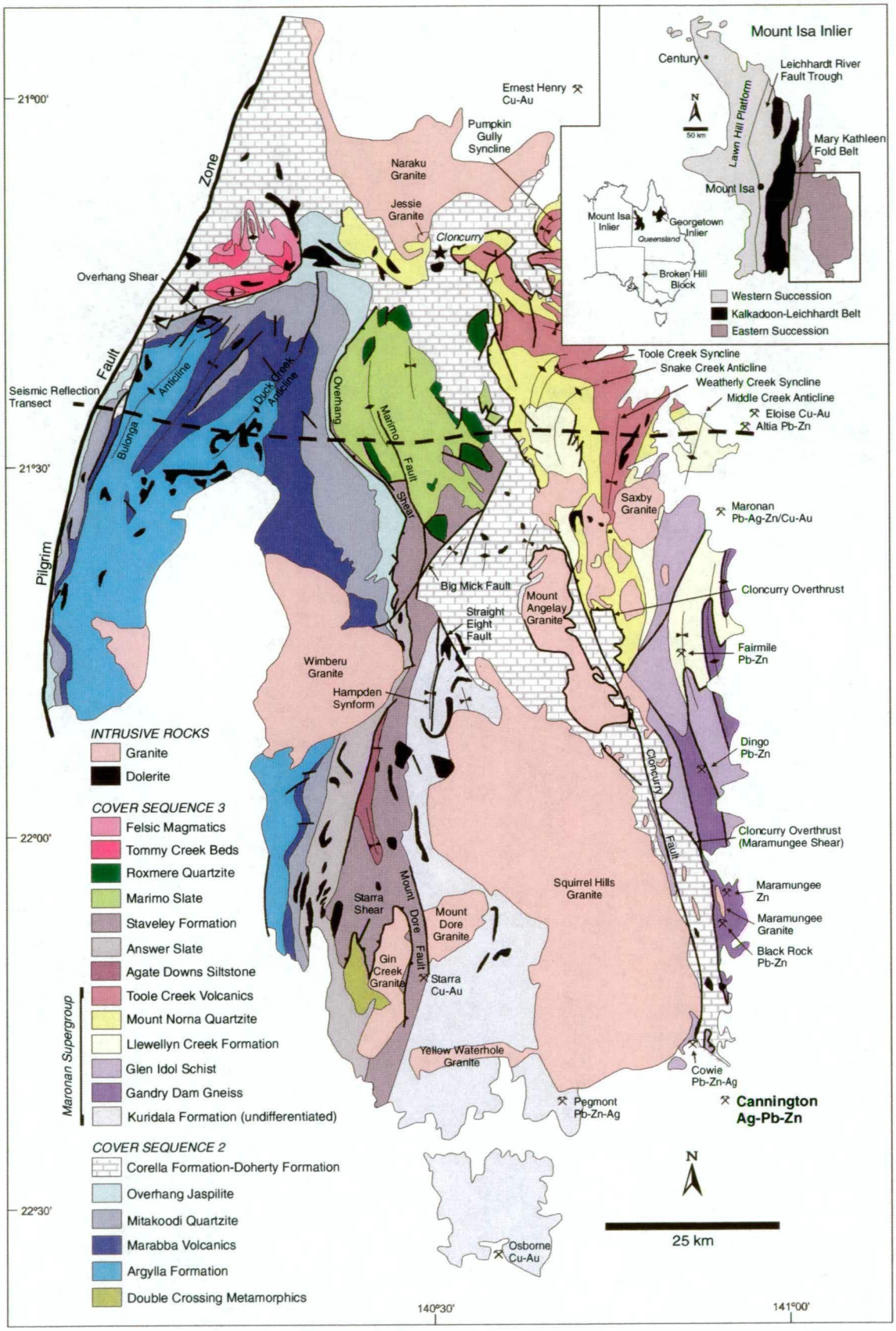

Figure 2.1 Geological map of the Eastern Succession displaying major stratigraphic units, structural elements, granites and significant ore deposits (compiled from BMR 1:500,000 Mount Inlier and Environs geological map of Blake (1987); Beardsmore et al., 1988; Beardsmore, 1992; Betts et al., 2000). Inset (top right) displays the location and main tectonostratigraphic belts of the Mount Isa Inlier after Blake and Stewart (1992).

circulation of voluminous hypersaline fluids within a mid-crustal regime (Oliver and Wall, 1987; Williams and Blake, 1993; de Jong and Williams, 1995; Oliver, 1995; Perkins and Wyborn, 1998; Giles, 2000).

This chapter presents a summary of the regional geology and geodynamic evolution of the Eastern Succession, covering the area east of the Pilgrim Fault Zone and south of the Naraku Granite. It aims to establish the geological background needed to place the Cannington deposit and its host rocks into a regional tectonostratigraphic and hydrothermal framework. In particular, the chapter draws correlations with the tectonostratigraphic framework of the Western Succession.

2.2 TECTONOSTRATIGRAPHIC EVOLUTION

2.2.1 Tectonostratigraphic framework of the Mount Isa Inlier

Blake and Stewart (1992) subdivided the stratigraphy of the Mount Isa Inlier into two major tectonostratigraphic cycles separated by the ca. 1890-1870 Ma Barramundi Orogeny. Rocks deposited after this orogeny during an extended period of episodic intracontinental rifting that affected much of northern Australia during the Early to Middle Proterozoic, comprise the second tectonostratigraphic cycle (Etheridge and Wall, 1994). Rocks comprising this second cycle were subdivided into three *Cover Sequences* separated by regional unconformities attributed to post-rift basin subsidence (Blake and Stewart, 1992; O'Dea et al., 1997a). Although O'Dea et al. (1997a) subdivided the stratigraphy into four cover sequences, much of the recent literature does not use this classification. Therefore, this review adheres to the subdivisions of Blake and Stewart (1992).

Cover Sequence 2 and 3 rocks, the distribution of which are illustrated in Figure 2.1, dominate the Proterozoic stratigraphy of the Eastern Succession. Figure 2.2 summarises the tectonostratigraphic framework and intrusive history of the Mount Isa Inlier including the names and ages of stratigraphic units and their inferred depositional settings with regard to recognised rifting events. Depositional ages and intrusive ages for the Eastern Succession are illustrated in Figure 2.3.

2.2.2 The Barramundi Orogeny (1890-1870 Ma) - Cover Sequence 1

The Barramundi Orogeny was an Early Proterozoic compressional event that affected much of northern Australia (Etheridge et al., 1987). Orogeny was preceded by a period of intraplate rifting and basin development, into which bimodal volcanic rocks and volcanosedimentary rift-sag sequences were deposited (O'Dea et al., 1997a). These rocks were subsequently deformed and metamorphosed during compressional tectonism ca. 1870 Ma (Etheridge et al., 1987; Etheridge and Wall, 1994). Pre-Barramundi age rocks, comprising the Yaringa Metamorphics and Kurbayia Migmatite, are poorly exposed in the central Kalkadoon-Leichhardt Belt of the Mount Isa Inlier (Page and Williams, 1988; Blake and Page, 1988; Blake and Stewart, 1992).

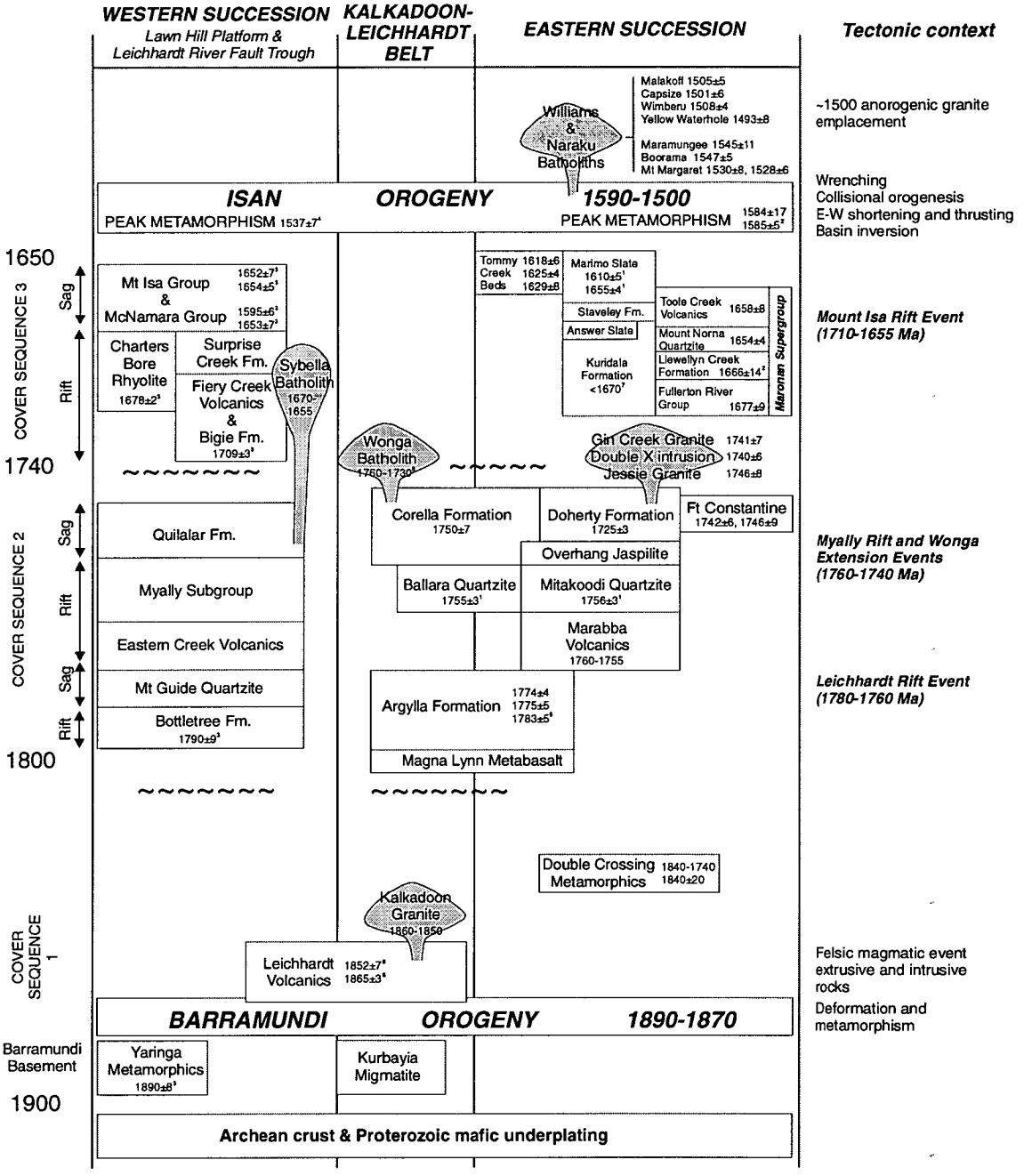

Figure 2.2 Summary of the tectonostratigraphic framework for the Mount Isa Inlier with the most recent published U-Pb (SHRIMP) zircon dates from the Eastern Succession (modified after Betts et al., 1997a; Giles and MacCready, 1997; O'Dea et al., 1997a; Page and Sun, 1998; Page and Sweet, 1998; Giles, 2000). 1—Page et al. (1997), 2—Giles (2000), 3—Page and Sweet (1998), 4—Connors and Page (1995), 5—Page (1983), 6—Page and Williams (1988), 7—Page (1998), 8—Pearson et al. (1992), ages without superscripts are from Page and Sun (1998). The age for high grade metamorphism in the Eastern Succession by Giles (2000) was determined from monazites in migmatitic gneiss at Cannington, i.e. the Gandry Dam Gneiss.

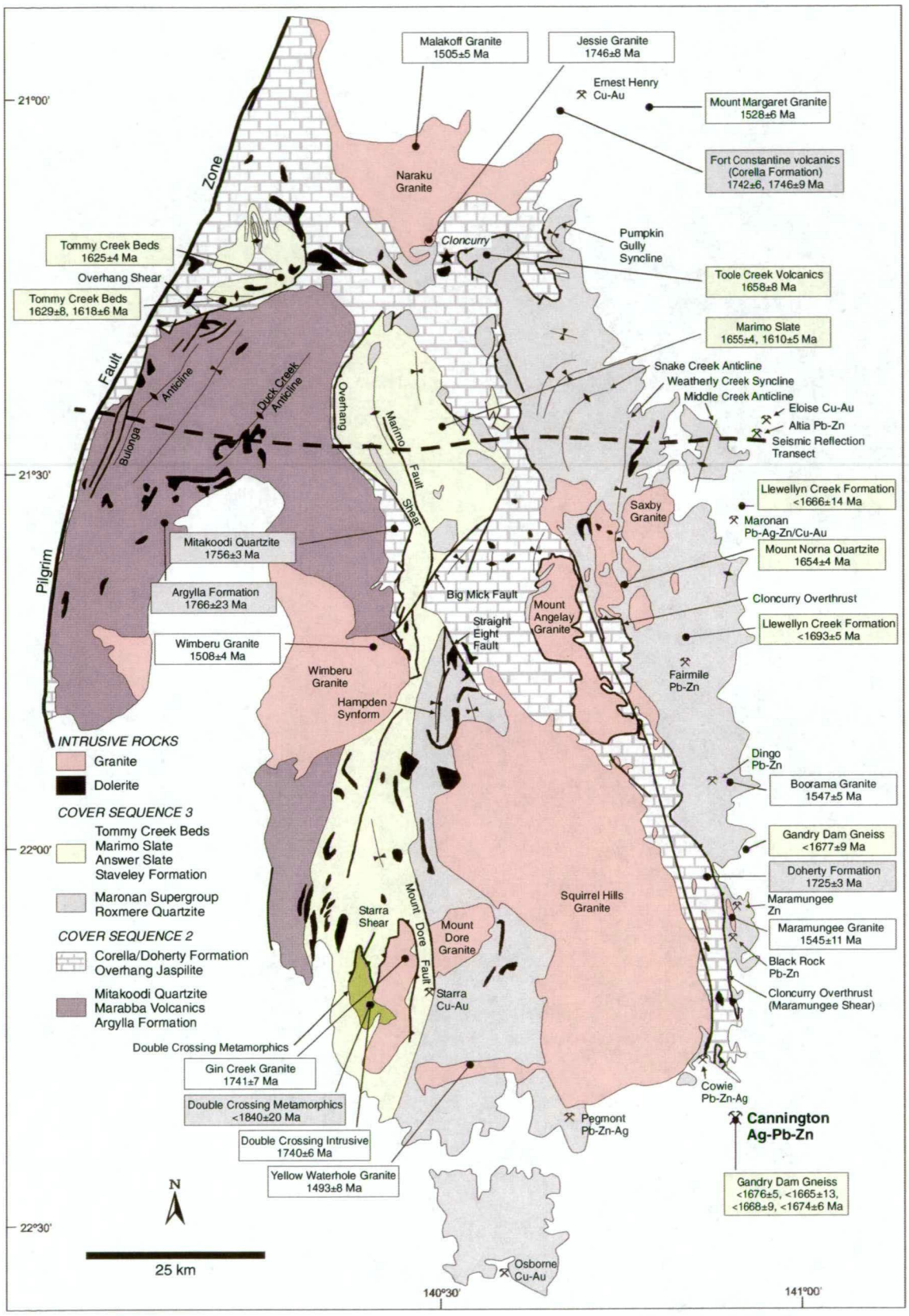

Figure 2.3 U-Pb$_{zircon}$ crystallisation ages of granites and depositional ages of major stratigraphic units comprising the Cover Sequences in the Eastern Succession (modified after Giles, 2000). White boxes are granites, whereas grey and yellow boxes are Cover Sequence 2 and 3 supracrustal rocks respectively. Data compiled from Page (1983), Page et al. (1997), Page and Sun (1998) and Giles (2000). The less than (<) symbol indicates maximum depositional ages determined from detrital zircon populations.

Voluminous felsic igneous activity associated with an Australia-wide 1880-1840 Ma felsic magmatic event (Wyborn, 1988) occurred during, or shortly after the Barramundi Orogeny, between ca. 1870-1850 Ma (Wyborn and Page, 1983; Page, 1988; Page and Williams, 1988; Wyborn, 1988; Wyborn et al., 1988; Blake and Stewart, 1992). Felsic igneous rocks of the Leichhardt Volcanics and comagmatic Kalkadoon and Ewen granites in the Kalkadoon-Leichhardt Belt correspond to this event and comprise Cover Sequence 1 in the Mount Isa Inlier (Blake and Stewart, 1992).

Collectively, pre-Barramundi and Cover Sequence 1 rocks do not outcrop east of the Pilgrim Fault in the Eastern Succession.

2.2.3 Episodic intracontinental rifting – Cover Sequence 2

Following the Barramundi Orogeny and deposition of Cover Sequence 1 rocks, the Mount Isa Inlier underwent a protracted period of episodic intracontinental rifting that spanned approximately 200 Ma between ca. 1780 Ma and 1590 Ma (Betts et al., 1997a; O'Dea et al., 1997a). Polydeformed and metamorphosed rocks presently exposed in the Eastern and Western Successions represent the younger Cover Sequences 2 and 3, which were deposited during at least three major periods of intracontinental rifting and associated post-rift subsidence without significant intervening compressional events (op. cit.; Fig. 2.2). This period of intermittent extension was then terminated by the onset of compressional tectonics related to the Isan Orogeny ca. 1590 Ma (op. cit.).

2.2.3.1 The Leichhardt Rift Event (1780-1760 Ma)

Rift-related bimodal volcanism in the Eastern Succession commenced ca. 1780 Ma with the extrusion of a 1-5km thick sequence of felsic volcanic rocks and continental flood basalts comprising the Argylla Formation and Magna Lynn Metabasalt respectively (Blake and Stewart, 1992; O'Dea et al., 1997a). The Argylla Formation (1766±23 Ma, Page, 1983; Fig. 2.1 and 2.3) constitutes the lowermost stratigraphic unit in the Eastern Succession and comprises rhyolitic tuffs, lavas and ignimbrites, together with quartzite, feldspathic arenite, minor intercalated schists and basaltic metavolcanic rocks (Blake and Stewart, 1992; Giles, 2000). This lithological grouping has been interpreted as an early rift-phase sequence (Beardsmore et al., 1988; Potma and Betts, 1997). Rifting was synchronous with volcanism and sedimentation (Derrick, 1980; Loosveld, 1989a) within a shallow-water to subaerial depositional environment (Giles, 2000).

The deformed and metamorphosed correlatives of this extensional period are preserved in the Leichhardt River Fault Trough of the Western Succession (O'Dea et al., 1997a; Fig. 2.2). Bimodal volcanic rocks and conglomerates of the Bottletree Formation and feldspathic sandstones of the lower Mount Guide Quartzite represent a basal rift-sag sequence that was deposited directly upon crystalline basement within an extensive north-south trending rift-basin called the Leichhardt Rift (op. cit.). Based on stratal geometries, the Leichhardt Rift was inferred to have formed during regional east-west extension with the deposition of the

volcanosedimentary succession into a series of fault-bounded half grabens (op. cit.). The deposition of the upper Mount Guide Quartzite and extrusion of voluminous continental flood basalts (up to 6km thick) of the Eastern Creek Volcanics in the Leichhardt Rift occurred shortly after the deposition of the basal sequence during ensuing post-rift thermal subsidence (O'Dea et al., 1997a; Giles, 2000).

2.2.3.2 The Myally and Wonga Extension Events (1760-1740 Ma)

Renewed rifting in the Eastern Succession between 1760-1740 Ma is indicated by the reconstructed geometry of normal faults intruded by dolerite in the Mitakoodi Quartzite (1756±3 Ma, Page et al., 1997; Fig. 2.1 and 2.3) that indicate north-south to northeast-southwest directed extension (Passchier and Williams, 1989; Williams, 1989). Reconstructed geometries of normal faults along the eastern limb of the Duck Creek Anticline indicate a similar extension direction (northwest-southeast; Potma and Betts, 1997). During this period the Argylla Formation was conformably overlain by more mature rift-related basaltic volcanic rocks and intercalated fine grained clastic sediments of the Marabba Volcanics (Fig. 2.1 and 2.3), which are believed to be temporally equivalent to the upper Eastern Creek Volcanics (Derrick, 1980; Betts et al., 1997a; Giles, 2000: Fig. 2.2). The Marabba Volcanics were subsequently overlain by arenites, quartzites, siltstones, basaltic and rhyolitic volcanic rocks of the Lower Mitakoodi Quartzite, which in turn was unconformably overlain by basal conglomerates, upward-fining interbedded pelites and quartzites, and basalt lenses of the Upper Mitakoodi Quartzite (Betts et al., 1997a; Potma and Betts, 1997) between ca. 1760-1750 Ma (Page et al., 1997). Reconstructed stratal geometries suggest that the Marabba Volcanics and Mitakoodi Quartzite were deposited in northwest dipping tilt blocks bounded by southeast dipping normal faults (Potma and Betts, 1997).

The Mitakoodi Quartzite has been interpreted to represent the transition from rift to sag phase sedimentation (Derrick et al., 1976). Ensuing conformable to unconformable sag-phase sedimentation in an inferred stable, shallow marine environment, involved the deposition of interbedded ferruginous and calcareous siltstones, pelites and intercalated red jaspers of the Overhang Jaspilite (Donchak et al., 1983; Potma and Betts, 1997). The Overhang Jaspilite was then overlain by stromatolitic carbonates and evaporitic protoliths of the Corella Formation (Betts et al., 1997a; O'Dea et al., 1997a; Fig. 2.1), which were deposited in a shallow water, possibly intertidal setting in which sedimentation was maintained contiguous with gradual thermal subsidence (Derrick, 1980).

This period of extension is preserved in the Mary Kathleen Fold Belt west of the Pilgrim Fault, where it has been referred to as the Wonga Event (Holcombe et al., 1991; Oliver et al., 1991; Pearson et al., 1992). The geometry of high-angle, south dipping imbricate normal faults in the Argylla Formation and Ballara Quartzite (a time correlative to the Mitakoodi Quartzite; Fig. 2.2) are consistent with north-south directed extension (Passchier, 1986; Passchier and Williams, 1989) related to ductile deformation along a shallowly west dipping, mid- to upper-crustal

detachment zone in Cover Sequence 2 rocks known as the Wonga-Shinfield Zone (Pearson et al., 1987; Holcombe et al., 1991; Oliver et al., 1991). Thermal weakening of the Wonga-Shinfield Zone is believed to have been induced by syntectonic granite emplacement (the Wonga Batholith; Pearson et al., 1992) resulting in ductile deformation overprinting earlier brittle extensional faults and attenuation of metamorphic isotherms along the detachment surface (Oliver et al., 1991). Efficacious circulation of large volumes of hydrothermal fluid manifested as extensive zones of metasomatism, spanned from the early stages of extension to intrusion of syntectonic granites of the Wonga Batholith (Oliver et al., 1993). However, such metasomatism is not observed around the similarly aged Gin Creek Granite east of the Pilgrim Fault (Fig. 2.1).

During the corresponding period in the Western Succession, following the extrusion of the Eastern Creek Volcanics in the Leichhardt River Fault Trough, renewed intermittent rifting and thermal subsidence related to the Myally Rift Event (Betts et al., 1997a; O'Dea et al., 1997a) initiated the deposition of coastal and shallow marine sediments of the Myally Subgroup in northerly tilted basins (Betts et al., 1997a; O'Dea et al., 1997a). The architecture of these basins suggests that they formed by syn-sedimentary reactivation of pre-existing faults in the Leichhardt Rift during north-south extension (O'Dea et al., 1997a; Giles, 2000). Dolomitic sandstones and mudstones of the upper Myally Group, and overlying shoreline to continental shelf quartzites and carbonates of the Quilalar Formation, are considered to represent the transition from rift to sag phase during thermal subsidence ca. 1750-1740 Ma (O'Dea et al., 1997a). These are temporally equivalent to the Mitakoodi Quartzite, Overhang Jaspilite and Corella Formation in the Eastern Succession respectively (Giles, 2000; Fig. 2.2). The evidence therefore suggests that broadly north-south directed extension spanned the entire Mount Isa Inlier between ca. 1760-1740 Ma (O'Dea et al., 1997a; Giles, 2000).

2.2.3.3 The Bigie Unconformity

Deposition of the Quilalar Formation in the Western Succession was terminated by a phase of regional east-west to northwest-southeast directed extension ca. 1740 Ma, believed to be related to the Wonga Event (O'Dea et al., 1997a; Betts and Lister, 2001). This caused tilt block rotation, uplift and erosion of pre-existing tilted half grabens, and truncation of Cover Sequence 2 units by the angular Bigie Unconformity (op. cit.). Renewed rifting initiated the deposition of the basal units of Cover Sequence 3 ca. 1710 Ma, namely the Bigie Formation and the Fiery Creek Volcanics (O'Dea et al., 1997a; Page and Sweet, 1998). Erosion therefore spanned a 30 Ma period between ca. 1740 and 1710 Ma. However, geochronological constraints from within the Wonga-Shinfield Zone indicate that extension occurred between ca. 1760 to 1730 Ma (Pearson et al., 1992) and was synchronous with the deposition of the Overhang Jaspilite and the Corella Formation in the Eastern Succession and Quilalar Formation in the Western Succession (Giles, 2000; ibid.). Giles (2000) argued that extension associated with the Wonga Event must have continued until after the deposition of the Corella Formation ca. 1720 Ma if it was responsible for uplift and erosion of the latter

carbonate sequence. This argument therefore raises the possibility that reactivation of the Wonga-Shinfield Zone occurred during the initial stages of rifting associated with deposition of the basal members of Cover Sequence 3 ca. 1710 Ma.

Evidence for a period of erosion in the Eastern Succession at this time is obscured by later deformation along the contact between Cover Sequences 2 and 3. However, Giles (2000) argued, on the basis of geochronological evidence, for a hiatus in sedimentation between the late sag-phase of Cover Sequence 2 (youngest ages of ca. 1720 Ma; Page and Sun, 1998) and the early rift-associated stages of Cover Sequence 3 (oldest ages of ca. 1690 Ma; Page and Sun, 1998). Furthermore, the basal to intermediate units of the Maronan Supergroup (specifically the Gandry Dam Gneiss and Llewellyn Creek Formation respectively) contain a significant population of zircons with inherited ages between 1780 and 1720 Ma, suggesting that a major proportion of detritus was sourced from an eroding terrain of Cover Sequence 2 age (Page and Sun, 1998; Giles, 2000).

2.2.4 The Mount Isa Rift Event (1710-1655 Ma) - Cover Sequence 3

Uplift and erosion in the Western Succession was interrupted by a third period of rifting between ca. 1710 and 1660 Ma, during which, sediments of the Isa Superbasin were deposited (Betts et al., 1997a, 1998 and 1999; Betts and Lister, 2001). This 50 Ma period of extension has been referred to as the Mount Isa Rift Event and was initiated in the Leichhardt River Fault Trough via reactivation of the Leichhardt Rift (Betts and Lister, 2001). Fluvial and shallow marine clastic sediments of the Bigie, Surprise Creek and Gunpowder Creek Formations, Fiery Creek Volcanics and Moondarra Siltstone were deposited in a series of southeast dipping half grabens, which produced wedge-shaped stratal geometries consistent with northwest-southeast directed extension (Betts et al., 1997a; Betts et al., 1999; Betts and Lister, 2001). During the post-rift evolution of the system, the basin depocentre moved toward the northwest, within the Lawn Hill Platform (Betts et al., 1998; Betts and Lister, 2001), where sag-phase, deep- to shallow-water marine carbonates and turbidites of the Mount Isa and McNamara Groups were deposited ca. 1660-1600 Ma (Andrews, 1998; Krassay et al., 2000a and b; Southgate et al., 2000). This shift in basin depocentre has been attributed to asymmetric extension in the lithosphere, with syn-rift sedimentation centred over the point of maximum crustal thinning and post-rift sedimentation centred above the greatest subcrustal lithospheric thinning and thermal subsidence (Betts, et al., 1998).

The extensional history and basin architecture during the deposition of Cover Sequence 3 in the Eastern Succession is poorly constrained in comparison to the Western Succession due to the obscuring of early extensional structures by deformation related to the Isan Orogeny. This aspect forms the focus of current research (e.g. PhD study by O. Hatton, University of Tasmania). Many of the possible early extensional structures have been reactivated during complex thrusting (Betts et al., 1997a and b; Potma and Betts, 1997; Giles, 2000; O'Dea, et al., in press; O. Hatton pers. comm., 2001). Likewise, intense deformation and metamorphism

has obliterated many primary sedimentary features, especially in the high grade metamorphic rocks in the southeast of the terrain (Jaques et al., 1982), e.g. the migmatitic Gandry Dam Gneiss (Beardsmore et al., 1988). However, some evidence for northwest-southeast directed extension at this time is preserved in the eastern limb of the Snake Creek Anticline where a series of northeast striking subvertical faults along the contact between the Llewellyn Creek Formation and the Mount Norna Quartzite may represent preserved and inverted normal faults that formed during the deposition of the latter unit (Giles, 2000; O. Hatton, pers comm., 2001). The apparent north-thickening wedge-shaped geometry of the Mount Norna Quartzite is consistent with a syn-sedimentary timing for these faults (op. cit.). Reconstruction of stratal geometries indicates that Cover Sequence 3 sedimentation took place within north to northwest tilted half grabens bounded by south to southeast dipping normal faults (Giles, 2000). This suggests that the entire Mount Isa Inlier was subjected to northwest-southeast directed extension between ca. 1700-1660 Ma.

In the Eastern Succession, the early stages of rifting commenced with the deposition of the basal members of the Maronan Supergroup, namely the Fullarton River Group (Beardsmore et al., 1988) between ca. 1690-1670 Ma (Page and Sun, 1998; Giles, 2000; Fig. 2.1, 2.2 and 2.3). High grade metamorphic quartzites, biotite-sillimanite-garnet schists, quartzofeldspathic migmatitic gneiss, amphibolites and minor intercalated iron formations, comprising the Gandry Dam Gneiss, represent a poorly bedded, immature basal rift-phase sequence of sandstones, siltstones, volcaniclastic rocks, felsic and mafic volcanic rocks and minor chemogenic iron formations, which were deposited as medial fans in shallow to moderate water depths (Beardsmore et al., 1988; Newbery, 1990, 1991). The Gandry Dam Gneiss was conformably overlain by quartzofeldspathic psammites, psammopelites and pelites of the Glen Idol Schist and temporally equivalent New Hope Arkose (Beardsmore et al., 1988). Protoliths of these metamorphosed rocks have been interpreted to be continental shelf to shoreline coarse-grained volcaniclastics, sandstones and siltstones deposited under shallow to moderate water depth (op. cit.).

Evidence for late-stage rifting is manifested by cyclically interbanded micaceous psammites, psammopelites, pelites and muscovite(-biotite) schists of the Llewellyn Creek Formation and lower Mount Norna Quartzite. These are believed to represent metaturbidites deposited as a series of submarine fans in a continental shelf to deep basin environment (Glikson and Derrick, 1970; Ryburn et al., 1988; Beardsmore et al., 1988) ca. 1670-1655 Ma (Page and Sun, 1998; Giles, 2000). Mafic volcanic rocks, and fine grained calcareous and carbonaceous metasediments comprising the Toole Creek Volcanics and upper Mount Norna Quartzite of the Maronan Supergroup (Beardsmore et al., 1988), and the calcareous and evaporitic sediments of the time equivalent Staveley Formation, Agate Downs Siltstone, Marimo Slates and possibly the Tommy Creek Beds, are consistent with a transition to more stable shallow water conditions in which sedimentation kept pace with gradual thermal subsidence ca. 1660-1600 Ma (Giles, 2000).

Contacts between Cover Sequence 2 and 3 units are typically characterised by north to northwest directed thrusts (O'Dea et al., in press). However, Giles (2000) recognised that in the northeastern area of Eastern Succession, the Toole Creek Volcanics are in direct contact with the Corella Formation (Cover Sequence 2); sections of the Mount Norna Quartzite and the entire lower members of the Maronan Supergroup are absent (Giles, 2000). Similar relationships were also noted in the Marimo Domain (also known as the Marimo-Staveley Block) and the Mitakoodi Culmination (op. cit.). Giles (2000) argued that these relationships implied that thrusts were either "reactivated extensional detachments in which younger sequences were juxtaposed against older prior to thrusting", or that they were inversion structures. The latter implied that present stratigraphic relationships possibly reflect the original depositional distribution, and that progressive onlapping of sediments toward the north and northwest during thermal subsidence resulted in deposition of upper Cover Sequence 3 rocks directly onto eroded Cover Sequence 2 (op. cit.).

Time correlatives in the Western Succession (e.g. the upper Bigie Formation, Surprise Creek Formation, Fiery Creek Volcanics and Moondarra Siltstone) to the early rift sequences of the Maronan Supergroup are lithologically dissimilar, and were deposited during the Mount Isa Rift Event in the Leichhardt River Fault Trough. Derrick et al. (1977) argued that the lithological differences, coupled with evidence for turbiditic sedimentation, inferred a continental rift margin setting for the deposition of Cover Sequence 3 in the Eastern Succession, rather than an intracontinental rift regime. However, sag-phase sedimentation in the Eastern Succession was synchronous with the deposition of the Mount Isa and McNamara Groups of the Isa Superbasin in the Western Succession (Page and Sun, 1998; Giles, 2000); the latter is also interpreted to have been deposited during thermal subsidence ca. 1660-1600 Ma, after the Mount Isa Rift Event (ibid.).

The culmination of extensional tectonics throughout the Mount Isa Inlier at approximately 1590 Ma coincided with the onset of a 90 Ma period of compressional tectonics known as the Isan Orogeny (Blake and Stewart, 1992; O'Dea et al., 1997a).

2.3 STRUCTURAL EVOLUTION - THE ISAN OROGENY (1590-1500 Ma)

2.3.1 Crustal-scale architecture of the Mount Isa Inlier

The recognition of the Mount Isa Deep Seismic Transect has played a pivotal role in the current understanding of the structural architecture of the Mount Isa Inlier (Goleby et al., 1996a and b; MacCready et al., 1997, 1998). In the Eastern Succession, the earliest structures in the seismic data are characterised by moderately east dipping shear zones with a reverse sense of displacement. Examples include the Bulonga Thrust in the east and the Cloncurry Overthrust in the west (Fig. 2.4). Macroscopic folds with overturned western limbs in the hanging wall of the shears have been interpreted as thrust propagation folds (MacCready et al., 1998; O'Dea et al., 1997a, in press; Betts et al., 2000). Localisation of thrusts may have been controlled to some degree, by pre-existing extensional structures that were operational

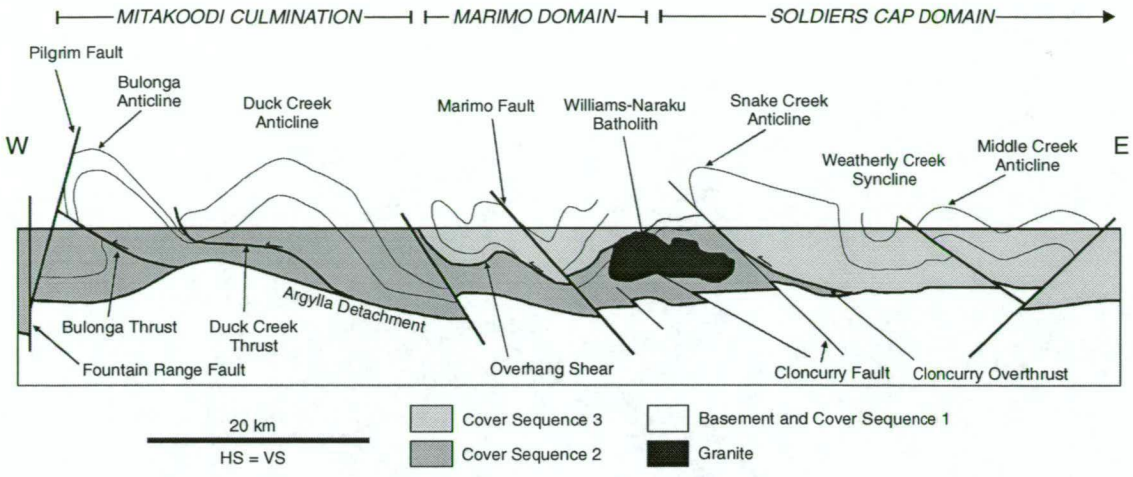

Figure 2.4 Interpretive geological cross section of the upper crust illustrating major structural elements of the Eastern Succession and distribution of Cover Sequence 2 and 3 rocks based on data from surface mapping and the Mount Isa Deep Seismic Transect (modified after MacCready et al., 1998; Giles and MacCready, 1997; Giles, 2000). The trace of the seismic transect is shown in Figure 2.1.

during deposition of Cover Sequences 2 and 3 (Betts et al., 1997a and b; O'Dea et al., 1997a; Potma and Betts, 1997; Giles, 2000). At depths between 3-9 km, the shears intersect a major mid-crustal, subhorizontal shear zone at low-angle (Fig. 2.4). This structure extends beneath the entire Eastern Succession and has been interpreted as a décollement that separates strongly deformed upper crustal Cover Sequence 2 and 3 rocks from less intensely deformed mid-crustal Cover Sequence 1 and Barramundi-aged basement rocks (MacCready et al., 1998). These relationships suggest that strain was preferentially partitioned into the upper crust during thrusting (MacCready et al., 1998). The early stages of orogeny in the Eastern Succession are therefore characteristic of a west-directed thrust and fold belt that was decoupled from the basement during "thin-skinned" tectonics (MacCready et al., 1997, 1998).

A series of steeply east dipping reverse faults displace the thrusts and propagation folds, and penetrate the middle crust to depths of 15-20 km where they offset the subhorizontal detachment by up to 2km (Fig. 2.4). The most striking of these reverse faults in the Eastern Succession, from west to east, include the Mitakoodi, Marimo and Cloncurry Faults (Giles, 2000). These structures are believed to have formed due to "thick-skinned" tectonics during the later stages of the Isan Orogeny (MacCready et al., 1998). The late stage of thick-skinned tectonics affected the entire Mount Isa Inlier, including basement, and produced the majority of structures in the Western Succession. In contrast, the earlier thin-skinned period of deformation was restricted to Cover Sequences 2 and 3 in the Eastern Succession (op. cit.).

2.3.2 Structural correlations

The Mount Isa Deep Seismic Transect highlights a two-stage evolution to the Isan Orogeny. In particular, it emphasises that the structural evolution of the Eastern Succession differed significantly from that of the Western Succession; it was more complex and protracted. Structural (and metamorphic) correlations must take this two-stage evolutionary model into

account (MacCready et al., 1998; Giles, 2000).

In consideration of this, Giles (2000) noted that the orogenic history of the Eastern Succession "...may be recorded to varying degrees in different fault-bound crustal slices," potentially leading to questionable structural correlations over large distances if based upon fold style and orientation (cf. Betts et al., 1997a and 2000). To overcome this conceivable problem, the Eastern Succession was subdivided into seven domains, each with unique, internally consistent structural and metamorphic elements (Giles, 2000; Fig. 2.5), viz.:

- Mitakoodi Culmination (Loosveld, 1989b; O'Dea et al., in press),
- Corella Domain (Donchak et al., 1983),
- Soldiers Cap Domain (Loosveld, 1989b; Rubenach and Barker, 1998),
- Maramungee Domain (host to Cannington; Newbery, 1990; Giles, 2000),
- Kuridala Domain (Loosveld, 1989b; Beardsmore, 1992; Betts et al., 2000; Giles, 2000),
- Marimo Domain (Loosveld, 1989b; Potma and Betts, 1997),
- Tommy Creek Block (Hill et al., 1992).

Structural correlations between these domains were based on temporal relationships between peak metamorphism and the development of deformation fabrics, assuming that peak metamorphic assemblages in each domain formed during a single protracted metamorphic event that affected the entire Eastern Succession (Giles, 2000). Geochronological evidence ($U\text{-}Pb_{zircon}$, e.g. Page, 1983; Page and Sun, 1998; Giles, 2000; and $^{40}Ar/^{39}Ar$, e.g. Perkins and Wyborn, 1998; Spikings 1999) from a variety of locations provides unequivocal support for this assumption (section 2.4). Three significant deformation events were recognised, with at least one to two additional events restricted to the higher metamorphic and more structurally complex Maramungee and southern Kuridala Domains. These correlations are summarised in Figure 2.6.

2.3.3 Pre-metamorphic fabrics

At least one pre-metamorphic schistose fabric that pre-dated major folding events is preserved in the higher metamorphic grade areas of the Eastern Succession, such as the Soldiers Cap, Maramungee and southern Kuridala Domains (Giles, 2000). These areas preserve more intricate structural histories compared to the lower metamorphic grade Mitakoodi, Marimo and northern Kuridala Domains. In the southern Kuridala Domain around the Pegmont deposit, a pre-metamorphic fabric is inferred by the differentiated nature of a second-generation shear fabric that is defined by the preferred alignment of peak-metamorphic biotite and sillimanite. Similarly, in the Soldiers Cap Domain, the differentiated nature of the axial planar fabric of the second-generation Snake Creek Anticline provides evidence for an earlier period of deformation prior to peak metamorphism. In the lower metamorphic grade areas to the north, the same generation axial planar differentiated fabric in the Toole Creek Syncline overprints a bedding parallel slaty cleavage (Ryburn et al., 1988; Huang, 1995; Giles, 2000).

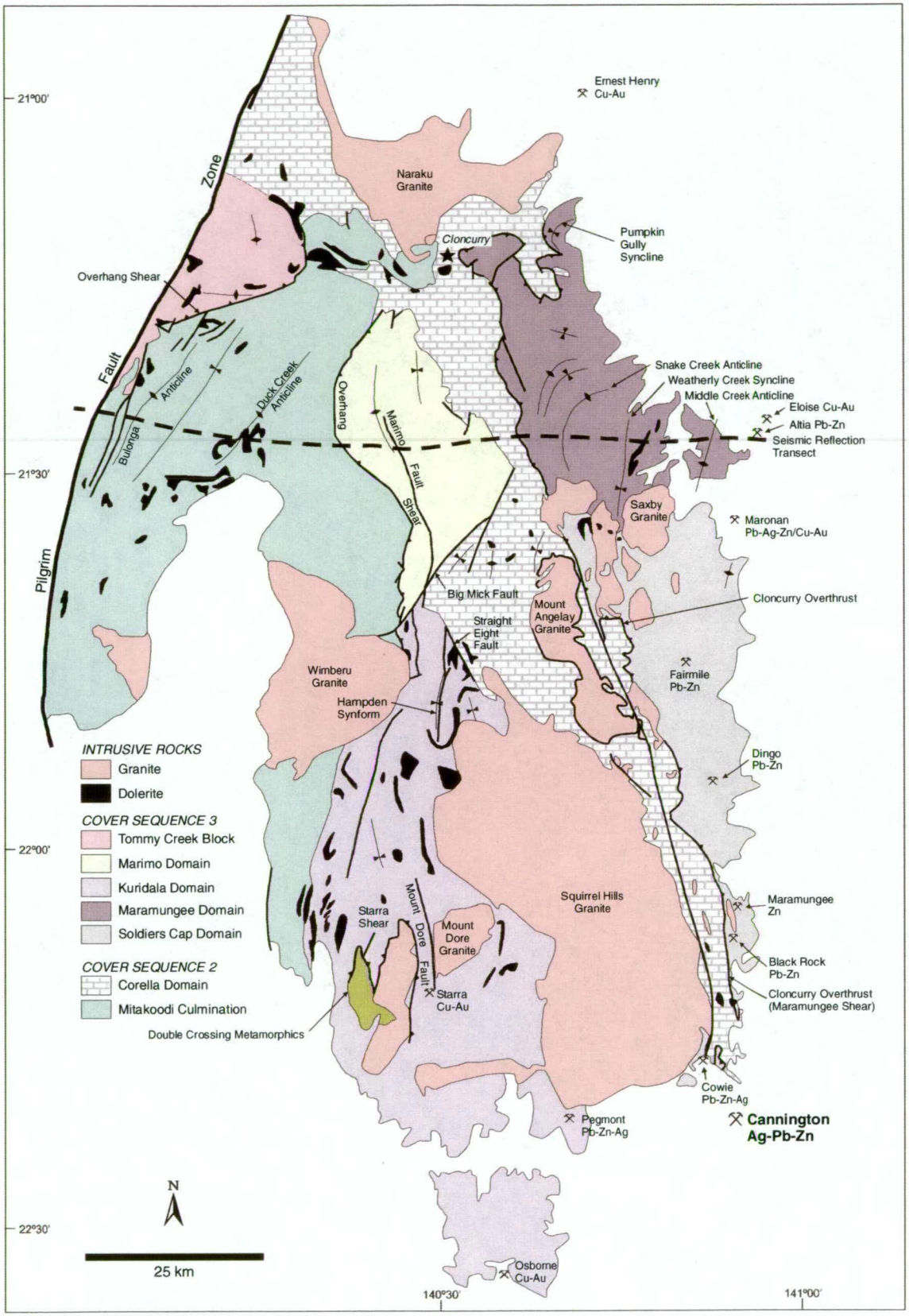

Figure 2.5 Structural domains of the Eastern Succession (modified after Giles, 2000).

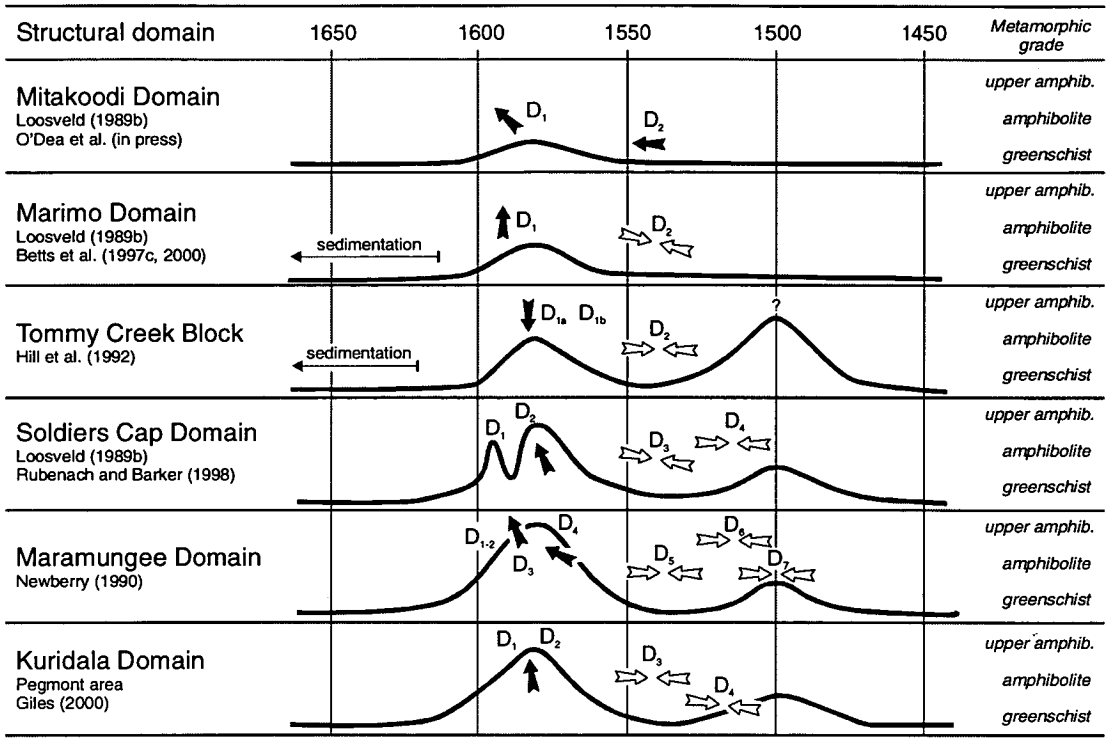

Figure 2.6 Time-temperature paths illustrating the correlations between the various structural and metamorphic events of the 1600-1500 Ma Isan Orogeny across the structural domains comprising the Eastern Succession (slightly modified after Giles, 2000). Temporal links are based on the assumption that peak metamorphism was essentially synchronous throughout the terrain and was related to a 1600-1580 Ma thermal event except for the anomalous high grade metamorphic event recognised in the Tommy Creek Block. Interpreted vergence directions during periods of "thin-skinned" thrusting and folding are indicated by the black arrows, whereas the white arrows indicate interpreted shortening directions during "thick-skinned" upright folding and faulting.

Newbery (1990) recognised seven generations of deformation in the Maramungee Domain that he termed S_1 to S_7. The dominant foliation in the area, S_4, is defined by the preferred alignment of peak metamorphic minerals. Earlier pre-metamorphic fabric forming events were largely inferred from the differentiated nature of S_3 and were considered to have developed during a period of east directed thrusting that preceded the major folding events.

Giles (2000) attributed the development of pre-metamorphic fabrics to a possible period of extensional tectonics just prior to or during the early stages of the Isan Orogeny (cf. Pearson et al., 1987; Betts et al., 1997a; Lister et al., 1997; O'Dea et al., 1997a). Evidence for this was largely based on the interpreted normal, hanging wall-to-the-south sense of displacement along the steeply east dipping Starra Shear prior to the main folding events in the central Kuridala Domain (Fig. 2.7). The normal sense of displacement, coupled with the recognition that the Starra Shear overprints the ca. 1740 Ma Gin Creek Granite (cf. Beardsmore, 1992), prompted Giles (2000) to compare the Starra Shear to the Wonga-Shinfield Zone in the Mary Kathleen Fold Belt (Pearson et al., 1987, 1992; Holcombe et al., 1991; Oliver et al., 1991;section 2.2.3.3). However, movement along the Starra Shear must have occurred, or continued after the deposition of the adjacent metasediments (Staveley Formation) ca. 1660 Ma, but before the main folding events during the very early stages of the Isan Orogeny (Giles, 2000). It is envisaged that extension was facilitated by large-scale, subhorizontal detachments that were then reactivated as thrusts during east-west compression shortly after (Betts et al., 1997a; Giles, 2000). However, the significance of early pre-metamorphic fabrics appears to

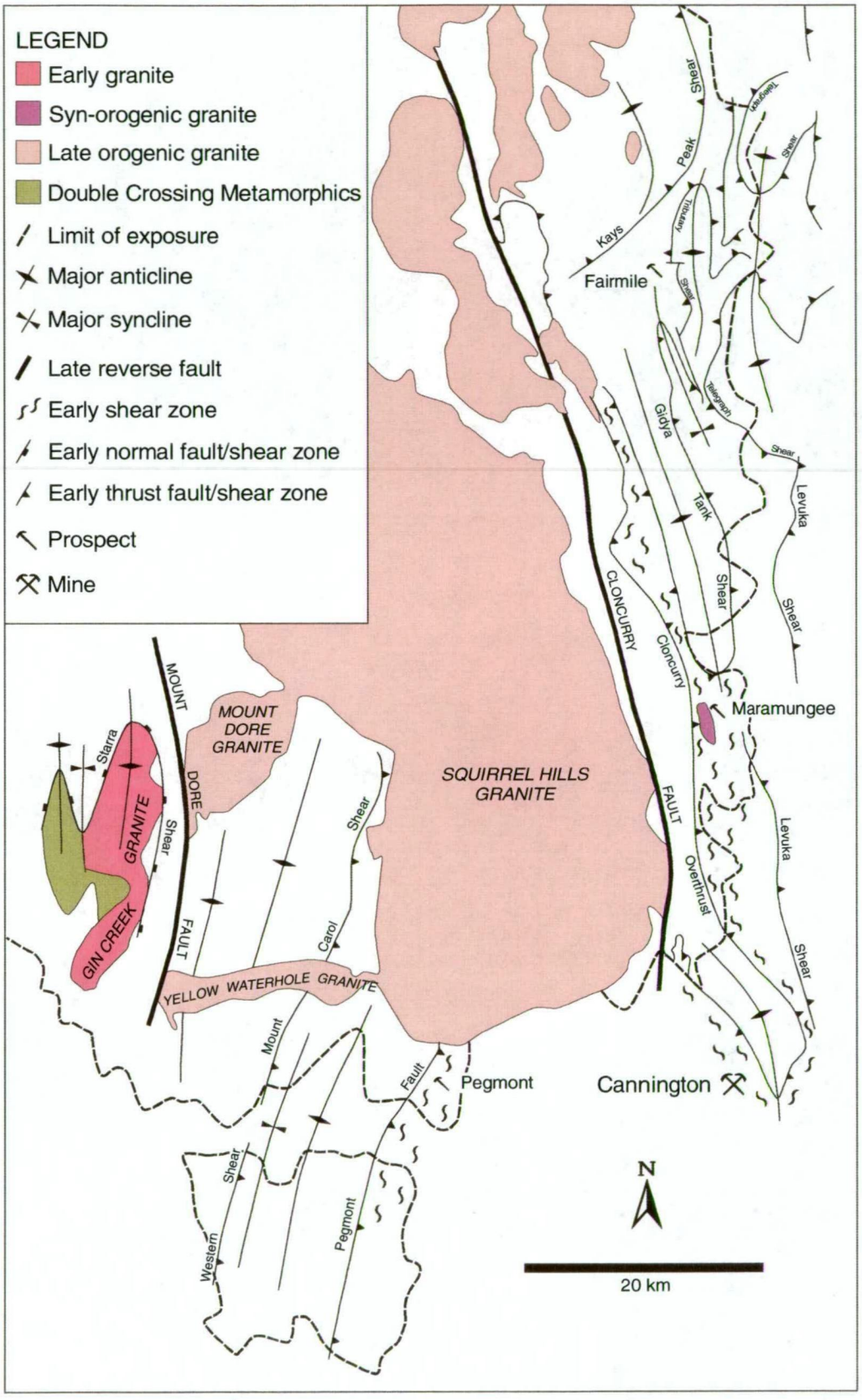

Figure 2.7 Major folds and shear zones in the southeastern region (Selwyn region) of the Eastern Succession (modified after Newbery, 1990; Giles, 2000).

be more complex.

The earliest thrusting event recognised in the Eastern Succession is preserved in the Marimo Domain (Betts et al., 1997c). Bedding parallel quartz mylonites that pre-dated peak metamorphism and subsequent major folding events, define the Marimo Shear (Betts et al., 1997c). Betts et al. (1997c) proposed that the Marimo Shear was a major subhorizontal thrust that emplaced the calcsilicates of the older Corella Formation (Cover Sequence 2) over the younger Marimo Slates (Cover Sequence 3) during the earliest compressional phase of the Isan Orogeny. They suggested that the transport direction was possibly toward the northwest, similar to the direction of the younger Overhang Shear (D_1) that, in contrast, juxtaposed younger Cover Sequence 3 rocks of the Marimo Domain over older Cover Sequence 3 rocks of the Mitakoodi Culmination (section 2.3.4 below). The temporal relationship between this compressional event and the proposed early extension is unclear (Giles, 2000) and constitutes an unresolved "pre-metamorphic paradox".

2.3.4 D_1 – northwest directed thrusting

D_1 is characterised by a period of largely northwest directed thrusting and nappe-style folding that was broadly synchronous with peak metamorphism. Higher metamorphic grade, younger Cover Sequence 3 rocks were thrust over lower metamorphic grade, older Cover Sequence 2 rocks, i.e. early shortening resulted in basin inversion (Betts et al., 1997a; Giles and MacCready, 1997; O'Dea et al., 1997a; Giles, 2000). Structures associated with D_1 were developed to varying degrees and styles in individual thrust slices throughout the terrain and were reoriented into their present positions by subsequent folding events (Betts et al., 1997a, b and c, 2000; Giles, 2000). It was during this period of early compressional, thin-skinned tectonics (MacCready et al., 1998), that the dominant axial planar, first generation slaty cleavages in the lower metamorphic grade domains, and the differentiated schistosities and later shear fabrics in the higher grade domains, were developed. These fabrics are defined by the alignment of peak metamorphic minerals.

Structures that formed in the Soldiers Cap Domain include the large-scale recumbent Snake Creek Anticline and smaller-scale Toole Creek Syncline; both exhibit a second generation axial planar differentiated fabric (Rubenach and Barker, 1998; Giles, 2000). The Snake Creek Anticline has an overturned and attenuated structurally lower western limb and a steeply to moderately east dipping axial surface. It is interpreted as a fold nappe that formed during north-northwest directed thrusting along the underlying Cloncurry Overthrust (Loosveld, 1989b; Giles, 2000). The Cloncurry Overthrust represents a detachment surface along which, the younger Soldiers Cap Group (Cover Sequence 3) was thrust over the older Corella Formation (Cover Sequence 2) and can be traced south through the Maramungee Domain (Fig. 2.7).
In the Maramungee Domain, north directed thrusting along six regional-scale, refolded, low-angle shear zones (Fig. 2.7) produced north-south trending, tight folds with steeply east dipping axial surfaces and differentiated axial planar schistosities (S_4 of Newbery, 1990; Giles,

2000). The Cloncurry Overthrust is the most prominent shear zone representing a detachment surface where the younger Fullarton River Group (Cover Sequence 3) was thrust over the older Corella/Doherty Formation (Cover Sequence 2). It is characterised by a 0.5-2 km wide shear zone (Newbery, 1990; Fig. 2.7) that contains a variety of intensely deformed rock types and elongate pods of calcsilicate breccia including areas of intense Na-Ca metasomatism (section 2.6). A prolonged history of episodic thrusting extending from prior to the main folding events through to reactivation during retrograde metamorphism, has been inferred (Newbery, 1990; Williams and Blake, 1993; de Jong and Williams, 1995; Mark, 1998; Giles, 2000). The Cloncurry Overthrust can be traced south toward Cannington using airborne magnetic interpretations (Newbery, 1990; Fig. 2.7).

In the Marimo Domain (Loosveld, 1989b; Betts et al., 1997c) and the northern area of the Kuridala Domain (Donchak et al., 1983; Lister, 1997; Betts et al., 2000) Cover Sequence 3 units were thrust over Cover Sequence 2 units during low-angle north to northwest directed thrusting along the Overhang Shear (Loosveld, 1989b; Betts et al., 1997b, 2000). Isoclinal, recumbent F_1 folds, with subhorizontal to shallowly east dipping axial surfaces and attenuated and truncated lower limbs, were developed in the hanging wall of the Overhang Shear in the Marimo and Kuridala Domains. In the footwall, however, a train of steeply plunging F_1 folds with northeast trending axial surfaces were developed in Cover Sequence 2 stratigraphy in the neighbouring Mitakoodi Culmination to the west (Betts et al., 1997b, 2000; O'Dea et al., in press; Fig. 2.8).

Structures produced during the early stages of shortening in the Tommy Creek Block consist of two generations of east-west trending, isoclinal, recumbent folds with north dipping axial surfaces (D_{1a} and D_{1b} of Hill et al., 1992) that were variably refolded by second generation structures to the north. Betts et al. (1997b) and O'Dea et al. (in press) suggested that the recumbent folds formed in response to thrusting along the Overhang Shear, and inferred that the Tommy Creek Block was possibly a member of the same thrust slice as the Marimo Domain (Fig. 2.8).

Early folds of this generation have not been recognised in the higher metamorphic grade, southern areas of the Kuridala and Maramungee Domains. Instead, a layer parallel differentiated schistosity persists (Giles, 2000).

2.3.5 D_2 – west directed thrusting

North-south to northeast-southwest trending, tight F_2 folds, with shallow plunges and steeply east dipping axial surfaces, define the main structural grain of the Eastern Succession (Betts et al., 1997a; O'Dea et al., 1997a; Giles, 2000). These structures are considered to have formed during a period of dominantly west directed thrusting (Betts et al., 1997a and b, 2000; MacCready et al., 1998; O'Dea et al., in press). The scale of F_2 folds can be enormous, e.g. the Mitakoodi Culmination is an anticlinorium approximately 50 km wide with an axial trace exposed over a strike length of some 100 km (O'Dea et al., in press; Fig. 2.1).

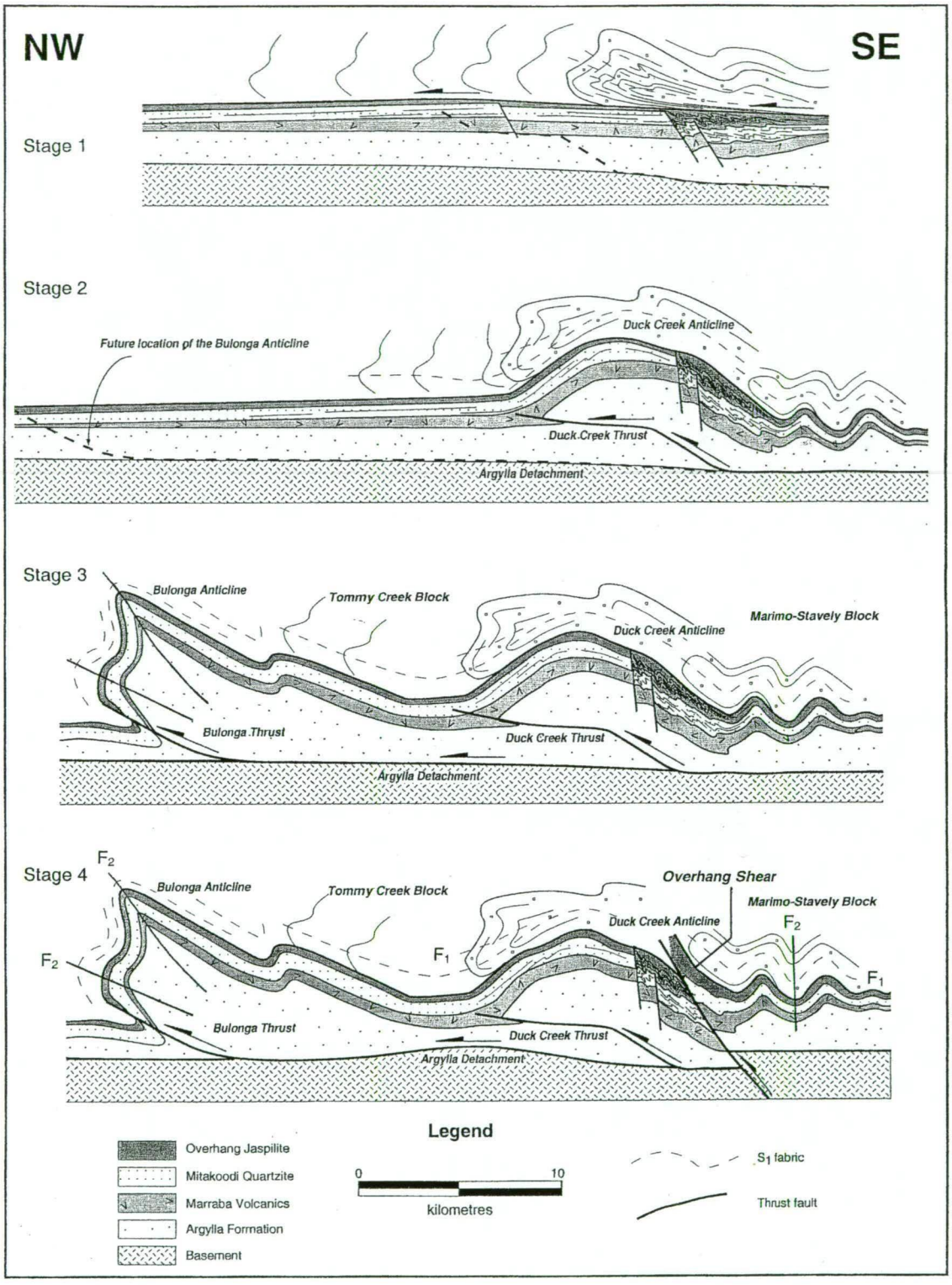

Figure 2.8 Schematic illustration of the interpreted structural evolution of the Mitakoodi Culmination and the Marimo Domain (slightly modified after Betts et al., 1997b; O'Dea et al., in press). This framework has been used as the basis for the fold and thrust model proposed for the Eastern Succession (see Betts et al., 1997b; O'Dea et al., in press). **Stage 1** – D_1 northwest directed thrusting within supracrustal rocks with the development of asymmetric isoclinal folds in the footwall and regional-scale recumbent folds in the hanging wall resulting in juxtaposition of the Marimo Slate and Overhang Jaspilite respectively. The development of F_1 folds in the footwall was influenced locally by pre-existing normal faults. **Stage 2 and 3** – D_2 west- to northwest directed thrusting resulting in decoupling from the crystalline basement along the Argylla Detachment and refolding of D_1 structures around the Duck Creek and Bulonga Anticlines. **Stage 4** – development of broad flexures along the Argylla Detachment, upright open folds in the supracrustal sequence and steeply east dipping basement piercing reverse faults during D_3.

The Mitakoodi Culmination consists of two regional-scale anticlines and an intervening syncline that have refolded earlier generation F_1 folds. From west to east, these are the Duck Creek Anticline, the Wakeful Syncline and the Bulonga Anticline (Betts et al., 1997b; O'Dea et al., in press; Fig. 2.5). These structures were interpreted to have formed during west-northwest directed thrusting along two major low-angle imbricate thrusts; the Bulonga Thrust in the west and the Duck Creek Thrust in the east (Fig. 2.5 and 2.8). From seismic reflection interpretations, these thrusts sole into the Argylla Detachment (MacCready et al., 1998; section 2.3.1). The isoclinal Bulonga Anticline, with its overturned and attenuated western limb, formed in the hanging wall of the Bulonga Thrust, whereas the more open, upright Duck Creek Anticline formed in the hanging wall of the Duck Creek Thrust (Betts et al., 1997b; O'Dea et al., in press; Fig. 2.8).

The neighbouring Marimo Domain to the east of the bounding Overhang Shear is essentially an F_2 synclinorium that consists of north-south trending, tight F_2 folds with shallow north plunging and steeply east dipping axial surfaces that have refolded rare isoclinal recumbent F_1 folds (Loosveld, 1989b; Betts et al., 1997c). These structures are analogous to the second generation folds in the northern Kuridala Domain, a region also dominated by a regional-scale F_2 synclinorium (Giles, 2000). D_2 structures in this domain are characterised by tight folds with steeply east dipping axial surfaces and overturned western limbs truncated, or attenuated, by east dipping faults, e.g. the Hampden Synform (Betts et al., 2000). The F_2 folds in both the Marimo and northern Kuridala Domains are believed to have formed during west-northwest directed thrusting along the inferred Duck Creek Thrust (Fig. 2.8). They are therefore, temporally related to the F_2 Duck Creek Anticline in the Mitakoodi Culmination (Betts et al., 1997b and c, 2000; O'Dea et al., in press). Overall, there is a transition, from east to west, from upright to overturned folding across the Marimo and northern Kuridala Domains and the Mitakoodi Culmination. The spatial geometry of these structures to second generation thrusts, coupled with kinematic relationships, are consistent with a fold-thrust complex in which deformation propagated toward the west and pre-existing first generation thrusts (e.g. Overhang Shear) and nappes were refolded by movement along younger underlying thrusts (Betts et al., 1997b and c, 2000; O'Dea, et al., in press). This framework forms the basis for the fold and thrust model proposed for the Eastern Succession (op. cit.; Fig. 2.8).

The axial traces of F_2 folds in the northern Kuridala Domain can be traced south to the west of the Pegmont deposit, where they have locally refolded an earlier layer parallel, differentiated, peak metamorphic fabric, indicating that they are at least third generation structures in this southern area (Giles, 2000). This is also supported by the differentiated nature of the axial planar schistosity. In contrast, isoclinal F_3 folds in the surrounds of the Pegmont deposit to the east display variable orientations due to refolding by north-northeast trending upright to steeply inclined F_4 folds. Removing the effects of F_4 folding indicates that these F_3 folds were originally "north to north-northeast trending with moderately west dipping axial surfaces and

overturned eastern limbs truncated by west to northwest dipping shear zones (Giles, 2000)." The observed increasing strain in the lower limbs adjacent to shear zones implies that F_3 folds formed during east-directed thrusting. This is the opposite direction to the remainder of the Eastern Succession and was attributed to an area of back-thrusting in a dominantly west vergent fold-thrust complex (Giles, 2000).

In the Soldiers Cap Domain, D_2 structures are characterised by north-south trending upright folds with steeply east dipping axial surfaces that refold earlier generation F_1 folds. Examples include the Weatherly Creek Syncline and Middle Creek Anticline that refold the earlier Snake Creek Anticline and Toole Creek Syncline (op. cit.; Fig. 2.1 and 2.5).

Hill et al. (1992) attributed refolding of earlier east-west trending F_1 recumbent folds by north-south trending upright folds in the northern area of the Tommy Creek Block to the regional D_2 event. In the fold-thrust model for the Eastern Succession (Betts et al., 1997b; O'Dea et al., in press), these folds correlate with D_2 structures in the adjacent Mitakoodi Culmination to the immediate south.

2.3.6 D_3 – wrenching and folding

D_3 deformation is characterised by a change in deformational style from thin-skinned folding and thrusting to thick-skinned folding and high-angle basement-piercing faulting during east-west compression (MacCready et al., 1998; Betts et al., 2000; Giles, 2000; O'Dea et al., in press). This transition was attributed to locking up of the thrust system, with subsequent further strain accommodated by the development of wrench tectonics (Lister et al., 1986; O'Dea et al., in press). Structures that formed vary between the structural domains of the Eastern Succession and overall, D_3 deformation did not account for a large percentage of crustal shortening; its overall significance with regard to reorienting pre-existing structures appears to have been minimal (Betts et al., 1997a; O'Dea et al., in press).

The most profound feature of D_3 is its temporal association with a significant period of mid- to upper-crustal fluid-flow that was facilitated by faulting and manifested by regional-scale sodic-calcic metasomatism of Cover Sequence 2 and 3 rocks, as well as late orogenic granitoids of the Williams Batholith. From numerous studies, this period of hydrothermal activity was temporally and genetically related to emplacement of the latter granitoids ca. 1540-1480 Ma (e.g. Williams and Blake, 1993; Phillips et al., 1994; de Jong and Williams, 1995; Baker, 1998; Baker and Laing, 1998; de Jong et al., 1998; Laing, 1998; Mark, 1998; Perkins and Wyborn, 1998; Mark and Foster, 2000; Perring et al., 2000, 2001; Pollard, 2001; Wang and Williams, 2001; and numerous others), further details of which are presented in section 2.6.

In the Mitakoodi Culmination, D_3 structures are manifested by north-south trending, open, upright folds along the overturned western limb of the Bulonga Anticline and immediately west of the Bulonga Thrust (O'Dea et al., in press). The Pilgrim Fault and other faults in the Mitakoodi Culmination are steeply east dipping reverse faults that show a component of dextral displacement. From seismic reflection interpretations, these faults offset the Argylla

Detachment by up to 3km (Betts et al., 1997b; MacCready et al., 1998; O'Dea et al., in press). Broad flexures in the Argylla Detachment are also considered to be related to D_3 deformation (op. cit.; Fig. 2.8).

In the northern Kuridala Domain, near the Hampden Synform, Betts et al. (2000) recognised two steeply dipping east-northeast and east-southeast striking S_3 cleavages that do not overprint one another. They attributed the development of these to possible perturbations in the local shortening direction during late wrenching. No associated folds were recognised, but a broad F_3 warp was inferred by fold interference patterns in the eastern limb of the Hampden Synform. The north-northeast striking, steeply east dipping Straight Eight Fault separates the older Corella Formation (Cover Sequence 2) from the younger Kuridala Formation (Cover Sequence 3; Fig. 2.5). The curvature of S_3 cleavages into parallelism with the fault provides evidence for a component of sinistral displacement (Betts et al., 2000). The same cleavages are recognised in the Marimo Domain to the north, but are poorly preserved (in contrast to their pervasive nature) in the northern Kuridala Domain (Betts et al., 1997c). In the more structurally complex southern Kuridala Domain, close to the Pegmont deposit, D_3 elements are actually fourth generation structures. They include localised north-northeast trending open, upright F_4 folds that may represent accommodation structures related to intrusion of the nearby Williams Batholith (Giles, 2000). Similar style (and orientation) F_4 folds have been recognised in the southern area of the Maramungee Domain (op. cit.)

In the Soldiers Cap and Maramungee Domains, D_3 is characterised by north to northwest trending upright, open folds and broad flexures with variable plunges, with or without a northwest to northeast striking steeply dipping axial planar crenulation cleavage (Beardsmore et al., 1988; Loosveld, 1992; Giles and MacCready, 1997; Mares, 1998). Northeast to northwest striking faults are common with brittle reactivation of pre-existing shear zones such as the Levuka Shear (Fig. 2.7) and the Cloncurry Overthrust (Newbery, 1990; Williams and Blake, 1993; de Jong and Williams, 1995; Baker, 1998; Baker and Laing, 1998; Laing, 1998). The most prominent of these faults is the north-northwest striking, steeply east dipping, basement–piercing Cloncurry Fault, which occurs in the calcsilicates of the older Corella/ Doherty Formation and in the metasediments of the younger Maronan Supergroup (Fig. 2.1). Elsewhere, it defines the contact between the latter units, where it represents brittle reactivation of the Cloncurry Overthrust. The Cloncurry Fault also overprints the undeformed Saxby Granite. A notable feature of the Cloncurry Fault is the pervasive sodic-calcic metasomatism that essentially occurs along its entire strike length for some 130 km (Williams and Blake, 1993; de Jong and Williams, 1995; section 2.6).

2.4 METAMORPHISM

Based on the relative timing between structural fabrics and peak metamorphic minerals, at least three discrete metamorphic events have been recognised in the Eastern Succession (Giles, 2000; Fig. 2.6). Evidence for the earliest of these events is restricted to metasediments of the Mount Norna Quartzite and Llewellyn Creek Formation in the area of the Snake Creek

Anticline, where it is characterised by both pre- to early D_1 and late D_1 porphyroblastic andalusite growth (Rubenach and Barker, 1998). It is possible that this apparent spatially restricted event represents an early thermal perturbation related to the second, broadly syn-D_2, high T-low P prograde(?) metamorphic event that was largely responsible for the observed regional-scale metamorphic zonation throughout the Eastern Succession (cf. Betts et al., 1997a; Rubenach and Barker, 1998; Giles, 2000; Fig. 2.9). U-Pb dating of metamorphic overgrowths on zircons from a variety of stratigraphic units spanning the Soldiers Cap and Maramungee Domains indicates that the peak of regional metamorphism occurred ca. 1580 Ma (Page, 1993; Page and Sun, 1998; Giles, 2000). This age is supported by additional $^{40}Ar/^{39}Ar$ determinations from rocks distal to the Williams-Naraku Batholith (Perkins and Wyborn, 1998; Spikings, 1999).

The regional metamorphic event is characterised by an anti-clockwise P-T-t path; the retrograde stage exhibited isobaric to slightly down pressure cooling (Loosveld, 1988, 1989a and b; Giles, 2000). Anti-clockwise P-T-t paths are typically attributed to lithospheric extension (van der Pluijm and Marshak, 1997); these are attributes of Giles's (2000) preferred, albeit slightly tentative, model for the terrain. In contrast, Loosveld (1988, 1989a) provided a convincing argument for crustal thickening and concomitant convective thinning of the mantle lithosphere to explain the anti-clockwise P-T-t metamorphic history for the region.

Jaques et al. (1982) recognised three peak metamorphic zones in the southeastern region (Selwyn region) of the Eastern Succession that ranged from upper greenschist facies in the west, through upper amphibolite facies in the east to the highest grade metamorphic facies in the southeast. Giles (2000) extended this zonation to cover the entire Eastern Succession after compiling Bureau of Mineral Resources mapping data (Derrick, 1980; Blake et al., 1983; Donchak et al., 1983; Ryburn et al., 1988); the metamorphic studies of Rubenach and Foster (1996), Rubenach and Barker (1998); and his own research at Cannington (Fig. 2.9). The lack of spatial correlation between the metamorphic isograds and granitoids suggests that regional metamorphism was unrelated to plutonism (Jaques et al., 1982; Loosveld, 1988, 1989a and c; Pollard et al., 1998; Rubenach and Barker, 1998; Giles, 2000) and this is unequivocally supported by recent geochronological studies that indicate the peak metamorphic event occurred ~50 Ma prior to intrusion of the Williams and Naraku Batholiths (Page and Sun, 1998; Perkins and Wyborn, 1998; Spikings, 1999; Giles, 2000; ibid.).

In the higher metamorphic grade areas, the peak metamorphic event is manifested by the alignment of sillimanite and biotite in differentiated schistosities and shear fabrics, porphyroblastic garnet growth and granoblastic textured feldspar in partially melted metasediments in the Maramungee and southern Kuridala Domains (Jaques et al., 1982; Mark et al., 1998; Giles, 2000). Using a combination of experimentally determined mineral equilibria and cation-exchange thermobarometry from exposed amphibolite and partially melted metapelites to the north of Cannington, Jaques et al. (1982) determined peak metamorphic conditions of ~4kbars and 600–680ºC and a geothermal gradient of 45-50°C/km^{-1}. Similar

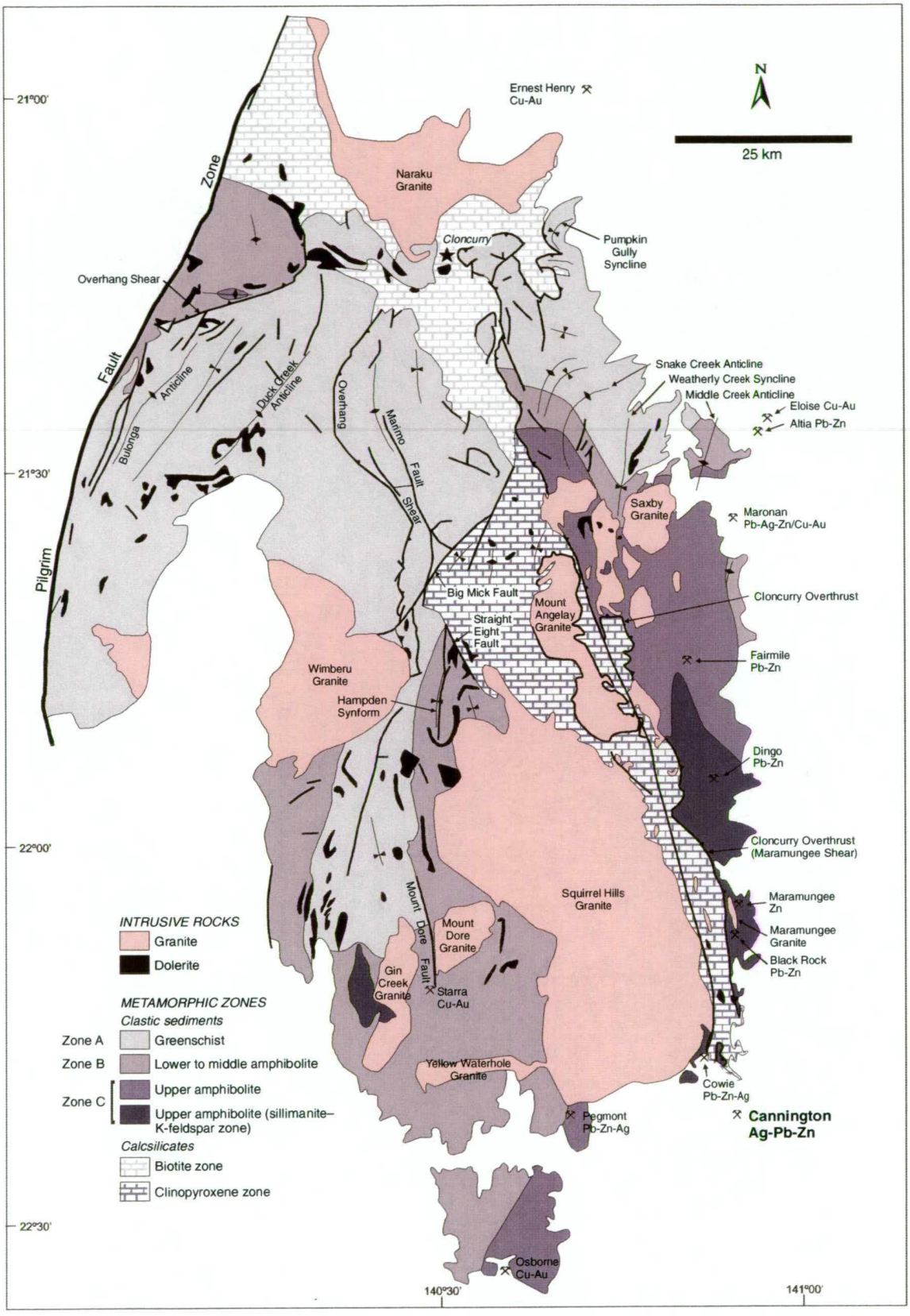

Figure 2.9 Peak metamorphic zones in the Eastern Succession compiled from Jaques et al. (1982), Rubenach and Foster (1996) and Rubenach and Barker (1998), and modified after Giles (2000). Zones A, B and C are from Jaques et al. (1982).

conditions were determined by Mark (1993), Mark et al. (1998) and Giles (2000) .

In the Soldiers Cap Domain, the transition from upper amphibolite facies in the south, to greenschist facies in the north, is marked by a restricted lower to middle amphibolite facies zone in the vicinity of the Snake Creek Anticline (Rubenach and Barker, 1998; Giles, 2000; Fig. 2.9). In the calcsilicates of the adjacent Corella Domain (Corella/Doherty Formation), this zone essentially corresponds to the transition between higher grade amphibolite facies hornblende-diopside-albite ± epidote ± quartz ± apatite ± grossularite assemblages in the south (Jaques et al., 1982), and lower grade greenschist facies quartz-calcite-albite-epidote-tremolite assemblages in the north (Derrick, 1980; Jaques et al., 1982; Ryburn et al., 1988). In the lower metamorphic grade domains to the north and west (i.e. the Marimo and northern Kuridala and Soldiers Cap Domains and the Mitakoodi Culmination), the peak metamorphic event is characterised by the alignment of muscovite and biotite in the first generation slaty cleavages, and porphyroblastic garnet and andalusite growth in metapelites (Rubenach and Foster, 1996; Rubenach and Barker, 1998; Betts et al., 1997b and c, 2000; Giles, 2000; O'Dea et al., in press).

The third metamorphic event is characterised by retrogression of sillimanite to coarse-grained muscovite in the upper amphibolite facies metasediments of the Maramungee and southern Kuridala Domains. The retrograde metamorphic event is believed to represent a transient thermal pulse coeval with intrusion of the Williams Batholith (Giles, 2000); the cognate relationship is supported by the increasing abundance of retrograde muscovite toward the batholith and the similarity in ages between granitoid intrusions (ca. 1520-1480 Ma; Page and Sun, 1998) and retrograde micas in the metasedimentary country rocks ($^{40}Ar/^{39}Ar$ ages of ca. 1510 Ma; Perkins and Wyborn, 1998; Spikings, 1999; Giles, 2000).

The Tommy Creek Block mainly consists of rocks that were metamorphosed to amphibolite facies and thrust over the greenschist facies rocks of the Mitakoodi Culmination and Corella Formation during D_1/D_2. However, peak metamorphism was characterised by local occurrences of upper amphibolite facies rocks in which sillimanite post-dated north-south trending upright F_2 folding (Loosveld, 1989a; Hill et al., 1992). This post-D_2 timing for peak metamorphism in the Tommy Creek Block is therefore enigmatic with respect to the remainder of the Eastern Succession and is believed to have been induced by radioactive heating of U-Th-K-rich felsic volcanic rocks in the Tommy Creek Beds causing local inversion of the geothermal gradient during the waning stages of the Isan Orogeny (Loosveld, 1988, 1989a; Giles, 2000). McLaren et al. (1999) attributed the peak metamorphic event adjacent to the Sybella Batholith in the Western Succession to a similar process.

2.4.1 Correlation with the Western Succession

U-Pb and Rb-Sr ages indicate that the peak metamorphic thermal event in the Western Succession occurred between 1540-1530 Ma – 1532±7 Ma (Connors and Page, 1995) and

1544±12 Ma (Page and Bell, 1986) respectively – in contrast to the older ca. 1580 Ma age in the Eastern Succession (Page, 1983; Page and Sun, 1998; Giles, 2000). This ~50 Ma disparity may indicate that regional metamorphism across the entire Mount Isa Inlier was either a single time transgressive event that migrated from east to west, or was spatially and temporally localised in different tectonostratigraphic terrains, i.e. possible multiple unrelated metamorphic events (Giles, 2000). $^{40}Ar/^{39}Ar$ geochronology from the Kalkadoon-Leichhardt Belt (Spikings, 1999) and Rb-Sr geochronology from the Western Succession (Page and Bell, 1986) provide evidence for a pre-peak metamorphic thermal event ca. 1590 Ma, supporting the latter of these possibilities (Giles, 2000).

The age of peak metamorphism in the Eastern Succession is broadly similar to that recorded in the Broken Hill Block (ca. 1600 Ma, Page and Laing, 1992; Nutman and Ehlers, 1998) and the Georgetown Inlier (ca. 1550 Ma, Black and Withnall, 1993; Black et al., 1998). The geochronological correlation between the terrains implies that heating in the Eastern Succession was possibly related to the Diamantina rather than the Isan Orogeny (Laing, 1990, 1996; Giles and MacCready, 1997; Page and Sun, 1998; Giles, 2000).

2.5 GRANITOIDS

Granites in the Eastern Succession can be divided into three groups on the basis of age. The youngest and most voluminous of these are the Williams and Naraku Batholiths, which are essentially late- to post-orogenic in age (i.e. post-D_2 and peak regional metamorphism, but pre- to post-D_3; Williams and Phillips, 1992; Pollard et al., 1998; Mark, 2001). These batholiths include the Yellow Waterhole, Squirrel Hills, Mount Dore, Wimberu, Mount Angelay, Saxby, and Naraku granites, as well as numerous smaller granitoid apophyses that intruded Cover Sequence 2 and 3 rocks between ca. 1520-1480 Ma ($U\text{-}Pb_{zircon}$ dating; Page and Sun, 1998; Fig. 2.1). These are commonly referred to as post-1540 Ma granitoids in the literature (e.g. Pollard et al., 1998; Wyborn, 1998) and are typically undeformed except for local crosscutting, late-orogenic, brittle faults, such as the Cloncurry and Mount Dore faults. Wyborn (1998) classified them as fractionated I-(granodiorite) type magmas using the nomenclature of Chappell and Stephens (1988), with compositions ranging from K-rich magnetite-hornblende-biotite diorites to high SiO_2, U, Th and K-enriched leucogranites. They are considered to have formed via partial melting of a plagioclase-stable mafic to intermediate underplate that was emplaced into the lower crust (Wyborn et al., 1988; Wyborn, 1998) ca. 2500-2200 Ma (depleted mantle Nd modal ages (T_{DM}); Page and Sun, 1998; Mark, 2001). Their Sr-depleted, Y-undepleted nature provides further support for a crustal prehistory as opposed to an active subduction environment in either a continental or island-arc setting (Wyborn et al., 1992; Wyborn, 1998).

Pollard et al. (1998) proposed an alternative classification scheme for post-1540 Ma granites of the Williams and Naraku Batholiths, dividing them into two geochemically distinct groups, both of which displayed A-type magmatic affinities, viz.:

- The subalkaline, high-K Cloncurry Supersuite consisting of mainly monzogranite and

syenogranite, e.g. the Saxby Granite, including the Wiley Igneous Complex, and parts of the Naraku Batholith (Molakoff and Capsize Granites),

- The alkaline, K-enriched Eureka Supersuite with compositions ranging from diorite to syenogranite and more mafic varieties containing hornblende and pyroxene, interpreted to represent a shoshinitic series, e.g. the Mount Angelay Igneous Complex, Squirrel Hills and Wimberu Granites.

On the basis of geochemistry both supersuites were interpreted to have formed via partial melting of the lower crust during mafic underplating. Partial melting of felsic source rocks with a dioritic to tonalitic composition were envisaged for the Cloncurry Supersuite intrusives, in contrast to variably immobile-element enriched gabbroic source rocks for the Eureka Supersuite.

Mark (2001) drew similar conclusions for the Mount Angelay Igneous Complex of the Eureka Supersuite, suggesting that mafic underplating provided the local heat source that facilitated partial melting of the crust (cf. Pollard et al., 1998). However, Mark (2001) further subdivided the intrusions into two compositional groups: i) monzodiorite-monzogranite; and ii) Na-enriched hornblende monzonite. Both types have T_{DM} ages of ca. 2200 Ma and, on the basis of chemistry and petrology, were classified as A-type granitoids (cf. Pollard et al., 1998). They were considered to have been derived from partial melting of a plagioclase-stable source; the felsic K-rich intrusions showing a broadly tonalitic to granodioritic source, whereas a possible mantle-derived gabbroic component was the suggested source for the K-rich tonalitic and mafic intrusions. The presence of these two crustal components is supported by the inverse relationship between εNd and SiO_2 and T_{DM} ages, suggesting incorporation of mantle-derived mafic material during melt generation, or partial melting of a younger mafic component in the crust (Mark, 2001).

A linear belt of slightly older, alkaline, subaluminous intrusions occur within the high strain zone adjacent to the boundary between the Maramungee and Corella Domains (i.e. the Cloncurry Overthrust) in the southeast of the Eastern Succession (Giles, 2000; Mark, 2001). In comparison to the post-1540 Ma granitoids they represent a volumetrically small, weakly foliated group that were emplaced ca. 1550 Ma (Williams and Heinemann, 1993; Page and Sun, 1998; Mark, 2001), and include the Maramungee (1548±11 Ma; Page and Sun, 1998) and Boorama Granites (1547±5 Ma; Page and Sun, 1998), and small irregular intrusive bodies in the Mount Angelay Igneous Complex (Mark, 2001; Fig. 2.1). Their spatial association with the Cloncurry Overthrust and late-syn to post-peak regional metamorphic timing possibly indicates that they are broadly associated with peak metamorphism (Mark, 2001), and that emplacement was possibly controlled by major regional-scale shear zones (Giles, 2000). These relationships indicate that the magmatic processes involved in their production differed from those of the post-1540 Ma K-rich intrusions of the Cloncurry and Eureka Supersuites, even though they are broadly similar in composition (Mark, 2001).

Compositionally, the ca. 1550 Ma intrusions are trondhjemitic, high Na-Al, Nb- and Y-depleted, and Sr-undepleted, unfractionated I-type melts with low Yb, HREE and Sc (Mark, 2001). T_{DM} ages of ca. 2200 Ma suggest that they were produced from similar aged crustal rocks as the younger K-rich post-1540 Ma intrusions (Mark, 2001). However, the Sr-undepleted, Y-depleted signature suggests they were produced via partial melting of an amphibole-bearing protolith, probably amphibolite, in which garnet was the stable phase as opposed to plagioclase (Mark, 2001). On geochemical grounds, Mark (2001) argued that the trondhjemites were produced by partial melting of the mafic underplate that provided the heat source for subsequent post-1540 Ma voluminous K-rich melts (ibid.).

Older foliated and metamorphosed granites east of the Pilgrim Fault include the Gin Creek and Jessie Granites (Fig. 2.1). Although little research has been carried out on these granites, U-Pb SHRIMP geochronology from igneous zircons indicate they were emplaced syn to post the deposition of Cover Sequence 2 rocks during the Wonga extensional event ca. 1740 Ma (Pearson et al., 1992; Page and Sun, 1998; section 2.2.3.2). The Gin Creek Granite in the central Kuridala Domain is a peraluminous, tourmaline-bearing granite that has a crystallisation age of 1741±7 Ma ($U\text{-}Pb_{zircon}$ age; Page and Sun, 1998). The Jessie Granite occurs within the Naraku Batholith ~5km west of the township of Cloncurry and is a microgranite with S-type geochemical affinities (op. cit.). It is muscovite-rich and contains abundant metasedimentary xenoliths (op. cit.). U-Pb SHRIMP analyses on igneous zircons and Sm-Nd isotopes suggest a crystallisation age of 1746±8 Ma and a T_{DM} age of ca. 2340 Ma respectively (op. cit.). The T_{DM} age is ~100 Ma older than T_{DM} ages for the ca. 1550 Ma and K-rich post-1540 Ma granitoids (op. cit., ibid.).

2.6 REGIONAL SODIC-CALCIC ALTERATION

The Eastern Succession is noted for spectacular occurrences of multistage sodic-calcic metasomatism that has affected large volumes of rock to varying degrees. Metasomatic zones are localised in a variety of brittle and ductile structures, such as contrasting brittle-ductile shear zones and faults, deformation fabrics related to regional deformation (Williams and Blake, 1993; de Jong and Williams, 1995; Oliver, 1995; Baker, 1998; Baker and Laing, 1998; Rubenach and Barker, 1998; Wang and Williams, 2001), breccia complexes and zones of brittle fracturing (Williams and Blake, 1993; de Jong and Williams, 1995; de Jong et al., 1998; Mark, 1998; Mark and Foster, 2000). The earliest sodic alteration event is preserved in metasediments at the Snake Creek Anticline in the Soldiers Cap Domain. Rubenach and Barker (1998) determined a pre- to syn-D_2 and broadly peak metamorphic timing for the event. The alteration is characterised by rare boudinaged albite veins up to 5cm thick that are subparallel to compositional layering and the S_2 foliation (op. cit.).

The later dominant post-peak metamorphic phase of sodic-calcic alteration is best exemplified in megabreccias along the Cloncurry Fault (Williams and Blake, 1993; de Jong and Williams, 1995; de Jong et al., 1998) and adjacent granitiods of the Mount Angelay Igneous Complex (Mark, 1998; Mark and Foster, 2000). Alteration zones can be up to 1km wide and collectively

span some 200km^2 in aerial extent (de Jong and Williams, 1995). Alteration occurred during the retrograde history of regional metamorphism and has been constrained to syn- to post-granitoid emplacement and pre- to post-D_3, based upon overprinting relationships between alteration assemblages, deformation fabrics and granitoid bodies (Williams and Blake, 1993; de Jong and Williams, 1995; Mark, 1998; Mark and Foster, 2000). U-Pb ages of ca. 1500 Ma from zircon overgrowths, considered to represent the time of albitisation in the 1505±5 Ma Molakoff Granite and the 1746±8 Ma Jessie Granite (Page and Sun, 1998), provide further support for the synchronicity of sodic-calcic alteration and emplacement of post-1540 Ma granitoids belonging to the Williams and Naraku Batholiths (Pollard et al., 1998).

Albite-actinolite-titanite-apatite (± quartz ± magnetite ± diopsidic clinopyroxene) is the most common alteration assemblage in sodic-calcic altered megabreccias (tens to hundreds of metres wide; Pollard, 2001) and vein systems in the Maramungee Creek and Fullarton River areas adjacent to the Cloncurry Fault (de Jong and Williams, 1995). In some areas, localised K-feldspar and quartz veins, and associated potassic alteration and silicification of clasts and wall rocks, overprint the sodic-calcic assemblages. This later stage of alteration has been interpreted to have occurred during the waning stages of metasomatism in a dominantly brittle regime, reflecting alteration at a lower temperature (de Jong and Williams, 1995; Pollard, 2001). At Maramungee Creek the distribution of alteration assemblages is strongly controlled by ductile structures such as shear zones (up to 150m wide) parallel to and typically within the limbs of F_2 folds (de Jong and Williams, 1995). In contrast, multistage sodic-calcic alteration in the Fullarton River area is dominated by pervasively albitised zones in granitoids (Mark, 1998), where fracture-localised replacement zones and multistage breccia systems display no apparent relationship to ductile structures (de Jong and Williams, 1995). Mark and Foster (2000) also recognised that sodic and sodic-calcic assemblages occurred in isolated pods of brecciated and/or altered metasediments, displaying no association with large fracture systems. Protoliths comprise a range of metamorphosed rocks (e.g. metabasites, calcsilicates, metapelites) and deformed trondhjemitic granitoids. In the breccia systems these form variably altered clasts up to tens of metres in size and at Maramungee Creek were ductilely deformed during subsequent shearing (op. cit.).

Pollard (2001) argued that the presence of rounded clasts and the polymict nature of breccias implied that they were at least partly of magmatic - hydrothermal origin and formed via upward expulsion of a magmatic vapour phase, which caused fracturing of rocks immediately above and within the roof of granitoid apophyses. This process facilitated the migration of later high temperature (>500°C and up to 650°C; Mark and Foster, 2000; Perring et al., 2000, 2001) hypersaline magmatic fluids, which interacted with the brecciated rock to produce the sodic-calcic alteration. Good evidence supporting such a process occurs in the roof of a small granitoid apophysis (the Roxmere pluton) belonging to the Saxby Granite of the Cloncurry Supersuite (Mark and Foster, 2000). Here, albite-actinolite-apatite-rich rocks capped by an actinolite-rich breccia form a carapace in the roof zone of the Roxmere pluton and are interpreted to have formed by the exsolution and release of magmatic volatiles via fluid

overpressuring (op. cit.). However, Mark and Foster (2000) argued that the low occurrence of such small Na-rich intrusive bodies and the limited amount of sodic-calcic alteration associated with them suggested that they were incapable of expelling a large enough volume of hydrothermal fluid required for regionally extensive sodic-calcic alteration, although a magmatic contribution was highly likely (cf. de Jong and Williams, 1995; Baker, 1998). An additional fluid source, such as regional metamorphic fluids, appears to be required (cf. de Jong and Williams, 1995; Mark and Foster, 2000).

2.7 BHT DEPOSITS IN THE EASTERN SUCCESSION

BHT deposits in the Eastern Succession only occur in two regional-scale ironstone horizons of the Maronan Supergroup (Laing, 1990, 1996; Beardsmore et al., 1988; Newberry, 1991; Derrick, 1993). The upper regional-scale ironstone horizon occurs in the Mount Norna Quartzite of the Soldiers Cap Group and can be further subdivided into three units (Fig. 2.10), namely; 1) the upper Mount Norna Quartzite / lower Toole Creek Volcanics; 2) the Weatherly Creek Ironstone; and 3) the Pegmont Ironstone. Ironstones within the upper Mount Norna Quartzite / lower Toole Creek Volcanics succession host the Maronan and Fairmile Pb-Zn prospects. They also host the Monakoff deposit, which is believed to be an epigenetic Cu deposit that is hosted in an ironstone formation with BHT geochemical affinities. The middle unit of the upper regional-scale horizon, the Weatherly Creek Ironstone, hosts no known mineralisation, while the lower unit, the Pegmont ironstone, is believed to host the significant Pegmont BHT deposit in stratigraphy that is laterally equivalent (Newbery, 1991). Ironstones in the Gandry Dam Gneiss of the Fullarton River Group form the lower, regional-scale BHT-favourable stratigraphic horizon. Ironstones, quartz-gahnite, Fe-Mn silicate units in this horizon host the Dingo, Maramungee, Black Rock, Cowie and Cannington BHT systems (Fig. 2.10).

Little is known about the deposits listed above and published reviews of deposit-scale features are scarce. However, Newbery (1991), Williams (1995a, 1998b) and Williams and Baker (1995) provide some information (Table 2.1). The Maronan deposit is associated with a shear zone and is hosted in an extensive package of Fe-Mn-rich rocks that include quartzite, psammopelites and garnetiferous muscovite-biotite schists and intercalated amphibolites (Williams, 1995a). Main stage hypogene sulphides include pyrite, chalcopyrite, pyrrhotite, galena, sphalerite, arsenopyrite and tetrahedrite (op. cit.).

The Fairmile Pb-Zn prospect is associated with an extensive stratiform ironstone unit chiefly comprising banded quartz-magnetite±garnet±apatite rock. Adjacent host rocks include quartzites, pelitic schists, amphibolites and marbles. Pb-Zn-Cu ore is closely associated with the ironstones (Williams and Baker, 1995).

Feldspathic psammites and quartzites and lesser amounts of andalusite- and sillimanite-bearing schists and amphibolites host the 11Mt Pegmont Pb-Zn-Ag BHT deposit (Vaughan

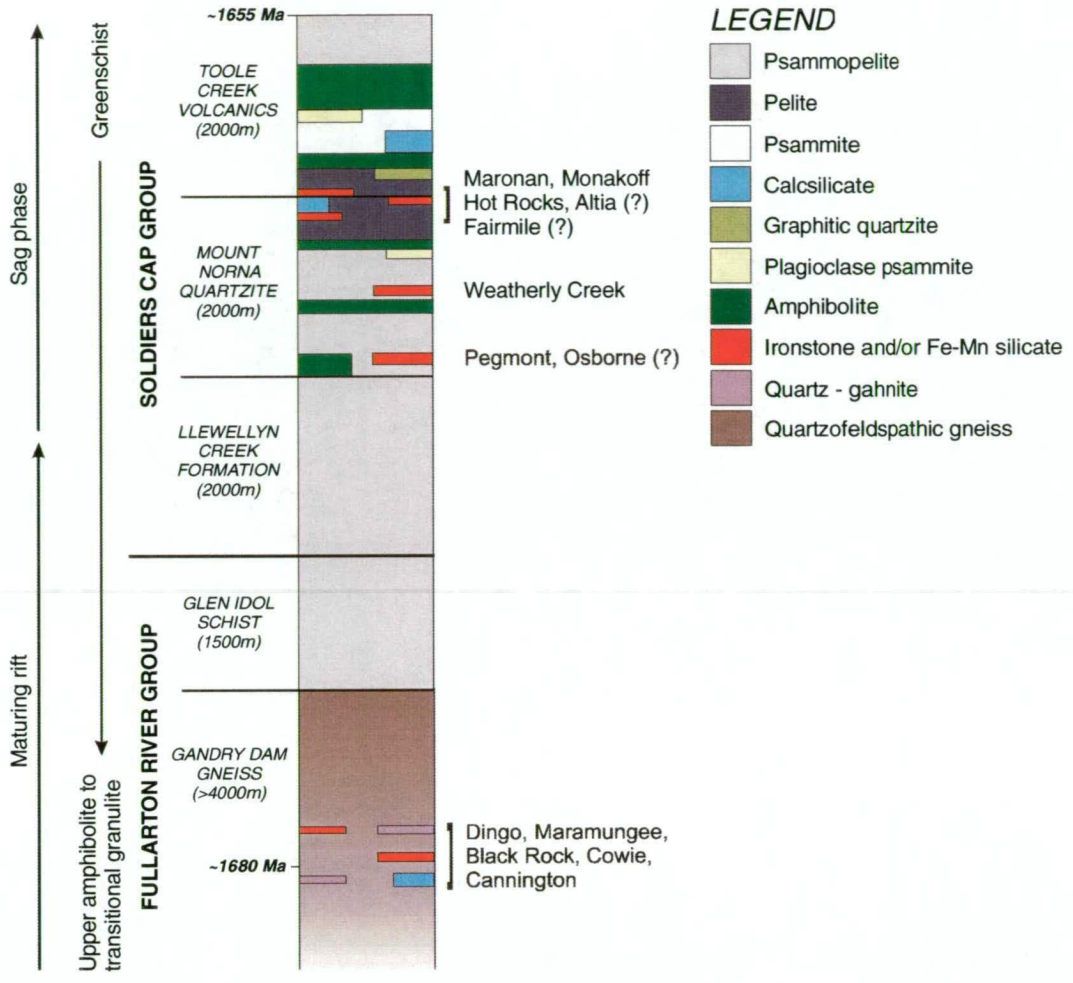

Figure 2.10 Stratigraphic positions of significant metalliferous stratiform ironstones, BIF and banded Fe-Mn silicate units with Broken Hill-type geochemical affinities in the Maronan Supergroup (modified after Laing, 1990, 1996 with additions from Beardsmore et al., 1988; Newbery, 1991; Derrick, 1993).

and Stanton, 1986; Williams, 1998b). The sulphides are restricted to a laterally zoned Ca-, Fe-, Mn- and P-rich silicate ironstone unit, which is enveloped by garnet-biotite-gahnite rocks. The highest metal grades and Pb:Zn ratios occur in the fayalite-rich core of the deposit (op. cit.). The host rocks of the Pegmont BHT deposit are regarded as the lateral equivalent of the Pegmont Ironstone (Newbery, 1991).

The third of the larger BHT deposits in the Eastern Succession is the 1.8Mt Maramungee Zn deposit. Zn-rich ores of this deposit are hosted in graphitic, Fe-Mn garnet-hedenbergite-apatite rocks and the sulphides resemble the Zn-ores at Cannington (Williams and Heinemann, 1993; Williams, 1998b).

Dingo, Black Rock and Cowie are smaller BHT prospects in the lower, regional-scale ironstone horizon in the Gandry Dam Gneiss of the Fullarton River Group. They are essentially similar deposits that are associated with Fe-Mn-silicate units hosted within gneiss, amphibolite and quartzite (Williams and Baker, 1995).

Table 2.1 Summary of Pb-Zn deposits in the Eastern Succession (compiled after Williams and Baker, 1995; Williams, 1995a, 1998b).

Locality	Morphology and scale	Host rocks Associated rocks	Resource	Status	References
Fairmile	isolated metre-scale outcrops	schist, quartzite, amphibolite, marble, ironstone		prospect	Williams & Baker (1995)
Gidya Tank	metre-scale	high-Fe amphibolite		prospect	Williams & Baker (1995)
Dingo	metre-scale (?) poorly exposed	calc-silicate amphibolite, gneiss		prospect	Williams & Baker (1995)
Maramungee	100 metre-scale	graphitic gneiss, amphibolite, calc-silicate, granite	1.4Mt @ 4.4% Zn	prospect	Williams & Baker (1995), Amoco (1976), Williams and Heinemann (1993)
Black Rock	metre-scale	gneiss, amphibolite, marble, quartzite, calc-silicate, granite		prospect	Williams & Baker (1995)
Cannington	100 metre-scale	migmatitic gneiss	45Mt @ 11.9% Pb, 4.8% Zn, 520g/t Ag	production	Skrzeczynski (1993), Chapman (1993), Roche (1994)
Maronan	100 metre-scale	psammopelite	Not published	prospect	Randell (1993), de Jong (1995)
Pegmont	100 metre-scale	gneiss	11Mt @ 8.35% Pb, 3.67% Zn, 11g/t Ag	development	Locsei (1977), Vaughan & Stanton (1986) Newbery (1990)

2.8 SUMMARY

The Eastern Succession comprises Cover Sequence 2 and 3 stratigraphy using the tectonostratigraphic framework of Blake and Stewart (1992). Cover Sequence 2 units were deposited during two periods of intracontinental extension. The first of these periods, termed the Leichhardt Rift Event, occurred between ca. 1780-1760 Ma and resulted in the extrusion of early rift-phase bimodal volcanic rocks of the Argylla Formation and Magna Lynn Metabasalt. The subsequent sag-phase was characterised by the deposition of feldspathic sediments and intercalated bimodal volcanic rocks of the Argylla Formation within a shallow-water to subaerial environment between ca 1760-1755 Ma. Based on dubious extensional structures in the Western Succession extension during this period was north-south directed.

A second period of north-south to northeast-southwest directed extension (the Myally and Wonga Events) occurred between ca. 1760-1740 Ma, possibly related to the development of a low-angle, mid- to upper-crustal detachment surface termed the Wonga-Shinfield Zone. It resulted in the deposition of more mature rift-related basaltic volcanic rocks and fine-grained clastic sediments of the Marabba Volcanics conformably over the Argylla Formation. Extension also broadly coincided with the intrusion of the Wonga Batholith and similarly aged granites east of the Pilgrim Fault, e.g. the Gin Creek and Jessie Granites. The Marabba Volcanics were subsequently overlain by transitional rift- to sag-phase sediments and bimodal volcanic rocks of the Mitakoodi Quartzite in northwest dipping half-grabens bounded by southeast dipping normal faults. Later sag-phase sedimentation involved the deposition of ferruginous and calcareous siltstones, pelites and red jaspers of the Overhang Jaspilite conformably and unconformably over the Mitakoodi Quartzite in a stable, shallow-marine environment. The Overhang Jaspilite was then overlain by stromatolitic carbonates and

evaporites of the Corella Formation under a shallow-water, possibly intertidal regime.

Cover Sequence 2 deposition was terminated by a short period of uplift and erosion between ca. 1720-1710 Ma, thought to be related to reactivation of the Wonga-Shinfield Zone possibly during the initial stages of a third period of rifting termed the Mount Isa Rift Event. This hiatus in sedimentation appears to have affected the entire Mount Isa Inlier, resulting in the development of the Bigie Unconformity in the Western Succession. The initiation of Cover Sequence 3 deposition coincided with the onset of northwest-southeast(?) directed extension that spanned a 55 Ma period from ca. 1710-1655 Ma. The initial rift-phase involved the deposition of immature siliciclastic sediments, bimodal volcanic rocks and minor chemogenic iron formations of the Gandry Dam Gneiss, Glen Idol Schist and New Hope Arkose (i.e. the Fullarton River Group) constituting the basal members of the Maronan Supergroup. It was during this early period of rifting that the metasedimentary host rocks to the Cannington Ag-Pb-Zn deposit were deposited ca. 1670 Ma. Metaturbidites comprising the lower members of the Soldiers Cap Group (e.g. the Llewellyn Creek Formation and lower Mount Norna Quartzite) were deposited as a series of submarine fans in a continental shelf to deep basin environment during ensuing late-stage rifting. Mafic volcanic rocks, calcareous and carbonaceous sediments, comprising the upper members of the Soldiers Cap Group (i.e. the upper Mount Norna Quartzite and Toole Creek Volcanics), represent a transition to shallow-water conditions indicative of the sag-phase. The termination of Cover Sequence 3 deposition coincided with the onset of compressional tectonics related to the Isan Orogeny ca. 1600-1590 Ma.

The Isan Orogeny spanned a 90 Ma period between 1590-1500 Ma. Interpretations from seismic reflection data depict a two-stage evolution for the structural architecture, commencing with an early thin-skinned period of north to northwest directed thrusting and folding related to decoupling of Cover Sequence 2 and 3 supracrustal rocks from crystalline basement along a regional-scale subhorizontal, mid-crustal shear zone (e.g. the Argylla Detachment) between ca. 1600-1550 Ma. Folds that developed presently form the main, broadly north-south trending structural grain of the Eastern Succession. Regional metamorphism (ca. 1590-1580 Ma) accompanied this early period of ductile deformation and ranged from upper greenschist facies in the north of the terrain to upper amphibolite facies in the southeast. Hotter Cover Sequence 3 units were thrust over and into cooler and older Cover Sequence 2 members along an array of imbricate, moderately east dipping listric thrusts (e.g. the Cloncurry Overthrust and Overhang Shear) that emanated from the regional-scale décollement. Based on seismic data interpretation, this early period of deformation was chiefly restricted to the Eastern Succession and had little effect on the Western Succession.

The second stage in the structural evolution of the Eastern Succession involved thick-skinned deformation (ca. 1550-1500 Ma) related to east-west compression that affected the entire Mount Isa Inlier. This event was largely responsible for the structural architecture that developed during orogeny in the Western Succession. In the Eastern Succession, this period

of transitional brittle-ductile deformation was attributed to locking up of the fold-thrust system, whereby additional strain was accommodated by wrenching. Characteristic structures that developed include steeply dipping basement-piercing faults with reverse displacements up to ~2 km, and upright north-south trending folds. Extensive sodic-calcic metasomatism and a second (retrograde) metamorphic pulse (ca. 1510 Ma) also occurred during this orogenic period and were associated with a discrete thermal perturbation consanguineous with the emplacement of voluminous granitic melts comprising the Williams and Naraku Batholiths (ca. 1520-1480 Ma).

Chapter 3

Geology and Geodynamic Evolution of the Host Succession

3.1 INTRODUCTION

This chapter documents the local geology of the Cannington mine, presenting a detailed account of the rocks comprising the host sequence and a summary of the most recent structural framework and macroscopic geometry of the deposit. The chapter is primarily concerned with establishing a sound geological framework that can then be used to underpin and augment interpretations of ore genesis in subsequent chapters. In particular, the textural and mineralogical criteria that define the structural and metamorphic history of the host succession provide a series of well constrained temporal 'base stations' that can be used as a correlative guide for the interpretation of ore paragenesis and ultimately, the evolution of the deposit and relative timing of ore formation. The objective is to correlate particular events recorded in the ores with metamorphic events recognised in the host sequence and thus the overall aims of this chapter are to:

- document all rock-types comprising the host sequence including spatial distribution and general petrology;
- present the current structural framework and macroscopic geometry of the deposit;
- summarise the metamorphic history of the host sequence;
- summarise previous U-Pb geochronology and $^{40}Ar/^{39}Ar$ thermochronology;
- determine the possible tectonostratigraphic setting in which the host sequence was deposited.

Rocks comprising the host sequence and their spatial distribution are initially described. Subsequent sections outlining the current structural and metamorphic framework, macroscopic geometry of the deposit, U-Pb geochronology and $^{40}Ar/^{39}Ar$ thermochronology draws heavily on the research of Giles (2000). The chapter is concluded by a discussion on the origins and lithotectonic setting of the host sequence.

3.1.1 Methods

Due to lack of outcrop, information on the types and distribution of host rocks has been gathered from drill holes spanning the entire deposit, as well as limited observations from underground. BHP drill logs and previous studies were also used to augment observations and interpretations. Reconciliation of the macroscopic geometry of the deposit has evolved beyond the work carried out during the period of this study due to the concurrent research of Giles (2000) that focussed on the geodynamic evolution of the Cannington host succession.

To facilitate the description of host rock types and their distribution, as well as the structural

framework and macroscopic geometry of the deposit, the Cannington area has been subdivided into two geographical domains termed the Northern and Southern Zones. The northwest striking Trepell Fault conveniently defines the boundary between these domains (Fig. 3.1). This division is ingrained in the local mine terminology and the literature, and will be adhered to here.

3.2 THE CANNINGTON HOST SUCCESSION

The host succession at Cannington is dominated by a monotonous, polydeformed succession of migmatitic quartzofeldspathic gneiss with intercalated pegmatites, amphibolites and quartzites (Walters, 1994a; Bailey, 1998; Bodon, 1998; Chapman and Williams, 1998; Mark et al., 1998; Walters and Bailey, 1998). Interbanded sillimanite-garnet schists and garnetiferous quartzites, as well as rare gahnite-bearing sillimanite-biotite-garnet schists envelop the entire deposit. The succession comprises some of the highest grade metamorphic rocks found in the Eastern Succession, and for that matter in the Mount Isa Inlier (Jaques et al., 1982; Giles, 2000).

Detailed lithostratigraphic correlation with other rock units in the Eastern Succession has been hampered by structural complexities, lack of outcrop and recognisable stratigraphic markers, and limited stratigraphic drilling outside the mine area. However, most workers agree that the host succession can be correlated with the Gandry Dam Gneiss (GDG) of the Maronan Supergroup (MSG), based on similar lithological features (Bailey, 1998; Bodon, 1998; Walters and Bailey, 1998; Chapman and Williams, 1998) and U-Pb_{zircon} ages (ca 1680 Ma; Page and Sun, 1996, 1998; Giles, 2000).

3.2.1 Quartzofeldspathic gneiss

Mark et al. (1998) recognised three types of quartzofeldspathic gneiss at Cannington, viz.

- migmatitic,
- nebulitic, and
- layered.

Migmatitic gneiss dominates the host sequence at Cannington (Figs. 3.1 and 3.2). It consists of coarse-grained, pegmatitic quartz-K-feldspar-plagioclase (± biotite, sillimanite, garnet) leucocratic segregations (<15cm thick) that are commonly bound by 1-2cm thick, schistose biotite-rich selvedges within fine- to medium-grained (1-3mm) equigranular schist. The latter comprises quartz (40-60 modal%) with subordinate biotite, K-feldspar, plagioclase, garnet and rare sillimanite (Fig. 3.3a and b; Mark, 1993; Mark et al., 1998). Sillimanite-garnet-quartz-plagioclase also occurs in the biotite–rich selvedges. Segregations typically comprise >10% of the rock volume and vary in lateral continuity over centimetre scales, forming bands and/or augen-like pods oriented subparallel to the biotite schistosity. Thicker segregations are more disconcordant than thin segregations, which have a near-concordant morphology. The schistosity wraps around the augen-like pods, suggesting that they may represent attenuated and/or boudinaged layers. Undulose extinction and deformation banding in quartz and K-feldspar, buckling of plagioclase twins, and the occurrence of cross-cutting sillimanite-quartz veins parallel to the biotite-sillimanite schistosity, indicate that segregations have been

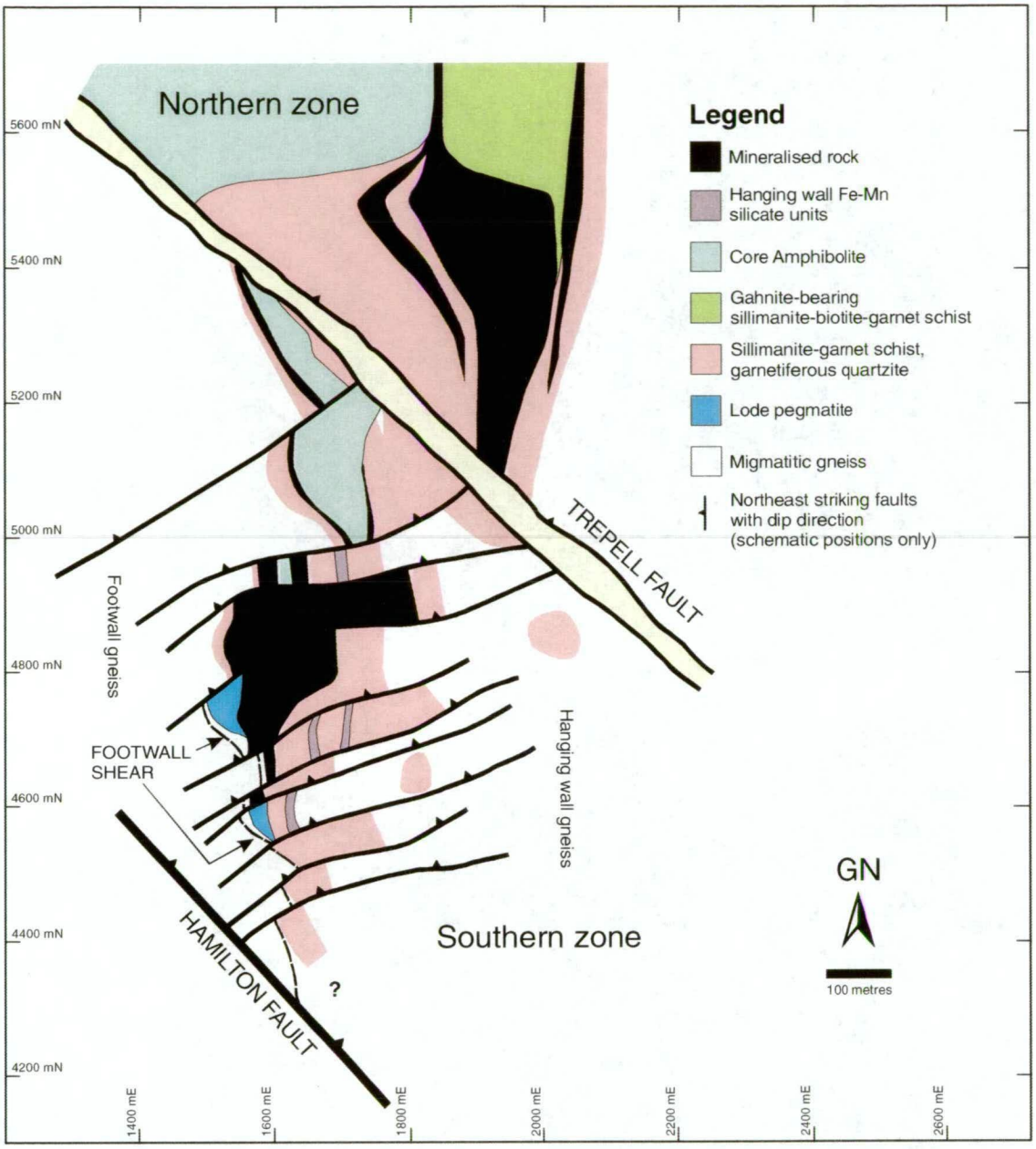

Figure 3.1 Interpreted Proterozoic geology of the Cannington deposit at the Cretaceous palaeosurface. Coordinates represent the local mine grid.

deformed (Mark, 1993; Sheehan, 1994; Mark et al., 1998; Giles, 2000).

Coherent quartzite units (1-10m thick) are commonly intercalated with the migmatitic gneiss, but individual units are difficult to trace between drill holes. Quartzites are comprised of fine- to medium-grained (1-3mm) equigranular quartz-plagioclase-K-feldspar and minor biotite, ± trace sillimanite, garnet assemblages. Leucocratic segregations are rare and when present, are oriented parallel to the schistosity in neighbouring biotite-rich bands. Biotite-sillimanite schists <2m thick also occur sporadically within the migmatitic gneiss and have a mineralogy of biotite-quartz-K-feldspar-plagioclase, garnet porphyroblasts and minor fibrolitic sillimanite (Fig. 3.3b). Rare bands grading from biotite-sillimanite-garnet to quartz-K-feldspar are also present (Walters, 1994a; Bodon, 1995, 1998; Bailey, 1998; Walters and Bailey, 1998).

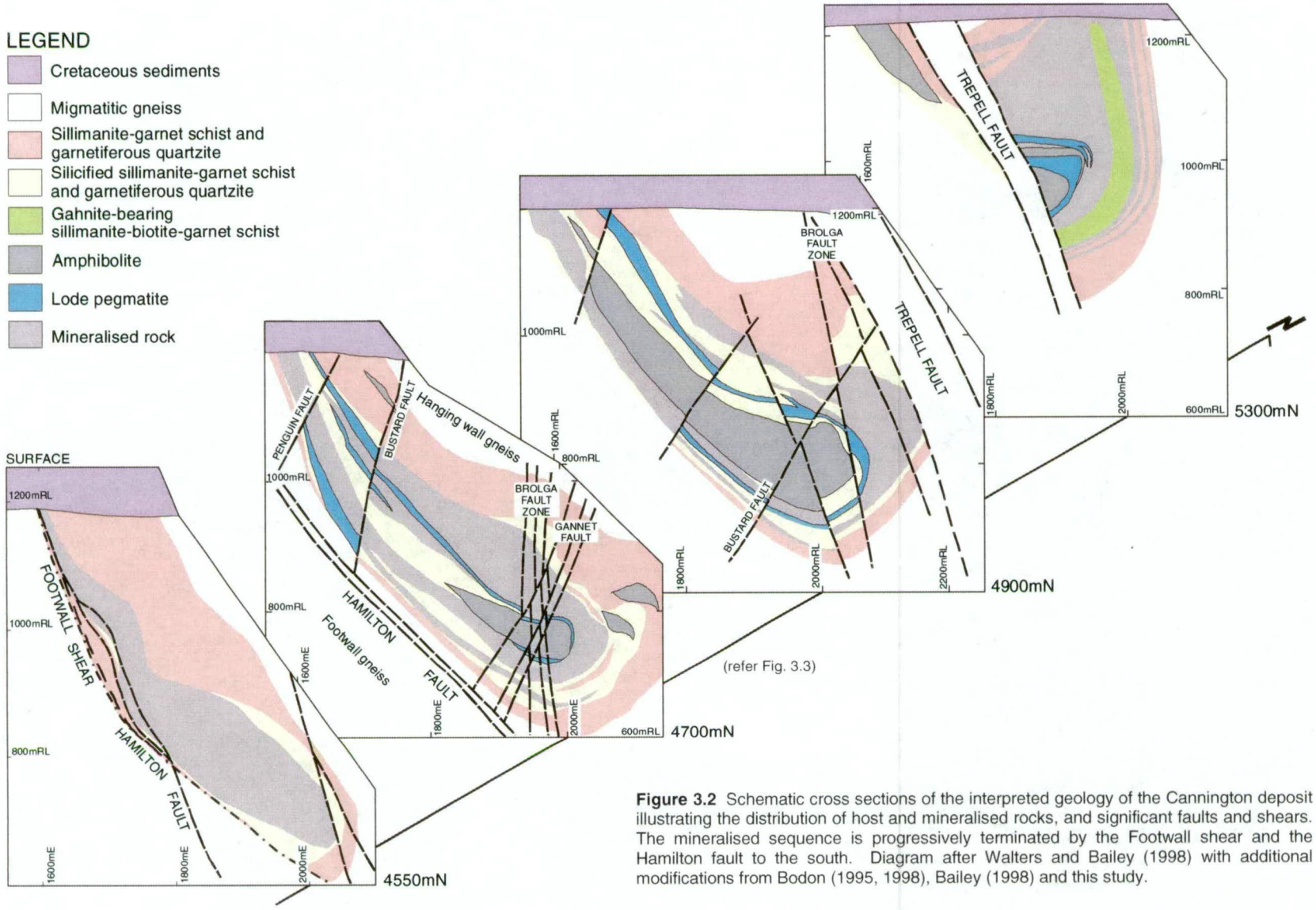

Figure 3.2 Schematic cross sections of the interpreted geology of the Cannington deposit illustrating the distribution of host and mineralised rocks, and significant faults and shears. The mineralised sequence is progressively terminated by the Footwall shear and the Hamilton fault to the south. Diagram after Walters and Bailey (1998) with additional modifications from Bodon (1995, 1998), Bailey (1998) and this study.

Nebulitic gneiss occurs in the periphery of the deposit and consists of 70-80% leucocratic segregations, 20-30% biotite-dominated mafic selvedges and rare quartzites (Mark et al., 1998). These components combine to form an irregularly banded gneiss (Fig. 3.3c). Leucocratic segregations occur as clots and/or clasts in a matrix of quartzofeldspathic material (op. cit.).

Layered gneiss is the least abundant of all gneiss types and occurs as localised, 2-12m thick layers within the migmatitic gneiss. Contacts between layered gneiss and migmatitic gneiss are abrupt. The gneiss is not routinely logged in drill core and therefore its spatial distribution is poorly constrained. However, units up to 25m thick have been logged on the 4800mN section (Chapman, 1993; Mark, 1993). Layered gneiss is characterised by a strong differential banding generally consisting of subparallel, 4-15mm thick bands of biotite-sillimanite-garnet and sillimanite-bearing garnetiferous quartzite (Fig. 3.3d). Mark et al. (1998) described the gneiss as a compositionally variable rock consisting of variable proportions of pelite, psammite, sillimanite-biotite-pelite and garnetiferous psammite bands. The mineralogy of each band-type is generally biotite-quartz-plagioclase-K-feldspar-sillimanite-garnet, the proportions of which vary between bands (Mark et al., 1998). Leucocratic segregations, typically subparallel to banding, comprise <10% of the rock volume. Segregations are more common in zones where garnetiferous quartzite and psammite are rare (op. cit.). The layered gneiss shows greater similarities to the garnet-rich rocks that envelop the orebody rather than to typical migmatitic gneiss, due to the presence of fine-grained garnetiferous quartzite bands (cf. Walters, 1994a).

3.2.2 Pegmatites

Mark (1993) and Mark et al. (1998) distinguished pegmatites from leucocratic segregations by the absence of biotite-rich selvedges and thicknesses in excess of 15cm (Fig. 3.3a, e and f). However, in reality, gradations occur particularly when there are a high proportion of segregations in the gneiss (cf. Walters, 1994a). The majority of pegmatites range from a few metres to 30m thick and grade into larger discordant leucocratic segregations on a deposit-scale (Mark et al., 1998). On a mine scale they are variably folded and boudinaged but are generally concordant with the prevailing schistosity in the area (cf. Walters, 1994a; Giles, 2000). Less commonly, some pegmatites are clearly discordant to schistosity and compositional banding (Fig. 3.3g and h). On a hand specimen scale, deformation fabrics are generally absent (cf. Walters, 1994a; Giles, 2000).

Pegmatites are mineralogically similar to leucocratic segregations; two end-member compositions have been recognised (Mark et al., 1998), namely: i) a more abundant K-feldspar-rich end-member comprised of K-feldspar-quartz, and rare plagioclase, biotite, garnet, muscovite and apatite; and ii) a plagioclase-rich end-member comprised of plagioclase-quartz-K-feldspar, rare biotite and garnet. Rare tourmaline-bearing pegmatites also occur in the migmatitic gneiss adjacent to the orebody (Fig. 3.4a). Grain sizes vary from 1cm to >5cm and in some instances, coarse books of biotite, and less commonly, muscovite are up to 3cm thick. Graphic textured intergrowths of quartz-K-feldspar are present in some examples (Fig. 3.3e). Incipient, texturally preserving sericite alteration of feldspars is ubiquitous, whereas hematite

Figure 3.3 Quartzofeldspathic gneiss and pegmatites.

Gneiss

A. Biotite-rich migmatitic gneiss with intercalated pegmatite zones and abundant leucocratic segregations. Garnet porphyroblasts up 1cm are sparsely disseminated throughout the biotite-schist units (CUD050, ~95.0m).

B. Close-up view of migmatitic gneiss with abundant leucocratic segregations. Not all segregations have biotite-rich selvedges in this sample. Garnet porphyroblasts up to 1cm occur in the most biotite-rich zones (CUD051, 112.8m).

C. Variety of nebulitic gneiss with abundant leucocratic material and minor biotite-rich selvedges (CAD159, 109.6m).

D. Banded gneiss comprised dominantly of psammitic (right) and more biotite-rich bands with minor leucocratic segregations. Fibrolitic sillimanite porphyroblasts have been stretched parallel to the schistosity (left; CAD048, 301.0m).

Pegmatite

E. Typical example of pegmatite with poorly developed graphic texture (CUD042, 103.1m).

F. Typical pegmatite with minor stringers of sillimanite-quartz (± biotite, garnet). The stringer material commonly forms in gradational zones adjacent to wall rock, consistent with partial assimilation of the latter during pegmatite emplacement (CUD043, 20.9m).

G. Post-deformation pegmatite crosscutting the strong foliation in biotite-schist at high angle (CAD155, 620.3m).

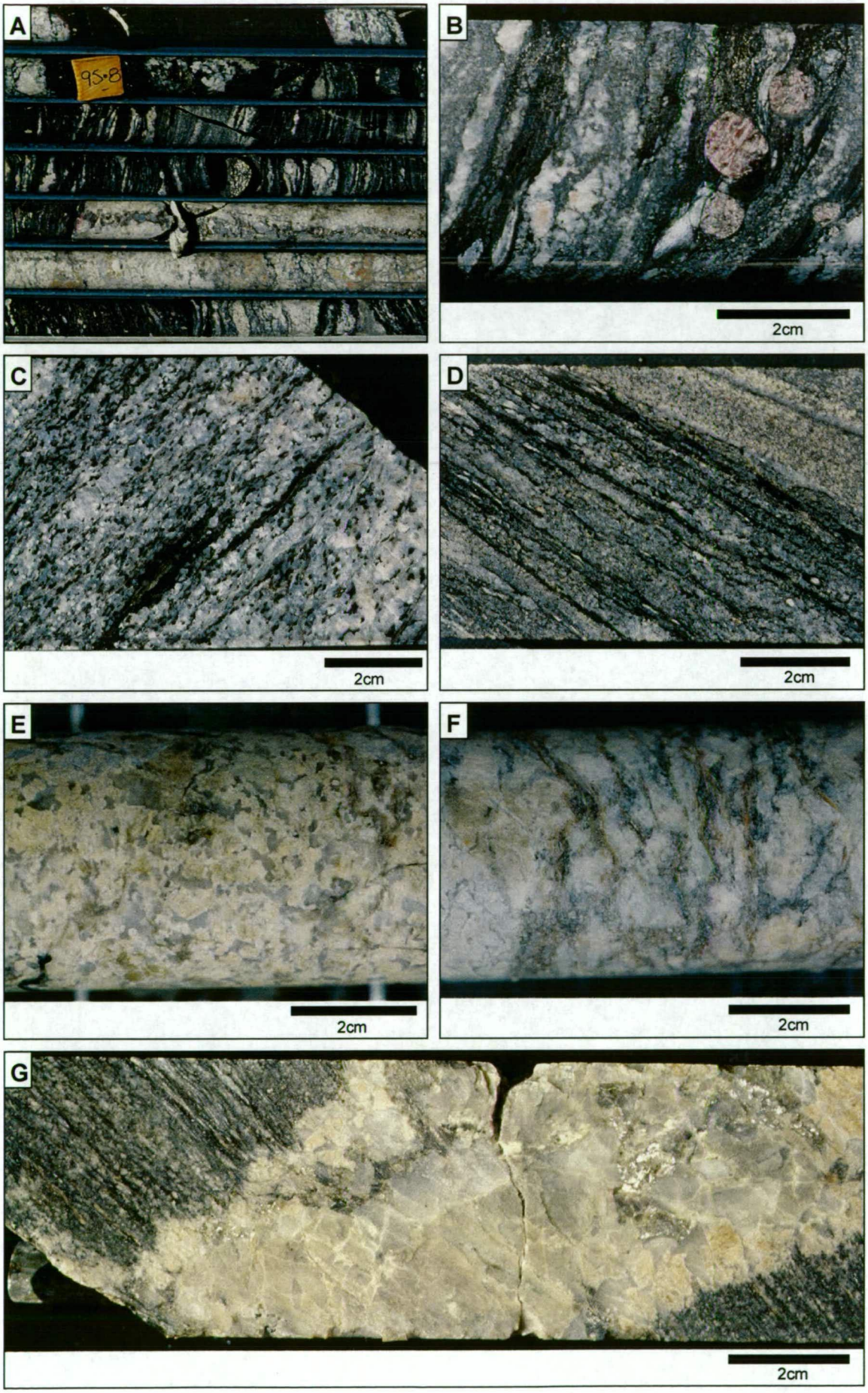
A
95-8
B
2cm
C
2cm
D
2cm
E
2cm
F
2cm
G
2cm

dusting of feldspars (red-orange feldspar) is more restricted.

Sillimanite-quartz (±biotite, garnet) stringers and clots, resembling partially assimilated wall rock, occur as nebulous zones in some pegmatites (Fig. 3.3f). Most pegmatite contacts have been obscured by intense alteration (garnet and/or late chlorite) and/or post-emplacement shearing/faulting. Where contacts have been preserved, they range from sharp (Fig. 3.3a) to obvious gradational, assimilated margins (Fig. 3.3a, bottom field of view).

3.2.2.1 Lode pegmatites

Pegmatites are also found within the orebody and are locally referred to as "lode" pegmatites (Walters, 1994a; Bailey, 1998; Bodon, 1998; Walters and Bailey, 1998). They are mineralogically and texturally similar to the pegmatites in the gneiss. However, the lode pegmatites typically contain nebulous clasts of sulphides and/or gneiss and garnetiferous host rocks. In some examples, green plumbian K-feldspar (amazonite) is diagnostic (Fig. 3.4b,c and d). In some drill hole intersections it is difficult to differentiate between large mineralised clasts and genuine interbanding of lode pegmatite and sulphide ore (Walters, 1994a). They have been used as local 'stratigraphic' markers due to their apparent localisation along contacts between various ore types, but in reality they transgress ore-type boundaries at low angle. Walters (1994a) recognised three major lode pegmatite bodies within the deposit, based on spatial distribution and broad associations with particular ore lode types, namely:

- lode pegmatites within the hedenbergite-fluorite-magnetite-rich Zn ore in the structural hanging wall, termed the Hanging wall Lode Pegmatite Zone (HLP);
- those spatially associated with high grade, olivine-pyroxenoid-magnetite-fluorite Pb-Ag ore in the structural footwall, called the Footwall Lode Pegmatite (FLP); and
- those mainly developed within the Core Amphibolite, called the Brolga Lode Pegmatite Zone (BLP).

The HLP is located close to the contact between hedenbergite-rich Zn ore and olivine-pyroxenoid-rich Pb-Ag ore and is up to 30m thick. It can be traced from subcrop in the southern area of the deposit for up to ~550m down-dip, and extends along strike for some 1000m where it gradually thins in the vicinity of the 5500mN section (Fig. 3.2). The southern extension of the HLP is terminated by the Footwall Shear and Hamilton Fault between the 4550mN and 4600mN sections. Clasts of sillimanite-garnet schist, garnetiferous quartzite, quartzite and hedenbergite-rich Zn ore sporadically occur within the pegmatite, as do localised concentrations of amazonite. The pegmatite also contains irregular sillimanite-garnet schist and quartzite interbands, especially just below subcrop, where weakly mineralised and silicified sillimanite-garnet schists and quartzites predominate (Walters, 1994a). Minor lenses of *in situ* lode pegmatite occur within sillimanite-garnet schist and minor quartzites higher in the mineralised hanging wall.

The FLP is significantly smaller (up to 15m thick) and not as laterally continuous as the HLP. It can be traced from the 4600mN section for ~500m along strike (Fig. 3.2). Limited intersections on the 5400mN section in the Northern Zone may suggest it continues for the entire ~1.2km

Figure 3.4 Tourmaline-bearing pegmatite and lode pegmatites.

A. Rare pegmatite containing large fractured crystals (up to 4cm) of tourmaline (CAD153, 354.2m).

B. Distinctly green amazonite in a lode pegmatite from the Brolga Lode Pegmatite (CAD004, 267.3m).

C. Typical example of amazonite-bearing garnetiferous lode pegmatite (CAD058, 285.2).

D. Sharp, intrusive contact between a lode pegmatite and banded ore. A garnet-rich zone is typical along the contacts (CAD029, 390.3m).

E. Contact between high grade olivine-magnetite-fluorite Pb-Ag ore and a lode pegmatite illustrating typical mineralogical zonation features. The ore contains abundant garnet-biotite along the contact, whereas the pegmatite has a green-grey K-feldspar zone that passes into a garnet zone. Garnets in the garnet zone have partially replaced K-feldspar grains. Late chlorite alteration overprints the garnet-biotite zone adjacent to the high grade ore. A tectonic banding is evident in the ore (CAD154, 489.1m).


A
3cm


B
N. 12004-2
cm


C


D
40
50


E
3cm

strike length of the deposit. To the south it is terminated by the Footwall Shear. On the 4600mN section it extends down-dip for ~400m and transgresses the footwall ore lodes. From the 4650mN section to the 4875mN section it occurs along the contact between the orebody and sillimanite-garnet schists. Beyond this it appears to move back into the mineralised rocks, where it occurs as a series of thin pegmatite lenses in the order of 1-2m thick. The FLP is characterised by abundant clasts of sulphides and host rock, and contains localised amazonite-bearing zones.

The BLP is up to 35m thick on the 5300mN section in the Northern Zone of the deposit (Fig. 3.2). However, in general the thickest intersections occur in the Southern Zone adjacent to a late subvertical fault zone termed the Brolga Fault zone. The strike extent of the pegmatite is unclear due to limited drilling, but appears to extend from ~4775mN to 5600mN as a series of lenses. Similarly the down-dip dimensions are poorly constrained; estimated at a maximum of 450m. Clasts of sulphides and sillimanite-garnet schist are conspicuously absent and only minor zones of amazonite occur in the Northern Zone of the deposit. Unlike the other lode pegmatites it is plagioclase-rich rather than K-feldspar-rich (Walters, 1994a).

Contact relationships between lode pegmatite and mineralised rock in the orebody range from gradational over several centimetres (Fig. 3.4d) to sharp over millimetre to centimetre scales (Fig. 3.4e and 3.5a). However, contacts are commonly obscured by faulting/shearing and alteration. Contacts are characterised by a 5cm to >2m wide zone of texturally preserving green to grey K-feldspar (± sulphide, gahnite) that progressively grades into a garnet (±quartz) assemblage (Fig. 3.4e). In some instances, either assemblage may be absent, e.g. green-grey K-feldspar only (Fig. 3.5a), or garnet-quartz only (Fig. 3.4d and 3.5c). Some pegmatites have been entirely replaced by garnet-quartz, although the pegmatitic texture has been preserved. Overprinting amphibole replacement of garnet is also common and in instances extends into adjacent ores. Sulphide veinlets and minor hedenbergite may also be present. Late stage quartz-chlorite (± sulphide) is commonly associated with zones of fracturing, brecciation and faulting in lode pegmatites and overprints earlier assemblages (Fig. 3.5c).

On a large scale, an exceptional, although complex, example of a lode pegmatite occurs in one of the early underground developments. Lobate apophyses in the order of 1-3m engulfed blocks of ore up to 50cm in diameter. Strong, texturally destructive to texturally preserving, amphibole-garnet-sulphide assemblages occur along the contacts of the lode pegmatite for up to 1-2m, and within recrystallised sulphide ore clasts. The adjacent ore contains abundant amphibole for up to 1m from the contact and beyond this, patches persists for ~5m to the limits of the underground exposure. Megacrysts of amphibole ranging from 5-12cm form coarse aggregates in the lode pegmatite and the adjacent host sulphide ore.

In drill core, sulphide clasts within lode pegmatites (except the BLP) typically have rounded morphologies with vaguely defined margins and range in size from 1cm to 20cm. In certain examples, clasts may be sub-angular (Fig. 3.5b). The abundance of clasts in individual drill

hole intersections is variable and they are generally dominated by the adjacent ore type. However, the FLP is enigmatic in some drill hole intersections in that it contains a large variety of clast types that do no match the host rocks. Gangue minerals within the clasts are commonly coarse-grained, up to 1cm. Gahnite may be present, as well as garnet and amphibole. In instances, ore clasts have a pegmatitic texture in which gangue minerals are intimately intergrown with feldspar and quartz. Sulphides occur both as fine inclusions in feldspars (including amazonite), and as coarse blebs to discontinuous veinlets that resemble small-scale piercement structures indicative of local remobilisation.

A distinctive gahnite-bearing sillimanite-biotite-garnet schist unit (refer below), located between ore lenses in the Northern Zone, also contains amazonite in *in situ* partial melt segregations (Fig. 3.5d). Biotite-sillimanite selvedges occur adjacent to and within the segregations. Small amazonite-bearing lode pegmatites up to 1m thick are also present and may contain patches of biotite-rich gahnite-bearing schist.

3.2.3 Garnetiferous rocks

Migmatitic gneiss grades into a sequence of K-feldspar-rich garnetiferous rocks that display a clear spatial association with the deposit, entirely enveloping it. Regional drilling throughout the Cannington area has failed to intersect similar rocks, suggesting them to be a rare component of the host succession (Walters, 1994a). Garnetiferous rocks have been collectively referred to as 'SHMU' by BHP exploration and mine geologists based on the BHP logging code of 'ScHist MUscovite' (cf. Walters, 1994a; Bodon, 1995) even though garnetiferous quartzite forms an appreciable proportion of the succession. Overall, SHMU comprises three end-member lithologies on the basis of mineralogy, texture and spatial distribution, namely:

- sillimanite-garnet schist and garnetiferous quartzite;
- variably silicified versions of the above, dominated by quartzites and sillimanite-biotite-garnet schist; and
- gahnite-bearing sillimanite-biotite-garnet schist.

Pink, fine-grained (<1 – 2mm across) disseminated garnet porphyroblasts are common to all types. They constitute up to ~60 modal% of the rock (e.g. garnetiferous quartzites) and have resulted in a distinct spotted texture. The leucocratic segregations and zones of orange-red feldspars that characterise migmatitic gneiss are uncommon (cf. Walters, 1994a), and K-feldspars typically have a distinct grey colour. Partial retrogression of fibrolitic sillimanite porphyroblasts to muscovite and weak, incipient sericitisation of K-feldspar has occurred.

3.2.3.1 Sillimanite-garnet schists and garnetiferous quartzites

Interbanded (<0.01 to 10m thick) sillimanite-garnet (-biotite-muscovite) schists and garnetiferous quartzites envelop the entire deposit (Fig. 3.5e and f). In the structural hanging wall of the Southern Zone they form a sequence up to 250m thick on sections north of 4650mN (Fig. 3.2). BHP geologists have informally referred to this enveloping sequence as the 'SHMU halo' (cf.

Figure 3.5 Lode pegmatites and garnet-rich host rocks. All garnet-rich rocks display a strong foliation defined by the alignment of biotite and fibrolitic sillimanite. The dominant foliation is typically a differentiated fabric that occurs at low-angle to compositional banding (see section 3.3.3 and Table 3.1 for further details).

Lode pegmatite

A. Contact between hedenbergite-rich Zn ore and lode pegmatite from the Hanging wall Lode Pegmatite Zone. In this example only a small green-grey K-feldspar zone in the lode pegmatite is developed along the contact (CAD043, 161.7m).

B. Weakly mineralised hedenbergite-garnet clasts in pegmatite have diffuse margins (CAD043, 184.8m).

C. Garnet-quartz in a lode pegmatite overprinted by late chlorite veinlets and incipient chlorite alteration of K-feldspar and garnet. However, the pegmatitic texture has been preserved (CAD164, 469.3m).

D. *In situ* partial melt containing abundant amazonite in gahnite-bearing biotite-garnet-sillimanite schist (CAD037, 494.6m).

Garnet-rich rocks

E. Typical garnetiferous quartzite (left) and sillimanite-garnet schist (right) that envelops the orebody. Sparse fibrolitic sillimanite porphyroblasts are disseminated in the garnetiferous quartzite, whereas they are very common in the schists and define the foliation in conjunction with biotite. The absence of leucocratic segregations in these rocks is an intrinsic feature of the host succession (CAD009, 108.2m).

F. Example of graded garnetiferous quartzite band (centre right). Garnet abundance progressively decreases in this band from right to left. Such a texture can be interpreted as a relic primary sedimentary feature suggesting that the garnetiferous rocks are a sequence of metasediments (CAD056, 466.2m).

G. Example of partially silicified, K-feldspar-rich sillimanite-garnet-biotite-schist found within the orebody in the Southern Zone. Sillimanite porphyroblasts have been partially replaced by quartz (CAD028, 380.6m).

H. Metapsammitic K-feldspar-rich rock found within the orebody of the Southern Zone. The piece of drill core on the right hand side of the photographs contains a quartz-gahnite vein parallel to the foliation and compositional banding. Light-brown coloured secondary sphalerite-sericite symplectite replaces gahnite along grain boundaries and fractures (CUD033, 17.0m).

Abbreviations: gh–gahnite, se–sericite, sp–sphalerite.

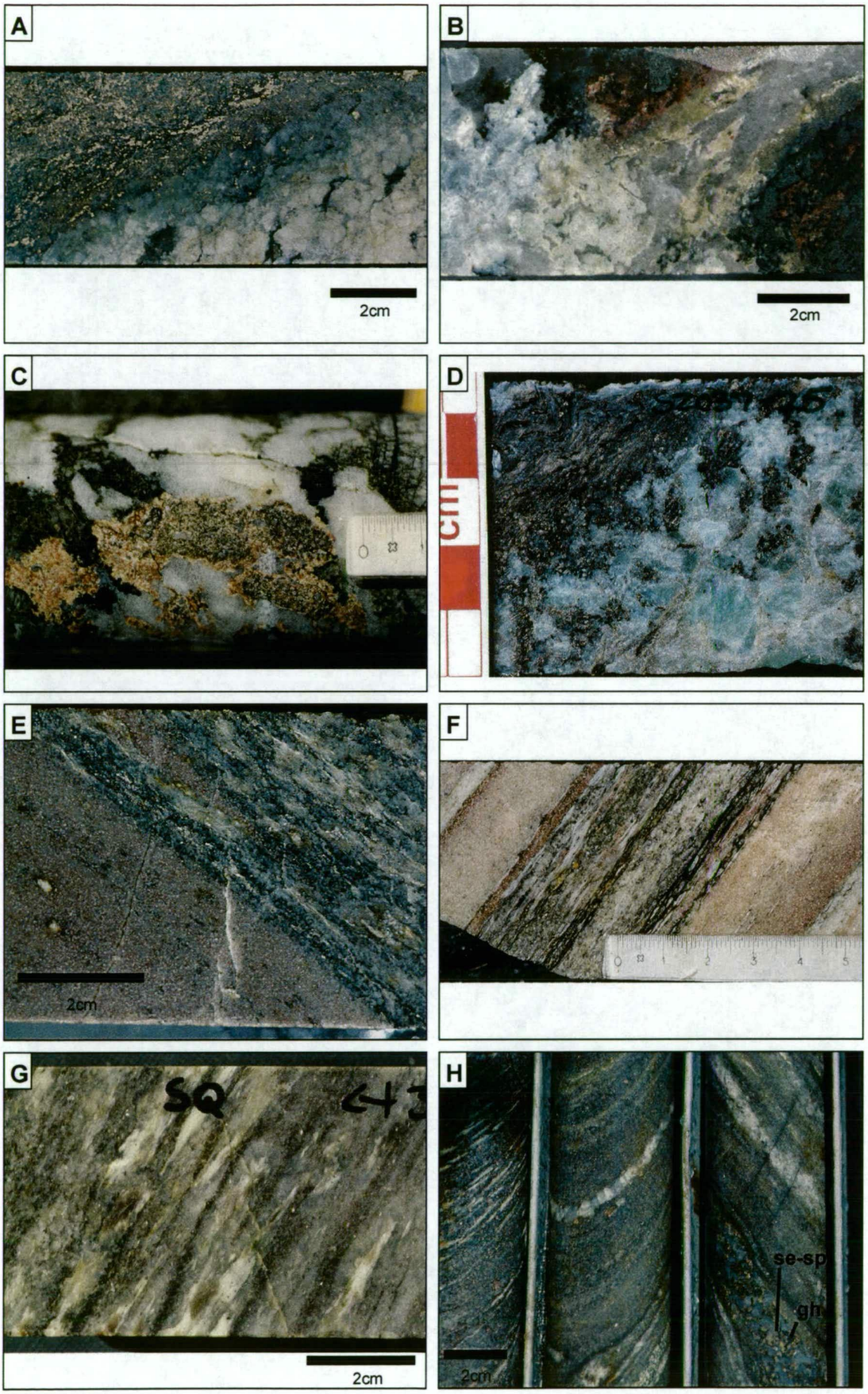
A
2cm
B
2cm
C
D
E
2cm
F
G
SQ
2cm
H
se-sp
gh
2cm

Walters, 1994a). To the south, the hanging wall sequence thins to ~40m on the 4450mN section before being truncated by the Hamilton Fault. The sparsity of these rocks in the footwall has been attributed to the combined effects of attenuation and truncation caused by movement along the Footwall Shear (cf. Walters, 1994a; Bailey, 1998; Giles, 2000).

A major proportion of the sillimanite-garnet schist and garnetiferous quartzite sequence in the structural hanging wall of the Northern Zone has been removed by erosion. It may have extended for up to 200m from mineralised rocks, based on its extensive development in the hanging wall of the Southern Zone. To the east, the sequence extends for up to 50m from mineralised rocks while its northern strike extension remains open due to lack of drilling. However, based on the current geometry of the deposit, and assuming no major intervening structural interruptions, the envelope may continue for another ~1.5km northward before being closed off at the Cretaceous palaeosurface.

The rocks display clear gradational relationships to migmatitic gneiss; the gradational zone characterised by fine-grained (<1 to 2mm), pink garnet porphyroblasts, and increasing abundance of sillimanite and muscovite commensurate with decreasing biotite. A possible weak zonation has been tentatively recognised within the hanging wall sequence of the Southern Zone whereby the proportion of garnetiferous quartzite increases toward the orebody (cf. Bailey, 1998). However, this relationship is not always apparent in drill hole intersections and due to extensive erosion, is unknown in the Northern Zone.

Cyclic interbanding between the quartzites and schists is a characteristic feature of the sequence. In detail, contacts between adjacent sillimanite-garnet schist and garnetiferous quartzite bands are typically sharp on a millimetre scale (Fig. 3.5e and f). However, rare bands grading from garnetiferous quartzite to sillimanite-garnet schist have been observed in some drill hole intersections. The proportion of garnet porphyroblasts in the schists and quartzites varies in drill hole intersections over tens of metres, but unfortunately this aspect was not logged in detail (cf. Walters, 1994a). Generally, garnet increases in abundance towards ore.

Garnetiferous quartzite bands are principally composed of quartz-K-feldspar, with variable garnet abundances and subordinate sillimanite, muscovite, zircon, biotite, ilmenite and rare apatite and graphite. Individual bands typically have an equigranular, sugary texture but may also display an internal grading defined by variations in garnet (Fig. 3.5f) or biotite abundances. Garnet abundances also vary between adjacent bands (Fig. 3.5f). The most garnet-rich quartzites may contain lenticular sillimanite porphyroblasts rimmed by muscovite (Fig. 3.5e).

Sillimanite-garnet schist bands contain variable proportions of quartz, K-feldspar, sillimanite, muscovite, biotite, and trace ilmenite, zircon, graphite and apatite (Fig. 3.5e and f). A strong foliation, typically sub-parallel to banding, is defined by the preferred alignment of fibrolitic sillimanite porphyroblasts and biotite. In some instances, individual bands display internal variations in mineral abundances similar to those observed in garnetiferous quartzite bands.

3.2.3.2 Silicified quartzites and sillimanite-biotite-garnet schists

Close to the contact with the orebody, the SHMU grades into a diverse suite of variably garnetiferous and K-feldspar-rich (commonly 15-20 modal%), quartzite dominated rocks that have been overprinted by local, patchy discordant zones of silicification, e.g. toward the eastern extremity of the Southern Zone in the immediate hanging wall and footwall adjacent to the Brolga Fault zone (cf. Bailey, 1998; Fig. 3.2). Contacts with the ore vary from sharp over millimetre to centimetre scales to gradational over metre scales. The rocks are most abundant within the orebody of the Southern Zone, where they form a lens up to ~50m thick on the 4700mN section (Fig.3.2). The lens reaches a maximum thickness of ~100m on the 4800mN section and forms the immediate structural hanging wall to the Core Amphibolite. The lens thins to the south and is absent by the 4550mN section. The quartzites also occur as sporadic thin lenses up to ~5m thick intercalated with ore lenses. Similar rocks are rare in the Northern Zone and appear to be confined to the hanging wall just above the Core Amphibolite on the 5500mN section, where they occur as a ~30m thick lens.

In the Southern Zone, the lens within the orebody is dominated by mottled grey to blotchy grey-green quartzites (Figs. 3.5g and h, and 3.6a and b). Smaller units of intercalated sillimanite-biotite-garnet schists may contain amazonite±gahnite-bearing *in situ* lode pegmatites. Locally, the quartzites grade into variably brecciated zones of intense silicification that commonly contain abundant sphalerite comprising a distinct siliceous Zn-rich ore (refer Chapter 4). Generally, these zones occur close to the contact with hedenbergite-rich ore lenses, but may occur as patchy zones elsewhere. Adjacent gradational zones are characterised by quartz, quartz-sphalerite (± minor gahnite, arsenopyrite/loellingite, chalcopyrite, pyrrhotite) and quartz-gahnite (± sphalerite) veins in weakly silicified quartzites. The veins typically have diffuse boundaries with adjacent quartzite wall rocks (Figs. 3.5h and 3.6a). Quartz in veins and silicified rock has a distinct blue-grey hue and is informally referred to as 'blue quartz'.

In hand specimen, the above veins can be discordant to relict banding in the quartzites. However, on a gross scale they anastomose subparallel to relict banding and the dominant foliation in the area (Fig. 3.6a). In some examples, they have been folded, boudinaged and attenuated in the plane of the dominant foliation of neighbouring schist bands. Open-space filling textures are conspicuously absent. Instead, quartz has a coarse granoblastic texture, with interstitial disseminated blebby sphalerite along grain margins, at grain margin triple junctions and filling fractures. Sphalerite also occurs as spheroidal inclusions in quartz and forms localised coarse-grained granoblastic textured aggregates. Deformation twinning and banding is common. Quartz displays undulose extinction, sub-grain and new grain development. Gahnite occurs as euhedral to subhedral grains, as euhedral inclusions in quartz and commonly as equigranular aggregates in the quartz veins. Late stage sericite-sphalerite symplectite overgrowths on gahnite grains and aggregates are common (see Chapter 4). Adjacent quartzite wall rock contains minor disseminated gahnite and has a granoblastic texture with interstitial disseminated, blebby to coarse-grained aggregates of sphalerite and pyrrhotite.

Sphalerite and pyrrhotite also fill fractures in the quartzites. In some examples, sulphides may comprise up to 20% of the rock and, in addition to sphalerite and pyrrhotite, contain an appreciable proportion of arsenopyrite/loellingite and chalcopyrite. Trace galena is also a common constituent. Rare hedenbergite-garnet-quartz (± carbonate) veins have also been observed, but are more prevalent immediately adjacent to hedenbergite-rich ores (Fig. 3.6b).

3.2.3.3 Gahnite-bearing sillimanite-biotite-garnet schists

A texturally and mineralogically distinct K-feldspar-rich, gahnite-bearing, sillimanite-biotite-garnet schist (SHGH), occurs within the Northern Zone (Bodon, 1995). The schist forms a subvertical lens that progressively thins as it is traced into the structural footwall (Figs. 3.1 and 3.2). It has a maximum thickness of ~30m on the 5200mN section and presumably continues south along strike to the Trepell Fault. To the north, it thins to ~10m thick on the 5600mN section, and the limit of its northern strike extension is unknown due to lack of drilling data. Contacts with ore lenses are sharp over centimetre scales where they have been preserved from faulting/shearing, and in instances the rock grades into a thin (10-30cm) biotite-garnet schist at the contact. Rare gahnite-bearing schists similar to those in the footwall of the Northern Zone occur in the hanging wall of the Southern Zone in section 4700mN (e.g. CAD028), and underground, structurally above hedenbergite-rich ore in the footwall.

In the footwall of the Northern Zone, the schist contains intercalated bands of garnetiferous quartzite and is very similar in appearance to interbanded sillimanite-garnet schist and garnetiferous quartzite (Fig. 3.6d). In thin section, gahnite poikiloblasts (up to 2mm across) and garnet porphyroblasts (up to 1mm across) with inclusion-rich cores are disseminated throughout the rock and form an integral part of the overall metamorphic texture (Fig. 3.6f, g and h). The majority of garnet occurs in the garnetiferous quartzite bands where it may comprise up to 60 modal% of the rock. In instances, K-feldspar displays a distinct porphyroblastic texture (Fig. 3.6e, f and g). Rare trace galena, sphalerite and pyrrhotite have been observed in some samples (Fig. 3.6h). A spaced, penetrative fabric is defined by the preferred alignment of biotite and fibrolitic sillimanite.

In contrast, the structurally higher, thicker portion of the unit in the Northern Zone has no garnetiferous quartzite bands or clearly definable compositional banding at drill core scale, resulting in a generally homogeneous rock with only local gradational variations in sillimanite content. A diagnostic feature is the abundance of large fibrolitic sillimanite porphyroblasts (up to 1.5cm and up to 60 modal% of the rock) with rounded cores, possibly after andalusite (Fig. 3.6c; Giles, 2000). Partial retrogression of sillimanite to muscovite is common. The groundmass is dominated by K-feldspar (up to ~40 modal%) with subordinate biotite, garnet, quartz, muscovite, minor gahnite, and trace apatite and graphite. Rare disseminated galena, sphalerite and pyrrhotite occur in some samples. Amazonite is common in *in situ* partial melts in the same zone (Fig. 3.5d) and in some instances, contains fine inclusions of galena (<5μm to 300μm).

Figure 3.6 Garnet-rich rocks continued, and gahnite-bearing sillimanite-biotite-garnet schist.

Garnet-rich rocks continued

A. K-feldspar-rich metapsammite within the orebody of the Southern Zone containing sphalerite-quartz-gahnite veins oriented subparallel to compositional banding in the rock. The sample occurs adjacent to a distinct siliceous Zn-rich ore; the latter comprising intensely silicified metapsammite overprinted by deformed quartz veins, vein stockworks and quartz-sphalerite breccias (see Chapter 4 for further details; CUD036, 46.8m).

B. Garnetiferous, K-feldspar-rich metapsammitic rock found within the orebody of the Southern Zone that has been overprinted by hedenbergite-garnet-quartz-carbonate veins. The veins crosscut the compositional banding locally (CAD030, 178.9m).

Gahnite-bearing sillimanite-biotite-garnet schist

C. Typical gahnite-bearing sillimanite-biotite-garnet schist from the Northern Zone. The rock has abundant large fibrolitic sillimanite porphyroblasts (up to 1cm in diameter) oriented parallel to the schistosity. These have typically been partially retrogressed to muscovite. Gahnite poikiloblasts (up to 3mm in diameter) are disseminated throughout the rock and are not obvious at drillcore scale during routine logging (CAD009, 177.8m).

D. A less common, but distinct example of gahnite-bearing sillimanite-biotite-garnet schist from the Northern Zone. Sillimanite porphyroblasts are less abundant in comparison to C. and are more lenticular shaped, defining the foliation. Small garnetiferous quartzite bands are a feature similar to typical garnetiferous sillimanite-garnet schists (e.g. Fig. 3.5e and f). Gahnite poikiloblasts (up to 3mm in diameter) are disseminated throughout the rock (CAD160, 368.4m).

E. Photomicrograph of porphyroblastic K-feldspar containing abundant fine inclusions of quartz and biotite. The texture is very similar to that observed in gahnite-bearing sillimanite-biotite-garnet schist that contains large porphyroblasts of sillimanite such as C. Coarser-grained biotite occurs interstitially and garnet porphyroblasts are disseminated throughout the rock (transmitted light; CAD070, 168.5m).

F. Photomicrograph of granoblastic to porphyroblastic K-feldspar grains and poikiloblastic gahnite. Biotite occurs interstitially (transmitted light; CAD160, 368.4m).

G. Photomicrograph displaying the morphology of two gahnite poikiloblasts. A large sillimanite porphyroblast (centre) has undergone near complete retrogression to muscovite. Matrix minerals are dominated by granoblastic K-feldspar and minor quartz, and interstitial biotite. Fine garnet porphyroblasts are disseminated throughout the rock (transmitted light; CAD027, 256.3m).

H. Photomicrograph of a garnetiferous quartzite band consisting of garnet, quartz, biotite, apatite and poikiloblastic gahnite with minor disseminated galena and graphite. Garnets have inclusion-rich cores with inclusion-free overgrowths (transmitted light; CAD160, 368.4m).

Abbreviations: ap–apatite, bt–biotite, ga–galena, gh–gahnite, gr–graphite, gt–garnet, ksp–K-feldspar, mu–muscovite, qz–quartz, sil–sillimanite, sp–sphalerite.

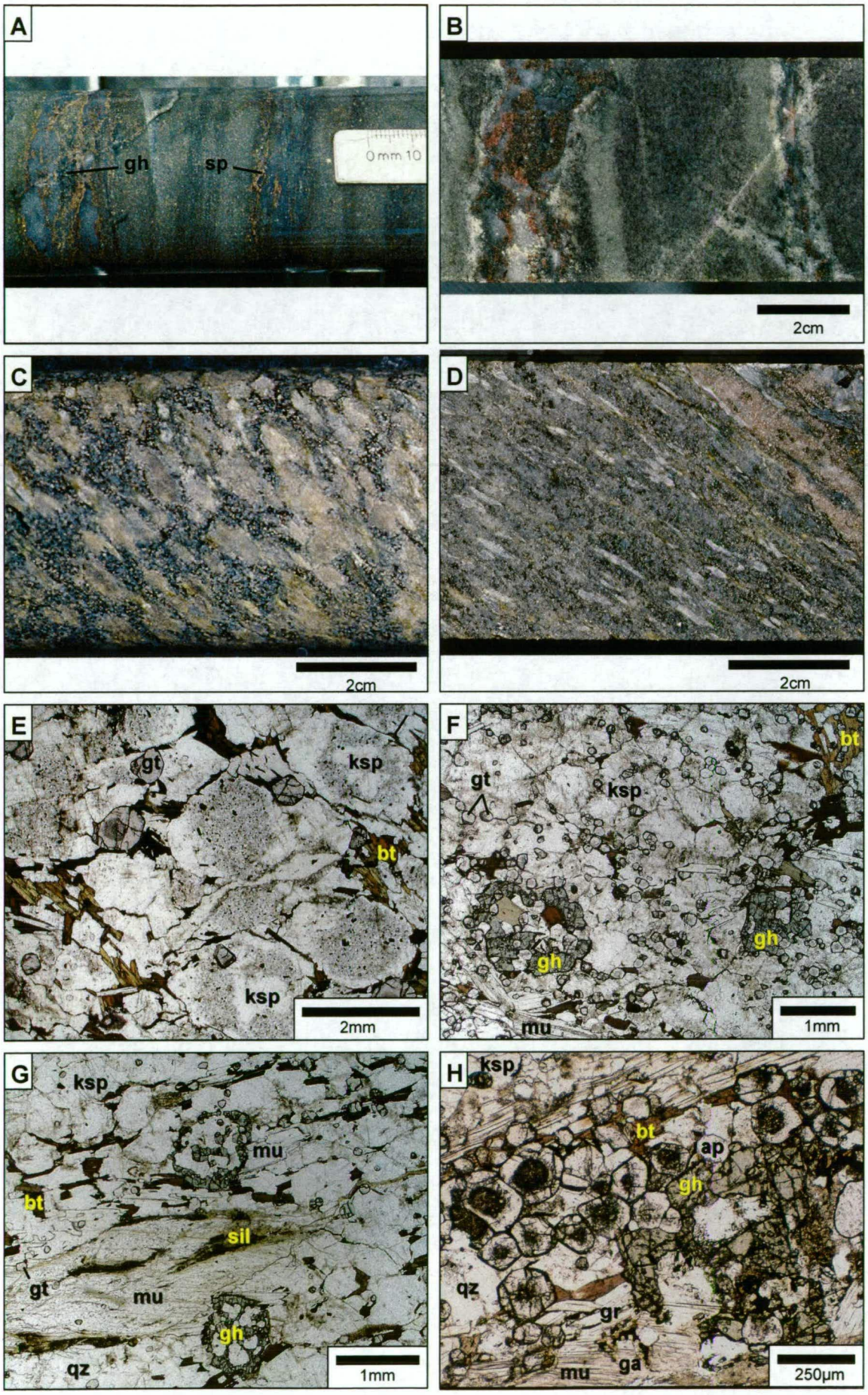
A
gh
sp
0 mm 10
B
2cm
C
2cm
D
2cm
E
gt
ksp
bt
ksp
2mm
F
bt
gt
ksp
gh
gh
mu
1mm
G
ksp
mu
bt
sil
gt
mu
gh
qz
1mm
H
ksp
bt
ap
gh
qz
gr
mu
ga
250µm

3.2.4 Amphibolites

Rare amphibolites occur in the migmatitic gneiss and interbanded sillimanite-garnet schists and garnetiferous quartzites of the SHMU halo (Figs. 3.2 and 3.7a). They form variably continuous lenses to boudinaged pods up to 50m thick that are typically concordant to banding in the gneiss and the SHMU. Biotite-garnet selvedges up to 20cm wide occur along contacts with other host rocks. In some cases, this assemblage is seen as sporadic zones within amphibolites. These features are a regional phenomenon and are not unique to the Cannington area (Williams and Heinemann, 1993; S. Walters and S. Konecny, pers. comm., 1995). Rare, garnet-bearing amphibolites are also present, but again are not restricted to the Cannington area (Fig. 3.7b).

The most significant and largest amphibolite at Cannington resides within the centre of the orebody and is known as the Core Amphibolite (Figs. 3.1 and 3.2: Walters, 1994a; Bailey, 1998; Bodon, 1995, 1998; Walters and Bailey, 1998). The Core Amphibolite attains a maximum thickness of ~240m in the 5600mN section in the Northern Zone. It progressively thins to the south and is absent by the 4600mN section in the Southern Zone. The limit of its northern strike extension is poorly defined owing to a lack of drilling data. The body is slightly transgressive to ore lenses on a gross scale, and contacts with mineralised rocks are typically sharp over 1-2cm where they have been preserved from faulting/shearing, or have not been intruded by pegmatite. In some instances, minor amphibole and disseminated sulphides occur along amphibolite contacts and elsewhere, rare pyroxferroite-hedenbergite occur (Fig. 3.7c).

Apart from these localised occurrences, the amphibolite is remarkably homogeneous with regard to texture and composition, except for localised intrusive pegmatite lenses up to ~20m thick (e.g. the BLP). It has a fine- to medium-grained, massive texture with a characteristic mineralogy of hornblende, plagioclase, quartz, biotite, minor ilmenite, and rare garnet and zircon. Granoblastic metamorphic textures are typical, with a weak foliation defined by the preferred alignment of biotite, and in some cases, hornblende (Fig. 3.7d and e). When present, garnet forms poikiloblasts (up to 1cm across) with inclusions of quartz, ilmenite and minor biotite (Fig. 3.7e). Incipient sericitisation of plagioclase is ubiquitous (Fig. 3.7d and e).

Weak sulphide mineralisation is spatially and temporally associated with fine microscopic chlorite veinlets, as well as overprinting chlorite alteration adjacent to late faults. Rare, weakly mineralised clinopyroxene-bearing pegmatite veins with biotite-garnet±clinopyroxene selvedges (Fig. 3.7f), and quartz-garnet veins with garnet selvedges have also been observed. Of particular significance is the occurrence of fine-grained galena, pyrrhotite and chalcopyrite inclusions in plagioclase grains that do not appear to be associated with late stage chlorite veinlets in some samples (Fig. 3.7g and h). Apart from these minor occurrences, the Core Amphibolite underwent no significant sulphide mineralisation, a particularly intriguing feature, given the abundance of high grade ore that envelops it (Chapter 6).

Figure 3.7 Amphibolite.

A. Typical massive medium grained amphibolite from the Core Amphibolite (CAD056, 371.0m).

B. Plagioclase-rich amphibolite with minor garnet poikiloblasts (up to 0.5cm in diameter). The schistosity (S_1/S_2) is defined by a poor, discontinuous mineralogical banding (CAD068, 435.7m).

C. Rare example of hedenbergite-pyroxferroite (-garnet) overprinting amphibolite along a contact with hedenbergite-rich ore (CUD049, 45.6m).

D. Photomicrograph of typical granoblastic texture in garnet-bearing amphibolite. The sample comprises hornblende-plagioclase-quartz-biotite-garnet. The schistosity (running from left to right) is defined by a weak preferred orientation to hornblende grains and minor biotite (polarised transmitted light; CAD068, 435.7m).

E. Photomicrograph displaying the schistosity (defined by biotite) wrapping around a large garnet poikiloblast containing inclusions of quartz, ilmenite, and minor hornblende and biotite. Sericitisation of plagioclase is common in amphibolite samples (plane-polarised transmitted light; CAD068, 435.7m).

F. Hedenbergite-bearing pegmatitic vein and associated hedenbergite and biotite selvedges. Hedenbergite occurs as porphyroblasts and fine bands that are oriented parallel to the foliation (CAD043, 186.8m).

G. Photomicrograph of fine pyrrhotite, chalcopyrite and galena inclusions in plagioclase. The sulphides are not spatially or temporally associated with the later sericitisation of the plagioclase (plane-polarised transmitted light, CAD056, 371.0m).

H. Reflected light view of G. displaying the subhedral morphology of pyrrhotite (plane-polarised reflected light).

Abbreviations: amph–amphibolite; bt–biotite, cpy–chalcopyrite, ga–galena, gt–garnet, hb–hornblende, hd–hedenbergite; il–ilmenite, pf–pyroxferroite; plg–plagioclase, po–pyrrhotite, qz–quartz; se–sericite.

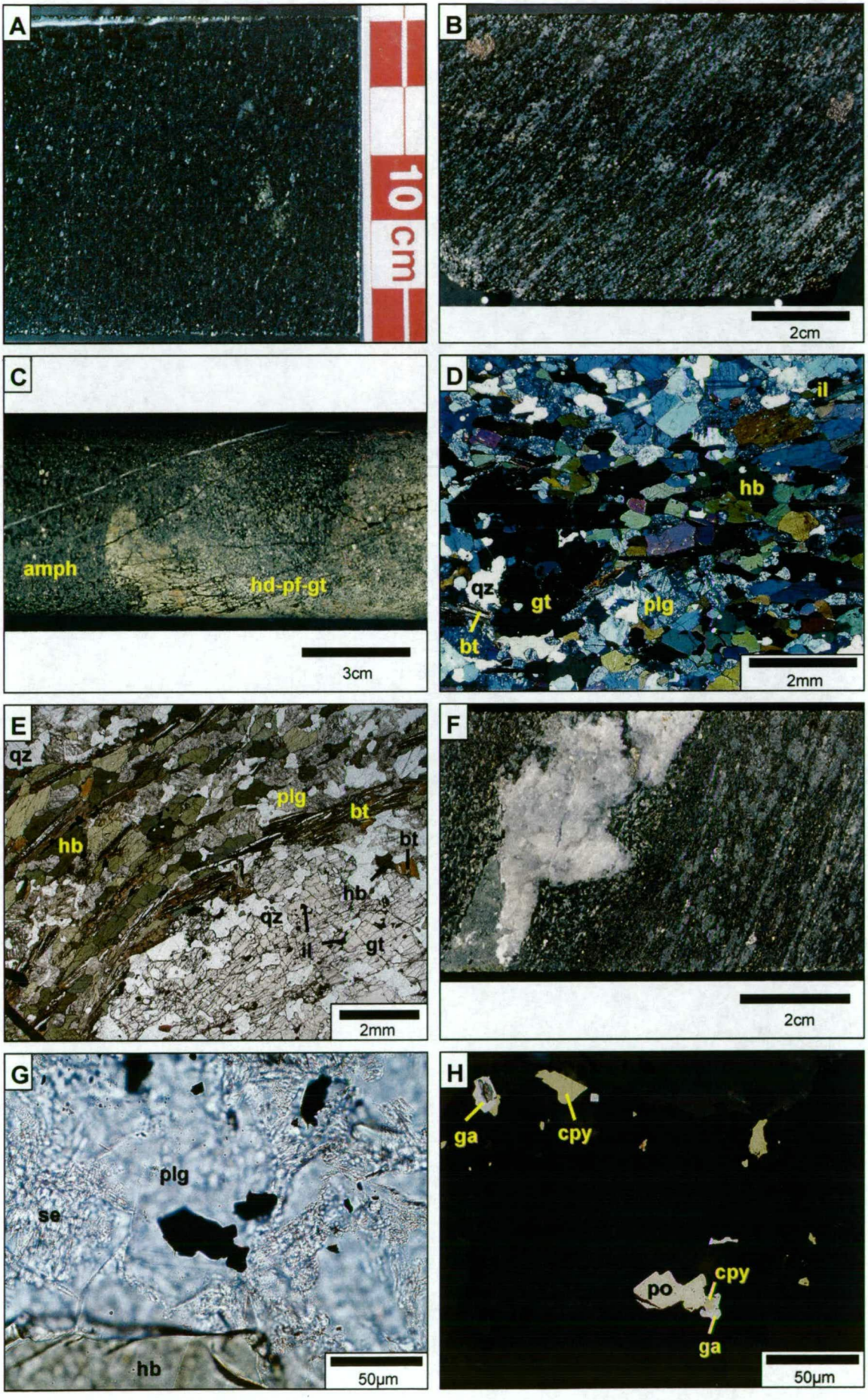
A
10 cm
B
2cm
C
amph
hd-pf-gt
3cm
D
il
hb
qz
gt
plg
bt
2mm
E
qz
plg
bt
hb
bt
hb
qz
il
gt
2mm
F
2cm
G
plg
se
hb
50µm
H
ga
cpy
po
cpy
ga
50µm

Based on geochemical affinities using various immobile elements such as Ti, Al, Zr, Nb, Y (Pearce and Cann, 1973; Floyd and Winchester, 1976; Winchester and Floyd, 1977; James et al., 1987; MacLean and Kranidiotis, 1987; MacLean, 1990; MacLean and Barrett, 1993; Barrett and MacLean, 1994a; and many others), the Core Amphibolite straddles the boundary between the andesite and subalkaline basalts field in Figure 3.8.

3.2.5 Fe-Mn silicate units

Two Fe-Mn silicate units occur in the hanging wall of the Southern Zone. The units range in thickness (1-5m) and can be traced from the Cretaceous palaeosurface to the Brolga Fault Zone on the 4700mN section (Fig. 3.2). They are hosted within the SHMU halo and in one area transgress into migmatitic gneiss on the 4700mN section. Only one unit can be traced south of the latter section to the 4550mN section. Both units can be traced north from the 4700mN to the 4775mN sections and beyond this, only sporadic intersections occur to the Trepell Fault. Similar Fe-Mn units can be traced throughout the Northern Zone. However, detailed correlation with the Southern Zone units is ambiguous.

The units have similar minerals and textures to the silicate component of particular ore types, varying from massive, equigranular to banded knebelite-magnetite-pyroxferroite-apatite (±garnet, fluorite; Fig. 3.9a), to finely banded knebelite-pyroxferroite-magnetite-garnet-biotite-amphibole-apatite (± fluorite, graphite; Fig. 3.9b). Areas of banded hedenbergite-garnet overprinted by hedenbergite-garnet-quartz (±carbonate) veins occur sporadically throughout the units (Fig. 3.9c). Contacts with interbanded sillimanite-garnet schists and garnetiferous

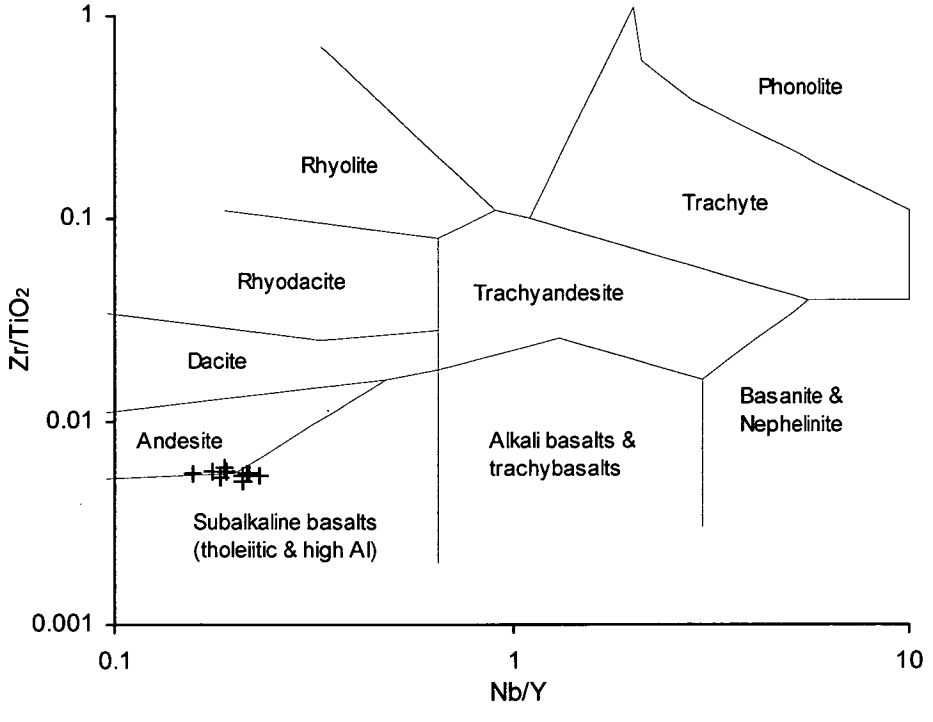

Figure 3.8 Classification and nomenclature for volcanic rocks using the Zr/TiO_2-Nb/Y immobile element plot after Winchester and Floyd (1977). The composition of the Core Amphibolite straddles the andesite-subalkaline basalt boundary.

Figure 3.9 Range in textural and mineralogical characteristics of Fe-Mn silicate units.

A. Massive knebelite-magnetite (± quartz, garnet, grunerite, apatite, galena, pyrrhotite) with minor coarse-grained retrograde pyroxferroite. Magnetite-pyrosmalite-fluorite-galena (± galena, pyrrhotite, freibergite) veinlets with pyrosmalite selvedges overprint the rock (CAD039, 104.6m).

B. Folded compositional banding. Bands are defined by variable proportions of garnet, quartz, biotite, apatite, knebelite, pyroxferroite, and minor hornblende, grunerite and graphite. Sulphides (chiefly galena, sphalerite and pyrrhotite) are disseminated throughout the rock and in instances, are concentrated in particular band-types (CAD252, 224.3m).

C. Hand specimen from underground displaying a vein of coarse grained hedenbergite overprinting relict compositional banding at high angle. Pre-existing knebelite-quartz bands have been replaced by hedenbergite-garnet (exact underground location unknown).

D. Typical sharp contact between the Fe-Mn silicate unit in B. and sillimanite-garnet schist. The contact is concordant to banding in the sillimanite-garnet schist. A small biotite-garnet selvedge is common along the contacts (CAD252, 223.75-224.1m).

Abbreviations: mt–magnetite; pf–pyroxferroite; ps–pyrosmalite.

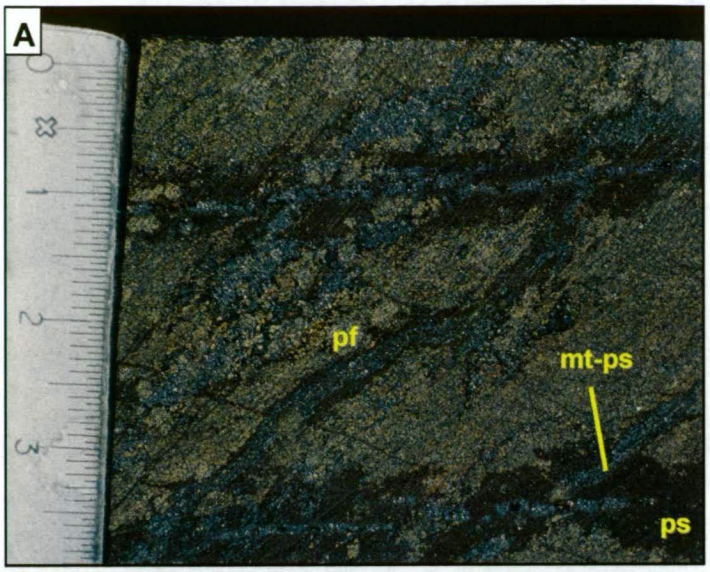
A
pf
mt-ps
ps

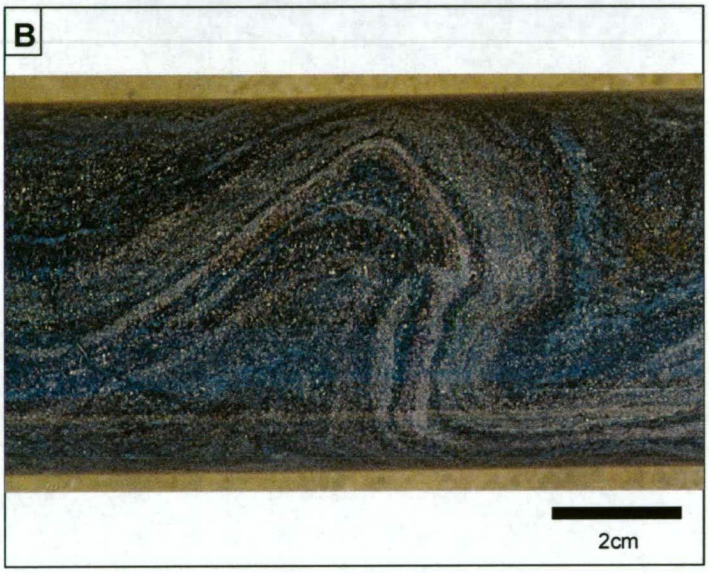
B
2cm

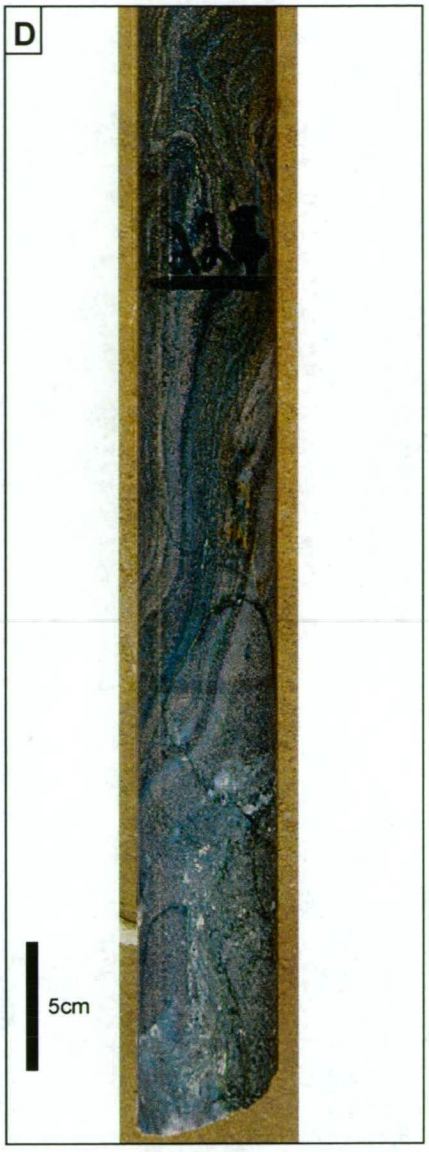
D
5cm

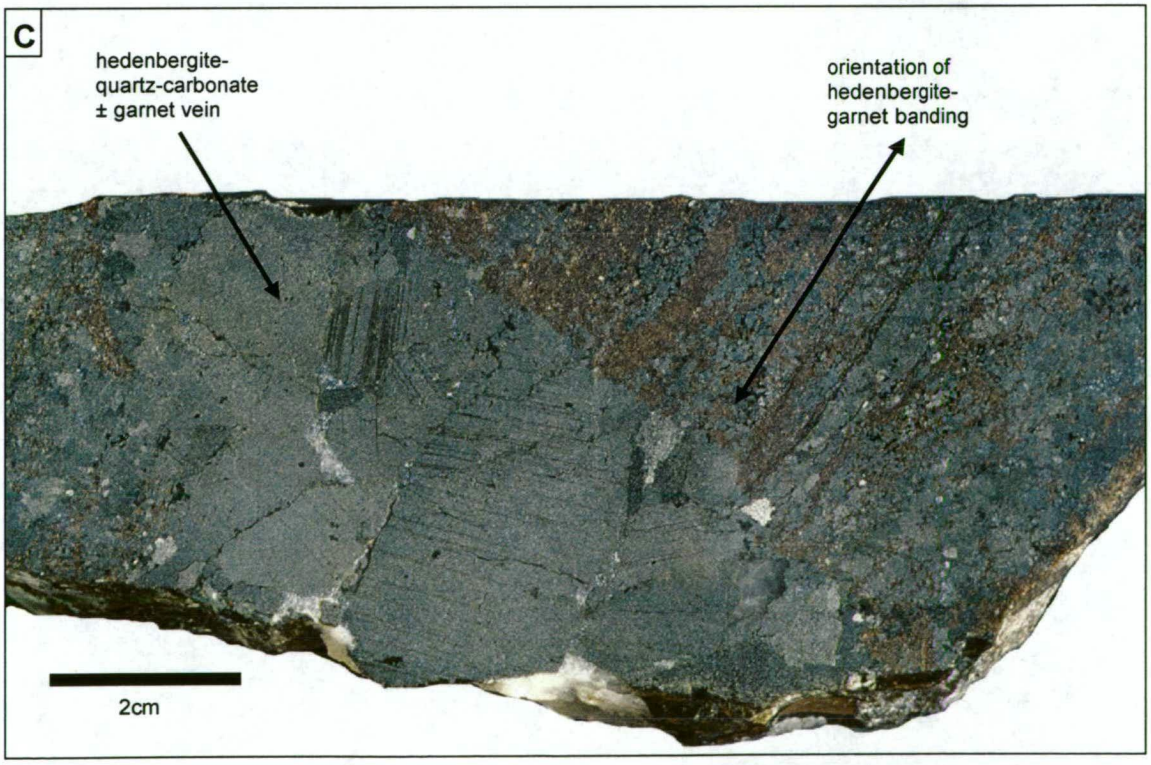
C
hedenbergite-
quartz-carbonate
± garnet vein
orientation of
hedenbergite-
garnet banding
2cm

quartzites are sharp over 5cm and are commonly characterised by a gradational zone of garnetiferous quartzite that ranges in thickness from 5cm to 1m (Fig. 3.9d).

3.2.6 Late alteration associated with joints and faults

Patchy zones of orange-red feldspar and a range of late overprinting assemblages are common to all gneiss types and intercalated pegmatites. Zones of orange-red feldspar occur in a plethora of rock types throughout the region and are not spatially related to sulphide deposits. Due to this, they are not routinely logged in drill core at Cannington and therefore, spatial distributions are poorly defined in the mine area. Zones up to ~50m thick have been observed in some drill hole intersections. The orange-red colouration is caused by fine hematite inclusions and is commonly referred to as red-rock alteration. However, it is unclear whether the hematite is due to a particular regionally extensive post-metamorphic hydrothermal event or is just an inherent regional diagenetic component.

Incipient alteration associated with joints and faults occurs within all host rocks. Alteration produced quartz-chlorite (-pyrite/marcasite), minor talc and various clays. All feldspars have undergone weak, pervasive, texturally preserving sericite alteration. Earlier albite veins with albite alteration selvedges are uncommon and are generally regarded as being temporally related to regionally extensive zones of Na-Ca metasomatism (section 2.4; see de Jong and Williams, 1995; Pollard, 2001).

Late alteration in the Fe-Mn silicate units is characterised by pyrosmalite-magnetite (± fluorite, galena, pyrrhotite, Ag-sulphosalts) veins and disseminations, and later chlorite-pyrite/ marcasite (± quartz, carbonate, galena, sphalerite) veins and disseminations.

3.3 STRUCTURAL GEOLOGY

The recent structural study of Giles (2000) represents the most robust structural framework for the Cannington deposit to date, and has overcome major shortfalls associated with previous deformational paradigms. These tended to focus only on the Southern Zone, or were based upon circumstantial and/or incomplete evidence (e.g. Gray, 1994; Sheehan, 1994, Bodon, 1995). All previous interpretations, were based on structural data collected from oriented drill core of mainly migmatitic gneiss and the enveloping garnetiferous rocks. Due to their banded nature, these are the most structurally fertile rocks in the area. The banding provides a means of identifying folds at drill core scale, and the abundance of biotite, sillimanite and garnet record multiple structural fabrics (cf. Gray, 1994; Sheehan, 1994; Giles, 2000).

Giles (2000) established six generations of deformation by measuring various structural fabrics and kinematic indicators in oriented drill core, which augmented previously collected structural data (e.g. Gray, 1994; Sheehan, 1994; BHP data). Of these, two ductile events (D_3 and D_4), and to a lesser degree, a later brittle event (D_5) control the macroscopic geometry of the Cannington deposit.

A traditional numerical scheme has been substituted for the deformational nomenclature of Giles (2000); note that it is internal to the deposit only. This approach simplifies the structural framework into a clearly defined and easily envisaged chronological sequence of events (Table 3.1). The structural framework is initially presented in terms of the meso- to microstructural criterion used to define each deformation event. This is followed by the macroscopic effects of each event and controls on the geometry of the deposit, and subsequent correlation with the regional structural framework proposed for the Eastern Succession.

3.3.1 D_i

A rare early mineral fabric (S_i) manifested by quartz inclusion trails in garnet porphyroblasts occurs in sillimanite-garnet-biotite schists adjacent to the orebody, and is equivalent to S_R of Giles (2000). It is unclear whether the fabric is related to the same deformation event that progressed throughout metamorphism and produced the dominant sillimanite-biotite schistosity in the area (S_1/S_2), or whether it formed in response to a discrete, unrelated event that pre-dated metamorphism. Strict interpretation suggests that garnet growth was post-kinematic with respect to S_i based on the undistorted linearity of the inclusions (cf. Vernon, 1987; van der Pluijm and Marshak, 1997).

3.3.2 D_1

D_1 elements are recognised by a biotite-sillimanite (fibrolite) schistosity (S_1) in melanocratic domains in migmatitic gneiss, and are essentially analogous to S_1 of Gray (1994) and Sheehan (1994) and S_M of Giles (2000) (Table 3.1). No macroscopic folds of this generation have been observed at Cannington, despite it being a major fabric-forming event. However, in some instances, S_1 sillimanite has been folded, by later events, into rootless, attenuated isoclines that vary from millimetre- to subcentimetre scale (Fig. 3.10a). A crenulated S_1 fabric is preserved within fibrolitic sillimanite aggregates that are aligned with the pervasive S_2, and within intrafolial zones between penetrative S_2 sillimanite microlithons (Fig. 3.10b; cf. Sheehan, 1994). There is clear textural evidence that S_1 has been transposed into the plane of S_2 in zones of high D_2 strain. Crenulated biotite occurs in areas of low D_2 strain and shows evidence for subsequent recrystallisation. The observation that S_1 is parallel to migmatitic layering in F_2 fold hinges indicates that the development of "...both fabric (S_1) and melt was controlled by syn-anatectic strain rather than pre-existing lithological variations" (Giles, 2000). This temporal relationship is particularly significant and it is at odds with previous structural studies, which suggested all partial melting occurred during D_2.

D_1 fabrics are poorly developed in garnetiferous rocks and are typically dominated by granoblastic textures and porphyroblastic garnet growth as well as rare poikiloblastic gahnite (Table 3.1). These textures are indicative of static mineral growth (Giles, 2000). The weak development of S_1 mineral fabrics may indicate that garnetiferous rocks experienced less D_1 strain in comparison with migmatitic gneiss.

The Core Amphibolite is dominated by similar D_1 elements, such as granoblastic textures and a

Table 3.1 Summary of the structural framework at Cannington (modified after Giles, 2000). Included are schematic depictions of the key meso– to microtextural criterion used to define the various deformation events. Correlation of the nomenclature used by Giles (2000) and this study appears in the left-hand column.

Giles (2000)	This study	Garnetiferous rocks (SHMU)	Migmatitic gneiss	Core Amphibolite	Macroscopic features
D_R	D_i	Enigmatic mineral fabric (S_i) preserved as quartz inclusions in garnet porphyroblasts 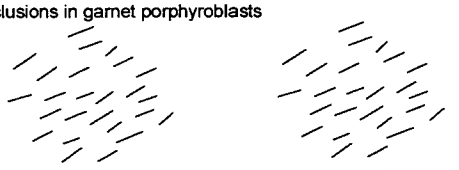		? not observed	Unknown
D_M	D_1	Granoblastic recrystallisation and porphyroblast growth 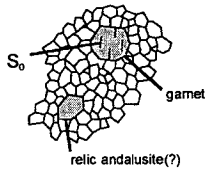	Syn-anatectic biotite-sillimanite fabric 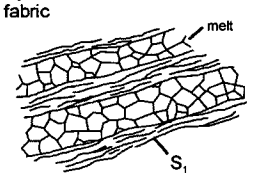	Granoblastic recrystallisation and porphyroblast growth 	Little effect on geometry of deposit. Syn-anatectic deformation. Mid to lower crustal sear zone?
D_Z	D_2	Microshears infilled with secondary sillimanite, and replacement 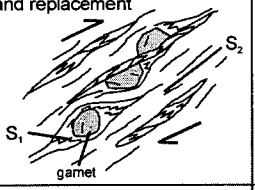	Differentiated fabric and isoclinal folding 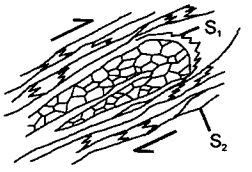	Fabric intensification and shearing 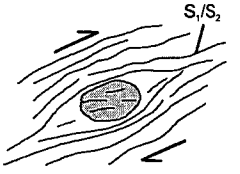	Little effect on geometry of deposit. Mid crustal high-temperature shear zone?
D_{F1}	D_3	Crenulation and isoclinal folding 	Crenulation and isoclinal folding 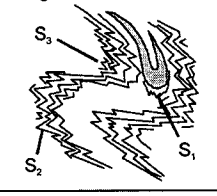	Crenulation 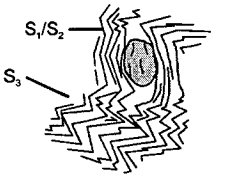	Significant effect on geometry of deposit. Inclined isoclinal folding during east-west shortening.
D_{F2}	D_4	Open, upright folding (no axial planar foliation) 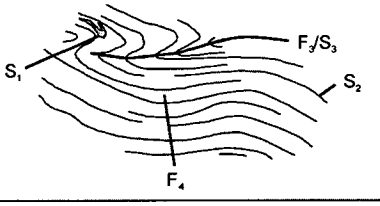			Moderate effect on geometry of deposit. Upright, open folding during east-west shortening.
FAULTING	D_5	Two faulting generations: - D_{5a} north-northeast striking Brolga Fault Zone. - D_{5b} conjugate fault set comprising the northwest striking Trepell and Hamilton faults and intervening northeast striking faults such as the Bustard and FOY faults.	 Brecciation	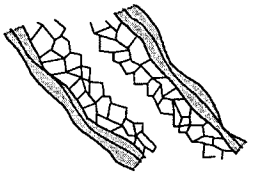 Vuggy carbonate-quartz veining	Minor effect on geometry of deposit. Regional-scale right lateral wrenching (Lister et al., 1986)

poorly defined S_1 fabric. However, the amphibolite preserves only one mineral foliation, which is defined by the preferred alignment of hornblende, plagioclase and biotite. This fabric has been interpreted as a composite S_1/S_2 fabric using evidence from garnet-biotite-rich zones along the margins of the amphibolite. Porphyroblastic garnets and the dominant foliation(s) recognised in these zones are similar to those of the migmatitic gneiss (Giles, 2000).

3.3.3 D_2

Penetrative sillimanite (fibrolite) and biotite schistosities (S_2) dominate the host sequence and are equivalent to the S_2 foliation defined by Gray (1994) and Sheehan (1994), and S_Z of Giles (2000). A well developed sillimanite lineation (L_2) typically occurs along the plane of S_2 and in the Southern Zone has a moderately to steeply dipping east or southeast plunge (Giles, 2000). The morphology of S_2 fabrics range between two end-members, type "A" and type "B", that are partly controlled by lithology (Giles, 2000). Type A morphologies consist of differentiated, spaced schistosities defined by millimetre-scale interbanded biotite-sillimanite domains and quartz-feldspar domains in melanocratic layers within migmatitic gneiss (Table 3.1). Crenulated (on a microscopic scale) fibrolite and biotite suggest that both minerals pre-date the dominant fabric and were re-oriented by it (op. cit.). However, some biotite that is aligned with the dominant S_2 fabric, appears to have overgrown crenulated fibrolite, indicating syn-kinematic recrystallisation, or new growth of secondary biotite. In quartz-feldspar domains, S_2 is defined by mineral elongation and truncation of grain boundaries along contacts with sillimanite-biotite-rich domains, suggesting that fabric development involved processes of crystal dislocation and/or dissolution. In some cases, sub-centimetre intrafolial, rootless, isoclinal F_2 folds, with thickened hinges and attenuated limbs, are defined by pre-existing leucocratic segregations, and provide evidence for significant transposition of earlier fabrics during D_2 (op. cit.; Table 3.1).

Type B fabrics are intrinsic to garnetiferous rocks and are characterised by the preferred alignment of disseminated biotite and elongate sillimanite porphyroblasts in a granoblastic textured groundmass of quartz, K-feldspar, porphyroblastic garnet and rare poikiloblastic gahnite. Textural evidence suggests that fibrolite grew within discrete curvilinear to anastomosing microshears at the expense of pre-existing silicates (Giles, 2000; Fig. 3.10b). Textures supporting this interpretation include:

- replacement of pre-existing silicate minerals (e.g. quartz, feldspar and preferentially aligned S_1 biotite) by sillimanite (Fig. 3.10b and c);
- truncation of quartz and feldspar grain boundaries and reduction in quartz grain sizes along contacts with sillimanite aggregates, suggesting strain-induced recrystallisation (Fig. 3.10c). This is also evidenced by quartz sub-grains and new-grains along larger granoblastic quartz grain boundaries (Fig. 3.10d);
- truncation and displacement of pre-existing garnet porphyroblasts and gahnite poikiloblasts (Fig. 3.10c; Table 3.1).

Figure 3.10 D_1 and D_2 structural elements.

D_1 elements

A. Transposed S_1 foliation defined by a rootless sillimanite isocline and folded leucocratic segregations in sillimanite-biotite-garnet schist. The dominant mineral fabric is a differentiated sillimanite-biotite S_2 foliation (CAD038, 40.75m).

B. Photomicrograph of a crenulated S_1 sillimanite foliation and a possible S_1 sillimanite isocline. The dominant foliation comprises a differentiated S_2 sillimanite shear fabric (i.e. S-C fabric) that is also defined by elongate, ribbon-like quartz grains between S_2 sillimanite microlithons (plane-polarised transmitted light, CAD028, 386.4m).

D_2 elements

C. Photomicrograph of the differentiated S_2 fabric in a sillimanite-garnet schist sample. S_2 is defined by the preferred alignment of sillimanite and intervening elongate quartz grains. Note the flattened porphyroblastic aggregate of garnet in the plane of S_2. Quartz grain boundaries have been truncated adjacent to the S_2 sillimanite microlithons (polarised transmitted light, CADCAD028, 386.4m).

D. Photomicrograph of the differentiated S_2 foliation defined by the preferred alignment of biotite, sillimanite and elongate quartz grains in sillimanite-biotite-garnet schist. Sub-grain development in quartz occurs along sutured grain boundaries that are indicative of strain-induced recrystallisation during D_2. Quartz sub-grains also rim biotite grains. It is difficult to ascertain whether the latter texture is due to dynamic recrystallisation, or is a metamorphic reaction corona around the biotites. Because biotite grains appear to be embayed by quartz, the latter interpretation implies biotite breakdown during S_2 fabric development (polarised transmitted light, CAD028, 420.9m).

E. Isoclinal F_2 fold in sillimanite-garnet schist with a well developed axial planar differentiated S_2 defined by sillimanite and biotite. Note the upper limb of the garnetiferous quartzite band has been attenuated and truncated by a second generation sillimanite-rich shear zone (CAD052, 299.0m).

F. Boudinaged garnetiferous quartzite band sub-parallel to the S_2 sillimanite fabric. The S_2 is locally diffracted around the boudins (CAD038, 59.75).

Abbreviations: bt–biotite, gt–garnet, mu–muscovite, qz–quartz, sil–sillimanite.

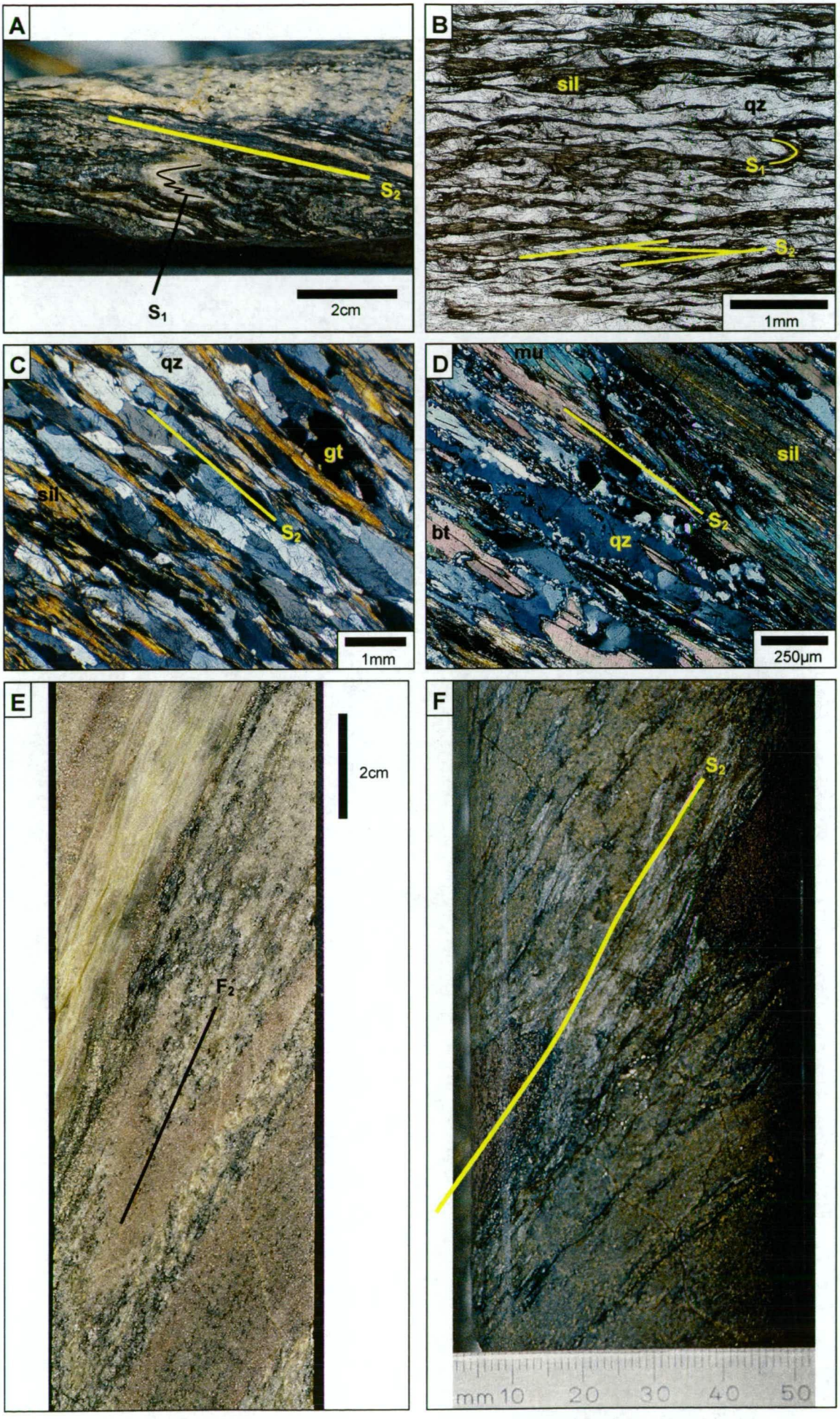
A
S2
S1
2cm
B
sil
qz
S1
S2
1mm
C
qz
gt
sil
S2
1mm
D
mu
sil
S2
bt
qz
250µm
E
2cm
F2
F
S2
mm 10 20 30 40 50

Chaotically folded and crenulated sillimanite beards in pressure shadows adjacent to interpreted relict andalusite porphyroblasts (now comprised of coarse-grained, optically continuous muscovite, with inclusions of fibrolite needles) are another textural variant of Type B fabrics typically found in areas of low D_2 strain (Giles, 2000) in gahnite-bearing sillimanite-biotite-garnet schists. The beards pass into narrow, discrete sillimanite microshears that propagate through the granoblastic fabric. Shears also bound the edges of porphyroblasts, forming a carapace of strongly aligned sillimanite, and propagate through the granoblastic groundmass in instances joining the carapace of a neighbouring porphyroblast (op. cit.). In some cases, silicates adjacent to the microshears have been replaced by sillimanite and flattened garnets were incorporated in the shear (op. cit.).

Overall, textures indicate that S_2 sillimanite fabrics were created by the transposition of S_1 sillimanite and biotite (e.g. the migmatitic gneiss), followed by biotite recrystallisation and/or new growth, and a later generation of secondary sillimanite (Giles, 2000). Hence, two generations of sillimanite occur at Cannington, a syn-D_1 and a syn-D_2 generation (op. cit.). Replacement of pre-existing minerals by secondary sillimanite implies the presence of a syn-D_2 fluid phase (op. cit.; section 3.4.3). It appears that fluid-flow was channelled through the microshears, where second generation sillimanite was precipitated. Porphyroblastic garnet and gahnite growth, and development of granoblastic textures clearly pre-date this process (op. cit.).

Meso- to microscopic F_2 fold styles are dominated by tight to isoclinal parallel folds that commonly have rounded, thickened hinge zones and a strong axial planar sillimanite-biotite schistosity (S_2; Fig. 3.10a and e). Attenuation of F_2 fold limbs (Fig. 3.10e) indicates significant transposition of pre-existing fabrics and compositional banding during D_2 under a regime of simple shear (Giles, 2000). Macro- to mesoscopic boudinaging of pegmatites and garnetiferous quartzite bands are an additional common feature of D_2 (Fig. 3.10f).

3.3.4 D_3

Tight to isoclinal folding of pre-existing mineral fabrics and compositional banding provides evidence for a third generation of deformation (D_3) that is analogous to Giles's (2000) D_{F1} (Fig. 3.11a, b and c; Table 3.1). It is also likely equivalent to the regional D_2 isoclinal fold event (O'Dea et al., 1997a). Gray (1994) and Sheehan (1994) misinterpreted mesoscopic F_3 folds as F_2. This was probably due to the similar, tight to isoclinal style of F_2 and F_3 folds, and the orientation of S_3 to differentiated S_1/S_2 fabrics in F_3 fold limbs, as well as the absence of overprinting fold relationships in drill core. However, the rounded parallel style of F_3 hinge regions gives the folds an apparent open character that can be recognised in drill core (Fig. 3.11a; Giles, 2000).

In F_3 fold hinges, an axial planar, spaced S_3 fabric has crenulated pre-existing fabrics within melanocratic zones in migmatitic gneiss and sillimanite-biotite-rich bands in garnetiferous rocks (Fig. 3.11a and b). S_3 is defined by weakly-aligned micas in leucocratic segregations. In zones of high D_3 strain, S_3 is the dominant fabric and has a very similar morphology to S_2 (i.e. fine

Figure 3.11 D_3 and D_5 structural elements.

D_3 elements

A. An asymmetric F_3 fold in sillimanite-garnet schist with an axial planar, spaced S_3 fabric defined by the preferred alignment of muscovite and biotite. Local diffraction of the foliation occurs in the garnetiferous quartzite band. Such structures were used by Giles (2000) to determine large-scale fold (F_3) vergence. A crenulated, differentiated S_2 sillimanite foliation occurs parallel to the compositional banding (CAD045, 232.0m).

B. Spaced S_3 fabric and crenulations overprinting a composite S_1/S_2 fabric in sillimanite-bearing migmatitic gneiss. Minor millimetre-scale F_1 intrafolial rootless, isoclinal folds are defined by sillimanite (S_1) and leucocratic segregations. A minor open F_3 fold is also apparent (CAD103, 152.2m).

C. Open to tight F_3 folding in interbanded biotite-garnet schist and quartzite adjacent to weakly mineralised hedenbergite-garnet-quartz rock (CAD030, 145.1).

D_5 elements

D. Carbonate-marcasite lined vugh in a carbonate vein adjacent to a possible north-northeast trending D_{5a} fault in the Brolga Fault Zone (CAD164, 166.0m).

E. Drillhole intersection of the D_{5b} Trepell Fault. The fault is characterised by abundant chlorite-clay gouge and friable, polymict breccias. Clasts consist of various silica-chlorite-pyrite-marcasite altered ore types and host rocks (CAD044, 538.0-544.0m).

F. Example of a silica-chlorite carbonate healed breccia and crustiform banded vuggy quartz-carbonate-marcasite veining in silicified quartzite, associated with a D_{5b} northeast trending fault . The latter open-space filling textures in veins and breccias are a characteristic feature of D_{5b} faults (CUD044, 60.9m).

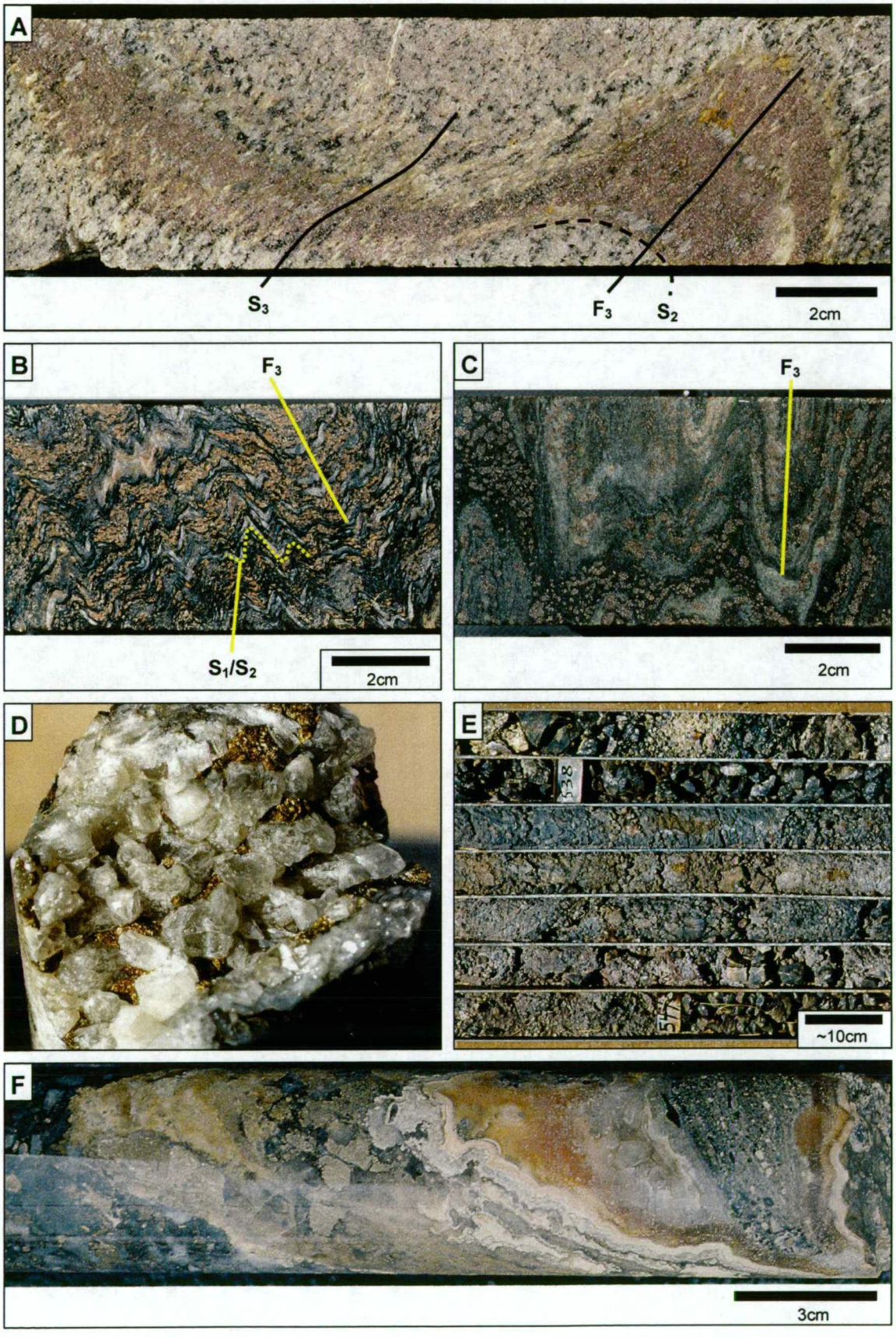
A
S3
F3
S2
2cm
B
F3
S1/S2
2cm
C
F3
2cm
D
E
538
537
~10cm
F
3cm

crenulations and differentiated fabrics) at drill core scale, but can be recognised on a microscopic scale by the presence of intrafolial crenulations of S_2 sillimanite (Giles, 2000). S_3 is also manifested by crenulation of the composite S_1/S_2 fabric in garnet-biotite-rich zones along the margin of the Core Amphibolite (Table 3.1).

Biotite is typically folded about open crenulations, whereas in the hinges of tight S_3 crenulations, it displays evidence of syn- to post-kinematic recrystallisation. These relationships suggest that biotite recrystallisation was strain-dependent, and/or was facilitated by a syn- to post-D_3 fluid phase (Giles, 2000). Texturally destructive replacement of K-feldspar, and crenulated S_2 sillimanite, by randomly oriented coarse-grained muscovite also occurred in zones of high D_3 strain (op. cit.). Curvilinear inclusion trails in the muscovite preserve the crenulated S_3 fabric. The textural evidence suggests that muscovite statically overgrew S_3 crenulations and therefore, replacement of sillimanite and K-feldspar by the latter mineral occurred syn- to post-D_3 (op. cit.).

3.3.5 D_4

A fourth generation of deformation (D_4) is recognised by broad open, upright folds (F_4) with no axial planar fabric (Table 3.1). Due to the lack of easily recognisable mesoscopic D_4 structures in drill core, F_4 folding has largely been inferred from variations in the orientation of S_3 fabrics and F_3 axial surfaces. D_4 is analogous to Gray (1994) and Sheehan's (1994) D_3, and D_{F2} of Giles (2000), and is interpreted to represent the last recognisable ductile event at Cannington. This is likely to be equivalent to the region D_3 event. F_4 orientations range from east-west trending, shallowly south to south-southwest plunging, to northeast trending, moderately to steeply southeast plunging fold sets (Sheehan, 1994; Giles, 2000). However, the average trend of F_4 fold hinges plunge moderately to the south (Fig. 3.12).

3.3.6 D_5

Two generations of faulting (D_{5a} and D_{5b}) displace all pre-existing structural elements and host rocks, including ore lenses. This brittle deformation event is equivalent to Gray and Sheehan's D_4 and the "Faulting" events of Giles (2000). Locally developed subvertical to steeply west dipping, north-northeast striking faults with curviplanar surfaces characterise the earlier D_{5a} event. The faults are locally developed and are most prolific in the Southern Zone, where they occur as series of irregular, anastomosing narrow structures concentrated in a north-northeast trending zone up to 150m wide forming the Brolga Fault Zone (Fig. 3.2, 3.12 and 3.13). Brecciation and intense fracturing with associated quartz-carbonate-chlorite-pyrite-marcasite alteration, and carbonate-quartz (sulphide) veins with obvious open–space filling textures (Fig. 3.11d; Table 3.1) is common within the fault zone. Healing of faults by intense silicification is also common (Walters, 1994a; McCarthy, 1996; Walters and Bailey; 1998; Giles, 2000). The Brolga Fault Zone appears to have an apparent reverse sense of movement, but degrees of displacement are not well constrained (Gray, 1994; Sheehan, 1994; Giles, 2000). Variability in interpreted displacements highlight the complexity of the Brolga Fault Zone; a complexity

possibly attributed to:

- a strike-slip component of movement (defined by subhorizontal chlorite slickensides on fault surfaces) that occurred either during D_{5a}, or to subsequent reactivation during D_{5b} (cf. Sheehan, 1994);
- interference by later D_{5b} fault offsets combined with pre-existing structural complications involving fold interference between F_3 and F_4 resulting in a chaotic series of fault bounded blocks.

D_{5b} consists of major northwest striking, steeply northeast dipping, and subordinate northeast striking, steeply northwest dipping faults. Subhorizontal chlorite slickensides on fault surfaces, indicate sinistral strike-slip displacements on northwest striking faults and dextral displacements on northeast striking faults. The Trepell and Hamilton Faults are the most prominent northwest striking faults in the mine area (Fig. 3.2). The Trepell Fault is up to 60m wide, whereas the Hamilton Fault is up to 40m wide. Both are characterised by polymict breccia zones infilled with chlorite-clay (± carbonate, pyrite-marcasite) gouge and rock flour (Fig. 3.11e). Angular clasts are dominated by various host rock and in cases, ore types. Quartz-carbonate-pyrite/marcasite (± base-metal sulphide) veining and strong texturally destructive, silica- chlorite-carbonate alteration occurred within the faults and in adjacent zones of intense fracturing (cf. McCarthy, 1996).

Smaller northeast trending D_{5b} faults occur between the Trepell and Hamilton Faults in the Southern Zone and are less common in the Northern Zone. Examples include the Penguin, Bustard and Gannet faults, amongst others (Figs. 3.2, 3.12 and 3.13). In the Southern Zone, the faults tend to be regularly spaced (~30–50m apart) and range in width from centimetres to several metres. They generally have a similar morphology to the major northwest trending faults, but display a greater range in styles, from breccia zones infilled with chlorite-clay (± carbonate) gouge, to narrow anastomosing faults with polished and slickensided surfaces (Giles, 2000), to zones of intense fracturing and broken ground. They also tend to be more open, dilatant-type structures locally. For example:

- in underground exposures cavernous openings lined with euhedral carbonate-pyrite-marcasite are up to 70cm wide and extend for several tens of metres along the fault plane, e.g. the FOY (Fountain of Youth) Fault; and
- within and adjacent to faults abundant quartz-carbonate-pyrite-marcasite (± base-metal sulphides, fluorite) veins are dominated by classic, open-space filling textures, such as vughs and crustiform banding, and breccias healed by vuggy carbonate-quartz (Fig. 3.11f).

Silica-chlorite-carbonate alteration of adjacent wall rocks is common, although in detail alteration assemblages vary depending upon the composition of the adjacent ore type (Walters, 1994a; Bodon, 1995, 1998; McCarthy, 1996).

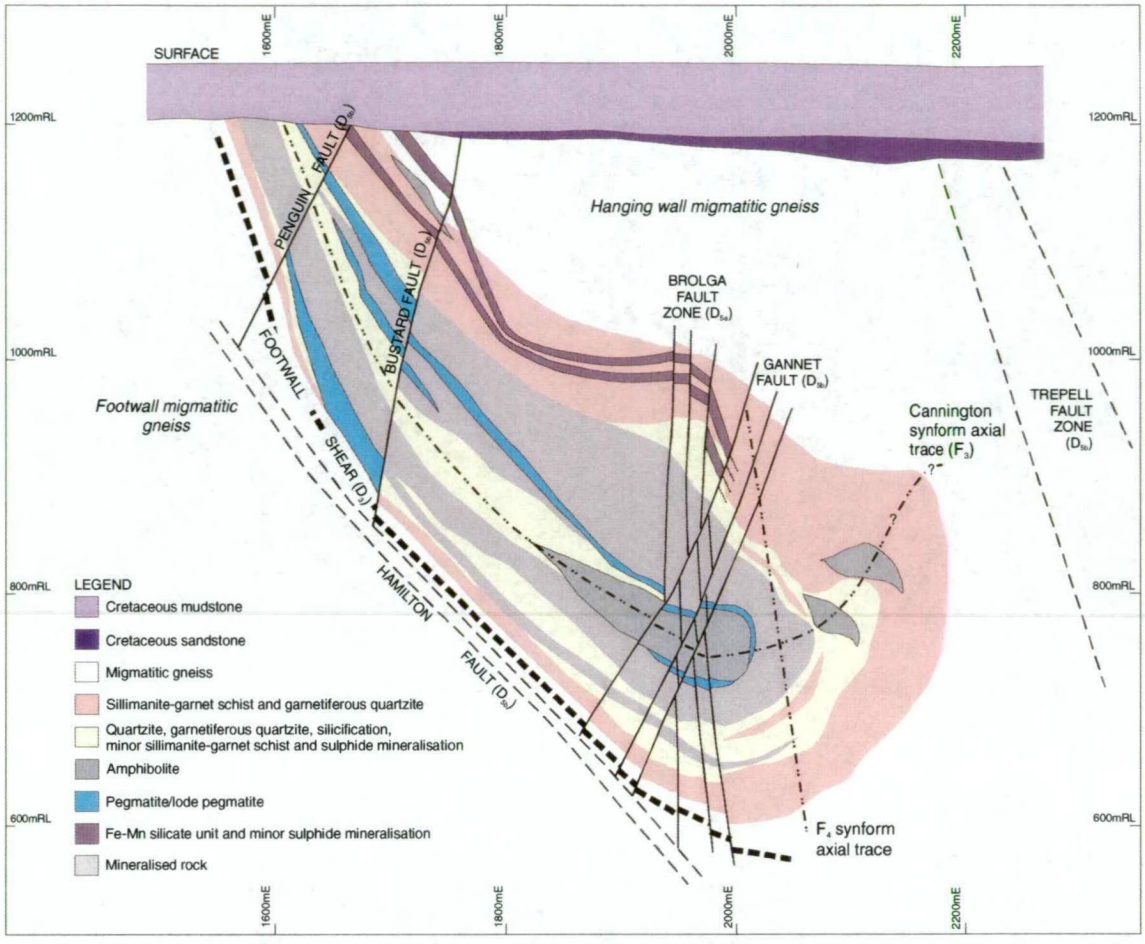

Figure 3.12 Interpretive 4700mN cross section of the Southern zone displaying the major structural elements controlling the geometry of the Cannington deposit using the deformational framework of Giles (2000). Diagram modified after Bailey (1998).

Orientations and displacements on the D_{5b} fault sets are consistent with a conjugate set geometry (Gray, 1994; Sheehan, 1994; Giles, 2000). It is envisaged that sinistral movement along the Trepell and Hamilton Faults resulted in the development of second order, northeast trending, dextral faults (op. cit.).

3.3.7 Macroscopic geometry

No D_i and D_1 macrostructures have been identified and it is possible that these events had little effect on the macroscopic geometry of the deposit. Gray (1994), using vergence relationships between early mineral fabrics and compositional banding, tentatively proposed that the deposit was located on the easterly dipping limb of a larger, regional-scale F_1 antiform (equivalent to F_z in Giles (2000) and F_2 in this study). The lack of clear evidence for macroscopic F_2 folding within the confines of the mine area implies that D_2 structures also had little influence on the geometry of the deposit.

Early structural studies identified a macroscopic isoclinal synform that plunged shallowly to the south-southwest (Gray, 1994; Sheehan, 1994; Giles, 2000) and was referred to as the Cannington Synform (Bodon, 1998). The fold geometry explained the gross repetition of ore types and host rocks in the Southern Zone, invoking a moderate, easterly-inclined axial surface through the centre of the Core Amphibolite (Fig. 3.12). A D_2 timing was inferred based on the

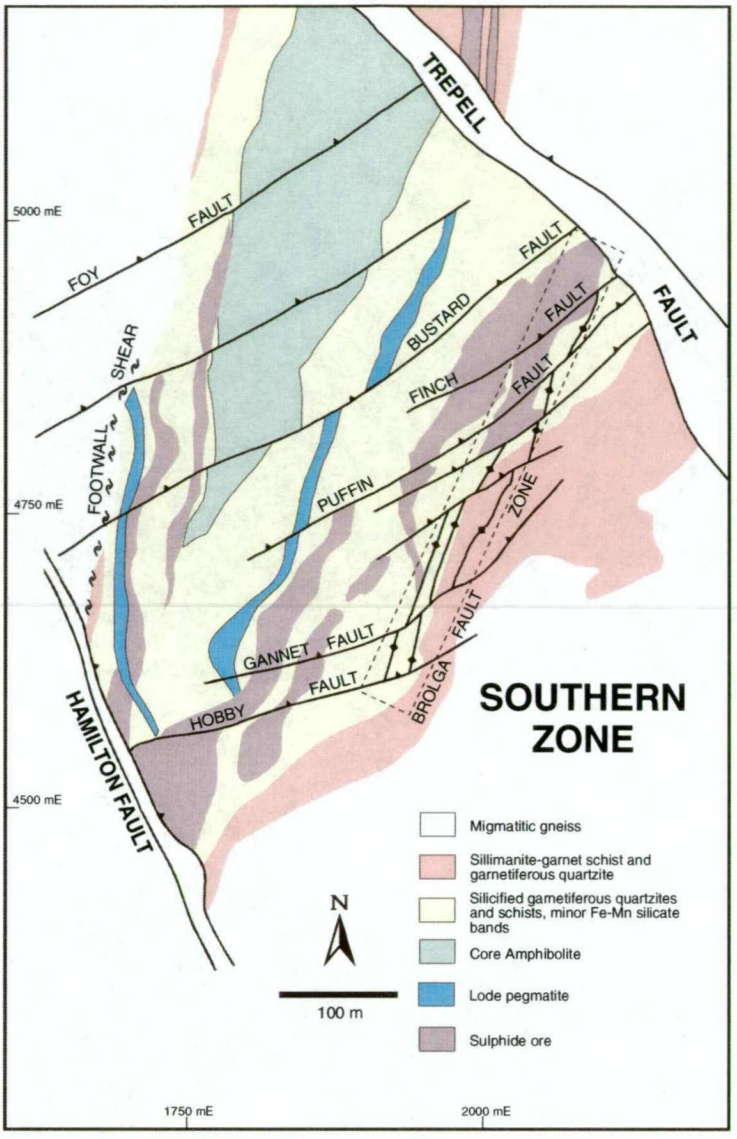

Figure 3.13 Interpreted Southern zone geology and geometry of D_{5a} (the Brolga fault zone), and conjugate D_{5b} northwest and northeast trending faults on the 900m mine RL approximately 350m below surface (modified after Bailey, 1998).

apparent axial planar orientation of the dominant S_2 fabric (analogous to S_2 in this study; op. cit.). However, other workers recognised that the S_2 fabric (S_2 in this study) was folded about the hinge of the Cannington Synform, implying that the fold was in fact a later generation, F_3 structure (Bodon, 1995; Giles, 2000). The consistent axial planar orientation of the S_3 fabric to the synform provided unequivocal evidence for a D_3 timing (Giles, 2000). It is now clear that macroscopic D_3 structures are the dominant influences on the geometry of the deposit.

The Cannington synform has a rounded, thickened hinge zone and attenuated limbs, with an "...arcuate axial surface that varies from steeply east dipping in the southern and western parts of the Southern Zone, to flat-lying or shallowly west dipping in the eastern parts of the Northern zone" (Giles, 2000). In the southern area of the Southern Zone, the host sequence and high grade ore lenses in the lower limb are progressively attenuated and truncated by the Footwall Shear (op. cit.; Fig. 3.12 and 3.13). Intensification of S_3 and development of a differentiated S_3 shear fabric as the shear is approached indicates that the Footwall Shear is a major third generation structure (Giles, 2000). The temporal and geometrical relationships between the

shear and the Cannington Synform are consistent with a fold-thrust pair (Giles, 2000). The Cannington Synform therefore represents "...an east or southeast vergent thrust propagation fold that has been rotated into a synformal orientation by later folding," although an original synformal closure is possible (op. cit.). Unfortunately, shear sense indicators in the Footwall Shear are masked by later pervasive silica-chlorite-carbonate alteration and intense fracturing associated with late stage brittle reactivation (Walters, 1994a; Giles, 2000). Given the present geometries, a normal sense of shear would be expected (Giles, 2000).

A possible macroscopic southeast plunging, open synform with a steep easterly dipping axial surface was initially proposed to explain apparent thickening of ore lenses in the structural hanging wall toward the hinge of the Cannington Synform, especially in the Northern Zone (Bodon, 1995). This was mainly based on circumstantial evidence collected from correlation of ore type lenses, and angles between compositional banding and the drill core axis. Ensuing structural studies confirmed the existence of this structure (Giles, 2000). Giles (2000) recognised that the synform folded earlier, pre-existing fabrics and the axial surface of the F_3 Cannington Synform, indicating a D_4 age.

The macroscopic F_4 synform intersects the host sequence north of about 4700mN and is characterised by a moderately east dipping western limb and a shallowly west dipping eastern limb with a broad, open hinge zone that plunges shallowly to the south (Giles, 2000; Fig. 3.12). The majority of the Southern Zone ore lenses occur on the western limb of the F_4 synform. Moving north, the axial trace of the F_4 fold progressively tracks across the Cannington Synform at a low angle resulting in ore lenses of the Northern Zone mainly occurring within the broad hinge region and eastern limb of the F_4 synform. Given the southerly plunge of the Cannington and F_4 synforms, as well as their sub-coaxial geometries, the host sequence appears as a large inverted U-shaped fold interference pattern at the Cretaceous palaeosurface between about 5900mN and 6100mN when looking north (Fig. 3.14).

D_5 faults further complicate the detailed distribution of ore types, especially in the region of the Brolga Fault Zone (ibid.; Figs. 3.13 and 3.14). The Trepell Fault (D_{5b}) is particularly significant as it displaces the Northern Zone by ~300m to the northwest (Giles, 2000). The Hamilton Fault has a similar sinistral strike-slip displacement of possibly 300m (Giles, 2000), and truncates the southern extension of the orebody and Footwall Shear (Fig. 3.13). As a result, a large portion of high grade ore and probable lower grade lateral equivalents have been displaced, presumably to the southeast, given the relative movement direction along the Hamilton Fault. However, exploration drilling and geophysical work to the south has been unsuccessful in locating this portion of the orebody. It is clear that the Hamilton Fault has had a significant effect on the geometry of the deposit, as well as on potential ore reserves. Numerous smaller northeast trending D_{5b} faults with dextral displacements in the order of metres to tens of metres locally offset ore lenses in the Southern Zone. On a deposit-scale, however, they do not significantly modify the macroscopic geometry of the deposit.

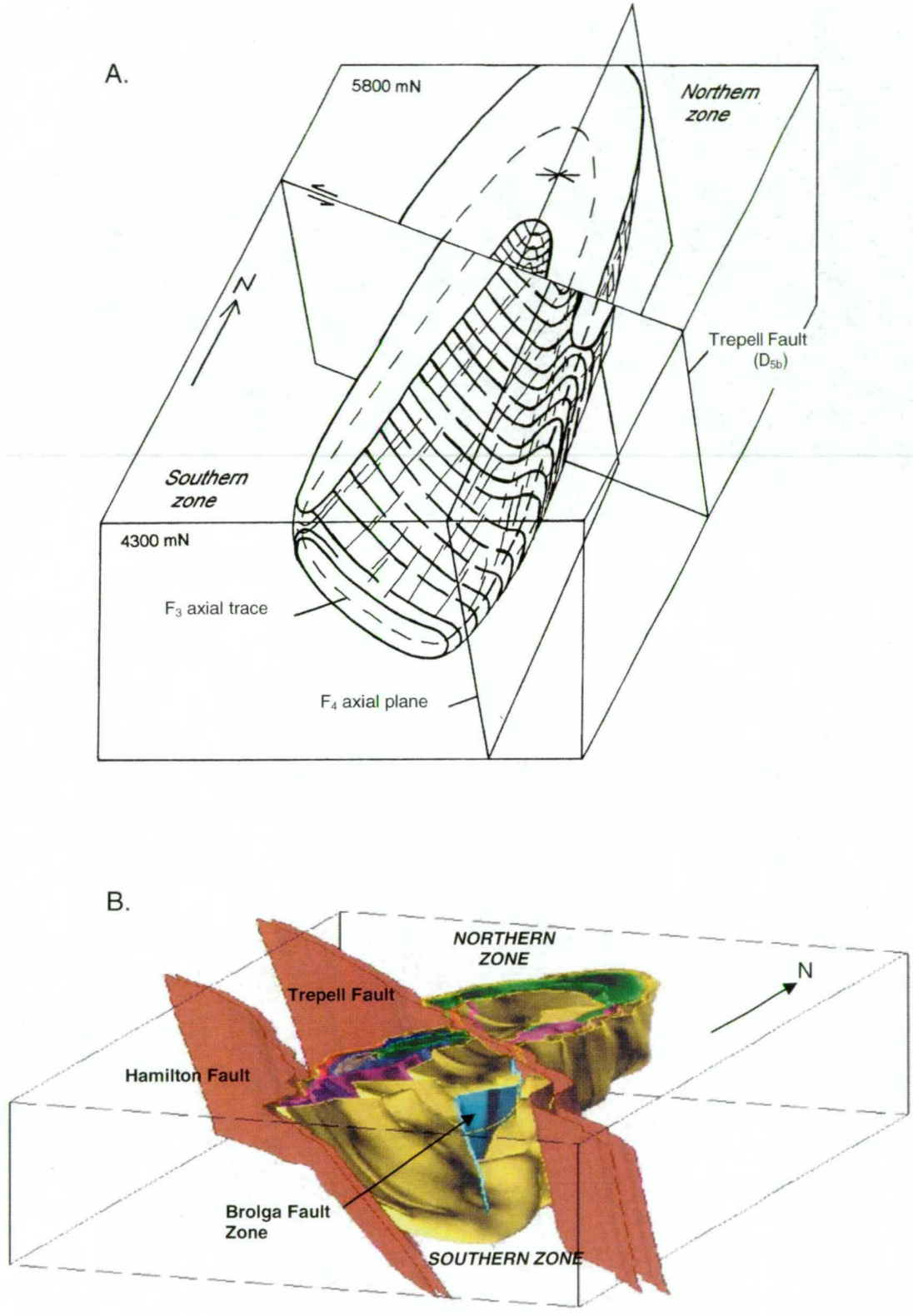

Figure 3.14 Three dimensional geometry of the Cannington deposit. **A.** schematic block diagram illustrating the main structural elements that control the macroscopic geometry (modified after Bodon, 1995; Giles, 1997). **B.** rendered surface model using the gOcad software package (modified from the Australian Crustal Research Centre web site, Monash University, 2000). The yellow surface depicts the limits of the garnetiferous alteration halo. The green surface represents the Core Amphibolite, and the purple, blue and red surfaces, various ore lenses.

3.4 METAMORPHIC HISTORY

Giles (2000) recognised that the host sequence at Cannington has experienced three periods of metamorphism (M_1, M_2 and M_3), two of which, M_1 and M_2, were temporally related to D_1 and D_2 fabric forming and destroying episodes of deformation respectively (section 3.3). Using a combination of phase equilibria for various key mineral assemblages and limited semiquantitative garnet-hornblende geothermometry, these periods collectively defined an anti-clockwise, low pressure-high temperature metamorphic P-T-t path (Fig. 3.15). Estimated P-T conditions for the subsequent periods of metamorphism (M_1 to M_3) are summarised forthwith.

3.4.1 The initial prograde path

Sillimanite porphyroblasts with cores of coarse grained muscovite in some garnetiferous rocks are morphologically similar to andalusite porphyroblasts with sillimanite beards found in the andalusite to sillimanite transition zone elsewhere in the region. On this basis, Giles (2000) considered that they were originally porphyroblasts of andalusite, or sillimanite after andalusite that were overgrown by later, second generation sillimanite. Subsequent retrogression of the cores to coarse-grained muscovite was attributed to post-D_3 retrogression. These features suggest that the initial M_1 prograde path passed through the andalusite stability field at pressures below 4kbars (op. cit.).

3.4.2 M_1 – peak metamorphism

Peak metamorphism (M_1) is characterised by the development of granoblastic textures and porphyroblastic garnet growth in all host rock types. Textural evidence indicates that extensive partial melting was synchronous with the development of a sillimanite-biotite fabric (S_1) in the gneiss host sequence (section 3.3.2). In garnetiferous rocks peak metamorphic assemblages are dominated by quartz-K-feldspar-sillimanite-biotite-garnet and rare gahnite, graphite and apatite, whereas in the Core Amphibolite they are dominated by hornblende-plagioclase, with minor biotite, quartz and ilmenite, and rare garnet. Overall, the peak metamorphic assemblages are consistent with upper amphibolite facies metamorphism (Yardley, 1989; Spear, 1993).

Using phase equilibria and semiquantitative garnet-biotite geothermometry from migmatitic gneiss and amphibolite, Mark (1993) and Mark et al. (1998) estimated peak metamorphic conditions of 665–690°C and 4–6kbars. Giles (2000) estimated similar conditions of ~650-700°C and ~4kbars using petrogenetic constraints for M_1 mineral assemblages in the migmatitic gneiss, garnetiferous rocks and the Core Amphibolite, as well as garnet–hornblende geothermometry (Graham and Powell, 1984) on the Core Amphibolite. Similarly, the estimates are comparable to those of Jaques et al. (1982), who determined peak metamorphic conditions of 600–680°C and ~4kbars from exposed amphibolites and partially melted metapelites ~10km north of Cannington using a combination of experimentally determined mineral equilibria and cation exchange thermobarometry, e.g. garnet-biotite (Ferry and Spear, 1978) and plagioclase-hornblende (modified after Spear, 1980) geothermometry, and clinopyroxene-quartz-plagioclase geobarometry (Ellis, 1980). However, rare porphyroblastic clinopyroxene restricted to

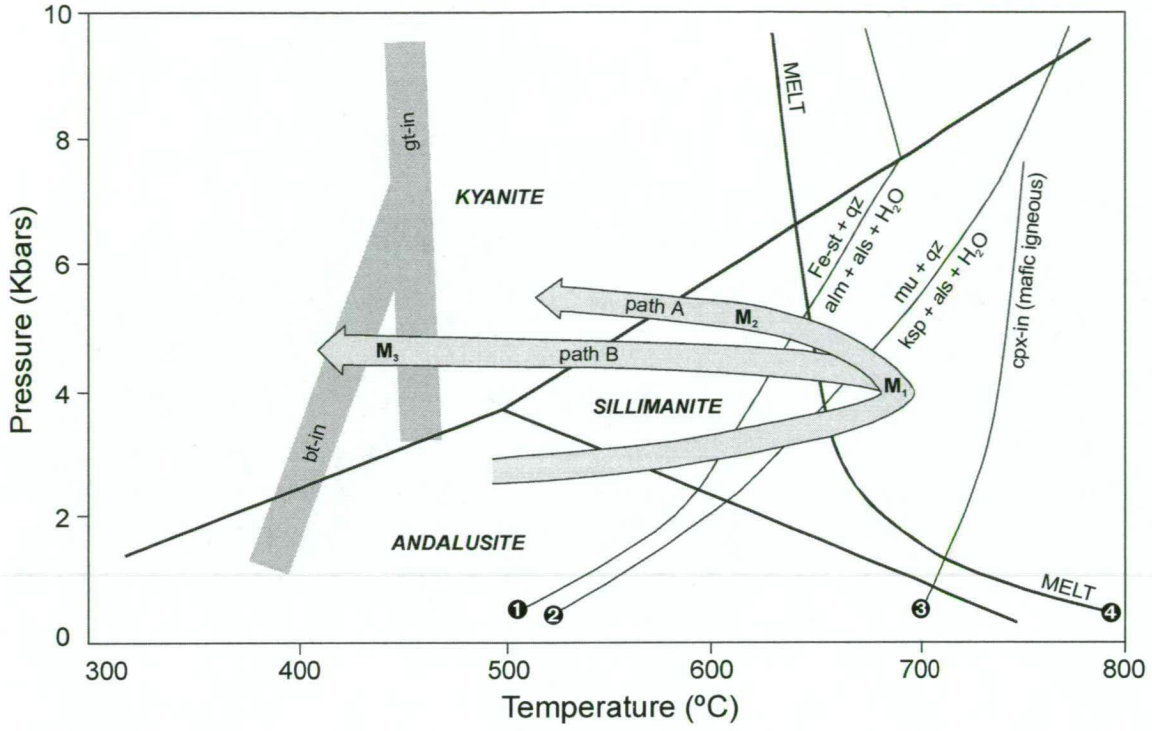

Figure 3.15 P-T diagram illustrating estimated conditions for the metamorphic events recognised at Cannington (modified after Giles, 2000). M_1 and M_2 are part of the same anticlockwise P-T-t metamorphic event (path A), whereas M_3 could either fall on the same path or be related to a discrete thermal pulse. The latter is supported by the temporal relationship between M_3 and D_3, as well as later biotite recrystallisation. Thermochronological evidence suggests that M_3 was synchronous with the emplacement of the Williams and Naraku batholith (see Fig. 3.17). Abbreviations: alm—almandine, als—aluminosilicate, bt—biotite, Fe-st—Fe-rich staurolite, gt—garnet, ksp—K-feldspar, mu—muscovite, q—quartz. Data sources for curves: 1—Yardley (1981), 2—Chatterjee and Johannes (1974), 3—Spear (1981) experimentally determined at fO_2 conditions equivalent to the hematite-magnetite buffer, 4—wet melting curve for common granite after Luth et al. (1964), aluminosilicate phase boundaries after Holdaway (1971). Large grey lines represent the approximate conditions of the biotite and garnet isograds.

selvedges adjacent to small clinopyroxene-bearing pegmatites in the Core Amphibolite, suggests that conditions were locally high enough to initiate hornblende breakdown via the reaction:

$$\text{hornblende} + \text{quartz} \leftrightharpoons \text{clinopyroxene} + \text{plagioclase} + H_2O \qquad 3.1$$

This reaction is characteristic of transitional upper amphibolite to granulite facies conditions (Yardley, 1989; Spear, 1993). However, the conditions under which hornblende commences to break down to clinopyroxene are variable and dependent on the bulk composition of the metabasite (Spear, 1993). From experimental studies the presence of quartz tends to lower the stability limit of hornblende under fO_2 conditions defined by the hematite-magnetite buffer (Spear et al., 1991; Fig. 3.15). In contrast, hornblende stability is enhanced in quartz undersaturated metabasics under more reduced conditions defined by the quartz-fayalite-magnetite buffer. A decrease in P_{H2O}, or introduction of a CO_2-rich fluid, may also drive reaction 3.1 to the right (Spear, 1993). The lack of quartz in the Core Amphibolite may indicate that peak metamorphic temperatures approached 800°C, at least on a spatially restricted scale. The absence of orthopyroxene in the assemblage provides an upper limit of ~820°C at 3-4kbars (Spear, 1993).

3.4.2.1 Partial melting of the host gneiss

Mark et al. (1998) ascribed leucocratic segregations in the gneiss to *in situ* partial melting of predominantly muscovite-rich units (67-75% partial melting) within a metasedimentary protolith that had overall experienced <10% partial melting during peak metamorphism. Enveloping biotite-sillimanite-rich melanocratic layers were interpreted as the residual product of the partial melting process. In typical metasediments, the breakdown of muscovite and quartz to sillimanite and K-feldspar during prograde metamorphism liberates H_2O that under P-T conditions in excess of the wet solidus of common granite (i.e. upper amphibolite facies) facilitates partial melting (Yardley, 1989; Spear, 1993). Peak metamorphic conditions at Cannington were in excess of the wet melting curve of common granite (Fig. 3.14). The amount of melt produced is directly proportional to the amount of H_2O available via muscovite dehydration (Spear, 1993). The absence of peak metamorphic muscovite in the gneiss is consistent with such dehydration and indicates that the rock is essentially "dry", i.e. all muscovite has been consumed (cf. Spear, 1993).

3.4.3 M_2 – retrograde secondary sillimanite

M_2 is characterised by sillimanite filled microshears (i.e. Type B S_2 fabrics) that overprint M_1 leucocratic segregations, granoblastic textures, truncate pre-existing mineral grain boundaries and displace garnet and gahnite porphyroblasts. Incipient replacement of M_1 K-feldspar, biotite, quartz and garnet by secondary sillimanite is intrinsic to M_2. These disequilibrium features suggest that secondary sillimanite did not form via typical prograde dehydration reactions but by some other process that occurred after peak metamorphism, syn-D_2. Giles (2000) attributed the formation of secondary sillimanite "alteration" to the interaction of pre-existing M_1 assemblages with a syn-D_2 fluid phase that exploited D_2 microshears and existing grain boundaries in the granoblastic matrix. Replacement of pre-existing minerals by secondary sillimanite probably involved reactions such as:

$$2\text{K-feldspar} + 2HCl^- \leftrightharpoons \text{sillimanite} + 5SiO_2 + 2KCl^- + H_2O \quad 3.2$$

$$2\text{biotite} + 14HCl^- \leftrightharpoons \text{sillimanite} + 5SiO_2 + 2KCl^- + 6(Fe,Mg)Cl_2^{-2}{}_{(aq)} + 9H_2O \quad 3.3$$

$$\text{garnet} + 2\text{biotite} + 16HCl^- \leftrightharpoons \text{sillimanite} + 6SiO_2 + 2KCl^- + 7(Fe, Mg)Cl_2^{-2}{}_{(aq)} + 10H_2O \quad 3.4$$

The reactions indicate that sillimanite stability is controlled by the pH of the fluid as well as the $a_{K+/H+}$. An acidic fluid with low $a_{K+/H+}$ will promote sillimanite alteration. Sillimanite may also form by the breakdown of muscovite and quartz via the reaction:

$$\text{muscovite} + \text{quartz} \leftrightharpoons \text{sillimanite} + \text{K-feldspar} + H_2O \quad 3.5$$

However, this dehydration reaction is typical of prograde metamorphism, and the lack of muscovite in the peak metamorphic assemblage suggests it was not a member of the reactant phases during retrograde events. The absence of secondary Fe-Mg and K-bearing phases, and the abundance of dissolution textures, suggests that secondary sillimanite alteration resulted in an overall reduction in the number of components (Giles, 2000). This process is essentially analogous to a high temperature form of base-cation leaching (Vernon, 1979; Ahmad and

Wilson, 1982; Vernon et al., 1987; Giles, 2000), i.e. leaching of Fe^{+2}, Mg^{+2} and K^{+}, and transport most likely as aqueous chloride complexes (reactions 3.2 to 3.4). The removal of more soluble cations drives reactions 3.2 to 3.4 to the right, resulting in further sillimanite precipitation in a zone of overall volume loss, until all Al-bearing phases are consumed or fluid-flow ceases. In this respect, the formation of Type B S_2 shear fabrics can be likened to a high temperature pressure dissolution (Wintsch and Andrews, 1988; Giles, 2000). The reactions also suggest that silica may precipitate as quartz or remain in solution. Giles (2000) argued that minor quartz-filled extensional veins accounted for a relatively minor amount of silica precipitation and that the majority of silica appears to have been removed from the system. However, diffuse zones of silicification in garnetiferous rocks adjacent to and within the orebody (section 3.2.3.2) may represent neighbouring areas where much of the silica was precipitated during M_2.

P-T conditions during M_2 cannot be constrained accurately because fibrolitic sillimanite stability spans a wide range of pressures and temperatures. A lower limit of ~500°C can be implied from the sillimanite stability field at the aluminosilicate triple point. This can be further constrained by the absence of retrograde staurolite that, in general terms, has an upper stability limit of ~600-650°C between 3-6kbars respectively (Fig. 3.15). The lack of partial melting during M_2 provides an upper constraint on temperatures, below the wet solidus of common granite, i.e. ~650°C at 4kbars (Fig. 3.15). These constraints infer that conditions during M_2 ranged between ~600-650°C and 3-6kbars (Giles, 2000).

3.4.4 M_3 – retrograde muscovite

M_3 is characterised by post-D_3 biotite recrystallisation in the hinges of tight F_3 crenulations and retrogression of pre-existing biotite, K-feldspar and both generations of sillimanite to coarse-grained muscovite. Muscovite commonly overgrows pre-existing fabrics defined by sillimanite, but itself does not display any preferred orientation, suggesting static growth mainly post-D_3. It likely that muscovite retrogression of sillimanite and K-feldspar was facilitated by a fluid phase via the reactions:

$$3\text{sillimanite} + 3\text{quartz} + 2KCl^{-} + 3H_2O \leftrightharpoons 2\text{muscovite} + 2HCl^{-} \qquad 3.6$$

$$\text{sillimanite} + \text{K-feldspar} + H_2O \leftrightharpoons \text{muscovite} + \text{quartz} \qquad 3.7$$

Reaction 3.6 indicates that muscovite retrogression requires the addition of $K^{+}_{(aq)}$ by a near neutral fluid in the absence of a pre-existing K-bearing phase, i.e. a fluid with a high $a_{K+/H+}$. Rewriting the reaction to include K-feldspar indicates that just the mere presence of a near-neutral fluid will promote muscovite retrogression (reaction 3.7). The latter is more realistic given the abundance of K-feldspar in the gneiss and garnetiferous rocks. Indeed, metamorphic petrologists regard reaction 3.7 as a common, rock buffered retrograde reaction in metasediments (Yardley, 1989; Spear, 1993). The selective replacement of secondary sillimanite filled microshears (i.e. Type S_2 fabrics) by retrograde muscovite suggests that fluid-flow was focussed along pre-existing zones of high strain (Giles, 2000). This is also supported by the occurrence of recrystallised biotite that is restricted to tight S_3 crenulations in contrast to more open crenulations. The textural and mineralogical relationships therefore imply the

involvement of a late- to post-D_3 neutral fluid that exploited pre-existing zones of high strain; both S_2 microshears and S_3 tight crenulations.

P-T conditions during M_3 are constrained by the lower stability limit of biotite and the upper stability limit of muscovite, i.e. between ~400-600°C at 3kbars. An additional constraint is provided by the existence of rare kyanite associated with retrograde muscovite. Giles (2000) considered that M_3 occurred after P-T conditions had entered the kyanite stability field based on the observation that kyanite contains aligned inclusions of sillimanite needles and is intergrown with retrograde muscovite. The presence of kyanite merely infers pressures were >3kbars. Based solely on these petrogenetic constraints, P-T conditions during M_3 are broadly constrained to ~400-600°C and >3kbars (Fig. 3.15).

Giles (2000) argued that M_3 was related to a discrete thermal event separate from M_1/M_2. This was largely based on three lines of evidence. Firstly, the spatially restricted character of static biotite recrystallisation (to tight S_3 crenulations) suggested that M_3 was of insufficient intensity and/or duration for pervasive recrystallisation to occur. Secondly, static growth of coarse-grained retrograde muscovite in metasediments external to the Cannington deposit increased in abundance toward the Williams and Naraku batholiths, suggesting a temporal and/or genetic link with late orogenic plutonism. Lastly, $^{40}Ar/^{39}Ar$ age determinations from amphiboles and muscovite correlated with the age of granite emplacement ca. 1520-1480 Ma (Perkins and Wyborn, 1998; section 3.4.6).

3.4.5 Source of retrograde fluids

Giles (2000) argued that the acidic M_2 fluid may have been sourced from the lower parts of the migmatitic zone via dehydration reactions related to partial melting during M_1. It was envisaged that fluids in equilibrium with crystallising partial melts of granitic composition in the lower part of the metamorphic pile were sufficiently enriched in CO_2 to cause separation of a CO_2-rich immiscible phase into which HCl was selectively partitioned (cf. Spear, 1993). The fluid was then channelled through a crustal-scale shear zone (the Maramungee Shear Zone) to higher parts of the metamorphic pile where it was focused through anastomosing S_2 microshears. Interaction with pre-existing mineral assemblages resulted in sillimanite alteration and formation of Type B S_2 shear fabrics. Water/rock ratios must have remained high enough to maintain fluid-buffered conditions during M_2, i.e. maintain disequilibrium between the rock and the fluid so that base-cation leaching and secondary sillimanite alteration could proceed. Because the fluid was considered to have been derived during M_1 partial melting, M_2 must have occurred shortly after peak metamorphism with P-T conditions remaining high enough to stabilise secondary sillimanite, i.e. >500°C. It is therefore possible that both M_1 and M_2 were related to the same thermal event (Giles, 2000).

It has been proposed that M_3 was essentially synchronous with the emplacement of the Williams and Naraku batholiths, so M_3 retrograde fluids may have had a magmatic origin (Giles, 2000). However, Spear (1993) noted that metamorphic fluid compositions are dynamic during

progressive metamorphism, so the fluids may also have had a metamorphic source. From reactions 3.2 to 3.4, the M_2 acidic fluid will become more alkaline, and the $a_{(K+\backslash H+)}$ will increase as reactions progress. In addition, cooling may have facilitated the production of late-stage retrograde muscovite, and secondary biotite, quartz, K-feldspar, i.e. the reverse of reactions 3.1 to 3.4. Retrograde staurolite and garnet may even have precipitated, but are of no consequence at Cannington, as they do not occur as retrograde phases. It is more likely that muscovite formed via reaction 3.7 (Spear, 1993). A scenario can be envisaged for M_3 in which plutonism caused a localised, transient thermal pulse, thereby initiating proximal hydrothermal cells of 'evolved' metamorphic fluids. Fluid-flow appears to have been facilitated by pre-existing zones of high strain, as evidenced by the selective replacement of secondary sillimanite in D_2 microshears (Type B S_2 fabrics) and in the hinges of tight S_3 crenulations (Spears, 1993; Giles, 2000).

3.4.6 Age of metamorphism and thermal history: U-Pb SHRIMP geochronology and $^{40}Ar/^{39}Ar$ thermochronology

A minimum age for M_1 of 1575±36 Ma and 1590±15 Ma was determined from U-Pb SHRIMP analyses of overgrowth rims on zircons from migmatitic gneiss and a single pegmatite sample (Giles and MacCready, 1997; Giles, 2000). The accuracy of these determinations was confirmed by U-Pb monazite ages from the same samples (ca. 1585 to 1578 Ma) and from interpreted metamorphic zircons from the Core Amphibolite (1578±7 Ma; op. cit.). The data indicate that M_1 occurred between ca. 1590 to 1580 Ma (Fig. 3.16). An age for M_2 was not determined, but based on the previous discussion (section 3.4.5), secondary sillimanite alteration appears to represent an early high temperature retrograde stage that occurred just after peak metamorphism (M_1) and was therefore related to the same thermal event.

$^{40}Ar/^{39}Ar$ thermochronology provides a method of quantitatively constraining the age and temperature of successive cooling stages and defining possible thermal events subsequent to peak metamorphism ca. 1580 Ma. Step heating experiments on various K-bearing minerals such as hornblende, biotite, muscovite and K-feldspar from samples of amphibolite (Core Amphibolite), pegmatite, gneiss and hedenbergite-garnet rich ore yielded cooling ages ranging between ~1510-640 Ma. Peak metamorphic ages of ca. 1580 Ma were not recorded in any of the samples possibly indicating that $^{40}Ar/^{39}Ar$ systematics were reset during a post-M1 thermal event.

Of particular relevance were $^{40}Ar/^{39}Ar$ age populations that emphasise two discrete thermal peaks between 1510-1440 Ma that post-dated M_1. The first of these was defined by ca. 1510 Ma ages determined from hornblendes in the Core Amphibolite and hedenbergite-garnet-rich ore. Based on the closure temperatures for the hornblendes, peak temperatures for the thermal event ranged between ~400-550°C (Fig. 3.16). The second thermal pulse occurred ca. 1440 Ma, and based upon estimated closure temperatures for hornblende and biotite, was less intense than M_3 at ~300°C (Fig. 3.16).

Giles (2000) argued that the 1510 Ma event correlated with M_3 based on textural evidence that implied M_3 was related to a discrete, transient thermal pulse broadly synchronous with intrusion of the Williams and Naraku batholiths (1520-1480 Ma; section 3.4.4). Ages of ca. 1490 Ma and closure temperatures of ~300-350°C for muscovite and biotite from pegmatite samples suggest a relatively slow cooling period after the thermal peak, i.e. from ~400-550° C to ~300-350°C over a period of about 20 million years (Fig. 3.16).

The lack of pre-1510 Ma ages implies that M_3 was of sufficient intensity to reset $^{40}Ar/^{39}Ar$ systematics in hornblendes. Plutonism must have had a significant, albeit ephemeral, effect on the thermal evolution of the region (op. cit.). The data therefore provide no indication of the cooling history for M_1/M_2. However, the possible cooling history of the latter events can be inferred from other regionally based $^{40}Ar/^{39}Ar$ and U-Pb studies. Samples taken from localities distal to the granites yielded cooling ages of 1586±16 Ma (hornblendes from the ca. 1745 Ma Fort Constantine Volcanics near the Ernest Henry Cu-Au deposit; Spikings, 1999) and 1576±18 Ma (hornblendes from the ca. 1740 Ma Gin Creek Granite; Spikings, 1999). Metamorphic actinolite and biotite from the Osborne deposit yielded maximum cooling ages of ca. 1590 Ma and ca. 1568 Ma respectively (Perkins and Wyborn, 1998). It appears that these areas did not experience the resetting effects of plutonism and the ages are within error of the of the U-Pb

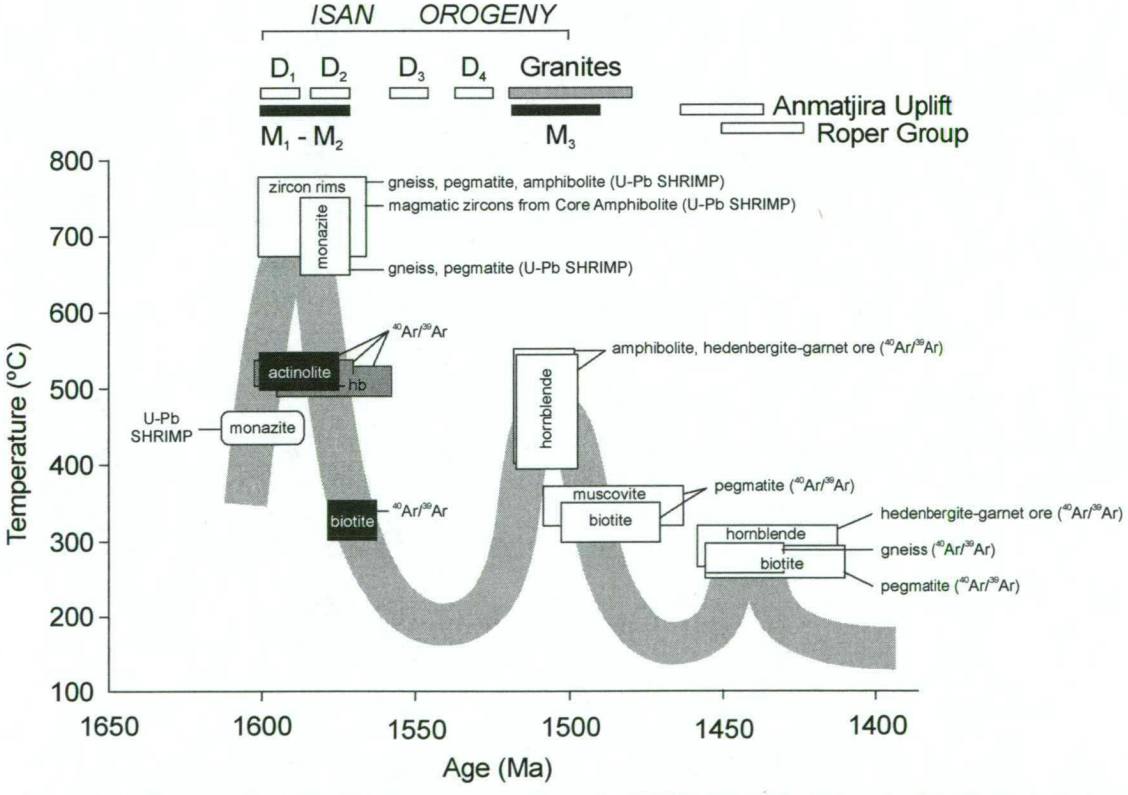

Figure 3.16 Temperature-time diagram summarising the pre-1400 Ma thermochronology for Cannington based on U-Pb SHRIMP and $^{40}Ar/^{39}Ar$ analyses (modified after Giles, 2000). $^{40}Ar/^{39}Ar$ systematics at Cannington do not record any thermal events prior to ca. 1510 Ma due to thermal resetting caused by the emplacement of the nearby Williams and Naraku batholith between 1520-1480 Ma. However, in more distal areas the $^{40}Ar/^{39}Ar$ systematics escaped thermal resetting and record the cooling history of M_1/M_2 prior to granite emplacement. The ca. 1600 Ma monazite age for M_1 (rounded box) was determined from a metasediment in the Llewellyn Creek Formation (Giles, 2000). Minerals listed in black boxes represent $^{40}Ar/^{39}Ar$ cooling ages for metamorphic actinolite and biotite from the Osborne deposit (Perkins and Wyborn, 1998), whereas those listed in grey boxes are for hornblendes from the ca 1745 Ma Fort Constantine Volcanics (near the Ernest Henry deposit) and the ca. 1740 Ma Gin Creek Granite (Spikings, 1999). Note that ages determined from hornblendes in hedenbergite-rich ores at Cannington represent maximum cooling ages rather than crystallisation ages (Giles, 2000).

ages for M_1 (ca. 1590-1580 Ma). A maximum cooling age of ca. 1568 Ma for metamorphic biotite at Osborne suggests a period of rapid cooling from estimated peak metamorphic temperatures of ~650°C to 300-350°C (the closure temperature of biotite) in <20 million years (Perkins and Wyborn, 1998; Giles, 2000; Fig. 3.16).

3.5 REGIONAL STRUCTURAL AND METAMORPHIC CORRELATIONS – THE ISAN OROGENY

Correlation between the various deformational and metamorphic events recognised in the structural domains comprising the Eastern Succession has been based on the relative timing between structural fabrics and metamorphism, in particular, peak metamorphism (Giles, 2000; Chapter 2). The presence of a schistose mineral fabric that pre-dated peak metamorphism appears to be restricted to structural domains that experienced higher grades of metamorphism, implying more complex structural histories in those regions. The apparent lack of folding related to this early event suggests that presumably (structurally) lower parts of the terrane underwent a period of very early extension prior to the Isan Orogeny (Giles, 2000). At Cannington, evidence for this early event is preserved as a relic fabric (S_i) in garnet porphyroblasts, and in the Pegmont area of the Kuridala Domain, within differentiated S_2 fabrics (op. cit.).

Subsequent to this localised period of deformation, two to three discrete metamorphic events related to the ca. 1600-1500 Ma Isan Orogeny occurred throughout the Eastern Succession (Giles, 2000). The earliest of these metamorphic events is recorded in the Snake Creek Anticline area where relationships between fabric development and porphyroblastic growth indicate a late-D_1 thermal event prior to peak metamorphism (Rubenach and Barker, 1998; Fig. 3.17).

The second of these thermal events is manifested by the preferred alignment of peak metamorphic minerals in differentiated schistosities that dominate the high grade metamorphic structural domains (i.e. the Soldiers Cap and southern Kuridala domains) and in early slaty cleavages of the lower grade structural domains (Giles, 2000). At Cannington this event corresponds to M_1/M_2 which occurred between ca. 1590-1580 Ma and correlates with the 1584±17 Ma thermal event recorded in overgrowth rims on detrital zircons in a garnetiferous gneiss (from the GDG) near Maramungee Creek ~45km to the north (Page and Sun, 1996, 1998), and with a peak metamorphic age of 1599±10 Ma determined from monazite grains in metasediments of the Llewellyn Creek Formation ~100km to the north (Giles and MacCready, 1997; Giles, 2000). $^{40}Ar/^{39}Ar$ cooling age determinations from metamorphic actinolite and biotite at the Osborne deposit (*ca.* 1590 Ma and 1568 Ma respectively; Perkins and Wyborn, 1998), and hornblendes from the Fort Constantine Volcanics near the Ernest Henry deposit and the Gin Creek Granite (ca. 1580 Ma; Spikings, 1999), are within error of the U-Pb zircon and monazite ages for M_1/M_2 at Cannington. These correlations suggest that peak metamorphism was a regional event that occurred between ca. 1600-1580 Ma. As a result, peak metamorphism can be used as a reference point for regional structural correlations (Betts et al., 1997a; Giles and MacCready, 1997; Giles, 2000: Fig. 3.17).

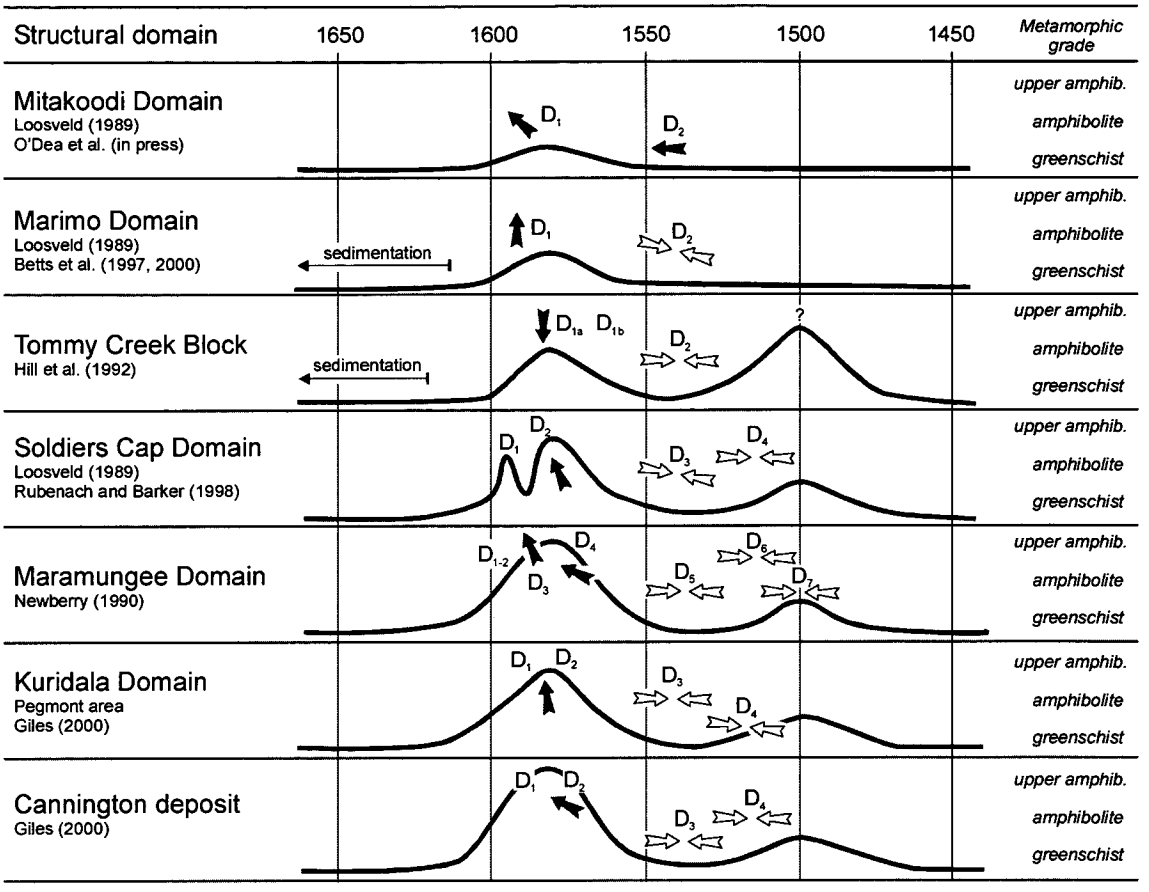

Figure 3.17 Correlation of the various structural and metamorphic events of the 1600-1500 Ma Isan Orogeny across the structural domains comprising the Eastern Succession (slightly modified after Giles, 2000). Temporal links are based on the assumption that peak metamorphism was essentially synchronous throughout the terrain and was related to a 1600-1580 Ma thermal event except for the anomalous high grade metamorphic event recognised in the Tommy Creek Block. Interpreted vergence directions during periods of "thin-skinned" thrusting and folding are indicated by the black arrows, whereas the open arrows indicate interpreted shortening directions during "thick-skinned" upright folding and faulting.

The third period of metamorphism is characterised by retrogression of peak metamorphic aluminosilicates to coarse-grained muscovite and recrystallisation of biotite in the hinges of crenulations (Giles, 2000). The thermal event is equivalent to M_3 at Cannington and was associated with a discrete, transient thermal perturbation (ca. 1510 Ma) related to the intrusion of the Williams and Naraku batholiths between ca 1520-1480 Ma (Betts et al., 1997a; Giles and MacCready, 1997; Giles, 2000).

Additional support for these correlations comes from the apparent consistency of north to northwest directed movements associated with the development of fold-thrust geometries that formed broadly synchronous with peak metamorphism (Giles and MacCready, 1997; MacCready et al., 1998; Giles, 2000) . This period of deformation (D_1) is manifested to varying degrees and structural styles in individual structural domains. Giles (2000) recognised that structures associated with this period included:

- peak metamorphic biotite-sillimanite schistosities (S_1) and differentiated S_2 fabrics at Cannington;
- high temperature mineral fabrics with shallow north to south plunging extension lineations in the Kuridala (Pegmont area) and Maramungee domains;
- the recumbent Snake Creek Anticline in the Soldiers Cap Domain;

- shear zones associated with northwest directed thrusting localised along the Overhang Shear and Cloncurry Overthrust; and
- the slaty cleavages and rare recumbent folds in the Marimo and northern Kuridala domains.

East-west shortening after peak metamorphism resulted in the development of north-south trending folds that form the dominant "structural grain" of the Eastern Succession (Betts, et al., 1997a; Giles and MacCready, 1997; Giles, 2000). Giles (2000) proposed that structures related to this event included:

- north-south trending, tight, upright folds with shallow plunges and steeply east dipping axial surfaces in the Kuridala and Marimo domains,
- the Maramungee Shear Zone and the Bulonga Thrust Maramungee Domain and Mitakoodi Culmination, where movement was related to east-west thrusting,
- the Footwall Shear and Cannington Synform (D_3) at Cannington, and similar style third generation inclined isoclinal folds in the Pegmont area of the Kuridala Domain.

However, thrusting at Cannington and in the Pegmont area was east vergent, rather than the common west vergent orientations in other domains. Collectively, these areas may represent "a zone of back thrusting in a dominantly west vergent fold and thrust terrane" (Giles, 2000).

3.6 AGE OF THE HOST SEQUENCE AND ZIRCON PROVENANCE

Two separate geochronological studies have been carried out at Cannington using U-Pb SHRIMP analysis of zircons and monazites. In order to augment a regional study of the Eastern Succession, Page and Sun (1998) analysed zircons from two migmatitic gneiss samples from the host sequence at Cannington. Giles (2000) undertook a more detailed geochronological study, preparing zircon and monazite separates from a range of host rocks including migmatitic gneiss, "garnetite" (i.e. weakly mineralised hedenbergite-garnet rock), pegmatite and amphibolite (Core Amphibolite). Results of the studies are summarised in Table 3.2 and Figure 3.17.

3.6.1 Migmatitic gneiss

All samples, except for the Core Amphibolite, contained zircons with rounded equant to sub-angular rounded morphologies consistent with a detrital heritage (Page and Sun, 1998; Giles, 2000). The gneiss samples and pegmatite also contained a variable component of rounded prismatic zircons with oscillatory zoning suggestive of a magmatic origin (op. cit.). U-Pb SHRIMP analyses highlighted a number of inherited age populations that were consistent amongst all samples, viz. (Fig. 3.18; Table 3.2):

- a large, and youngest, population between ca. 1680-1660 Ma,
- a distinct population between 1750-1700 Ma,
- a very small component of zircons aged between ca. 1850-1800 Ma,
- no zircon grains with ca. 2300-1850 Ma inherited ages,
- a small population of ca. 2600-2300 Ma inherited ages.

Table 3.2 Summary of geochronology based on U-Pb SHRIMP dates determined from zircons and monazites in various rocks from Cannington. Ages are cited in Ma.

Sample	Location	Detrital/ magmatic zircon ages	Metamorphic zircon ages	Metamorphic monazite ages	Inherited zircon ages	Discordant ages	Source
Migmatitic gneiss	6000mN section, *CAD005*	1676±5*			1715±5, 1820, 2400, 3250		Page and Sun (1996, 1998)
Altered albitic gneiss	6000mN section, *CAD005*	*ca.* 1680 (small discordant population)			1712±6 (main population), 1750-1770, 2520-2565		Page and Sun (1998)
Migmatitic gneiss	5300mN section, *CAD159*, 198.4m	1665±13*	1575±36 (M_1)	1577±5 (M_1)	1720±16, 2497±18	*ca.* 500	Giles (2000)
Pegmatite	465mRL (underground exposure), intrusive pegmatite in the Core Amphibolite	1688±9 (youngest inherited component)	1590±15 (M_1)	1578±4 (M_1)	*ca.* 1800, 2460		Giles (2000)
Core Amphibolite	400mRL (underground exposure)	1578±15 (equivalent to M_1 age)	As for magmatic zircon age			*ca.* 450	Giles (2000)
Metasomatic garnetite	4700mN section, *CAD051*, 593.0m	1674±6*, 1621±7 (partial resetting of detrital zircons)			2300-2400		Giles (2000)

* – maximum depositional age.
Drillhole numbers are listed italics.

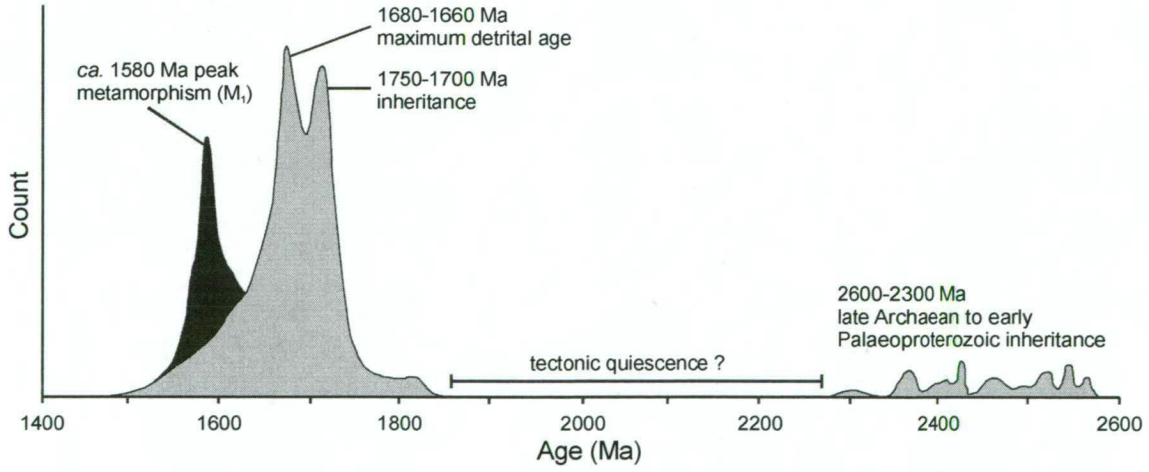

Figure 3.18 Probability plot summarising all U-Pb SHRIMP data from Cannington (after Giles, 2000). Data from Page and Sun (1998) is also included. The grey field represents zircon analyses, the dark grey field represents monazites.

Giles (2000) suggested that the inheritance patterns in the zircon analyses from samples of gneiss and pegmatite confirmed previous interpretations for a sedimentary heritage (e.g. Mark, 1993; Walters, 1994a; Bailey, 1998; Mark, et al., 1998; Walters and Bailey, 1998). Coincident ages between magmatic and detrital zircons in the migmatitic gneiss indicated that the volcanic component in the sedimentary protolith was contemporaneous (Page and Sun, 1998; Giles, 2000), and the observed prismatic morphology of the magmatic zircons provided evidence for a short residence time in the sedimentary environment, i.e. relative immaturity of the magmatic component (Giles, 2000). Maximum depositional ages (Table 3.2) are therefore very similar to the true depositional age of the sedimentary protolith (~1675 Ma; op. cit.). Coincident maximum depositional ages and similar zircon inheritance patterns between pegmatite and migmatitic gneiss confirm that pegmatitic melts were formed via partial melting of the local metasedimentary sequence during peak metamorphism (M_1) ca. 1580 Ma.

A large population of inherited zircon ages between 1750-1700 Ma suggests a significant component of detrital material was sourced from Cover Sequence 2 aged rocks (1740-1710 Ma; Page and Sun, 1998; Giles, 2000).

The lack of zircons with inherited ages spanning 2300-1850 Ma implies an extended period of tectonic quiescence (Giles, 2000). Giles (2000) suggested that thermal conditions during this period were of insufficient intensity for the growth of new zircons or resetting of U-Pb systematics in existing zircons. In particular, a small population of inherited zircon ages corresponding to the Barramundi Orogeny (ca. 1900-1840) suggest a very minor component of detrital material was either sourced directly or recycled from the similar aged magmatic and sedimentary edifice comprising the Kalkadoon-Leichhardt Belt. This implies that rocks of the Kalkadoon Leichhardt Belt and rocks aged between 2300-1850 Ma were exposed to limited erosion and magmatic sampling during deposition of the host sequence at Cannington ca. 1670 Ma (Giles, 2000), or that the majority of detrital material was possibly shed into an alternative basin.

The oldest inherited ages (2600-2300 Ma) indicate that a small component of detrital zircons was sourced from a late Archaean to early Palaeoproterozoic basement of unknown affinities (Giles, 2000). The similar slightly rounded prismatic morphology of Archaean and Palaeoproterozoic zircons, suggests similar, relatively short-lived residence times in the sedimentary environment. It is likely therefore, that Archaean and Palaeoproterozoic basement was exposed to erosional forces during deposition of the host sequence (op. cit.). Giles (2000) argued that these features implied that the host sequence and rocks comprising Cover Sequence 2 were directly deposited on late Archaean to early Palaeoproterozoic basement that was undergoing extension.

Discordant ages of ~500 Ma (Table 3.2) indicate a period of Pb loss possibly related to Pb mobility and partial resetting of U-Pb systematics during the early Phanerozoic (Giles, 2000). Late stage vuggy carbonate-quartz veins containing galena and associated with D_5 brittle

deformation may relate to this period (op. cit.). If this is correct, then Pb isotope systematics may also have been affected by late stage hydrothermal activity (Chapter 7).

3.6.2 Emplacement of the Core Amphibolite

Analyses of magmatic and metamorphic zircons in the Core Amphibolite yielded coincident ages of 1578±15 Ma, suggesting that emplacement (and crystallisation of the melt) was essentially synchronous with peak metamorphism (M_1). Giles (2000) argued that thermal resetting of U-Pb systematics in magmatic zircons from the Core Amphibolite could be discounted as a causative mechanism for the coincident ages, as zircons in the migmatitic gneiss had not been reset even though both rock-types had experienced the same metamorphic history. Furthermore, Giles (2000) recognised that thermal resetting at upper amphibolite facies conditions was unlikely based on experimental studies, but could be induced if the rock was flushed by an acidic or saline fluid. However, there is no evidence for the latter in the Core Amphibolite (Bodon, 1998; Walters and Bailey, 1998; Giles, 2000: section 3.2.4).

3.7 DISCUSSION

3.7.1 Relict sedimentary features

Zircons do not undergo appreciable re-equilibration and recrystallisation during upper amphibolite facies metamorphism and primary detrital and magmatic morphologies are commonly preserved. At Cannington, Page and Sun (1998) and Giles (2000) recognised that migmatitic gneiss contained both detrital and magmatic zircon populations of essentially equivalent age, indicating a contemporaneous, locally derived volcanic or intrusive input (section 3.6.1). No other unequivocal relic primary sedimentary clastic textures and/or volcanic textures were observed in the migmatitic gneiss at Cannington. It appears that syn-anatectic partial melting has obliterated primary sedimentary features. However, in rocks that have experienced very little partial melting larger scale features such as primary lithological variations (e.g. bedding and graded bedding) may be preserved, although texturally and mineralogically modified to some extent (Laing et al., 1978; Haydon and McConachy, 1987; Wright et al., 1987;Haydon et al., 1993). The host sequence at Broken Hill, New South Wales contains particularly good examples where modified bedding and graded bedding were preserved up to granulite facies metamorphism (Laing et al., 1978; Page and Laing, 1992).

Garnetiferous rocks at Cannington appear to have had a bulk composition that was not conducive to partial melting during M_1 and therefore primary sedimentary features may be preserved. Cyclic interbanding between sillimanite-biotite-garnet schist and garnetiferous quartzite units provide possible evidence for primary bedding. This is supported by rare occurrences of bands grading from sillimanite-biotite-garnet to garnet-quartz-K-feldspar that resemble relict turbiditic graded beds (Walters, 1994a; I. Willis, pers. comm., 1995; Bodon, 1998; Walters and Bailey, 1998) similar to those recognised at Broken Hill in New South Wales (e.g. Laing et al., 1978). Other possible primary sedimentary features include:

- a weak vertical lithostratigraphic zonation from predominantly sillimanite-garnet schist

with intercalated garnetiferous quartzite, to garnetiferous quartzite with intercalated sillimanite-garnet schist as the orebody is approached, i.e. an increase in the predominance of quartzite over schist toward the orebody (cf. Bailey, 1998),

- variations in mineral abundances between adjacent garnetiferous quartzite bands, e.g. variations in the proportions of garnet, quartz and K-feldspar,
- internal grading within individual bands defined by variations in mineral abundances, e.g. garnet-rich to garnet-poor in garnetiferous quartzite bands (Fig. 3.5f), and sillimanite-rich to sillimanite-poor in gahnite-bearing sillimanite-biotite-garnet schists.

Mark (1993) and Walters (1994a) suggested that the migmatitic gneiss sequence represents a siliciclastic package of immature arkosic sediments. Geochemical affinities indicate that the gneiss has variable compositions ranging through wackes, litharenites, arkoses and shales (Fig. 3.19). However, this classification must be regarded with some scepticism as it involves elements that are inherently mobile (except for Al_2O_3) during post-depositional processes such as metamorphism and hydrothermal alteration (Pearce and Cann, 1973; Floyd and Winchester, 1978;MacLean, 1990; MacLean and Barrett, 1993; and many others).

The interpretation that the migmatitic gneiss is a metamorphosed package of sedimentary rocks concurs with the interpretations of Beardsmore et al. (1988) for the Gandry Dam Gneiss (GDG). From Chapter 2, the metasediments of the GDG were deposited during a period of rapid subsidence associated with an early ensialic rifting phase in the region (Beardsmore et al., 1988) ca. 1680 Ma (Page and Sun, 1998; Giles, 2000). The interpreted depositional environment consisted of shallow to moderate water depth dominated by traction current to medial fan sedimentation and intermittent pulses of mafic and felsic volcanism, as well as exhalation of metalliferous fluids forming a sequence of poorly-sorted, immature sands and silts

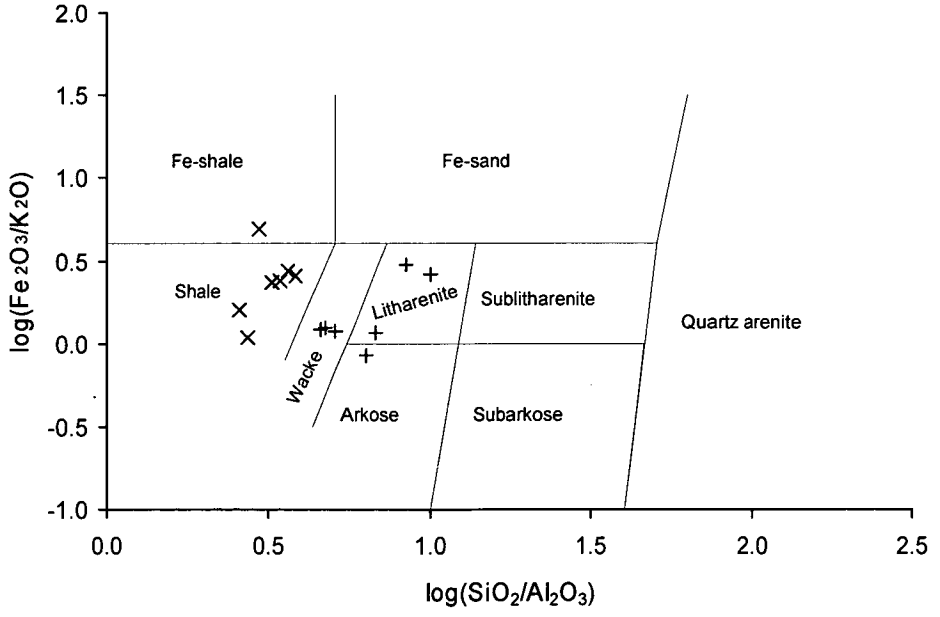

Figure 3.19 Classification and nomenclature for sandstones and shales using the $\log(Fe_2O_3/K_2O)$ versus $\log(SiO_2/Al_2O_3)$ diagram after Herron (1988). The majority of pelitic gneiss plot within the shale field (x), whereas the psammitic gneiss (+) are dispersed in the wacke, litharenite and arkose fields (refer Appendix 2 for wholerock geochemical data).

with intercalated volcaniclastic horizons, mafic and felsic volcanics, and minor chemogenic sediments (Beardsmore et al., 1988). Considering the deposit is hosted in the GDG, the latter interpretation is the best attempt to date at resolving the depositional environment for the host rocks at Cannington. However, emplacement of mafic melts may be related to a period magmatism synchronous with peak metamorphism at ca. 1580 Ma.

3.7.2 Origin of garnetiferous rocks

Because garnetiferous rocks have a laterally extensive distribution, spatial association with mineralised rocks and gradational relationships to migmatitic gneiss, they have been interpreted to represent an Fe-Mn(-Ca) alteration halo that was superimposed upon the original sedimentary host succession (French et al., 1994; Richmond, 1994; Walters, 1994a and b; Bodon, 1995, 1996b, 1998; Williams et al., 1996; Richmond et al., 1996b; Bailey, 1998; Walters and Bailey, 1998; Williams and Chapman, 1998; Giles, 2000). The observation that garnet compositions are atypical for normal metasedimentary compositions found in pelites also suggests that the sedimentary protoliths have been altered (Richmond et al., 1996; Williams et al., 1996). Further evidence supporting this comes from strong textural, mineralogical and geochemical similarities with rocks considered to represent the metamorphosed alteration halo that surrounds the Broken Hill deposit in New South Wales (Lottermoser, 1988; Spry and Wonder, 1989; Parr and Plimer, 1993). However, of critical importance, is the timing of this alteration event with respect to deformation and peak metamorphism.

Temporal relationships between porphyroblastic garnet growth, metamorphism and mineral fabric development in the metasediments, provides a rigorous means of constraining the relative timing of the alteration halo. Williams et al. (1996) recognised that garnet porphyroblasts and granoblastic K-feldspar were truncated by fibrolitic sillimanite. Giles (2000) also recognised that garnet porphyroblasts were consistently overprinted and truncated by microshears filled with secondary sillimanite (i.e. S_2 shear fabrics), suggesting a pre-D_2/M_2 timing.

Peak metamorphic textures are characterised by the development of granoblastic fabrics in garnetiferous rocks (Giles, 2000). Garnet porphyroblasts form an integral part of the granoblastic texture, suggesting a pre- to syn-peak metamorphic timing. However, the preservation of an early foliation (S_i), defined by quartz inclusion trails in garnet porphyroblasts, suggests a pre-D_i and clearly pre-peak metamorphic (M_1) timing for the alteration halo.

Richmond et al. (1996) and Williams et al. (1996) argued that the coherent composition of garnets in garnetiferous rocks and garnet altered pegmatites implied a common heritage related to a high temperature alteration event that must have post-dated pegmatite emplacement, and therefore post-dated peak metamorphism. However, the timing of garnet alteration selvedges along the margins of pegmatites with respect to mineral fabric development, is poorly constrained and the selvedges are not common to all pegmatites hosted in the garnetiferous rocks. Indeed, it is possible that the alteration was produced by contact metasomatic processes

during pegmatite emplacement syn-M_1 (section 3.7.3.3) and may therefore, be temporally unrelated to garnet alteration in the metasediments. If this is correct, then it is likely that alteration in the adjacent metasediments pre-dated pegmatite emplacement.

The post-peak metamorphic model does not explain the typically higher abundance of garnet in garnetiferous quartzite compared to sillimanite-garnet schist, nor does it adequately explain observed internal variations in garnet abundance within bands. Assuming that quartzites are comparatively less permeable than schists, due to annealing of quartz and feldspar during metamorphism, it would be expected that fluid-flow would have been facilitated through the schists. Richmond et al. (1996) implied that garnet abundance was related to the intensity of Fe-Mn(-Ca) alteration, and in this scenario, it should be the schists that are most intensely altered and therefore, the most garnet-rich. However, the opposite is the case.

Considering the pre-metamorphic model, the higher abundance of garnet in garnetiferous quartzite compared to sillimanite-garnet schists is possibly related to the influence of primary sedimentary features on hydrothermal fluid pathways. Hydrothermal fluid may have been selectively focussed through psammitic rocks prior to metamorphism owing to their higher primary and/or secondary porosities and permeabilities compared to pelites. Such a process may provide an explanation for the presence of garnetiferous quartzite bands that display an internal grading in garnet abundance, i.e. mimicking and subsequent preservation of primary sedimentary grading. A similar, larger-scale process is thought to have occurred at Broken Hill prior to metamorphism, whereby hydrothermal fluids were thought to have been selectively channelled through, and ponded within upward coarsening, deltaic psammitic wedges (Haydon and McConachy, 1987; Wright et al., 1987; Haydon et al., 1993). At the Currawong volcanic-hosted massive sulphide deposit in northeastern Victoria, pyritic replacement fronts in sandstone laminations in turbidites adjacent to the orebody provide clear evidence for primary porosity- and permeability-controlled fluid-flow (Bodon and Valenta, 1995).

3.7.3 Timing of pegmatite and lode pegmatite emplacement and Pb-Zn mineralisation

3.7.3.1 Timing of emplacement

The timing of partial melting can be constrained to syn-D_1/M_1 (section 3.3.2 and 3.4.2). However, the timing of pegmatite emplacement appears to be more complex. In general, pegmatite emplacement was synchronous with migmatisation, and formed via partial melting of the precursor gneiss protolith during peak metamorphism (Mark, 1993; Mark et al., 1998; Giles, 2000). However, rare pegmatites that crosscut the differentiated S_2 schistosity provide evidence for emplacement after peak metamorphism (D_1/M_1) and secondary sillimanite (D_2/M_2; Fig. 3.3g and h). Such an observation indicates that pegmatite emplacement either continued over a protracted period of time from syn-D_1/M_1 to post-D_2/M_2, but related to the same M_1/M_2 thermal event, or was associated with a subsequent unrelated and transient thermal pulse. Lode pegmatites display similar temporal relationships to deformation and peak

metamorphism (refer below).

3.7.3.2 Temporal relationships with the ores – lode pegmatites

Evidence for the temporal relationship between lode pegmatite emplacement and sulphide mineralisation can be gleaned from a variety of textural observations. Based on overprinting quartz-albite alteration and coeval sulphide veining localised along the margins of lode pegmatites, Mark (1993) concluded that the main ore formation event post-dated pegmatite emplacement and therefore peak metamorphism (cf. Richmond et al., 1996; Williams et al., 1996; Williams and Chapman, 1998). Such a scenario is considered unlikely because firstly, albite is not a gangue mineral in the ores apart from minor amounts in silicified sillimanite-biotite-garnet schists and garnetiferous quartzites. Secondly, fine sulphide veinlets are a common feature along many lode pegmatite contacts with a variety of ore types and are clearly related to a series of late stage alteration events associated with fracture zones, brecciation and faulting. In certain examples, discontinuous sulphide veinlets emanating from the ore contact overprint lode pegmatites locally. The sub-perpendicular orientation of these veins to the dominant deformation fabric in the adjacent ore suggests they represent small-scale piercement or extensional pull-apart veins that formed in response to competency contrasts between lode pegmatite and ore. These relationships indicate that sulphide veining is more likely related to localised remobilisation of pre-existing sulphides during deformation. Thirdly, the transgressive nature of lode pegmatites to ore lenses and the presence of coarse-grained, diffuse-edged ore clasts within unaltered lode pegmatites indicates that they intruded the orebody after ore formation (Walters, 1994a; Bodon, 1998; Walters and Bailey, 1998).

Textures of sulphide-bearing clasts in lode pegmatites are consistent with partial assimilation of ore during the emplacement of the melt. Critical textures supporting this interpretation include:

- diffuse margins of ore clasts,
- recrystallisation of sulphides and incorporation as inclusions in feldspar and quartz,
- pegmatitic to granoblastic intergrowths between gangue-sulphide minerals and quartz-feldspar within the clasts,
- presence of Pb-bearing amazonite with fine inclusions of galena,
- lobate, intrusive-like margins between lode pegmatites and ore suggestive of localised assimilation and mingling between melt and ore where the nature contacts have been preserved from shearing.

An underground exposure of a lode pegmatite with lobate apophyses that intrude and "stope-out" ore is a particularly good example that illustrates the assimilation and ore-melt mingling process. However in this case, the lode pegmatite crosscuts deformation fabrics and compositional banding in the adjacent ore suggesting a post-peak metamorphic timing.

3.7.3.3 Alteration selvedges

Alteration along lode pegmatite contacts appears to be related to the rock type in which the melt intruded. Lode pegmatites hosted in garnetiferous rocks have minor to absent garnet-quartz

alteration along their contacts, whereas green-grey K-feldspar, garnet-quartz, amphibole and instances quartz-gahnite alteration was characteristic along the margins of lode pegmatites that intruded Fe-Mn-Ca ores (Walters, 1994a; Bodon, 1995, 1998). This relationship is perhaps due to the stark compositional contrasts between lode pegmatite and ore, insomuch as lode pegmatites have reacted with the ores during emplacement (cf. Walters, 1994a). The observation that high temperature minerals define the alteration assemblage, and that alteration is restricted to contacts tends to support this. These relationships imply an alteration process somewhat analogous to contact metasomatism between marbles and hornfelses with local diffusive exchange of cations across the contact. The presence of amphibole±sulphide alteration and veins overprinting earlier garnet alteration suggests the involvement of a late retrograde fluid that was preferentially focused along lode pegmatite-ore contacts and facilitated solution-associated remobilisation of pre-existing sulphides.

Minor alteration, or lack thereof, along lode pegmatite margins in sillimanite-biotite-garnet schists and garnetiferous quartzites suggests that compositional contrasts were not great. However, the presence of minor quartz-gahnite assemblages implies that the host rocks were probably anomalous in Zn, particularly in the Northern Zone, where gahnite-bearing schist contains up to ~3000ppm Zn (see Chapter 6 and Appendix 2). Subsequent, lower temperature alteration events, such as that producing chlorite, are clearly related to late, overprinting fracture zones and faults in the lode pegmatites (ibid.) and are not necessarily localised along pegmatite contacts, i.e. they occur as patchy zones throughout lode pegmatites. Overall, the relationships indicate that alteration defined by high temperature mineral assemblages was contiguous with lode pegmatite emplacement. It is likely therefore, that amazonite and gahnite in lode pegmatites formed via assimilation of pre-existing Pb and Zn phases, probably sulphides (Chapter 7).

3.7.3.4 Lode pegmatite protoliths

Sillimanite-biotite-garnet schists and garnetiferous quartzites within the mineralised package have been considered the likely protolith to lode pegmatites due to the occurrence of amazonite-bearing *in situ* leucocratic segregations and lode pegmatites within these rocks (Walters, 1994a). In the Northern Zone of the deposit, gahnite-bearing sillimanite-biotite-garnet schists are the likely protolith due to the proliferation of amazonite-bearing, *in situ* melts (Fig. 3.5d). Such an interpretation is logical, but protoliths may not necessarily be restricted to just these rocks. It is a distinct possibility that lode pegmatites were sourced from nearby migmatitic gneiss and simply inherited their characteristic compositions via assimilation of ore, and/or sillimanite-biotite-garnet schists and garnetiferous quartzites anomalous in Pb and Zn. In either case, the presence of amazonite-bearing lode pegmatites and *in situ* partial melts in schists and quartzites essentially defines a specific stratabound horizon anomalous in Pb that may be regionally extensive and therefore useful in exploration for further BHT deposits. Similar lode pegmatites occur at many other BHT deposits. At Broken Hill in New South Wales they are present in the Main Lode (e.g. the Separation pegmatite) and as semi-regional stratabound marker units (Walters, 1994a and 2000; A. Webster, pers. comm., 1998).

3.7.4 Temporal relationships between the Core Amphibolite and the ores

Williams (1998a) suggested that high-Fe metatholeiites associated with BHT deposits in the Eastern Succession, including the Core Amphibolite at Cannington, had geochemical affinities consistent with basalts erupted in a propagating rift setting, and that rifting was synchronous with deposition of the sedimentary rocks comprising the Fullarton River Group. However, U-Pb ages, determined from magmatic zircons, indicate that the Core Amphibolite intruded the metasedimentary sequence broadly synchronously with peak metamorphism (ca. 1580 Ma) during compressional tectonics related to the Isan Orogeny some 100 Ma after ensialic rifting and deposition of the host sediments ca. 1670 Ma.

Considering that the Core Amphibolite resides within the orebody and has sharp contacts with ores and silicified garnetiferous rocks, the lack of evidence of significant sulphide mineralisation and hydrothermal alteration, and its slightly transgressive nature to the ore lenses (section 3.2.4), implies emplacement after most ore formation. The presence of galena, pyrrhotite and chalcopyrite inclusions in granoblastic plagioclase that do not appear to be temporally related to late-stage retrograde sericite and chlorite alteration (section 3.2.4), provide evidence for possible assimilation of pre-existing ore during emplacement. This would explain the enigmatic Pb and Zn anomalism in comparison to other amphibolites in the region that are not spatially associated with sulphide deposits (Chapter 7). If this is correct, it is likely that original geochemical affinities have been modified to some extent and present geochemical features may not accurately reflect true igneous affinities.

3.8 SUMMARY

The Cannington deposit is hosted by migmatitic gneiss with intercalated pegmatites and amphibolites. Garnetiferous rocks envelop the orebody for up to 250m and occur within it. Two Fe-Mn silicate units are hosted within the garnetiferous rocks of the structural hanging wall in the Southern Zone, and have similar mineralogical and textural features to particular Fe-Mn silicate ores. A large, texturally and compositionally homogeneous amphibolite body, the Core Amphibolite, resides within the deposit and contains no significant sulphide mineralisation or hydrothermal alteration, and was emplaced synchronous with pea metamorphism (M_1).

Six discrete generations of deformation have been recognised in the local mine area (Table 3.1). The macroscopic geometry of the deposit is largely controlled by D_3, D_4 ductile, and to a lesser degree, D_5 brittle structures, that formed subsequent to partial melting of the host sequence. A macroscopic, shallowly south plunging, isoclinal F_3 fold (the Cannington Synform), with a variable, moderate east to west dipping axial surface, interpreted to pass through the centre of the deposit, is responsible for the broad repetition of ore types in the structural hanging wall and footwall. The lower limb of the Cannington Synform has been attenuated and truncated by the Footwall Shear (D_3) in the southern area of the Southern Zone. This has resulted in partial truncation of ore lenses and displacement of the entire host sequence in the structural footwall. An open, shallowly south plunging F_4 synform with a moderate to steeply

east dipping axial surface progressively refolds the axial surface of the Cannington Synform to the north. The Southern Zone occurs within the easterly dipping limb of the F_4 synform, whereas the Northern Zone occurs within the broad hinge region and steeper westerly dipping limb.

Geometrical relationships suggest that the Cannington Synform and Footwall Shear may represent an east vergent fold-thrust pair that was reoriented into its present position by subsequent F_4 folding. Due to the similar shallow southerly plunge of the F_3 and F_4 folds the structures are essentially coaxial and both appear to have formed in response to east-west shortening.

Two generations of D_5 faulting variably offset the macroscopic fold geometry. The earlier generation (D_{5a}) is characterised by narrow and commonly healed subvertical north-northeast striking anastomosing faults with marginal displacements that collectively form the Brolga Fault Zone. The later generation (D_{5b}) comprise a conjugate set of northwest and northeast striking faults with variable sinistral and dextral strike-slip displacements respectively. The northwest striking, steeply northeast dipping Trepell Fault offsets the Northern Zone of the deposit ~300m to the northwest, whereas the northwest striking Hamilton Fault truncates the southern extension of the orebody.

Three periods of metamorphism are recorded in the host rocks. The thermal evolution is characterised by a high temperature, low pressure anti-clockwise P-T-t path that involved up-pressure heating during prograde metamorphism and isobaric or up-pressure cooling during retrogression (Giles, 2000). Key mineralogical and textural criteria used to define the metamorphic events and estimate P-T conditions for each, as well as temporal relationships with deformation can be summarised as follows:

M_1 — *Syn-D_1 peak metamorphism ca. 1580 Ma:* sillimanite-biotite mineral fabric (S_1), porphyroblastic garnet and gahnite growth, granoblastic textures, extensive partial melting (sillimanite-K-feldspar-biotite-quartz). Estimated P-T conditions of ~650-700°C and ~4kbars (*upper amphibolite facies*) determined from petrogenetic constraints and garnet–hornblende geothermometry. Rare hornblende breakdown and growth of new clinopyroxene adjacent to clinopyroxene-bearing pegmatite in the Core Amphibolite indicates that conditions reached *transitional upper amphibolite to granulite facies* locally.

M_2 — *Syn-D_2 retrogression ca. 1580 Ma:* secondary sillimanite (differentiated S_2 fabric) replacement and overgrowth of M_1 mineral assemblages, granoblastic textures, leucocratic melt segregations and possible relic andalusite porphyroblasts (secondary sillimanite beards). Involvement of a syn-D_2 fluid phase (base-cation leaching by an acidic fluid) focussed along S_2 microshears (pressure solution pathways). Estimated P-T conditions of 500-650°C and 3-6kbars (*middle to upper amphibolite facies*) determined from fluid-mineral equilibria involving sillimanite, absence of staurolite and muscovite, and lack of partial melting, i.e. below wet solidus of common granite. Represents retrogression during initial stages of cooling following peak metamorphism (M_1).

M_3 — *Post-D_3 retrogression ca. 1510 Ma:* biotite recrystallisation in hinges of S_3 crenulations. Rare kyanite intergrown with muscovite. Muscovite±kyanite replacement of sillimanite, biotite and K-feldspar. Static overgrowth of pre-existing S_1/S_2 fabrics and S_3 crenulations by coarse-grained muscovite. Involvement of a post-D_3 fluid phase focussed along pre-existing S_2 sillimanite microshears. Fluid-mineral equilibria suggests conditions of >400°C and >3kbars (*upper greenschist to lower amphibolite facies*). Represents a discrete ephemeral thermal event associated with late orogenic plutonism, i.e. intrusion of the Williams and Naraku batholiths.

The host rocks are interpreted to represent an immature siliciclastic sedimentary sequence with a variable contemporaneous volcanic component that was deposited directly on late Archaean to early Palaeoproterozoic basement that was undergoing extension during a period of rapid subsidence associated with an ensialic rifting phase ca 1675 Ma. The vast majority of detrital material was sourced from nearby Cover Sequence 2 rocks (1750-1700 Ma) and a small component from the late Archaean to early Palaeoproterozoic basement of unknown affinities. Garnetiferous rocks are interpreted to represent a premetamorphic Fe-Mn(-Ca) alteration halo superimposed upon psammites and psammopelites, that was spatially and temporally associated with major ore formation. The preservation of an early S_i fabric defined by quartz inclusion trails in garnet porphyroblasts provides evidence of a pre-metamorphic timing for the alteration event.

Based on geochemical affinities, the Core Amphibolite and other high-Fe amphibolites in the MSG appear to represent shallow-level, differentiated Fe-rich andesitic sills indicative of a propagating rift environment. In contrast, U-Pb ages determined from magmatic zircons indicate that the Core Amphibolite was emplaced essentially synchronous with peak metamorphism ca. 1580 Ma in a compressional regime during the early stages of the Isan Orogeny. Sharp contacts with the ores and presence of sulphide inclusions in plagioclase that are unrelated to retrogression, suggests the Core Amphibolite was emplaced after ore formation and that some degree ore assimilation took place. Assimilation probably accounts for the anomalous Pb-Zn tenor of the amphibolite in addition to minor late stage overprinting sulphide-bearing veinlets. It is likely therefore, that the original igneous geochemistry has been affected to some extent.

Pegmatites were generated via partial melting of the host metasedimentary sequence syn-D_1/ M_1 (ca. 1580 Ma). Coherent inheritance patterns in U-Pb zircon ages and similar zircon morphology populations between pegmatites and migmatitic gneiss provide further supporting evidence for this interpretation. Rare pegmatites that crosscut the differentiated S_2 shear fabric in migmatitic gneiss indicate that emplacement occurred either over protracted period of time related to the same M_1/M_2 thermal event, or during a subsequent unrelated and transient thermal perturbation. Lode pegmatites within the orebody display similar temporal relationships. The transgressive nature of the latter to ore lenses, presence of partially assimilated ore clasts and evidence for ore-melt mingling provides unequivocal evidence for emplacement after ore formation. Small-scale sulphide-bearing piercement veinlets associated with late stage

hornblende alteration along lode pegmatite margins are consistent with remobilisation of pre-existing sulphides and appears to have been facilitated by a late retrograde fluid phase that was focussed along the contacts during deformation. This retrograde event appears to be related to a more deposit-wide metasomatic event that will be addressed in subsequent chapters.

Chapter 4

Ores Types and Paragenetic Relationships

FOREWORD

The contents of this chapter have been published in a special issue of Economic Geology on the McArthur River-Mount Isa Inlier-Cloncurry Minerals Province, i.e. Bodon (1998). A copy of the paper can be found in Appendix 5. An expanded and updated version of the publication is presented here, including additional research that was not published in Bodon (1998).

4.1 INTRODUCTION

This chapter examines the temporal relationships between sulphide deposition, deformation, metamorphism and retrograde alteration, by presenting detailed paragenetic sulphide and host rock relationships on a deposit-wide scale. Reconciling the paragenesis of the deposit provides a method of determining the relative timing of ore formation with respect to deformation and metamorphism. It also provides a means of characterising particular events recorded in the ores into an organised sequence of events (i.e. an evolutionary framework) that serves as a guide for subsequent research. Moreover, paragenetic relationships form the basis for deciphering the genesis of the deposit.

Initially major ore types are defined. Thereafter, each ore type is described in terms of its mineralogy, distribution, metal association and paragenesis (i.e. textures). Principal gangue mineral compositions and metal zonation in the Cannington deposit are also described. More empirical aspects, such as mineralogical and major metal zonation features of the ores, are then addressed. This is followed by a discussion on the interpreted paragenesis of Cannington and a comparison of mineralogical, metal zonation and paragenetic features with typical Zn-Pb skarn deposits as defined by Meinert (1992, 1993 and 1998). The chapter is closed with a comparison between the Cannington and Broken Hill, Australia, deposits.

4.2 METHODS

Textural observations have been gathered from underground mapping, logging of approximately 30km of drill core, some 1,000 hand specimen samples and microtextural investigations on over 180 polished thin sections. These observations provide vital constraints on the timing of metal introduction, as well as the evolutionary history of the deposit.

Geochemical data used for determining metal zonation features was provided by BHP Minerals. Mineral compositional data was determined using a Cameca SX50 electron microprobe at the University of Tasmania. Instrument settings and analytical data can be found in Appendix 1.

4.3 OVERVIEW OF MAJOR ORE TYPES

Sulphide and sulphosalt minerals occur in a range of mineralogically and texturally diverse siliceous and Fe-Mn silicate (skarnoid) rocks . Strong metal zonation trends involving Pb-Ag- and Zn-rich mineralised rocks are a feature of the deposit and correlate with mineralogical zonation patterns on a deposit scale (Bodon, 1998; Walters and Bailey, 1998; Chapman and Williams, 1998; Pringle, 1999). On the basis of these distinct associations, mineralised rocks have been divided into three major groups that are independent of economic cut-offs and therefore, mine terminology (Tables 4.1 and 4.2). These are:

i) graphitic ore (variable Fe up to 15 wt%, up to 5 modal% graphite);
ii) Fe-Mn silicate ore (>15 wt% Fe); and
iii)siliceous ore (<10 wt% Fe; quartz is principal gangue mineral; rare graphite).

All ore types occur as a series of low aspect ratio lenses that have been dissected by subvertical D_5 faults. Two large pegmatite bodies up to 30m thick intrude the deposit and are locally transgressive to the ore lenses (refer Chapter 3; Figs. 4.1-4.3). Lode pegmatites up to 5m thick, are randomly distributed and locally contain partially assimilated blocks of ore (refer Chapter 3; Bodon, 1998; Walters and Bailey, 1998). In underground exposures, some lode pegmatites have definite intrusive contacts with the ore.

A wide diversity of minerals and associated complex textural relationships are intrinsic to the ores (Table 4.1). For example, ten Ag-sulphosalt minerals have been recognised in a small area of olivine-pyroxenoid ore in the footwall of the Southern Zone alone (Dugmore, 1998). Compositions of silicate gangue minerals display complex variations, commonly involving substitution between Fe, Mn and to a lesser extent Ca (see section 4.5). Some minerals display compositional variations relative to their paragenesis (Richmond et al., 1996; Pringle, 1999). However, compositional variations/zonations for individual gangue minerals with regard to spatial distribution have not been fully established (cf. French et al., 1994).

Thin (over 2 to 10cm) contact zones between mineralised Fe-Mn silicate rocks and host rocks are a key feature of the deposit. No crosscutting relationships are evident apart from localised, weakly mineralised hedenbergite-garnet-quartz veining, and associated quartz-garnet alteration and silicification of host rocks. In contrast, siliceous ores commonly display gradational and crosscutting relationships with host rocks, as well as Fe-Mn silicate and graphitic ores.

4.4 GRAPHITIC ORE

Graphitic ore constitutes <5% of the current economic resource (unpublished BHP reports) at Cannington. It occurs predominantly in the hinge region, and footwall areas of the Southern Zone, as small lenses intercalated with mineralised, banded Fe-Mn silicate rocks. These lenses progressively coalesce and thicken north of the 4800mN section into a discrete lens up to 20m thick. Graphitic ore is more prevalent in the weakly mineralised Northern Zone,

Table 4.1 Classification of ore types comprising the Cannington deposit (modified after Bodon, 1995, 1996b, 1998; Walters and Bailey, 1998)

Ore type	Chemical association	Characteristic mineralogy	Pb/Zn	Common textures	Equivalent mine terminology
Graphitic (variable Fe up to 15%, up to 5 modal % graphite)	Pb, Zn, Ag *Si, P, Fe, Mn, C*	Quartz, apatite, graphite, amphibole[1], biotite, garnet[2], knebelite, pyroxferroite, galena, sphalerite (minor pyrosmalite, pyrrhotite, loellingite-arsenopyrite)	Variable, but commonl y Pb≥Zn	Laterally continuous (over metre scales) millimetre to centimetre compositional banding, granoblastic, spheroidal sulphide inclusions in silicates	Inveravon
Fe-Mn silicate (>15% Fe)	Pb-Ag *Fe-Mn-F*	*Olivine-pyroxenoid (quartz absent)* Knebelite, pyroxferroite, fluorite, magnetite, pyrosmalite, galena, pyrrhotite, Ag-sulphosalts (minor apatite, antimonides, sphalerite, loellingite-arsenopyrite)	Pb»Zn	Durchbewegung, mylonitic fabrics to granoblastic, spheroidal sulphide inclusions in Fe-Mn silicates, blebby coarse grained sulphides	Nithsdale/ Burnham
	Pb-Ag *Fe-Mn-P*	*Banded olivine-pyroxenoid* Knebelite, pyroxferroite, quartz, garnet[2], apatite, amphibole[1], galena, pyrrhotite (minor fluorite, graphite, magnetite, pyrosmalite, Ag-sulphosalts, antimonides, sphalerite, loellingite-arsenopyrite)	Pb»Zn	Laterally continuous (over metre scales) from millimetre to tens of centimetres, granoblastic, spheroidal sulphide inclusions in Fe-Mn silicates	Broadlands/ Warenda
	Zn *Fe(-Mn-Ca)-F*	*Hedenbergite (<10 modal % quartz)* Hedenbergite, garnet[3], amphibole[4], fluorite, ilvaite, magnetite, pyrrhotite, sphalerite, chalcopyrite, loellingite-arsenopyrite (minor quartz, pyrosmalite, apatite, galena)	Zn>Pb	Durchbewegung, mylonitic fabrics to granoblastic, spheroidal sulphide inclusions in Fe-Mn silicates, blebby coarse grained sulphides	Kheri/Colwell
	Zn *Fe(-Mn-Ca)-P*	*Banded hedenbergite* Hedenbergite, garnet[3], quartz, amphibole[4], apatite, pyrrhotite, sphalerite, chalcopyrite (minor fluorite, magnetite, loellingite-arsenopyrite, ilvaite, pyrosmalite, pyroxferroite, galena)	Zn>Pb	Syn- to post-D_2 hedenbergite (± quartz, garnet, carbonate, hornblende) veins and associated hedenbergite-garnet-quartz alteration	Broadlands/ Warenda
Siliceous (<10% Fe)	Pb-Zn-Ag *Si-P*	Quartz, carbonate, apatite, chlorite, galena, sphalerite, Ag-sulphosalts (minor antimonides, fluorite, graphite, loellingite-arsenopyrite)	Variable but commonl y Pb≥Zn	Quartz-sulphide breccias, syn- to post-D_2 quartz veins, minor relic compositional banding in nebulous quartz clasts	Glenholme/ Glenholme Breccia
	Zn *Si*	Quartz, K-feldspar, muscovite, garnet[3], sillimanite, gahnite, sphalerite, loellingite-arsenopyrite, pyrrhotite (minor hedenbergite, chalcopyrite, galena)	Zn»Pb	Massive quartz, granoblastic, disseminated blebby sulphide, syn- to post-D_2 quartz veins, quartz-sulphide breccias	Cukadoo

[1] — manganoan grunerite, hornblende
[2] — manganoan almandine
[3] — calcic almandine
[4] — hornblende, ferro-actinolite
[5] — terminology after Bailey (1998), and Walters and Bailey (1998)
N.B. Hornblende compositions range from edenite to hastingsite and contain up to 3.5 wt% Cl (French et al., 1994; this study). Pyrosmalite contains up to 4.3 wt% Cl (French et al., 1994; this study)

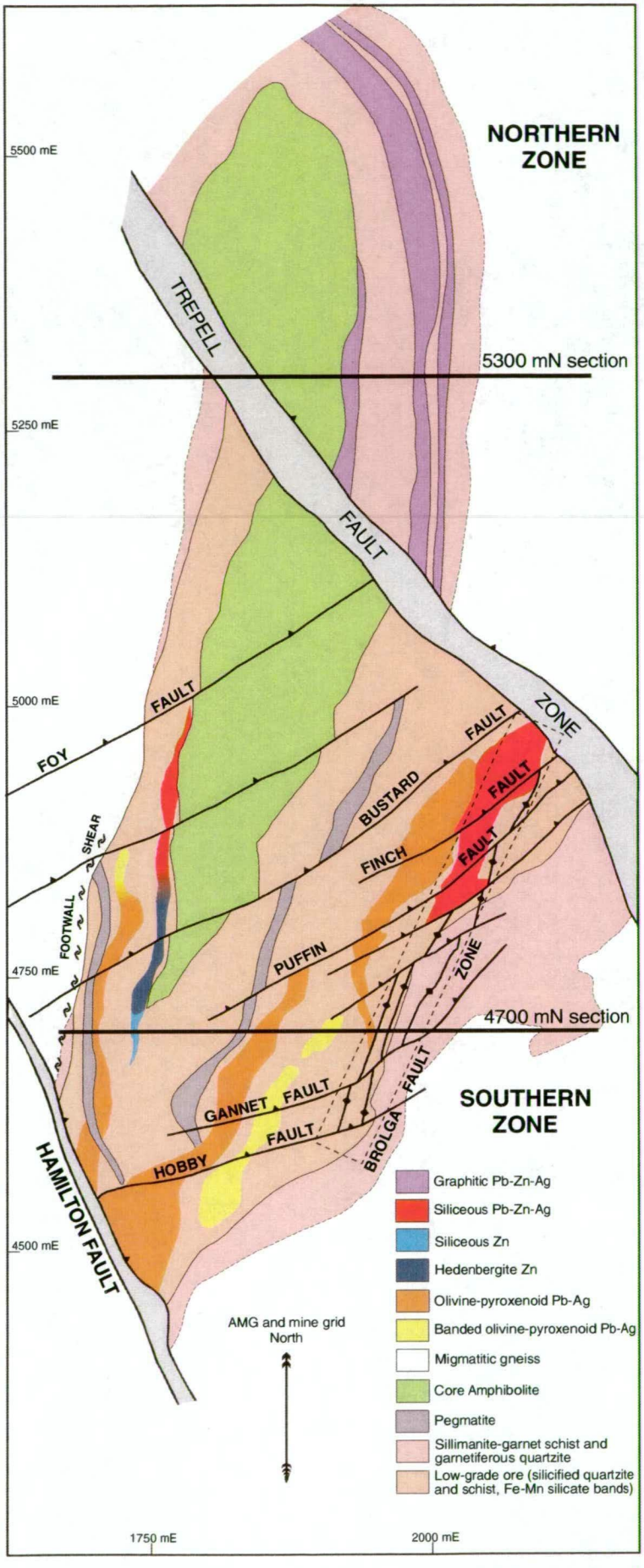

Figure 4.1 Interpretive geology and distribution of major ore types on the 900mRL, approximately 350m below surface (modified after Bailey, 1998).

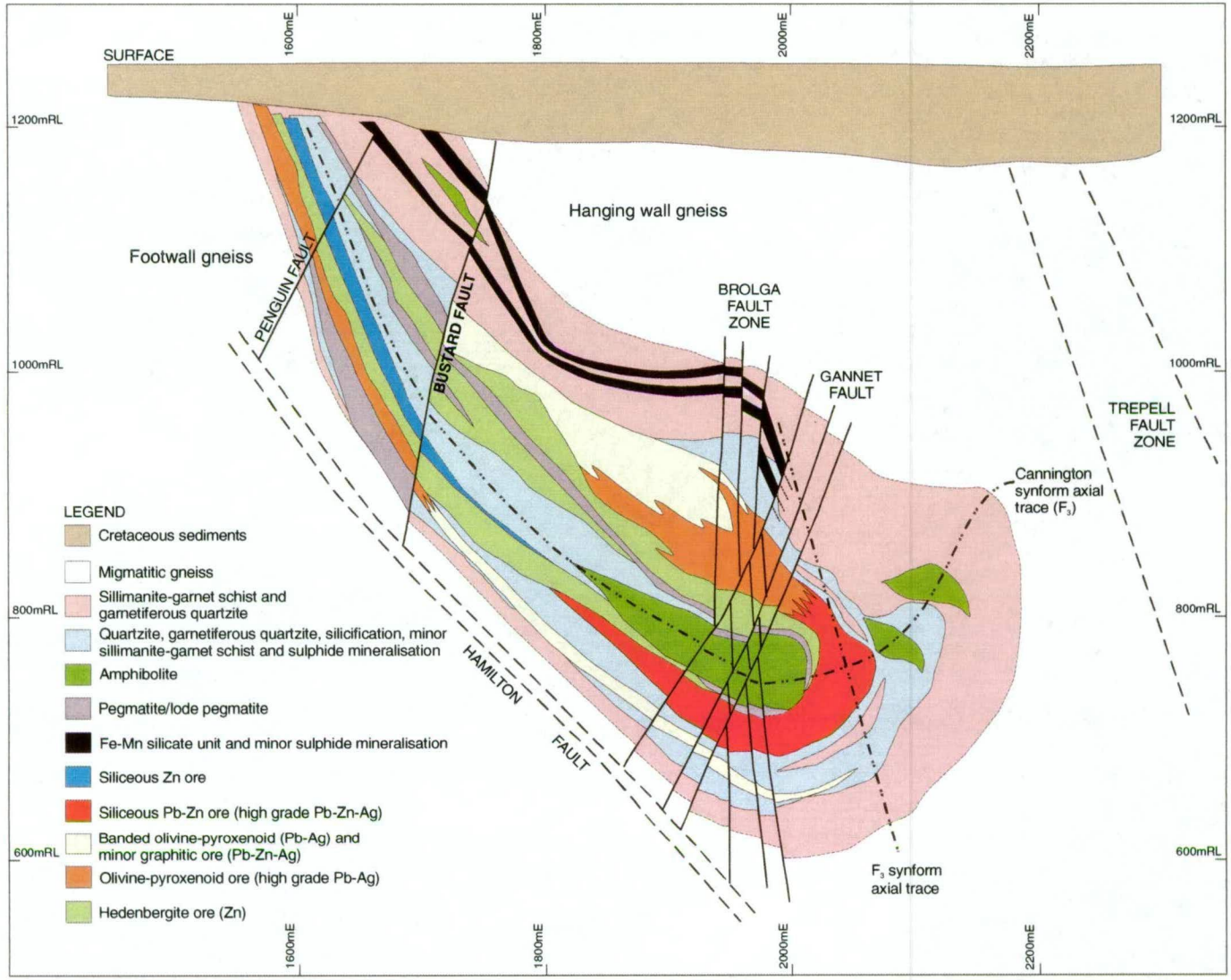

Figure 4.2 Interpretive geological cross section 4700mN of the Southern Zone (modified after Bailey, 1998; Bodon, 1998). Refer to Table 4.1 for explanation of ore types.

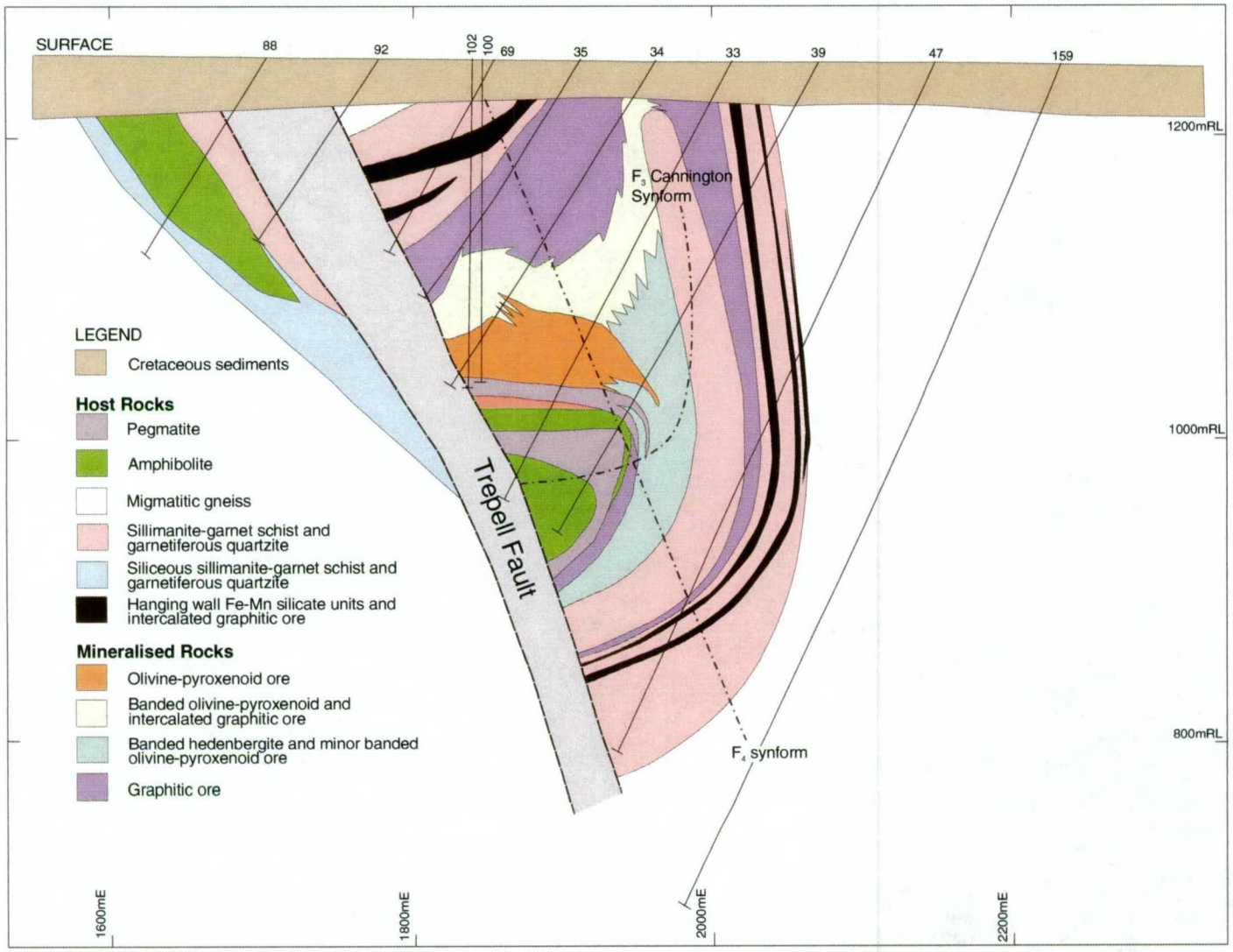

Figure 4.3 Interpretive geological cross section 5300mN of the Northern Zone (after Bodon, 1998).. Refer to Table 4.1 for explanation of ore types.

Table 4.2 Ore types comprising the Southern Zone lode horizons, including relative ore grades and intrinsic metal associations (compiled after Walters, 1994a; Bailey, 1998; Bodon, 1995, 1998; Walters and Bailey, 1998). Refer to Table 4.1 for mineralogies and Table 4.3 for average grades and compositions.

Mine lode horizon (% of Southern Zone resource)	Ore type	Mine terminology	Dominant metal association
Hanging wall Pb (56.5%)	Olivine-pyroxenoid	Burnham	Pb-Ag (Sb)
	Banded olivine pyroxenoid and banded hedenbergite, minor Graphitic	Broadlands	Pb-Ag
Hanging wall Zn (1.4%)	Hedenbergite	Kheri	Zn (As-Cu)
Footwall Zn (18.9%)	Hedenbergite	Colwell	Zn (As-Cu)
	Siliceous Zn	Cukadoo	Zn (As-Cu)
	Siliceous Pb-Zn-Ag (type1 > type2)	Glenholme	Pb-Zn-Ag (Sb-As)
Footwall Pb (12.3%)	Olivine-pyroxenoid	Nithsdale	Pb-Ag (Sb)
	Banded olivine-pyroxenoid, minor Graphitic	Warenda	Pb-Ag
Glenholme Breccia (10.9%)	Siliceous Pb-Zn-Ag (type2 > type1)	Glenholme Breccia	Pb-Zn-Ag (Sb-As)

occurring as lenses that typically range from 1-20m thick, intercalated within mineralised banded Fe-Mn silicate rocks, and as discrete lenses in the footwall and hinge region of the Cannington Synform. The largest of these lenses occurs to the east and reaches a maximum thickness of approximately 35m on section 5300mN (Fig. 4.3), extending some 600m along strike to the north, where it outcrops at the Cretaceous palaeosurface.

Contacts between graphitic ore and host rocks are sharp over centimetre scales, and lenses are concordant to surrounding host rocks. Similarly, laterally continuous (over several metres when exposed) compositional banding, a striking feature of graphitic ore, is concordant to possible bedding in the host rocks. Hence, there is no evidence that the ore type transgresses host metasediments.

Coherent metal zonation does not occur in graphitic ore. However, there is some correlation between elevated Pb and Ag, and Fe and Mn (Fig. 4.4, Table 4.3). In comparison to other ore types, graphitic ore possesses the highest P content with some drillhole intersections averaging 1-2 wt% wholerock P (Fig. 4.4, Table 4.3).

Graphitic ore, also called "Inveravon" using the Cannington mine terminology, is the most mineralogically diverse of all ore types (Table 4.1). Common gangue minerals include quartz, manganoan almandine, graphite (up to 5 modal%), grunerite, hornblende, biotite, apatite, minor pyrosmalite ($(Fe,Mn)_8Si_6O_{15}(OH,Cl)_{10}$), pyroxferroite, knebelite, minor magnetite, manganoan calcite, fluorite and allanite. Sulphides include galena, sphalerite, minor pyrrhotite, loellingite ($FeAs_2$), arsenopyrite, and rare pyrargyrite (Ag_3SbS_3), freibergite ($Cu_6(Ag,Fe)_6Sb_4S_{13}$), and antimonial silver of no fixed composition (French et al., 1994; Table 4.1). The silicate gangue minerals combine in variable proportions to define the compositional

Table 4.3 Average compositions of major ore types in the Southern Zone. After Bodon (1998) modified from Walters (1994a), and Walters and Bailey (1998).

Major ore type (mine terminology)	Pb %	Zn %	Ag ppm	Sb ppm	Fe %	Mn %	As ppm	Cu ppm	F %	P ppm	Au ppm	Pb/Zn ratio
Graphitic (Inveravon)	4.9	3.1	147	157	10.0	1.40	465	178	0.8	15060	0.04	1.6
Olivine-pyroxenoid (Nithsdale/Burnham)	14.8	2.3	820	680	20.8	1.95	575	503	5.06	875	0.07	6.4
Banded olivine-pyroxenoid and hedenbergite (Broadlands/Warenda)	11.5	1.7	430	505	6.2	0.8	210	180	1.53	2100	0.03	6.8
Hedenbergite (Kheri/ Colwell)	2.0	12.4	84	58	15.0	0.30	2600	1100	0.28	750	0.27	0.2
Siliceous Pb-Zn-Ag (Glenholme/ Glenholme Breccia)	18.3	10.5	695	920	3.5	0.20	1300	400	0.28	2100	0.10	1.7
Siliceous Zn (Cukadoo)	2.4	12.3	82	80	5.9	0.10	2300	900	0.1	500	0.35	0.2

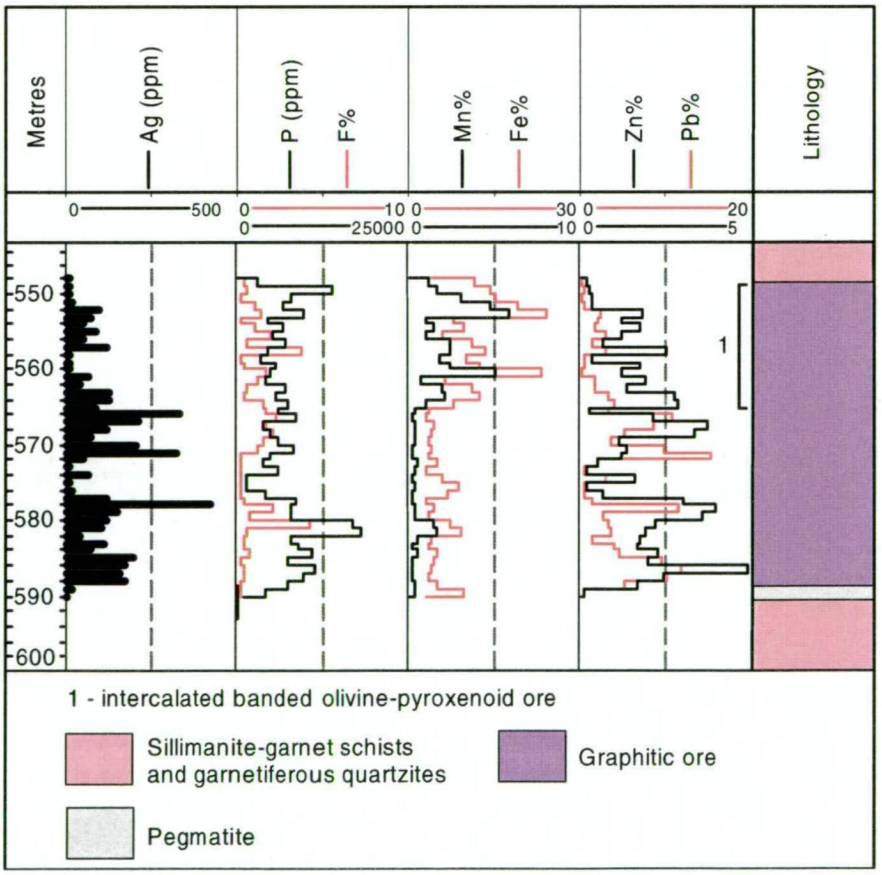

Figure 4.4 Downhole geochemical plot of graphitic ore (CAD163 Southern Zone, see Fig. 4.2), modified after Bodon (1998). Refer to Table 4.1 for explanation of ore types.

banding that characterises graphitic ore. Four principal band types have been recognised based on characteristic mineral assemblages, viz:

- olivine-pyroxenoid-rich,
- quartz-apatite-graphite-rich,
- biotite-garnet-hornblende-graphite-rich,
- and apatite-garnet-rich.

These discrete band types are typically interbedded, the relative proportions of which define an 'ore facies'. In this context, the criteria used to constitute the distinction of a discrete facies based on band type is one in which the predominance of a particular band type extending over an interval of >1m is commonplace. On this basis, three ore facies have been recognised and named using mineralogical rather than textural criterion. These are the:

- olivine facies,
- quartz-apatite facies,
- and biotite-garnet(-hornblende) facies.

Contacts between the ore facies are transitional over several metres and are typically characterised by intercalations rather than uniform gradational trends. Apatite-garnet-rich bands do not occur in high enough concentrations to predominate over other band types for intervals >1m. Hence, the criterion used to define a facies distinction (ibid.) is not satisfied and is therefore unwarranted. In fact, apatite-garnet-rich bands are found in all facies to varying degrees, but have never been observed as the predominant band type. Even though bands are laterally continuous over several metres, they rarely attain thicknesses >1cm; sub-millimetre to sub-centimetre thicknesses are the norm.

Granoblastic microscopic textures and spheroidal inclusions in silicate gangue minerals are features common to all ore facies. In particular, granoblastic sulphide-silicate textures and spheroidal inclusions of sulphide in silicates are intrinsic features of graphitic ore. Generally speaking, inclusion types typically reflect the mineralogy of the particular band type. For example, hedenbergite in a hedenbergite-knebelite-pyroxferroite-quartz band will typically contain inclusions of the latter minerals. However, mutual inclusions do not occur between constituent minerals comprising a particular band. For example, hedenbergite and pyroxferroite inclusions in knebelite are extremely rare, but knebelite inclusions in hedenbergite and pyroxferroite are common.

4.4.1 Olivine facies

The olivine facies comprises olivine-pyroxenoid(± manganoan almandine, hedenbergite, hornblende) bands <1cm to 20cm thick. Interbands are dominated by 1mm to 20cm thick quartz-apatite-graphite ± biotite-garnet-hornblende (Fig. 4.5a to c). Rare fluorite-rich bands have also been observed (Fig. 4.5b). Zones up to 3m thick of massive olivine-pyroxenoid occur in some drillhole intersections. Magnetite is typically absent, although when present,

Figure 4.5 Graphitic ore — the olivine facies.

A. Diffuse olivine-pyroxferroite band (position 1) and apatite-manganoan almandine band (position 2) within massive quartz-apatite-galena (position 3). An S_1 foliation is defined by the preferred alignment of pyroxferroite-knebelite aggregates (position 1) and disseminated, ovoid hornblende poikiloblasts (position 4; CAD034, 115.4m).

B. Pyroxferroite-knebelite banding with abundant coarse-grained disseminated galena (position 1). Other bands types comprise minor apatite-manganoan-rich almandine (position 2), and fluorite-rich bands (position 3; CAD160, 346.4m).

C. Hedenbergite-rich variety of olivine facies ore, comprising hedenbergite-pyroxferroite bands (position 1), quartz-apatite-galena-graphite bands (position 2), manganoan almandine-apatite bands (position 3), quartz-graphite-galena bands (position 4), and fluorite-rich bands (position 5). Minor irregular F_1 or F_2 folds are evident (CAD160, 351.6m).

D. Photomicrograph of coexisting knebelite, hedenbergite, garnet, hornblende, quartz and sulphides displaying characteristic mutual grain boundary relationships. Knebelite occurs as inclusions in hedenbergite and garnet. There is no retrograde alteration of silicate phases. Galena occurs as fine inclusions in garnet and knebelite, and forms an integral part of the overall granoblastic texture (plane-polarised transmitted light, NZ043-18).

E. Photomicrograph of pyroxferroite containing inclusions of knebelite, garnet, and minor grunerite. Knebelite-quartz also forms the matrix between pyroxferroite grains. Some pyroxferroite grain boundaries are manifested by knebelite-quartz inclusion trails (centre of view) that represent the remnants of the knebelite-quartz matrix prior to coalescence of pyroxferroite grains. There is no evidence of retrograde alteration. Minor sulphide also fills interstices between pyroxferroite grains (plane-polarised transmitted light, NZ160-25).

F. Photomicrograph of a knebelite-pyroxferroite-quartz band and adjacent quartz-graphite-apatite galena band. Both band types are characterised by granoblastic textures, although not as well developed in the knebelite-rich band. Comparatively large pyroxferroite grains occur along the contact between the band types. An S_1 foliation is defined by the very weak alignment of knebelite grains and is more obvious at hand-specimen scale (plane-polarised transmitted light, NZ035-2).

G. Photomicrograph of displaying the retrogression of pyroxferroite to grunerite (plane-polarised transmitted light, NZ069-4).

Abbreviations: ga-galena, gr-graphite, gt-manganoan almandine, gu-grunerite, hb-hornblende, hd-hedenbergite, kn-knebelite, qz-quartz, pf-pyroxferroite.

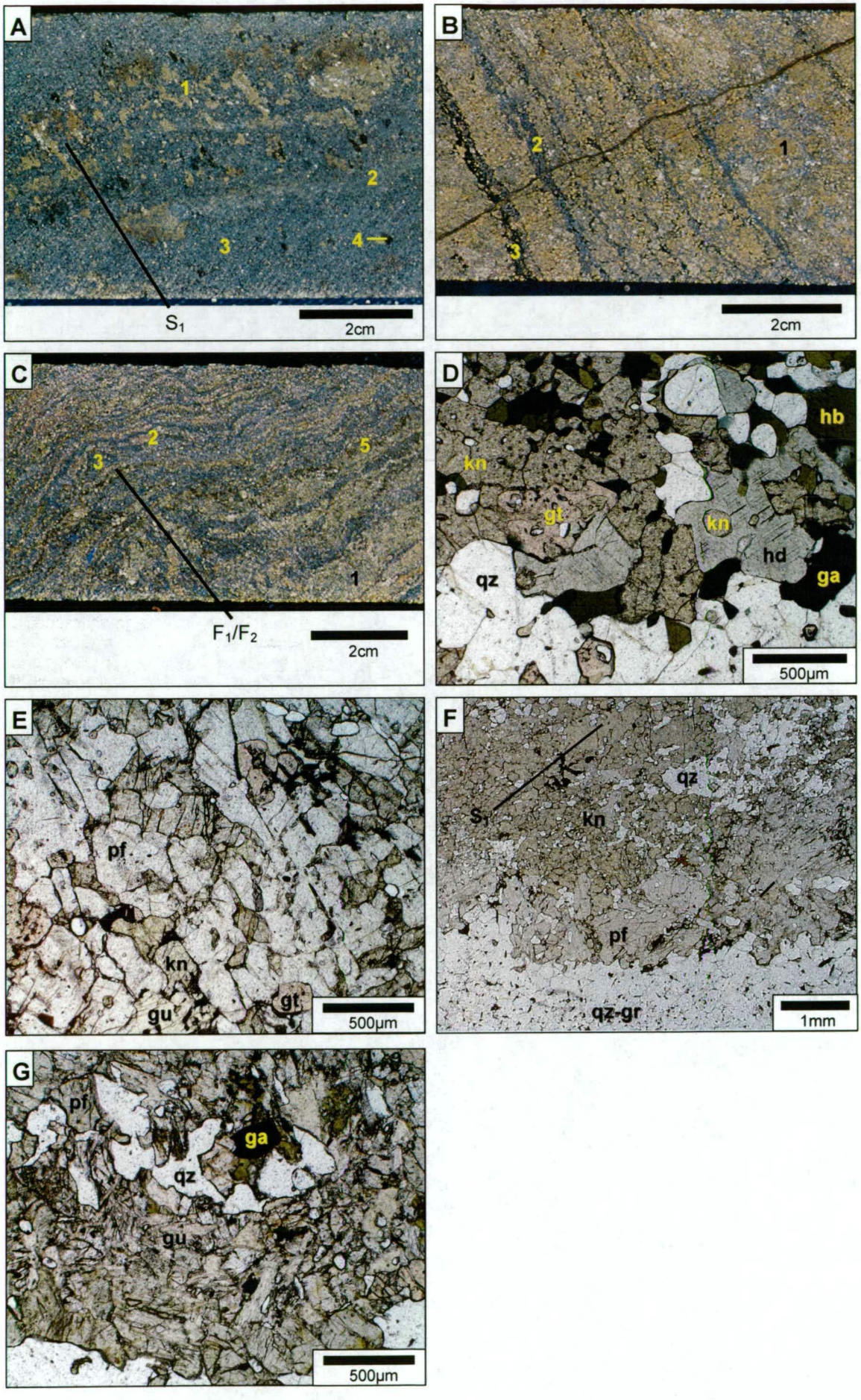
A
1
2
3
4
S1
2cm
B
2
1
3
2cm
C
2
3
5
1
F1/F2
2cm
D
hb
kn
gt
kn
hd
ga
qz
500µm
E
pf
kn
gt
gu
500µm
F
qz
S1
kn
pf
qz-gr
1mm
G
pf
ga
qz
gu
500µm

occurs in association with knebelite ± pyroxferroite-rich bands. Rare monomineralic bands of apatite, up to 5mm thick, have also been observed. Disseminated galena occurs predominantly in the quartz-apatite-graphite bands, but in instances is concentrated in thicker, more massive textured knebelite-pyroxferroite bands (Fig. 4.5b).

Knebelite-pyroxferroite bands are characterised by granoblastic textures in thin section. Mutual spheroidal inclusions in silicates are typical, such as knebelite inclusions in hedenbergite (Fig. 4.5d), and knebelite inclusions in pyroxferroite (Fig. 4.6e). Pyroxferroite and/or hedenbergite inclusions in knebelite are very rare. Manganoan almandine contains inclusions of quartz and rarely apatite. Pyroxferroite, when present, commonly occurs along the contact between knebelite and quartz-apatite-graphite bands where it forms coalesced porphyroblasts and poikiloblasts (Fig. 4.5e and f). Grunerite typically occurs in knebelite-pyroxferroite bands where it is a retrograde product of the latter minerals (Fig. 4.5g). In other cases, granoblastic textural relationships between grunerite, pyroxferroite and knebelite prevail. Hornblende displays similar textural features to grunerite. As a retrograde mineral however, hornblende is the product of garnet and hedenbergite breakdown, such as hornblende reaction coronas encompassing garnet porphyroblasts.

Galena (±sphalerite, pyrrhotite) occurs as rounded inclusions in knebelite, pyroxferroite, hedenbergite, quartz and manganoan almandine. Sulphides also fill interstices between granoblastic silicates. In particular, granoblastic sulphides are not associated with retrograde alteration (Fig. 4.5d). Magnetite displays similar granoblastic textures to the sulphides. Graphite is restricted to quartz-apatite bands and displays the same granoblastic textures as those in other ore facies (see next section). Incipient pyrosmalite alteration of the Fe-Mn silicates is associated with overprinting pyrosmalite (± magnetite) veinlets that contain galena (± freibergite, pyrargyrite, antimonial silver).

When present, an S_1 foliation is defined by the weak alignment of knebelite-pyroxferroite aggregates (Fig. 4.5a and f) and ovoid hornblende poikiloblasts (Fig. 4.5a). Folding of compositional bands is evident in some samples (Fig. 5.4c).

4.4.2 Quartz-apatite facies

The quartz-apatite facies is spatially associated with the olivine facies and commonly occurs as intervals up to 10m thick. The facies has a simple mineralogy of quartz-apatite-graphite-galena ± garnet-fluorite-biotite (Fig. 4.6a and b). Compositional banding is poorly developed and the ore facies has a more massive texture. Where banding is present, it is defined by grain size and/or subtle mineralogical variations (Fig. 4.6b). Apatite-garnet and monomineralic apatite bands, up to 3mm thick may also occur. Apatite also occurs as disseminated subhedral grains and as inclusions in quartz. Fluorite occurs as overprinting veinlets with selvedges depleted in galena, disseminations intergrown with quartz and apatite, and rarely as definable compositional bands (Fig. 4.6b). The facies is typically enriched in galena that occurs as disseminations and isolated coarse grained aggregates (Fig. 4.6a and b).

Figure 4.6 Graphitic ore — the quartz-apatite facies.

A. Massive granoblastic quartz-apatite with abundant disseminated galena (position 1), with areas of very coarse-grained, remobilised galena (position 2). Disseminated, ragged garnet porphyroblasts are evident throughout the rock (position 3) as well as minor pale yellow, fluorite-rich patches (position 4; CAD035, 148.2m).

B. Fluorite-rich quartz-apatite-galena with minor F_2 folding and coarse-grained, remobilised galena (position 1) within fluorite-rich zones (position 2) to bands (position 3). Fluorite-rich and diffuse garnet bands define the F_1 or F_2 folding (CAD016, 113.3m).

C. Photomicrograph of typical granoblastic textured quartz-fluorite-galena. Minor allanite is also present. The high magnification inset displays fluorite inclusions in quartz, and well developed triple junctions between all phases. Retrograde alteration is absent (plane-polarised transmitted light, NZ018-13).

D. Photomicrograph of typical granoblastic sulphide-silicate texture, with blebby, disseminated galena-sphalerite filling interstices and occurring along granoblastic quartz grain margins. Some quartz grains contain fine inclusions of galena. The sample contains no retrograde phases (plane-polarised reflected light, NZ042-8).

E. Photomicrograph of garnet porphyroblasts containing relic pseudomorphs after possible chlorotoid laths overgrown by inclusion-rich garnet in a matrix of granoblastic quartz-graphite(-apatite-sulphide). Inclusions in the porphyroblasts are chiefly quartz and minor graphite and sulphide. Some porphyroblasts have coalesced (plane-polarised transmitted light, NZ023-1).

F. Photomicrograph of a manganoan almandine-apatite band displaying the nature of the sharp contact with adjacent granoblastic quartz-apatite-graphite-sulphide. The textures of the garnets are a diagnostic feature of the band, and appear to have nucleated along the band margins, growing inward. In instances such garnets display radiating inclusion trails producing a pseudo-radial type texture from the nucleation point, e.g. the two garnets in the lower left corner of the field of view (plane-polarised transmitted light, NZ023-1).

Abbreviations: aa-allanite, at-apatite, bt-biotite, fl-fluorite, ga-galena, gr-graphite, gt-manganoan almandine, qz-quartz, sp-sphalerite.

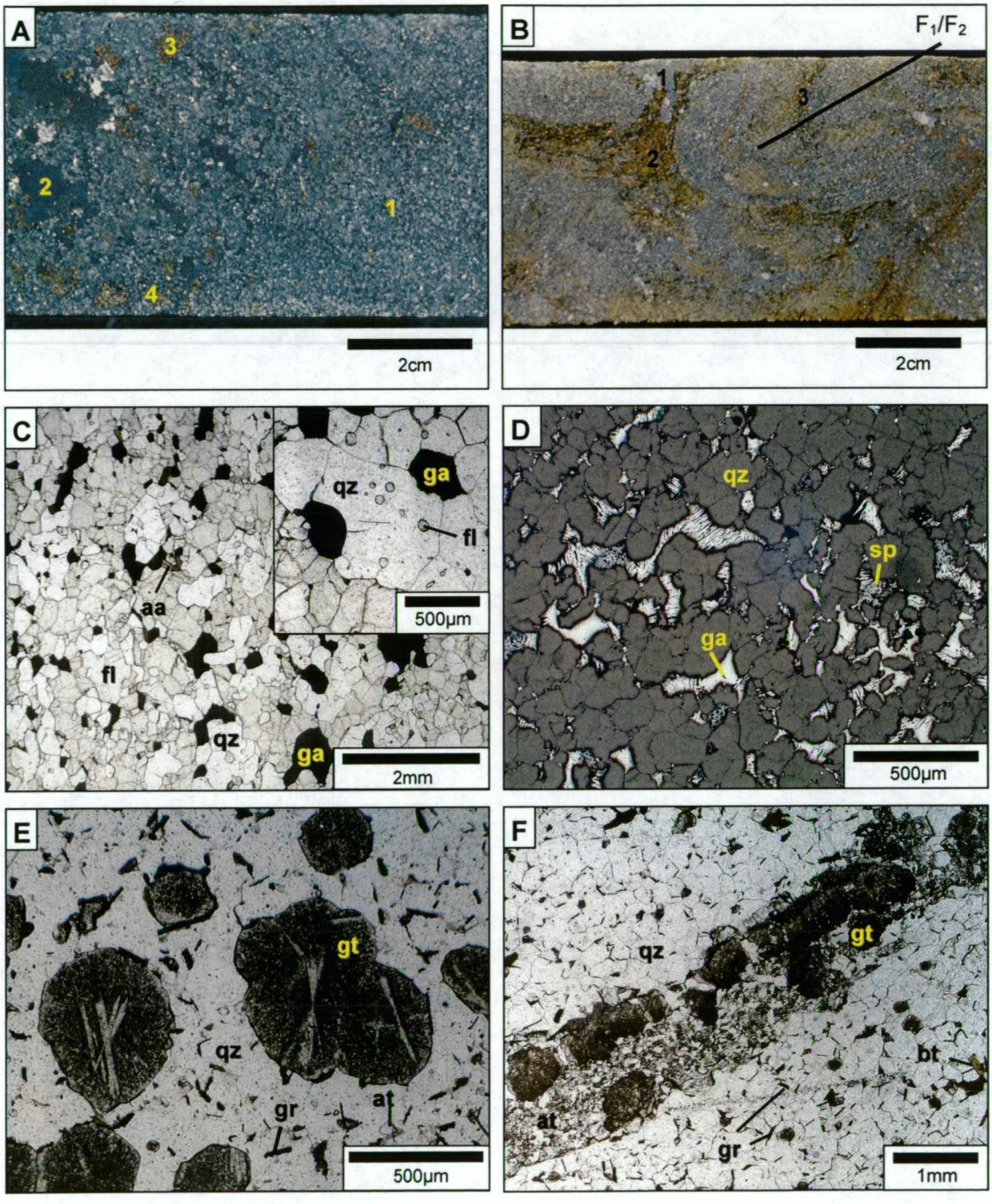
A
3
2
1
4
2cm
B
F1/F2
1
3
2
2cm
C
qz
ga
fl
500µm
aa
fl
qz
ga
2mm
D
qz
sp
ga
500µm
E
gt
qz
gr
at
500µm
F
qz
gt
bt
at
gr
1mm

The facies is characterised by granoblastic sulphide-silicate textures in thin section (Fig. 4.6c and d). Well developed granoblastic textures are developed in quartz-graphite bands (Fig. 4.6f). Galena typically fills interstices between granoblastic quartz and occurs along quartz grain boundaries (Fig. 4.6d). Galena may also occur as spheroidal inclusions in quartz. Similarly, fluorite has a granoblastic texture and occurs as spheroidal inclusions in quartz in some samples (Fig. 4.6c). Sector-twinned manganoan almandine porphyroblasts occur in some samples and in instances contain bow-tie textures that possibly reflect chlorotoid pseudomorphs (cf. Stanton, 1989; Fig. 4.6e). Other garnets display radial textures (see chapter 5) defined by fine quartz inclusion trails (cf. Burton, 1986; Stanton, 1989). Garnets in apatite bands typically occur along the margins of the band and in some samples form a laterally continuous garnet margin (e.g. Fig. 4.7f). These garnets display similar radial textures to those in sector-twinned porphyroblasts, but also show an intriguing banded texture (Fig. 4.6f).

An S_1 foliation is evident in some samples where it is defined by weakly aligned biotite and graphite. F_1/F_2 folds occur in more fluorite-rich varieties (Fig. 4.6b).

4.4.3 Biotite-garnet(-hornblende) facies

The biotite-garnet-hornblende facies occurs as laterally continuous lenses over several tens of metres interbedded with and gradational to both other facies. Thickest intersections occur toward the periphery of the orebody in the Northern Zone. Fine-scale compositional bands (sub-millimetre to tens of centimetres) are a definitive feature of this facies and are defined by variations in proportions of chiefly quartz, apatite, biotite, garnet, hornblende, graphite (Fig. 4.7a to g), including sphalerite and galena (Fig. 4.7a to g). Knebelite and pyroxferroite are rare. Individual bands are laterally continuous and maintain constant thickness over several metres. Some bands display sharp margins (Fig. 4.7b, d, e and f), whereas other bands appear to grade into one another (Fig. 4.7a and d), or display an internal grading from garnet-poor to garnet-rich (Fig. 4.7c and d). Apatite, garnet and rarely graphite locally occur as monomineralic bands up to 5mm thick. Rare fluorite occurs as overprinting veinlets, disseminations, and within apatite-garnet bands.

Granoblastic sulphide–silicate textures are common to all band types. Garnet porphyroblasts typically have an inclusion-rich core overgrown by an inclusion-free rim (Fig. 4.7h). Inclusion types consist of abundant quartz and minor apatite, graphite, sphalerite, galena and rare pyrrhotite and biotite. Figure 4.7g is a particularly good example of large spheroidal sphalerite inclusions in garnet porphyroblasts hosted in a sphalerite-rich band (position 3 in the figure). Other textural types include sector-twinned garnets, and disseminated garnet poikiloblasts in graphite absent quartz-apatite bands. In some samples, granoblastic quartz grains contain similar inclusion types to garnets such as sphalerite, galena, graphite and apatite, and have inclusion free overgrowths (Fig. 4.7i). Poikiloblastic hornblende intergrown with quartz and poikiloblastic garnet occur in quartz-apatite-rich bands. There is little evidence to suggest that poikiloblastic hornblende formed as a retrograde product of garnet; grain boundary

Figure 4.7 Graphitic ore — the biotite-garnet-hornblende facies.

A. Fine-scale compositional banding with small-scale F_3 folds. The S_1/S_2 foliation is parallel to banding. Bands consist of apatite-garnet (position 1), quartz-sphalerite (position 2), quartz-galena (position3), manganoan almandine-apatite (position 4), quartz-biotite-graphite-apatite containing manganoan almandine porphyroblasts (position 5), and hornblende-rich bands (position 6). A veinlet filled with remobilised galena-sphalerite is also present (position 7; CAD157, 312.0m).

B. Convoluted to ptygmatic folding of possible D_3 origin. Veinlets of remobilised sphalerite and galena (position 1) define a weakly developed fracture cleavage (CUD134, 265.0m).

C. Fine-scale compositional banding defined by biotite-manganoan almandine-graphite-rich (position 1), manganoan almandine-apatite-rich (position 2), quartz-biotite-graphite-rich (position 3), quartz-galena-graphite-rich (position 4), and a manganoan almandine-biotite-graphite-rich (position 5) bands. At position 5, variations in garnet porphyroblast abundance and size define an apparent grading (CAD004, 109.1m).

D. Garnet-rich (position 1 and 2) and apatite-rich (position 3) banding as well as a carbonate-rich band (position 4). Note the graded garnet bands at positions 1 and 2 (CAD160, 353.9m).

E. Scanned thin section view of the folded compositional banding in B. Bands are comprised of three basic types, namely garnet-apatite (1), hornblende-garnet-quartz-sphalerite-galena (2), and quartz-apatite-graphite-biotite-sphalerite-galena. The thicker hornblende-rich band to the left of view contains a higher abundance of sphalerite toward its right-hand margin and a higher concentration of galena toward its left-hand margin. The thinner hornblende-rich band also displays a similar intraband sulphide zonation, with sphalerite enrichment along its right-hand margin. However, a galena-rich zone is absent. The far right-hand garnet-apatite band shows spectacular ptygmatic folding. The sample contains minor overprinting pyrosmalite alteration associated with fine fractures that contain remobilised sphalerite and galena (transmitted light, SZU134-1).

F. Photomicrograph of folded bands defined by garnet-apatite (position 1), quartz-graphite-sulphide (position 2), garnet-biotite-sulphide (position3) and biotite-graphite-quartz-sulphide bands. Sulphides, intergrown with silicates, form a component of the granoblastic texture. Sulphides also occur as inclusions in garnet and quartz. There is no retrograde alteration present in the sample. The preferred alignment of biotite and graphite define an S_1 foliation parallel to banding, which has been folded by a small F_2 fold (plane-polarised transmitted light, NZ160-31).

G. Photomicrograph of the same sample as that in F. displaying a folded S_1 foliation at low angle to the banding. S_1 is defined by the preferred alignment of biotite and graphite. Folded bands (F_2) consist of the same mineral assemblages as those in C., i.e. garnet-apatite (position1), quartz-graphite-sulphide (position 2) and garnet-biotite-sulphide bands (position 3). Spheroidal sulphide inclusions occur in the garnet porphyroblasts. There is no retrograde alteration in the sample (plane-polarised transmitted light, NZ160-31).

H. Photomicrograph of granoblastic textured biotite-graphite-quartz band containing a garnet porphyroblast and minor disseminated sulphides. The preferred alignment of biotite and graphite define an S_1 foliation that wraps around the garnet porphyroblast. Recrystallised biotite, with no preferred orientation, occurs in the pressure shadow sites adjacent to the porphyroblast (position 1). Retrograde alteration is absent (plane-polarised transmitted light, NZ040-8).

I. Photomicrograph of displaying well developed 120° triple junctions in coexisting quartz and sulphide. Quartz grains consist of a core containing abundant spheroidal sulphide inclusions and blades of graphite (qz1), that is overgrown by a later generation of inclusion free quartz (qz2). Graphite laths are also aligned along quartz grain boundaries (plane-polarised transmitted light, SZ157-2).

Abbreviations: bt-biotite, ga-galena, gr-graphite, gt-manganoan almandine, qz-quartz, sp-sphalerite.

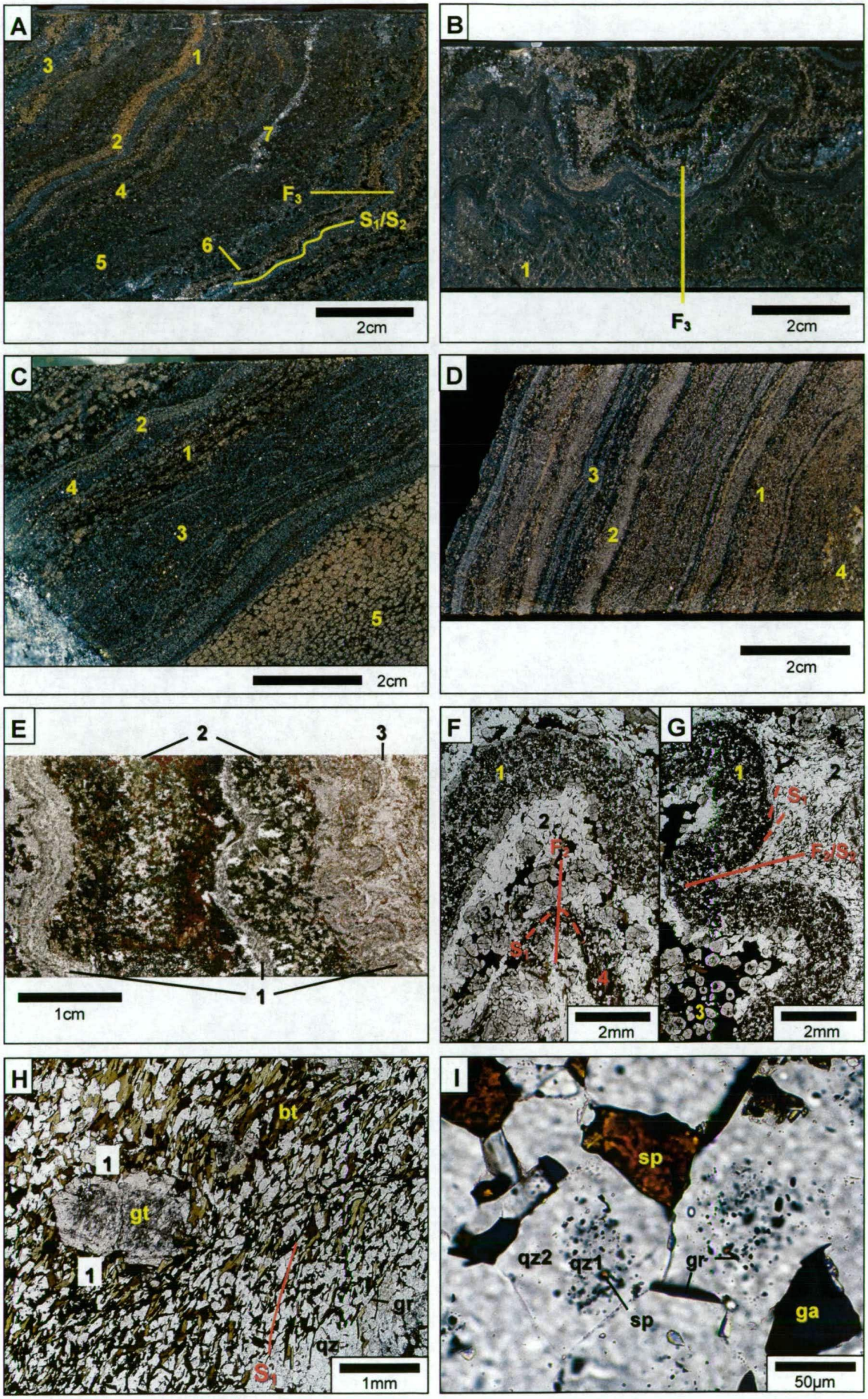
A
3
1
2
7
4
F3
S1/S2
6
5
2cm
B
1
F3
2cm
C
2
1
4
3
5
2cm
D
3
1
2
4
2cm
E
2
3
1
1cm
F
1
2
F2
3
S1
4
2mm
G
1
2
S1
F2/S2
3
2mm
H
bt
1
gt
1
gr
qz
S1
1mm
I
sp
qz2
qz1
gr
sp
ga
50μm

relationships suggest they formed contemporaneously. In contrast, granoblastic textures persist in hornblende-rich bands. Inclusions in hornblende comprise quartz, apatite and minor sphalerite, galena, chalcopyrite, pyrrhotite and garnet. Graphite laths (up to 0.5mm) are typically arranged along quartz grain boundaries (Fig. 4.7h and i); they also crosscut quartz grain boundaries. Sphalerite and galena occur as isolated, disseminated curvilinear grains in triple junction sites between quartz grains, and lenticular shaped blebs along quartz grain boundaries (Fig. 4.7i). Rare pyrosmalite veins overprint the banding and contain galena, and minor freibergite and sphalerite. Localised incipient pyrosmalite alteration of hornblende and biotite is associated with the veining.

Folds and mineral foliations are developed to varying degrees. Folding of compositional banding is common (Fig. 4.7b), with some samples displaying spectacular ptygmatic folding (Fig. 4.7e). The alignment of graphite and biotite defines both the S_1 and S_2 foliation that have the same orientation as the pervasive S_1/S_2 observed throughout the mine area (Fig. 4.7f and g). A biotite-graphite schistosity (S_1) wraps around garnet porphyroblasts in biotite-rich bands (Fig. 4.7h). Coarse grained remobilised galena (± sphalerite) fills extensional veinlets normal to S_1/S_2 forming small-scale piercement veins and localised durchbewegt-textured breccia zones. Elsewhere remobilised galena and sphalerite infills a spaced S_3 fracture cleavage (Fig. 4.7b). Other deformation textures include boudinaged garnet-rich bands, convoluted to brecciated compositional banding (Fig. 4.7b), and centimetre-scale rootless F_1/F_2 folds and isoclines with attenuated fold limbs. The earliest deformation fabric is preserved in garnet porphyroblasts where rare quartz inclusion trials define a relict foliation that is morphologically similar to the S_i foliation preserved garnet porphyroblasts in the proximal garnetiferous metasediments.

4.5 Fe-Mn SILICATE ORE

Fe-Mn silicate ore is characterised by wholerock Fe contents >15 wt%, with some intersections averaging 30-40 wt% Fe (Fig. 4.8). Gangue minerals include quartz, hedenbergite, pyroxferroite, knebelite and variable proportions of fluorite, magnetite, garnet, apatite, amphiboles (ferro-actinolite and hornblende), pyrosmalite, chlorite (greenalite, chamosite) and epidote group minerals (ilvaite and allanite). Common sulphide minerals include galena, sphalerite, loellingite, arsenopyrite, pyrrhotite, various Ag-sulphosalts (chiefly freibergite and pyrargyrite) and variable proportions of chalcopyrite. Minor antimonides (allargentum) and arsenides (gudmundite) are also present. These minerals combine to form four sub-types of ore, each having distinct Fe-Mn silicate assemblages (Table 4.1) and metal associations (Fig. 4.8, Tables 4.2 and 4.3), viz.:

i) Olivine-pyroxenoid (Pb-Ag(-Sb), Fe-Mn(-Ca); quartz absent).
ii) Banded olivine-pyroxenoid (Pb-Ag(-Sb), Fe-Mn(-Ca); quartz-rich).
iii) Hedenbergite (Zn(-As), Fe-Ca(-Mn); quartz-poor <10 modal%).
iv) Banded hedenbergite (Zn(-As), Fe-Ca(-Mn), quartz-rich >10 modal%).

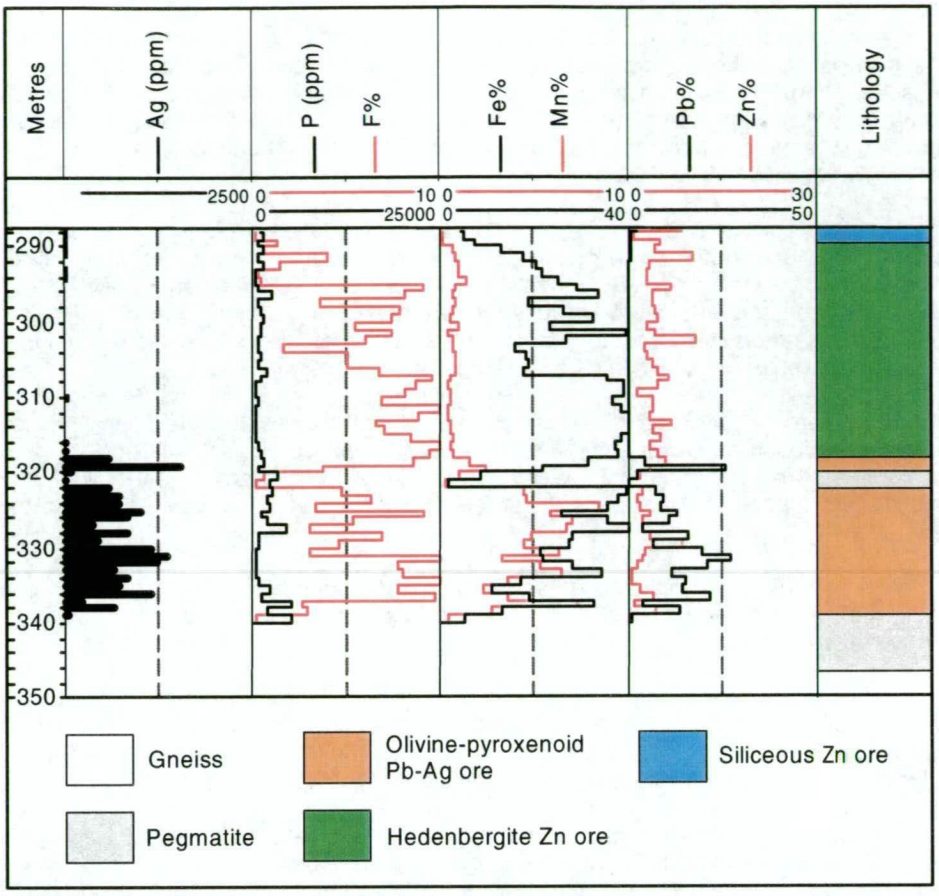

Figure 4.8 Downhole geochemical plot of olivine-pyroxenoid and hedenbergite ores (CAD214, Southern Zone), modified after Bodon (1998). Refer to Table 4.1 for explanation of ore types.

4.5.1 Olivine-pyroxenoid ore

This type constitutes nearly 70% of the currently defined Southern Zone resource, occurring as two major lenses in the hanging wall and footwall; the Footwall Pb lode and the Hanging wall Pb lode (Bailey, 1998; Table 4.2). In the footwall of the Southern Zone it has a lenticular geometry that attains a maximum thickness of approximately 25m on section 4700mN (Fig. 4.2), and extends some 350m along strike and 420m down-dip. In the hanging wall of the Southern Zone it reaches a maximum thickness of approximately 45m on section 4700mN (Fig. 4.2), and extends for 1km along strike and some 580m down-dip (more commonly 250m down-dip). To the south, the hanging wall and footwall lenses are truncated by the Footwall shear and Hamilton fault. Olivine-pyroxenoid ore only occurs in the hanging wall of the Northern Zone, where it attains a maximum thickness of approximately 65m on section 5300mN (Fig. 4.3), extending northward along strike for approximately 250m.

The ore type is characterised by strong correlations between elevated Mn (>2 wt% wholerock Mn) and Pb-Ag grades (Fig. 4.8; Table 4.3). Contacts with hedenbergite ore are sharp to gradational over centimetre scales, and are characterised by abrupt changes in Mn, Pb, Zn and Ag concentrations (Fig. 4.8). Characteristic gangue minerals include ferroan knebelite, fluorite (up to 50-60 modal% in some samples), magnetite, pyrosmalite, localised manganoan pyroxferroite, minor apatite, and widespread trace allanite (Table 4.1). Manganoan grunerite is rare and quartz is notably absent. Sulphides include galena, pyrrhotite, freibergite, pyrargyrite,

Figure 4.9 Olivine-pyroxenoid ore.

A. Fluorite-rich ore displaying typical contrasting brittle-ductile breccia textures (durchbewegung). Clasts consist of knebelite (±pyroxferroite; position 1) and magnetite (position 2) grain aggregates and solitary porphyroclasts hosted in a matrix of recrystallised fluorite and blebby, coarse-grained galena (and minor sphalerite, pyrrhotite, Ag-sulphosalts). Fine, discontinuous fractures infilled with galena emanate from the coarse grained blebs, and commonly resemble small-scale piercement veins (CAD058, 286.3m).

B. Photomicrograph of a fluorite-rich zone displaying classic durchbewegt deformation textures. Solitary knebelite and magnetite grains form porphyroclasts in a matrix of recrystallised fluorite and ribbons of galena. Incipient pyrosmalite alteration of knebelite is a characteristic feature. It is difficult to correlate the durchbewegt textures to a particular deformation event. However, given the intensity of deformation and the static recrystallisation of fluorite after the shearing, a D_1 to D_3 timing is likely (plane-polarised transmitted light, SZ037-13).

C. Photomicrograph of coexisting knebelite, apatite, magnetite and sphalerite displaying mutual grain boundary relationships. Apatite and knebelite both contain spheroidal inclusions of one another. Sphalerite occurs along grain boundaries, in triple junction sites and as spheroidal inclusions in knebelite and apatite. Likewise, magnetite displays similar textures (plane-polarised transmitted light, NZ034-4).

D. Photomicrograph displaying curvilinear and smooth, rounded grain boundary relationships between phases, similar to those in C., but involving calcite rather than apatite (plane-polarised transmitted light, NZ034-4).

E. Photomicrograph of spheroidal galena (ga1) and fluorite (fl1) inclusions in a rounded knebelite grain. Incipient pyrosmalite alteration of knebelite occurs along intragranular fractures and grain boundaries. Abundant later stage galena (ga2) and fluorite (fl2), is intergrown with the pyrosmalite and forms a matrix to knebelite grains (polarised transmitted light, SZ052-24).

F. Photomicrograph of rounded knebelite and magnetite grains in a matrix of later stage galena(ga2)-sphalerite-pyrrhotite-fluorite(fl2). Knebelite contains spheroidal inclusions of an earlier galena generation (ga1). Magnetite (mt1) contains spheroidal inclusions of knebelite and fluorite (fl1). A later generation of magnetite (mt2) is associated with pyrosmalite alteration of knebelite, and typically occurs as thin overgrowths and rinds along knebelite grains (plane-polarised reflected light, SZ043-8).

G. Photomicrograph of a pyrosmalite veinlet containing secondary magnetite (mt2), with selvedges of pyrosmalite alteration of granoblastic textured knebelite. Fluorite remains unaltered. Early magnetite (mt1) occurs as spheroidal inclusions in knebelite and as curvilinear grains filling interstices between knebelite grains. Fluorite displays a similar textural occurrence (plane-polarised transmitted light, NZ034-13).

H. Photomicrograph of relict granoblastic sulphide-silicate texture. Knebelite has been pseudomorphed by ferroan pyrosmalite (ps). However, the relic granoblastic texture has been preserved. Secondary magnetite (mt2) and manganoan pyrosmalite overgrowths (mps) have invaded relic curvilinear textured galena producing a characteristic flaser texture indicative of localised solution-associated remobilisation (plane-polarised reflected light, NZ035-32).

Abbreviations: at-apatite, ca-calcite, fl-fluorite, ga-galena, kn-knebelite, mps-manganoan pyrosmalite, mt-magnetite, pg-pyrargyrite, po-pyrrhotite, ps-ferroan pyrosmalite, sp-sphalerite.

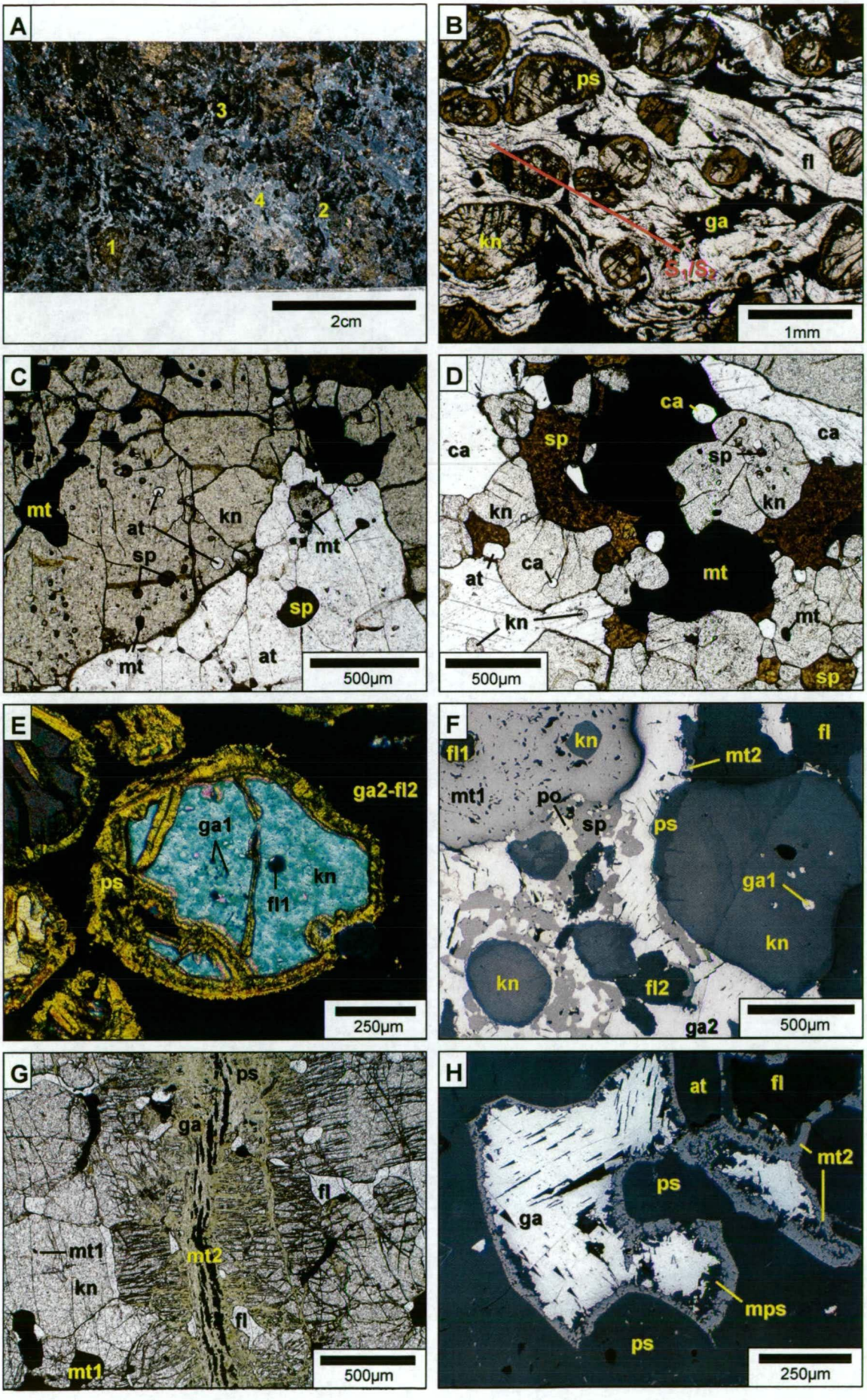
A
3
4
2
1
2cm
B
ps
fl
ga
kn
S_1/S_2
1mm
C
mt
at
kn
sp
mt
sp
mt
at
500μm
D
ca
sp
ca
ca
sp
kn
kn
at
ca
mt
kn
mt
500μm
sp
E
ga2-fl2
ga1
ps
kn
fl1
250μm
F
fl1
kn
mt2
fl
mt1
po
sp
ps
ga1
kn
kn
fl2
ga2
500μm
G
ps
ga
fl
mt1
mt2
kn
fl
mt1
500μm
H
at
fl
mt2
ps
ga
mps
ps
250μm

minor sphalerite, arsenopyrite, gudmundite (FeSbS), and trace pyrite and marcasite (Table 4.1). Loellingite ($FeAs_2$), with arsenopyrite overgrowths, and antimonial silver (approaching allargentum compositions ($Ag_{1-x}Sb_x$); French et al., 1994) may also be present. Chalcopyrite is uncommon, but does occur as localised disseminated patches in the ore.

The ore is characterised by contrasting brittle-ductile breccias indicative of durchbewegt textures (Vokes, 1969; Marshall and Gilligan, 1989; Table 4.1). Clasts comprise sulphide-bearing equigranular aggregates (from 0.5mm to 10cm) of knebelite-magnetite (± pyroxferroite) in a matrix of coarse grained (up to 2mm) recrystallised fluorite (Fig. 4.9a). Penetrative anastomosing mylonitic zones up to 10cm thick are common in fluorite-rich zones, and comprise porphyroclasts of magnetite, knebelite, apatite and minor pyroxferroite in a matrix of recrystallised fluorite containing ribbons of galena and/or pyrrhotite (Fig. 4.9b). The enveloping surface of the mylonitic zones is parallel to the S_2 foliation in host rocks to the deposit. More coherent granoblastic textures occur in fluorite-poor areas that are dominated by knebelite, magnetite and minor pyroxferroite. Coarse-grained (up to 1cm), recrystallised galena infills fractures and intergranular pull-aparts forming irregular blebby textures with fine veinlets of galena emanating from their margins (Fig. 4.9a). Rare folded magnetite bands indicate that parts of the ore may have been compositionally banded prior to deformation.

Microscopic textures are characterised by mutual grain boundary relationships between magnetite, knebelite, apatite, pyroxferroite, fluorite and accessory allanite and extremely rare carbonate. All of these minerals contain spheroidal inclusions of one another (Fig. 4.9c to f). Fluorite also fills intergranular spaces between magnetite, knebelite, apatite and pyroxferroite, displaying more granoblastic and curvilinear grain boundary textures within knebelite-rich aggregates. Spheroidal galena, and more rarely sphalerite, form inclusions (<250µm in diameter) in knebelite (Fig. 4.9c to f) and to a lesser degree in magnetite and pyroxferroite. Spheroidal pyrrhotite, composite galena-pyrrhotite, sphalerite-pyrrhotite inclusions have also been observed in knebelite.

Pyrosmalite alteration of knebelite and pyroxferroite is common along grain boundaries, intragranular fractures (Fig. 4.9e, g and h) and along cleavage surfaces in pyroxferroite. In all instances, pyrosmalite displays no preferred orientation. Ferroan pyrosmalite and fine-grained "lace" textured galena pseudomorphs knebelite grains, although the granoblastic fabric is preserved (Fig. 4.9h and 4.10a). However, pyroxferroite grain fabrics are commonly destroyed, leaving relic corroded grains in a groundmass of fine grained ferroan pyrosmalite and galena. Magnetite, apatite, fluorite and accessory allanite remain unaltered and retain their original grain fabrics (Fig. 4.9g). Fibrous manganoan pyrosmalite intergrown with secondary magnetite, galena and Ag-sulphosalts, have overgrown pseudomorphed knebelite grains in strongly altered samples (Fig. 4.9h and 4.10a). Fibrous terminations project into coarse grained recrystallised galena (Fig. 4.10a), and characteristic 'flaser' textures are formed in relict isolated curvilinear blebs of galena interstitial to pyrosmalite altered knebelite (Fig. 4.9h). Manganoan pyrosmalite-secondary magnetite overgrowths also occur on early,

Figure 4.10 Olivine-pyroxenoid and banded olivine-pyroxenoid ores.

A. Photomicrograph of knebelite grain pseudomorphed by ferroan pyrosmalite with fibrous manganoan pyrosmalite overgrowths intergrown with pyrargyrite, galena and minor secondary magnetite (mt2). Galena intergrown with the ferroan pyrosmalite has replaced knebelite forming delicate "lace-like" textures. Late stage galena, pyrargyrite, and minor pyrite and sphalerite form the matrix to altered knebelite grains (plane-polarised reflected light, SZ074-5).

B. Photomicrograph of subhedral to anhedral pyrargyrite and freibergite-pyrrhotite inclusions in galena. Strong, red internal reflections in pyrargyrite are a diagnostic feature. Although the textures in the sample are inconclusive, Dugmore (1998) suggests that pyrargyrite formed via the breakdown of freibergite during retrogression (plane-polarised reflected light, NZ035-32).

C. Photomicrograph of euhedral crystals of gudmundite growing into a microscopic vugh infilled with later generation fluorite. Secondary magnetite (mt2) rims the margins of the galena. Intergrown pyrrhotite and allargentum typically occur along the margins of coarse-grained galena (plane-polarised reflected light, SZ048-3).

D. Photomicrograph of pyrrhotite-allargentum inclusion in galena displaying typical emulsoid-type texture. Minor secondary magnetite(mt2)-pyrosmalite is also present (plane-polarised reflected light, SZ037-13).

E. Knebelite-pyroxferroite bands (position 1) and quartz-apatite ± graphite bands (position 2) are overprinted by an S_1 foliation that is defined by the preferred alignment of knebelite-pyroxferroite aggregates. Note the fine pyrosmalite veinlets to the left of the field that overprint the S_1 foliation (CUD128, 26.7m).

F. Photomicrograph of E. displaying the preferred alignment of knebelite-pyroxferroite aggregates that define the S_1 foliation (plane-polarised transmitted light, SZU128-1).

G. Hedenbergite vein (position 1) with an associated zoned alteration selvedge comprising a proximal hedenbergite-garnet-quartz zone (position 2), and an outer pyroxferroite zone (position 3) overprinting banded olivine-pyroxenoid ore and the S_1/S_2 foliation (CAD061, 531.0m).

H. Photomicrograph displaying alteration of knebelite to secondary pyroxferroite. Strongly corroded knebelite grains intergrown with quartz, occur as inclusions within the pyroxferroite poikiloblast and along grain margins (plane-polarised transmitted light, NZ004-5).

Abbreviations: ag-antimonial silver, at-apatite, bt-biotite, fl-fluorite, fr-freibergite, gd-gudmundite, kn-knebelite, ga-galena, gt-garnet, mps-manganoan pyrosmalite, mt2-secondary magnetite, pf-pyroxferroite, pg-pyrargyrite, po-pyrrhotite, ps-pyrosmalite, qz-quartz, sp-sphalerite.

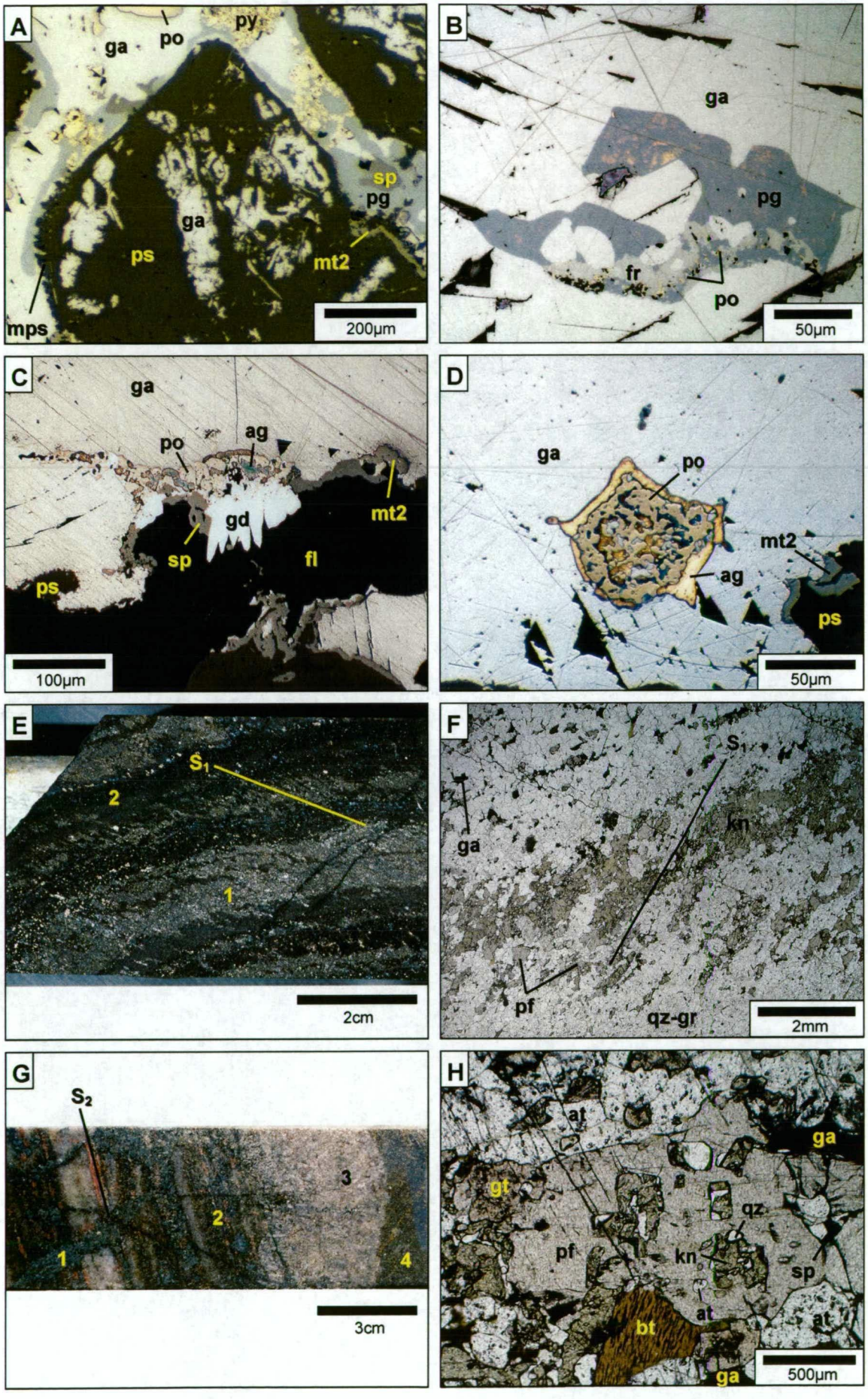
A
ga
po
py
sp
pg
ga
ps
mt2
mps
200µm
B
ga
pg
fr
po
50µm
C
ga
po
ag
mt2
gd
sp
fl
ps
100µm
D
ga
po
mt2
ag
ps
50µm
E
S1
2
1
2cm
F
S1
ga
kn
pf
qz-gr
2mm
G
S2
3
2
1
4
3cm
H
at
ga
gt
qz
pf
kn
sp
at
bt
at
ga
500µm

comparatively coarser grained magnetite grains, as well as filling fractures in the latter. Pyrosmalite-secondary magnetite-galena (± freibergite, pyrargyrite, antimonial silver) veinlets commonly overprint the rock, and possess alteration selvages of pyrosmalite and minor late stage fine grained galena (Fig. 4.9g).

Freibergite occurs as inclusions in coarse grained galena, and is commonly associated with pyrosmalite-galena alteration of Fe-Mn silicates. Pyrargyrite, antimonial silver and gudmundite display similar textural habits to freibergite, but are more common in intensely pyrosmalite altered samples along the margins of coarse grained galena, and within manganoan pyrosmalite overgrowths (Fig. 4.10a) where they have replaced freibergite (Fig. 4.10b). Rare euhedral gudmundite crystals occur along the margins of fluorite filled cavities (Fig. 4.10c). Pyrrhotite, gudmundite and antimonial silver also form emulsoid-textured aggregates after freibergite (Fig. 4.10d). Pyrrhotite also occurs as subhedral and bladed inclusions in coarse grained galena and has been variably altered to birds-eye textured pyrite and marcasite (cf. Craig and Vaughan, 1981, p. 139), especially in strongly pyrosmalite altered samples. Minor sphalerite hosted in coarse-grained galena, contains fine pyrrhotite and rare chalcopyrite inclusions.

Carbonate-chlorite (± quartz) alteration is spatially associated with late subvertical D_5 faults that overprint the ore (Bodon, 1995; McCarthy, 1996; Dugmore, 1998). Within these zones, carbonate veins and breccias contain minor amounts of remobilised galena, sphalerite and fluorite, as well as a diverse suite of late stage Ag-sulphosalts (Dugmore, 1998).

4.5.2 Banded olivine-pyroxenoid ore

This type comprises alternating knebelite-pyroxferroite and quartz-apatite (± manganoan almandine, graphite, amphibole) bands (Fig. 4.10e; Table 4.1) that are continuous over metre scales, and are parallel to possible bedding in adjacent host rocks. Contacts with host rocks are marked by a ~10cm thick garnet zone and there is no evidence of transgressional relationships. The ore type displays clear spatial associations with graphitic (olivine facies specifically) and olivine-pyroxenoid ore, occurring as a transitional style of banded ore between these two types. Due to these gradational relationships, metal zonation characteristics tend to be intermediate between graphitic and olivine-pyroxenoid ore. Correlation between Fe-Mn, and Pb-Ag are not as clear as olivine-pyroxenoid ore (e.g. Fig. 4.4, position 1, 548-564m). Elevated P (up to 2.5 wt%) occurs in some intervals transitional to graphitic ore (Fig. 4.4).

In the Southern Zone, banded olivine-pyroxenoid ore forms the down-dip extension of footwall olivine-pyroxenoid ore and is up to 35m thick on section 4700mN (Fig. 4.2). North of section 4800mN, it is intercalated with graphitic ore. In the hanging wall, banded olivine-pyroxenoid ore forms a laterally continuous lens that can be traced over the full strike length of the deposit (approximately 1.5km) in the same structural position. On section 4700mN in the Southern Zone, the hanging wall lens forms the up-dip extension to olivine-pyroxenoid ore and is up to

50m thick (Fig. 4.2). To the north, this lens contains minor intercalated graphitic ore and is up to 170m thick on section 5300mN in the Northern Zone (Fig. 4.3).

Ore consists of disseminated galena that typically occurs in quartz-apatite bands, although locally abundant concentrations occur in knebelite-pyroxferroite-fluorite-magnetite-rich intervals (up to 5m thick) in transitional zones adjacent to significant olivine-pyroxenoid ore lenses. Zones up to 3m thick of massive equigranular knebelite-pyroxferroite occur in some intervals. Magnetite and fluorite are typically absent, although minor amounts occur in some knebelite bands, especially in transitional zones adjacent to high grade olivine-pyroxenoid ore.

Granoblastic fabrics dominate microscopic textures. In quartz-apatite bands, quartz displays similar textures and inner inclusion-rich cores to quartz in graphitic ore. Inclusions consist of galena, pyrrhotite, sphalerite, apatite and graphite. Knebelite and pyroxferroite display mutual grain boundary relationships (Fig. 4.10f). In more sulphide-rich bands, the latter minerals host spheroidal inclusions of sphalerite, galena and pyrrhotite.

Rare secondary pyroxferroite forms an outer alteration zone to hedenbergite-garnet-quartz alteration that transgresses compositional banding (Fig. 4.10g). In other samples, pyroxferroite alteration is located along the margins of knebelite-rich bands, and forms porphyroblasts in a groundmass of quartz and corroded knebelite. Composite inclusions of quartz and corroded knebelite occur in the pyroxferroite porphyroblasts (Fig. 4.10h), and form inclusion trails along sutured margins where pyroxferroite porphyroblasts have coalesced similar to textures found in olivine facies graphitic ore (Fig. 4.5e).

Hornblende occurs as inclusion-rich poikiloblasts in quartz-apatite (± graphite) bands, and as an alteration product of garnet. Grunerite is restricted to knebelite-pyroxferroite bands, where it typically appears to be contemporaneous, and intergrown with knebelite and pyroxferroite. However, in some cases, secondary grunerite replaces knebelite-pyroxferroite. Overprinting veinlets of pyrosmalite-galena (± freibergite, and antimonial silver) produce minor incipient pyrosmalite alteration of these Fe-Mn silicates.

Local folding of compositional banding is commonly accompanied by an axial plane foliation that is defined by the preferred alignment of knebelite-pyroxferroite aggregates (Fig. 4.10e and f), and when present, ovoid hornblende poikiloblasts. There is no microtextural evidence that the latter Fe-Mn silicates have replaced an earlier foliation, or were precipitated during foliation development. The preferred alignment of graphite and/or biotite in more graphitic samples also defines the foliation. The orientation of these folds and foliations are consistent with D_1/D_2 fabrics seen in the host rocks. Small-scale piercements of coarse grained remobilised sulphide occur locally, as well as sulphide filled intergranular pull-aparts normal to the foliation.

4.5.3 Hedenbergite ore

Hedenbergite ore is widely distributed in the hanging wall and footwall of the Southern Zone, typically forming an inner zone to olivine-pyroxenoid ore. Like olivine-pyroxenoid ore, the geometry of the Zn lodes is lensoidal and up to 40m thick on section 4700mN (Fig. 4.2), extending for some 250m down-dip and 450m along strike. In the southern sections of the Southern Zone, footwall and hanging wall hedenbergite ore coalesces to form a single 60m thick lens that is terminated by the Footwall Shear and Hamilton Fault to the south. In the Northern Zone, zones up to 10m thick occur in banded hedenbergite-garnet-quartz rocks north of section 5300mN, and extend less than 100m down-dip and along strike.

Contact relationships between hedenbergite ore and host rocks are characterised by a transgressive zone (up to 10m) of hedenbergite veining and associated quartz-garnet (± hornblende) alteration that grades into silicification. Similar transgressive hedenbergite-garnet-quartz alteration zones occur along the contacts between banded olivine-pyroxenoid and hedenbergite ore. Compared to olivine-pyroxenoid ore, hedenbergite ore has low wholerock Mn (<1 wt%), Pb and Ag, but elevated Zn, Cu, As, and Au (Fig. 4.8; Tables 4.2 and 4.3).

Hedenbergite ore is dominated by hedenbergite, hornblende, ferro-actinolite, magnetite, fluorite, ilvaite, calcic almandine, and minor quartz, apatite, pyrosmalite (Table 4.1), and rare accessory pyroxferroite and knebelite that form small patches up to 10cm wide. Sulphides include pyrrhotite, arsenopyrite, sphalerite, variable chalcopyrite and minor galena. Again, loellingite occurs as cores in arsenopyrite grain. Ag-sulphosalts are typically associated with pyrosmalite veinlets and alteration, but are rare.

Macroscopic and microscopic textures are similar to olivine-pyroxenoid ore, and durchbewegt breccia textures are common (Fig. 4.11a). Anastomosing mylonitic zones up to 2m wide occur in fluorite-rich ore, and are characterised by porphyroclasts and equigranular aggregates (from 0.5mm to 10cm) of hedenbergite, magnetite and minor calcic almandine, quartz and apatite, contained in a recrystallised matrix of fluorite with ribbons of pyrrhotite and sphalerite (Fig. 4.11b). Arsenopyrite has a patchy distribution, and occurs as euhedral to subhedral crystals up to 1cm across, and where locally abundant, forms interlocking grains (<3cm across).

In thin section, hedenbergite and magnetite form granoblastic aggregates with curvilinear blebby fluorite, sphalerite, pyrrhotite and minor chalcopyrite infilling interstices between grains and triple junction sites. Hedenbergite hosts spheroidal inclusions of magnetite, quartz, apatite, fluorite, sphalerite, pyrrhotite and rare composite sphalerite-pyrrhotite-chalcopyrite inclusions (e.g. the spheroidal sphalerite inclusions toward the top of the field of view in Fig. 4.11b). Rare inclusions of knebelite in magnetite also occur. Quartz contains a variety of spheroidal to euhedral shaped inclusions, the most common being hedenbergite, hornblende, allanite, calcic almandine, pyrrhotite and sphalerite. In some samples, rare hypersaline

Figure 4.11 Hedenbergite and banded hedenbergite ores.

A. Typical example of hedenbergite ore with a durchbewegt textured zone characterised by porphyroclasts of hedenbergite and magnetite grain aggregates and solitary grains in a matrix of recrystallised fluorite, and ribbons of sphalerite and pyrrhotite (position 1). The textures are very similar to durchbewegt olivine-pyroxenoid ore. In contrast, more massive, granoblastic hedenbergite-fluorite-magnetite-sphalerite-pyrrhotite also occurs (position 2; CAD045, 368.7m).

B. Photomicrograph of durchbewegt textured, fluorite-rich hedenbergite ore. Porphyroclasts consist of hedenbergite and magnetite and are contained within a matrix of recrystallised fluorite and ribbons of sphalerite-pyrrhotite and minor chalcopyrite. Sulphide ribbons wrap around the porphyroclasts and in instances are folded. Sphalerite and pyrrhotite also occur as spheroidal inclusions in hedenbergite (top of field; plane-polarised transmitted light, SZ058-6b).

C. Photomicrograph displaying retrograde hornblende alteration of hedenbergite, and a later generation of ferro-actinolite alteration (plane-polarised transmitted light, SZ153-25).

D. Photomicrograph of pseudomorphic replacement of hedenbergite by ilvaite–ferro-actinolite–galena. Galena and sphalerite fill interstices between ferro-actinolite blades (plane-polarised reflected light, SZ037-23b).

E. Pre- to possibly syn-D_2 hedenbergite-hornblende vein (position 1) overprinting compositional banding. Alteration comprises hornblende-quartz (position 2), quartz (position 3), and outer zone of quartz-calcic almandine (position 4; CUD149, 94.6m).

F. Post-D_2 hedenbergite vein (position 1) overprinting compositional banding and the S_1/S_2 foliation that is defined by the preferred alignment of knebelite-pyroxferroite aggregates in banded olivine-pyroxenoid ore. Knebelite-pyroxferroite bands (position 2) are selectively altered to hedenbergite and minor calcic almandine (position 3), and/or quartz-calcic almandine (position 4). Quartz-apatite bands have been silicified with minor calcic almandine alteration (position 5; CAD016, 81.3m).

G. Transitional zone between strong hedenbergite-garnet-quartz alteration (right of field) and banded olivine-pyroxenoid ore (left of field). The weakly altered zone is characterised by the development of coarse grained, ragged hedenbergite porphyroblasts and coalesced porphyroblastic aggregates at position 4. Position 1–massive granoblastic hedenbergite, position 2–granoblastic quartz-calcic almandine, position 3–olivine-quartz band, position 4–partially coalesced hedenbergite porphyroblasts in hornblende alteration of an olivine-pyroxenoid band (CAD043, 94.7m).

H. Photomicrograph of coalesced hedenbergite porphyroblasts in a knebelite-quartz band in banded olivine-pyroxenoid ore. Relic knebelite and quartz grains occur along sutured hedenbergite grain boundaries. Relic knebelite-quartz inclusion trails in hedenbergite highlight stages in the growth and coalescence of hedenbergite porphyroblasts (plane-polarised transmitted light, NZ020-21).

Abbreviations: aa-allanite, act-ferro-actinolite, fl-fluorite, ilv-ilvaite, kn-knebelite, ga-galena, hb-hornblende, hd-hedenbergite, mt-magnetite, po-pyrrhotite, qz-quartz, sp-sphalerite.

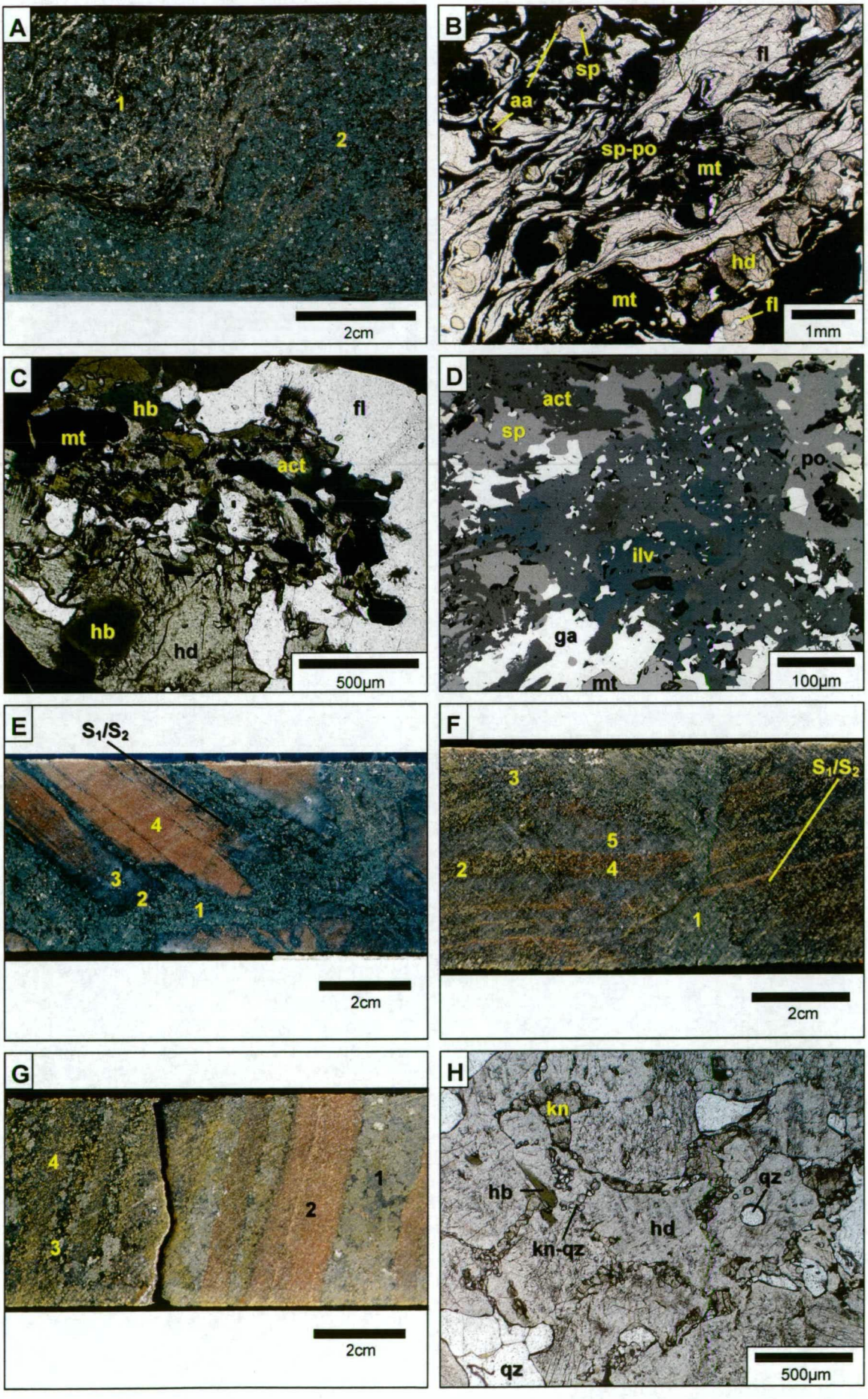
A
1
2
2cm
B
sp
fl
aa
sp-po
mt
hd
mt
fl
1mm
C
hb
fl
mt
act
hb
hd
500µm
D
act
sp
po
ilv
ga
mt
100µm
E
S1/S2
4
3
2
1
2cm
F
3
S1/S2
5
2
4
1
2cm
G
4
1
2
3
2cm
H
kn
hb
qz
hd
kn-qz
qz
500µm

multiphase fluid inclusions (up to 20μm) with up to four daughter crystals are hosted in quartz (cf. Dong et al., 1997a).

Hedenbergite and calcic almandine have been altered to hornblende along grain boundaries, fractures, as well as along cleavage planes in hedenbergite. Veinlets of fibrous ferro-actinolite overprint the rock in some samples and typically contain minor sphalerite, pyrrhotite, chalcopyrite and rarely fluorite. Associated wall-rock alteration is characterised by ferro-actinolite alteration of hedenbergite and hornblende along grain boundaries, cleavage planes and fractures, with fine grained sphalerite, pyrrhotite and chalcopyrite commonly intergrown with the ferro-actinolite alteration (Fig. 4.11c). In some instances, these veinlets crosscut equigranular aggregates and individual grains of earlier pyrrhotite and sphalerite. Ilvaite and minor secondary magnetite replace hedenbergite and hornblende along fractures and cleavage planes, and rarely pseudomorph hedenbergite grains (Fig. 4.11d). Minor arsenopyrite may be associated with the ilvaite. Minor pyrosmalite, commonly associated with fine grained galena and sphalerite, replaces hedenbergite, hornblende, ferro-actinolite and ilvaite. Pyrosmalite also occurs as overprinting veinlets that contain galena, sphalerite and rare chalcopyrite. Pyrrhotite, sphalerite and chalcopyrite, associated with minor pyrosmalite, have partially replaced magnetite along fractures.

4.5.4 Banded hedenbergite ore

Hedenbergite ore grades into weakly mineralised quartz-rich (>20 modal%), banded (1-10cm thick) hedenbergite-quartz-calcic almandine-hornblende rock, termed banded hedenbergite ore (Figs. 4.10g, and 4.11e to g; Table 4.1). In the hanging wall of the Southern Zone the ore type forms the down-dip extension of hedenbergite ore, where it is up to 25m thick on section 4700mN (Fig. 4.2), and forms transgressive patchy zones up to 10m thick in banded olivine-pyroxenoid ore. It also forms similar transgressive zones in silicified metasediments, forming a transitional zone between the latter and hedenbergite ore. In the Northern Zone, it occurs in the hinge region of the Cannington Synform and is up to 100m thick on section 5300mN (Fig. 4.3), grading over several metres into banded olivine-pyroxenoid ore.

Where banded hedenbergite ore is spatially associated with banded olivine-pyroxenoid ore, it is characterised by alternating hedenbergite (± calcic almandine, hornblende bands), calcic almandine-quartz, and hornblende-quartz (± garnet) bands. Bands vary from anastomosing to lenticular to laterally continuous. Deformed and undeformed hedenbergite veins overprint the compositional banding (Fig. 4.11e and f), with multiple vein generations commonly present. Veins possess a zoned alteration selvage that grades outward from hornblende-quartz, to quartz, to quartz-garnet (Fig. 4.11e).

In the Northern zone, the contact between banded hedenbergite and banded olivine-pyroxenoid ore is characterised by hedenbergite veins that overprint compositional banding in the latter ore type. Hedenbergite veins also overprint the S_1/S_2 foliation defined by the preferred alignment of knebelite and pyroxferroite (Fig. 4.11f). Associated alteration typically

involves the selective replacement of knebelite-pyroxferroite bands by hedenbergite, and alteration of intervening quartz-apatite (± graphite) bands to quartz and/or quartz-calcic almandine (Fig. 4.11f); apatite remains unaltered. In some instances, knebelite-pyroxferroite bands are altered to quartz-calcic almandine (Fig. 4.11f), but the primary banded texture of the protolith is typically preserved. Quartz commonly contains hypersaline, multiphase fluid inclusions that are similar to those found in quartz in hedenbergite ore.

In other examples, the contact is characterised by a quartz-calcic almandine alteration front containing hedenbergite porphyroblasts (Fig. 4.11g). At a microscopic scale, individual hedenbergite porphyroblasts coalesce with increasing alteration intensity, forming porphyroblastic hedenbergite aggregates. Individual hedenbergite grains have sutured boundaries that typically contain relic, fine-grained quartz and knebelite (Fig. 4.11h). In less altered samples, quartz and strongly corroded knebelite form the groundmass to hedenbergite porphyroblasts and porphyroblastic aggregates. Rarely, an outer pyroxferroite alteration front to hedenbergite-quartz-calcic almandine alteration and veining, overprints knebelite bands (Fig. 4.10g). Discordant pyroxferroite-bearing veins have also been observed (cf. Chapman, 1993; Chapman and Williams, 1998), but unequivocal examples tend to be rare. In the transitional zones between banded hedenbergite and graphitic ore, alteration is manifested by silicification and/or quartz-calcic almandine alteration, with hedenbergite commonly absent.

Similar textural features are observed in the hanging wall Fe-Mn silicate units of the Southern Zone where banded hedenbergite ore forms transgressive alteration zones associated with crosscutting D_2 tension gashes filled with quartz (Fig. 4.12a). Megacrysts of euhedral hedenbergite, garnet and carbonate up to 10cm in size have been observed in some tension gashes (Fig. 4.12b; cf. Chapman and Williams, 1998).

Banded hedenbergite ores in metasediments are also characterised by hedenbergite veining, in addition to disseminated hedenbergite aggregates and intense silicification. Hedenbergite veins are folded, boudinaged, or undeformed and crosscut one another. This transitional zone between the metasediments and hedenbergite ore, grades into either less silicified metasediments, or intensely silicified rock with abundant sphalerite. The latter forms a distinct ore type termed siliceous Zn ore (section 4.6.1). Patchy concentrations of calcic almandine (up to 60 modal%) are common.

4.6 SILICEOUS ORE

Siliceous ore is characterised by <10 wt% Fe, <1 wt% wholerock Mn and abundant quartz (up to 70 modal%). Pb:Zn ratios and mineral components highlight two end-members (Tables 4.1 and 4.2):

i) Siliceous Zn ore (Zn>>Pb), and

ii) Siliceous Pb-Zn-Ag ore (variable Pb/Zn, but commonly Pb≥Zn).

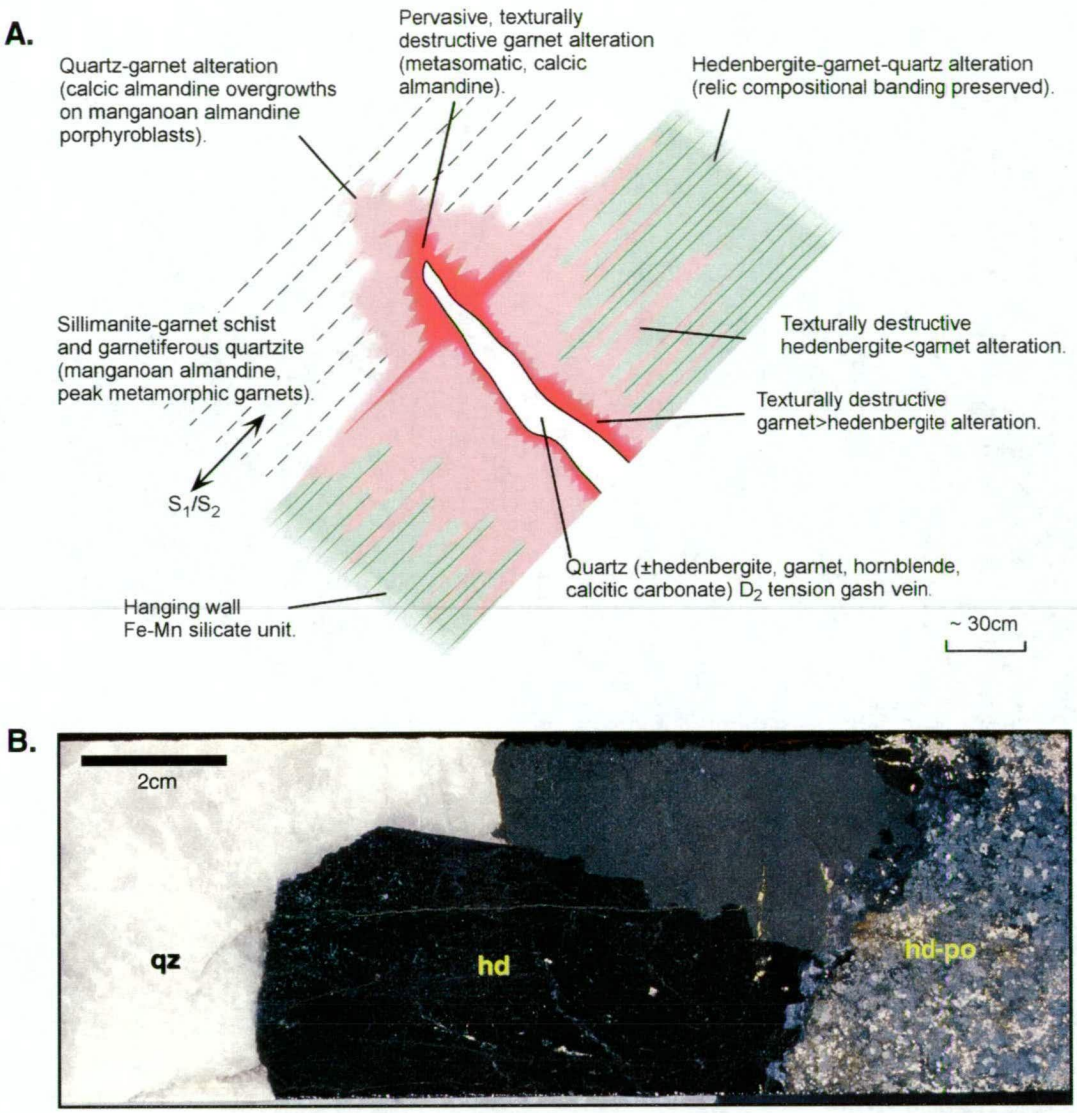

Figure 4.12 Examples of quartz-hedenbergite filled D_2 tension gashes. **A.** sketch of alteration features associated with a D_2 tension gash in a hanging wall Fe-Mn silicate unit of the Southern Zone, modified after Bodon (1998). **B.** drillcore photograph of euhedral hedenbergite megacrysts within a large (~1m thick) tension gash vein in hedenbergite ore (CAD038, 212.3m).

Siliceous Zn ore has elevated As, Cu, Au and low P, Ag, Sb compared to siliceous Pb-Zn-Ag (Table 4.2). However, both types contain quartz with similar multiphase hypersaline fluid inclusions to those in banded hedenbergite ore.

4.6.1 Siliceous Zn ore

Siliceous Zn ore constitutes <5% of the currently defined Southern Zone resource (Bailey, 1998). On section 4700mN in the Southern Zone, it displays a close spatial relationship to the axial surface of the Cannington Synform, and to the western extremity of the Core Amphibolite, where it is up to 40m thick (Fig. 4.2). Weak siliceous Zn ore occurs structurally above and below the Core Amphibolite on this section. The ore type reaches a maximum thickness of approximately 100m north of section 4700mN, and extends some 500m along strike and up to 600m down-dip. Only rare isolated zones of poorly developed siliceous Zn ore are found in the north of the Northern Zone.

Siliceous Zn ore consists of strongly silicified rock that displays gradational relationships to host metasediments, and shares similar geochemical features to hedenbergite ore, e.g. Pb/Zn ratio between 0.1 to 0.4, low Ag, Sb, and elevated As, Cu and Au (Table 4.2). Correlations between Pb and Ag are characteristic, but unlike Fe-Mn silicate ore, do not show positive correlations with elevated Fe and Mn (Fig. 4.13).

Gangue minerals include abundant quartz and K-feldspar with lesser muscovite, sillimanite, calcic almandine and gahnite (Table 4.1); quartz is distinctly bluish in hand specimen. The ore contains numerous accessory phases such as apatite, biotite, hedenbergite, hornblende, epidote, pyrosmalite, sericite, chlorite and rare graphite. Sulphides include sphalerite, pyrrhotite, arsenopyrite, and minor chalcopyrite and galena (Table 4.1). Arsenopyrite grains typically have loellingite cores, and Ag-sulphosalts are rare.

Siliceous Zn ores display a diversity of textures such as:

- anastomosing sphalerite-pyrrhotite veinlets and disseminations (Fig. 4.14a),
- quartz-gahnite-sphalerite-pyrrhotite veins up to ~10cm thick (Fig. 4.14b),
- sulphide-bearing crackle breccias in intensely silicified rock consisting of rounded silicified clasts (up to ~2cm diameter) in a matrix of recrystallised sphalerite and minor pyrrhotite and galena (Fig. 4.14c),
- disseminated gahnite in intensely silicified rock (Fig. 4.14d),
- diffuse zones of disseminated sphalerite, pyrrhotite, euhedral arsenopyrite (up to 1cm) and minor gahnite,
- quartz-sphalerite (± pyrrhotite, gahnite) veins up to ~20cm wide in weakly mineralised

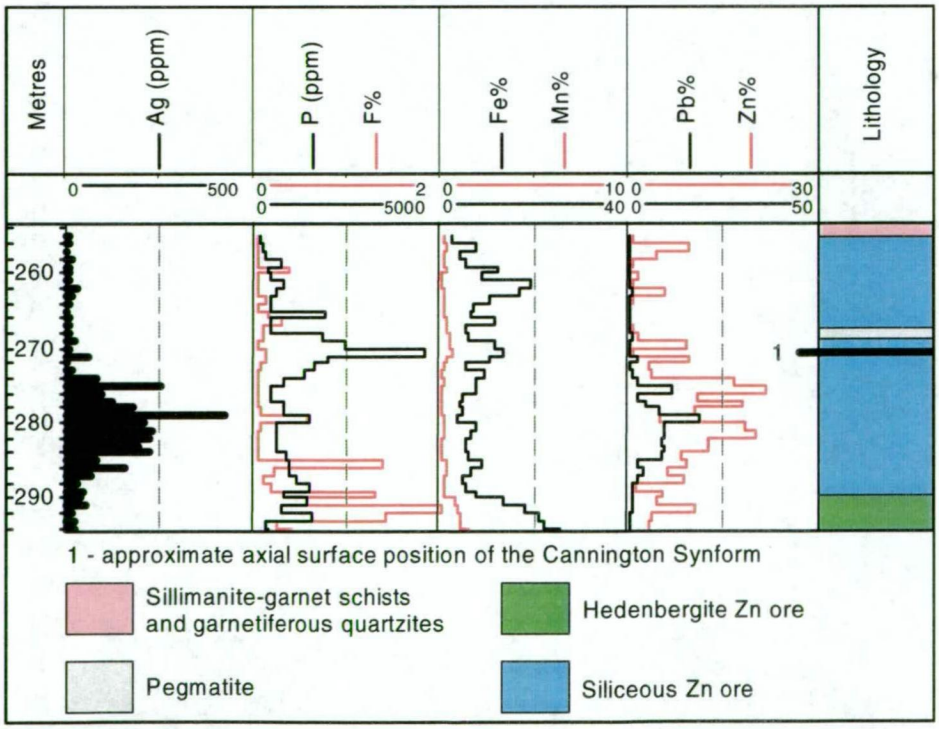

Figure 4.13 Downhole geochemical plot of siliceous Zn ore (CAD214 Southern Zone). Refer to Table 4.1 for explanation of ore types.

and silicified host rocks that in some instances have the appearance of stockwork zones (up to ~10m wide) with associated intense silicification.

In thin section, quartz in strongly silicified metasediments displays granoblastic textures. In other samples, quartz displays sutured grain boundaries, sub-grains and new grains, and undulose extinction on a microscopic scale. Quartz in deformed veins displays similar textures indicative of dynamic recrystallisation (Fig. 4.14e) and open-space filling textures are absent. In most cases, sulphides fill interstices between quartz new grains and sutured grain boundaries, and occur as inclusions in quartz (Fig. 4.14e). Contacts between quartz-gahnite veins and the silicified wallrock are typically sharp to diffuse (Fig. 4.14g). Euhedral to subhedral gahnite grains have been partially pseudomorphed by sericite, and have fibrous sericite overgrowths with an outer fine grained sphalerite rim (Fig. 4.14f to h). In contrast, euhedral gahnite inclusions in quartz remain unaltered (Fig. 4.14f and h). Sphalerite typically contains abundant inclusions of pyrrhotite and/or chalcopyrite aligned along cleavage traces and grain boundaries.

Veins and stockwork zones display varying degrees of deformation, ranging from folding to transposition of quartz and quartz-gahnite±sphalerite-pyrrhotite veins into the plane of S_1/S_2, (Fig. 4.14b), brecciation (Fig. 4.14c) and boudinaging. In other samples, S_1/S_2 is defined by the alignment of anastomosing sphalerite-pyrrhotite veinlets (Fig. 4.14a), and the alignment of gahnite aggregates (Fig. 4.14d). However, relatively rare, possible undeformed veins and stockworks also occur and in some cases, sillimanite porphyroblasts that define S_2 are partially silicified and have diffuse, "ghostly" outlines.

4.6.2 Siliceous Pb-Zn-Ag ore

This ore type constitutes approximately 11% of the currently defined Southern Zone resource (Bailey, 1998), and in the Southern Zone, occurs in the hinge region of the Cannington Synform where it has possibly undergone thickening due to folding. On section 4700mN it has a maximum thickness of approximately 70m in the hinge zone (Fig. 4.2), and occurs as a lens in the footwall up to 45m thick, extending >350m along strike and up to 450m up dip. Moving north it's location progressively moves around the Cannington Synform, so that by the 4900mN section a large portion of the lens is located in the hanging wall. This geometry suggests that Siliceous Pb-Zn-Ag ore has a steeper plunge to the south than the Cannington Synform and has essentially been folded by it. Similarly in the Northern Zone, siliceous Pb-Zn-Ag ore occurs in the hinge region of the Cannington Synform north of section 5400mN. However, it is only weakly developed in comparison to the Southern Zone.

Siliceous Pb-Zn-Ag ore displays similar geochemical features to graphitic ore, sharing a common Pb:Zn ratio between 1.5 to 2.0 and elevated wholerock P (up to >2.0 wt%; Table 4.2). Pb and Ag correlate in downhole geochemical plots, but do not correspond to elevated Fe and Mn (Fig. 4.15). Siliceous Pb-Zn-Ag ore grades laterally into graphitic and to a lesser extent, banded olivine-pyroxenoid ore. In the Northern Zone, quartz veins overprint compositional

Figure 4.14 Siliceous Zn ore.

A. A small mineralised breccia zone and sphalerite-pyrrhotite veining, with euhedral crystals of arsenopyrite in partially silicified, feldspathic metapsammite to metapsammopelite. An S_1/S_2 foliation is defined by the weak alignment of biotite (CAD215, 102.5m).

B. Quartz-gahnite-sphalerite-pyrrhotite veining in partially silicified, feldspathic metapsammite. An S_1/S_2 foliation is defined by elongate 'pods' of quartz and gahnite vein material, and the alignment of sphalerite-pyrrhotite blebs and stringers within the veins. Translucent, blue coloured vein quartz is a characteristic feature of the ore type. Open-space filling textures are absent (CUD036, 46.8m).

C. Characteristic breccia textures in sulphide-rich, intensely silicified metapsammite. Clasts of silicified metapsammite and possibly vein quartz, are hosted in a matrix of recrystallised sphalerite-galena. Breccias vary in texture from clast supported to matrix supported , displaying gradations to disseminated sulphide and/or fine sulphide stringer in the silicified rock. A weak S_1/S_2 foliation is defined by the alignment of disseminated sulphide blebs (CUD036, 38.5m).

D. Disseminated gahnite porphyroblasts and porphyroblastic aggregates in strongly silicified metapsammopelite. Gahnite porphyroblasts are typically rimmed by sericite and secondary sphalerite; an intrinsic late alteration feature in siliceous Zn ores. An S_1/S_2 foliation is defined by the alignment of gahnite aggregates and minor biotite pseudomorphed by late chlorite (CUD033, 60.4m).

E. Photomicrograph of quartz-sulphide textures. Fine stringers of sphalerite occur along the margins of strained quartz grains. Sphalerite also fills interstices between quartz grains and occurs as spheroidal inclusions in quartz. Sub-grain and new-grain development (position 1), undulose extinction in quartz and sutured grain boundaries provide evidence for dynamic recrystallisation during D_1/D_2. Plane-polarised transmitted light (left), polarised transmitted light (right; sample no. DSCK01, location unconstrained).

F. Photomicrograph of a quartz-gahnite vein. The majority of gahnite porphyroblasts have been pseudomorphed by late sericite and have spectacular symplectite-like sericite overgrowths with an outer rim of secondary sphalerite. Possible minor secondary sillimanite alteration of gahnite has been observed in some of the overgrowths. In contrast, euhedral gahnite inclusions in quartz have been protected from the retrograde fluid and remain unaltered. Open-space filling are absent. Instead quartz has a granoblastic texture and has undulose extinction. The mineralogy and textural features indicate that the veining predates peak metamorphism (M_1) and D_1 (plane-polarised transmitted light, SZ028-7).

G. Photomicrograph depicting the nature of the contact between the quartz-gahnite vein in F. and the silicified wallrock (dashed line). Gahnite grains illustrate the sharp nature of the contact. However, Quartz contacts tend to be more diffuse and are largely defined by a change to coarser grained quartz. Symplectite overgrowths on gahnite contain possible minor secondary sillimanite (polarised transmitted light, SZ028-7).

H. Photomicrograph of coexisting gahnite, muscovite and K-feldspar. Again gahnite grains have been pseudomorphed by fine grained sericite and have been overgrown by bladed sericite with an outer rim of secondary sphalerite. The symplectite overgrowth also contains spheroidal inclusions of sphalerite, as well as possible minor secondary sillimanite (plane-polarised transmitted light, SZ028-7).

Abbreviations: apy-arsenopyrite, ga-galena, gh-gahnite, ksp-K-feldspar, mu-muscovite, po-pyrrhotite, qz-quartz, se-sericite, si-sillimanite, sp-sphalerite.

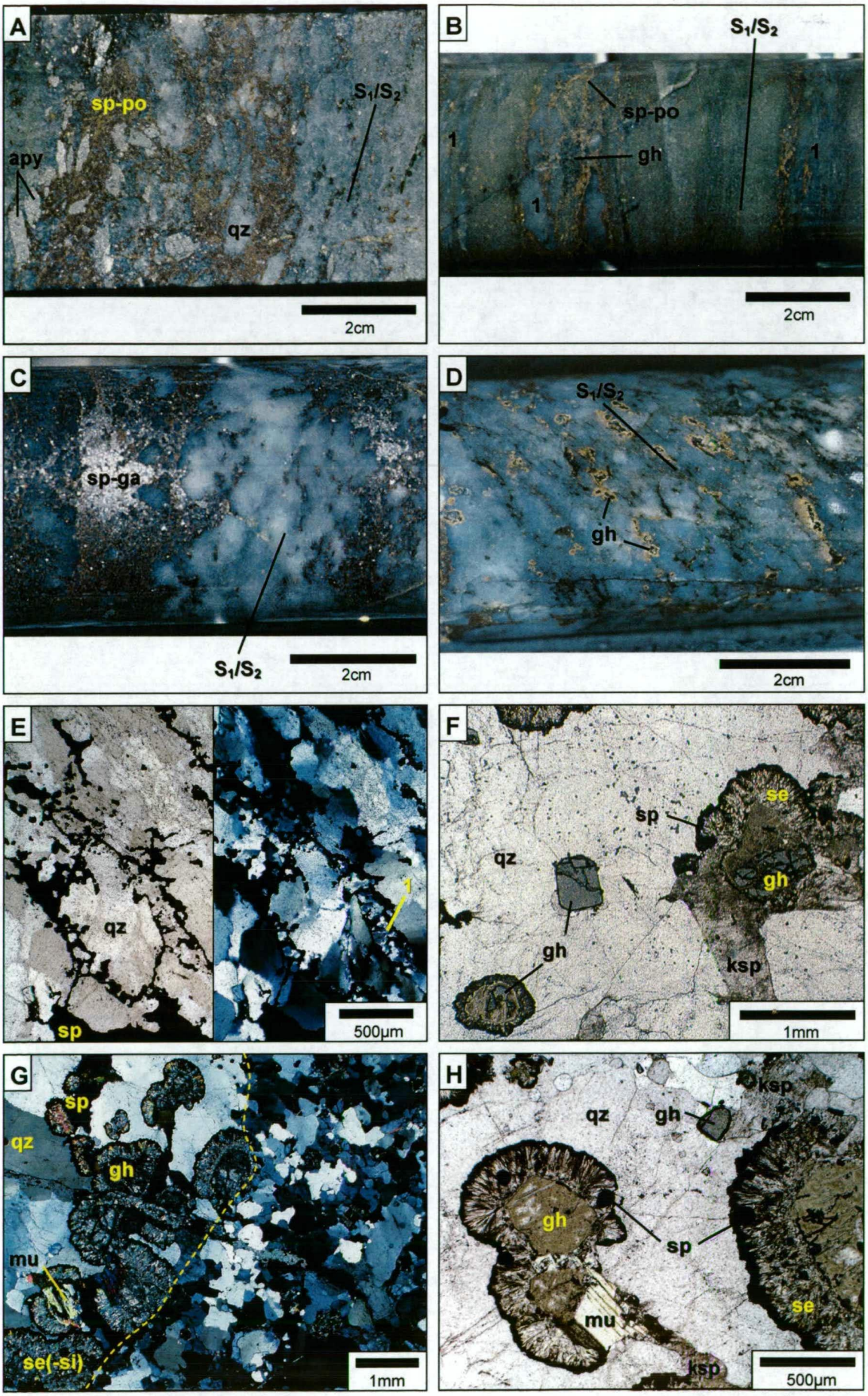
A
sp-po
S_1/S_2
apy
qz
2cm
B
S_1/S_2
sp-po
gh
1
1
1
2cm
C
sp-ga
S_1/S_2
2cm
D
S_1/S_2
gh
2cm
E
qz
sp
1
500µm
F
se
sp
qz
gh
gh
ksp
1mm
G
sp
qz
gh
mu
se(-si)
1mm
H
ksp
qz
gh
gh
sp
mu
se
ksp
500µm

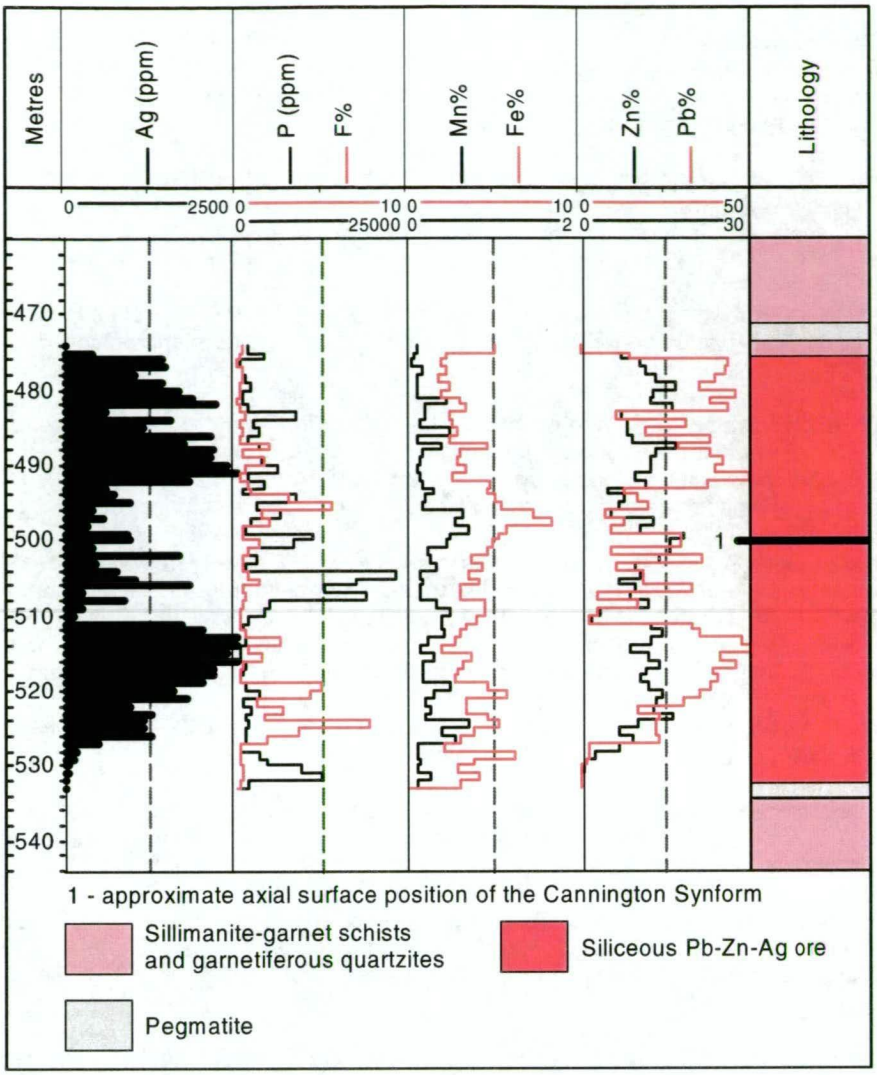

Figure 4.15 Downhole geochemical plot of siliceous Pb-Zn-Ag ore (CAD163 Southern Zone). Refer to Table 4.1 for explanation of ore types.

bands in graphitic ore and characterise gradational zones. Relict folded (F_2 or F_3) compositional bands are common in partially silicified graphitic ore adjacent to veins (Fig. 4.16a), whereas texturally destructive silicification is typically associated with sulphide-rich breccia zones. The ore type is characterised by spectacular sulphide-rich breccias (Fig. 4.16b and c), and two sub-types have been identified on the basis of subtle mineral and textural differences.

Type 1 breccias comprise clasts of silicified rock containing minor disseminated sphalerite galena, apatite and graphite, and have ragged to diffuse margins (Fig. 4.16b). The matrix consists of coarse grained (up to 1.5cm diameter), recrystallised sphalerite, galena, and quartz, with total sulphides constituting up to 60 modal% of the breccia. In thin section, all sulphides and sulphosalts occur interstitially to quartz. Minor intergrowths of gudmundite, freibergite and blades of veenite ($Pb_2Sb_2S_5$) ± pyrosmalite, occur as isolated grain aggregates along the margins of coarse grained galena (Fig. 4.16c), and in places fill fractures and cleavage traces in the latter. Freibergite also occurs as poikiloblastic inclusions in galena, and rare antimonial silver forms complex emulsoid intergrowths with pyrrhotite and gudmundite. Very minor disseminated euhedral to subhedral arsenopyrite is present in most samples and

Figure 4.16 Siliceous Pb-Zn-Ag ore.

A. Silicified graphitic ore displaying relic compositional banding and $F_{1(?)}$ folding in the transitional zone to siliceous Pb-Zn-Ag ore. A weak axial plane $S_{1(?)}$ is defined by the alignment of disseminated sphalerite and galena (CAD215, 102.5m).

B. Breccia textured Type 1 siliceous Pb-Zn-Ag ore comprised of rounded, ragged clasts of weakly mineralised silicified rock (position 1) in a matrix of finer grained milled clasts and coarse grained recrystallised galena and sphalerite (position 2). Clast sizes are typically ≤2cm in this sample (position 3; CAD152, 447.7m).

C. Late stage intergrowth of sphalerite, veenite, freibergite, gudmundite and arsenopyrite along the margin of coarse grained galena in Type 1 siliceous Pb-Zn-Ag ore (plane-polarised reflected light, SZ063-2a).

D. A subhedral arsenopyrite grain in coarse grained galena in Type 1 siliceous Pb-Zn-Ag ore. The grain has been partially replaced by galena along intragranular fractures and grain boundaries. A highly reflective gudmundite inclusion occurs within the arsenopyrite grain, in addition to fine inclusions of galena (plane-polarised reflected light, SZ063-2b).

E. Brecciated Type 2 siliceous Pb-Zn-Ag ore comprised of rounded, weakly mineralised silicified clasts hosted in a matrix of sulphide and late stage manganoan calcite. Veinlets of calcite and remobilised galena (±sphalerite) overprint some silicified clasts (position 1). The ore type typically has a spongy appearance (position 2) and contains numerous small vughs lined with carbonate. The alignment of wispy sphalerite and galena defines a weak foliation that appears to wrap around silicified clasts. However, it is difficult to correlate this foliation with a particular deformation event and it may be an artefact of rebrecciation during D_5 as seen in other samples (CAD083, 570.8m).

F. Vuggy quartz-carbonate-fluorite-sulphide vein breccia associated with a D_5 fault in siliceous Pb-Zn-Ag ore. Clasts consist of weakly mineralised silicified rock (position 1). Vughs are lined with euhedral quartz, manganoan calcite (position 2) and fluorite (position 3; CAD004, 219.6m).

G. Smaller-scale view of position 2 in G. displaying euhedral fluorite lining a vugh. The existence of late stage fluorite in syn- to post-D_5 carbonate veins and breccias suggests remobilisation of pre-existing fluorite from the ores. Remobilised galena is also present in the sample (CAD004, 219.6m).

H. Spongy textured galena grains indicative of dissolution by late stage fluid associated with pyrosmalite alteration. The protolith is difficult to establish due to pervasive pyrosmalite alteration. However, a relic granoblastic texture and pyrosmalite as an alteration product suggests an Fe-Mn silicate precursor, possibly an intensely altered clast of olivine-pyroxenoid ore (plane-polarised reflected light, SZ083-7).

Abbreviations: apy-arsenopyrite, cb-manganoan carbonate, fl-fluorite, fr-freibergite, ga-galena, gd-gudmundite, ps-pyrosmalite, sp-sphalerite, ve-veenite.

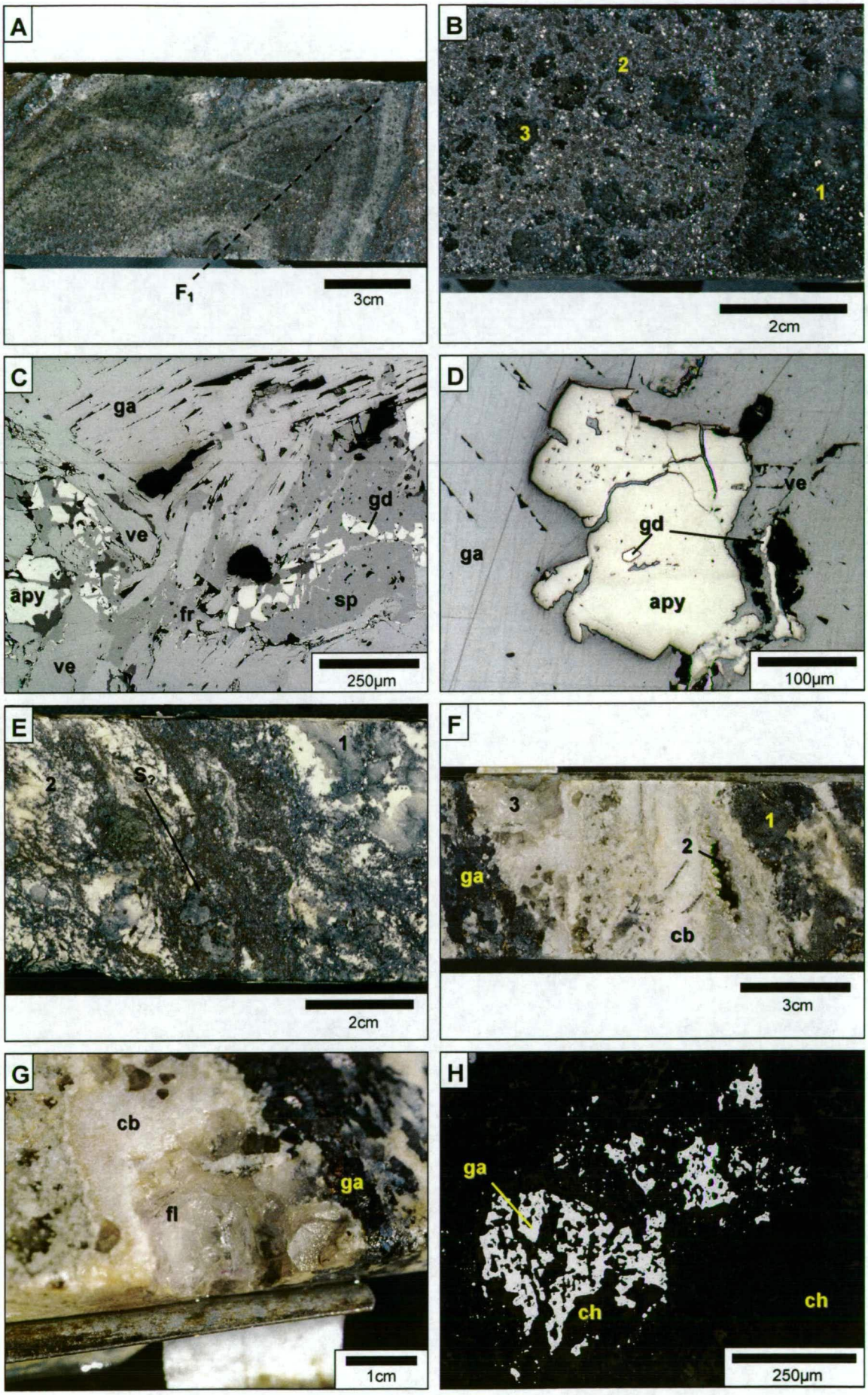
A
F1
3cm
B
2
3
1
2cm
C
ga
gd
ve
apy
fr
sp
ve
250µm
D
ve
gd
ga
apy
100µm
E
1
2
S?
2cm
F
3
1
2
ga
cb
3cm
G
cb
ga
fl
1cm
H
ga
ch
ch
250µm

can contain inclusions of gudmundite or possible allargentum (Fig. 4.16d). Bladed pyrrhotite generally forms "clusters" in galena. Accessory pyrite and marcasite form birds-eye textures indicative of the breakdown of pyrrhotite. Fluorite is rarely present, but does occur as localised veins that overprint the ore.

Relict compositional banding is present in some silicified clasts, where it may be folded around an S_1/S_2 foliation defined by the preferred alignment of sulphides. However, the orientation of folds and foliations varies between clasts in some samples, indicating that folding pre-dated brecciation. Quartz veins are also present and contain minor coarse grained sphalerite and galena (up to 4cm diameter). Veins are folded, boudinaged, and dismembered producing a brecciated mass of quartz clasts and recrystallised sulphide. Elsewhere, quartz veins appear undeformed.

Type 2 breccias comprise similar minerals to type 1 breccias, plus additional quartz, carbonate, chlorite and Ag-sulphosalt minerals. They occur as restricted zones (up to ~10m thick) spatially related to the D_5 subvertical Brolga Fault Zone, where they overprint Type 1 ore. The breccias commonly have a vuggy, porous texture with euhedral carbonate, quartz and/or pyrite, marcasite, galena, sphalerite and rare fluorite lining cavities (Fig. 4.16f to h). Multiple generations of vuggy, crustiform banded quartz-manganoan calcite veins adjacent to D_5 faults, commonly contain minor remobilised sulphides and rare fluorite (Fig. 4.16f and g).

In thin section, secondary silicification is manifested by strain-free quartz overgrowths on strained quartz. Carbonate alteration is characterised by euhedral manganoan calcite overgrowths on fine grained spongy textured ankerite and ferroan dolomite. Minor intergrowths of veenite, acanthite, freibergite, gudmundite, antimonial silver, and rare "canningtonite" ($4PbS.3Ag_2S.3Sb_2S_3$, a previously unknown Ag-sulphosalt; French et al., 1994) occur along galena margins. In Fe-Mn silicate-bearing breccias, sponge textured galena grains, indicative of dissolution by late stage fluids, occur in pervasively chlorite altered samples (Fig. 4.16h).

4.7 MINERAL COMPOSITIONS

A summary of gangue mineral compositions is presented in Table 4.4. Compositions of the principal silicate minerals (olivine, pyroxenoid, pyroxene and garnet) are plotted on ternary diagrams in Figure 4.17 (see Appendix 1 for microprobe data).

Microprobe data confirms that olivine compositions range from ferroan knebelite to knebelite, with compositions falling into three broad groups based on their Mn contents (Table 4.4; Fig. 4.17a and b). Olivines in the first group are characterised by 15-20wt% MnO and are restricted to olivine-pyroxenoid ores. The second group contains 10-15wt% MnO and are the most widespread, occurring in olivine-pyroxenoid, banded olivine-pyroxenoid and olivine facies graphitic ore. Olivines containing the least amount of MnO (<10wt%) are restricted to hedenbergite ore.

Table 4.4 Summary of gangue mineral compositions.

Mineral group	Mineral	Number of microprobe analyses	Features/comments
Olivine			
$(Fe,Mn)_2SiO_4$	Ferroan-knebelite	49	15-20 wt% MnO - olivine-pyroxenoid ore 10-15 wt% MnO - olivine-pyroxenoid, banded olivine pyroxenoid, olivine facies graphitic ore <10 wt% MnO - hedenbergite Zn, olivine facies graphitic ore
Pyroxenoid			
$(Fe,Mn,Ca)SiO_3$	Manganoan pyroxferroite	42	14-22 wt% MnO
Clinopyroxene			
$Ca(Fe,Mn)Si_2O_6$	Hedenbergite	28	16-21 wt% CaO 2-6 wt% MnO
Garnet			
$(Fe,Mn,Ca)_3(Al,Fe)_2Si_3O_{12}$	manganoan to calcic almandine	90	0-8 wt% CaO with some rare compositions to ~12 wt% CaO 1-21 wt% MnO 15-34 wt% FeO
Amphibole			
$(Na,K)_{0-1}Ca_2(Mg,Fe,Al)_5(Si,Al)_8O_{22}(OH,F,Cl)_2$	Hornblende	24	0.2-1.0 wt% MnO 10-11 wt% CaO 1-3.5 wt% K_2O 0.5-2.5 wt% Cl 0.2-0.6 wt% F
$Ca_2(Mg,Fe)_5Si_8O_{22}(OH,F,Cl)_2$	Ferro-actinolite	16	0.7-6.0 wt% MnO 5-11.8 wt% CaO 0.01-0.4 wt% Cl 0-0.08 wt% F
$(Mg,Fe,Mn)_7Si_8O_{22}(OH,F,Cl)_2$	Manganoan grunerite	8	2.5-6.0 wt% MnO 0.65-2.0 wt% MgO 0.07-0.3 wt% Cl 0-0.1 wt% F
Biotite			
$K_2(Mg,Fe)_{6-4}Al,Fe,Ti)_{0-2}Si_{6-5}Al_{2-3}O_{20}(OH,F)_4$	Annite	17	35-38 wt% FeO 0.4-2.7 wt% Cl 0.2-0.8 wt% F
$(Fe,Mn)_8Si_6O_{15}(OH,Cl)_{10}$	Ferroan to manganoan pyrosamlite	41	inter-sample variations 5-24 wt% MnO 0.2-5.5 wt% Cl
Phosphate			
$Ca_5(PO_4)_3(OH,F,Cl)$	Fluorapatite	9	0-0.02 wt% Cl 3-4.8 wt% F
Carbonate			
$CaCO_3$	Manganoan calcite	3	1.7-1.8 wt% $FeCO_3$ 6.3-7.0 wt% $MnCO_3$

Pyroxenoids are dominated by manganoan pyroxferroite. In general they range in composition from 14-22 wt% MnO, with the most Mn-rich containing the highest Ca contents. Hence there is a compositional trend toward more rhodonitic compositions rather than the pyroxmangite end-member (Fig. 4.17a and b). By far the greatest range in compositions occurs in olivine-pyroxenoid ore, whereas compositions in banded olivine-pyroxenoid ore show very little variation and are the most Fe-rich (Fig. 4.17a and b). Pringle (1999), also recognised this compositional trend in graphitic ore in the Northern Zone, and subdivided pyroxferroite into two compositional groups based on Fe and Ca content. The most Fe-rich and Ca-poor pyroxferroite, with an interpreted peak metamorphic origin, correlate with ores in which Pb>Zn. Ca-rich, Fe-poor pyroxferroite, of interpreted metasomatic origin (secondary pyroxferroite in

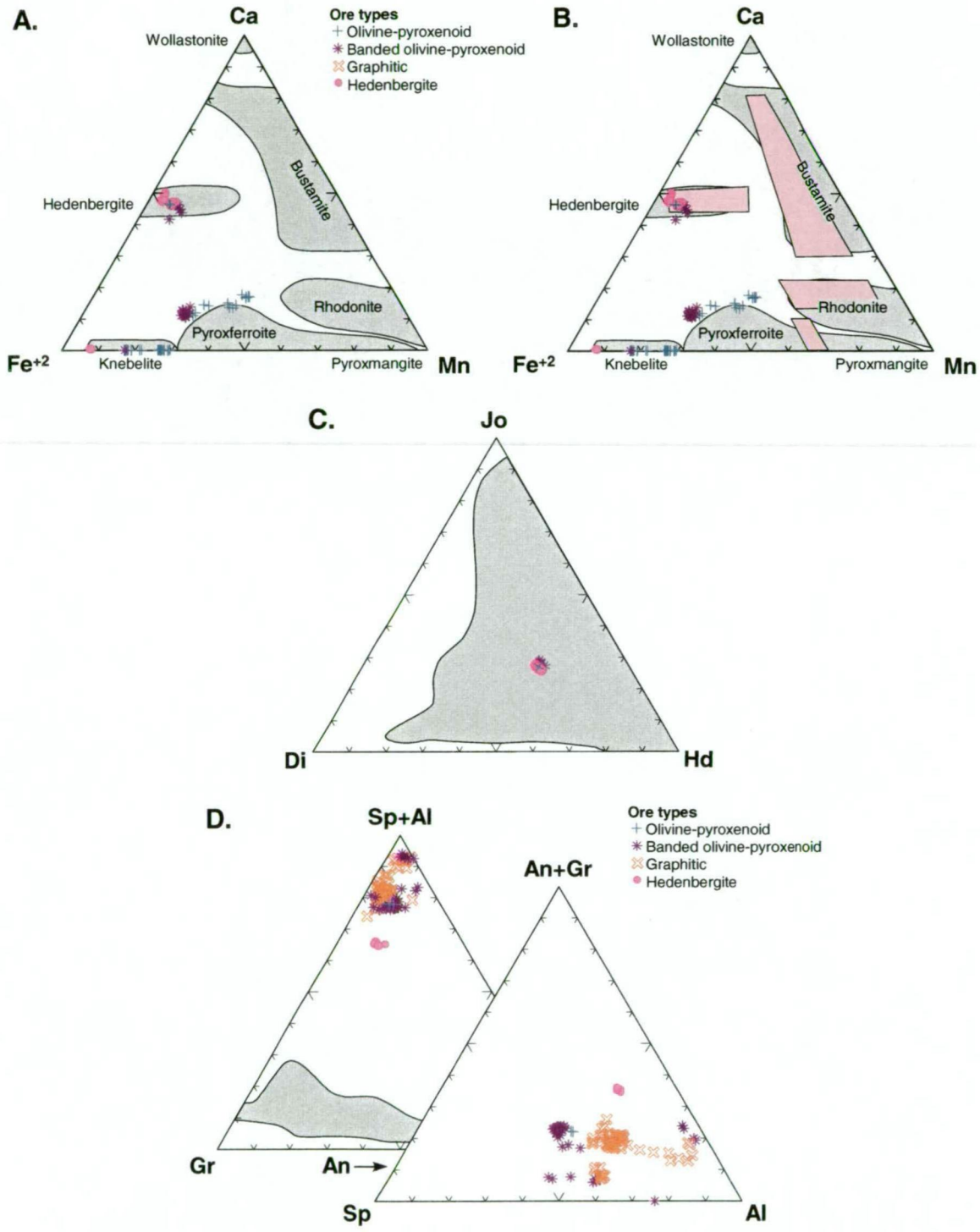

Figure 4.17 Ternary plots of olivine, clinopyroxene and pyroxenoid compositions from the dominant ore types at Cannington. **A.** olivine, clinopyroxene and pyroxenoid compositions (mineral fields after Brown et al., 1980). **B.** compositional fields of gangue minerals from Broken Hill, Australia (after Birch et al., 1983) duplicated upon the same diagram in A. The diagram highlights the Mn-Ca-enrichment at Broken Hill in comparison to the Fe-dominated compositions at Cannington. **C.** hedenbergite compositions with respect to end-member clinopyroxene mol fractions. The shaded region represents the range in clinopyroxene compositions found in Zn-Pb skarn deposits (Meinert, 1993). End-members are: Jo–johannsenite, Di–diopside, Hd–hedenbergite. **D.** garnet compositions with respect to end-member mol fractions. The shaded region represents the range in garnet compositions found in Zn-Pb skarn deposits (Meinert, 1993). End-members are: Al–almandine, An–andradite, Gr–grossularite, Sp–spessartine.

this study), correlate with ores that have variable Pb and Zn contents (op. cit.).

Hedenbergite, the principal clinopyroxene in all ore types, shows very little compositional variation (Fig. 4.17a, b and c). Based on limited microprobe data, Mn contents define two compositional groups, viz.:

- A Mn-poor group, containing <~5wt% MnO, restricted to hedenbergite ore,
- A Mn-rich group (5–8wt% MnO), occurring in banded olivine-pyroxenoid ore.

A summary of garnet compositions from all ore types is presented in Table 4.4 and illustrated in Figure 4.17d. The data confirm that garnet compositions range from calcic to manganoan almandine. The most calcic garnets occur in hedenbergite ore, whereas the most spessartine-rich garnets occur in olivine-pyroxenoid and banded olivine-pyroxenoid ores. Garnets in graphitic ores show the largest variation in Fe and Mn, ranging from manganoan almandine to almandine. Further discussion of garnet compositions, including those from host rocks, is presented in Chapter 5.

Three principal amphiboles occur in the deposit. These are hornblende, ferro-actinolite and manganoan grunerite (Table 4.4, Appendix 1). Hornblende occurs in all ore types, however, grunerite is restricted to olivine-pyroxenoid assemblages. Ferro-actinolite is restricted to hedenbergite ore. Other gangue mineral compositions, such as pyrosmalite, are summarised in Table 4.4. Biotite compositions are summarised in detail in Chapter 5.

4.8 METAL ZONATION

Metal zonation in the Southern Zone at Cannington has a close association with gangue mineralogy. Olivine-pyroxenoid ores form an outer Mn zone enriched in Pb-Ag, while hedenbergite ores form an inner Mn-depleted zone enriched in Zn (Tables 4.2 and 4.3; Fig. 4.8). This laterally continuous zonation is mirrored on either side of the Cannington Synform. The contact between these zones is characterised by a marked increase in Pb, Ag and Mn moving from hedenbergite ore to olivine-pyroxenoid ore (section 4.5); Zn decreases only marginally over the same interval.

In the hinge region of the Cannington Synform siliceous Zn ore forms an inner silica-Zn-rich zone west of the Core Amphibolite. In contrast, siliceous ore in the hinge zone east of the Core Amphibolite is characteristically Pb-Ag- and Zn-rich, with Pb:Zn ratios very similar to graphitic ore (1.5-2.0; section 4.6.2).

In contrast, metal zonation trends in the Northern Zone are more erratic. On section 5300mN, a representative section of the Northern Zone hanging wall, Pb and Ag show strong spatial correlations, with highest grades occurring as a large (~140m wide), thick (~50m) zone structurally above the Core Amphibolite and a smaller east dipping lens above this (Fig. 4.18). Fe shows a strong correlation with the lower, thicker lens, which corresponds to the northern continuation of the hanging wall olivine-pyroxenoid ore lens in the Southern Zone. In contrast,

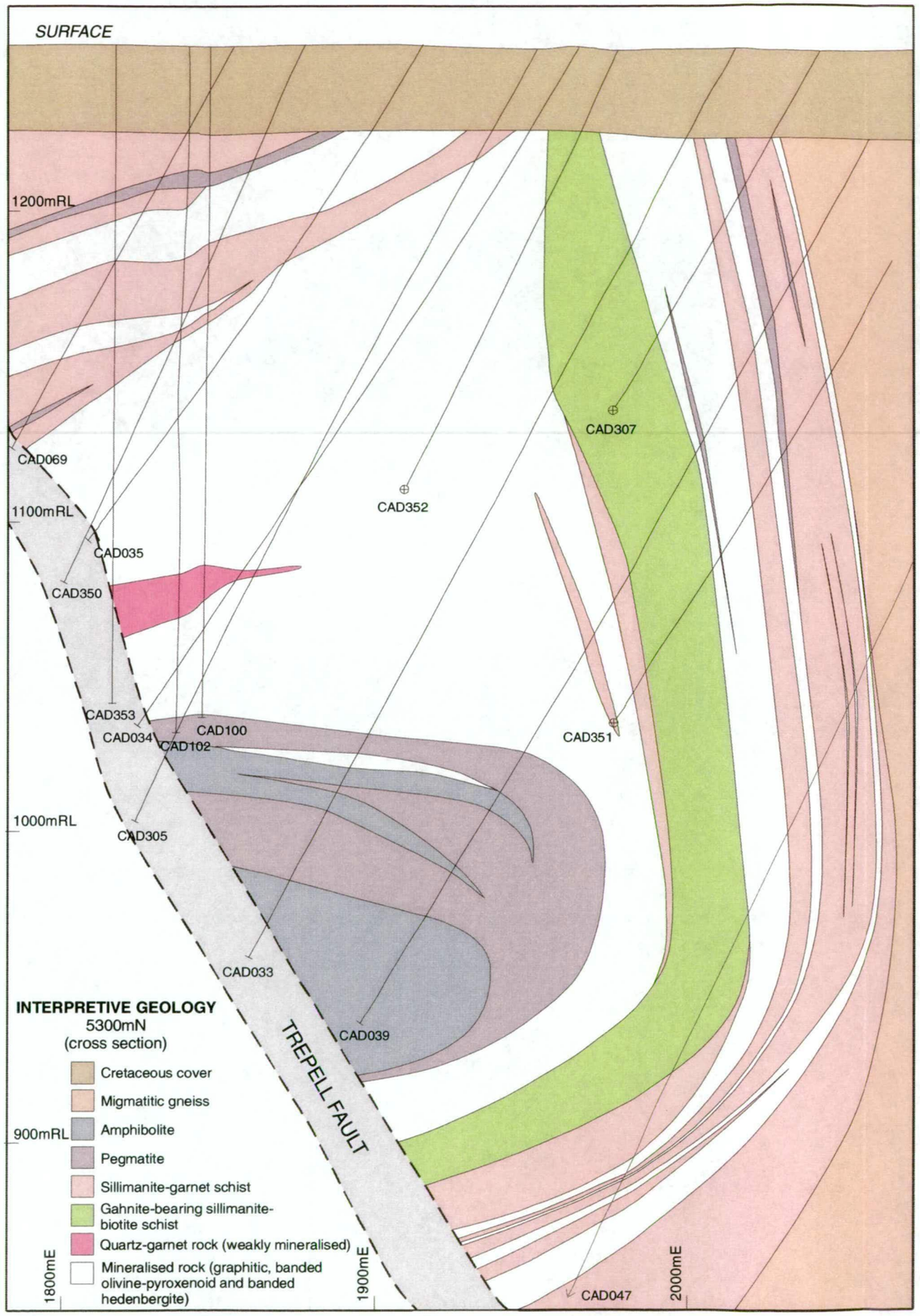

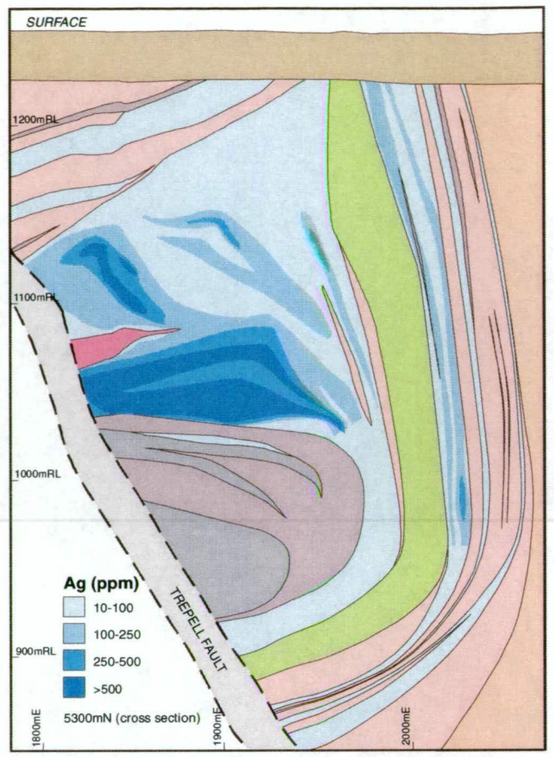

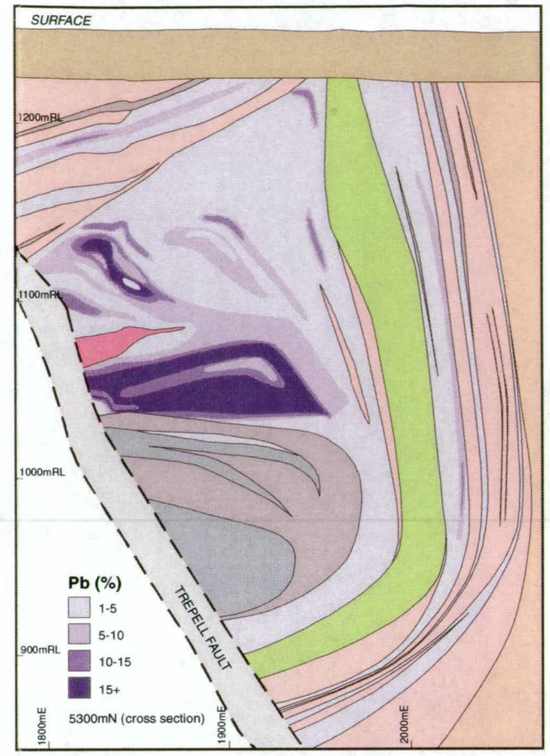

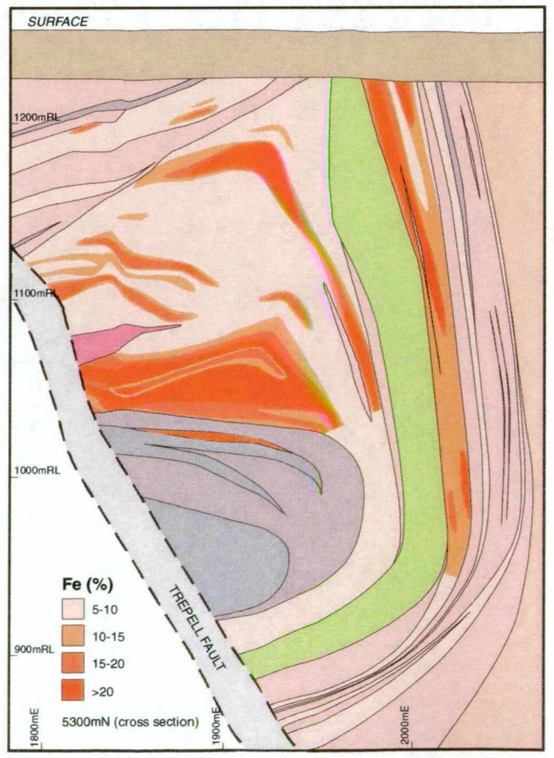

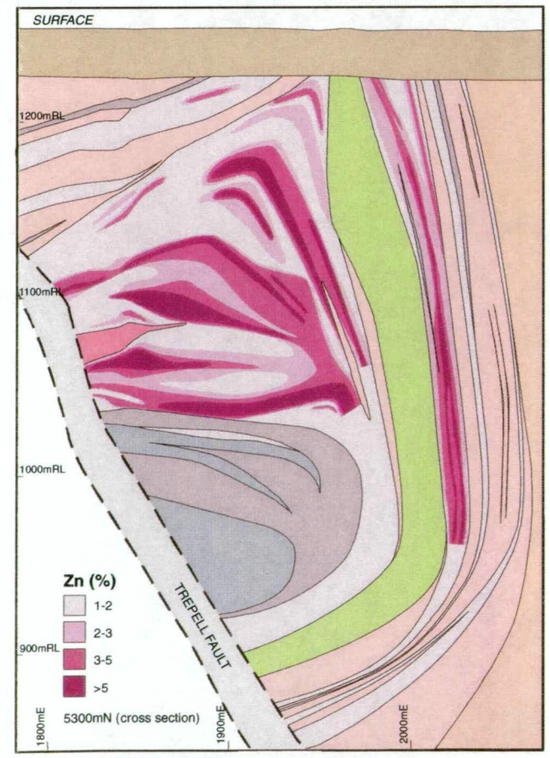

Figure 4.18 Cross section 5300mN showing metal zoning in the Northern Zone.

Fe shows a weak correlation with the structurally higher, east dipping lens. Elevated Fe also occurs as another structurally higher, Zn-rich lens closer to the Cretaceous palaeosurface. A similar correlation between Fe and Zn is also seen in the subvertical ore lens to the east. Zn distribution is erratic, forming a series of lenses that show variable correlations with Pb, Ag or Fe-rich zones.

Similar correlations between the various metals in the Northern Zone exist in long section (Fig. 4.19). The lower high grade Pb-Ag lens on the 1900mE long section correlates with olivine-pyroxenoid ore, while the upper lenses are erratically distributed. A zone of high grade Pb-Ag-Zn on the 5200mN section correlates with quartz-apatite facies ore containing subordinate olivine facies graphitic ore and increased modal abundance of fluorite. Overall, the lack of systematic metal zonation corresponding to an inner Zn-rich zone that grades outward into a Pb-Ag-rich zone is a notable difference between the Northern Zone and the Southern Zone

4.9 DISCUSSION

Resolution of the evolutionary history of Cannington lies in reconciling the relative timing between sulphide deposition, metamorphism, deformation and metasomatism. Correlation between the deformational history recorded in the host rocks and that recorded in the ores provides the key to deciphering the timing of ore formation and subsequent post-depositional events. Correlation based on fold-style must be applied with extreme caution due to complexities caused by fold interference geometries, the coaxial nature of folding events, similarity in fold styles and in fact, lack of recognisable fold geometries with particular deformation events such as D_1.

It is well established that rheologically incompetent ores behave as strain sinks during deformation, especially in high grade metamorphic terrains like the Cannington region (Gilligan and Marshall, 1987; Marshall et al., 2000; Marshall and Spry, 2000). Deformation fabrics in the ores typically reflect the last major deformation event. Pre-existing deformation events are commonly obliterated by recrystallisation (both static and dynamic), including remobilisation of sulphides (op. cit.). Phenomena such as this may result in erroneous conclusions for the timing of ore formation. More subtle textural criteria must be used in such instances when establishing a more accurate relative timing for ore formation. In metamorphosed terrains, the application of metamorphic textural criteria in conjunction with more traditional lower temperature overprinting and replacement textures, such as those used in the study of epithermal deposits for example, is required, especially in high grade terrains (e.g. Lawrence, 1973).

In the migmatitic gneiss and the enveloping garnetiferous alteration halo at Cannington, evidence for the earliest fabric-forming deformation event is recorded in garnet porphyroblasts, where quartz inclusion trails define a relict S_i fabric (section 3.3.1; Giles, 2000). S_1 and S_2 are defined by the preferred alignment of sillimanite and biotite, with the latter characterised by the development of a differentiated fabric and microshears infilled with secondary sillimanite

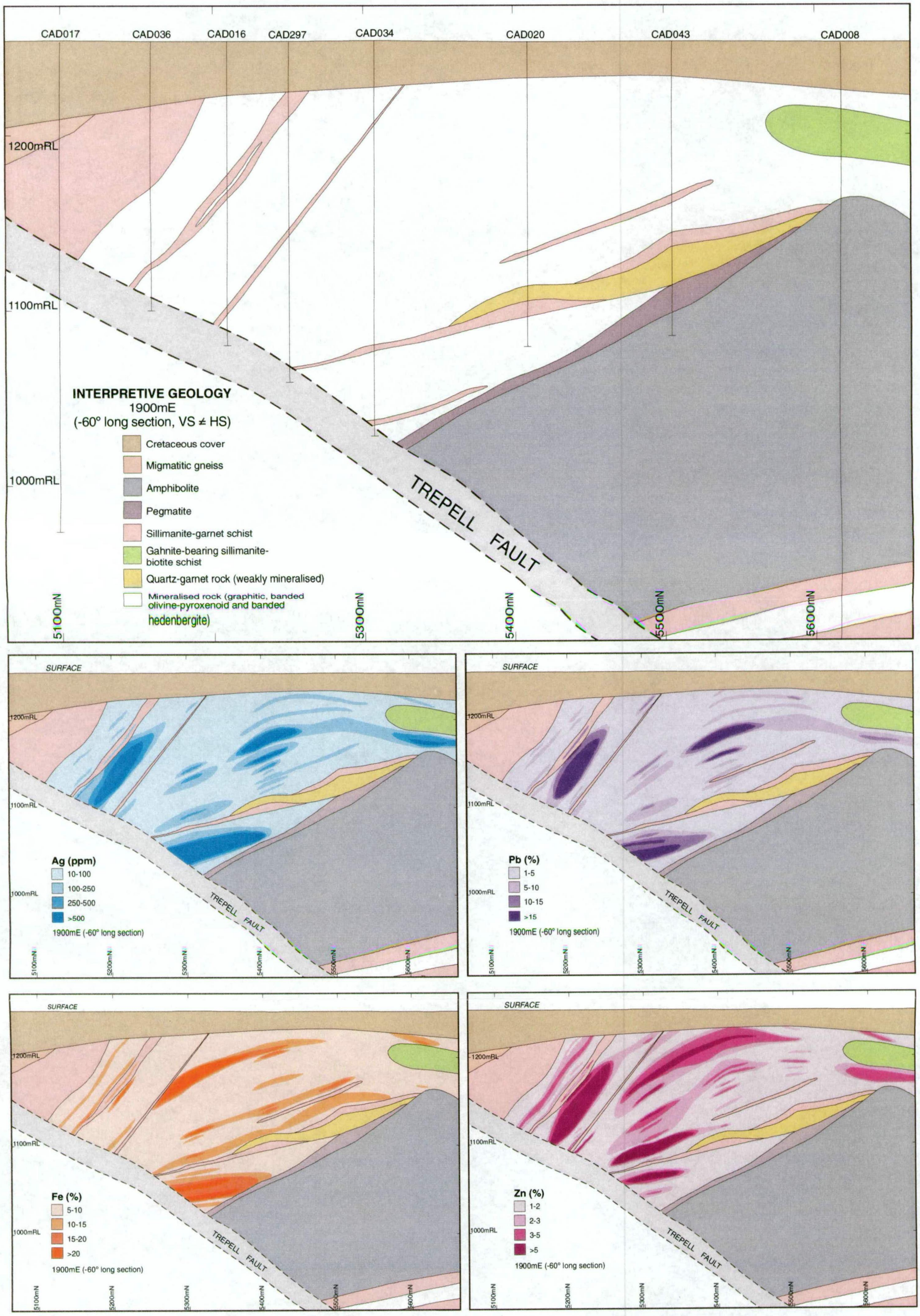

Figure 4.19 Long section 1900mE showing metal zoning in the Northern Zone.

(section 3.3.2 and 3.3.3; Giles, 2000). Macroscopic isoclinal folds characterise F_1 and F_2 folds. S_3 is manifested by crenulation of the S_1/S_2 differentiated fabric, and static recrystallisation of crenulated biotite and replacement of sillimanite by muscovite (section 3.3.4; Giles, 2000). F_3 folds are also characterised by macroscopic- to prospect-scale isoclinal folds. Subsequent deformation did not involve the formation of mineral fabrics, but rather open, upright folding (D_4) and subvertical faulting (D_5). Microscale deformation textures are either absent (D_4), or are spatially restricted (D_5).

M_1 involved the development of granoblastic textured, peak metamorphic assemblages and partial melting of the host succession during D_1 (section 3.4.2; Giles, 2000). U-Pb zircon and monazite ages indicate that M_1 occurred ca. 1580 Ma (Page and Sun, 1998; Giles, 2000). In contrast, M_2 involved a fluid phase that caused base-ion leaching of pre-existing peak metamorphic assemblages commensurate with deposition of secondary sillimanite in S_2 microshears (ibid.; section 3.4.3). M_3 was associated with a discrete thermal pulse related to the intrusion of the Williams Batholith (section 3.4.4; op. cit.). $^{40}Ar/^{39}Ar$ thermochronology from hornblendes in banded hedenbergite ore and the Core Amphibolite indicate that M_3 occurred ca. 1510 Ma (op. cit.). This post-D_3 thermal event also involved a retrograde fluid phase, in which fluid-flow appears to have been facilitated by pre-existing shear zones and fabrics.

The above characteristics preserved in the host rocks provide a textural guide for correlation with deformation textures in the ores. For example, particular mineral assemblages in the ores that display M_1 peak metamorphic characteristics, such as granoblastic textures and D_1 mineral fabrics defined by high grade metamorphic assemblages (and have orientations consistent with S_1 in the host sequence), are interpreted to be the products of prograde metamorphism and D_1. These are therefore peak metamorphic assemblages and are interpreted to be the same generation as those in the host rocks. Mineral assemblages that overprint D_1 fabrics and M_1 assemblages are interpreted to be genetically related to subsequent events. Using these criteria, the paragenesis of the deposit can be broken down into prograde (Stage I, peak metamorphic), retrograde, (Stage II, retrograde alteration) and late stage hydrothermal alteration assemblages related to D_5 faulting (Stage III, near-surface hydrothermal), all of which contain characteristic mineral assemblages and associated textures.

4.9.1 Fe-Mn silicate and graphitic ore

4.9.1.1 Stage I peak metamorphic assemblages

Graphitic and banded olivine-pyroxenoid ores are dominated by granoblastic sulphide-silicate textures indicative of M_1. An S_1 fabric, with an orientation consistent with the S_1 in host rocks, is defined by the preferred alignment of graphite and biotite, and aggregates of knebelite, pyroxferroite, hedenbergite, grunerite, hornblende, and poikiloblastic manganoan almandine. Manganoan almandine bands are commonly boudinaged and folded, and the S_1 foliation wraps around inclusion-rich garnet porphyroblasts. In addition to quartz, apatite and rare calcite, the former minerals constitute M_1 peak metamorphic assemblages.

The presence of characteristic granoblastic textures and mutual curvilinear grain boundary relationships between sulphides and silicates are features indicative of annealing during prograde metamorphism (Lawrence, 1973). The general absence of retrograde assemblages and associated replacement-type textures, except for localised breakdown of garnet to hornblende, and knebelite-pyroxferroite to secondary grunerite, indicates that assemblages are dominantly prograde. Hence, minerals that define S_1 are interpreted as prograde metamorphic assemblages and therefore represent Stage I of the paragenesis (Fig. 4.20).

Spheroidal inclusions of sphalerite, galena and pyrrhotite in interpreted peak metamorphic knebelite, pyroxferroite, hedenbergite, manganoan almandine porphyroblasts and cores of granoblastic quartz, indicate that sulphides must have present in the rocks during prograde metamorphism. Further supporting evidence comes from the observation that sulphides are not associated with later retrograde minerals in many instances. Sulphide inclusions in peak metamorphic silicates and magnetite are indicative of 'spheroidation' (a metallurgical term), a process that occurs by co-recrystallisation of phases during annealing (Lawrence, 1973). In addition, isolated curvilinear galena and sphalerite grains in triple junction sites, and in narrow lenses along quartz grain boundaries, form an integral part of the characteristic granoblastic sulphide-silicate texture of the rock. Such textures have been interpreted as co-recrystallisation of quartz and sulphide during prograde metamorphism (Lawrence, 1973), and are similar to interpreted metamorphic sulphide-silicate textures described by Stanton (1965), and Stanton and Gorman (1968).

Textural evidence supporting a pre-peak metamorphic timing for graphitic ores is provided by garnet porphyroblasts that exhibit bow-tie textures. Such textures are interpreted to have formed by pseudomorphic replacement of possible bladed chlorotoid by garnet during prograde metamorphism (cf. Vaughan and Stanton, 1986; Stanton, 1989). However, the timing of graphitic ores can be traced back even further, possibly to prior the earliest recorded deformation event, D_i. Evidence for a relict S_i fabric is preserved in garnet porphyroblasts as rare quartz inclusion trails. These are texturally similar to those preserved in garnet porphyroblasts that characterise the S_i fabric in the proximal garnetiferous alteration halo. Thus, if graphitic ores and the proximal alteration halo are temporally equivalent, as suggested by spatial relationships, geometries and the latter textural evidence, then both the ores and proximal halo predate the earliest, pre-peak metamorphic generation of deformation, D_i. Indeed, the preservation of S_i in garnet porphyroblasts suggests the fabric-forming event occurred prior to garnet formation, during the earliest stage of orogeny (section 3.3; Giles, 2000). Garnet equilibria for pelitic rocks indicates that thermal conditions during D_i must have been below ~450°C (Yardley, 1989).

The close spatial relationship between banded olivine-pyroxenoid and olivine-pyroxenoid ore implies that the two ore types share similar prograde assemblages and temporal features. Fluorite-sulphide-rich olivine-pyroxenoid and hedenbergite ores are dominated by high strain fabrics, such as durchbewegt textures and mylonite-like shear fabrics. The highly strained

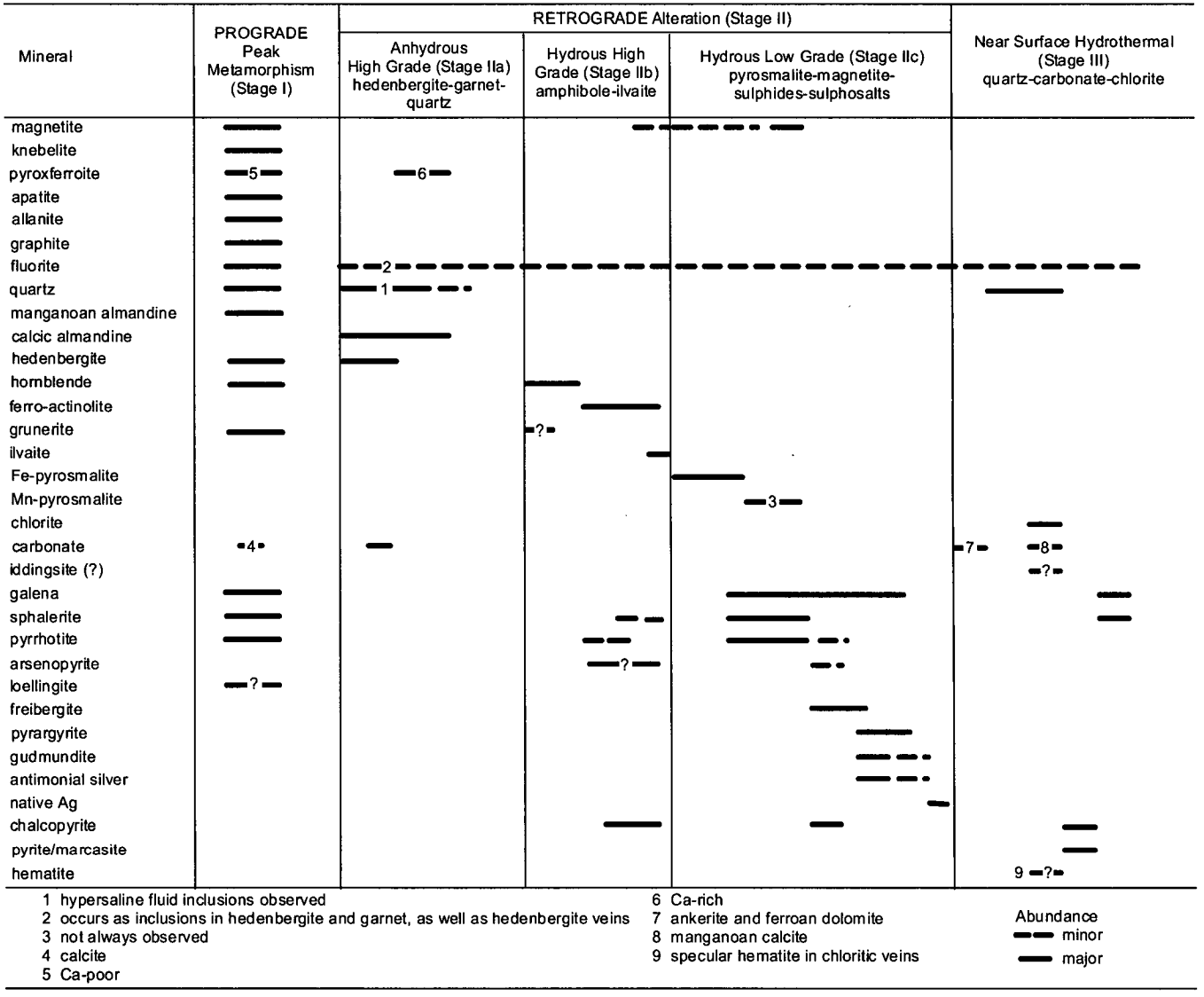

Figure 4.20 Mineral paragenesis of olivine-pyroxenoid Pb-Ag, hedenbergite Zn and graphitic Pb-Zn-Ag mineralisation. Refer to Table 4.1 for explanation of ore types.

nature of the fabrics, recrystallisation of fluorite and the observation that fabrics are defined by peak metamorphic assemblages rather than by retrograde minerals such as pyrosmalite, suggests a D_1/D_2 timing for fabric development. Consequently, the deformation textures are interpreted as differentiated S_1/S_2 fabrics.

Ribbons of galena and/or pyrrhotite in mylonitic, durchbewegt zones in olivine-pyroxenoid ore, wrap around knebelite, pyroxferroite, magnetite, apatite and allanite porphyroclasts and equigranular grain aggregates, indicating that the latter minerals predate D_1/D_2 deformation. The observation that knebelite and pyroxferroite grains contain spheroidal inclusions of magnetite, apatite and fluorite that are not associated with retrograde phases, supports a prograde metamorphic timing for their development. Similar mutual inclusion relationships exist in hedenbergite ores, including the occurrence of sphalerite, pyrrhotite and chalcopyrite inclusions in peak metamorphic hedenbergite and garnet. In both ore types, allanite rarely occurs as inclusions in peak metamorphic silicates, but does occur as equigranular annealed grain aggregates and porphyroclasts in highly strained S_1/S_2 durchbewegt fabrics. Consequently it too, is interpreted to have a prograde metamorphic timing. Mutual inclusions of knebelite and carbonate, and curvilinear to granoblastic grain boundary relationships indicate that minor carbonate is also part of the peak metamorphic assemblage in some rare examples of olivine-pyroxenoid ore (Fig. 4.20).

Stage I peak metamorphic assemblages should have been subjected to the same peak metamorphic conditions as those determined for the host rocks, i.e. 650-700°C and ~4kbars (Mark et al., 1998; Giles, 2000). This aspect will be explored in more detail in the next chapter.

4.9.1.2 Stage IIa anhydrous metasomatic assemblages

Evidence for a post-peak metamorphic timing for hedenbergite veining and associated hedenbergite-calcic almandine-quartz alteration is manifested in banded olivine-pyroxenoid ore, where interpreted peak metamorphic knebelite and pyroxferroite have been selectively altered to secondary hedenbergite. In some examples, mutual grain boundary relationships between hedenbergite, pyroxferroite and knebelite indicate that equilibrium was attained during metasomatism. However, in other samples, disequilibrium textures are present, where coalesced porphyroblasts of hedenbergite occur in a groundmass of strongly corroded knebelite intergrown with quartz.

Other examples contain similar disequilibrium textures, but in contrast, these involve the replacement of knebelite by later post-peak metamorphic secondary pyroxferroite that formed in association with hedenbergite alteration during high grade Stage IIa metasomatism. Further supporting evidence for post-peak metamorphic pyroxferroite comes from the presence of hedenbergite-pyroxferroite veins that overprint compositional banding and S_1/S_2. Pringle (1999) also recognised a second generation of pyroxferroite in graphitic ores, which could be distinguished from Stage I peak metamorphic pyroxferroite by its comparatively Ca-rich composition (section 4.7).

The symmetrical distribution of metasomatised ores around the margins of the Core Amphibolite and in the hinge region of the Cannington Synform may be an artefact of F_3 folding, or focussed fluid flow along the margins of the Core Amphibolite and in the hinge region of the Cannington Synform where D_3 dilational structures might be expected to have developed. In the latter case, D_3 dilational structures would have facilitated the ingress of Stage IIa fluids and therefore metasomatism would have a syn- to post-D_3 timing; a feature that is inconsistent with the textural evidence. In the former case, metasomatism would predate D_3 (cf. Giles, 2000). Metasomatised ores tend to be folded around the F_3 Cannington synform rather than exclusively located in the hinge region, suggesting a pre-D_3 timing. The abundance of folded hedenbergite-calcic almandine-quartz veins with axial surfaces parallel to the F_3 Cannington Synform provide addition evidence for a pre-D_3 timing for Stage IIa metasomatism (op. cit.).

Evidence for a syn- to post-D_2 timing for Stage IIa metasomatic assemblages is manifested by:

- hedenbergite veins and associated hedenbergite-calcic almandine-quartz (±pyroxferroite) alteration that overprint the S_1/S_2 foliation in banded olivine-pyroxenoid ore, as well as hedenbergite veins that have been folded and overprinted by D_2 structures and fabrics;
- the localisation of hedenbergite-calcic almandine-quartz alteration around D_2 tension gash veins in hanging wall Fe-Mn silicate units, and the presence of hedenbergite and calcic almandine megacrysts within these tension gashes indicative of open-space filling. The occurrence of carbonate megacrysts indicates that some carbonate was also deposited during this stage (Fig. 4.20); and
- the observation that calcic almandine consistently overgrows earlier Stage I manganoan almandine in sillimanite-garnet schists adjacent to hedenbergite-calcic almandine alteration in the hanging wall Fe-Mn silicate unit (Richmond et al., 1996a).

Based on the similarity between Stage IIa assemblages and the characteristic hedenbergite, minor calcic almandine and quartz mineralogy of hedenbergite ores, Bodon (1998) argued for a temporal relationship between the two. However, the work presented here suggests that this is not the case. Fluorite-sulphide-rich hedenbergite ores preserve durchbewegt S_1/S_2 fabrics (section 4.9.1.1), indicating that hedenbergite, calcic almandine and quartz in hedenbergite ore are Stage I prograde metamorphic minerals and therefore predate Stage IIa assemblages. Similarly, Stage I peak metamorphic hedenbergite occurs in graphitic and banded olivine-pyroxenoid ores.

In summary, the textural evidence indicates a syn- to post-D_2 timing for Stage IIa hedenbergite-calcic almandine-quartz metasomatism. Metasomatism was associated with the ingress of a high temperature (~450-500°C), hypersaline fluid (Dong et al., 1997a and b) facilitated by pre-existing dilational D_2 structures (cf. Pringle, 1999; Giles, 2000), such as fractures and tension gashes that developed in more competent banded ores and the hanging

wall Fe-Mn silicate. Considering that D_2 and M_2 were essentially synchronous, with the latter characterised by the influx of an acid fluid phase and concomitant deposition of secondary sillimanite in S_2 microshears in the surrounding garnetiferous rocks, a genetic relationship between the M_2 hydrothermal event and Stage IIa metasomatism is inferred (cf. Giles, 2000). Stage IIa metasomatism is therefore interpreted as an initial high grade, retrograde event (Fig. 4.20) related to syn-M_2 fluid-fluxing of the orebody.

Thermal constraints determined from multiphase hypersaline fluid inclusions in Stage IIa quartz (Dong et al., 1997a) are similar to the 500°C conditions estimated from mineral equilibria for M_2 (section 3.4.3; Giles, 2000). Estimates based on petrogenetic considerations from assemblages in the metasediments indicate that pressures ranged between 4-6kbars (op. cit.). These P-T conditions are clearly great enough to account for the coarse grained textures and anhydrous mineral assemblage that characterise Stage IIa metasomatism (op. cit.).

4.9.1.3 Stage IIb hydrous metasomatic assemblages

Hydrous retrogression is characterised by the alteration of Stage I and Stage IIa anhydrous assemblages to a variety of amphiboles and ilvaite. In olivine-pyroxenoid, banded olivine-pyroxenoid and graphitic ore, hydrous retrogression involved the breakdown of knebelite and pyroxferroite to secondary grunerite, and manganoan almandine to hornblende. Minor ilvaite alteration of knebelite and pyroxferroite also occurred. In hedenbergite ore, hedenbergite and calcic almandine were altered to hornblende, which was subsequently altered to ferro-actinolite and minor ilvaite. Sphalerite-pyrrhotite-chalcopyrite intergrown with ferro-actinolite and within ferro-actinolite veinlets indicates that some sulphide deposition took place during this stage (Fig. 4.20).

Replacement of hedenbergite and hornblende by ilvaite in some samples was accompanied by the deposition of minor secondary magnetite, sphalerite, pyrrhotite and chalcopyrite. Overprinting ilvaite veinlets also contain minor sphalerite, pyrrhotite and arsenopyrite. Given that hedenbergite ore contained sulphides prior to Stage IIb, it is likely that sulphides associated with the ferro-actinolite and ilvaite veining and alteration represent local solution-associated remobilisation. In summary, Stage IIb hydrous retrogression was characterised by hornblende and grunerite alteration, followed by a later ferro-actinolite and ilvaite(-magnetite) veining and alteration, commensurate with deposition of locally remobilised sphalerite-pyrrhotite-chalcopyrite and minor arsenopyrite (Fig. 4.20).

The exact timing of the event relative to deformation is difficult to resolve accurately because the retrograde assemblages display variable degrees of deformation, i.e. deformed and undeformed veinlets, randomly oriented ferro-actinolite versus the preferred alignment of ferro-actinolite. Initial impressions suggest a syn- to post-D_2 timing for Stage IIb metasomatism based on its spatial relationship with Stage IIa assemblages. However, detailed timing relationships relative to deformation are more complex than this. Early Stage IIb retrogression is characterised by hornblende that occurs in folded hedenbergite veins with axial surfaces

parallel to the large-scale F_3 Cannington Synform, indicating a pre-D_3 timing. The preferred alignment of later ferro-actinolite retrogression in some samples also indicates a pre- to syn-D_3 timing. However, in the majority of cases, ferro-actinolite does not define a mineral fabric, and appears to have formed by static-grain growth after D_3. Ilvaite displays similar static grain growth. The presence of undeformed ferro-actinolite and ilvaite veinlets provides the best evidence for a post-D_3 timing for the latest stages of Stage IIb metasomatism.

Stage IIb metasomatism therefore occurred over a protracted period from syn- to post-D_2, to post-D_3. Overall, the earliest hornblende-grunerite retrogression most likely reflects the waning stages of the M_2 metasomatic event. Later ferro-actinolite and ilvaite retrogression occurred syn- to chiefly post-D_3, and has the same relative timing as post-D_3 static biotite recrystallisation and replacement of sillimanite by coarse grained muscovite in the host rocks that define M_3 (section 3.4.4). M_3 is characterised by the influx of a fluid phase post-D_3 and was associated with the intrusion of the Williams Batholith (Giles, 2000). It is likely that the later ferro-actinolite-ilvaite stage of Stage IIb metasomatism is related to this ca. 1510 Ma discrete thermal event (M_3). Minimum P-T conditions during M_3 were ~400°C and ~3kbars based on petrogenetic and textural evidence from host metasediments (Giles, 2000).

4.9.1.4 Stage IIc late stage hydrous metasomatic assemblages

Overprinting of Stage I prograde and Stage IIa and b retrograde Fe-Mn silicates by pyrosmalite veinlets and associated pyrosmalite alteration represents a lower grade hydrous alteration stage of the paragenesis (Stage IIc; Fig. 4.20). There is a strong correlation between the intensity of pyrosmalite alteration and abundance of Ag-sulphosalts. Pyrosmalite (± minor secondary magnetite) alteration in olivine-pyroxenoid ore preferentially affected knebelite and pyroxferroite. Galena and minor sphalerite, pyrrhotite and freibergite formed complex intergrowths with pyrosmalite, replacing Fe-Mn silicates. Intense alteration involved further retrogression to manganoan pyrosmalite, which occurs as undeformed fibrous overgrowths on Stage I magnetite and Stage IIc ferroan pyrosmalite pseudomorphs after knebelite. These manganoan pyrosmalite overgrowths also contain intergrown galena, pyrargyrite, secondary magnetite and rare freibergite. Pyrargyrite, antimonial silver, gudmundite, minor pyrrhotite and chalcopyrite are breakdown products of freibergite (Dugmore, 1998). A similar decomposition trend for tetrahedrite is recognised at Broken Hill, New South Wales (Lawrence, 1968). In some samples, Stage I galena interstitial to equigranular knebelite, displays characteristic flaser textures, providing evidence for the local dissolution and remobilisation of pre-existing sulphides during this stage of the paragenesis (Fig. 4.9h).

Pyrosmalite alteration in graphitic ore displays the same textural relationships as those observed in olivine-pyroxenoid ore, although alteration is significantly less abundant and tends to be incipient rather than pervasive and restricted to olivine-pyroxenoid bands. Pyrosmalite alteration in hedenbergite ore is also poorly developed, and is characterised by the alteration of hedenbergite, hornblende, ferro-actinolite and ilvaite to minor pyrosmalite and galena. As in olivine-pyroxenoid ore, pyrosmalite occurs in undeformed crosscutting veinlets that clearly

overprint pre-existing fabrics in both graphitic and hedenbergite ore.

In summary, Stage IIc was characterised by initial pyrosmalite-secondary magnetite alteration and the deposition of abundant galena and freibergite, followed by the deposition of manganoan pyrosmalite in intensely altered ore, with the concomitant breakdown of freibergite to pyrargyrite, gudmundite, antimonial silver, and minor pyrrhotite and chalcopyrite (Fig. 4.20). Given the presence of pre-existing Stage I ore as inclusions in Fe-Mn silicates and interstitial curvilinear grains, it is possible that Stage IIc sulphides, sulphosalts, arsenide and antimonide minerals formed by local remobilisation of earlier Stage I ore.

The observation that Stage IIc assemblages are undeformed suggests static grain growth, which implies a post-D_3 timing similar to Stage IIb ferro-actinolite and ilvaite. It is also likely that Stage IIc metasomatism was related to ingress of M_3 fluids, but represents the waning stages of M_3 (Giles, 2000). However, a genetic link between Stage IIb ferro-actinolite-ilvaite and Stage IIc is difficult to establish given the spatial restriction of the former and the widespread distribution of the latter even though they share a similar relative timing to D_3 and M_3. The most intense Stage IIc alteration occurs in olivine-pyroxenoid ore adjacent to the D_3 Footwall Shear and at the termination of the Core Amphibolite within the hinge of the F_3 Cannington Synform in siliceous Pb-Zn-Ag ore. These spatial relationships suggest that Stage IIc fluids were focussed along pre-existing D_3 structures.

4.9.1.5 Stage III near-surface hydrothermal assemblages

Quartz-carbonate veining and incipient quartz-carbonate-chlorite alteration of pyrosmalite within graphitic, and Fe-Mn silicate ore is spatially and temporally associated with D_5 faults (cf. McCarthy, 1996). During this stage pyrrhotite was altered to birds-eye textured pyrite and marcasite (Fig. 4.20). Minor remobilised galena, sphalerite, Ag-sulphosalts and fluorite occur in quartz-carbonate veins and quartz-carbonate healed breccias. Overall, Stage III of the paragenesis represents a near-surface hydrothermal system that exploited brittle faults during D_5.

4.9.2 Siliceous Pb-Zn-Ag ore

Gradational relationships indicate that siliceous Pb-Zn-Ag ore was produced by the silicification and brecciation of graphitic ore. Given this relationship, it is likely that siliceous Pb-Zn-Ag ore contained similar Stage I prograde assemblages to those in graphitic ore, such as apatite, graphite, allanite and some quartz (Fig. 4.20). A syn- to post-D_2 timing for silicification is indicated by quartz veins that overprint the S_1/S_2 foliation in weakly silicified graphitic ore, whilst elsewhere veins are folded and brecciated in strongly silicified zones. An association between strong silicification and brecciation illustrates the importance of structural controls on the intensity of retrograde alteration and the formation of siliceous Pb-Zn-Ag ore.

Quartz associated with siliceous Pb-Zn-Ag ore, and that associated with Stage IIa hedenbergite-calcic almandine-quartz assemblages rarely coexist. However, quartz grains in

both ore types host similar multiphase hypersaline fluid inclusions. This similarity coupled with a consistent syn- to post-D_2 timing, provide evidence for a temporal and therefore genetic link between silicification and Stage IIa metasomatism in other ore types (Fig. 4.21). The general absence of hedenbergite in siliceous Pb-Zn-Ag ores can be explained by the lack of peak metamorphic Fe-Mn silicates such as knebelite and pyroxferroite in the precursor graphitic ore. Hence, the style of metasomatism is host rock-dependent.

Stage IIb of the paragenesis is not evident in siliceous Pb-Zn-Ag ore, possibly due to the absence of mafic minerals such as hedenbergite, garnet, magnetite, pyroxferroite and knebelite. Instead, retrograde assemblages comprise minor undeformed Stage IIc pyrosmalite intergrown with galena, freibergite, veenite, gudmundite and sphalerite in overprinting veinlets, and filling cleavage traces and fractures in coarse-grained recrystallised galena (Fig. 4.21). Stage III in siliceous Pb-Zn-Ag ore is characterised by quartz-carbonate veining and alteration spatially associated with D_5 subvertical faults, which forms vuggy textured Type 2 siliceous Pb-Zn-Ag ore. Detailed mineral paragenesis is summarised in Figure 4.21.

4.9.3 Siliceous Zn ore

Siliceous Zn ore displays clear gradational relationships to sillimanite-garnet schists and garnetiferous quartzites. Partially silicified host rocks share the same peak metamorphic assemblages that occur in the sillimanite-garnet schists and garnetiferous quartzites. These characteristics indicate that protoliths to siliceous Zn ore are host metasediments.

Euhedral inclusions of gahnite in peak metamorphic quartz and K-feldspar indicate that gahnite is a peak metamorphic mineral; an interpretation supported by disseminated gahnite poikiloblasts in gahnite-bearing sillimanite-biotite-garnet schists in the Northern Zone (section 3.2.3.3). Hence, Stage I prograde minerals in siliceous Zn ore comprise quartz, K-feldspar, sillimanite, biotite, manganoan almandine, and minor gahnite (Fig. 4.22). Subsequent secondary sillimanite filled microshears formed during D_2/M_2, whereas incipient retrogression of sillimanite to muscovite occurred during M_3 (Giles, 2000).

Texturally destructive silicification of sillimanite-garnet schists and garnetiferous quartzites is associated with quartz veining and development of siliceous breccias. Partial silicification of peak metamorphic sillimanite porphyroblasts suggests that the silicification post-dated peak metamorphism (M_1). The observation that quartz veins have been folded and transposed into the plane of S_2 or have overprinted the S_2 foliation, provides evidence for a syn- to post-D_2 timing for silicification. Minor hedenbergite-calcic almandine-quartz veining with hypersaline fluid inclusions, provides a temporal link with Stage IIa retrogression associated with hedenbergite and banded hedenbergite ore (Fig. 4.22).

High grade hydrous retrogression is characterised by minor hornblende alteration of hedenbergite and calcic almandine, and is equivalent to Stage IIb of the deposit paragenesis. Post-D_2 retrograde alteration is characterised by undeformed sericite, chlorite and illite

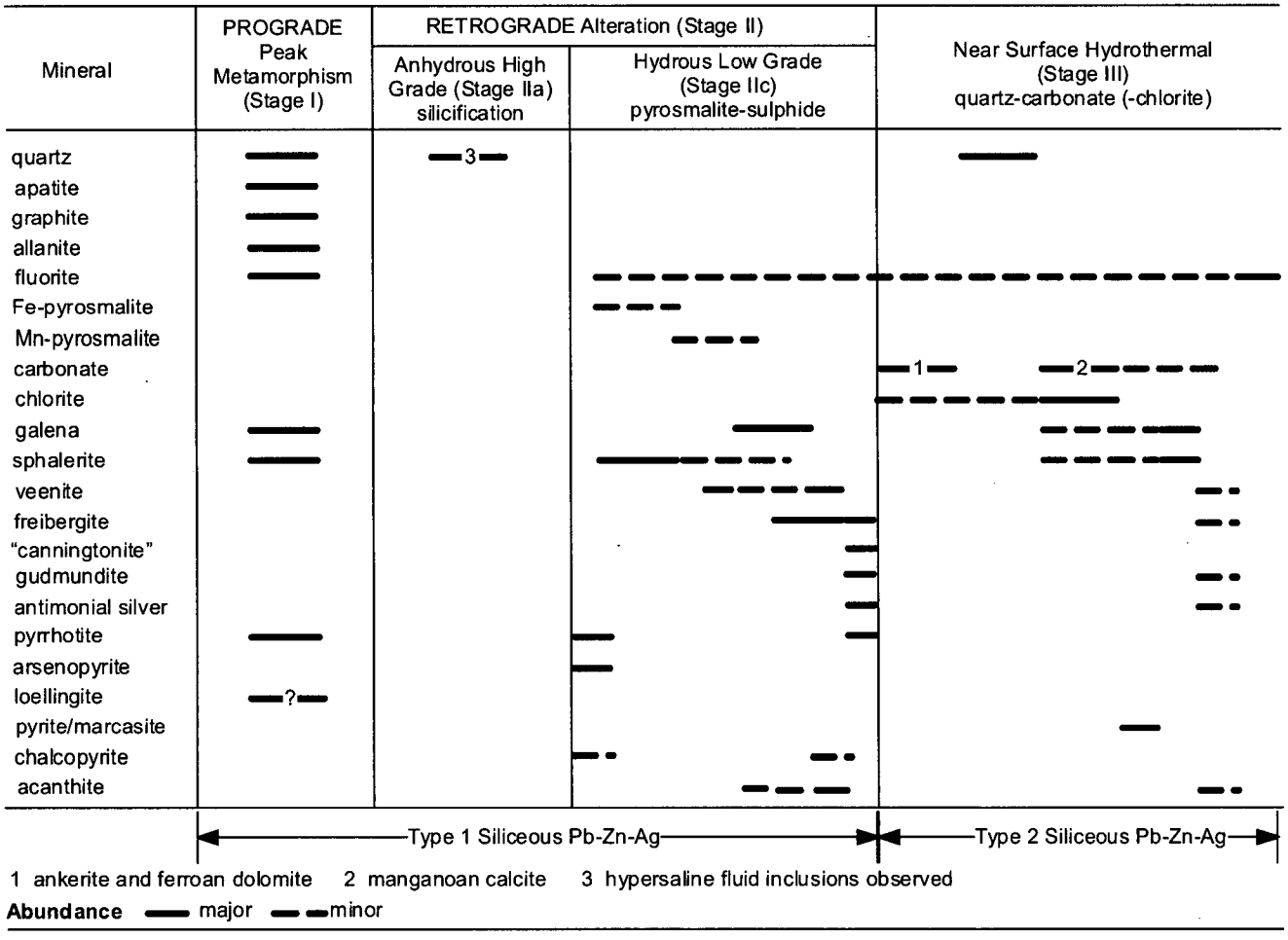

Figure 4.21 Mineral paragenesis of siliceous Pb-Zn-Ag mineralisation. Refer to Table 4.1 for explanation of ore types.

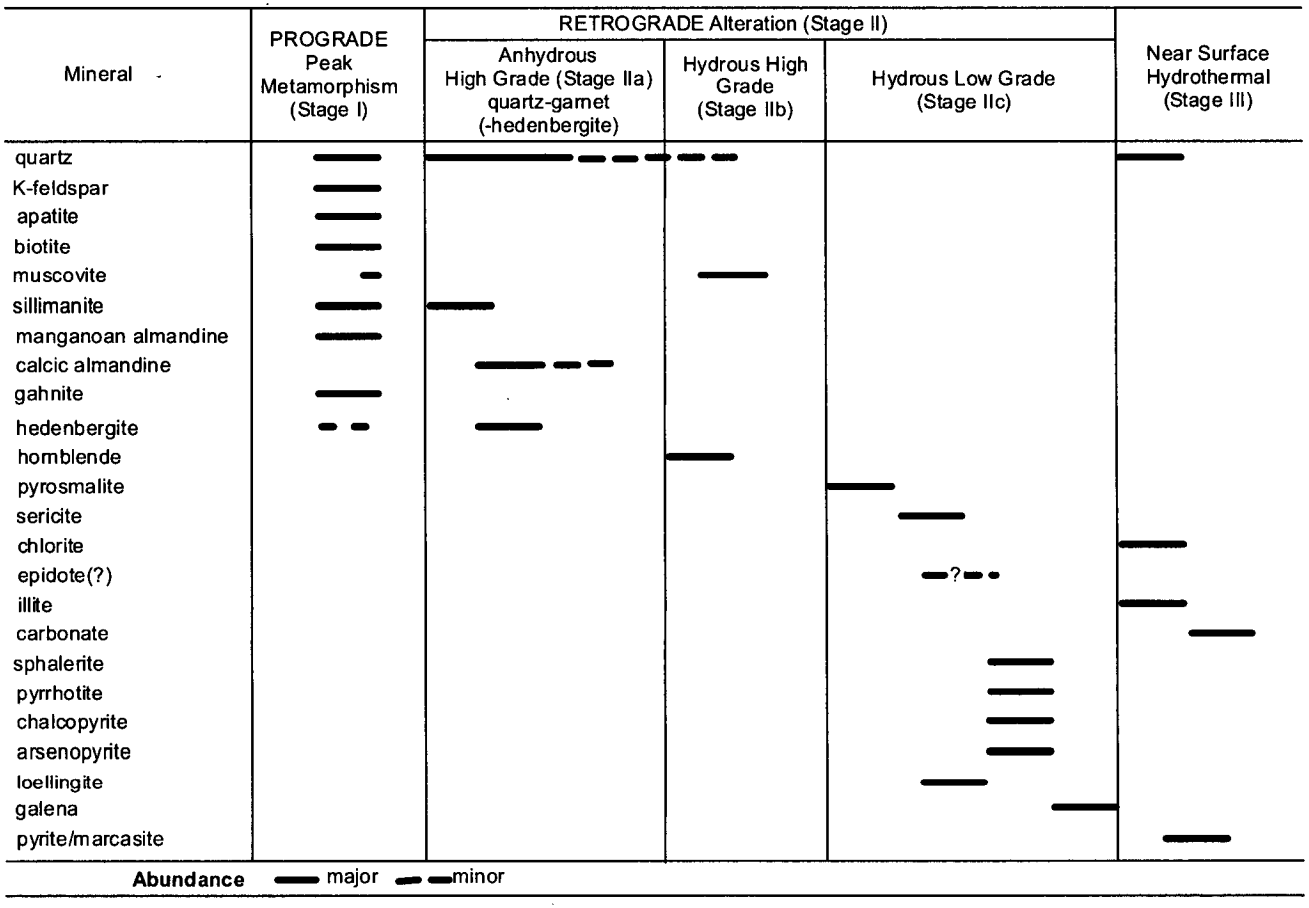

Figure 4.22 Mineral paragenesis of siliceous Zn mineralisation including silicified metasediments. Refer to Table 4.1 for explanation of ore types.

(Stage IIc) replacement of peak metamorphic sillimanite, K-feldspar, biotite, garnet and gahnite. Sphalerite, pyrrhotite, chalcopyrite and minor galena also display a late timing and are typically intergrown with Stage IIc alteration minerals. Stage III includes vuggy quartz-carbonate veining and alteration spatially associated with D_5 subvertical faults (Fig. 4.22).

4.9.3.1 The significance of gahnite

The presence of peak metamorphic gahnite porphyroblasts and poikiloblasts in some unsilicified sillimanite-garnet schists (e.g. gahnite-bearing sillimanite-biotite-garnet schists in the Northern Zone), indicates that anomalous Zn was present in some host rocks prior to metamorphism (section 3.2.3.3). Deformed quartz-gahnite veins in these rocks typically display granoblastic textures and diffuse margins with wallrocks. Adjacent silicified rocks are also characterised by peak metamorphic granoblastic textures. Disseminated sphalerite and minor galena form typical granoblastic textures and are localised along sutured quartz grains, as well as inclusions in quartz. These textures are indicative of peak metamorphic features. The occurrence of aligned gahnite aggregates and microscopic penetrative recrystallised zones in quartz, define an S_1 fabric. Sillimanite filled microshears are consistent with D_2/M_2 features. Overall, the textural evidence indicates that quartz-gahnite veins and associated silicification and mineralisation pre-date peak metamorphism and D_1.

A pre-peak metamorphic timing is also supported by the observed absence of gahnite in Stage IIa syn- to post-D_2 quartz veins and associated silicification. Quartz-gahnite veins are therefore unrelated to, and predate Stage IIa quartz veins and silicification. Hence, there is good evidence that quartz-gahnite veins possibly represent metamorphosed quartz-sphalerite veins that overprinted metasediments prior to peak metamorphism. Gahnite most likely formed by the breakdown of sphalerite in the presence of aluminosilicate during prograde metamorphism via the reaction (Spry, 2000):

$$\underset{\text{sphalerite}}{ZnS} + \underset{\text{aluminosilicate}}{Al_2SiO_5} + 0.5O_2 \rightleftharpoons \underset{\text{gahnite}}{ZnAl_2O_4} + \underset{\text{quartz}}{SiO_2} + 0.5S_2$$

This reaction also provides an explanation for the observed silicification. Overall, a possible premetamorphic quartz-sphalerite stockwork zone is inferred from the textural evidence.

4.9.4 Fluorite paragenesis

Fluorite is not exclusive to any particular paragenetic stage. It can be traced as far back as Stage I, where rounded inclusions of fluorite occur in peak metamorphic knebelite and pyroxferroite, and within garnet-apatite and olivine-pyroxferroite bands in graphitic ore. Disseminated fluorite also occurs in some quartz-apatite facies graphitic ores, where it forms characteristic peak metamorphic granoblastic fluorite-quartz textures. Fluorite deposition also occurred during Stage IIa, where it occurs in hedenbergite veins that overprint compositional banding in banded olivine-pyroxenoid ore. Fluorite veins also overprinted Stage IIa silicification in siliceous Pb-Zn-Ag ore. The latest stage of fluorite deposition occurred in D_5, where euhedral fluorite crystals line vughs in Stage III quartz-carbonate veins spatially

associated with D_5 faulting. The textural evidence indicates that fluorite was present prior to peak metamorphism, and was remobilised during subsequent Stage II syn-D_2 to post-D_3 retrogression and Stage III syn- to post-D_5 hydrothermal activity.

4.9.5 Mineralogical and paragenetic comparison with Broken Hill, Australia

Walters and Bailey (1998) classified the Cannington deposit as a BHT deposit based on close mineralogical, textural and chemical similarities with the Broken Hill deposit, New South Wales (Chapter 1; cf. Beeson, 1990; Parr and Plimer, 1993; Walters, 1996). Textures of the ores at Broken Hill have been documented by many workers since the late 1800's (e.g. Andrews, 1922; Lawrence, 1968, 1973; Hodgson, 1975; Johnson and Klingner, 1975; Plimer, 1980, 1984, 1987; Parr and Plimer, 1993; Webster, 1994, 1996; and many others). In particular, the paragenetic significance of ore textures at Broken Hill were addressed by Lawrence (1968 and 1973), Hodgson (1975), Plimer (1980, 1984 and 1987), Parr and Plimer (1993) and Webster (1994).

Lawrence (1973) suggested that the presence of granoblastic sulphide-silicate textures and spheroidal inclusions of sulphide in peak metamorphic Fe-Mn silicates (i. e. "spheroidation" textures) at Broken Hill indicated co-recrystallisation during prograde metamorphism, and therefore that sulphides were present in the rock during prograde metamorphism. Ores that exhibited these textures underwent subsequent textural modification during retrogression adjacent to shear zones (Lawrence, 1973; Webster, 1994). Ramdohr (1950) also noted spheroidation and granoblastic sulphide-silicate textures in some ores at Broken Hill and attributed these to metamorphic recrystallisation, noting that primary paragenetic features had been obliterated. Similar prograde spheroidation and granoblastic sulphide-silicate textures with subsequent textural modification during retrogression are manifested in the ores at Cannington.

Lawrence (1973), Plimer (1980, 1984, 1987) and Parr and Plimer (1993), recognised that Broken Hill consisted of prograde ore that subsequently underwent a series of retrograde events characterised by progressively lower temperature alteration assemblages and associated textural modification; Cannington displays a very similar evolutionary and textural history. A striking similarity between Broken Hill and Cannington is the occurrence of retrograde hedenbergite-garnet-quartz alteration and silicification, which at Broken Hill is spatially associated with retrograde shear zones and post-peak metamorphic dilational structures such as tension gashes and extensional veins (Webster, 1994, 1996). At Cannington, it is also associated with zones of dilatancy that facilitated post-peak metamorphic fluid flow during D_2/M_2.

Even though mineral assemblages at Broken Hill (Lawrence, 1968; Worner and Mitchell, 1983; Plimer, 1984) are similar to Cannington, there are some major differences, for example:

i) magnetite is common at Cannington and rare at Broken Hill;

ii) carbonate is common at Broken Hill and rare at Cannington, except for late stage carbonate associated with D_5 faults;
iii) Fe-Mn silicates at Cannington approach Fe-rich end-members (French et al., 1994; this study), whereas at Broken Hill they approach Mn-rich end-members (Fig. 4.17b; Lawrence 1968, 1973; Hodgson, 1975; Birch, 1983); and
iv) graphite is present at Cannington and relatively rare at Broken Hill.

In summary, the Broken Hill and Cannington deposits display similar evolutionary histories with regard to paragenetic relationships and ore textures. Both deposits exhibit an early prograde metamorphic stage, followed by subsequent post-peak metamorphic retrogression manifested by a series of later overprinting metasomatic assemblages. There is good textural evidence for the presence of sulphides prior to peak metamorphism at both deposits. Compositional variations in the gangue minerals and their relative abundances are the main differences between Cannington and Broken Hill.

4.9.6 Other genetic aspects and models

Walters and Bailey (1996 and 1998) prefer a genetic model for Cannington that involves the interaction of externally derived, post-peak metamorphic hypersaline fluids with a pre-existing zoned, Broken Hill-type protolith to produce the resulting "zone-refined" hybrid deposit. The external derivation of the retrograde hypersaline fluid is supported by the occurrence of structurally controlled, late orogenic metasomatism associated with Cu-Au deposits (Williams and Blake, 1993; Williams and Baker, 1995; Williams et al., 1996; Baker, 1996; Mark and Foster, 2000; Pollard, 2001) elsewhere in the Eastern Succession, including the extensively metasomatised Cloncurry Fault (section 2.6; de Jong and Williams, 1995; Mark and de Jong, 1996) approximately 10km northwest of Cannington.

Hypersaline fluid inclusions of similar composition to those in Stage IIa retrogression at Cannington occur in a range of Cu-Au and BHT Pb-Zn deposits throughout the Cloncurry district (Williams et al., 1996; Dong et al., 1997a and b). Therefore, the interpretation that Stage II retrograde alteration was produced by the introduction of regional hypersaline metasomatic fluid is reasonable. This process best explains local solution-associated remobilisation of pre-existing metals and sulphur (i.e. internal reworking), textural modification of the ore, and the large diversity of mineral assemblages within the deposit. However, the source of the metasomatic fluid, both at Cannington and on a regional scale, remains speculative, although a magmatic heritage related to intrusions associated with the Williams Batholith is preferred (section 2.6; de Jong and Williams, 1995; Mark and Foster, 2000; Pollard, 2001). However, the timing of Stage IIa metasomatism at Cannington is syn- to post-D_2/M_2, ca. 1550 Ma, i.e. it predates intrusion of the Williams batholith and the thermal pulse associated with it, M_3, by ~40Ma. If this is correct, then Stage IIa metasomatism at Cannington is unrelated to regional metasomatism. Stage IIb metasomatism, characterised by ferro-actinolite-ilvaite-magnetite alteration, has a timing that is more consistent with regional metasomatism based on textural evidence. Age dating of actinolite at Cannington would either

substantiate or discount this apparent temporal relationship.

4.9.6.1 Comparison to Zn-Pb skarn deposits

A common theme in recent literature on Cannington is the interpretation that the deposit resembles an epigenetic skarn that formed after peak metamorphism (Chapman, 1993; Strain, 1993; Richmond, 1994; Jenkins, 1994; Richmond et al., 1996a and b; Williams et al., 1996; Chapman and Williams, 1998).

To compare Cannington to Zn-Pb skarn deposits, it is necessary to define the typical characteristics of Zn-Pb skarn deposits. Meinert (1998) provided a key reference that described the mineral compositions and metal zonation typical of Zn-Pb skarns. Below follows a summary of the relevant aspects of Meinert's (1998) publication with respect to this type of deposit.

In general, Zn-Pb skarn deposits are zoned in terms of gangue mineralogy from proximal garnet (high garnet:pyroxene ratios), through pyroxene, to distal pyroxene-pyroxenoid (low garnet:pyroxene ratio) relative to the associated intrusion. Overall, zonation in silicate compositions is characterised by proximal Mg, to distal Fe and Mn. For example, proximal pyroxenes are more diopsidic, whereas distal pyroxenes are more hedenbergitic to johannsenitic. Similar Mn-enrichment in distal garnet (spessartine), olivine (tephroite), ilvaite and pyroxenoid (bustamite/rhodonite) is also noted. Concomitant Fe-enrichment may also be evident in the distal silicates (e.g. fayalite/knebelite, pyroxmangite/pyroxferroite). In general, however, despite the zonation in gangue mineralogy, Zn-Pb skarns are characterised by an overall low garnet:pyroxene ratio. Epidote/ilvaite may also be present directly adjacent to or within the associated intrusion.

Metal associations are also zoned in Zn-Pb skarn deposits so that proximal garnet-rich assemblages have associated sphalerite-pyrrhotite(± magnetite)-chalcopyrite-galena, while distal pyroxene-rich assemblages have associated pyrite-sphalerite-galena-(± hematite)-rhodochrosite. Pb:Zn ratios increase from proximal to distal. Some Zn-Pb skarn deposits also show vertical zonation, where Zn-Pb grades increase higher in the systems (i.e. distal), with a concomitant increase in the Pb:Zn ratio. The overall metal zonation in classic Zn-Pb skarns is therefore characterised by;

- Proximal - high Zn:Pb, Cu:Zn and Cu:Pb, i.e. Cu>Zn>Pb.
- Distal - low Zn:Pb, Cu:Zn and Cu:Pb, i.e. Pb>Zn>Cu.

On a regional scale, a metal zonation with respect to proximity to the associated intrusion is also evident; Cu skarns are typically proximal, whereas Zn-Pb skarns are typically distal to their associated intrusions.

Chapman and Williams (1998) proposed that the Cannington deposit displays several features

typical of Zn-Pb skarn deposits. These include:

- Fe- and Mn-rich pyroxenoid rocks with associated Pb-Ag that occur in an outer envelope which encloses an inner Fe-Ca-rich, hedenbergite zone associated with Zn(-Cu-As).
- Both Pb-Ag and Zn mineralisation is associated with magnetite and fluorite assemblages.
- Pyroxenoid compositions are characteristically Ca-rich, which is consistent with crystallisation in equilibrium with hedenbergite (a feature of skarns formed at temperatures several hundreds of degrees cooler than peak metamorphism at Cannington).
- Geochemical constraints indicate that pyroxene–pyroxenoid–garnet alteration could be partly developed in distinctly carbonate/calcsilicate rocks or chemical sedimentary units.

However, it should be noted that Ca-rich pyroxenoid compositions are stable at the higher temperatures (e.g. Brown et al., 1980) proposed for peak metamorphic conditions at Cannington. In addition, Chapman and Williams (1998) suggested that another feature arguing against a late metasomatic (skarn) origin for mineralisation and alteration, was the highly reduced nature of the silicate assemblages, especially the garnets, since this is atypical of skarn deposits. They explained this apparent anomaly by suggesting that the reduced character of the host rocks (graphite-stable) would have allowed high temperature saline fluids to transport large amounts of Fe and Mn. Further, if these fluids were subsequently reduced (on contact with the host rocks), they could be responsible for the alteration assemblages characterised by low-andradite garnet and anhydrous Fe-Mn-silicates.

In particular, Chapman (1993), and Chapman and Williams (1998) focussed on an intersection in one drillhole (CAD155) located in the Southern Zone, and they realised that "this is an isolated deep hole and the illustrated intersection cannot be correlated with other Fe-rich alteration zones associated with economic mineralisation" (Figure 6 of Chapman and Williams, 1998). In fact, a reinterpretation of the same drillhole reveals that this area is a particularly good example of Stage IIa and b metasomatism of olivine facies graphitic ore and banded olivine-pyroxenoid ore. Moreover, the intersection does not accurately represent a microcosm of the entire orebody, but a component of a much larger and extremely diverse system.

Based on textural observations, the model proposed by Chapman (1993), Williams et al. (1996) and Chapman and Williams (1998) involves the deposition of sulphides after initial post-peak metamorphic anhydrous alteration (hedenbergite-calcic almandine-quartz and (secondary) pyroxferroite), when magnetite, fluorite and minor pyrosmalite were deposited. Even though there is a general consensus that anhydrous alteration occurred syn- to post-D_2 and was followed by subsequent hydrous retrogression, several key observations suggest that the proposed post-D_2 paragenesis and timing of sulphide mineralisation is not an accurate

representation of the textural diversity of ore types comprising the entire deposit, viz.:

- spheroidal inclusions of sulphide, fluorite and magnetite in prograde Fe-Mn silicates indicate that sulphides, fluorite and magnetite can be traced back to the earliest premetamorphic, prograde stage of the paragenesis;
- sulphides occur in ores that contain no retrograde alteration and form classic granoblastic sulphide-silicate textures indicative of co-crystallisation during prograde metamorphism (e.g. graphitic ores); and
- textures indicate that fluorite was deposited throughout the retrograde history, and is not exclusive to any particular paragenetic stage after peak metamorphism.

While mineral and metal zonation patterns at Cannington are similar to Zn-Pb skarns, numerous features suggest that deposit is not a skarn. These include:

- The mineral paragenesis and temporal relationships between sulphides and silicates are very different from Zn-Pb skarns (ibid.).
- Garnet compositions are unlike typical Zn-Pb skarn deposits, being significantly more Fe-Mn rich (Fig. 4.17d).
- The association of Pb-Zn-Ag ore with siliceous and finely banded graphitic rocks enriched in P (up to ~2 wt%).
- Erratic metal zonation features in the Northern Zone unlike the clearly defined Pb-Zn zonation observed in the Southern Zone (section 4.8).
- The abundance of coexisting magnetite and fluorite in both olivine-pyroxenoid and hedenbergite ores.

These major differences are supported by Meinert (1995; pers. comm., 2000) who, in addition to mineralogical compositions and assemblages, suggested that ore textures at Cannington were atypical of Zn-Pb skarn deposits. In an unpublished report to BHP (1995), Meinert argued that several major factors, similar to those presented here, discounted a skarn-model for Cannington, viz.;

- The abundance of more Fe-Mn mineral compositions and absence or scarcity of andraditic garnet, johannsenite and bustamite. More johannsenitic pyroxene and andraditic garnet compositions would be expected in a fluid dominated metasomatic skarn system.
- Olivine is rare in Zn-Pb skarns, and like pyroxenoids at Cannington, compositions fall along the Fe-Mn join rather than the Ca-Mn join typical of skarns.
- Scarcity of crosscutting stockwork veins and abundance of laminated mineralised rocks "which, although strongly metamorphosed, appear to reflect original stratigraphic layering" Meinert (1995).
- Presence of a garnetiferous alteration halo enveloping the deposit.

Williams et al. (1996) and Chapman and Williams (1998) have also suggested that the presence of high temperature (~450-500°C) hypersaline, metal-rich fluid inclusions in quartz is

consistent with a metasomatic model (see also Dong et al., 1997a). However research presented here suggests that such a feature could be re-interpreted as evidence for solution-associated remobilisation of pre-existing metals within the deposit by the introduction of externally derived hypersaline metasomatic fluids syn- to post-D_2, i.e. localised solution-associated remobilisation associated with the ingress of Stage IIa fluid during M_2.

4.10 CONCLUSIONS

The deposit paragenesis and temporal relationships to metamorphism and deformation are summarised in Table 4.5. The most pronounced deformation fabrics in the ores at Cannington correlate with D_1/D_2 (Gray, 1994; Sheehan, 1994; Bailey, 1998; Bodon, 1995, 1998; Walters and Bailey, 1998; Giles, 2000; this study). Premetamorphic sulphides (Stage I of the paragenesis) occur in graphitic, olivine-pyroxenoid and banded olivine-pyroxenoid ore, as spheroidal inclusions in peak metamorphic minerals and as recrystallised curvilinear sulphide grains in granoblastic textured rocks overprinted by D_1 fabrics. Rare pseudomorphic bow-tie textures and S_i quartz inclusions trails preserved in garnet porphyroblasts in graphitic ores indicate that the timing of ore formation can be traced back to very early prograde metamorphic times below garnet stability. The ores were subsequently subjected to prograde metamorphism where P-T conditions eventually breached the upper stability of possible chloritoid. Peak metamorphic conditions of ~650-700°C and ~4kbars occurred ca. 1580 Ma.

Syn- to post-D_2 retrogression caused widespread hedenbergite-quartz-calcic almandine (Stage IIa) and amphibole-ilvaite alteration (Stage IIb) of pre-existing Fe-Mn silicate ore, as well as silicification of graphitic ore and host rocks. Stage IIa retrogression was associated with the ingress of M_2 fluids facilitated by D_2 dilational structures that formed in response to competency contrasts between rock types. These structures provided the necessary plumbing

Table 4.5 Summary of key minerals associated with each stage of the deposit paragenesis (modified after Bodon, 1995, 1998). Minerals in italics are restricted to siliceous Zn ore.

Metamorphism	Stage I prograde, peak metamorphic (pre–D_1)
M_1	Knebelite, pyroxferroite, hedenbergite, fluorite, magnetite, apatite, quartz, manganoan almandine, hornblende, grunerite, *sillimanite, K-feldspar, gahnite*, biotite, galena, sphalerite, pyrrhotite, allanite, rare carbonate (possible loellingite)
	Stage II retrogression (syn–D_2 to post–D_3)
M_2	*Stage IIa anhydrous (syn– to post–D_2)* Hedenbergite, calcic almandine, quartz, *sillimanite,* pyroxferroite, carbonate, fluorite
M_2 (waning)	*Stage IIb hydrous high grade (syn– to post–D_2)* Hornblende, grunerite, fluorite, minor sphalerite, pyrrhotite, chalcopyrite, arsenopyrite
M_3	*Stage IIb hydrous (syn– to post–D_3)* Ferro-actinolite, ilvaite, magnetite, fluorite, *muscovite(?)*, sphalerite, pyrrhotite, chalcopyrite, arsenopyrite, minor galena
M_3 (waning)	*Stage IIc hydrous low grade (post–D_3)* Pyrosmalite, magnetite, fluorite, *sericite*, galena, sphalerite, pyrrhotite, chalcopyrite, freibergite, pyrargyrite, arsenopyrite, gudmundite, antimonial Ag, minor veenite, acanthite, rare native Ag
	Stage III near-surface hydrothermal alteration (syn– to post–D_5)
	Quartz, fluorite, carbonate, chlorite, illite, galena, sphalerite, freibergite, gudmundite, veenite, antimonial Ag, acanthite, launyaite, "canningtonite", pyrite, marcasite, rare specular hematite

systems for the circulation of the retrograde fluid through the deposit. It is likely that the high competency of the Core Amphibolite influenced the fold geometry and hence zones of dilatancy during D_2. On a larger scale, the distribution of Stage IIa retrograde alteration coincides with postulated dilational zones in the hinge region of the F_3 Cannington Synform and pressure shadow zone adjacent to the Core Amphibolite. However, the syn- to post-D_2, pre-D_3 timing for Stage IIa metasomatism suggests that these spatial relationships are apparent only.

Later Stage IIb ferro-actinolite-ilvaite retrogression occurred syn- to chiefly post-D_3 and was related to the ingress of retrograde fluid coincident with the transient M_3 event related to intrusion of the Williams Batholith. Later hydrous retrogression during the waning stages of M_3 was characterised by the deposition of abundant sulphide, and a large variety of sulphosalt and antimonide minerals associated with pyrosmalite veining and pyrosmalite-secondary magnetite alteration (Stage IIc). Fluid-pathways were controlled by pre-existing D_3 structures such as the Footwall Shear. Textural evidence suggests that solution-associated remobilisation of premetamorphic sulphides occurred during the retrograde events, possibly causing deposit-wide reworking and zone refining over a range of thermal conditions and protracted period of time of primary deposit features.

The presence of premetamorphic sulphides indicates that Cannington is not a syn- to post-D_2 metasomatic deposit, but a premetamorphic zoned deposit that underwent modification by later metamorphism, deformation, and syn-D_2/M_2 to post-D_3/M_3 retrograde alteration associated with the introduction of regional metasomatic fluids. It is difficult to confidently estimate the spatial scale of remobilisation associated with particular retrograde events. However, it appears to be restricted to only several metres in most instances, albeit highly variable depending on the rheological properties of the pre-existing ore (i.e. degree of strain), as well as proximity to D_2 and D_3 structures that facilitated retrograde fluid-flow (e.g. the Footwall Shear). On this basis, the gross premetamorphic metal zonation features and distribution of ore types is interpreted to have remained largely intact (cf. Meinert, 1995). Assemblages comprising premetamorphic ores that show no evidence of subsequent Stage II retrogression, in particular graphitic ore, should therefore record a prograde P-T-t path and peak metamorphic conditions equivalent to those preserved in the host rocks, and this aspect forms the focus of the next chapter.

Chapter 5

Thermobarometric Estimation of Metamorphic Conditions, M_1

5.1 INTRODUCTION

Textural evidence from unmetasomatised ores such as graphitic ore, indicate that sulphide mineralisation predated peak metamorphism. In fact, the timing of mineralisation can be traced back through prograde metamorphism prior to garnet formation pre- to syn-D_i (section 4.9.1). If this is correct, then the ores should have been subjected to the same metamorphic history as the host rocks as previously proposed in Chapter 4.

The dominance of K-feldspar-sillimanite assemblages and ubiquitous partial melting in the migmatitic gneiss, indicate that peak metamorphic conditions during M_1 reached upper amphibolite facies grade (section 3.4; Mark, 1993; Gray, 1994; Sheehan, 1994; Mark et al., 1998; Giles, 2000). Jaques et al. (1982) determined peak metamorphic conditions of ~4kbars and 600–680°C from exposed metapelites and amphibolite to the north of Cannington using a combination of experimentally determined dehydration reactions and cation-exchange thermobarometry, e.g. garnet-biotite (Ferry and Spear, 1978) and plagioclase-hornblende geothermometry (modified after Spear, 1980), and clinopyroxene-quartz-plagioclase geobarometry (Ellis, 1980). A comparable range in peak metamorphic conditions of 4–6kbars and 665–690°C was estimated from pelitic and mafic rocks at Cannington, also using experimentally determined dehydrations reactions, phase equilibria and garnet-biotite geothermometry (Mark, 1993; Mark et al., 1998). Subsequent thermobarometric work at Cannington concurred with these estimates, yielding results of 650–690°C and 4–5kbars using a combination of mineral equilibria and garnet-biotite (from migmatitic gneiss) and garnet-hornblende (from the Core Amphibolite) geothermometry (Giles, 2000).

However, previous work at Cannington has not included pressure estimates calculated using cation exchange geobarometry, and calculated peak metamorphic temperatures using the Fe-Mg garnet-biotite geothermometer (Ferry and Spear, 1978) lack corrections for elevated Mn (and Ca) in garnet, and F and Cl in biotite. Including these corrections allow thermometric calculations to be carried out on Mn-rich rocks that contain garnets with compositions that would otherwise fall outside the calibration limits of the original Fe-Mg garnet-biotite geothermometer of Ferry and Spear (1978). This is particularly relevant to Cannington where widespread Mn anomalism characterises the garnetiferous alteration halo and significant Mn-F enrichment occurs within the orebody. Moreover, the calibrations can be applied to garnet-biotite pairs in mineralised banded rocks that are feature of the Northern Zone of the deposit.

In light of the aforementioned aspects, this chapter focuses on resolving the perennial question of whether particular ores having an interpreted premetamorphic origin, such as graphitic ore, were subjected to the same peak metamorphic conditions (M_1) as the surrounding host rocks. Metamorphic conditions have been estimated from a range of host and mineralised rock types using various cation exchange thermobarometers.

The chapter starts by firstly describing the mineral assemblages and structural fabrics within the samples used in the study. Mineral compositions are presented in conjunction with the latter, including chemical zonation trends in garnet. The applicability of various thermobarometers is then reviewed and results of the thermobarometric calculations presented. This is followed by a discussion on the estimated peak metamorphic conditions (M_1) and implications with regard to the timing of sulphide mineralisation.

5.2 METHODS

All samples used in the study were collected from drill core. Host rock samples included:

- amphibolite from the Core Amphibolite (sample no. SZ068-14),
- pelitic gneiss (sample no. SZU51-1),
- and gahnite-bearing sillimanite-biotite-garnet schist (sample no. NZ160-33).

Three graphitic ore samples were collected from the Northern Zone of the deposit. These included:

- biotite-garnet-rich banded ore from the biotite-garnet-hornblende facies (sample no. NZ040-8),
- biotite-garnet-hornblende-apatite-rich banded ore also from the biotite-garnet-hornblende facies (sample no. NZ042-4),
- and garnet-knebelite-grunerite-biotite-rich banded ore from the olivine facies (sample no. NZ039-2).

Thermobarometric calculations based on cation exchange equilibria between minerals within a given rock require the determination of mineral compositions. The most commonly used thermobarometers in metapelite and metabasic rocks require quantitative analyses of garnet, biotite, plagioclase and hornblende. The latter minerals were analysed using a Cameca SX50 electron microprobe at the Central Science Laboratory, University of Tasmania. Analytical procedures and data can be found in Appendix 1.

Microprobe traverses across garnet porphyroblasts were conducted from either core to rim, or complete rim-core-rim, with analyses taken at regular intervals to determine internal compositional zonation. Rim analyses were situated as close as possible to the porphyroblast margins and core analyses in the interpreted centre. Some garnet porphyroblasts, especially in the banded ores, contain fine inclusion trails of quartz that radiate outward from the core of the porphyroblast. These provided a means by which garnet cores could be identified with a high degree of visual accuracy in two dimensions.

Biotite grains in contact with garnet rims were analysed, as well as grains located away from the garnets (i.e. matrix biotite). Biotite inclusions in garnet porphyroblasts are rare, but when present were analysed to constrain compositional variations during garnet growth. Hornblende-plagioclase pairs in amphibolite were also analysed.

5.3 SAMPLE DESCRIPTIONS AND MINERAL COMPOSITIONS

5.3.1 Amphibolite

With the exception of biotite-garnet alteration zones along contacts with migmatitic gneiss and ores, garnet in the Core Amphibolite is rare. However, one example from the Southern Zone was chosen for the study. Mineral abundances have been visually estimated at 50% hornblende, 20% plagioclase, 12% quartz, 7% biotite, 5% garnet, 2% ilmenite, 2% sericite, and trace amounts of sphene and pyrite. A granoblastic fabric characterises the sample, with a weak S_2 foliation defined by the alignment of biotite and hornblende grains. Garnet occurs as poikiloblasts up to 1cm in diameter and contain inclusions of quartz, minor ilmenite and rare biotite (Fig. 5.1a). Weak retrograde alteration of plagioclase to a fine dusting of sericite occurs throughout the sample.

Compositions of garnet porphyroblasts are summarised in Table 5.1 and Figure 5.2. Core to rim compositional zonation is illustrated in Figure 5.3. The analytical data indicates that garnets have an average end-member composition of almandine and contain a significant component of grossularite (15.2 mol% average). Compositional zonation across one garnet porphyroblast is characterised by a decrease in MnO concentrations from core to rim, whilst CaO concentrations increase. MgO and FeO increase toward the rim before MgO starts to decrease and FeO remain constant.

Average compositions for biotite, hornblende and plagioclase are presented in Table 5.2. No zonation was detected in the latter minerals and it appears that compositions have been homogenised during metamorphism. Plagioclase has an average composition of An_{42}. Hornblende compositions are consistent with ferro-pargasite using the nomenclature of

Table 5.1 Average garnet analysis and end-member compositions of two garnet porphyroblasts from the Core Amphibolite. Total analyses (n) = 17. Refer Appendix 1 for detailed analytical results.

Oxide	Average analysis (wt%)	End members	Average composition (mol%)	Range in compositions (mol%)
SiO_2	36.89	pyrope	7.5	6.7-8.2
TiO_2	0.07	almandine	64.2	61.9-65.4
Al_2O_3	21.14	spessartine	8.2	6.5-10.6
Cr_2O_3	0.01	andradite	5.0	1.9-8.2
Fe_2O_3	1.70	grossularite	15.2	11.5-18.7
FeO	28.35			
MnO	3.59			
MgO	1.85			
CaO	6.96			
ZrO_2	0.04			
Y_2O_3	0.02			
V_2O_3	0.02			
TOTAL	100.56			

Figure 5.1 Photomicrographs of garnet porphyroblasts and biotite microprobed for garnet-biotite geothermometry on various host rocks and banded ores.

A. Poikiloblastic garnet from the Core Amphibolite containing large inclusions of quartz and finer inclusions of ilmenite and hornblende (plane-polarised transmitted light, SZ068-14, 435.7m).

B. Garnets from gahnite-bearing sillimanite-biotite-garnet schist with inclusion-rich cores (inset). Inclusions are dominated by quartz and possible minor K-feldspar. Sillimanite defines a composite S_1/S_2 foliation (M_1/M_2) and has been partially retrogressed to muscovite during M_3. A small poikiloblastic-like, corroded clot of gahnite intergrown with biotite and K-feldspar occurs in the lower left corner of the photomicrograph. The inset is a high magnification view of the garnets and one of the biotites that was microprobed within the black circle outlined in the top right of the photomicrograph (plane-polarised transmitted light, NZ160-33, 368.4m).

C. A large garnet porphyroblast from a biotite-rich migmatitic gneiss. A strong composite S_1/S_2 foliation is defined by the alignment of biotite and sillimanite. Secondary sillimanite replaces biotite and is indicative of D_2/M_2. M_2 sillimanite and M_1 biotite has subsequently been replaced by muscovite and possible fine grained euhedral kyanite indicative of M_3 (plane-polarised transmitted light, SZU51-1, 112.8m).

D. Poikilitic garnets from banded quartz-biotite-garnet-graphite ore in a matrix of granoblastic quartz-biotite±graphite. Fine inclusions in the garnets are dominated by quartz and rare biotite and sphalerite. The weak alignment of biotite defines a mineral fabric. The lack of retrograde minerals defining a later overprinting mineral fabric and the preservation of the granoblastic texture suggests that the foliation is equivalent to S_1 in the host sequence. The majority of garnet growth pre-dates S_1/M_1. However syn-D_1/M_1 growth is evidenced by inclusion–free garnet overgrowths that incorporate biotite (plane-polarised transmitted light, NZ040-8, 168.2m).

E. Sector-twinned garnet porphyroblasts in banded quartz-biotite-garnet-hornblende-apatite-graphite ore. The garnets typically have fine quartz-apatite and larger galena inclusions that radiate outward from the core of the porphyroblast. The garnets occur within an apatite-quartz±fluorite band which is as thick as the diameter of the garnets. A weak foliation at moderate angle to the banding is defined by the alignment of disseminated biotite and in other areas, the crystallographic alignment of apatite grains. The lack of a pre-existing fabric or overprinting fabric defined by retrograde minerals, coupled with the preservation of granoblastic textures indicates that the foliation is indicative of S_1. Elsewhere in the sample, S_1 is axial planar to millimetre-scale, tight F_1 folds (plane-polarised transmitted light, NZ042-4, 92.3m).

F. As for E. but poikiloblastic variety of garnet typically associated with poikilitic hornblende aggregates. These garnets typically occur in bands that lack graphite and have distinct corroded, embayed type textures (plane-polarised transmitted light, NZ042-4, 92.3m).

G. Garnet porphyroblasts from banded quartz-garnet-knebelite-grunerite-biotite ore. Garnets in the knebelite-grunerite band (left) form coalesced porphyroblasts to bands, whereas garnets in granoblastic quartz-rich bands (right) form comparatively finer grained inclusion-rich porphyroblasts. Late stage pyrosmalite alteration of biotite and minor grunerite is common. The sample lacks any discernable mineral foliation that is axial planar to millimetre scale open folds (plane-polarised transmitted light, NZ039-2, 108.4).

Abbreviations: bt–biotite, gh–gahnite, gt–garnet, gu–grunerite, hb–hornblende, ksp–K-feldspar, mu–muscovite, plg–plagioclase, qz–quartz, sil–sillimanite.

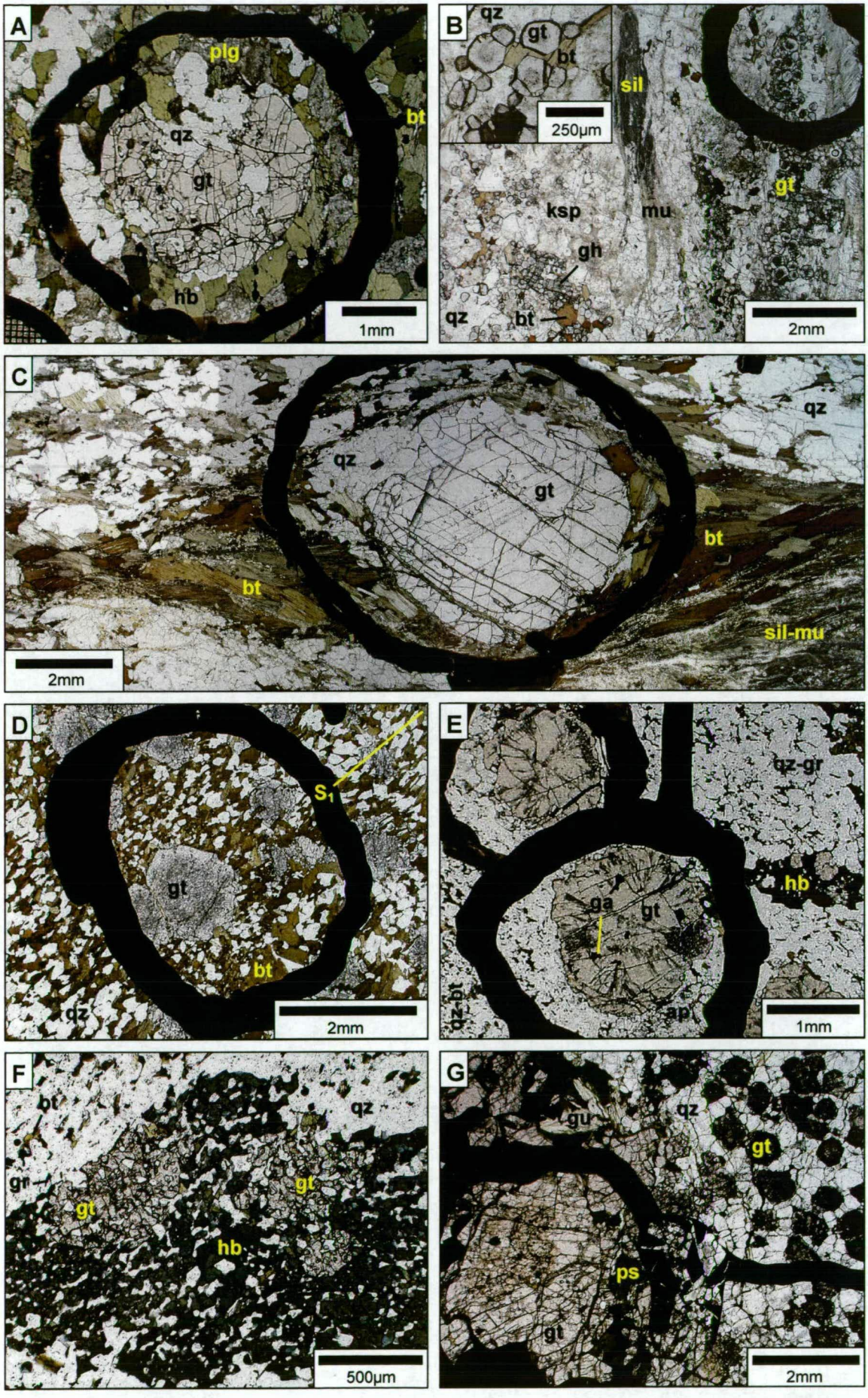
A
plg
bt
qz
gt
hb
1mm
B
qz
gt
bt
250µm
sil
gt
ksp
mu
gh
qz
bt
2mm
C
qz
qz
gt
bt
bt
sil-mu
2mm
D
S1
gt
bt
qz
2mm
E
qz-gr
hb
ga
gt
qz-gr
ap
1mm
F
bt
qz
gr
gt
gt
hb
500µm
G
gu
qz
gt
ps
gt
2mm

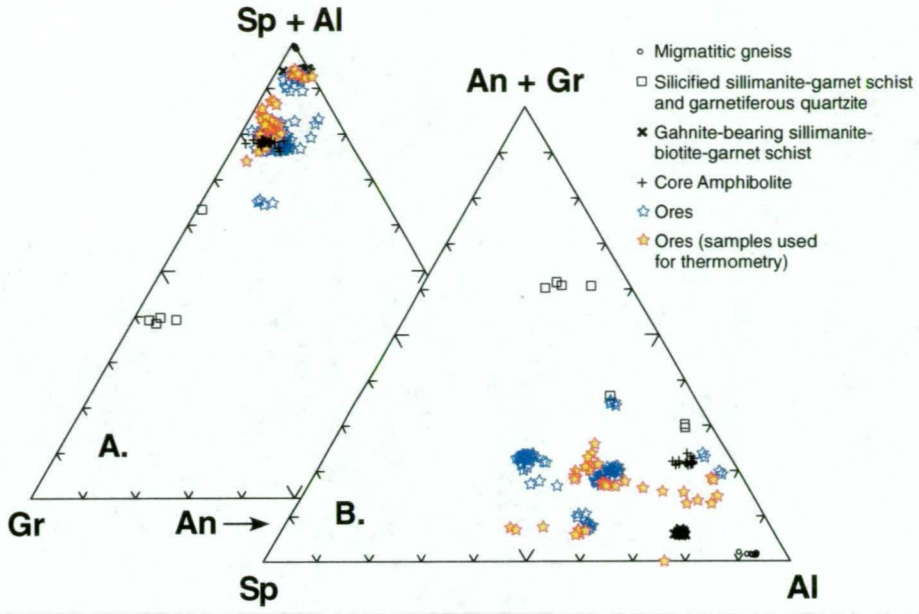

Figure 5.2 Ternary plots of garnet compositions for samples used in the thermometric calculations. Refer Appendix 1 for microprobe analyses. **A.** mol fractions of spessartine+almandine, grossularite. **B.** mol fractions of grossularite+andradite (ΣCa-garnet), spessartine, almandine. Abbreviations: Sp—spessartine (mol %), Gr—grossularite (mol%), An—andradite (mol%), Al—almandine (mol%). Garnet compositions from silicified sillimanite-garnet schist and garnetiferous quartzites are from French et al. (1994).

Leake et al. (1997).

5.3.2 Pelitic gneiss

A sample of pelitic gneiss was collected from the footwall of the Southern Zone. Mineral abundances in the sample have been visually estimated at 40% quartz, 30% biotite, 20% sillimanite, 5% garnet, 3% K-feldspar, 2% plagioclase and trace graphite, sericite, chlorite and pyrite (Fig. 5.1c). A granoblastic texture characterises the rock, with the preferred alignment of fibrolitic sillimanite and biotite defining a well developed S_1/S_2 foliation that wraps around garnet porphyroblasts. Decussate textured biotite-rich domains adjacent to garnet porphyroblasts have been overgrown by minor secondary sillimanite (M_2) that has subsequently been partially replaced by fine grained muscovite (white mica) and minor kyanite(?) consistent with M_3. Garnet porphyroblasts (≤8mm in diameter) contain minor quartz

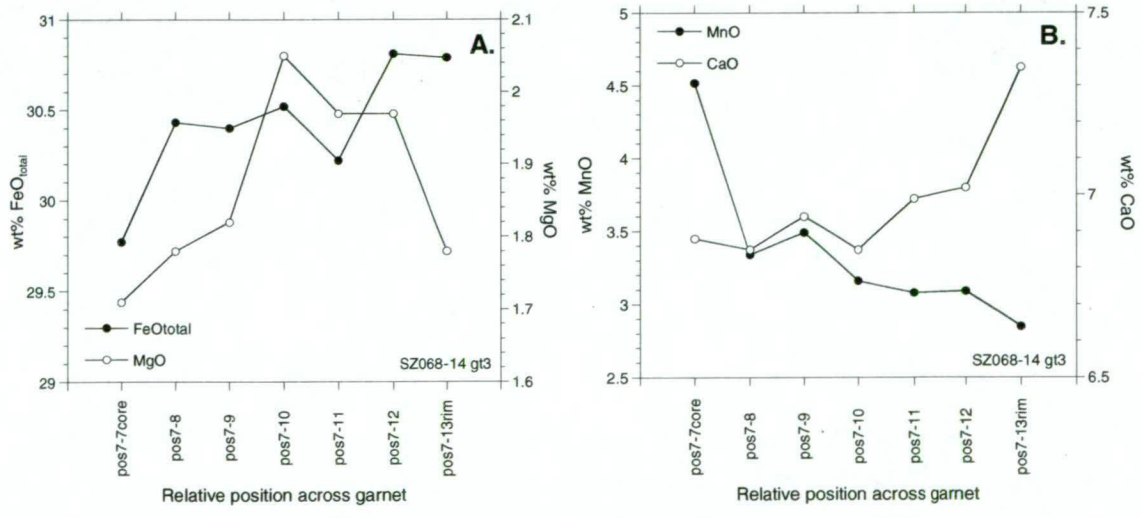

Figure 5.3 Compositional variations across a garnet porphyroblast in garnet-bearing amphibolite from the Core Amphibolite. Sample numbers appear in the bottom right of the graphs.

Table 5.2 Average biotite, hornblende and plagioclase analyses from the Core Amphibolite. Average plagioclase composition is An_{42}. Refer Appendix 1 for detailed analytical results.

Oxide/element (wt%)	Biotite	Hornblende	Plagioclase
SiO_2	32.84	39.92	57.23
TiO_2	3.30	1.34	0.02
Al_2O_3	15.44	13.71	27.64
Fe_2O_3	-	4.70	0.06
FeO	-	18.70	-
FeO_{total}	27.20	-	-
MnO	0.12	0.26	0.00
MgO	7.53	5.56	0.00
CaO	0.17	11.41	8.95
Na_2O	0.12	1.49	6.83
K_2O	7.58	1.18	0.15
F	0.23	0.15	-
Cl	0.23	0.18	-
Analyses (n)	4	8	4

inclusions and development of adjacent syn-kinematic quartz pressure shadows. Low grade retrogression is minimal with the alteration of sillimanite and K-feldspar to minor sericite, and biotite to trace chlorite.

The composition of one garnet porphyroblast is summarised in Table 5.3 and Figure 5.2. Compositional variations across the porphyroblast are illustrated in Figure 5.4. The analytical data indicates that the garnet has an average end-member composition of almandine (80.9 mol% average) and contains a significant component of pyrope (12.3 mol% average). FeO concentrations generally increase from core to rim, whereas MgO has an opposite trend. The core also contains elevated MnO that initially decreases toward the rim and then increases abruptly on the rim. CaO displays a similar trend of decreasing concentrations toward the rim and then an abrupt increase on the rim.

The average composition of biotite is presented in Table 5.4. No zonation was detected suggesting compositions were homogenised during metamorphism.

Table 5.3 Average garnet analysis and end-member compositions of a garnet porphyroblast from pelitic gneiss. Total analyses (n) = 9. Refer Appendix 1 for detailed analytical results.

Oxide	Average analysis (wt%)	End members	Average composition (mol%)	Range in compositions (mol%)
SiO_2	36.27	pyrope	12.3	8.3-13.7
TiO_2	0.01	almandine	80.8	79.5-82.9
Al_2O_3	21.09	spessartine	5.8	4.8-8.1
Cr_2O_3	0.02	andradite	1.1	0.9-1.6
Fe_2O_3	1.27	grossularite	0.0	-
FeO	35.06			
MnO	2.47			
MgO	2.99			
CaO	0.38			
ZrO_2	-			
Y_2O_3	-			
V_2O_3	-			
TOTAL	99.56			

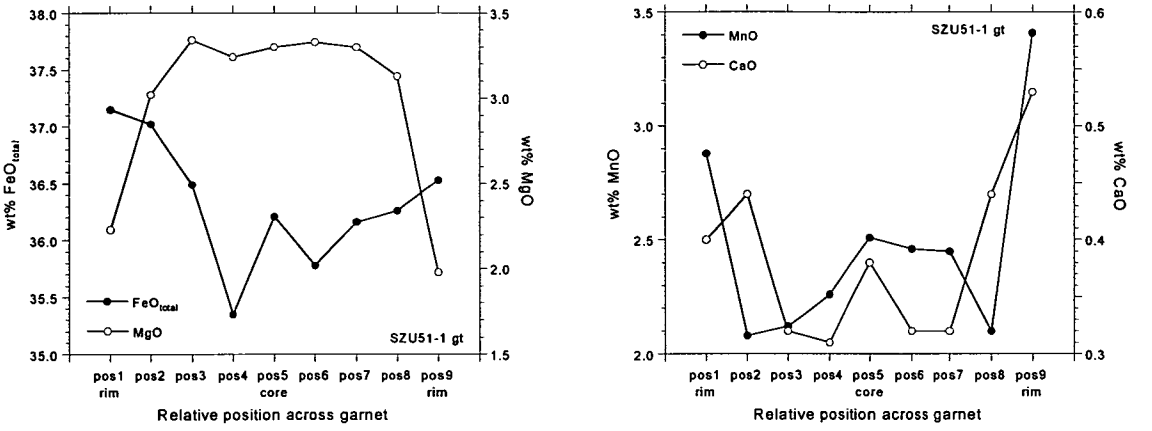

Figure 5.4 Compositional variations across an almandine porphyroblast in a pelitic gneiss sample (sample numbers appear in the bottom right of the graphs).

5.3.3 Gahnite-bearing schist

A sample of gahnite-bearing sillimanite-biotite-garnet schist was collected from the Northern Zone of the deposit. Mineral abundances have been visually estimated at 50% K-feldspar, 15% sillimanite, 15% garnet, 8% quartz, 6% biotite, 5% muscovite, 1-2% gahnite and trace amounts of graphite and galena (Fig. 5.1b). A granoblastic texture characterises the rock, with an anastomosing S_2 foliation defined by the alignment of elongate fibrolitic sillimanite porphyroblasts and biotite. Fine-grained inclusion-rich garnet porphyroblasts (≤1mm in diameter) with inclusion free rims are disseminated throughout the rock. Inclusion minerals are difficult to confidently resolve optically, but appear to be dominated by a mixture of quartz and K-feldspar(?). Garnet abundances increase dramatically to ~50% in quartz dominated, K-feldspar-sillimanite absent augen. Retrogression of sillimanite to muscovite (M_3) is pronounced in the sample along with minor late, fine-grained sericite alteration of K-feldspar.

Garnet compositions are summarised in Table 5.5 and Figure 5.2. Compositional variations across two porphyroblasts are illustrated in Figure 5.5. Microprobe analyses indicate that garnets contain a significant component of almandine (72.3 mol% average) and spessartine (16.8 mol% average); the average spessartine component ~3 times greater than that of garnet in the pelitic gneiss sample. FeO concentrations generally increase from the core toward the rim of porphyroblasts before decreasing abruptly in the rims. MgO contents remain relatively constant, but decrease in the garnet rims. CaO contents display similar trends, but show an

Table 5.4 Average biotite composition from a pelitic gneiss. Refer Appendix 1 for detailed analytical results.

Oxide/element (wt%)	Biotite
SiO_2	34.38
TiO_2	1.96
Al_2O_3	20.62
FeO_{total}	22.42
MnO	0.07
MgO	6.74
CaO	0.00
Na_2O	0.17
K_2O	8.75
F	0.20
Cl	0.31
Analyses (n)	4

Table 5.5 Average garnet analysis and end-member compositions of four garnet porphyroblasts from gahnite-bearing sillimanite-biotite-garnet schist. Total analyses (n) = 24. Refer Appendix 1 for detailed analytical results.

Oxide	Average analysis (wt%)	End members	Average composition (mol%)	Range in compositions (mol%)
SiO_2	35.84	pyrope	5.0	4.0-5.5
TiO_2	0.03	almandine	72.3	71.2-73.4
Al_2O_3	20.63	spessartine	16.8	16.0-18.3
Cr_2O_3	0.03	andradite	4.3	1.1-6.1
Fe_2O_3	1.42	grossularite	1.7	0.0-4.7
FeO	30.97			
MnO	7.12			
MgO	1.19			
CaO	2.01			
ZrO_2	-			
Y_2O_3	-			
V_2O_3	-			
TOTAL	99.23			

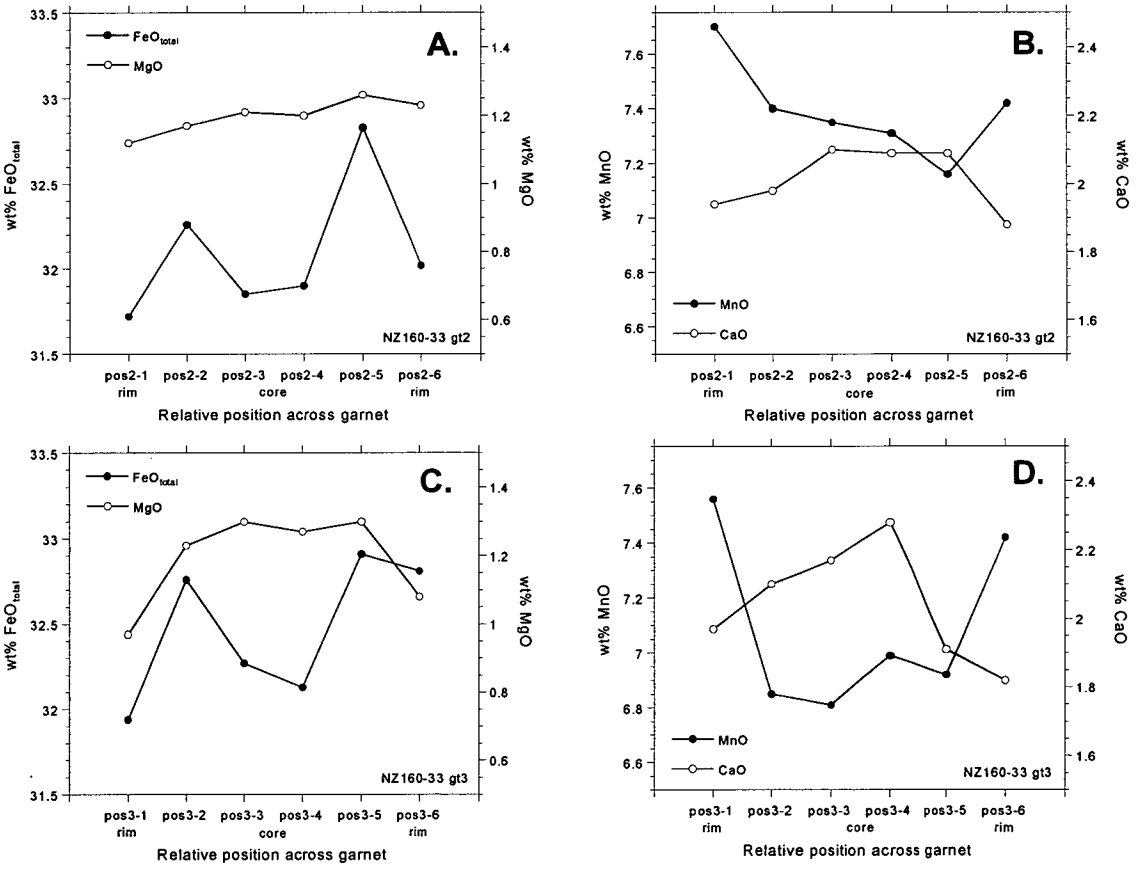

Figure 5.5 Compositional variations across two garnet porphyroblasts from gahnite-bearing sillimanite-biotite-garnet schist. **A.** garnet 2. **B.** garnet 3. Sample numbers appear in the bottom right of the graphs.

Table 5.6 Average biotite composition from gahnite-bearing sillimanite-biotite-garnet schist. Refer Appendix 1 for detailed analytical results.

Oxide/element (wt%)	Biotite
SiO_2	34.33
TiO_2	3.03
Al_2O_3	19.03
FeO_{total}	22.86
MnO	0.19
MgO	6.07
CaO	0.02
Na_2O	0.11
K_2O	9.87
F	1.34
Cl	0.34
Analyses (n)	24

overall progressive decrease from core to rim. MnO concentrations show a general increase from core to rim, with an abrupt increase in garnet rims.

Biotite is enriched in F (Table 5.6) compared to biotite in the pelitic gneiss. No zonation was detected suggesting compositions were homogenised during metamorphism.

5.3.4 Banded ores

5.3.4.1 Banded quartz-biotite-garnet-graphite

Mineral abundances for the banded quartz-biotite-garnet-graphite ore sample (NZ040-8) have been visually estimated at 55% quartz, 30% biotite, 10% garnet, 3% graphite, 2% sphalerite, 2% galena and trace apatite and hornblende (Fig. 5.1d). These minerals combine in variable proportions defining quartz-biotite-rich bands, and biotite-garnet-quartz-graphite-rich bands, both up to 1.5cm thick. The preferred alignment of biotite and graphite define the S_1 foliation (Fig. 5.1d) that is oriented at moderate angle to the compositional banding. Garnet porphyroblasts (≤3mm in diameter) occur predominantly in the biotite-rich bands, and contain abundant fine inclusions of quartz and rare biotite. In general, S_1 wraps around the porphyroblasts and minor randomly oriented, decussate biotite occurs in adjacent pressure shadow zones. Inclusion free garnet overgrowths typically display irregular, serrated margins with matrix minerals and in instances appear to overgrow biotite suggesting minor garnet growth after deformation. Quartz grains in quartz-biotite bands contain abundant inclusions of sphalerite. No retrogression is apparent in the sample.

The composition of one garnet porphyroblast is presented in Table 5.7 and Figure 5.2. Zonation features are illustrated in Figure 5.6a and b. Microprobe analyses indicate that the garnet contains a significant component of almandine (66.1 mol% average), spessartine (17.0 mol% average) and grossularite (12.5 mol% average). A strong symmetrical zonation from core to rim is characterised by increasing FeO and MgO, and decreasing MnO and CaO. Rims are enriched in CaO, and show slight depletion in MgO. The zonation differs from garnets in the pelitic gneiss and gahnite-bearing schist samples in that MgO increases and CaO decreases from core to rim, and MnO enriched rims are absent. MgO contents are very low, <0.5 wt%.

Table 5.7 Average garnet analyses and end-member compositions of garnet porphyroblasts from various banded ores. Refer text for sample descriptions and Appendix 1 for detailed analytical results.

	Sample		
Oxide (wt%)	**NZ040-8**	**NZ042-4**	**NZ039-2**
SiO_2	36.50	36.39	36.23
TiO_2	0.02	0.05	0.01
Al_2O_3	21.35	20.86	20.79
Cr_2O_3	0.01	0.01	0.01
Fe_2O_3	1.15	1.99	1.70
FeO	28.88	22.07	21.59
MnO	7.34	12.32	18.15
MgO	0.24	0.11	0.19
CaO	5.42	6.90	2.35
ZrO_2	0.02	0.05	0.00
Y_2O_3	0.03	0.07	0.00
V_2O_3	0.02	0.06	0.02
TOTAL	100.98	100.89	101.04
Analyses (n)	14	10	5
End member (mol%)			
pyrope	1.0 *(0.5-1.6)*	0.5 *(0.3-0.7)*	0.8 *(0.5-1.3)*
almandine	66.1 *(55.5-77.6)*	50.6 *(49.1-52.6)*	49.8 *(43.0-57.0)*
spessartine	17.0 *(5.4-26.7)*	28.6 *(25.5-31.8)*	42.4 *(35.0-48.9)*
andradite	3.4 *(1.4-5.8)*	5.9 *(3.9-7.7)*	5.1 *(3.3-7.3)*
grossularite	12.5 *(9.7-14.2)*	14.4 *(11.6-16.8)*	1.9 *(0.2-2.6)*

N.B. Text in italics represents ranges in compositions

The average composition of biotite (Table 5.8) is notably more Fe- and Cl-rich than biotite in the pelitic gneiss and gahnite-bearing schist. No zonation was detected suggesting compositions were homogenised during metamorphism.

5.3.4.2 Banded quartz-biotite-garnet-hornblende-apatite-graphite

Mineral abundances for the quartz-biotite-garnet-hornblende-apatite-graphite ore sample (NZ042-4) have been visually estimated at 65% quartz, 20% biotite, 5% garnet, 4% hornblende, 3% apatite, 2% galena, 1% graphite and trace fluorite. These minerals have combined in variable proportions to define garnet-biotite-hornblende, garnet-apatite-quartz (± fluorite, graphite), and quartz-biotite-apatite-graphite bands. The rock has a granoblastic texture with an S_1 foliation, defined by weakly aligned biotite and minor graphite, oriented at moderate angle to the compositional banding. The alignment of acicular apatite grains in

Table 5.8 Average biotite compositions from various banded ores. Refer text for sample descriptions and Appendix 1 for detailed analytical results.

	Sample		
Oxide/element (wt%)	**NZ040-8**	**NZ042-4**	**NZ039-2**
SiO_2	32.32	33.25	32.87
TiO_2	1.45	1.84	1.46
Al_2O_3	15.45	12.89	12.13
FeO_{total}	33.06	35.98	35.54
MnO	0.20	0.57	0.62
MgO	1.77	1.92	1.86
CaO	0.01	0.00	0.01
Na_2O	0.05	0.03	0.06
K_2O	9.24	9.26	9.23
F	0.33	0.25	0.86
Cl	1.42	1.87	2.51
Analyses (n)	2	2	2

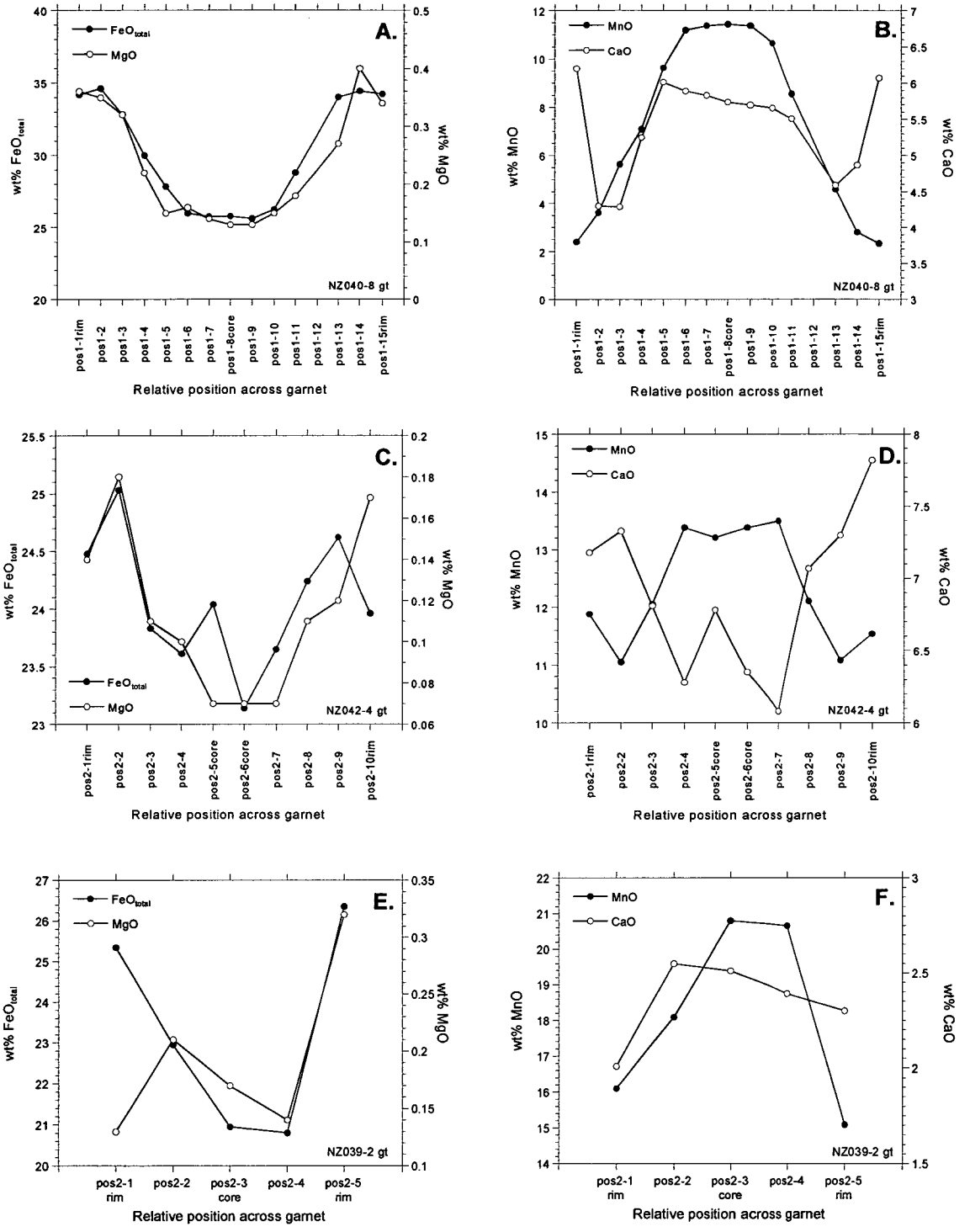

Figure 5.6 Compositional variations across garnet porphyroblasts in banded ores. **A.** and **B.** banded quartz-biotite-garnet-graphite ore. **C.** and **D.** banded quartz-biotite-garnet-hornblende-apatite-graphite ore. **E.** and **F.** banded quartz-garnet-knebelite-grunerite-biotite ore. Sample numbers appear in the bottom right of the graphs.

garnet-apatite bands also defines S_1 in instances. Garnet occurs as rounded sector-twinned porphyroblasts (≤2mm in diameter; Fig. 5.1e), and spongy textured poikiloblasts (≤2mm in diameter; Fig. 5.1f). In general, sector-twinned porphyroblasts predominate in garnet-apatite-rich bands and contain abundant fine inclusions of quartz and apatite that radiate outward from the core (Fig. 5.1e). Inclusions of galena and graphite may also be present. The characteristic morphology of these garnets is indicative of crystallisation in the presence of graphite during prograde metamorphism (Burton, 1986). Garnet poikiloblasts occur in graphite-poor garnet-biotite-hornblende bands, and in instances form aggregates with hornblende poikiloblasts (Fig. 5.1f). Inclusions are dominated by quartz. In garnets that are less poikilitic, inclusions include rare biotite, graphite, hornblende, apatite and galena. No retrogression is apparent in the sample, apart from very minor retrogression of garnet to secondary hornblende.

The composition of one sector-twinned garnet porphyroblast in a garnet-apatite band is presented in Table 5.7 and zonation features illustrated in Figure 5.6c and d. The garnet is more spessartine-rich (28.6 mol% average) than the garnet in sample NZ040-8 (Table 5.7), and displays similar compositional zonation, apart from an overall increase in CaO content from core to rim and Mn enrichment in the rims. Asymmetric zonation occurs chiefly in the garnet rims. MgO concentrations are extremely low, <0.2 wt%; too low to be of any great significance (R. Berry, pers. comm., 2000).

The average composition of biotite (Table 5.8) is similar to biotite in sample NZ040-8. No zonation was detected suggesting compositions were homogenised during metamorphism.

5.3.4.3 Banded quartz-garnet-knebelite-grunerite-biotite

Mineral abundances for the banded quartz-garnet-knebelite-grunerite-biotite ore sample (NZ039-2) have been visually estimated at 40% garnet, 25% quartz, 10% grunerite, 10% galena, 7% knebelite, 3% biotite, 2% magnetite, 2% pyrosmalite, and trace sphalerite, graphite, apatite and pyrrhotite (Fig. 5.1g). These minerals combine in variable proportions to define garnet-knebelite-grunerite-biotite, and quartz-garnet (± apatite, graphite) bands. A granoblastic texture characterises the rock, and grunerite aggregates display decussate textures. Garnet in knebelite-grunerite bands forms large coalesced porphyroblasts (≤0.5cm in diameter) and bands (≤1cm thick). Inclusions of biotite, sphalerite and quartz occur in interpreted cores, whereas rims are generally inclusion free (Fig. 5.1g). Garnets in the quartz-rich bands have a very different morphology, consisting of fine-grained, disseminated poikilitic porphyroblasts ≤0.5mm in diameter (Fig. 5.1g). Inclusions are dominated by extremely fine opaques (sulphides) and quartz. Minor alteration of knebelite and biotite to pyrosmalite is evident in the sample. The lack of disequilibrium textures such as symplectite and pseudomorphic replacement indicates that grunerite is not a retrograde product of knebelite, but a peak metamorphic mineral. This is also supported by instances of knebelite overgrowing grunerite grain boundaries.

The average composition of one garnet porphyroblast in a knebelite-grunerite-biotite band is presented in Table 5.7 and zonation features illustrated in Figure 5.6e and f. The garnet is significantly more spessartine-rich (42.4 mol% average) than garnets in samples NZ040-8 and NZ042-4 (Table 5.7). Zonation trends are characterised by decreasing CaO and MnO, and increasing FeO toward garnet rims. No inversion of trends in the rims is evident. MgO concentrations are too low to be of significance (R. Berry, pers. comm., 2000).

Biotite is enriched in Cl in comparison to the other ore samples (Table 5.8). No zonation was detected suggesting compositions were homogenised during metamorphism.

5.4 GARNETS

5.4.1 Compositional populations

Richmond et al. (1996a) and Williams et al. (1996) subdivided garnets from sillimanite-garnet schists and garnetiferous quartzites in the hanging wall of the Southern Zone into two compositional groups based on variations in the molecular proportion of total Ca-garnet (andradite + grossularite); i) type A with total Ca-garnet values of <12 mol%, and ii) type B garnets with total Ca-garnet values of >22 mol%. Almandine is the dominant molecular component in both populations with spessartine typically ranging between 3-30 mol%. Type A Ca-poor garnets are most common in the proximal garnetiferous alteration halo (sillimanite-garnet schists and garnetiferous quartzites), and garnet alteration zones along pegmatite contacts and leucocratic segregations (Fig. 5.7). The compositions are unlike typical garnets in metapelites that have compositions similar to garnets in the migmatitic gneiss, i.e. spessartine >~5 mol% and total Ca-garnet <~3 mol% (Richmond et al., 1996a).

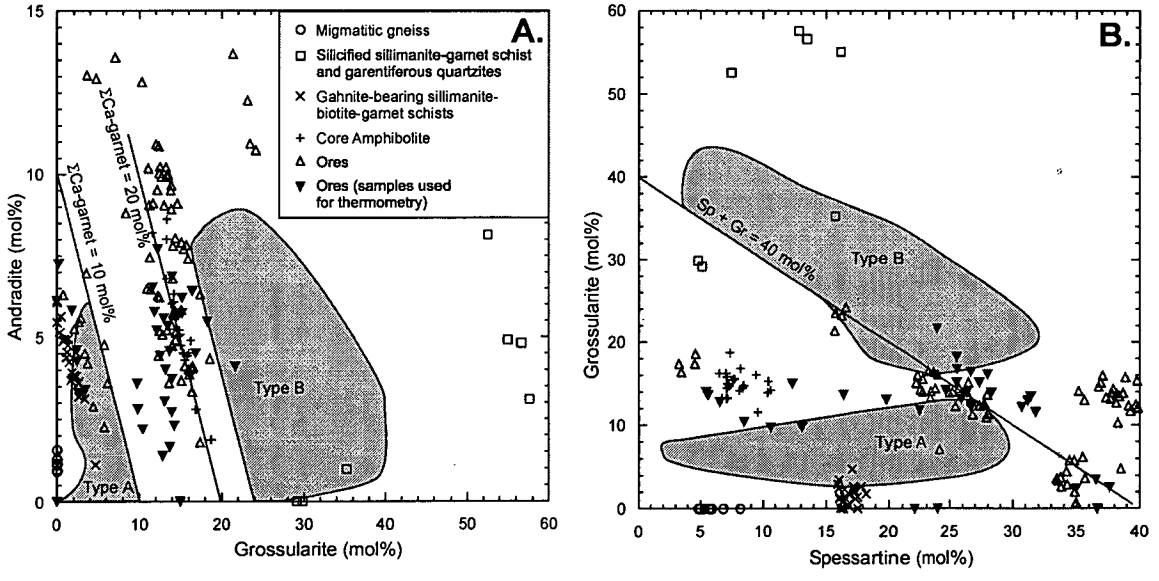

Figure 5.7 Binary plots of garnet compositions for samples used in the thermometric calculations based on the proposed discrimination criteria of Richmond et al. (1996a) and Williams et al. (1996). Refer Appendix 1 for microprobe analyses. **A.** andradite versus grossularite mol% fractions. **B.** Grossularite versus spessartine mol% fractions. Type A and B fields refer to the compositional populations defined by Richmond et al. (1996a) and Williams et al. (1996).

Type B Ca-rich garnets are found in garnet-quartz altered sillimanite-garnet schists, garnetiferous quartzites and pegmatites adjacent to hedenbergite-bearing Fe-Mn silicate units in the hanging wall of the Southern Zone. Type B garnets are believed to be related to post-peak metamorphic metasomatism due to their occurrence as overgrowths on type A garnets in localised areas where quartz veins overprint sillimanite-garnet schists and garnetiferous quartzites adjacent to a hedenbergite-bearing Fe-Mn silicate unit in the Southern Zone (Richmond et al., 1996a; Williams et al., 1996). They are believed to be the sole garnet-type found in hedenbergite-bearing Fe-Mn silicate units within this region of the deposit. These textural relationships and association with quartz veins and hedenbergite are consistent with Stage IIa of the deposit paragenesis (section 4.9.1.2).

Data from this study indicate that peak metamorphic garnet compositions are more variable and the distinction between type A and B populations tend to be blurred by intermediate compositions (Fig. 5.7). In particular, the greatest variations in garnet compositions occur in mineralised rocks. For example, silicified and mineralised schists and quartzites spatially associated with siliceous Zn ore are the most grossularite-rich of all samples, with compositions ranging from calcic almandine to ferroan grossularite (Figs. 5.2 and 5.7). In contrast, garnets in graphitic ore are characterised by variations between spessartine and almandine end-members, i.e. Fe and Mn rather than Fe and Ca (section 4.7). Garnets in host rocks display more homogenous compositions (Figs. 5.2 and 5.7). In fact, many of the garnets analysed do not fall into the type A and B compositional fields of Richmond et al. (1996a) and Williams et al. (1996; Fig. 5.2). This is probably due to the avoidance of rocks that have been affected by Stage IIa metasomatism and the lack of garnet analyses from sillimanite-garnet schists in this study.

5.4.2 Zonation in porphyroblasts

Compositional zoning in garnet represents a record of the chemical evolution of garnet growth and therefore the chemical reaction history of the particular rock in which the garnet occurs (Spear, 1993). This in turn, is governed by the P-T path of metamorphism. Zonation is produced by changes in the composition of material supplied to the garnet rim as the garnet grows with time (op. cit.). The resultant compositional profile is faithfully preserved so long as diffusion within the garnet is sufficiently slow.

Zoning is caused by two dominant mechanisms (Spear, 1993): i) growth zoning, and; ii) diffusion zoning. Growth zoning involves the addition of new, compositionally different garnet to the rims of the growing garnet crystal. Assuming no other exotic components are added to or subtracted from the rock (e.g. via metasomatism), the major causes of variations in composition of material added to the garnet rims are:

- changes in the external P-T conditions that drive reactions in the matrix,
- changes in the mineral assemblage during garnet growth or,
- equilibrium fractional crystallisation.

The latter involves fractionation of a particular element (or elements) into the core of the garnet, thereby causing a change in the bulk composition of the reactant phases in the matrix. As a result, garnet rim equilibrium compositions will vary over P-T-t space resulting in primary growth zoning (Spear, 1993). In nature, equilibrium fractional crystallisation results in smooth, typically monotonic profiles that can be emulated reliably using a Rayleigh fractionation model (Hollister, 1966; Loomis, 1983; Spear, 1993). Perturbations in profiles are interpreted to signify the initiation and/or culmination of certain garnet forming and consuming reactions during metamorphism; they essentially reflect step functions in garnet growth zoning (e.g. Fig. 17-12 on page 596 of Spear, 1993).

Diffusion zoning involves the modification of pre-existing growth zoning by volume diffusion (Spear, 1993). Like growth zoning, it is also caused by variations in the external P-T conditions, but does not involve growth nor consumption of the garnet grain (op. cit.). The rate of diffusion is strongly temperature dependent, increasing exponentially with increasing metamorphic grade. The process is therefore much more efficient in high grade rocks and of lesser importance in low grade rocks (op. cit.). Diffusion causes homogenisation of garnet compositions, and is manifested by flattened compositional profiles in the interior of garnets. Generally speaking, there is a change in the mechanism of garnet zoning from growth dominated to diffusion dominated with increasing metamorphic grade (Loomis, 1983; Spear, 1993). However, in reality garnet zonation is influenced by both processes. Hence, it is likely that the nature of compositional profiles in garnets from Cannington largely reflect prograde metamorphic growth zoning in contrast to diffusion zoning; the latter appears to be less significant.

Growth zoning caused by fractional crystallisation in almandine garnets in metapelites is typically characterised by an antipathetic relationship between Fe-Mg and Mn zonation during prograde metamorphism, with cores enriched in Mn and rims enriched in Fe-Mg (Turner, 1981; Yardley, 1989; Deer et al., 1992; Spear, 1993). This relationship is due to the high distribution coefficient (K_D) of Mn for garnet in comparison to other Fe-Mg-Mn-bearing silicates in the metapelite assemblage, insomuch as most of the Mn in the rock will be sequestered into early formed garnet. This causes the Mn content of the reactant phases in the matrix to decrease, resulting in progressively lower Mn contents in garnet as growth continues. Slow diffusion kinetics in garnet promotes the preservation of the Mn-enriched core and as growth continues the garnet progressively becomes more enriched in Fe and Mg (op. cit.). Typically, the Fe/Fe+Mg ratio of the garnet increases.

In instances, Ca may have a "bell-shaped" profile similar to Mn, consistent with the consumption of plagioclase that becomes more albitic as garnet growth continues during isobaric heating (Spear, 1993). In more mafic rocks such as metabasalts, compositional trends in plagioclase are the reverse due to the presence of other Ca-bearing reactant phases in the matrix such as amphibole and epidote, i.e. plagioclase compositions become more

calcic during isobaric heating. The appearance of clinopyroxene at higher grades (i.e. transitional granulite facies) involves hornblende and plagioclase consumption, the net effect of which results in more albitic plagioclase compositions. In either case, Ca can be sequestered by garnet at an early stage in the metamorphic history of the rock.

Similar zonation profiles involving Mn and Ca exist in garnets from amphibolite and pelitic gneiss at Cannington, although Mg remains relatively constant in the latter. The zonation trends in garnets from these samples therefore reflect typical growth zoning profiles during prograde metamorphism. Mn-enriched cores suggest preservation of early growth histories. However, an increase in the Fe/Fe+Mg ratio in garnet rims indicates garnet consumption during late retrograde mineral growth via removal of Mg from garnet rims by other reactant phases in the rock matrix such as biotite and/or hornblende (Frost and Tracey, 1991). Corresponding Mn enrichment in the rims supports this. A high Ca core is consistent with plagioclase consumption during prograde metamorphism, i.e. plagioclase becomes more albitic. Whereas, high Ca rims indicate late stage Ca exchange with plagioclase during retrogression. Either an isothermal pressure increase, or isobaric cooling can cause the latter, assuming that garnet rims are in equilibrium with the plagioclase (Spear, 1993). It is more likely that Ca enrichment in rims represents isobaric cooling considering the interpreted isobaric cooling path for metamorphism at Cannington (section 3.4; Giles, 2000). This is especially applicable to the amphibolite sample where plagioclase comprises ~20 modal% of the rock. In the case of the pelitic gneiss, plagioclase is the only Ca-bearing phase besides the garnet itself.

Zonation profiles in garnets from gahnite-bearing schist differ from garnet in the pelitic gneiss with regard to the lack of a Mn-enriched core, and slightly Fe, Mg and Ca depleted rims. However, Fe depletion and Mn enrichment in the rims are the most significant inversions from garnet core trends. Mn enrichment in the rim is consistent with garnet consumption during late retrograde mineral growth, and this is consistent with minor Fe (and lesser Mg) depletion in the rim. However, the lack of a Ca enriched rim suggests that Ca exchange did not occur possibly because of the lack of a Ca-bearing matrix phase that would facilitate Ca exchange. A Mn enriched core is not evident suggesting that the early prograde history has not been preserved in the garnet potentially due to the homogenising effects of diffusion zoning. The small size of the garnets (≤250μm in diameter) suggests that diffusive processes would have had a far greater effect on zoning compared to larger sized porphyroblasts (2-5mm in diameter) in the amphibolite and pelitic gneiss (cf. Loomis, 1983; Spear, 1993).

In contrast, zonation profiles in garnets from the ore samples display variable trends in Mn and Ca. Increasing trends in Fe and Mg from core to rim is consistent with normal zonation trends during prograde metamorphism. Mn enriched cores suggests that early prograde histories have been preserved in the garnets. The lack of Mn enrichment in garnet rims for samples NZ040-8 and NZ039-2 (Fig. 5.6b and f respectively) suggests that garnet was not consumed, and the small variation in FeO content in the rims suggests negligible compositional

readjustment during late mineral growth for sample NZ040-8. Incorporation of biotite along garnet margins in sample NZ040-8 is also consistent with garnet growth, rather than consumption. Ca enrichment in the rim of NZ040-8 indicates that local exchange of Ca occurred with matrix phases during initial cooling and was related to either: i) the introduction of a new Ca-bearing phase, or; ii) the consumption of a pre-existing Ca-bearing phase. Considering that Ca-bearing matrix phases are absent in the sample, the latter option is more appealing, although evidence for the mineral consumed is lacking. Overall, there is little compositional evidence for consumption of garnet during cooling.

The only ore sample that shows some evidence for minor retrograde readjustment is NZ042-4. Mn enrichment and Fe depletion in garnet rims indicates garnet consumption during late retrograde mineral growth, involving the exchange of Fe from garnet rims into other reactant phases in the matrix such as biotite and/or grunerite.

5.5 THERMOBAROMETRIC CALCULATIONS

5.5.1 Thermobarometers

The choice of applicable thermobarometers is not only based upon the mineral assemblages comprising a rock, but also the compositional range for which the thermobarometers have been calibrated. This is particularly relevant at Cannington where many of the rocks are anomalous in Mn and F. All samples used in the study contain biotite and garnet in their mineral assemblages, thus allowing the application of the well established garnet-biotite geothermometer of Ferry and Spear (1978). As a side issue, this commonality augments the validity of comparisons made between various rock types, i.e. internal consistency to the thermometric estimates. The Ferry and Spear (1978) geothermometer is based on ideal mixing between Fe-Mg, and it is clear from the analytical data that garnets at Cannington also contain significant Mn and Ca, so much so that garnet compositions do not fall within the compositional range of the Ferry and Spear (1978) calibration.

The application of the Ferry and Spear (1978) calibration to Mn-Ca bearing rocks commonly results in underestimation of temperature by ~50°C (c.f. Hodges and Spear, 1982; Ganguly and Saxena, 1984; Berman, 1990; Williams and Grambling, 1990; Kleeman and Reinhardt, 1994; Holdaway et al., 1997) and in instances, overestimation by ~50°C (this study). The thermometer becomes increasingly erratic at upper amphibolite and granulite conditions because of Ca in garnet (Essene, 1982, 1989) and nonideal mixing behaviour (Berman, 1990; Berman and Kozoil, 1991). A number of calibrations for Mn-Ca and nonideal mixing behaviour in garnet have been developed (e.g. Williams and Grambling, 1990). These calibrations essentially expand the calibration to cover a broader range of garnet compositions and higher grade metamorphic conditions.

The Williams and Grambling (1990) calibration also caters for nonideality and the oxidation state of biotite (i.e. $Fe^{3+}/Fe^{3+} + Fe^{2+}$). In particular, the oxidation state of biotite affects the

calibration and for accurate determinations should be accounted for (Williams and Grambling, 1990; Holdaway et al., 1997). Another consideration is the F and Cl content of biotite in the samples from Cannington, especially the ores (Table 5.8). Zhu and Sverjensky (1992) modelled the effects of F and Cl content in biotite on the garnet-biotite geothermometer of Ferry and Spear (1978). F in biotite stabilises the Mg-component (Munoz, 1984; Perchuk and Aranovich, 1984; Zhu and Sverjensky, 1991), thereby causing temperature to be underestimated by conventional garnet-biotite geothermometry if ignored (Zhu and Sverjensky, 1992). For example, 0.3 wt% F in biotite will cause an increase of ~25°C in estimated temperature (op. cit.). The effects of Cl are the opposite, although less significant by a factor of ~2 (op. cit.). For example, 2 wt% Cl in biotite will cause a decrease of ~50°C in estimated temperature. A compounding factor is the somewhat erratic behaviour of the Ferry and Spear (1978) calibration at upper amphibolite to granulite facies conditions due to increasing amounts of F, Cl, Ti and Al^{VI} in biotite (op. cit.; Essene, 1982, 1989; Valley et al., 1990). These effects have been accounted for in the calibration of Zhu and Sverjensky (1992) who recommend its usage in high grade metamorphic rocks. The Ferry and Spear (1978) garnet-biotite geothermometer, with corrections for Mn and Ca in garnet (Williams and Grambling's (1990) model 3), and F and Cl in biotite (Zhu and Sverjensky, 1992), was used in this study.

Other calibrations for the garnet-biotite geothermometer were also tried to verify the results of the latter calculations. These included the models of Hodges and Spear (1982), Berman (1990) and Holdaway et al. (1997). The hornblende-plagioclase geothermometer (Holland and Blundy, 1994) was also used as an independent check on garnet-biotite geothermometry in the Core Amphibolite sample. The composition of hornblende in the amphibolite (ferro-pargasite) falls within the compositional range for the calibration. Both the edenite-tremolite and edenite-richterite models were applied to hornblende-plagioclase pairs.

Garnet, hornblende and plagioclase compositions for the amphibolite fall within the compositional limits of the garnet-hornblende-plagioclase-quartz geobarometer. Specifically, the pargasite Fe-models I and II (Kohn and Spear, 1989) were used in the study. Barometric calculations were carried out on the amphibolite only.

P-T estimates for peak metamorphism were calculated using the Geothermobarometry program (version 2.1) of Spear and Kohn (1999). A spreadsheet was developed to incorporate the compositional corrections of Williams and Grambling (1990) and Zhu and Sverjensky (1992) into the calibration of the Ferry and Spear (1978) garnet-biotite geothermometer (R. Berry, pers. comm., 2000).

5.5.2 Estimated peak metamorphic conditions (M_1)

Minimum criteria for the resolution of P-T-t paths determined from zoned garnets have been outlined by Frost and Tracy (1991) and include:

- Knowledge of the equilibrium assemblage or assemblages present during the whole period of garnet growth.
- Measured constraints on the compositional changes in other phases that have participated in garnet producing reactions, especially biotite and plagioclase.
- Any post-growth modification of the original zoning in garnet via diffusive processes needs to be recognised and understood.
- Estimated P-T-t paths must be supported by textural and structural evidence.

The temperature range over which metamorphism spanned can be estimated if the composition of biotite is known at all stages of garnet growth. Biotite inclusions in garnet are rare in the samples from Cannington and only one example has been microprobed. However, in samples that contain a significantly higher proportion of biotite than garnet, biotite compositions can be approximated. In a given sample, if biotite clearly predominates as the major Fe-Mg bearing phase then any changes in P-T conditions will have an insignificant effect on the Fe-Mg content of the biotite in comparison to changes in Fe-Mg during garnet growth assuming the system remains closed throughout metamorphism, i.e. the composition of biotite is buffered by its high abundance and lack of other Fe-Mg bearing phases. This assumption is reasonable for peak and post-peak metamorphism in metapelites where biotite is the major Fe-Mg bearing phase, but is unreasonable for rocks that contain an abundance of hornblende such as the Core Amphibolite, and ore samples that contain greater proportions of knebelite, grunerite, hornblende and garnet in comparison to biotite.

Plagioclase compositions are likely to have varied throughout metamorphism as well (section 5.4.2; Spear, 1993). Generally, the Ca content of garnet increases with pressure and as a result there is a corresponding decrease in the Ca content in plagioclase (Frost and Tracy, 1991; Spear, 1993). The situation is reversed during isobaric heating, i.e. Ca from garnet is partitioned into plagioclase. Overall, whether plagioclase becomes more calcic or sodic depends on the slope in P-T space of the heating (and cooling) path in addition to the presence of other Ca-bearing phases such as epidote and amphiboles (op. cit.). Isobaric cooling results in more albitic compositions for plagioclase and increasing Ca content in garnet.

As previously mentioned the slight increase in Ca content in garnet rims for the amphibolite sample from Cannington is consistent with isobaric cooling. This implies that plagioclase compositions in the Core Amphibolite were slightly more calcic prior to cooling. Retracing the prograde path of the garnet suggests that plagioclase was more albitic at lower grade. Assuming an average plagioclase composition for all stages of metamorphic growth can lead to large errors in pressure estimates except for the final stages of garnet growth assuming

equilibrium. For example, application of the garnet-plagioclase-sillimanite-quartz (Kozoil, 1989) and the garnet-biotite-plagioclase-quartz (Hoisch, 1990) geobarometers results in pressure overestimates. An artificial upper limit for P-T can be calculated assuming a composition of ~An_{100}. However, the opposite effect occurs using the garnet-hornblende-plagioclase-quartz geobarometer (Kohn and Spear, 1989) and the hornblende-plagioclase geothermometer (Holland and Blundy, 1994), insomuch as arbitrarily adjusting plagioclase to more calcic, presumably peak metamorphic compositions, results in overestimation of P-T. For example, pressure estimates of 9-10kbars at 700°C, and temperature estimates of >1000° C at 5kbars were calculated using a composition of An_{98} for the amphibolite sample.

In summary, compositional variations in matrix phases during garnet growth are poorly constrained for the amphibolite sample because no inclusion relics exist in the garnet. Thermobarometric estimates must be regarded within these limitations. Implicitly, estimates using garnet rim compositions will provide an accurate estimation of conditions during the final stages of garnet growth, whereas garnet core compositions will yield less accurate P-T-time estimations. However, it is reasonable to assume that biotite, hornblende, plagioclase and quartz in the amphibolite, and biotite in the remaining samples used in the study, were stable phases throughout much of garnet growth even though compositional variations remain unknown.

Due to the absence of zonation in plagioclase, hornblende and biotite, average compositions for these minerals have been assumed. Temporal relationships between garnet growth and deformation, and textural relationships between phases have been outlined in section 5.3. Hence, the criteria of Frost and Tracy (1991) for the determination of P-T-t paths involving zoned garnets are fulfilled within the limitations of the data.

Figure 5.8 illustrates estimated peak metamorphic conditions for the Core Amphibolite, i.e. the intersection of K_D equation lines (K_{eq}) for the thermobarometers. Red lines represent estimates using the garnet-biotite geothermometer with calibrations for Mn-Ca-F-Cl, and black lines, the original Ferry and Spear (1978) calibration. Results of the thermobarometric calculations indicate that peak metamorphic conditions ranged between 730–770°C and 5.0–6.4kbars (Fig. 5.8, Table 5.9), with estimates from garnet rims indicating 735–765°C and 5.7–6.3kbars (Table 5.10) using the garnet-biotite geothermometer with corrections for Mn-Ca-F-Cl and the garnet-hornblende-plagioclase-quartz geobarometer. Similar temperature estimates were calculated using the hornblende-plagioclase geothermometer (Holland and Blundy, 1994; Table 5.9, Fig. 5.9d). These estimates are ~50-80°C higher than the uncorrected Ferry and Spear (1978) garnet-biotite geothermometer (Fig. 5.8).

Application of various alternative garnet-biotite corrections (e.g. Hodges and Spear, 1982; Berman, 1990; Holdaway et al., 1997) to garnet in the amphibolite sample suggests that temperatures may have approached granulite facies conditions, in the order of >800°C (Fig. 5.9a, b and c). However, mineral assemblages in the amphibolite are inconsistent with

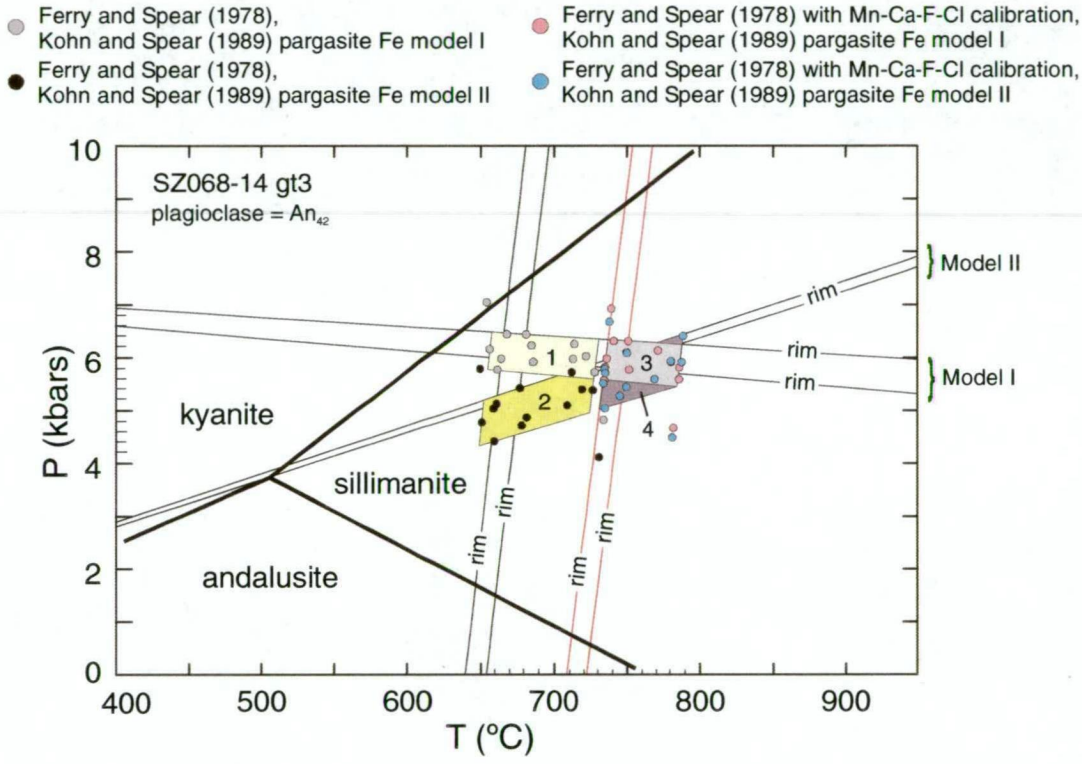

Figure 5.8 P-T diagram illustrating the range in metamorphic conditions determined from a garnet porphyroblast in the Core Amphibolite using garnet-biotite and garnet-hornblende-plagioclase-quartz thermobarometry. Ranges in P-T are due to compositional variations in garnet porphyroblasts. Fields: 1–garnet-biotite geothermometer (Ferry and Spear, 1978) and garnet-hornblende-plagioclase-quartz pargasite Fe model I geobarometer (Kohn and Spear, 1989); 2–as for 1 but using the garnet-hornblende-plagioclase-quartz pargasite Fe model II geobarometer; 3–garnet-biotite geothermometer with calibrations for Mn-Ca in garnet (Williams and Grambling, 1990) and F-Cl in biotite (Zhu and Sverjensky, 1992; red K_{eq} lines), and the pargasite Fe model I geobarometer; 4–as for 3 but using the pargasite Fe model II geobarometer. Temperatures calculated using the Mn-Ca-F-Cl calibrations are ~50°C higher than the Ferry and Spear (1978) model. Estimates from garnet rims are labelled "rim".

Table 5.9 Summary of estimated ranges in peak metamorphic conditions determined using thermobarometric calculations on a zoned garnet in the Core Amphibolite. Garnet-biotite geothermometry (Ferry and Spear, 1978) without calibrations for Mn-Ca in garnet and F-Cl in biotite are included for comparison only.

Geothermometer	Temperature (°C) Garnet 3	Geobarometer	Pressure (kbars) Garnet 3
gt-bt	660 - 730	gt-plag-hb-qz (pargasite, Fe model I)	5.7 - 6.2
	650 - 725	gt-plag-hb-qz (pargasite, Fe model II)	4.4 - 5.5
gt-bt (Mn-Ca-F-Cl)	735 - 785	gt-plag-hb-qz (pargasite, Fe model I)	5.6 - 6.3
	735 - 785	gt-plag-hb-qz (pargasite, Fe model II)	5.0 - 6.1
hb-plag (edenite-richterite)	735 - 740	gt-plag-hb-qz (pargasite, Fe model I)	5.5 - 6.3
	730 - 740	gt-plag-hb-qz (pargasite, Fe model II)	5.0 - 6.0
hb-plag (edenite-tremolite)	760 - 765	gt-plag-hb-qz (pargasite, Fe model I)	5.5 - 6.3
	760 - 765	gt-plag-hb-qz (pargasite, Fe model II)	5.2 - 6.2
Range	*730 - 785*		*5.0 - 6.3*

Abbreviations: bt—biotite, gt—garnet, hb—hornblende, plag—plagioclase.

Table 5.10 Summary of estimated ranges in peak metamorphic conditions determined using thermobarometric calculations on garnet rims in the Core Amphibolite. The two estimations for represent opposing rims respectively.

Geothermometer	Temperature (°C) Garnet 3 rims	Geobarometer	Pressure (Kbars) Garnet 3 rims
gt-bt (Mn, F, Cl)	735 / 750	gt-plag-hb-qz (pargasite, Fe model I)	5.8 / 6.3
	735 / 750	gt-plag-hb-qz (pargasite, Fe model II)	5.8 / 6.1

Abbreviations: bt—biotite, gt—garnet, hb—hornblende, plag—plagioclase.

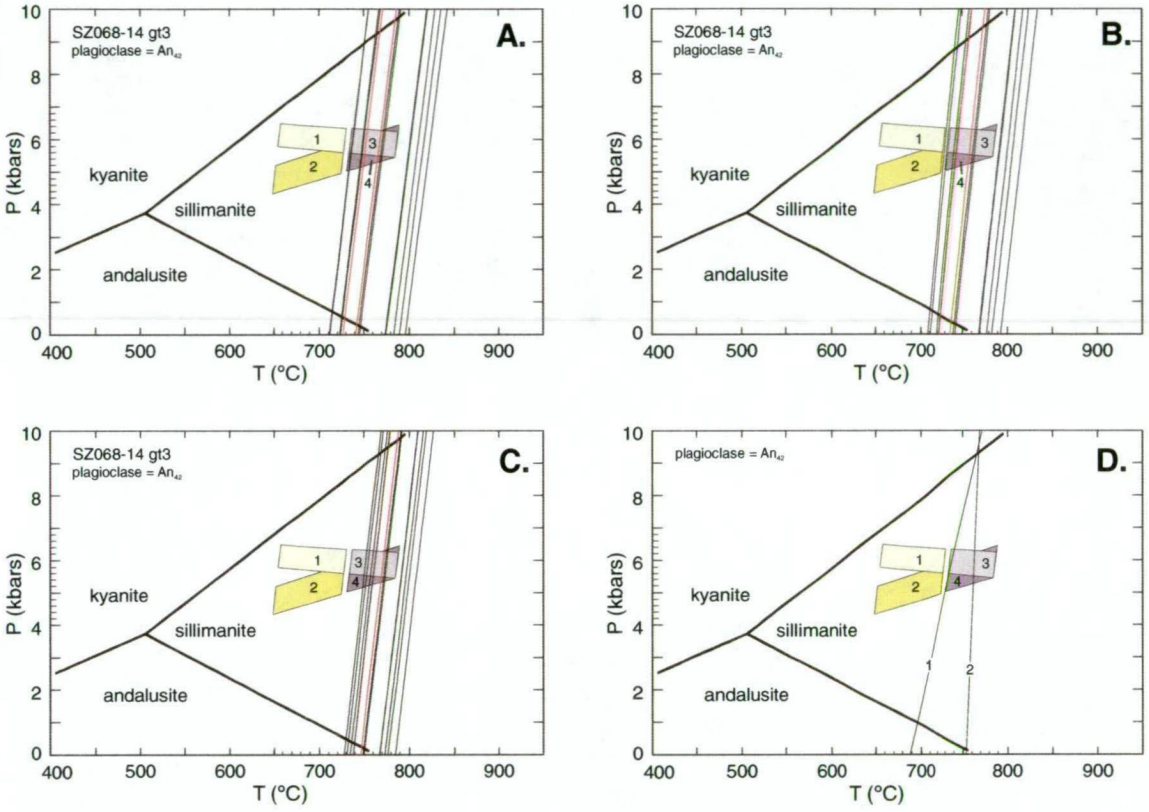

Figure 5.9 P-T diagrams comparing metamorphic conditions determined using the Ferry and Spear (1978) garnet-biotite geothermometer (fields 1 and 2) and additional corrections for Mn-Ca-F-Cl (fields 3 and 4) with alternative garnet-biotite calibrations for garnet in the Core Amphibolite. Hornblende-plagioclase thermometric determinations are also included for comparison. Red lines indicate temperatures determined from opposing garnet rims in the microprobe traverse. **A.** Ferry and Spear (1978) garnet-biotite geothermometer with additional corrections of Berman (1990). **B.** Hodges and Spear (1982) garnet-biotite geothermometer. **C.** Holdaway et al. (1997) garnet-biotite geothermometer. **D.** Holland and Blundy (1994) hornblende-plagioclase geothermometer using the edenite-richterite calibration (line 1) and the edenite-tremolite calibration (line 2). Fields 1 to 4 are the same as those in Figure 5.8. Temperatures determined from the alternative garnet-biotite geothermometers are similar to those determined using the Ferry and Spear (1978) model with corrections for Mn-Ca-F-Cl (Williams and Grambling, 1990; Zhu and Sverjensky, 1992). Some compositions plot at higher temperatures (>800°C) approaching granulite facies conditions. However, mineral assemblages are inconsistent with such high grade metamorphism.

Table 5.11 Summary of temperature estimates calculated at 6kbars for various host rocks and banded ores using the garnet-biotite geothermometer (Ferry and Spear, 1978) with corrections for Mn-Ca-F-Cl (Williams and Grambling, 1990; Zhu and Sverjensky, 1992).

Host rocks	Range (°C)
Core Amphibolite (SZ068-14)	735 - 790
Pelitic gneiss (SZU51-1)	600 - 780
Gahnite-bearing schist (NZ160-33)	640 - 750
Banded ores	
quartz-biotite-garnet-graphite (NZ040-8)	550 - 760
quartz-biotite-garnet-hornblende-apatite-graphite (NZ042-4)	450 - 660
quartz-garnet-knebelite-grunerite-biotite (NZ039-2)	570 - 780

granulite facies conditions except for rare occurrences of clinopyroxene that indicate transitional granulite facies (section 3.4). It is therefore likely that these higher temperatures are overestimates. Rim temperatures are comparable to the results obtained from the garnet-biotite Mn-Ca-F-Cl calculations (Fig 5.9a, b and c).

Temperature profiles in garnet porphyroblasts calculated at 6kbars using the garnet-biotite geothermometer with corrections for Mn-Ca-F-Cl are illustrated in Figure 5.10 and ranges summarised in Table 5.11. In general, maximum temperature estimates for peak metamorphism from the pelitic gneiss, gahnite-bearing schist and the banded ores (~745-780°C) are very similar to that of the amphibolite (~750–790°C) except for the banded quartz-biotite-garnet-hornblende-apatite-graphite banded ore (~665°C). However, ranges in temperature estimates are much larger (up to ~280°C) than those of the amphibolite. Because matrix biotite compositions were used in the calculations, rim temperatures are the most reliable estimates, assuming biotite and garnet are in equilibrium.

Garnet from the amphibolite displays an increase in temperature from the core, followed by a decrease on the rims consistent with the interpreted isobaric cooling path (Fig. 5.10a). As previously mentioned, Mn enrichment in the core of the garnet is consistent with the expected growth zoning profile developed during prograde metamorphism. This suggests that the primary growth zoning profile has been preserved. If this is correct, then the trend of increasing temperature from the core toward the rim is a record of garnet growth during prograde metamorphism. However, the accuracy of the temperature estimates decreases from the rim to the core as the composition of biotite at the time early garnet growth (i.e. the core) is unknown.

Temperature profiles in garnets from the pelitic gneiss (Fig. 5.10b) and gahnite-bearing schist (Fig. 5.10c) display convex, bell-shaped paths in contrast to the concave path for garnet in the amphibolite. The correlation between Mn enrichment and decreasing temperature along garnet rims suggests minor garnet consumption during interpreted isobaric cooling. Flattened temperature profiles from the core toward the rim may provide circumstantial evidence for homogenisation by subsequent diffusion zoning. However, such an interpretation remains speculative considering the preservation of Mn and Ca enriched cores in the garnet from the pelitic gneiss. Given these ambiguities, it is unlikely that the temperature profiles are an

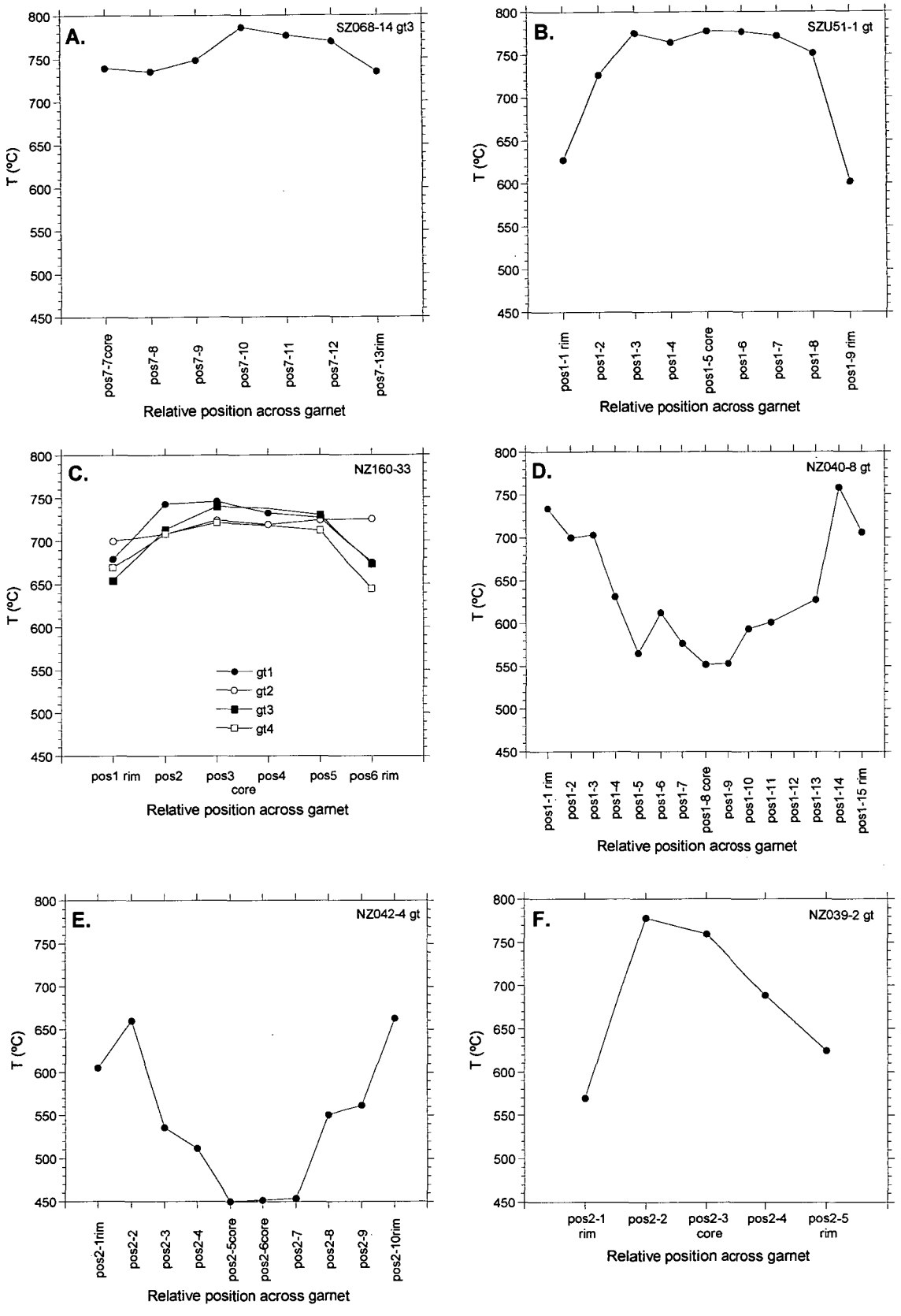

Figure 5.10 Temperature variations calculated at 6kbars for garnet porphyroblasts from various host rocks and banded ores using the garnet-biotite geothermometer (Ferry and Spear, 1978) with calibrations for Mn-Ca in garnet (Williams and Grambling, 1990), and F-Cl in biotite (Zhu and Sverjensky, 1992). **A.** Core Amphibolite. **B.** pelitic gneiss. **C.** gahnite-bearing schist. **D.** banded quartz-biotite-garnet-graphite ore. **E.** banded quartz-biotite-garnet-hornblende-apatite-graphite ore. **F.** banded quartz-garnet-knebelite-grunerite-biotite ore. Sample numbers appear in the top right of the graphs.

accurate reflection of the prograde path of metamorphism, i.e. garnets in the pelitic gneiss and gahnite-bearing schist preserve peak metamorphic and late stage cooling temperatures only.

The ores display concave temperature profiles similar to the garnet in the amphibolite sample except for the banded quartz-garnet-knebelite-grunerite-biotite ore. Differences of ~40-50°C between cooling temperatures and interpreted peak metamorphic temperatures (i.e. those slightly inside the rim) are also similar, except for the banded quartz-garnet-knebelite-grunerite-biotite ore that displays a discrepancy of ~200°C. Mn enriched cores in all the ore samples suggest that early prograde growth zoning has been preserved in the garnets. This is supported by the convex shape of the temperature profiles. Hence, the early prograde metamorphic path appears to have been preserved in the garnets. The presence of relic possible chlorotoid pseudomorphs that form bow-tie textures in the cores of some sector-twinned garnets, provide additional textural evidence that the garnets grew during prograde metamorphism (section 4.9.1.1).

Since in many cases peak temperatures are associated with garnet rims, there is little evidence for significant readjustment during cooling. This suggests that the ores have

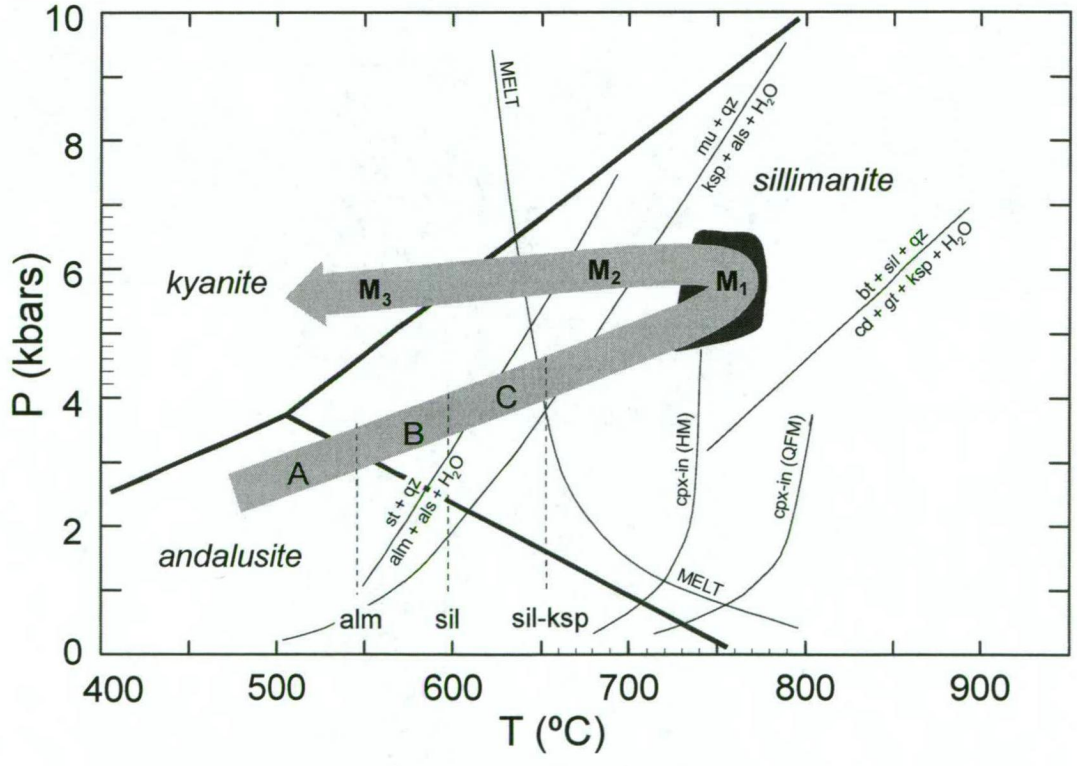

Figure 5.11 P-T diagram summarising the metamorphic history (anti-clockwise P-T-t path) for Cannington. The black field represents the range in peak metamorphic conditions determined from the thermobarometric calculations. The regional metamorphic zones of Jaques et al. (1982) from east (A) to west (C) across Selwyn Range district are duplicated on the diagram. Isograds bounding these zones (dashed lines) are; A–almandine, B–sillimanite and, C–sillimanite-K-feldspar. Aluminosilicate phase boundaries are after Holdaway (1971). Minimum melting point curve (wet solidus) for common granite is after Turner (1981). Cpx-in (QFM) and cpx-in (HM) curves for mafic igneous rock determined for fO_2 conditions defined by the quartz-fayalite-magnetite (QFM) and hematite-magnetite (HM) buffers respectively are after Spear (1981). Muscovite+quartz↔K-feldspar+aluminosilicate+H_2O curve is after Helgeson et al. (1978). Staurolite+quartz↔almandine+aluminosilicate+H_2O curve is after Pigage and Greenwood (1982). Biotite+sillimanite+quartz↔cordierite+garnet+K-feldspar+H_2O curve is after Holdaway and Lee (1977). Abbreviations: alm–almandine, als–aluminosilicate, bt–biotite, cd–cordierite, cpx–clinopyroxene, gt–garnet, ksp–K-feldspar, mu–muscovite, qz–quartz, sil–sillimanite, st–staurolite.

undergone minimal post-peak metamorphic re-equilibration during the interpreted isobaric cooling path. Of particular significance is that growth zoning in the garnets and the thermobarometric estimates indicate that the ores have been subjected to the same peak metamorphic conditions recorded in the surrounding host rocks. The existence of sulphide inclusions within garnets (and other silicates) implies that sulphide minerals were present during all stages of the P-T-t history, and must have existed prior to garnet formation during early prograde metamorphism, M_1 (cf. section 4.9.1).

5.6 CONCLUSION

Calculated peak metamorphic conditions and the interpreted P-T-t path for Cannington are summarised in Figure 5.11. The black field in Figure 5.11 represents the range in peak metamorphic conditions determined from the thermobarometric calculations. All results plot below the K-feldspar-sillimanite univariant curve. The peak metamorphic temperatures determined in this study are ~50-80°C higher than those estimated by past workers (e.g. Jaques et al., 1982; Mark, 1993, Mark et al., 1998; Giles, 2000). Pressure estimates fall within the range proposed by Mark (1993) and Mark et al. (1998), but are ~2kbars higher than those calculated by Jaques et al. (1982).

The thermobarometric calculations indicate that graphitic ores were subjected to the same metamorphic event (M_1) that is recorded in the host rocks. The presence of spheroidal sulphide inclusions in peak metamorphic garnets indicates that sulphide mineralisation predates M_1 and early prograde metamorphism.

Chapter 6

Geochemistry of Altered Rocks and the Origin of Graphitic Ore: Mass Changes and Carbon Isotopes

6.1 INTRODUCTION

The Northern Zone of the Cannington deposit is dominated by facies comprising graphitic ore, which are interpreted to be the distal, weakly mineralised transitional components of well-mineralised ores in the Southern Zone. Delicate centimetre- to millimetre-scale mineral bands in graphitic ore are laterally continuous over tens of centimetres to metre scales and concordant with possible sedimentary layering in the enclosing garnetiferous rocks. The contact between the ores and the garnetiferous metasediments is also concordant to possible sedimentary layering. These basic observations, coupled with textural (Chapter 4) and thermobarometric (Chapter 5) evidence are consistent with premetamorphic replacement and synsedimentary genetic models.

Geochemical examination of the transitional, distal graphitic ores may provide insights into possible primary genetic aspects of ore formation that are likely to have been modified or destroyed by strong deformation and retrogression in olivine-pyroxenoid Pb-Ag and hedenbergite Zn ores in the Southern Zone. The evidence presented so far suggests that graphitic ores were possibly formed by either:

i) exhalation of hydrothermal fluid in a basin-floor environment and coeval accumulation of chemical and detrital sediment, and/or sub-surface replacement of detrital sediments; or

ii) replacement of detrital sediments at some stage after the deposition of the host sequence, but prior to deformation and metamorphism.

Previous geochemical studies on sulphide-bearing interbanded hedenbergite-garnet and garnet-quartz-apatite rocks at Cannington demonstrated that the ores contain an alkali-depleted pelitic component (Chapman, 1993; Chapman and Williams, 1998). Chapman and Williams (1998) argued that the geochemical evidence suggested the ores were possibly derived from a mixed detrital-chemical sedimentary protolith that may also have contained carbonate or calc-silicate rocks. Subsequent geochemical work on graphitic ore in the Northern Zone generally agreed with these earlier interpretations (e.g. Pringle, 1999).

Understanding the origin of ubiquitous minor graphite (up to 5 modal%; Chapter 4) in graphitic ore may help constrain genetic processes. For example graphite may have formed by: i) the interaction of reduced, CH_4-bearing hydrothermal fluid with pre-existing carbonate, or; ii) by metamorphism of biogenic material. Determination of $\delta^{13}C$ isotopic compositions of graphite will help reconcile carbon sources for graphite in the ores at Cannington, as well as clarify

possible genetic processes and associations.

The aims of this chapter are to:

- Determine mass changes associated with premetamorphic hydrothermal alteration of the metasedimentary host sequence, and construct an alteration index that can be used as a geochemical exploration tool.
- Identify geochemical components comprising graphitic ore and quantify their relative contributions using mass balance calculations.
- Quantify the geochemical changes associated with Stage IIa metasomatism of graphitic ore.
- Determine the $\delta^{13}C$ isotopic composition of graphite in graphitic ore to establish carbon sources.

In this chapter, sampling strategies and analytical procedures will be presented, followed by the determination of immobile elements and estimated protolith compositions of garnetiferous rocks and geochemical components comprising graphitic ore. This is followed by mass balance calculations and determination of hydrothermal rare-earth element (REE) signatures. The discussion section presents an alteration index specific to the Cannington deposit, as well as the origin of geochemical components in graphitic ore and genetic implications. The last major section of the chapter is the carbon isotope study.

6.2 METHODS: WHOLEROCK GEOCHEMISTRY

6.2.1 Samples

Representative drillcore samples of host rocks and ores were collected from Northern Zone drillholes, and within the immediate vicinity of the orebody. All samples were analysed for wholerock major, trace and rare-earth element concentrations (see below). Particulars of the sample set are summarised in Tables 6.1 and 6.2. Sample descriptions and locations can be found in Appendix 2.3.

Host rock samples included typical least altered migmatitic gneiss (n=4), amphibolite (from the Core Amphibolite; n=10), and garnetiferous rocks (n=10) from the interpreted metamorphosed proximal alteration halo (Table 6.1). Samples of garnetiferous rocks included:

- sillimanite-garnet schist (n=4);
- garnetiferous quartzite (n=1), and;
- gahnite-bearing sillimanite-biotite-garnet schist (n=5).

Very weak, incipient sericite alteration of feldspars is common to all samples, and is typically spatially associated with joints and fractures in the rocks. This type of alteration is a regionally extensive phenomenon and unfortunately is unavoidable when sampling. Based on mineral assemblages and recognised geochemical classifications of sedimentary rocks (e.g. Herron, 1988; Garcia et al., 1991, 1994), samples of gneiss were subdivided into psammite dominant

Table 6.1 Summary of host rock samples used in the geochemical study (refer Appendix 2.1 for XRF analytical detection limits, Appendix 2.2 for wholerock analytical data determined in this study and Appendix 2.3 for sample data).

Sample	Source of data	Number of samples	Method of analysis	Comments
Amphibolite	This study	10	XRF ICP-MS (REE)	Samples from the Core Amphibolite.
Quartzofeldspathic gneiss	This study	4	XRF IE-XRF ICP-MS (REE)	
	BHP Minerals	10	XRF ICP-MS (REE)	50% of samples affected by red-rock alteration* of variable intensity.
Sillimanite-garnet schist	This study	4	XR IE-XRF ICP-MS (REE)	
	Chapman (1993)	1	XRF	Not used in the mass balance calculations presented here. Analyses performed at James Cook University, Townsville.
Garnetiferous quartzite	This study	1	XRF ICP-MS (REE)	
	Chapman (1993)	2	XRF	Not used in the mass balance calculations presented here. Analyses performed at James Cook University, Townsville.
Gahnite-bearing sillimanite-garnet-biotite schist	This study	5	XRF IE-XRF ICP-MS (REE)	
	TOTAL	37		

* – regionally extensive albite alteration with hematitic dusting.
N.B. all analyses were performed at the Centre of Ore Deposit Research and School of Earth Sciences, University of Tasmania unless otherwise stated.

Table 6.2 Summary of ore samples used in the geochemical study (refer Appendix 2.1 for XRF analytical detection limits, Appendix 2.2 for wholerock analytical data determined in this study and Appendix 2.3 for sample data).

Ore type	Sample	Number of samples	Method of analysis
Graphitic (Pb-Zn-Ag)	Quartz-apatite facies	3	XRF IE-XRF ICP-MS
	Biotite-garnet facies	8	XRF IE-XRF ICP-MS
	Olivine facies	10	XRF IE-XRF ICP-MS
	Hedenbergite metasomatised banded olivine-pyroxenoid ore	1	XRF IE-XRF ICP-MS
Olivine-pyroxenoid (Pb-Ag)	Olivine-fluorite ore	3	XRF IE-XRF ICP-MS
Hedenbergite	Hedenbergite-garnet-quartz altered olivine facies	1	XRF IE-XRF ICP-MS
	TOTAL	25	

IE-XRF — ionic exchange XRF for determination of REE geochemistry.
ICP-MS — As, Bi, W, Rb, and U and Th (some samples) analysed by Analabs due to interference with Pb and Zn on XRF instrument.
N.B. all analyses were performed at the Centre of Ore Deposit Research and School of Earth Sciences, University of Tasmania unless otherwise stated.

($TiO_2/Zr<0.003$, ≥70 wt% SiO_2, <6 wt% total Fe_2O_3) and pelite dominant ($TiO_2/Zr>0.003$; ≤65 wt% SiO_2, >6 wt% total Fe_2O_3). None of the samples have intermediate compositions between 63-68 wt% SiO_2, making the distinction between psammitic and pelitic gneiss more apparent. This classification assisted in: i) ascertaining whether compositional variations could be attributed to primary sedimentary sorting processes and/or variable provenance, and; ii) establishing whether graphitic ore contains a compositionally unique detrital sedimentary component.

Typical representative samples of graphitic ore were collected mainly from the 5300mN section in the Northern Zone, and included all ore facies, viz. (Table 6.2):

- quartz-apatite facies (massive to banded quartz-apatite-graphite; n=3)
- biotite-garnet facies (banded quartz-apatite-graphite-almandine-biotite-amphibole; n=8), and;
- the olivine facies (interbanded knebelite-apatite-almandine-pyroxferroite, and quartz-apatite-graphite-almandine; n=10).

Detailed mineralogical and textural characteristics of the facies comprising graphitic ore are outlined in Chapter 4. However, it is important to reiterate that the ore facies are variably interbanded over centimetre to metre scales. An additional three samples of well mineralised olivine-pyroxenoid Pb-Ag ore were collected from the Northern Zone, and represent the extreme end-member hydrothermal composition in the ore sample set.

To avoid potential contamination by post-peak metamorphic hydrothermal alteration products, only least altered ore samples were used in the study, i.e. samples devoid of Stage IIa hedenbergite-garnet-quartz ± pyroxferroite, Stage IIb amphibole-ilvaite, Stage IIc pyrosmalite-magnetite and/or Stage III carbonate-chlorite alteration assemblages (see Chapter 4 for textural descriptions). Hence, ore samples chiefly comprised interpreted Stage I peak metamorphic assemblages. This approach enabled valid lithogeochemical comparisons between the host rocks and the ores, as well as provided a means of best estimating the primary premetamorphic bulk composition of the ores. To assess the effects of Stage IIa syn- to post-D_2 metasomatism, a well constrained 'altered-unaltered' sample pair was collected from a centimetre-scale hedenbergite-garnet-quartz alteration selvedge adjacent to a discordant hedenbergite vein within banded olivine facies ore. A description of the sample can be found in section 6.5.4.

Densities of all samples used in the subsequent mass balance studies were determined using the standard water-bath technique to measure rock volumes (Holtzclaw et al., 1984, p. 17).

6.2.2 Analytical procedures

Samples were crushed and pulverised in a chrome-steel mill and then made into fused glass beads and pressed powdered pellets in preparation for XRF analysis. Wholerock major and

trace element analyses were determined on a Phillips PW1480 X-ray fluorescence spectrometer by Mr. P. Robinson (Analyst) at the School of Earth Sciences, University of Tasmania. Detections limits for the instrument are listed in Appendix 2.1. Samples were not analysed for Cr due to contamination from the chrome-steel mill. Fe contamination was negligible because all samples contain >100ppm Fe (P. Robinson, pers. comm., 1997). Analytical results can be found in Appendix 2.2, and the average compositions of host rocks and ores presented in Table 6.3.

Loss on ignition (LOI) is intrinsic to the sample preparation stage prior to major element XRF analyses and must be quantified for accurate geochemical determinations. Volatiles that are lost on ignition include C, H, O, N and S. LOI values presented here include S, even though S was independently determined during analysis. LOI values were treated as a separate component of the samples in this study and therefore analyses have not been recalculated to 100% volatile free. This allows the volatile components to be included in the mass balance calculations. It is important to note that the LOI values are not a true measurement of the volatile content of the samples prior to metamorphism.

High Pb concentrations in the ore samples interfered with XRF determinations for As, Bi, Rb, Th and Y. High Zn concentrations interfered with W analyses. To overcome these problems, Y was determined in conjunction with the REE by ionic exchange XRF (see below), and As, Bi, Rb and W were determined by ICP-MS at Analabs (Perth, Western Australia) after being digested using an aqua regia, perchloric acid and hydrofluoric acid technique. U and Th analyses on selected samples were also determined by ICP-MS at Analabs.

REE concentrations were determined by XRF using a slightly modified version of the Na_2O_2 digestion and procedure (Robinson et al., 1986) prior to the commissioning of a new HP4500 inductively coupled plasma, quadrapole mass spectrometer (ICP-MS) at the School of Earth Sciences, University of Tasmania. This modification to the standard ionic exchange-XRF procedure was necessary due to incomplete digestion of the majority of graphitic ore samples. The undigested residue consisted of an unusual brown colloidal flocculent (in the acid liquor) that was possibly refractory carbonaceous matter from the ore samples. To dissolve this substance, a 6M HCl acid digestion technique was devised specifically for the ore samples, to replace the Na_2O_2 sinter step of the standard procedure. Subsequent REE analyses on 10 host rock samples were carried out by ICP-MS by Dr. Z. Yu (School of Earth Sciences, University of Tasmania).

A selection of graphitic ores were analysed for C, H and S on a Carlo Erba IA 1108 elemental analyser by Dr. G. Rowbottom of the Central Science Laboratory, University of Tasmania, using standard analytical procedures. This augmented the C isotope data on graphite. Analytical procedures for the carbon study can be found in section 6.8.1 and Appendix 3.

Table 6.3 Average wholerock major and trace element compositions of host rocks and ores used in the study.

	Host rocks				Graphitic ore facies			Olivine-pyroxenoid ore
(wt%)	Amphibolite	Gneiss	Sillimanite-garnet schist	Gahnite-bearing schist	Biotite-garnet	Quartz-apatite	Olivine	
SiO_2	48.41	66.33	63.94	57.76	45.23	77.26	38.09	18.47
TiO_2	1.16	0.61	0.62	0.84	0.28	0.12	0.09	0.04
Al_2O_3	14.34	15.15	17.42	21.92	6.83	1.65	1.88	0.21
Fe_2O_3	13.26	6.68	7.26	7.39	16.89	5.11	34.70	38.34
MnO	0.24	0.09	0.77	0.45	2.94	0.95	8.08	6.92
MgO	7.84	2.02	0.62	0.90	0.79	0.18	0.40	0.41
CaO	10.83	0.61	0.44	0.43	5.69	2.62	6.24	8.90
Na_2O	2.00	1.87	0.33	0.37	0.25	0.07	<0.1	<0.1
K_2O	0.71	3.53	6.33	5.56	1.14	0.30	0.15	<0.01
P_2O_5	0.08	0.10	0.15	0.17	3.40	1.40	3.20	0.39
ZnO	-	0.01	0.02	0.81	6.68	1.40	1.19	1.98
PbO	-	0.02	0.06	0.10	6.31	8.44	5.84	18.14
LOI (incl. S)	1.08	2.58	1.61	3.74	3.18	1.33	0.00	1.49
TOTAL	99.95	97.72	99.54	100.09	99.51	100.79	99.62	95.28
S	0.08	0.05	0.05	0.07	4.45	1.95	1.62	4.56
C	-	-	-	-	1.24	-	-	-
S	-	-	-	-	3.36	-	-	-
H	-	-	-	-	0.08	-	-	-
(ppm)								
Pb	112.44	34.00	738.80	723.00	-	-	-	-
Zn	228.22	62.36	128.80	3902.00	-	-	-	-
Cu	-	36.50	21.00	41.33	-	-	-	-
Ni	-	51.50	29.33	52.67	-	-	-	-
Sb	<2	<2	<2	8.82	118.98	124.77	159.74	409.00
Cd	<1	<2	<2	4.88	187.11	53.67	36.67	67.83
Ag	<2	<2	<2	<2	193.47	95.13	132.42	777.03
Nb	4.07	14.35	14.72	17.96	4.89	2.40	2.21	<1
Zr	64.78	209.19	188.54	152.58	67.03	30.43	25.38	13.97
Sr	129.00	75.58	41.34	36.86	45.99	20.73	39.69	8.00
Ba	51.89	544.47	569.56	459.48	144.49	71.10	30.17	9.00
Y	20.67	29.35	24.81	33.22	25.00	10.58	21.44	76.22
As	41.00	6.00	7.50	17.60	62.38	111.33	70.50	483.33
Bi	<2	0.70	0.77	0.43	0.75	16.10	0.93	9.53
W	<2	10.20	9.60	12.94	292.34	182.70	55.14	22.83
Rb	21.33	174.21	272.20	244.00	119.74	31.90	14.53	1.34
U	<1.5	7.25	2.95	7.55	8.77	4.39	2.78	-
Th	<1.5	16.55	18.80	21.40	4.82	3.09	1.60	-
La	5.30	43.88	48.01	54.51	29.49	49.12	44.38	108.75
Ce	11.06	82.52	85.42	97.18	46.78	71.81	64.67	163.63
Pr	1.71	10.53	10.72	11.95	5.50	7.65	7.31	17.56
Nd	8.91	39.84	42.39	44.54	20.97	27.91	27.84	65.96
Sm	2.75	7.14	8.10	7.60	4.19	5.26	6.15	14.60
Eu	1.07	1.05	1.63	1.57	5.51	15.18	14.85	15.22
Gd	3.56	5.26	5.70	5.45	3.86	4.05	5.47	15.65
Tb	0.67	0.87	0.88	1.03	0.65	0.58	0.87	2.70
Dy	3.85	4.56	4.36	5.39	3.43	2.00	3.18	12.32
Ho	0.82	1.01	0.57	0.83	-	-	-	-
Er	2.21	2.76	2.50	3.56	1.96	0.80	1.51	5.16
Tm	0.31	0.44	0.22	0.35	-	-	-	-
Yb	1.97	2.70	2.46	3.39	1.52	0.50	1.11	2.47
Lu	0.27	0.41	0.21	0.33	-	-	-	-
Sc	37.76	12.81	9.81	16.77	-	-	-	-
Th	0.57	17.60	14.06	14.38	-	-	-	-
U	0.20	3.85	2.83	6.28	-	-	-	-
Y	21.20	28.25	15.88	22.38	-	-	-	-

6.2.3 Additional data

BHP Minerals provided an additional 10 samples of gneiss with associated wholerock multi-element geochemical data determined by conventional XRF. This brought the total number of gneiss samples to 14 in the final dataset. Samples in the BHP dataset were collected from drillholes located from immediately south of the Hamilton Fault and up to ~1.2km north of the orebody. Some of the gneiss samples contained weak, incipient post-peak metamorphic albite alteration: a regionally extensive Na-metasomatism manifested in instances, as a 'red-rock' alteration owing to the orange-red discolouration of affected rocks. These albite-altered rocks were not included in the mass balance calculations. However, they have been included in the subsequent bivariate plots to statistically augment the determination of immobile elements.

Geochemical analyses (XRF) of one sillimanite-garnet schist and two garnet quartzite samples, both from the Southern Zone, were obtained from Chapman (1993). This data has also been used in the subsequent bivariate plots to statistically augment the determination of immobile elements. However, they were not included in the mass balance calculations.

6.3 ELEMENT IMMOBILITY

6.3.1 Concepts and criteria

A major objective of this geochemical study is to quantify compositional changes resulting from hydrothermal alteration of various rock types. During alteration, the addition or removal of a mobile element will affect the concentrations of all other elements (Gresens, 1967; Grant, 1986; Kranidiotis and MacLean, 1987; MacLean, 1990; MacLean and Barrett, 1993; Barrett and MacLean, 1994b). To accurately quantify these compositional variations it is necessary to consider factors such as changes in mass and volume, and element mobility (Gresens, 1967; Grant, 1986; MacLean and Kranidiotis, 1987; MacLean, 1988, 1990; Barrett and MacLean, 1991, 1994a and b; Elliott-Meadows and Appleyard, 1991; Shriver and MacLean, 1993; MacLean and Barrett, 1993; and others). The concept of element immobility forms the basis for mass-balance and composition-volume calculations. Moreover, determination of immobile elements is particularly important for reconciling protoliths to altered rocks, and in the case of altered igneous rocks, primary magmatic fractionation trends that can be used for reliable discrimination of magmatic affinity (Pearce and Cann, 1973; Floyd and Winchester, 1978; MacLean, 1990; MacLean and Barrett, 1993). The latter has received greatest attention in understanding the hydrothermal alteration of volcanosedimentary sequences that host VHMS deposits (MacLean and Kranidiotis, 1987; Liaghat and MacLean, 1992; MacLean and Barrett, 1993; Barrett and MacLean, 1994b; and many others).

During high-grade metamorphism (i.e. amphibolite to granulite facies) of altered rocks, some immobile elements may become mobile (Finlow-Bates and Stumpfl, 1981; Leitch and Lentz, 1994). Generally however, if the rocks have not endured extensive shear deformation, or have not been overprinted by later hydrothermal events, premetamorphic lithogeochemical signatures are largely retained, insomuch as elements that were immobile during alteration

remain immobile during metamorphism (MacLean, 1990; Elliott-Meadows and Appleyard, 1991; Shriver and MacLean, 1993; MacLean and Barrett, 1993; Barrett and MacLean, 1994b). Implicitly, the same suite of immobile elements determined in unmetamorphosed rocks, can therefore be used for discriminating magmatic affinity and reconciling least-altered precursors to altered rocks in high grade metamorphic terrains (Pearce and Cann, 1973; Floyd and Winchester, 1978; MacLean and Barrett, 1993; Barrett and MacLean, 1994b). In particular, the alteration trends and mass changes determined will reflect primary alteration processes (MacLean and Barrett, 1993; Barrett and MacLean, 1994b).

The high field strength (HFS), incompatible elements (from an igneous point of view) such as Ti, Al, Nb, Zr, Y and the heavy rare-earth elements (HREE) typically remain immobile during hydrothermal alteration (MacLean, 1990; MacLean and Barrett, 1993; and others). In instances, only a few of these elements may display immobile behaviour, whereas other elements, such as P, may display immobility (MacLean and Barrett, 1993; Barrett and MacLean, 1994b; Leitch and Lentz, 1994). Y and Nb mobility has been reported in a variety of altered rocks around volcanic-hosted massive sulphide (VHMS) deposits (Finlow-Bates and Stumpfl, 1981; Costa et al., 1983). Weak REE mobility has been recognised in some studies of low grade metamorphic (Hellman, et al., 1979; Ludden and Thompson, 1979; Bartley, 1986) and hydrothermally altered rocks (Kerrich and Fryer, 1979; Campbell et al., 1984; Ludden et al., 1982; Bence and Taylor, 1985; Lesher et al., 1986; MacLean, 1990). Due to these variations, element immobility needs to be clearly demonstrated to ensure that: i) ensuing mass balance calculations are an accurate reflection of alteration processes, and; ii) interpreted igneous and sedimentary fractionation trends are a valid indication of primary magmatic and sedimentary sorting processes respectively.

Element immobility is determined by plotting anticipated immobile element pairs on a bivariate graph. If the data form a clear linear trend (r=0.9-0.99), and the associated regression line passes through the origin and composition of the least-altered precursor, then the elements are considered immobile (MacLean and Kranidiotis, 1987; MacLean, 1990; MacLean and Barrett, 1993; Barrett and MacLean, 1994b). In other words, constant element ratios between the hydrothermally altered rock and its least-altered precursor are an indication of immobile behaviour during hydrothermal alteration. Scatter of data along this trend is caused by mass gains and losses in mobile elements due to alteration processes, resulting in the concomitant dilution and concentration of the immobile elements respectively (MacLean and Kranidiotis, 1987; MacLean, 1990; Liaghat and MacLean, 1992; MacLean and Barrett, 1993; Barrett and MacLean, 1994a, 1994b). Mass gains during alteration are manifested by compositions moving toward the origin from the least-altered precursor composition, whereas mass losses are defined by compositions moving in the opposite direction along the same "alteration trend" (MacLean and Kranidiotis, 1987; MacLean, 1990; MacLean and Barrett, 1993; Barrett and MacLean, 1994a, 1994b). These relationships are illustrated in a hypothetical example in Figure 6.1a. Linear to curvilinear trends that do not pass through the origin may indicate

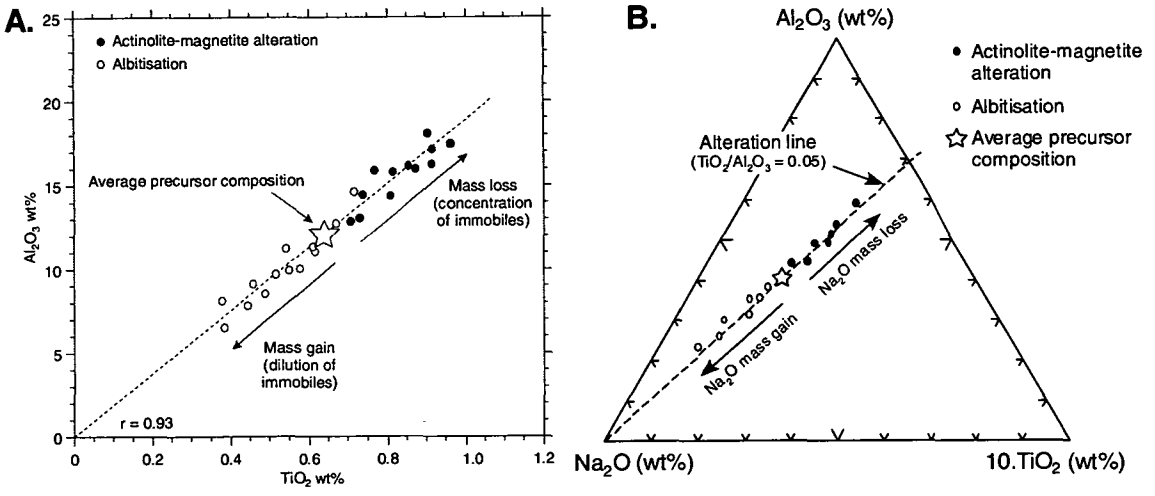

Figure 6.1 Linear alteration trends illustrating the effects of mass gains and losses in mobile elements caused by hydrothermal alteration. In this hypothetical example, albitisation involves a mass gain, whereas actinolite-magnetite alteration involves a mass loss. **A.** Al_2O_3-TiO_2 bivariate plot (modified after Barrett and MacLean, 1993). **B.** Al_2O_3-TiO_2-Zr ternary plot developed from Garcia et al. (1991, 1994).

magmatic fractionation processes and therefore magmatic affinity (MacLean and Kranidiotis, 1987; MacLean and Barrett, 1993; Barrett and MacLean, 1994a, 1994b), or fractionation related to sedimentary sorting processes and/or provenance variations (Garcia et al., 1991, 1994).

Whilst bivariate plots are a preliminary step for the determination of immobile elements, a more rigorous approach involving ratios between possible immobile elements is required thereafter. As previously mentioned, immobility of a particular element during hydrothermal alteration is defined by constant ratios between two elements in the altered rock and its least altered precursor. If for example, Al, Ti and Zr demonstrate immobile behaviour on bivariate plots, then ratios between these elements should be the same in the altered and least altered precursor. Hence, on bivariate plots involving ratios between immobile elements, the composition of the altered rock should plot in the same position as its least altered precursor. If this is not the case, and instead a trend or large dispersion of the data is evident, then one of the elements is mobile.

Determining which element is mobile can be difficult to quickly establish when using immobile-mobile element ratios on bivariate plots. However, it is particularly easy to resolve on a ternary plot involving the elements in question using a similar method to Garcia et al. (1991, 1994). In fact, ternary plots have the advantage of allowing mass changes to be easily visualised in a similar fashion to more simple bivariate plots involving only two elements (op. cit.). Primary magmatic or sedimentary fractionation trends and mixing trends can also be easily defined on ternary plots (e.g. Garcia et al., 1994). Figure 6.1b illustrates a hypothetical example of the fundamental dynamics of a ternary plot when applied to hydrothermal alteration studies. Mass gains and losses of a particular mobile element during alteration are exemplified by scattering of the data along a linear alteration trend from the least altered precursor. The orientation of the alteration trend is an indication of which element is mobile. In the example in Figure 6.1b, Al and Ti are immobile, i.e. ratios between these elements are the same in the altered rock

and its least altered equivalent. Compositions of the altered rock define a linear trend that when projected, passes through the Mg apex suggesting that whilst Ti/Al ratios remain constant (i.e. immobile), Mg is mobile. Mass gains in Mg plot between the precursor composition and the Mg apex, whereas mass losses plot between the precursor composition and the Al-Ti join. If a curvilinear trend is evident, then all the elements are behaving in a mobile, but systematic manner that can be mathematically modelled. Such curvilinear trends are indicative of fractionation related to magmatic or sedimentary processes, or may even be related to systematic mixing between two sources (e.g. Garcia et al., 1994).

6.3.2 Major and trace element geochemistry of host rocks

Bivariate plots of traditionally accepted immobile elements (Al, Ti, Nb, Y, Zr) are presented in Figure 6.2 for all host rock types and ores. The lack of linear trends that pass through the origin on all plots involving Y (Fig. 6.2d, g, i and j) indicates Y mobility in all host rocks and ores. Linear trends in the amphibolite data are related to variations in TiO_2 only (Fig. 6.2e, f and g). Apart from this, the Core Amphibolite plots as a discrete, tight cluster on all bivariate plots and is therefore remarkably homogeneous.

Linear trends ($r > 0.9$) that pass close to the origin and satisfy the criteria for immobile behaviour (ibid.) occur between Al, Ti and Nb (to a notably lesser degree) for gneiss and garnetiferous rocks (Fig. 6.2a, b and e). The latter immobile elements are also useful for discriminating between psammitic and pelitic gneiss. However, on Al_2O_3 and TiO_2 versus Zr plots, gneiss and garnetiferous host rocks display a scattered distribution, forming a broad negative trend (Fig. 6.2c, f and h). This variation provides evidence for Zr mobility.

A TiO_2-Zr plot reveals that psammitic gneiss form a scattered population with no recognisable trend (Fig. 6.2f). In contrast, pelitic gneiss form a weak linear trend that when extrapolated passes very close to the origin, suggesting Ti and Zr immobility. Hence, whilst Ti and Zr display immobile behaviour in the pelitic gneiss, they display mobile behaviour in the psammitic gneiss. These relationships are also apparent on a Nb-Zr plot (Fig. 6.3h). Evidence for Al mobility in both pelitic and psammitic gneiss is provided by the lack of linear trends passing through the origin on an Al_2O_3-Zr plot (Fig. 6.2h). Further evidence for Al mobility relative to Ti and Zr immobility in the pelitic gneiss is illustrated by a linear trend in the data projecting through the origin on an Al_2O_3/TiO_2 versus Al_2O_3/Zr bivariate plot (Fig. 6.3).

Overall, the relationships between Al, Ti and Zr are clearly depicted on an Al_2O_3-TiO_2-Zr ternary plot where the gneiss define a broad trend that projects toward the Zr apex (Fig. 6.4a). Strict interpretation of this trend indicates Zr mobility and relatively constant Al_2O_3/TiO_2 ratios. However, in detail, the slight trend in the pelitic gneiss data toward the Al_2O_3 apex is indicative of minor Al mobility, whilst Ti and Zr are immobile. The linear trend in the psammitic population toward the Zr apex is indicative of Zr mobility. However, this trend is slightly offset from the Zr apex, suggesting that Al and Ti are also slightly mobile, i.e. TiO_2/Zr ratios vary (Fig. 6.4a). This is confirmed by the lack of linear trends for the psammitic gneiss populations on

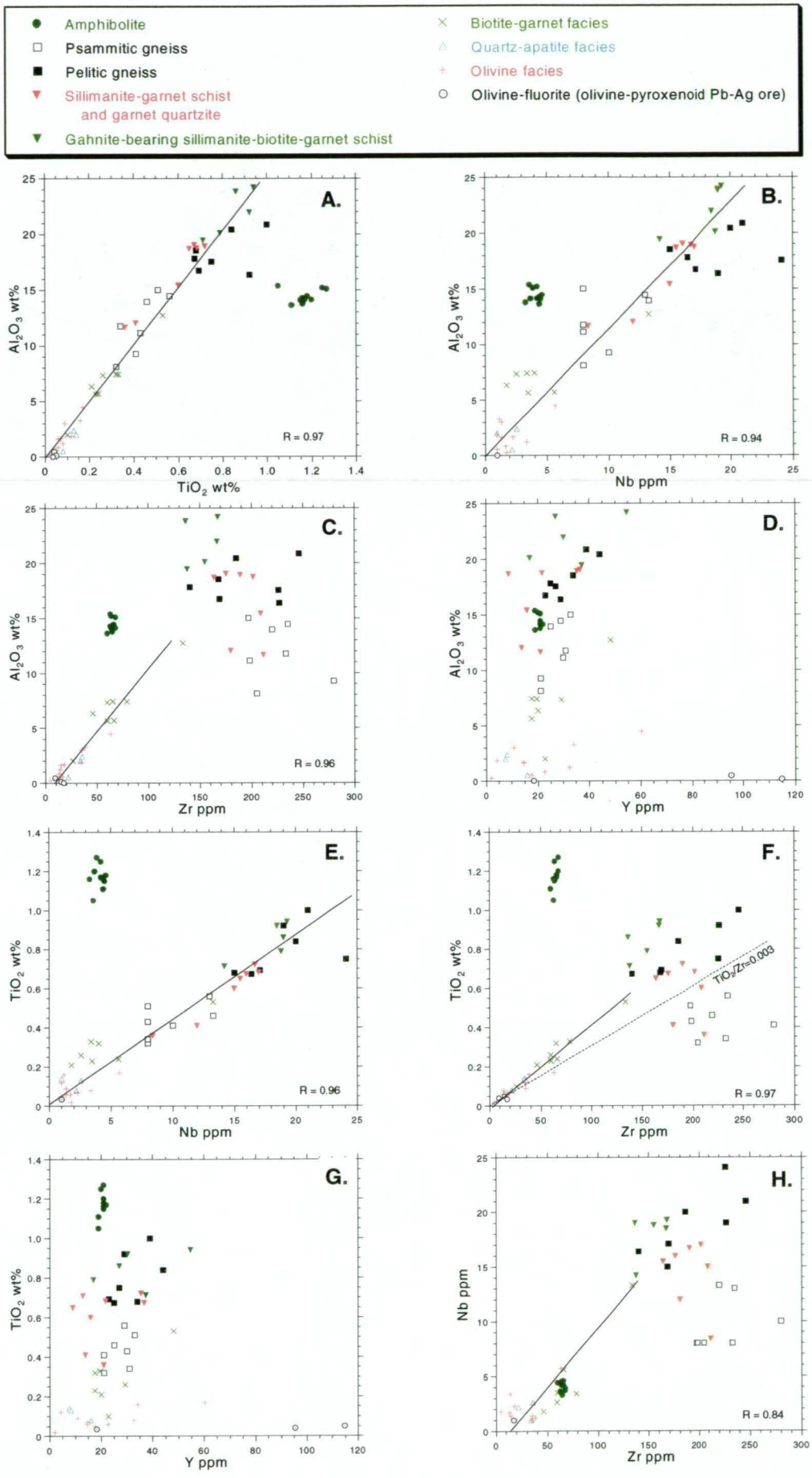

Figure 6.2 Bivariate plots of traditionally accepted immobile elements (Al, Ti, Zr, Y, Nb) for host rocks and ores. The figure is continued overleaf.

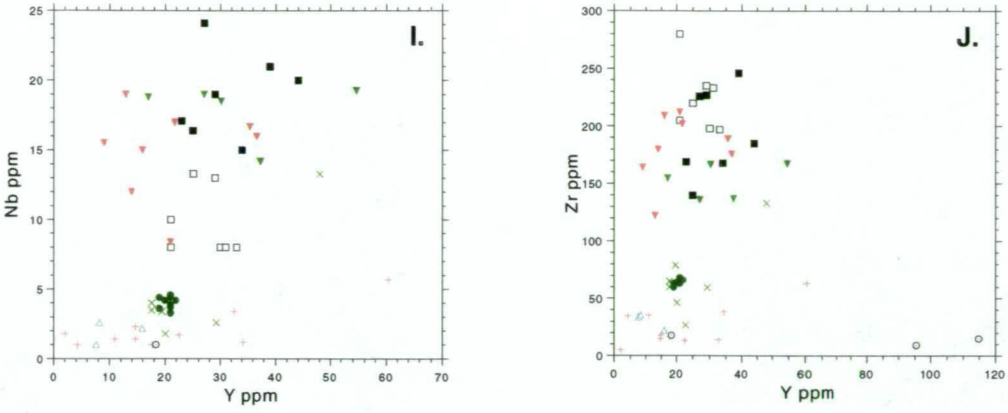

Figure 6.2 — continued.

Al_2O_3 and TiO_2 versus Zr bivariate plots (Fig. 6.2c and f). Even though Al, Ti and Zr demonstrate variably mobile behaviour in the psammitic gneiss, the trend on the ternary plot illustrates that relationships are systematic. Such systematic variations are indicative of processes that cause fractionation, or mixing between two end-member compositions (Garcia et al., 1991, 1994). The latter will be addressed in more detail in section 6.4.1.

Sillimanite-garnet schists and garnetiferous quartzites plot within the pelitic and psammitic gneiss populations respectively, and mimic the characteristic geochemical relationships of the gneiss on bivariate plots (Fig. 6.2) and the ternary plot (Fig. 6.4a). Garnetiferous quartzites plot within the psammitic gneiss population, whereas sillimanite-garnet schists plot within the pelitic gneiss population. This relationship confirms that sillimanite-garnet schists and garnetiferous quartzites represent hydrothermally altered metasediments (see sections 3.7.2 and 6.4.3). The gahnite-bearing schist also displays similar geochemical relationships to the gneiss, plotting along the same trends on bivariate plots, including the broad negative trend on Al_2O_3 and TiO_2 versus Zr bivariate plots. On an Al_2O_3-TiO_2-Zr ternary plot the gahnite-bearing

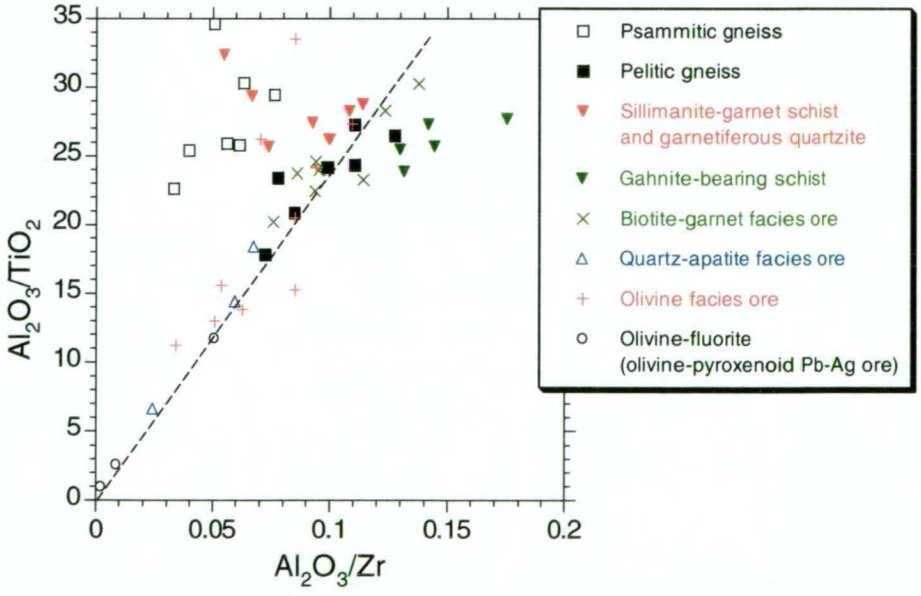

Figure 6.3 Al_2O_3/TiO_2 versus Al_2O_3/Zr bivariate plot. The pelitic gneiss population define a linear trend that project through the origin, suggesting Al mobility. Graphitic ores plot along the same trend. Garnet-biotite facies ores plot within the pelitic population, whereas quartz-apatite and olivine facies ores define the linear trend back to the origin from the pelitic population. The relationships suggest a genetic link between the ores and the pelitic gneiss.

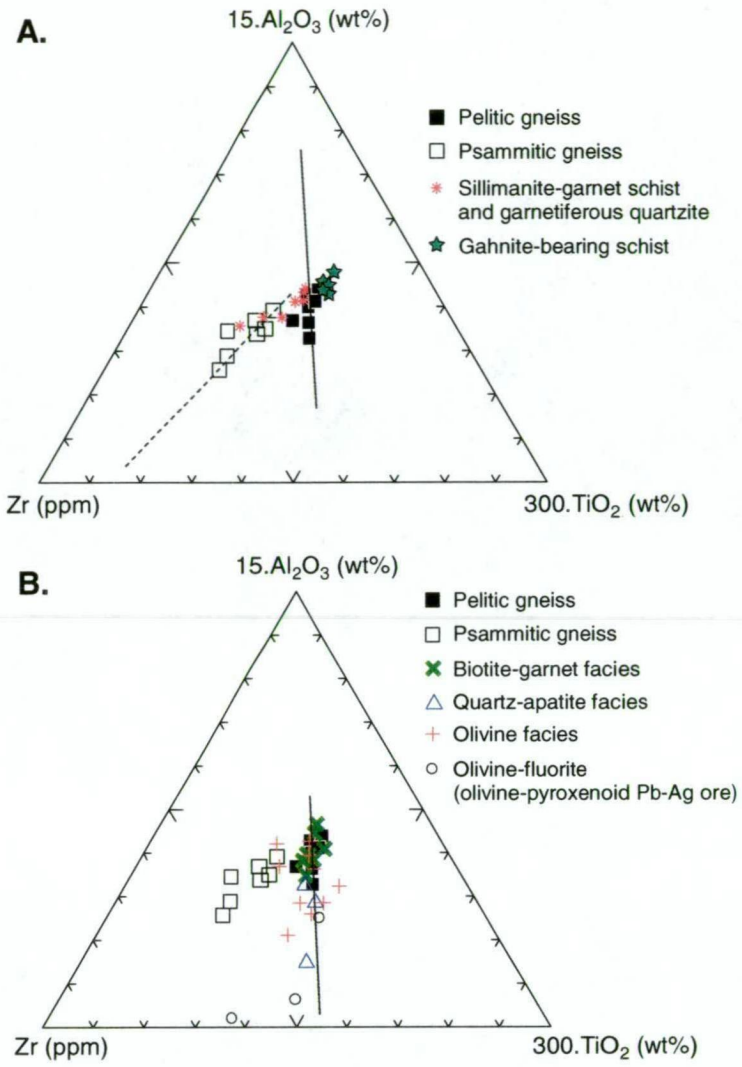

Figure 6.4 Al_2O_3-TiO_2-Zr ternary plots of gneiss, garnetiferous rocks and ores. **A.** gneiss and garnetiferous host rocks (including garnetiferous rocks) define a broad trend toward the Zr apex. Gahnite-bearing schists define a tight population, whereas sillimanite-garnet schists plot within the pelitic gneiss population. Garnetiferous quartzites plot within the psammitic population. The psammitic gneiss population, define a linear trend (dashed line) that is offset from the Zr apex. The pelitic gneiss define a linear trend (solid line) that extrapolates back to the Al_2O_3 apex, indicating Al mobility, and Ti and Zr immobility. **B.** graphitic ores plot along the same "Al mobility" trend as the pelitic gneiss (solid line). Biotite-garnet facies ores plot within the pelitic gneiss population, whereas quartz-apatite and olivine facies ores define a broad linear trend toward lower Al_2O_3 values suggesting comparatively greater mass losses in Al_2O_3. TiO_2/Zr ratios are the same as the pelitic gneiss suggesting a genetic relationship.

schist plots as a discrete cluster along the same broad trend defined by the gneiss providing evidence for Al, Ti and Zr immobility (Fig. 6.4a). However, the schist is comparatively depleted in Zr relative Al_2O_3 and TiO_2.

Overall, the gahnite-bearing schist is the only host rock type that displays evidence for Al, Ti and Zr immobility. Ti and Zr are the most reliable immobile elements in the pelitic gneiss and sillimanite-garnet schist, whereas the latter elements display mobile behaviour in the psammitic gneiss and garnetiferous quartzite, especially Zr.

6.3.3 Major and trace element geochemistry of graphitic ores

Graphitic ores do not define clear linear trends ($r > 0.9$) on bivariate plots involving Nb and Y, indicating that these elements display mobile behaviour (Fig. 6.2b, d, e, g, i and j). Linear

trends ($r > 0.9$) that pass close to the origin and satisfy the criteria for immobile behaviour (section 6.3.1) occur between Al, Ti and Zr (Fig. 6.2a, b and e). However, the linear trend defined by the ores on an Al_2O_3-Zr plot is slightly offset from the origin, consistent with Al mobility. Al mobility is also supported by scattering of the data off the linear trend. The same Al_2O_3/TiO_2-Al_2O_3/Zr bivariate plot used to substantiate Al mobility in the pelitic gneiss can also be used for the same purpose for graphitic ore based on Ti and Zr immobility. On such a diagram, the graphitic ores define a clear linear trend that passes through the origin, therefore confirming Al mobility (Fig. 6.3). These relationships are easily envisaged on an Al_2O_3-TiO_2-Zr ternary plot (Fig. 6.4b) where the ores define a broad linear trend that when projected, passes through the Al_2O_3 apex. Overall, the most reliable immobile elements in graphitic ores are Ti and Zr.

6.3.4 Rare-earth element geochemistry

REE immobility was tested by including previously determined immobile elements (Ti, Al, Zr and Nb; ibid.) in Pearson correlation coefficient matrices calculated for metasediments (i.e. gneiss and garnetiferous host rocks) and graphitic ores (Table 6.4). Correlation coefficients between the REE and established immobile elements (Ti, Al, and Zr) are poor. These relationships are exemplified by scattering of the data and lack of discernable linear trends on bivariate plots of TiO_2 versus REE (Fig. 6.5a to k). REE abundances are similar to the metasediments, except for significant Eu enrichment and slightly lower HREE abundances (Fig. 6.5). Overall, the REE display mobile behaviour in the host rocks and ores.

6.4 PRECURSOR COMPOSITIONS

Chemical changes associated with hydrothermal alteration of a particular rock can be quantified by comparing the altered rock to its least-altered protolith via mass balance calculations (section 6.3.1). The integrity of these calculations is contingent on reconciling the true protolith of the altered rock. Ideally, the altered and least-altered sample pair(s) should be in close proximity to one another (MacLean and Barrett, 1993; Barrett and MacLean, 1994b). Such an example can be regarded as a single precursor system (MacLean and Barrett, 1993;

Table 6.4 Pearson correlation coefficients between REE and immobile elements (Ti, Al, Nb and Zr) for the host rocks and ores.

	La	Ce	Pr	Nd	Sm	Eu	Gd	Tb	Dy	Er	Yb	TiO_2	Al_2O_3	Nb	Zr
Gneiss and garnetiferous rocks															
TiO_2	0.356	0.433	0.383	0.384	0.344	0.398	0.316	0.402	0.303	0.416	0.426	1.000			
Al_2O_3	0.332	0.356	0.328	0.331	0.303	0.388	0.279	0.340	0.286	0.389	0.396	0.874	1.000		
Nb	0.134	0.337	0.286	0.305	0.305	0.429	0.255	0.248	0.099	0.200	0.225	0.888	0.807	1.000	
Zr	0.055	0.115	0.143	0.162	0.235	0.104	0.276	0.109	0.060	-0.117	-0.085	-0.334	-0.624	-0.295	1.000
Garnet-biotite ore facies															
TiO_2	-0.636	-0.546	-0.502	-0.491	-0.426	-0.615	0.040	0.251	0.659	0.717	0.779	1.000			
Al_2O_3	-0.592	-0.551	-0.497	-0.476	-0.439	-0.736	0.008	0.242	0.649	0.732	0.812	0.974	1.000		
Nb	-0.904	-0.773	-0.767	-0.714	-0.408	-0.483	0.426	0.559	0.813	0.757	0.692	0.895	0.869	1.000	
Zr	-0.759	-0.655	-0.624	-0.614	-0.527	-0.631	0.004	0.242	0.673	0.738	0.780	0.977	0.941	0.952	1.000
Olivine facies ore															
TiO_2	0.690	0.716	0.703	0.676	0.632	0.144	0.567	0.533	0.645	0.757	0.766	1.000			
Al_2O_3	0.776	0.792	0.781	0.751	0.707	0.189	0.633	0.620	0.661	0.776	0.770	0.899	1.000		
Nb	0.724	0.672	0.691	0.715	0.758	0.436	0.773	0.761	0.748	0.729	0.650	0.386	0.461	1.000	
Zr	0.811	0.814	0.810	0.787	0.760	0.262	0.689	0.656	0.675	0.758	0.694	0.919	0.943	0.503	1.000

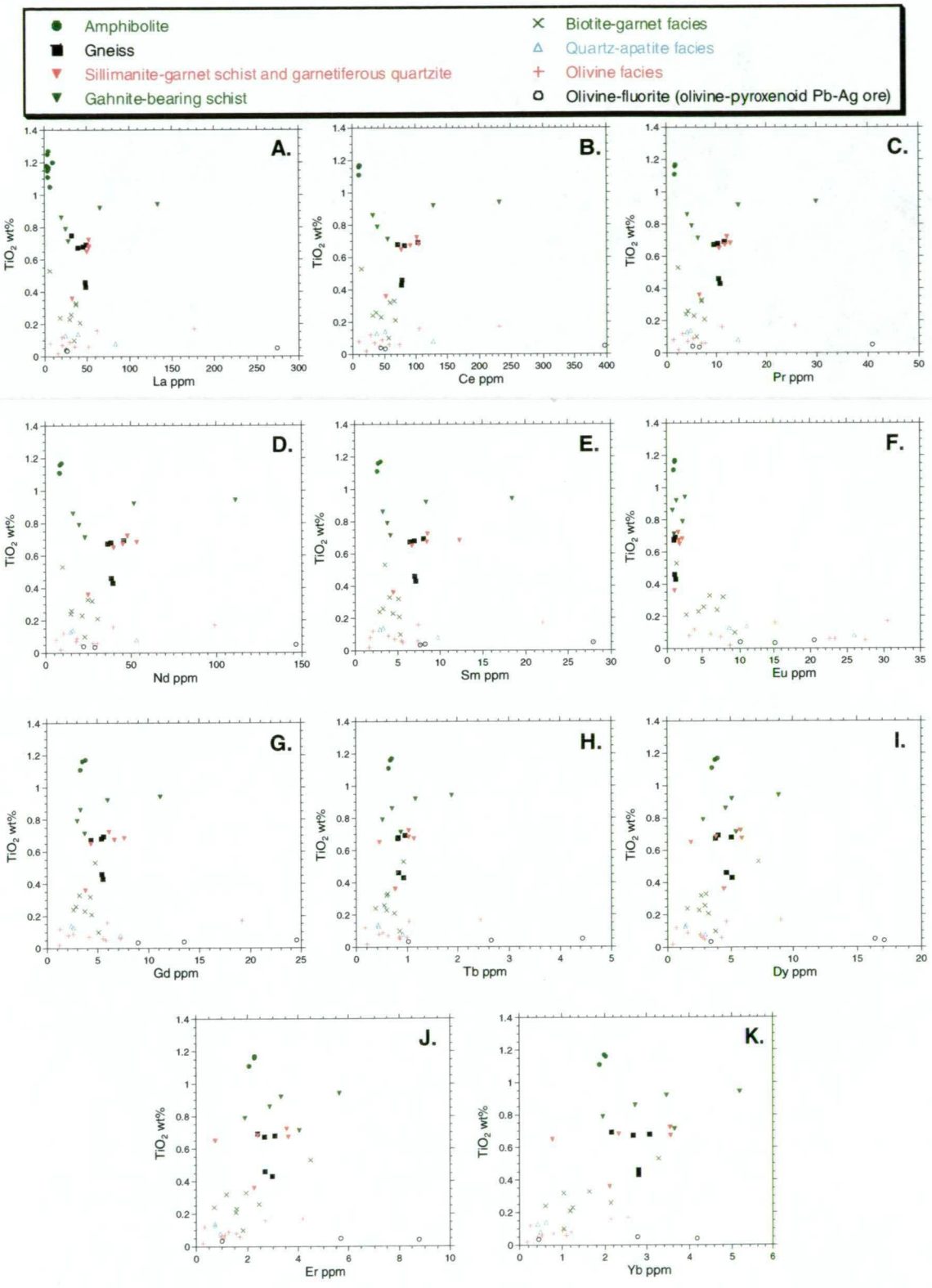

Figure 6.5 Bivariate plots of TiO_2 versus REE for host rocks and ores.

Barrett and MacLean, 1994b). Apart from the metasomatic sample set collected, none of the samples from Cannington represent single precursor systems due to the perennial problem of heterogeneity in the altered and unaltered gneissic rocks and graphitic ore, and the lack of exposure between drillholes. However, precursor compositions can be estimated using a multiple precursor system approach similar to that used in many alteration studies of VHMS districts in Canada, i.e. where protoliths of altered rocks cannot be confidently constrained in the field (e.g. Finlow-Bates and Stumpfl, 1981; MacLean and Kranidiotis, 1987; MacLean, 1990; MacLean and Barrett, 1993; Barrett and MacLean, 1994a, 1994b).

The multiple precursor method relies on establishing primary magmatic fractionation trends in unaltered igneous rocks using immobile compatible-incompatible (TiO_2-Zr, Al_2O_3-Zr), or immobile compatible (TiO_2-Al_2O_3) element pair discriminants (MacLean and Barrett, 1993; Barrett and MacLean, 1994a). On bivariate plots involving these elements, the intersection between the regression line for the altered samples (i.e. the alteration line that passes through the origin) and the curvilinear fractionation trend represents the precursor composition (Fig. 6.6a). However, if the fractionation line is subparallel to the alteration line, precursor compositions cannot be reliably estimated, e.g. plotting immobile incompatible element pairs (Nb-Y, Th-Zr, Y-Zr) yield fractionation lines that are superimposed on alteration lines. A similar approach can be applied to immobile element ternary plots. However, the altered rock will plot at some point *on* the fractionation trend, and this point represents the precursor composition.

On mobile-immobile element bivariate plots, the displacement of the altered sample from the fractionation curve is random, and the precursor composition cannot be readily determined. Instead, the immobile element concentration can be used to constrain the precursor composition and concentration of the particular mobile element (Fig. 6.6b). On a ternary plot involving one mobile and two immobile elements, the intersection of the alteration trend with the fractionation trend represents the precursor composition (Fig. 6.6c).

Whilst this method has direct application to altered igneous suites with definable fractionation trends, determination of precursor compositions in hydrothermally altered sedimentary rocks can be more difficult. This is largely due to primary geochemical heterogeneities caused by a combination of sedimentary processes (e.g. sorting and weathering) and provenance variations (Taylor and McLennan, 1985; Argast and Donnelly, 1987; Garcia et al., 1991, 1994; and many others). This is particularly relevant to immobile element systematics in the gneissic metasediments at Cannington. Typical fractionation trends related to sedimentary processes are reviewed below.

6.4.1 Al-Ti-Zr fractionation in the sedimentary environment

The effects of sedimentary processes on Al, Ti and Zr geochemistry in clastic sedimentary sequences have been studied by Garcia et al. (1991 and 1994). It is well established that the transport and deposition of detrital sediment involves various degrees of mechanical sorting. Sorting is analogous to the unmixing of a bulk sediment composition, resulting in the formation

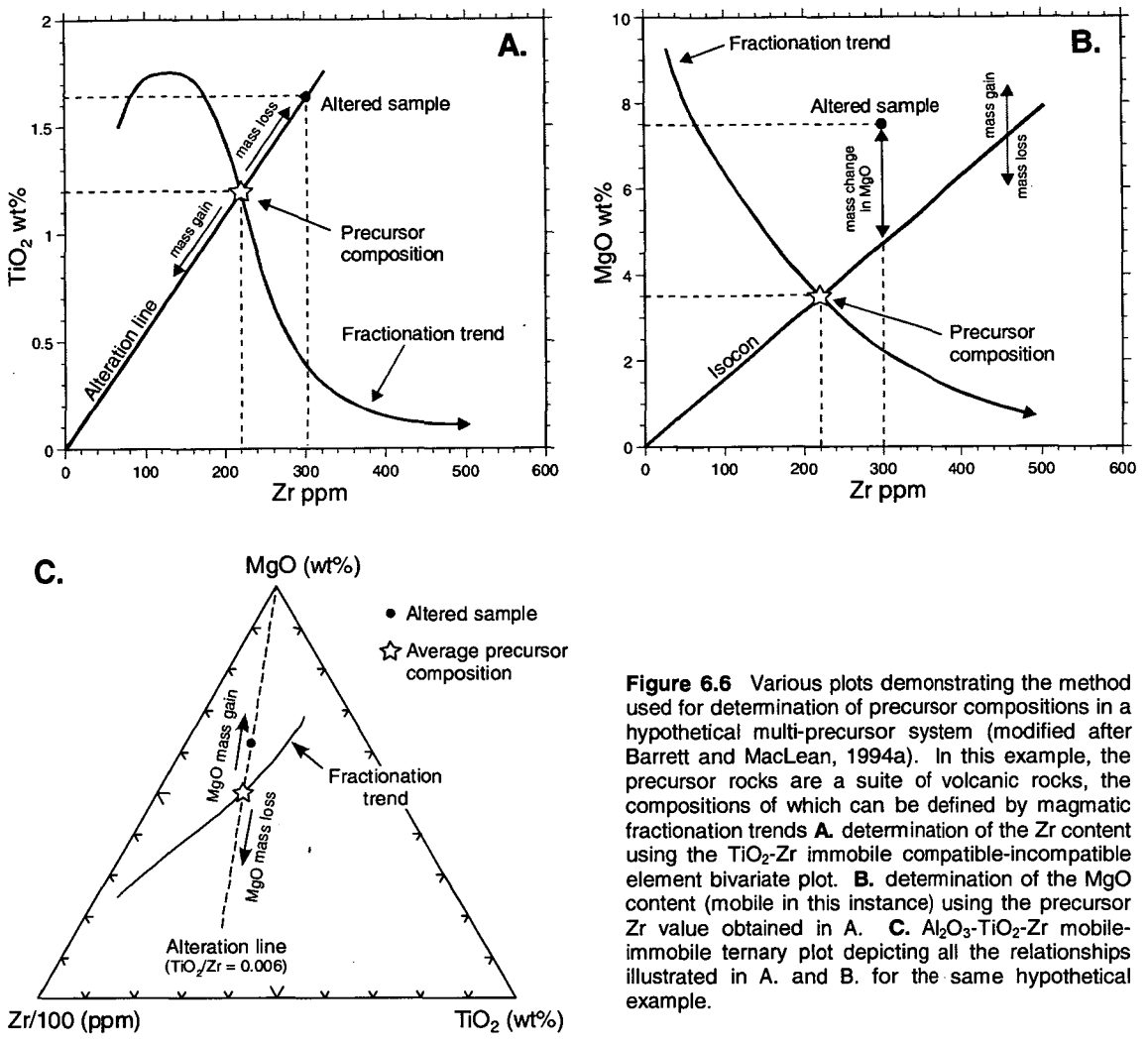

Figure 6.6 Various plots demonstrating the method used for determination of precursor compositions in a hypothetical multi-precursor system (modified after Barrett and MacLean, 1994a). In this example, the precursor rocks are a suite of volcanic rocks, the compositions of which can be defined by magmatic fractionation trends **A.** determination of the Zr content using the TiO_2-Zr immobile compatible-incompatible element bivariate plot. **B.** determination of the MgO content (mobile in this instance) using the precursor Zr value obtained in A. **C.** Al_2O_3-TiO_2-Zr mobile-immobile ternary plot depicting all the relationships illustrated in A. and B. for the same hypothetical example.

of complementary shale and sandstone sedimentary sequences. In particular, the geochemistry of the sedimentary products is controlled by the sorting process and can be used as a measure of sedimentary maturity. The distribution of chemical components between the sorted end-members is controlled by the physical properties of the detrital minerals. Shales chiefly consist of clay minerals and are therefore enriched in Al_2O_3, whilst sandstones contain abundant quartz and are enriched in SiO_2. Feldspars, heavy minerals (e.g. rutile, ilmenite, zircon) and lithic fragments are also preferentially concentrated into the coarser-grained sandstone fraction. TiO_2 is mainly concentrated in the fine-grained pelitic component even though it occurs in heavy minerals in the sandstone fraction. Nb is also typically enriched in the pelitic fraction. As a consequence, TiO_2 and Al_2O_3 typically increase as Zr decreases and therefore Al_2O_3 typically increases with increasing TiO_2/Zr ratios from sandstones to shales within a particular sedimentary sequence. This intrinsic variability in chemistry caused by mechanical sorting of a bulk sediment has been referred to as 'sedimentary fractionation' (Garcia et al., 1991 and 1994).

Geochemical systematics of sedimentary fractionation are best illustrated on an Al_2O_3-TiO_2-Zr ternary diagram for common sandstones and shales (Fig. 6.7a; Garcia et al., 1991). The diagram illustrates that for an arbitrary bulk sediment composition (BS), Zr is strongly

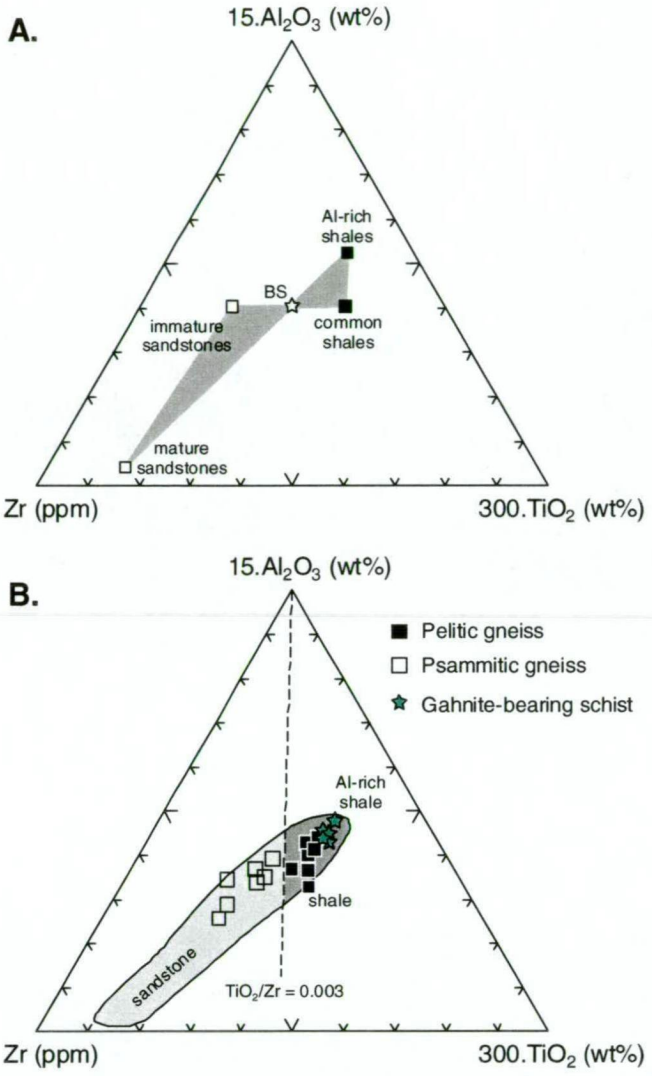

Figure 6.7 Al_2O_3-TiO_2-Zr ternary plots depicting the effects of sedimentary sorting on immobile elements (modified after Garcia et al., 1991, 1994). **A.** geochemical systematics of sedimentary sorting on the fractionation of Al_2O_3, TiO_2 and Zr using an initial arbitrary bulk sediment composition (BS). Zr is strongly fractionated during sorting, whilst Al_2O_3/TiO_2 ratios remain relatively constant. The diagram is useful for determining the degree of sedimentary maturity of a particular complementary sandstone-shale sequence, as well as defining source rock compositions. **B.** psammitic and pelitic gneiss from Cannington plot within the common sandstone (light grey) and shale (dark grey) fields respectively. Gahnite-bearing schists are comparatively enriched in Al_2O_3 and plot toward more mature Al-rich shale compositions. The distribution and trend of the data indicate that Al-Ti-Zr systematics are consistent with primary sedimentary fractionation (op. cit.). The short spread in psammitic gneiss compositions indicates that the host succession comprises immature siliciclastic sediments, except for the more mature Al-rich shale protolith of the gahnite-bearing schist.

fractionated during sorting in comparison to Al and Ti, and that the greatest fractionation occurs in sandstones. As the degree of fractionation increases, sandstones become progressively enriched in Zr relative to Al and Ti, and TiO_2/Zr ratios decrease. This is due to the combined effects of Ti and Al dilution by excess quartz and preferential concentration of zircon in the sandstone during sorting (op. cit.). The degree of fractionation is proportional to the degree of sorting. Well-sorted, mature sandstones are enriched in Zr relative to Ti and Al, and are characterised by large ranges in TiO_2/Zr ratios (op. cit). Poorly-sorted, immature sedimentary sequences are characterised by a small degree of fractionation that is manifested on the ternary diagram by a small spread in sandstone compositions, i.e. sandstone compositions are closer to the bulk sediment composition (BS), and ranges in TiO_2/Zr ratios are comparatively less (op. cit.).

Even though Al_2O_3-TiO_2-Zr abundances vary between shales and sandstones due to the addition and subtraction of mobile elements via weathering, transport, mixing from other sources, leaching and sedimentary sorting, "their relative proportions are transferred from the source area into the bulk sediment without any modification" (Garcia et al., 1994). Hence, the refractory properties of Al, Ti and Zr are useful for provenance studies, such that ratios between these elements in the source are faithfully preserved in the bulk sedimentary products. Because the majority of sedimentary suites are characterised by simple mixing trends between Al_2O_3-TiO_2-Zr due to sorting, the bulk composition of the source is constrained to this mixing trend on bivariate and ternary plots (Garcia et al., 1991, 1994). Hence, the mathematical equation that describes a particular mixing trend represents a unique lithogeochemical fingerprint of the sedimentary sequence and its source (op. cit.). More than one mixing trend for a given sedimentary sequence indicates more than one source.

The unique Al_2O_3-TiO_2-Zr sedimentary fractionation trend for a particular sedimentary sequence will be preserved during subsequent metamorphism and/or hydrothermal alteration due to the inherent immobile behaviour of Al, Ti and Zr during the latter post-depositional processes (section 6.3.1). Hence, these elements are particularly useful for lithogeochemical fingerprinting of detrital components within a given sedimentary sequence that has been subjected to high grade metamorphism and/or hydrothermal alteration, provided immobility can be demonstrated (Garcia et al., 1991). Moreover, the systematics provide a powerful tool for determining precursor compositions in metamorphosed alteration systems, such as the proximal garnetiferous alteration halo at Cannington, and provide a sound basis for subsequent mass balance calculations.

In summary, coherent systematics during sedimentary sorting and immobile properties of Al, Ti and Zr provides a basis for:

i) lithogeochemical discrimination;
ii) gauging sedimentary maturity and characterising source rocks;
iii) hydrothermal alteration studies involving: 1) the determination of protoliths to hydrothermally altered rocks in multi-precursor systems, and; 2) determination of mass changes;
iv) determining all of the above in metamorphosed terrains, provided immobile behaviour can be demonstrated.

6.4.2 Al-Ti-Zr systematics in the gneiss

The preceding discussion provides a firm basis for the interpretation of Al_2O_3-TiO_2-Zr geochemistry in the gneiss. The preferential enrichment of Al_2O_3 and TiO_2 (and Nb) in pelitic gneiss and enrichment of Zr in psammitic gneiss, are features consistent with typical sedimentary sorting processes. Increasing TiO_2 and decreasing Zr from psammitic to pelitic compositions on TiO_2-Zr plots is also consistent with normal sedimentary sorting processes. These relationships are depicted on an Al_2O_3-TiO_2-Zr ternary diagram (Fig. 6.7b). Pelitic and psammitic gneiss form a trend consistent with Al, Ti and Zr fractionation due to sedimentary

sorting, and plot within the common shale and sandstone fields respectively. The short scatter in the psammitic population along this trend indicates that only limited Zr fractionation occurred during sedimentary sorting and confirms earlier interpretations that the host succession comprises immature siliciclastic sediments (section 3.2.1; Beardsmore et al., 1988; Walters, 1994a and b; Walters and Bailey, 1998).

Linear trends on Al_2O_3-TiO_2 bivariate and Al_2O_3-TiO_2-Zr ternary plots therefore represent mixing lines related to sorting (cf. Garcia et al., 1991). A single trend on these diagrams suggests a single source, the bulk composition of which lies along the trend between the psammitic and pelitic populations. The observation that the gneiss plots within the common sandstone and shale fields suggests the gneiss has a composition essentially the same as common clastic sedimentary sequences found around the world, and that it was sourced from rocks with similar relative abundances of Al_2O_3, TiO_2 and Zr. In particular, the primary sedimentary fractionation trends have not been significantly modified during later upper amphibolite facies metamorphism (M_1) and retrogression (M_2 and M_3).

6.4.3 Protoliths of garnetiferous host rocks

On immobile-immobile element plots involving Ti, Al and Nb, garnetiferous rocks form a coherent linear trend that projects through the origin (Fig. 6.2a, b and e). As such, this trend is interpreted as an alteration trend (section 6.3.1; MacLean and Barrett, 1993). The composition of the unaltered protolith lies along this trend (see Figure 6.6). Amphibolites can be disregarded as possible least altered precursors, because they do not plot along the same immobile element alteration trends (Fig. 6.2). The only least altered rock type with compositions superimposed along the same alteration trends is the gneiss. This relationship provides strong geochemical evidence for a gneiss precursor composition for the garnetiferous rocks. However, it is possible to resolve the precursor composition more accurately by examining the geochemistry of the gneiss with respect to pelitic versus psammitic compositions and sedimentary fractionation between Al, Ti and Zr (section 6.4.1 and 6.4.2 above).

On a TiO_2-Zr plot, sillimanite-garnet schists plot along the same trend as the pelitic gneiss (Fig. 6.2f), indicating that the latter rock is the likely precursor; the composition of which lies within the pelitic population along this trend. Further resolution of the pelitic precursor composition is not possible due to the scatter of the pelitic population along this trend. This precursor composition is confirmed on an Al_2O_3-TiO_2-Zr ternary plot where sillimanite-garnet schists plot within the pelitic gneiss population (Fig. 6.4a). In contrast, garnetiferous quartzites plot within the psammite field, suggesting that the psammitic gneiss is the likely precursor for these altered rocks. It is apparent that variations in immobile element abundances in the garnetiferous rocks are due to a combination of premetamorphic hydrothermal alteration processes (i.e. mass gains and losses in mobile elements) superimposed upon primary sedimentary fractionation features (i.e. mass gains and losses related to sedimentary sorting). Consequently, detailed precursor compositions must vary amongst the samples to some

degree. An average pelitic gneiss precursor composition for the sillimanite-garnet schists was used for the subsequent mass balance calculations (Table 6.5). Mass balance calculations were not carried out on garnetiferous quartzites due to a lack of wholerock analyses.

The precursor to gahnite-bearing schists is less obvious. Unlike sillimanite-garnet schists, gahnite-bearing schists have marginally higher TiO_2/Zr ratios (~0.005) than the pelitic gneiss and therefore plot slightly above the trend defined by the latter rocks on a TiO_2-Zr plot (Fig. 6.2f). A possible least-altered protolith with the same TiO_2/Zr ratios has not been recognised at Cannington. It is however, unlikely that higher TiO_2/Zr ratios indicate a discernable variation in provenance because the gahnite-bearing schists lie along the same linear trend as the host gneiss on immobile-immobile bivariate plots involving Al_2O_3, TiO_2 and Nb (Fig. 6.2). The Al_2O_3-TiO_2-Zr ternary plot provides further evidence supporting this common heritage, as the gahnite-bearing schists plot as a tight cluster on the same sedimentary fractionation trend defined by the gneiss (Fig. 6.4a). The compositional relationships indicate that the gahnite-bearing schist is more akin to Al-rich shales, suggesting that the possible precursor was a more mature Al-rich pelitic sediment (Fig. 6.7b). If this is correct, it has important genetic significance with regard to the depositional setting of the ores considering the gahnite-bearing schists have a strong spatial association with the deposit (see section 6.7.3).

Even though the pelitic gneiss has similar Al_2O_3/TiO_2 ratios to the gahnite-bearing schist, the disparity in TiO_2/Zr has the potential to cause large errors in mass balance calculations if an average pelitic gneiss precursor composition is assumed. To overcome this compositional mismatch, an Al_2O_3 enriched precursor composition was calculated by normalising the average pelitic gneiss composition to the TiO_2/Zr ratio of the gahnite-bearing schist (Table 6.5). This method effectively approximates the sedimentary fractionation trend with respect to the relative abundances of Al, Ti and Zr in the metasediments. The calculated composition will therefore fall on the sedimentary fractionation trend and within the gahnite-bearing schist population on the Al_2O_3-TiO_2-Zr ternary diagram. The calculated Al-rich pelitic precursor composition was used in the subsequent mass balance calculations for the gahnite-bearing schists (Table 6.5).

6.4.4 Detrital components in graphitic ores

Graphitic ores plot along the same linear trends as the gneiss and garnetiferous rocks on bivariate plots involving Ti, Al and Nb, suggesting a genetic link (Fig. 6.2a, b and f). Immobile element abundances are significantly lower in the ores compared to the metasedimentary host rocks, but the similar immobile element ratios provide evidence that the ores contain minor amounts of locally derived detrital sediment rather than material from an alternative or additional exotic Al, Ti and Zr bearing source. It is interpreted that an amphibolite component in graphitic ores can be discounted because amphibolite compositions do not plot along the same immobile element alteration trends as the graphitic ores (Fig. 6.2).

Table 6.5 Composition of the average pelitic gneiss and calculated Al-rich pelitic precursors used in the mass balance calculations.

Oxide (wt%)	Average pelitic gneiss	Standard deviation	Calculated Al-rich pelite
SiO_2	57.86	*3.59*	54.04
TiO_2	0.73	*0.07*	0.93
Al_2O_3	18.22	*1.40*	23.32
Fe_2O_3	10.26	*3.75*	9.58
MnO	0.11	*0.06*	0.10
MgO	2.81	*0.62*	2.62
CaO	0.48	*0.30*	0.45
Na_2O	1.58	*0.98*	1.48
K_2O	4.20	*1.30*	3.92
P_2O_5	0.10	*0.04*	0.10
LOI (incl. S)	2.75	*0.64*	2.57
TOTAL	99.10		99.11
S	0.11	*0.10*	0.11
Traces (ppm)			
Pb	28.4	*20.31*	28.4
Zn	56.8	*35.52*	56.8
Sb	<2	-	<2
Cd	<2	-	<2
Ag	<2	-	<2
Nb	18.5	*3.61*	18.5
Zr	177.5	*31.62*	165.8
Sr	74.2	*36.90*	74.2
Ba	592.7	*349.73*	592.7
Y	30.6	*8.59*	30.6
As	6.0	*4.24*	6.0
Bi	0.7	*0.57*	0.7
W	10.2	*11.45*	10.2
Rb	221.8	*54.86*	221.8
REE (ppm)			
La	44.84	*4.97*	44.84
Ce	85.69	*16.44*	85.69
Pr	10.50	*1.00*	10.50
Nd	40.33	*4.85*	40.33
Sm	7.18	*0.82*	7.18
Eu	1.01	*0.11*	1.01
Gd	5.12	*0.66*	5.12
Tb	0.87	*0.08*	0.87
Dy	4.34	*0.63*	4.34
Ho	-	-	-
Er	2.71	*0.34*	2.71
Tm	-	-	-
Yb	2.64	*0.46*	2.64
Lu	-	-	-

The composition of the locally derived sedimentary component within the ores can be determined by considering the sedimentary fractionation trends in Al, Ti and Zr in the gneiss. Projection of the ore trend on a TiO_2-Zr bivariate plot highlights a distinct genetic relationship between the ores and pelitic gneiss (Fig. 6.2f). This relationship can also be seen on the Al_2O_3-Zr plot (Fig. 6.2c), and is clearly depicted on the Al_2O_3/TiO_2-Al_2O_3/Zr plot (Fig. 6.3). In detail however, the latter plot reveals that biotite-garnet ores fall within the pelitic gneiss population and therefore ranges in Al_2O_3, TiO_2 and Zr ratios are essentially the same. This suggests that the relative abundances between Al_2O_3, TiO_2 and Zr in the pelitic gneiss have been faithfully preserved in biotite-garnet facies ores. Quartz-apatite and olivine facies ores lie along the same linear trend, but Al_2O_3/TiO_2 and Al_2O_3/Zr ratios are less than or equal to those of biotite-garnet facies ores and pelitic gneiss. This relationship suggests that whilst TiO_2/Zr ratios support a pelitic gneiss component, variable Al_2O_3 mobility is evident.

The same relationships are revealed and the Al_2O_3-TiO_2-Zr ternary plot (Fig. 6.4b). The vertical orientation of the ore trend essentially represents an alteration or mixing line indicating variable mass losses in Al_2O_3 in quartz-apatite and olivine facies ores relative to TiO_2 and Zr. However, three olivine facies ores plot within the pelitic gneiss population, suggesting that in some samples Al_2O_3 remained immobile during ore formation. In addition, two olivine facies ore samples plot within the psammitic gneiss population providing evidence for a minor immature (in a sedimentary context) psammitic component in some olivine facies ores.

Overall, the data indicate that graphitic ores contain a recognisable component of pelitic gneiss (cf. Chapman, 1993; Chapman and Williams, 1998; Pringle, 1999), as well as a subordinate immature psammitic component in some olivine facies samples. Relative abundances of Al, Ti and Zr in the pelitic gneiss have been faithfully preserved in the biotite-garnet ore facies in contrast to quartz-apatite and olivine ore facies that display evidence for variable Al mobility (ibid.; Figs. 6.3 and 6.4b). The geochemical evidence indicates that no other exotic rock types are present in the ores. Dilution of the immobile elements compared to abundances in the pelitic gneiss therefore suggest that graphitic ores contain additional constituents of hydrothermal origin. Hence, the ore facies are comprised of only two principle components: i) pelitic detritus, and; ii) hydrothermal constituents. Appropriately, an average pelitic gneiss precursor composition was used in the subsequent mass balance calculations (Table 6.5). This precursor composition is equivalent to that used in the mass calculations for the garnetiferous schists. Mass balance studies were not carried out on olivine facies ores that contain a recognisable psammitic component.

6.5 MASS CHANGES

In order to accurately determine compositional changes resulting from hydrothermal alteration, mass changes between the altered rock and its least altered equivalent must be quantified. Application of the same principles can be used to quantify the pelitic component in the graphitic ores. The methods used to quantify mass (and volume) changes during hydrothermal alteration are summarised by Leitch and Lentz (1994). All methods rely on

particular elements remaining immobile during alteration, as they serve as a basis for the measurement of mass changes in mobile elements (section 6.3.1).

The Gresens analysis (Gresens, 1967) is one such method for determining mass changes associated with alteration, and over the years has evolved into two different approaches. The first of these are modifications by Grant (1986) and Huston (1993), which are graphical solutions to the Gresens composition-volume calculation and cater for single precursor systems, i.e. the "isocon method". Construction of an isocon diagram is essentially a data presentation tool only, and an optional preliminary step to ensuing mass-balance calculations. The diagram depicts the relative mass changes between elements, rather than absolute mass changes and should therefore be interpreted with caution.

The second approach is that of MacLean and Kranidiotis (1987), MacLean (1990) and MacLean and Barrett (1993). It has the advantage of catering for both single and multiple precursor systems, whereby individual samples in a variety of altered rocks can be related back to appropriate precursor compositions. It is referred to here as the "MacLean method". The MacLean method is particularly useful in terrains where least-altered precursors cannot be readily identified in the field, and where multiple sources are evident in the protolith (section 6.4), such as in mixed clastic-chemical sediments (e.g. Liaghat and MacLean, 1992). Rock densities are not required for calculating the mass changes and no assumptions are made with regard to constant volume or constant mass (Barrett and MacLean, 1994a). Furthermore, the method overcomes the deceptive effects of closure (constant sum of 100%) on relationships between elements in untreated lithogeochemical data (Barrett and MacLean, 1994b). Both the isocon and MacLean methods use very similar formulas, the main difference being the reversal of immobile element ratios between the altered and least-altered compositions. This simply changes the algebraic relationships in the equations, but both methods yield very similar results.

The MacLean method was chosen for this study because a multiple precursor approach was used to determine precursor rocks (section 6.4). The Huston (1993) isocon method was used to validate the calculated mass and volume changes; results of which were very similar, but are not presented here.

6.5.1 Mass-volume calculations

Mass balance calculations are based upon changes in concentration of immobile elements between the altered rock and its least-altered precursor. In the MacLean method, mass changes are calculated by normalising the immobile element in the altered sample to its original concentration in the precursor. Concentrations of the mobile elements are then recalculated using the same 'dilution' factor to produce a reconstructed concentration (C_r), e.g.:

(1) $C_r = (Zr_p/Zr_a) \times C_a$

where Zr_p = concentration of Zr in the precursor, Zr_a = concentration of Zr in the altered rock,

and C_a = the concentration (%) of the mobile element in the altered rock. The reconstructed composition reflects the absolute mass of the altered rock in wt% (wt% = g/100g). Subtraction of the precursor concentration from the reconstructed concentration yields the absolute mass change (ΔC) for the particular component, e.g.:

(2) $\Delta C = C_r - C_p$

where C_r = reconstructed concentration of the particular component, and C_p = concentration of the particular component in the precursor. The sum of ΔC for all components equals the absolute net mass change (ΔM) in the altered rock. This may also be calculated by:

(3) $\Delta M = \sum C_r - \sum C_p$

where $\sum C_r$ = the sum of all components in the reconstructed composition, and $\sum C_p$ = the sum of all components in the precursor composition. The relative % net mass change ($\Delta MR\%$) can be calculated by:

(4) $\Delta MR\% = [(Zr_p/Zr_a) - 1] \times 100$

and the relative % net mass changes ($\Delta CR\%$) for the mobile elements can be calculated by:

(5) $\Delta CR\% = [(Cr/Cp) - 1] \times 100$

Net relative % volume change ($\Delta V\%$) can be calculated from rock densities together with the mass changes by:

(6) $\Delta V\% = [(Zr_p/Zr_a \times \rho_p/\rho_a) - 1] \times 100$

where ρ_p = the density of the precursor (g/cc), and ρ_a = the density of the altered rock (g/cc)[†].

Several external limitations may lead to errors in the mass balance calculations (Barrett and MacLean, 1994a), such as:

i) Accuracy of the precursor compositions determined from fractionation trends in multiple precursor systems. For instance, correlation coefficients for magmatic fractionation trends may suggest errors of up ±10% for possible for precursor immobile element concentrations in altered samples.

ii) Accuracy of the analytical instrument used for geochemical analyses, which translates into the accuracy of the fractionation curve on bivariate plots.

In multi-precursor systems these potential errors combined may lead to mass change errors of up to ±25%, but more commonly in the range between ±10-15% (Barrett and MacLean, 1994a).

Al_2O_3 was not used as a basis for mass balance calculations because of its variably mobile behaviour in the pelitic gneiss, sillimanite-garnet schists and graphitic ores. As previously mentioned the most reliable immobile elements in the latter rocks are TiO_2 and Zr (section 6.3). Hence, an average of the Ti_p/Ti_a and Zr_p/Zr_a ratios (i.e. an average dilution factor) was used in the mass balance calculations. Because the calculated precursor composition was based on the relative abundances of Al, Ti and Zr in the gahnite-bearing schist, the mass

[†] To account for volume, absolute mass changes for the mobile elements can be calculated by:
$\{[(Zr_p/Zr_a) \times (\rho_p/\rho_a)] \times C_a\} - C_p$
and relative % mass changes by:
$\{\{[(Zr_p/Zr_a) \times (\rho_p/\rho_a) \times C_a]/C_p\} - 1\} \times 100$
The mass calculations here assumed constant volume and only the net relative % volume change was calculated.

balance calculations were based on an average of the Al_p/Al_a, Ti_p/Ti_a and Zr_p/Zr_a.

Oxide wt% and ppm concentrations for the major and trace elements respectively were converted to % concentrations to standardise concentration units so that absolute net mass changes could be calculated. Units for absolute mass changes are therefore expressed in g/100g for major elements. Mass change units for the trace elements were converted from g/100g to g/tonne (i.e. ppm) by multiplying the results by 10,000, i.e. % (g/100g) x 10,000 = g/tonne.

6.5.2 Garnetiferous host rocks

Calculated mass changes for four sillimanite-garnet schist samples are presented in Table 6.6 and Figure 6.8. Calculated mass changes are small, ranging between -2.2 to 4.8g/100g, with an average absolute net mass gain of 0.8g/100g (Table 6.6). The small net mass changes are consistent with sillimanite-garnet schists plotting within the pelitic gneiss population on bivariate and ternary plots. The most significant average mass changes include additions in Si (2.5g/100g), Al (0.6g/100g), Mn (0.4g/100g) and K (2.3g/100g), and Pb (918ppm), Zn (76ppm) and Rb (81ppm) for the trace elements. The most significant average mass losses occur in Fe (-2.2g/100g), Mg (-1.3g/100g) and Na (-0.9g/100g) for the major elements (Fig. 6.8a), and Sr (-31ppm) and Ba (-13ppm) for the traces (Fig. 6.8b). Mass changes in REE are depicted in the absolute mass change REE profiles, and are characterised by comparatively larger mass gains in light REE (LREE) compared to heavy REE (HREE), with mass losses in HREE occurring in same samples (Fig. 6.8c). The greatest mass changes occur in Ce and Nd.

Calculated mass changes for five gahnite-bearing schist samples are presented in Table 6.7 and Figure 6.9. Gahnite-bearing schists are characterised by greater average net mass gains compared to sillimanite-garnet schists (e.g. an average absolute net mass gain of 5.9g/100g, and average relative net mass gain of 9.4%; Table 6.7), possibly indicating that alteration was slightly more intense. The most significant average mass gains for the major elements include Si (4.3g/100g), Al (0.3g/100g), Mn (0.3g/100g) and K (1.8g/100g), LOI (1.5g/100g), and Pb (762ppm), Zn (4855ppm) and Rb (44ppm) for the trace elements (Table 6.7; Fig. 6.9a and b). Fe, Mg, Na, Sr and Ba comprise the most significant mass losses. Average mass changes in REE for the gahnite-bearing schist are minor and are characterised by greater mass changes in LREE in comparison to the HREE (Fig. 6.9c). However, in detail the mass losses and gains in LREE vary between samples with the greatest changes occurring in La, Ce and Nd. Compared to the sillimanite-garnet schist, the REE profiles are consistent amongst the samples, suggesting more coherent REE behaviour during hydrothermal alteration. Overall, elements that have undergone the most significant mass changes are essentially the same as those determined for the sillimanite-garnet schist.

6.5.3 Graphitic ores

Mass balance calculations were performed on eight biotite-garnet facies, three quartz-apatite and six olivine facies ore samples. Calculated mass changes for biotite-garnet facies ores are

Table 6.6 Calculated absolute mass changes in sillimanite-garnet schists using an average precursor pelitic gneiss composition.

Sample no.	NZ009-2	NZ047-1	SZ048-6	SZ048-27	Average	Standard deviation
(g/100g)						
Si	6.6	1.7	1.8	-0.1	2.5	2.9
Ti	0.0	0.0	0.0	0.0	0.0	0.0
Al	1.2	0.0	0.9	0.1	0.6	0.6
Fe	-4.9	-4.0	1.0	-0.8	-2.2	2.7
Mn	0.1	0.3	1.0	0.2	0.4	0.4
Mg	-1.3	-1.3	-1.2	-1.2	-1.3	0.1
Ca	-0.2	-0.1	0.3	0.0	0.0	0.2
Na	-0.8	-0.9	-1.0	-0.9	-0.9	0.1
K	3.9	2.8	0.7	1.5	2.3	1.4
P	0.0	0.0	0.0	0.0	0.0	0.0
S	-0.1	-0.1	-0.1	0.0	-0.1	0.1
LOI	0.0	-0.6	-1.1	-0.6	-0.6	0.4
(g/tonne)						
Pb	2359.0	597.8	257.0	457.6	917.9	970.9
Zn	78.6	104.6	27.9	91.9	75.8	33.6
Sb	-0.1	-0.1	-0.1	5.9	1.4	3.0
Cd	-0.1	-0.1	-0.1	-0.1	-0.1	0.0
Ag	-0.1	-0.1	-0.1	-0.1	-0.1	0.0
Nb	-1.5	-2.0	-1.8	-2.3	-1.9	0.3
Zr	3.0	18.6	6.1	6.5	8.5	6.9
Sr	-18.1	-18.7	-46.6	-41.9	-31.3	15.1
Ba	74.3	110.8	-103.9	-132.2	-12.8	123.1
Y	-20.7	-9.4	7.8	3.9	-4.6	13.0
As	-0.1	3.8	9.3	8.6	5.4	4.4
Bi	-0.1	0.1	1.9	0.1	0.5	0.9
W	2.1	10.2	23.8	7.2	10.8	9.3
Rb	189.9	89.4	-25.3	67.9	80.5	88.3
La	10.3	6.5	10.0	6.2	8.3	2.2
Ce	-0.8	16.1	9.8	13.2	9.6	7.4
Pr	1.2	1.8	1.7	1.2	1.5	0.3
Nd	3.7	11.6	7.1	6.3	7.2	3.3
Sm	0.2	4.8	1.6	1.1	2.0	2.0
Eu	0.9	1.1	0.7	0.5	0.8	0.2
Gd	-0.3	2.3	1.8	0.8	1.2	1.2
Tb	-0.4	0.1	0.3	0.1	0.1	0.3
Dy	-2.3	-0.5	1.7	1.2	0.0	1.8
Er	-1.9	-0.4	1.1	0.7	-0.1	1.3
Yb	-1.8	-0.4	1.1	0.8	-0.1	1.3
DF	1.10	0.97	1.05	0.97	1.02	0.06
ΔMR%	10.1	-2.8	4.5	-2.8	2.3	6.2
ΔM (g/100g)	4.8	-2.2	2.3	-1.8	0.8	3.4
density (g/cc)	2.7	2.7	2.7	2.7	2.7	0.0
ΔV%	10.1	-2.8	4.5	-2.8	2.3	6.3

DF — dilution factor, which is the average of the Zr_p/Zr_a and Ti_p/Ti_a immobile element ratios (<1 – net mass loss, >1 – net mass gain).
ΔMR% — relative net mass change.
ΔM — absolute net mass change.
ΔV% — relative net volume change.

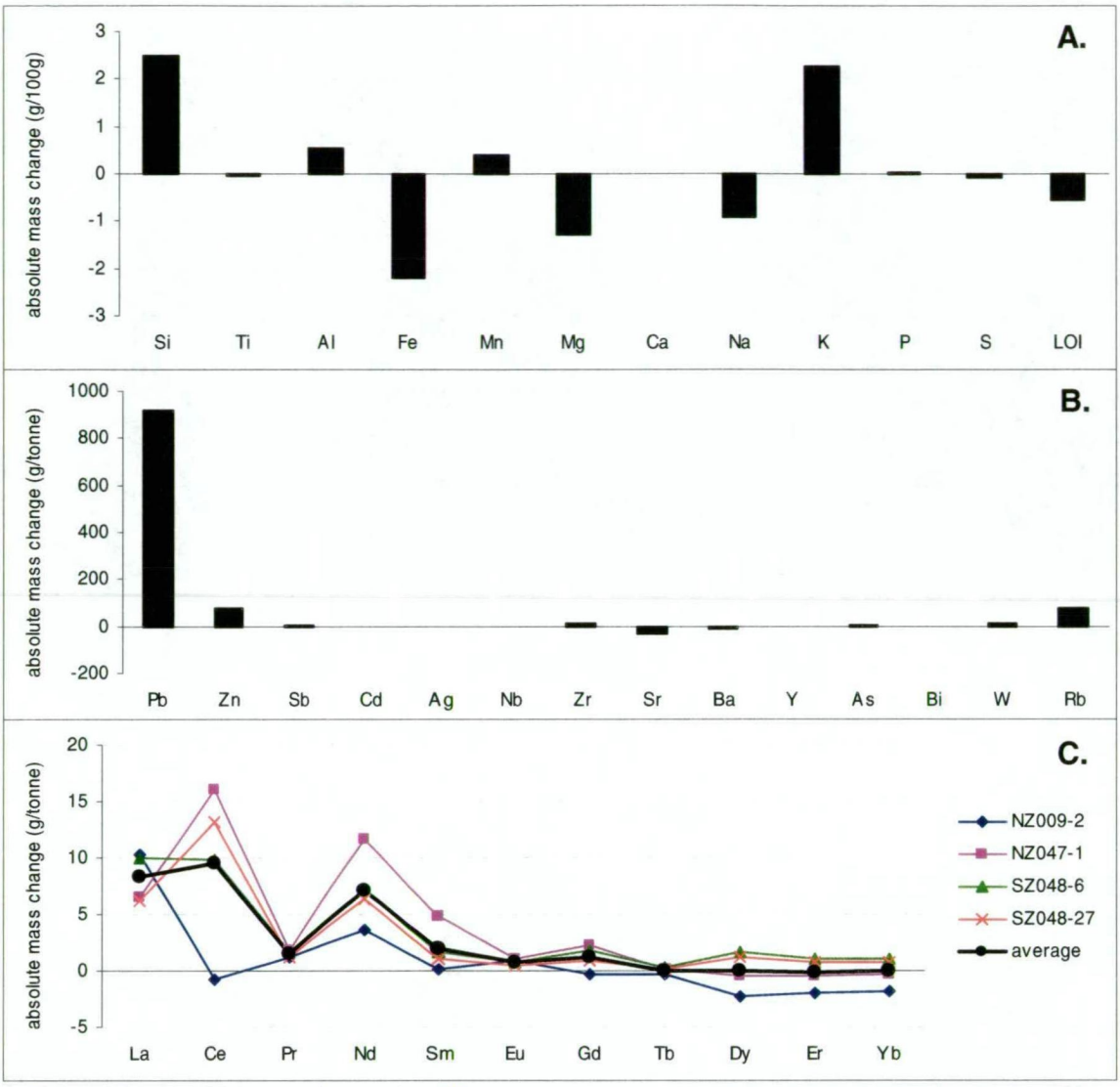

Figure 6.8 Absolute mass changes for sillimanite-garnet schist calculated using an average precursor pelitic gneiss composition. **A.** average mass changes for major elements. **B.** average mass changes for trace elements. **C.** absolute REE profiles. See Table 6.6 for standard deviations.

presented in Table 6.8 and Figure 6.10. Due to variations in the immobile element concentrations amongst the samples, there are considerable ranges in calculated mass changes. Absolute net mass gains are common to all samples and range from 25.0 to 15.7g/100g. Relative net mass gains range from 35.3 to 596.1%. The most significant average mass gains occur in Si, Fe, Mn, Ca, P, and S for the major elements, and Pb, Zn, Sb, Cd, Ag, As, and W for the trace elements (Fig. 6.10a and b). Absolute mass losses in Mg, and Na are characteristic to most samples, whereas variable mass losses or gains occur in Al, K, LOI, Zr, Sr, Ba, and Rb. Addition in total REE occurs in all samples except for one: the latter possesses the lowest net mass gain. Absolute mass change profiles for the REE are consistent between all the samples, with the greatest mass changes restricted to the LREE, especially La, Ce and Nd (Fig. 6.10c). Mass gains in Eu are also a significant feature of the REE profiles. Large net mass gains suggest that large net volume gains were associated with the formation of biotite-garnet facies ores. Calculated relative volume changes range from 13.8% for samples with the lowest net mass gains, to 478.3% for samples with the greatest.

Calculated mass changes for apatite-quartz facies ores are presented in Table 6.9 and Figure

Table 6.7 Calculated absolute mass changes in gahnite-bearing sillimanite-biotite-garnet schists using an average pelitic precursor gneiss composition.

Sample no.	NZ027-4	NZ004-10	NZ047-7	SZ061-50	NZ160-33	average	Standard deviation
(g/100g)							
Si	2.5	4.0	8.5	7.6	-0.9	4.3	3.8
Ti	0.0	0.0	0.0	0.0	0.0	0.0	0.0
Al	-0.5	1.5	0.4	-0.2	0.2	0.3	0.7
Fe	-1.6	-1.3	0.3	-1.6	-1.0	-1.1	0.8
Mn	0.2	0.2	0.4	0.1	0.6	0.3	0.2
Mg	-0.9	-1.1	-0.9	-1.0	-1.1	-1.0	0.1
Ca	-0.1	0.0	0.0	0.0	0.0	0.0	0.1
Na	-0.8	-1.0	-0.4	-0.9	-0.9	-0.8	0.2
K	0.9	1.0	3.0	1.3	2.7	1.8	1.0
P	0.0	0.0	0.0	0.0	0.1	0.0	0.0
S	-0.1	-0.1	0.0	-0.1	0.1	0.0	0.1
LOI	1.4	2.0	1.3	1.7	1.2	1.5	0.4
(g/tonne)							
Pb	470.2	807.9	1111.0	426.9	991.6	761.5	305.8
Zn	4702.4	1774.2	14654.9	284.9	2858.9	4855.1	5710.1
Sb	7.2	3.2	7.4	3.3	24.3	9.1	8.8
Cd	4.0	4.3	5.0	-0.1	7.2	4.1	2.6
Ag	-0.1	-0.1	-0.1	-0.1	2.6	0.4	1.2
Nb	0.4	2.2	-1.0	2.8	0.4	1.0	1.5
Zr	4.8	-17.2	4.0	10.2	-1.5	0.1	10.5
Sr	-36.1	-42.5	-21.8	-40.2	-29.5	-34.0	8.4
Ba	-98.5	-221.0	129.3	-331.6	54.7	-93.4	190.1
Y	0.3	-1.1	15.6	-11.3	23.0	5.3	13.8
As	8.1	13.0	23.4	4.4	44.0	18.6	15.9
Bi	0.3	-0.1	0.1	-0.1	0.6	0.2	0.3
W	5.6	7.6	24.1	9.0	23.9	14.0	9.2
Rb	16.3	23.1	72.6	43.9	63.6	43.9	24.5
La	22.4	-22.9	-10.0	-16.5	86.2	11.8	45.1
Ce	45.4	-51.4	-17.1	-41.8	141.9	15.4	80.2
Pr	4.0	-6.0	-2.6	-4.7	18.9	1.9	10.2
Nd	12.7	-22.4	-11.5	-17.7	68.7	6.0	37.6
Sm	1.4	-3.7	-2.0	-2.9	10.9	0.7	6.0
Eu	0.4	-0.1	0.2	1.5	1.5	0.7	0.8
Gd	1.0	-1.5	-0.5	-1.7	5.8	0.6	3.1
Tb	0.3	-0.1	0.2	-0.3	1.0	0.2	0.5
Dy	0.9	0.7	2.4	-1.0	4.4	1.5	2.0
Er	0.7	0.4	2.3	-0.6	2.8	1.1	1.4
Yb	0.9	0.3	1.9	-0.4	2.4	1.0	1.1
DF	1.02	1.09	1.24	1.14	0.98	1.09	0.10
ΔMR%	2.2	9.3	23.7	13.5	-1.9	9.4	10.0
ΔM (g/100g)	1.5	5.6	14.1	7.0	1.4	5.9	5.2
density (g/cc)	2.7	2.7	2.7	2.7	2.7	2.7	0.0
ΔV%	2.2	9.3	23.7	13.5	-1.9	9.4	10.0

DF — dilution factor, which is the average of the Al_p/Al_a and Ti_p/Ti_a immobile element ratios (<1 – net mass loss, >1 – net mass gain).
ΔMR% — relative net mass change.
ΔM — absolute net mass change.
ΔV% — relative net volume change.

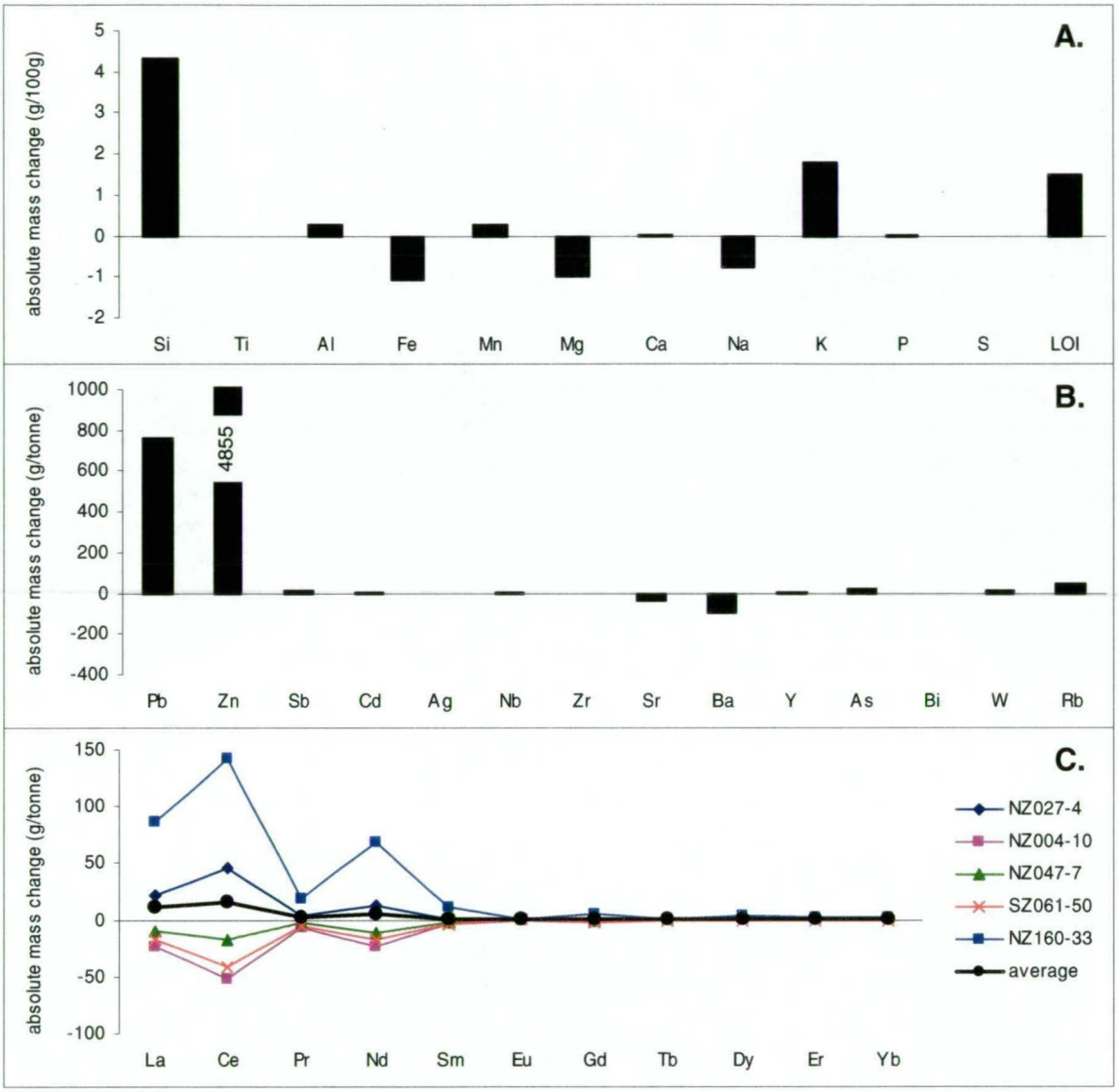

Figure 6.9 Absolute mass changes for gahnite-bearing schist using a calculated Al-rich pelite precursor (see Table 6.5). **A.** average mass changes for major elements. **B.** average mass changes for trace elements. **C.** absolute REE profiles. See Table 6.7 for standard deviations.

6.11. Absolute net mass gains range from 227.1 to 398.7g/100g, with an average of 301.7g/100g. Relative net mass gains range from 421.6 to 759.9%, with an average of 537.1%. The most significant average absolute mass gains occur in Si, Fe, Mn, Ca, P, and S for the major elements, and Pb, Zn, Sb, Cd, Ag, As, and W for the trace elements (Fig. 6.11a and b). Absolute mass losses in Al, Mg, Na, K, Nb, Ba and Rb are characteristic to most samples. Significant mass gains in total REE occur in all samples. Absolute REE profiles are consistent between all the samples, with the greatest mass changes occurring in Eu and the LREE, especially La, Ce and Nd (Fig. 6.11c). Calculated relative volume changes range from 326.8 to 603.5%, with an average of 421.2%.

Calculated mass changes for olivine facies ores are presented in Table 6.10 and Figure 6.12. Absolute net mass gains in olivine facies ores are higher than biotite-garnet and quartz-apatite facies ores. Calculated mass changes are extremely variable due to variations in the immobile element concentrations amongst the samples. Absolute net mass gains range from 267.7 to 1834.4g/100g, with an average of 743.5g/100g. Relative net mass gains range from 357.8 to

Table 6.8 Calculated absolute mass changes in biotite-garnet facies ores using an average precursor pelitic gneiss composition.

Sample no.	NZ016-1	NZ029-8	NZ033-2	NZ039-3	NZ047-8	NZ029-13	SZ157-11	NZ160-31	Average	Standard deviation
(g/100g)										
Si	145.7	14.2	29.0	29.2	1.7	15.3	73.3	26.6	41.9	43.9
Ti	0.0	0.0	0.0	0.0	0.0	0.0	0.0	0.0	0.0	0.0
Al	-2.2	-0.9	1.6	-0.5	-0.5	0.2	-1.0	2.7	-0.1	1.5
Fe	18.7	18.3	26.5	35.9	19.6	28.6	16.8	33.4	24.7	6.9
Mn	3.3	7.2	6.9	7.9	4.6	9.1	0.9	7.0	5.9	2.6
Mg	-0.5	-0.9	-0.6	1.3	-0.9	-0.2	-0.7	-0.1	-0.3	0.7
Ca	37.0	11.1	13.2	15.8	2.0	12.3	6.0	11.0	13.5	9.7
Na	-1.2	-0.8	-1.2	0.1	-1.1	-0.9	-1.2	-1.2	-0.9	0.4
K	-2.4	-0.5	0.6	1.1	-1.7	0.4	-3.0	-3.3	-1.1	1.6
P	14.1	4.6	4.5	6.5	0.6	5.3	1.3	3.6	5.1	3.9
S	30.7	6.4	13.4	12.6	1.9	9.8	0.5	50.1	15.7	15.7
LOI	13.5	3.1	5.5	11.1	-1.5	7.5	0.0	23.4	7.8	7.6
Pb	145.7	24.8	16.7	8.4	0.1	12.4	3.5	0.2	26.5	45.7
Zn	12.5	5.1	16.6	17.8	0.3	12.3	0.2	80.5	18.2	24.4
(g/tonne)										
Sb	2491.2	150.6	831.9	284.6	6.4	110.3	150.0	158.4	522.9	780.5
Cd	501.8	178.6	478.1	457.4	9.9	391.8	-0.1	2476.2	561.7	748.5
Ag	2171.0	906.8	963.9	493.2	-0.1	224.5	84.7	73.7	614.7	684.5
Nb	-18.5	-11.0	-11.0	-7.8	-0.5	-8.5	-2.5	-11.9	-9.0	5.3
Zr	8.3	-1.7	-5.4	6.2	2.5	-14.7	11.7	-8.8	-0.2	8.5
Sr	273.1	80.0	65.6	142.3	-51.8	135.6	-19.4	-38.8	73.3	103.4
Ba	-305.9	79.0	-236.6	275.8	-432.4	52.2	-550.5	-541.2	-207.5	290.1
Y	128.1	12.8	54.0	23.2	34.5	13.4	-30.6	42.9	34.8	42.6
As	62.5	160.1	684.3	97.8	14.8	59.8	242.5	105.8	178.5	202.0
Bi	3.4	1.0	8.3	1.1	0.0	0.6	0.5	3.9	2.4	2.6
W	2659.0	1422.0	51.9	1495.3	1009.3	11.9	33.0	176.3	857.3	901.5
Rb	-173.1	187.7	332.7	252.2	43.4	285.3	-186.1	-191.2	68.9	211.0
La	196.7	37.7	45.6	45.4	-36.3	47.6	6.8	108.1	56.5	65.3
Ce	311.1	61.0	17.5	49.2	-66.5	61.9	1.9	160.8	74.6	107.7
Pr	31.6	5.4	1.9	6.5	-7.4	7.3	0.5	17.7	7.9	11.1
Nd	120.5	15.1	3.9	25.4	-26.8	28.4	1.9	71.7	30.0	43.1
Sm	29.7	1.8	2.1	6.4	-2.5	5.5	0.8	11.8	7.0	9.5
Eu	64.0	12.5	14.1	12.7	0.8	18.6	19.1	8.9	18.9	17.9
Gd	30.3	2.0	3.1	6.3	1.4	5.5	2.3	10.9	7.7	9.0
Tb	5.1	0.5	0.7	0.9	0.4	0.6	0.2	1.9	1.3	1.5
Dy	22.5	2.6	4.5	3.5	5.3	2.5	0.2	7.8	6.1	6.5
Er	10.0	1.6	4.4	2.1	3.4	0.2	-0.7	2.9	3.0	3.1
Yb	4.7	1.0	3.5	1.2	1.8	0.0	-0.9	1.7	1.6	1.7
DF	6.96	2.23	2.89	3.01	1.35	2.50	2.85	3.65	3.18	1.56
ΔMR%	596.1	122.6	188.8	205.8	35.3	149.8	185.4	265.3	218.6	155.9
ΔM (g/100g)	415.7	92.1	133.0	147.5	25.0	112.1	96.5	234.3	157.0	112.3
density (g/cc)	3.3	3.3	3.5	3.5	3.2	3.3	2.8	3.5	3.3	0.2
ΔV%	478.3	83.8	126.0	133.2	13.8	104.4	171.3	180.2	161.4	129.4

DF — dilution factor, which is the average of the Zr_p/Zr_a and Ti_p/Ti_a immobile element ratios (<1 – net mass loss, >1 – net mass gain).
ΔMR% — relative net mass change.
ΔM — absolute net mass change.
ΔV% — relative net volume change.

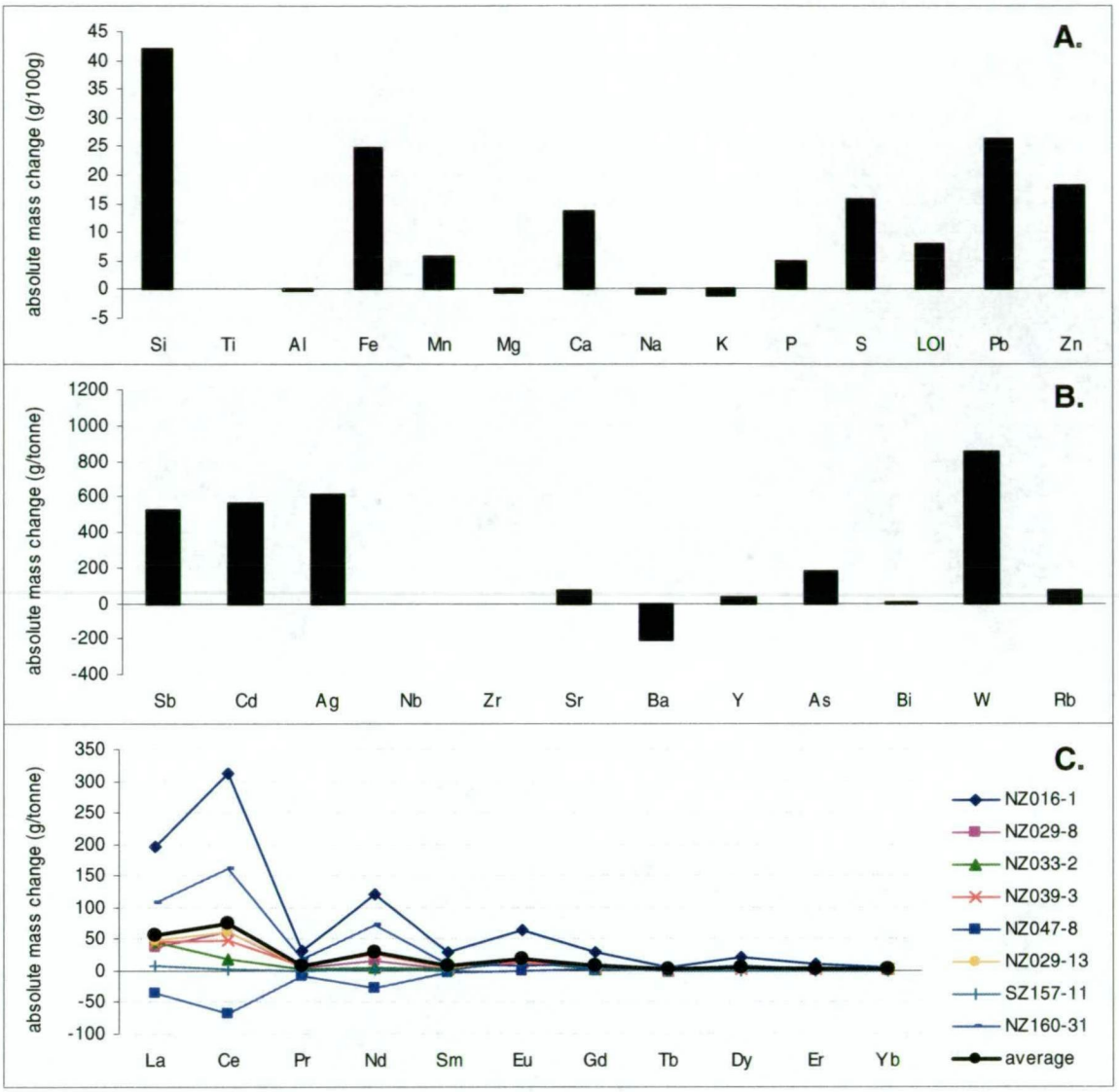

Figure 6.10 Absolute mass changes for biotite-garnet facies ores calculated using an average precursor pelitic gneiss composition. **A.** average mass changes for major elements. **B.** average mass changes for trace elements. **C.** absolute REE profiles. Standard deviations are very high for some elements (see Table 6.8).

3458.7%, with an average of 1244.6%. The most significant average absolute mass gains occur in Si, Fe, Mn, Ca, P and S for the major elements, and Pb, Zn, Sb, Cd, Ag, Sr, Y, As, and W for the trace elements (Fig. 6.12a and b). Nb shows both mass losses and gains amongst the samples. The largest average absolute mass losses occur in Na, K, LOI, Ba and Rb. Significant mass gains in total REE occur in all samples and absolute REE profiles are the same as quartz-apatite ores (Fig. 6.12c). Calculated relative volume changes are extremely large, ranging from 217.8 to 2469.1%, with an average of 868.5%.

Overall, graphitic ores consistently display absolute net mass gains, the smallest associated with biotite-garnet facies ores and the largest with olivine facies ores. The most significant gains occur in Si, Fe, Mn, Ca, P and S for the major elements, and Pb, Zn, Sb, Cd, Ag, As and W. The most significant mass losses occur in Na, K and Ba. Gains in Rb are characteristic of the biotite-garnet facies, whereas losses are intrinsic to the quartz-apatite and olivine ore facies. Mass gains and losses occur in Al in the biotite-garnet ore facies, whereas consistent mass losses occur in the quartz-apatite and olivine ore facies. Mass gains in total REE occur

Table 6.9 Calculated absolute mass changes in quartz-apatite facies ores using an average precursor pelitic gneiss composition.

Sample no.	NZ040-4b	NZ030-13	NZ035-13	Average	Standard deviation
(g/100g)					
Si	320.6	132.4	170.8	207.9	99.4
Ti	0.0	0.0	0.0	0.0	0.0
Al	-7.2	-4.1	-2.9	-4.7	2.2
Fe	7.3	14.7	18.5	13.5	5.7
Mn	4.2	0.8	8.0	4.4	3.6
Mg	-1.4	-0.8	-1.1	-1.1	0.3
Ca	15.6	6.4	12.8	11.6	4.7
Na	-0.6	-1.2	-1.0	-0.9	0.3
K	-3.4	-0.5	-2.6	-2.2	1.5
P	6.8	1.0	4.4	4.1	2.9
S	12.8	17.2	5.3	11.8	6.0
LOI	12.5	4.0	2.1	6.2	5.5
Pb	12.3	107.3	7.9	42.5	56.2
Zn	18.9	1.4	4.8	8.3	9.3
(g/tonne)					
Sb	561.4	1280.9	335.8	726.0	493.6
Cd	896.7	117.3	181.1	398.4	432.8
Ag	284.5	1200.6	117.0	534.0	583.3
Nb	0.4	-18.5	-4.7	-7.6	9.8
Zr	10.8	-0.7	10.5	6.9	6.6
Sr	139.9	-12.2	60.3	62.7	76.0
Ba	-497.3	61.4	-185.9	-207.3	279.9
Y	106.1	9.1	13.1	42.8	54.9
As	1091.9	505.8	582.6	726.8	318.5
Bi	0.8	167.3	-0.1	56.0	96.4
W	178.8	2712.2	38.6	976.5	1504.8
Rb	-197.6	126.1	-83.0	-51.5	164.1
La	674.0	161.2	83.7	306.3	320.8
Ce	1009.8	180.8	109.9	433.5	500.3
Pr	110.3	14.6	11.2	45.4	56.3
Nd	416.3	42.6	37.7	165.5	217.2
Sm	76.2	9.7	7.9	31.3	38.9
Eu	222.6	55.8	44.8	107.7	99.6
Gd	56.6	7.3	8.6	24.2	28.1
Tb	6.9	1.3	1.4	3.2	3.2
Dy	22.1	3.5	3.1	9.6	10.9
Er	5.5	1.0	1.2	2.6	2.5
Yb	1.5	0.5	-0.5	0.5	1.0
DF	8.60	5.22	5.30	6.37	1.93
ΔMR%	759.9	421.6	429.8	537.1	193.0
ΔM (g/100g)	398.7	279.4	227.1	301.7	87.9
density (g/cc)	3.3	3.3	3.3	3.3	0.0
ΔV%	603.5	326.8	333.4	421.2	157.9

DF — dilution factor, which is the average of the Zr_p/Zr_a and Ti_p/Ti_a immobile element ratios (<1 – net mass loss, >1 – net mass gain).
ΔMR% — relative net mass change.
ΔM — absolute net mass change.
ΔV% — relative net volume change.

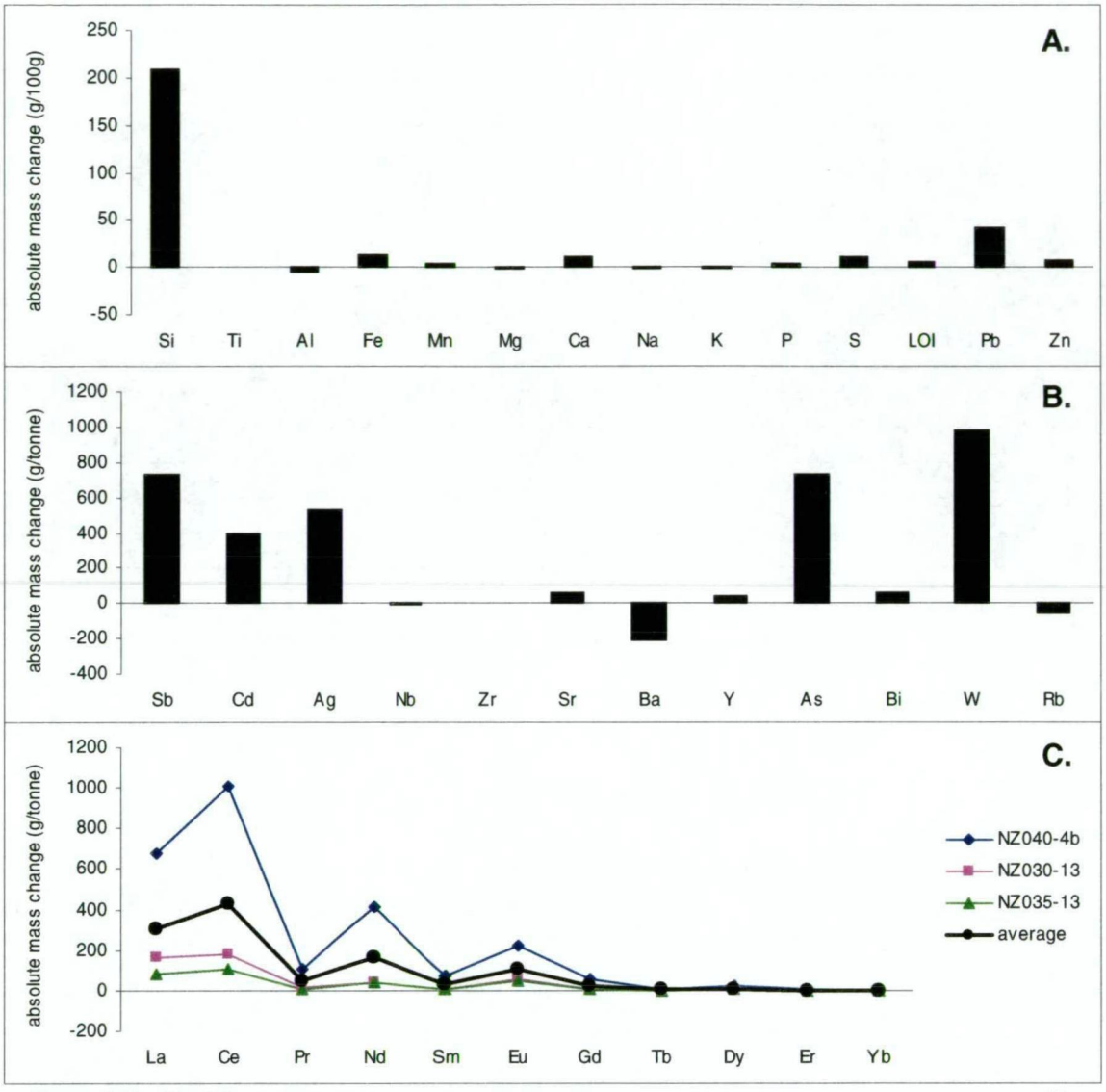

Figure 6.11 Absolute mass changes for quartz-apatite facies ores calculated using an average precursor pelitic gneiss composition. **A.** average mass changes for major elements. **B.** average mass changes for trace elements. **C.** absolute REE profiles. Standard deviations are very high for some elements (see Table 6.9).

in all ore facies, with the greatest gains occurring in the LREE, especially La, Ce and Nd. Absolute mass change profiles for the REE in all ore facies are very similar, except for mass losses in LREE in some biotite-garnet facies ores. The calculations indicate that the LREE were significantly more mobile than the HREE during ore formation. In particular, the profiles are very similar to the gahnite-bearing schist, suggesting that the same hydrothermal fluids responsible for ore formation interacted with the gahnite-bearing schist protolith.

6.5.4 Stage IIa Metasomatism

Stage IIa hedenbergite-garnet-quartz alteration is common throughout the orebody. To gauge the geochemical effects of alteration on pre-existing ores, a well constrained altered and unaltered pair was chosen. The sample consists of banded olivine facies ore overprinted by a hedenbergite (-fluorite-galena) vein at high angle to the banding (Fig. 6.13). The vein overprints a weak S_1/S_2 foliation defined by the preferred alignment of olivine grain aggregates in the olivine facies ore, indicating a post-D_2 timing. Such examples are common in parts of the deposit (Chapter 4; Chapman, 1993; Bodon, 1995, 1998; Chapman and Williams, 1998;

Table 6.10 Calculated absolute mass changes in olivine facies ores using an average precursor pelitic gneiss composition.

Sample no.	NZ040-4a	NZ044-2	NZ044-5	NZ070-4	NZ160-20	NZ047-2	Average	Standard deviation
(g/100g)								
Si	212.7	23.0	189.6	1202.8	121.7	31.2	296.8	450.7
Ti	0.0	0.0	0.0	0.0	0.0	0.0	0.0	0.0
Al	-4.0	-1.7	-0.6	-4.7	0.8	-4.1	-2.4	2.2
Fe	345.3	93.8	240.3	546.7	245.8	150.1	270.3	160.7
Mn	99.6	31.1	90.7	104.4	98.6	34.4	76.5	34.2
Mg	0.3	0.0	0.3	0.2	2.5	-0.3	0.5	1.0
Ca	40.0	36.9	28.6	32.2	111.6	8.2	42.9	35.5
Na	-1.2	-0.5	-1.2	0.4	0.6	-1.2	-0.5	0.8
K	-3.5	-3.4	-3.5	-2.3	-3.0	2.3	-2.2	2.3
P	10.7	7.9	8.2	4.9	40.8	3.1	12.6	14.1
S	20.0	12.1	3.5	2.7	29.2	21.3	14.8	10.6
LOI	-32.5	2.0	-23.7	-72.1	-21.8	9.8	-23.1	29.0
Pb	6.2	60.9	9.0	11.7	82.3	88.3	43.1	38.5
Zn	35.8	5.2	5.1	7.1	26.6	2.6	13.7	13.9
(g/tonne)								
Sb	533.0	1311.1	493.4	377.1	2853.1	1622.7	1198.4	953.4
Cd	1451.0	185.3	99.4	99.5	909.1	48.6	465.5	581.1
Ag	159.7	1349.6	497.4	181.4	1927.2	1356.3	911.9	733.6
Nb	3.2	-13.0	4.8	45.5	-1.8	-12.9	4.3	21.6
Zr	-8.8	-1.3	4.2	4.0	2.1	16.1	2.7	8.1
Sr	349.0	120.4	147.1	135.7	1344.0	24.8	353.5	496.7
Ba	-470.0	-565.7	-498.3	-137.2	-496.9	560.6	-267.9	433.2
Y	258.4	126.5	118.6	44.2	145.5	-6.3	114.5	91.0
As	166.1	160.1	40.5	177.8	2347.7	318.9	535.2	892.3
Bi	-0.1	7.7	2.9	-0.1	1.1	10.0	3.6	4.3
W	213.4	1291.0	60.8	323.7	141.2	245.0	379.2	455.6
Rb	-196.5	-207.4	-213.4	-29.6	-195.8	449.7	-65.5	261.9
La	409.0	239.9	160.8	513.9	576.8	68.6	328.2	203.0
Ce	653.3	394.6	251.4	654.5	797.1	69.4	470.0	278.8
Pr	80.3	40.2	31.8	71.4	83.2	6.8	52.3	30.8
Nd	349.6	140.5	139.8	266.8	293.9	17.9	201.4	123.3
Sm	86.7	26.8	39.4	48.7	57.5	4.0	43.9	28.1
Eu	288.3	68.3	75.0	308.2	279.0	20.6	173.2	131.6
Gd	86.7	22.0	36.7	36.9	61.2	1.8	40.9	29.8
Tb	11.8	3.8	5.4	-0.9	9.1	0.1	4.9	5.0
Dy	50.6	17.0	22.6	9.5	29.3	-0.5	21.4	17.7
Er	19.0	9.6	8.6	6.2	8.9	-0.9	8.6	6.4
Yb	11.4	7.2	5.3	-2.6	3.6	-1.3	3.9	5.3
DF	12.79	4.58	10.13	35.59	11.98	5.6	13.44	11.4
ΔMR%	1178.5	357.8	915.4	3458.7	1097.8	459.6	1244.6	1134.8
ΔM (g/100g)	729.8	267.7	546.6	1834.3	736.9	346.1	743.5	568.0
density (g/cc)	3.2	3.9	3.7	3.7	4.4	3.9	3.8	0.4
ΔV%	972.1	217.8	633.0	2469.1	628.4	290.4	868.5	829.9

DF — dilution factor, which is the average of the Zr_p/Zr_a and Ti_p/Ti_a immobile element ratios (<1 – net mass loss, >1 – net mass gain).
ΔMR% — relative net mass change.
ΔM — absolute net mass change.
ΔV% — relative net volume change.

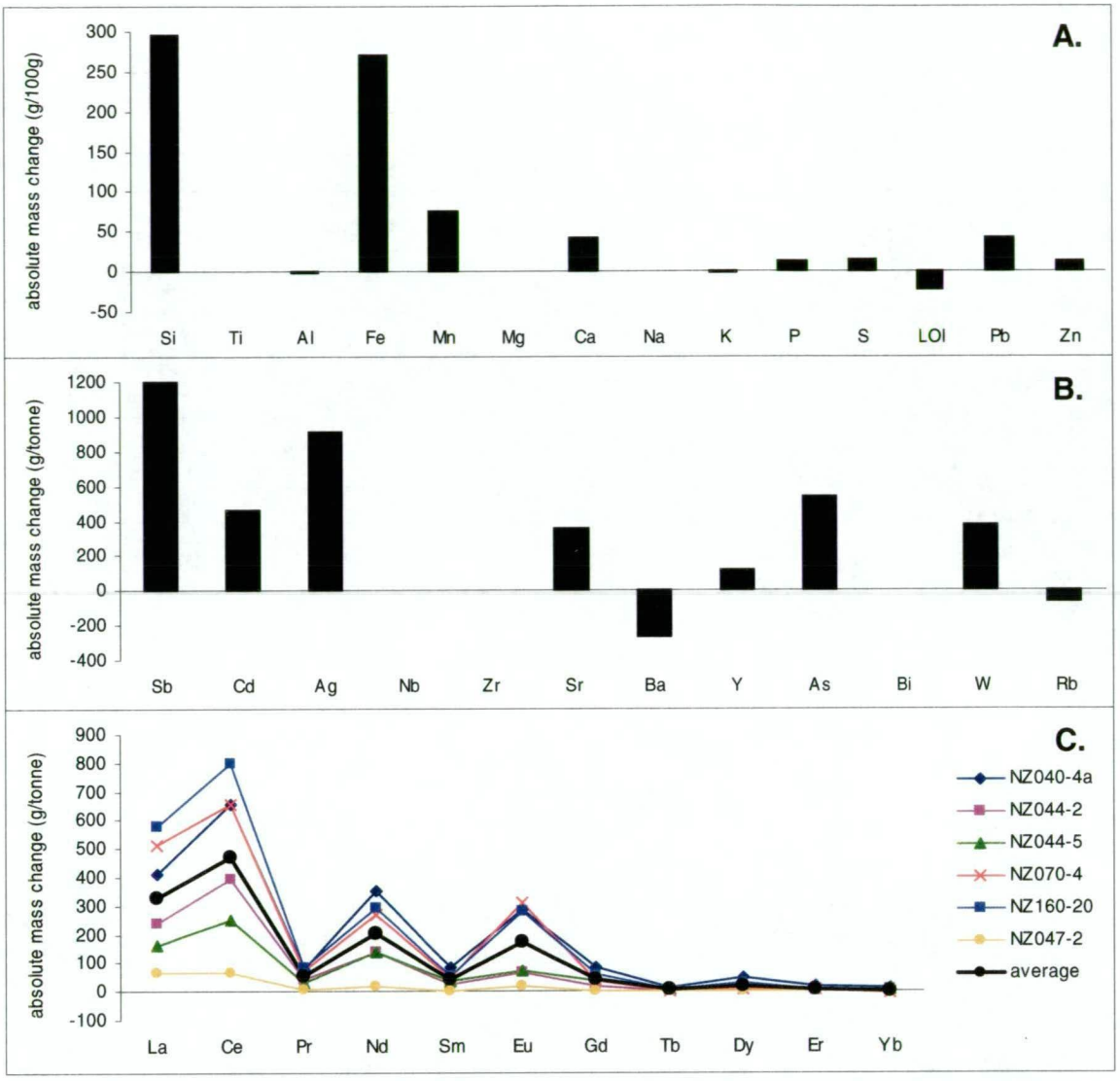

Figure 6.12 Absolute mass changes for olivine facies ores calculated using an average precursor pelitic gneiss composition. **A.** average mass changes for major elements. **B.** average mass changes for trace elements. **C.** absolute REE profiles. Standard deviations are very high for some elements (see Table 6.10).

Pringle, 1999). An ~5cm wide alteration selvedge is characterised by garnet-quartz and hedenbergite-garnet alteration of the olivine-rich bands, and silicification of quartz-apatite bands (Fig. 6.13). The "altered" sample taken from the selvedge did not include the hedenbergite vein. Bivariate plots involving Al, Ti and Zr indicate that these elements were immobile during metasomatism (not shown). Ti is the most consistent immobile element and was therefore chosen as the basis for the mass balance calculation.

Calculated mass changes are presented in Table 6.11 and Figure 6.14. Stage IIa metasomatism resulted in an overall absolute net mass loss of -5.1g/100g, or an absolute relative net mass loss of -11.1%. Relative net volume loss is equivalent to the relative net mass loss because the densities of the altered and unaltered samples are the same. Hence, the volume losses were negligible. The most significant absolute mass gains occur in Ca (0.94g/100g), S (0.57g/100g), LOI (1.64g/100g), Pb (4.88g/100g), Sb (30.20ppm), Ag (51.69ppm), and Y (27.1ppm). Absolute mass losses occur in Si (-4.12g/100g), Fe (-7.20g/100g), Mn (-2.06g/100g), Zn (-0.29g/100g), As (-30.56ppm), with smaller losses in Cd (-

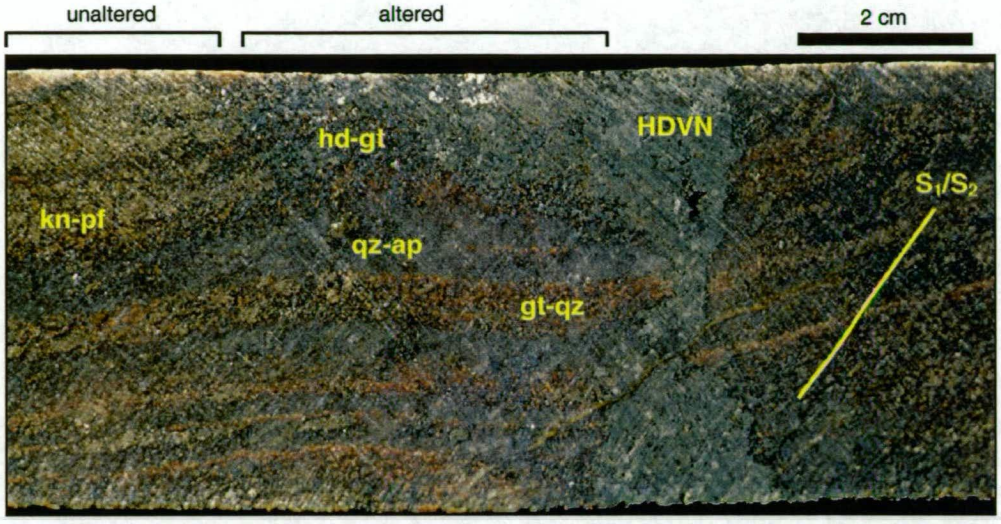

Figure 6.13 Photograph of the sample used to calculate mass changes associated with Stage IIa hedenbergite-garnet-quartz alteration of banded olivine facies ore. A post-D_2 hedenbergite vein (HDVN) overprints the compositional banding and the S_1/S_2 foliation (defined by the alignment of knebelite-pyroxferroite aggregates). Knebelite-pyroxferroite bands (kn-pf) have been selectively altered to garnet-quartz (gt-qz) and hedenbergite-garnet (hd-gt). Quartz-apatite bands (qz-ap) have been silicified. The zones marked 'unaltered' and 'altered' depict the portions of the rock that were sampled for wholerock geochemistry. The sample is the same as that in Figure 4.11f (NZ016-2, CAD016, 81.3m).

Table 6.11 Calculated absolute mass changes associated with hedenbergite-garnet-quartz alteration of olivine facies ore (sample no. NZ016-2).

Element	Absolute mass change (g/100g)	Element	Absolute mass change (g/tonne)
Si	-4.12	Sb	30.20
Ti	0.00	Cd	-2.37
Al	0.56	Ag	51.69
Fe	-7.20	Nb	-1.62
Mn	-2.06	Zr	10.41
Mg	0.02	Sr	-3.07
Ca	0.94	Ba	-1.49
Na	0.05	Y	27.13
K	0.01	As	-30.56
P	-0.10	Bi	0.27
S	0.57	W	-7.73
LOI	1.64	Rb	-0.27
Pb	4.88	La	-0.90
Zn	-0.29	Ce	-0.67
		Pr	-0.16
		Nd	-0.69
DF	0.89	Sm	-0.33
ΔMR%	-11.11	Eu	-0.63
ΔM (g/100g)	-5.09	Gd	-0.09
density (g/cc)	3.91	Tb	0.01
ΔV%	-11.11	Dy	1.23
		Er	1.94
		Yb	1.97

DF — dilution factor, which is the average of the Al_p/Al_a and Ti_p/Ti_a immobile element ratios (<1 — net mass loss, >1 — net mass gain).
ΔMR% — relative net mass change.
ΔM — absolute net mass change.
ΔV% — relative net volume change.

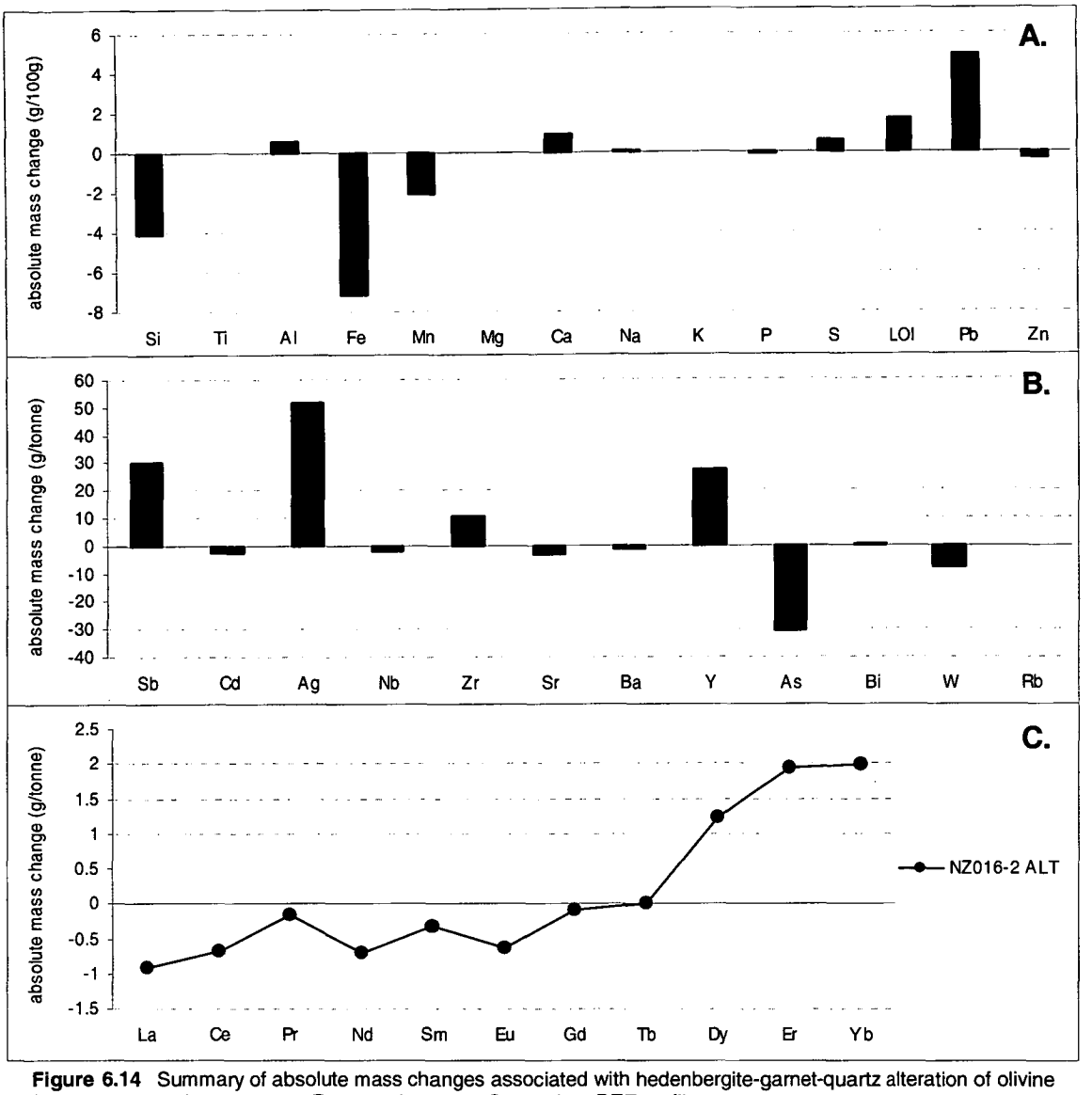

Figure 6.14 Summary of absolute mass changes associated with hedenbergite-garnet-quartz alteration of olivine facies ore. **A.** major elements. **B.** trace elements. **C.** absolute REE profiles.

2.37ppm), Sr (-3.07ppm), Ba (-1.49ppm) and W (-7.73ppm). Total HREE have undergone a mass gain of 5.06ppm, whereas total LREE including Eu, have undergone a mass loss of -3.39ppm. These trends in REE are also manifested in their absolute abundances when normalised to chondrite (Fig. 6.15h). Overall, these alteration trends are very different to those in graphitic ores.

6.6 HYDROTHERMAL REE SIGNATURES

Chondrite normalised REE patterns for host rocks, ores and the metasomatised sample are presented in Figure 6.15. La/Sm and Gd/Yb ratios and calculated Eu anomalies (Eu/Eu*=Eu/$\sqrt{SmxGd}$; Taylor and McLennan, 1985) are presented in Table 6.12. Amphibolites are characterised by flat REE profiles (Fig. 6.15a), whereas profiles in the gneiss are similar to the average crustal shale profile (NASC shale after Gromet et al., 1984), displaying comparatively slight LREE enrichment and HREE depletion and a stronger negative Eu anomaly (Fig. 6.15b). The REE profiles in the gneiss are similar to those in host gneiss from the Broken Hill and Pinnacles deposits in New South Wales (Lottermoser, 1989; Parr, 1992). However, the gneiss

at Cannington do not display the notable negative Eu anomalies that characterise the gneiss at the Pinnacles deposit (Parr, 1992).

Garnetiferous rocks have similar REE profiles to the gneiss (Fig 6.15c and d), but abundances and La/Sm and Gd/Yb ratios are more variable (Table 6.12). Eu anomalies are slightly larger in comparison to the gneissic rocks (Table 6.12). One gahnite-bearing schist sample has a distinct positive Eu anomaly (Eu/Eu*=2.01; Fig 6.15d), and one sillimanite-garnet schist sample is depleted in HREE compared to other sillimanite-garnet schist samples (Fig 6.15c).

Positive Eu anomalies are intrinsic to graphitic ores (Fig. 6.15e to g). However, the Eu

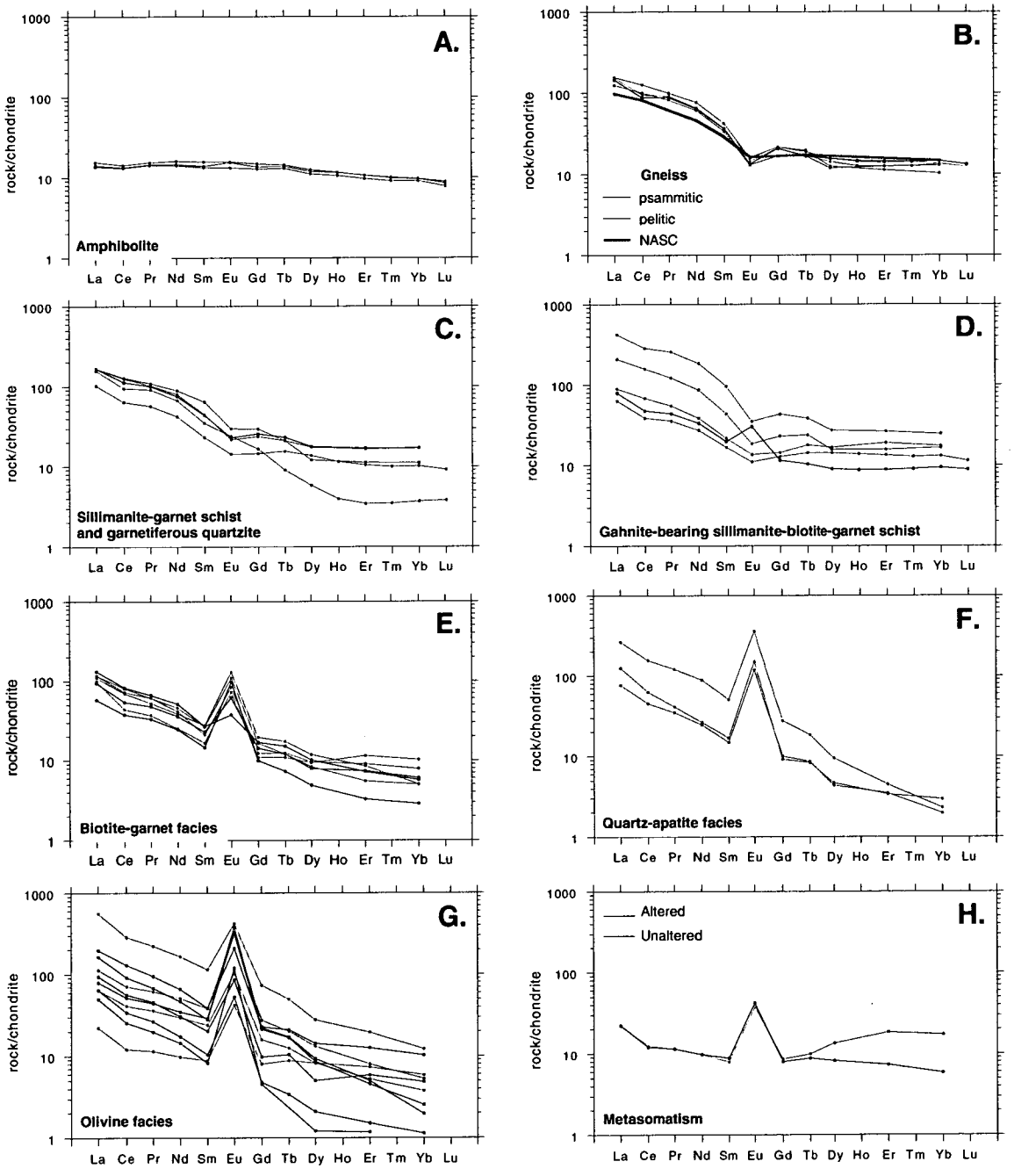

Figure 6.15 Chondrite normalised REE plots for host rocks, graphitic ores and hedenbergite-garnet-quartz metasomatised olivine facies ore. **A.** amphibolite. **B.** psammitic and pelitic gneiss. **C.** sillimanite-garnet schist and garnetiferous quartzite. **D.** gahnite-bearing sillimanite-biotite-garnet schist. **E.** biotite-garnet facies. **F.** quartz-apatite facies. **G.** olivine facies. **H.** metasomatised olivine facies ore.

Table 6.12 Chondrite normalised ranges in La/Sm, Gd/Yb ratios and Eu anomalies (Eu/Eu*) for host rocks and graphitic ores.

Rock/ore type	La/Sm	Gd/Yb	Eu/Eu*
Amphibolite	0.99 - 1.03	1.55 - 1.39	1.01 - 1.12
Psammitic gneiss	4.17	1.55 - 1.59	0.52 - 0.57
Pelitic gneiss	3.72 - 3.99	1.31 - 2.08	0.48 - 0.54
Sillimanite-garnet schist	2.61 - 4.54	1.39 - 4.55	0.67 - 1.00
Gahnite-bearing sillimanite-biotite-garnet schist	3.79 - 4.79	0.83 - 1.74	0.55 - 2.01
Biotite-garnet facies ore	1.11 - 5.95	1.07 - 3.89	1.02 - 8.07
Quartz-apatite facies ore	5.19 - 7.45	3.13 - 12.04	9.62 - 9.81
Olivine facies ore	2.52 - 6.18	1.37 - 11.32	4.60 - 19.73
Unmetasomatised olivine facies ore	2.52	1.37	5.03
Metasomatised olivine facies ore	2.73	0.50	4.54

$Eu/Eu^* = Eu/\sqrt{Sm \times Gd}$

anomalies in biotite-garnet facies ores are smaller than those in quartz-apatite and olivine facies ores (Table 6.12; Fig. 6.15e to g). Quartz-apatite facies ores generally have the highest La/Sm and Gd/Yb ratios (Table 6.12). In the metasomatised-unmetasomatised sample pair, metasomatism resulted in enrichment of HREE (Fig. 6.15h).

6.6.1 Methods

Hydrothermal REE signatures in the garnetiferous host rocks and graphitic ores can be calculated using a similar normalising method to the mass balance calculations. By normalising the immobile element in the altered sample to its original concentration in the precursor it is possible to calculate the relative percentages of the combined hydrothermal and precursor components that comprise the altered rock or ore. For altered rocks and ores that have undergone net mass gains this can be calculated by:

(7) $P\% = (Ti_a/Ti_p) \times 100$

Where P% = the percentage of combined precursor components in the altered rock or ore, Ti_a = the concentration of Ti (%) in the altered rock or ore, and Ti_p = the concentration of Ti (%) in the precursor. The percentage of hydrothermal components comprising the altered rock or ore can be calculated by:

(8) $H\% = [1-(Ti_a/Ti_p)] \times 100$

Where H% = the percentage of combined hydrothermal components in the altered rock or ore. For rocks that have undergone a net mass loss, P% and H% can be calculated by simply reversing the immobile element dilution factor in the latter equations. For example:

(9) $P\% = (Ti_p/Ti_a) \times 100$

(10) $H\% = [1-(Ti_p/Ti_a)] \times 100$

Absolute concentrations of the REE in the hydrothermal component of the altered rock or ore can then be recalculated knowing H%, i.e. using the same immobile element dilution factor to produce a reconstructed concentration (C_r) using equation (1) in the mass calculations. The absolute concentrations (i.e. mass changes) can then be calculated using equation (2). These values represent the *absolute* REE abundances in the hydrothermal component only.

Negative concentrations (or mass losses) however, cannot be plotted on log-scale spidergrams. Instead, calculating the changes in REE concentrations relative to the precursor provides an arithmetic measurement of the changes in *relative* REE abundances, i.e. normalisation of the reconstructed composition of the altered rock or ore to the precursor. In this way, the hydrothermal REE signature can be isolated using:

(11) Hydrothermal REE signature = C_r/C_p

where C_r = reconstructed concentration of the particular element, and C_p = concentration of the particular element in the precursor. The calculation differs slightly from the relative % mass change for mobile elements in the mass balance equations, insomuch as values <1 equate to mass losses and values >1, mass gains. A value of 1 indicates that the element has not changed and was therefore immobile during hydrothermal alteration. Because negative values are not involved, the hydrothermal REE signatures can be easily plotted on a log-scale spidergram without having to apply an arbitrary correction factor.

From a mathematical point of view, normalisation reduces small versus large absolute mass changes to a common level, so that small variations in signatures can be easily detected. The method is therefore appropriate for resolving hydrothermal REE signatures in the altered host rocks and graphitic ores. It should be emphasised however, that normalised REE profiles differ from REE profiles of absolute mass changes. Overall, the method is more accurate than simply normalising the altered rock to its corresponding precursor, as it takes into account the mass changes associated with alteration and ore formation.

6.6.2 Results

In comparison to precursor compositions, all graphitic ores and garnetiferous host rocks have calculated hydrothermal REE signatures that possess lower La/Sm and Gd/Yb ratios, and variable positive Eu anomalies (compare Tables 6.12 and 6.13). Hydrothermal signatures in the sillimanite-garnet schists are generally flat (low La/Sm and Gd/Yb ratios), especially the LREE. Slight positive Eu anomalies occur in all samples (Fig. 6.16a). Two of the samples display notable depletion in HREE. The gahnite-bearing schists are also characterised by slightly negative to positive profiles with the majority displaying recognisable positive Eu anomalies (Fig. 6.16b). Two of the samples have near flat REE profiles with no Eu anomaly.

Table 6.13 Ranges in %hydrothermal component, La/Sm, Gd/Yb and Eu anomalies (Eu/Eu*) for calculated hydrothermal REE signatures in altered host rocks and graphitic ores.

Altered rock/ore type	%hydrothermal component	La/Sm	Gd/Yb	Eu/Eu*
Sillimanite-garnet schist	0.6 - 10.6	0.68 - 1.19	0.89 - 2.92	1.30 - 1.93
Gahnite-bearing sillimanite-biotite-garnet schist	1.1 - 23.4	1.00 - 1.26	0.53 - 1.11	1.06 - 3.90
Biotite-garnet facies ore	54.6 - 86.2	1.04 - 1.56	0.68 - 2.50	3.41 - 15.64
Quartz-apatite facies ore	80.7 - 89.0	1.36 - 1.96	2.01 - 7.70	18.65 - 23.53
Olivine facies ore	76.6 - 97.2	0.66 - 1.62	0.89 - 7.26	8.91 - 38.21
Metasomatised olivine facies ore		1.08	0.37	0.90

$Eu/Eu^* = Eu/\sqrt{Sm \times Gd}$

Mass balance calculations indicate that graphitic ores are enriched in ΣREE. Hydrothermal REE profiles are close to flat and all samples display strong positive Eu anomalies. Eu anomalies in biotite-garnet facies ores are less intense compared to quartz-apatite and olivine facies ores (Table 6.13; Fig. 6.16c to e). In addition, the calculated % total hydrothermal component in biotite-garnet facies ores is less than the quartz-apatite and olivine facies ores (Table 6.13), i.e. the % total pelitic precursor component is greater. Much of the variation in the hydrothermal profiles is restricted to the HREE for all ore facies.

The hydrothermal REE profile in the metasomatised sample displays no Eu anomaly and the Gd/Yb ratio is significantly less than the La/Sm ratio (Table 6.13, Fig. 6.16f). The sample differs from all other rock types, insomuch as the precursor positive Eu anomaly is greater than the calculated hydrothermal Eu anomaly signature. Like all other rock types, the greatest variations occur in the HREE relative to the precursor composition.

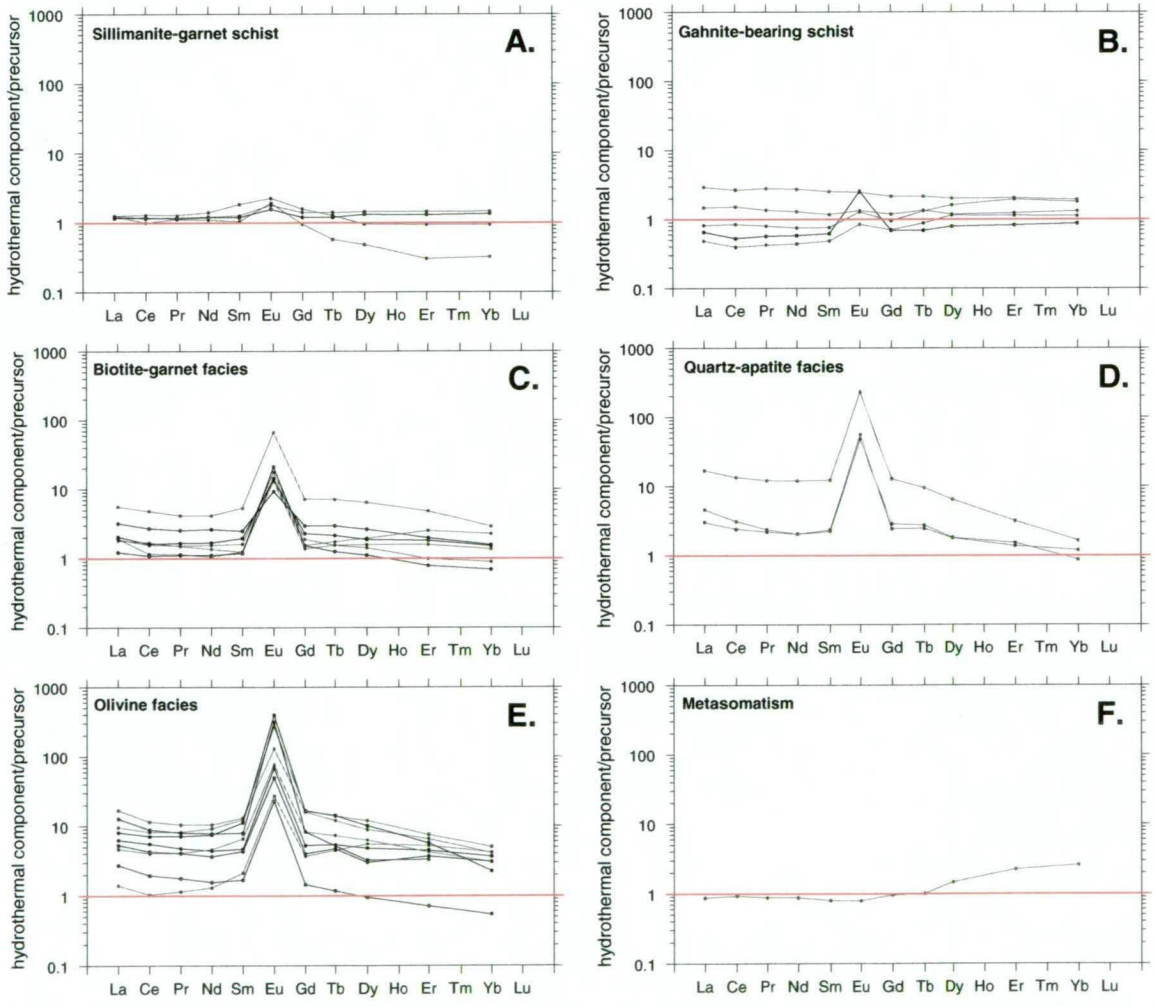

Figure 6.16 Calculated hydrothermal REE signatures in garnetiferous rocks (A. and B.), graphitic ores (C. D. and E.), and hedenbergite-garnet-quartz metasomatised olivine facies ore (F.). Values <1 equate to a mass loss (i.e. leaching by the hydrothermal fluid), whereas data >1 signify mass gain (i.e. precipitation from the fluid).

6.7 DISCUSSION

6.7.1 Mass changes in garnetiferous rocks

Small absolute net mass gains and losses in sillimanite garnet schists (-2.2 to 4.8g/100g) and gahnite-bearing schists (1.4 to 14.1g/100g), suggest that premetamorphic alteration involved subtle changes in the major element geochemistry of the host metasediments. In particular, alteration of the sediments involved leaching of Fe, Mg, Ca and Na from pelitic protoliths and addition of Si, Mn and K. These changes are consistent with the high K-feldspar and sillimanite abundances, and Mn-enrichment in garnet and biotite in the garnetiferous rocks compared to pelitic gneiss (Chapter 5). Pb and Zn enrichment also occurred during alteration in the proportions Pb>>Zn in the sillimanite-garnet schists, and Zn>>Pb in the gahnite-bearing schists. Overall, the mass balance calculations indicate that the garnetiferous rocks represent a metamorphosed Si-K-Mn alteration halo superimposed on immature siliciclastic sediments (section 3.7.2; Walters, 1994b).

Mass gains in Al_2O_3 for sillimanite-garnet schists may be due to either subtle changes in Al abundances relative to TiO_2 and Zr in the precursor pelitic gneiss due to primary sedimentary fractionation, or are due to hydrothermal alteration. Considering the variability in Al_2O_3 abundances relative to TiO_2 and Zr in the pelitic gneiss (section 6.3.2), it is likely that mass gains in Al_2O_3 are an inherited primary sedimentary artefact caused by assuming an average pelitic gneiss precursor composition, rather than an alteration effect. If this is correct, and Al_2O_3 immobility during alteration is assumed, then the calculated mass change in Al_2O_3 is an indication of the inherent compositional mismatch between the altered and least-altered rock (cf. Grant, 1986; Barrett and MacLean, 1994b). Small mass gains in Zr (~8ppm) are also likely to be a reflection of the compositional mismatch of the average precursor composition rather than hydrothermal alteration. Mass gains and losses in Al_2O_3 for gahnite-bearing schists is also a manifestation of the compositional mismatch between the calculated Al-rich pelitic precursor and individual gahnite-bearing schist samples.

The calculated mass changes for the garnetiferous rocks at Cannington (pelitic sediments specifically) favour a possible premetamorphic alteration assemblage of principally quartz-sericite (enrichment in SiO_2 and K_2O) ± minor Mn-chlorite (enrichment in MnO and depletion in FeO_{total} and MgO; cf. Stanton, 1976; Plimer, 1979). The existence of Mn-Fe carbonate (e.g. rhodochrosite to manganosiderite) as an alteration phase is difficult to substantiate. If it was present, it was entirely consumed by devolatilisation reactions during prograde metamorphism. Depletion in CaO and Na_2O may reflect the breakdown of plagioclase during alteration of the feldspathic sediments.

It is worth noting that enrichments and depletions in particular major elements, and the interpreted quartz-sericite ± Mn-chlorite alteration assemblage at Cannington, are similar to those associated with VHMS deposits, except for MgO and FeO_{total} depletion in the pelites at Cannington (cf. Ishikawa et al., 1976; Lydon, 1988; Large et al., 2001). This similarity was

also noted by Walters (1994b).

6.7.1.1 Alteration geochemistry at Broken Hill, Australia

Few lithogeochemical studies on the garnetiferous rocks enveloping the Broken Hill deposit in New South Wales have been published. Plimer (1979) recognised that interpreted premetamorphic alteration is characterised by progressive depletion in Na and enrichment in Fe, Ti and Mn as the orebody is approached. Within 500 vertical metres of the deposit, depletions in Na, Ca, Sr and Mg, and enrichments in Si, K, Rb, Pb, S, Mn, Fe and Ti are apparent (Plimer, 1979). Elliot (1979) argued that quartzofeldspathic gneiss is depleted in Na, Ca, Mg and Sr, and enriched in Pb, Zn, Ba, Si, Fe, Mn, K and Rb. In the near-ore environment, Main et al. (1983) recognised enrichment in Al, Fe, Mg, Ca, K, Ti and Mn, and depletion in Na, P and Ba in the Potosi Gneiss. Based on MnO enrichment and Na_2O depletion, Main et al (1983) developed a discriminant function to illustrate geochemical trends toward ore. Haydon et al. (1993) and Wright et al. (1993) also recognised that geochemical trends toward ore were characterised by progressive enrichment in Mn and K, and concomitant depletion in Na, as well as an increase in the Pb/Zn ratio. These workers suggested that the Na_2O/MnO ratio was the most sensitive indicator for alteration and determining geochemical trends toward ore, confirming the earlier study of Main et al. (1983).

These previous studies involved a statistical and/or element ratio approach, independent of calculated mass changes based on established immobile elements. Nevertheless, there appears to be general agreement that alteration at Broken Hill involved Si, K, Mn, Fe and Rb enrichment, and Na, Ca, Mg and Sr depletion. These geochemical trends are very similar to the calculated mass changes at Cannington, except for Fe enrichment.

6.7.1.2 The BHT alteration index

An alteration index is a mathematical function that quantifies the degree of principle chemical changes that have occurred in a given rock due to hydrothermal alteration. The expression is a simple ratio between mass gains over mass gains plus losses normalised to 100 (Ishikawa et al., 1976). For example:

(12) Alteration index (AI) = 100 x enrichments / (enrichments + depletions)

An alteration index provides a useful method for discriminating altered rocks from their unaltered protoliths. In particular, alteration indexes are capable of detecting and discriminating subtle geochemical variations related to particular alteration assemblages and/ or phases, and are therefore sensitive to the intensity of alteration within a given rock. These properties have direct implications for the development of geochemical vectors in exploration for ore deposits.

Numerous indexes have been devised for detecting various types of alteration assemblages associated with particular deposit classes, such as the Ishikawa index (Ishikawa et al., 1976) and the chlorite-carbonate-pyrite index (CCPI; Large et al., 2001) for VHMS systems, and the

SEDEX index for sediment-hosted Zn-Pb-Ag deposits (Large and McGoldrick, 1998). The Ishikawa index for example, is based on an alteration model involving Na_2O and CaO depletion in volcanics rocks reflecting breakdown of plagioclase and volcanic glass, and MgO and K_2O enrichment related to the formation of chlorite and sericite alteration assemblages with increasing intensity of alteration. As a result, the index increases as alteration becomes more intense around major ore-forming fluid pathways proximal to massive sulphides.

Based on the mass balance calculations presented here and in other studies (e.g. Walters, 1994b), K_2O/Na_2O ratios can be used to discriminate BHT alteration in metasediments, i.e. can be used as a quantitative indicator. Walters (1994b) proposed an alkali alteration index as a preliminary approach for discriminating BHT alteration in metasediments using the formula:

(13) Alkali index = $100 \times K_2O / (K_2O + Na_2O)$

However, the simplicity of the ratio and presence of various hydrothermal events, such as regionally extensive, late orogenic Na-metasomatism in the Cannington region, precludes its application for discriminating BHT alteration alone. Instead, Walters (1994b) developed a BHT specific alteration index after an extensive lithogeochemical study of host rocks from Cannington. Based on fundamental geochemical differences between altered and unaltered gneiss at Cannington, and previous lithogeochemical studies at Broken Hill in New South Wales (section 6.7.1.1), Walters (1994b) concluded that BHT alteration involved enrichment in K, Fe and Mn, and depletion in Ca, Mg and Na. Using equation 13 above, the BHT alteration index was expressed as:

(14) BHT AI = $100 \times (K_2O + Fe_2O_{3\,(total)} + 10MnO) / (K_2O + Fe_2O_{3\,(total)} + 10MnO + CaO + MgO + Na_2O)$

MnO was factored by 10 to equalise it with the magnitudes of other components (Walters, 1994b). The index is essentially a quantitative measure of the abundance of K-feldspar (and biotite) versus plagioclase, as well as the bulk Fe+Mn/Mg ratio, which accounts for changes in garnet (and biotite) compositions. An increase in the index corresponds to K_2O enrichment (K-feldspar and biotite), and Na_2O and CaO depletion (plagioclase) in conjunction with an increase in the Fe+Mn/Mg ratio with increasing alteration intensity. The index provides a quantitative method for discriminating BHT alteration amongst other less significant alteration types, whilst retaining sensitivity to the intensity of BHT alteration. Thus, the index can be used to determine geochemical vectors to ore. However, it is not suitable for discriminating BHT alteration in protoliths such as amphibolites, calc-silicate rocks, iron-formations or graphitic shales (Walters, 1994b).

The BHT index has similarities to the previously mentioned Ishikawa index (Ishikawa et al., 1976) and CCPI (Large et al., 2001) used in VHMS districts, the most significant difference being that MgO is depleted rather than enriched. The BHT index has stronger similarities to the SEDEX alteration index (Large and McGoldrick, 1998), but recognises the significance of K_2O enrichments and CaO and Na_2O depletions.

The BHT index proved successful for discriminating fertile BHT alteration systems, but its

sensitivity to the intensity of alteration was poor and therefore, its application for geochemical vectors to ore in an exploration scenario was limited. The index was also unable to discriminate between large and small BHT systems. However, it was particularly useful for determining subtle BHT alteration in typical metasediments where other routine geochemical methods failed (Walters, 1994b). This has the advantage of expanding the size of BHT targets.

The mass calculations presented here support the enrichments and depletions for BHT alteration at Cannington as interpreted by Walters (1994b), with one notable exception; Fe was depleted from pelitic gneiss protoliths rather than added. Modification of the BHT alteration index to account for this results in the equation:

(15) Mod BHT AI = 100 x (K_2O + 10MnO) / (K_2O + 10MnO + $Fe_2O_{3\,(total)}$ + CaO + MgO + Na_2O)

MnO was factored by 10 to equalise it with the magnitudes of other components. The modified BHT alteration index results in the expansion of the BHT alteration field on bivariate plots. Highly prospective rocks fall between values of 42% to 100% instead of 80% to 100% for the original BHT index (Fig. 6.17a to d). Like the original BHT index of Walters (1994b), the modified index is a measure of the abundance of K-feldspar (and biotite) versus plagioclase and the bulk Mn/Fe+Mg ratio, which accounts for changes in garnet (and biotite) compositions. The Mn/Fe + Mg ratio is a better indicator of compositional variations in garnet than the original BHT index. This is suggested because garnet compositions vary between Fe and Mn end-members rather than Mg and Ca end-members (section 5.4). An increase in the index corresponds to K_2O enrichment (high K-feldspar and biotite abundances), and Na_2O and CaO depletion (low plagioclase abundance) in conjunction with an increase in the Mn/Fe+Mg ratio of garnets (and biotite) with increasing alteration intensity. Overall, the modified BHT alteration index is likely to be more sensitive to the intensity of alteration in metasediments. The latter aspect and potential for determining vectors to ore require testing in drillhole intersections that span the entire alteration system at Cannington. However, a preliminary assessment of the modified BHT index can be made using the available data.

On plots involving MnO and Pb, the pelitic and psammitic gneiss populations define positive linear trends that extrapolate toward the sillimanite-garnet and gahnite-bearing schist populations using both BHT indexes (Fig. 6.17a to d). These trends indicate that the samples used in the study are in fact, weakly altered. In particular, the linear trends in the gneiss are better defined using the modified BHT index. The same linear trend is clearly defined on a Zn versus the modified BHT index plot, which also highlights the anomalous Zn content of gahnite-bearing schists in comparison to sillimanite-garnet schists (Fig. 6.17e). Plotting an immobile element sensitive to sedimentary fractionation processes, such as TiO_2, against the modified BHT index provides a method for discriminating between pelitic versus psammitic gneiss, and sillimanite-garnet schist versus garnetiferous quartzite (Fig. 6.17f).

Plotting the alkali index against the modified BHT index also distinguishes pelitic versus psammitic compositions (Fig. 6.18). However, the plots indicate that the modified BHT index

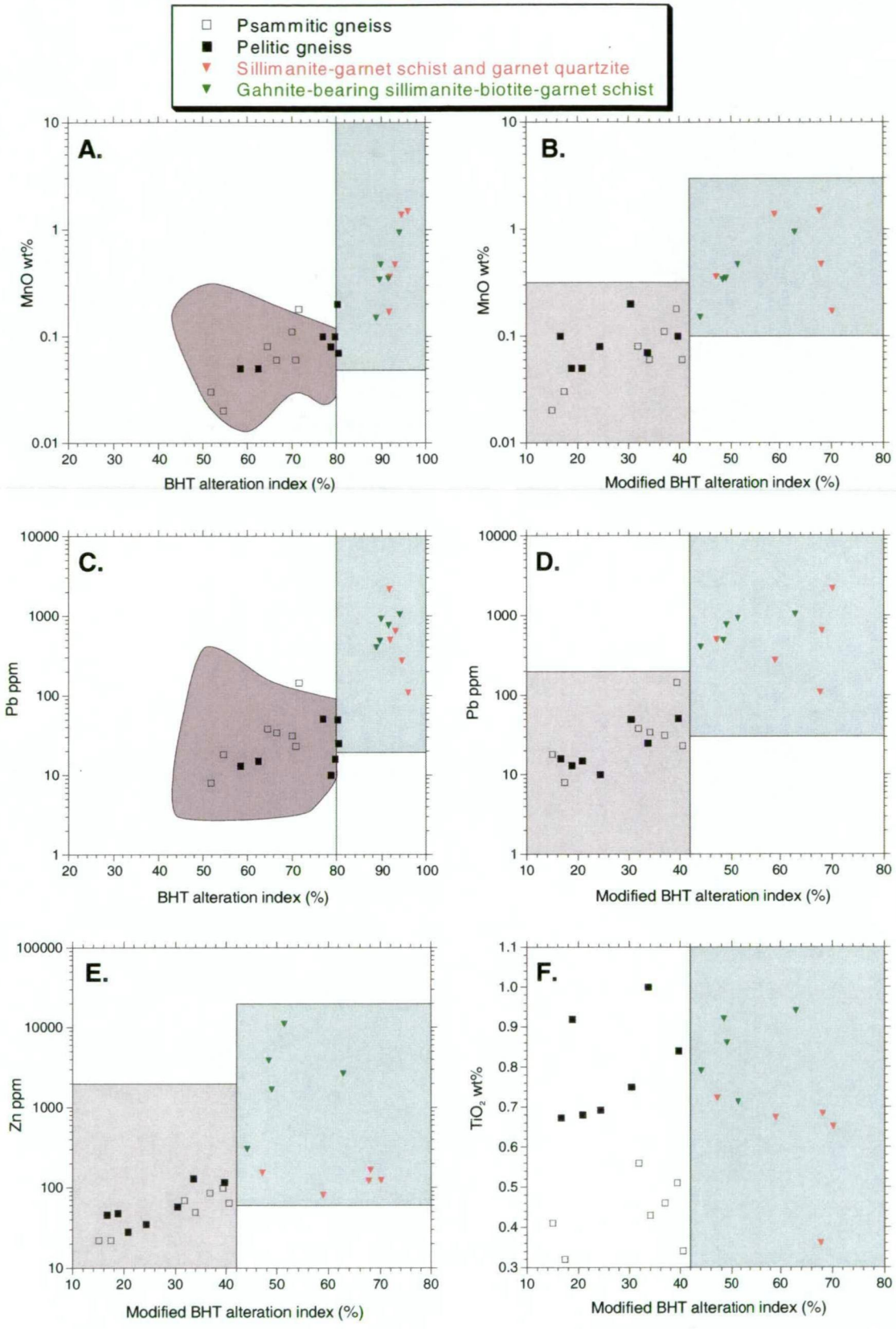

Figure 6.17 Bivariate plots of the BHT alteration (Walters, 1994b) and modified BHT alteration indexes (this study). Garnetiferous rocks plot within the green "BHT alteration" field. Pelitic and psammitic gneiss plot within the grey fields. **A.** MnO versus the BHT index. **B.** MnO versus the modified BHT index. **C.** Pb versus the BHT index. **D.** Pb versus the modified BHT index. **E.** Zn versus the modified BHT index. **F.** TiO_2 versus the modified BHT index. Grey fields in A. and C. represent gneiss from the Cannington region, including typical host rock gneiss from the local mine area (Walters, 1994b). Positive liner trends defined by the gneiss are stronger on plots involving the modified BHT index.

does not discriminate between pelitic and psammitic compositions (Fig. 6.18b), unlike the original BHT index and alkali index (Fig 6.18a). Trends in the data using the latter indexes could be related to primary sedimentary compositional variations and /or BHT alteration. The modified BHT index is therefore advantageous because it eliminates the potential for primary sedimentary variations being misinterpreted as alteration trends. If the original BHT index is adopted, the metasediments should be subdivided into pelitic and psammitic populations so that primary sedimentary trends can be distinguished from BHT alteration trends. In addition, the modified BHT index is more sensitive to BHT alteration in pelitic gneiss than the original BHT index. Considering the clear genetic relationship between pelitic gneiss and the ores (section 6.4.4), this latter aspect is significant.

The alkali index versus BHT index plots are useful for determining Na_2O enrichment versus K_2O enrichment in gneisses (Fig. 6.18). Walters (1994b) proposed that gneissic rocks with alkali indices below 40% were anomalously enriched in Na_2O, and attributed this enrichment to albite alteration associated with regional Na-metasomatism (section 2.6). However, it is unclear whether Na_2O enrichment is due to metasomatism, or is related to primary sedimentary variations. Regardless of which process causes Na_2O enrichment in the gneiss, it can be readily discriminated from "prospective" BHT alteration by both BHT indexes and the alkali index (Fig. 6.18). However, the geochemical effects of Na-metasomatism on pre-existing BHT alteration has not been assessed. It is possible that Na-metasomatism has the potential to mask BHT alteration with regard to the alteration indexes, due to a change in the K_2O/Na_2O ratio.

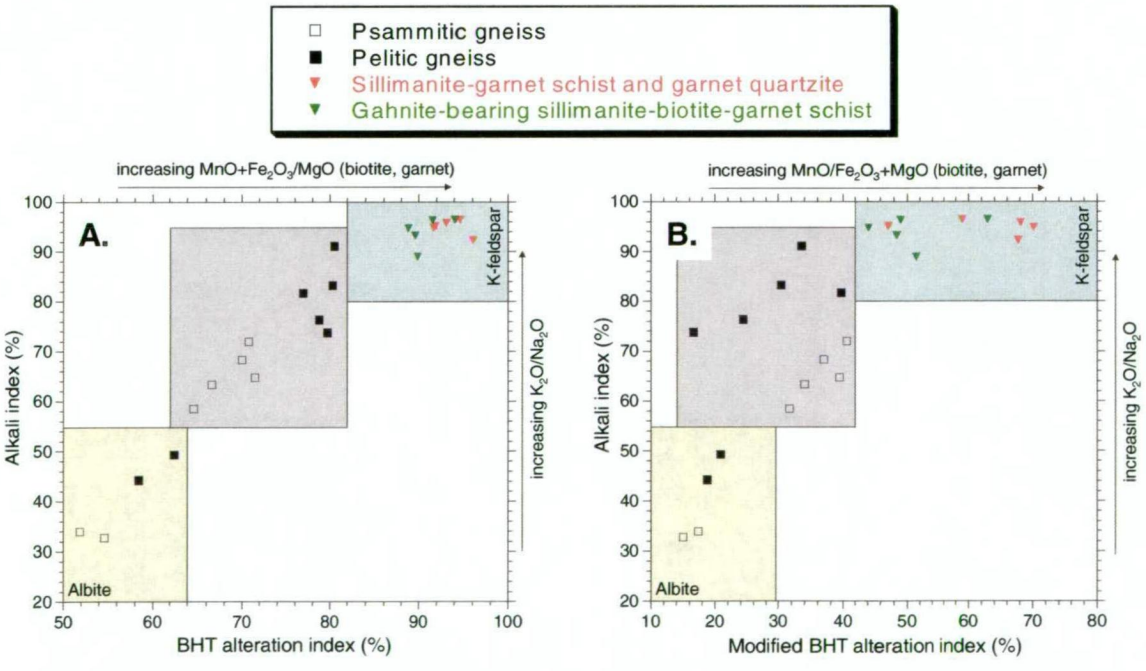

Figure 6.18 Bivariate plots discriminating between regional albitic alteration and BHT alteration in altered and least altered migmatitic gneiss and garnetiferous rocks. **A.** alkali alteration index versus the BHT alteration index proposed by Walters (1994b). **B.** as for A. but using the modified BHT alteration index developed in this study. Alteration fields correspond to BHT K-Mn-alteration (blue) and regional Na-metasomatism (yellow). Psammitic and pelitic compositions are readily distinguishable in the least-altered gneiss field (grey). Expansion of the BHT alteration field using the modified BHT alteration index suggests that it is possibly more sensitive to the intensity of BHT alteration in comparison to the BHT alteration index of Walters (1994b).

6.7.2 Mass changes in graphitic ores: genetic implications

Geochemical evidence indicates that graphitic ores consist of two principle components: i) pelitic gneiss, and; ii) hydrothermal constituents (cf. Chapman, 1993; Chapman and Williams, 1998). It is unlikely that sedimentary fractionation processes caused dilution of immobile elements in the various ore facies via the addition of detrital quartz, because the major detrital component in the ores is pelitic, not psammitic. The latter aspect is supported by the disparity between the ore trend and the sedimentary fractionation trend on the Al_2O_3-TiO_2-Zr ternary plot (Fig. 6.4b). The ore facies may therefore have formed by either coincident deposition of pelitic detritus and chemical sediment, or replacement of pelite dominated clastic material, or a combination of both processes. These processes would result in dilution of immobile elements in the pelitic fraction, resulting in the calculated net mass gains.

The greatest dilution of immobile elements occurs in quartz-apatite and olivine facies ores (e.g. Fig. 6.2a and f), suggesting that these ore facies have undergone the greatest mass gains and are dominated by hydrothermal constituents. In contrast, higher abundances of immobile elements in biotite-garnet facies ores suggest a greater proportion of pelitic detritus. However, in detail, these relationships are more complex.

Such large mass gains (25 to ~1800g/100g) suggest that large volume changes must have occurred during the formation of the graphitic ores. For example, given that the density of the precursor pelitic gneiss is 2.7g/cc and an average of 3.3g/cc for biotite-garnet facies ores, alteration could only have produced ~20% dilution of the immobile elements. Therefore, changes in volume of at least 480% must have occurred in conjunction with mass gains of 500% to account for the dilution in some samples (cf. Chapman and Williams, 1998). Calculated relative volume changes are highly variable, ranging from ~14% for samples with the lowest relative net mass gains, to 2469% for samples with the greatest. Mass and volume changes of this calibre are extreme, and it is unlikely that the ores were formed exclusively by alteration and replacement processes. For example, the primary porosity in unconsolidated pelite ranges between ~60-70% and psammites between 35-50% (Dickinson, 1985; Dzevanshir et al., 1986; Wilson and McBride, 1988). Volume changes greater than the porosity imply a replacement process, and extreme volume changes >100% imply that other constituents are present in addition to the sediment, e.g. interbanded clastic sediments and hydrothermal sediment, or some other exotic component (cf. Chapman and Williams, 1998). Chapman and Williams (1998) proposed that the other component possibly comprised an exotic carbonate/calc-silicate rock with additional silica, phosphate and Fe-Mn phases. However, they did not discount the possibility that Ca, P, Mn and Fe enrichment was of hydrothermal origin. The geochemical evidence presented here does not support the presence of an exotic Al_2O_3, TiO_2 and Zr bearing rock type in the ores, irrespective of a replacement or chemical sediment model for ore formation.

The only feasible process to account for such large and extremely variable mass-volume gains

is a model involving coincident deposition of mixed pelitic detritus and hydrothermal sediment. Such a process is consistent with the preservation of Al_2O_3, TiO_2 and Zr ratios in biotite-garnet facies ores that are indicative of the pelitic gneiss component (Fig. 6.4b), i.e. these elements were immobile during the formation of biotite-garnet facies ores. The delicate millimetre- to centimetre-scale mineral banding in biotite-garnet facies ores is more indicative of primary depositional banding rather than textural features associated with replacement of pelitic sediments. Considering these aspects it can be concluded that biotite-garnet facies ores in particular, are mixed chemical-clastic metasediments. Mixed chemical-clastic sedimentation was proposed for the formation of garnetites (Billington, 1976; Plimer, 1986; Lottermoser, 1989; Spry and Wonder, 1989) and "lode horizon" rocks (Stanton, 1976; Barnes et al., 1983; Slack et al., 1984; Plimer, 1986, Parr and Plimer, 1993) at Broken Hill, New South Wales.

Evidence for Al mobility in quartz-apatite and some olivine facies ores suggests that not all ores formed by coincident accumulation of pelitic detritus and hydrothermal sediment. Even though relative abundances between Ti and Zr in these ore facies support the existence of a pelitic gneiss component, some process caused systematic Al_2O_3 depletion relative to TiO_2 and Zr in the pelitic component (Fig. 6.4b; section 6.4.4). Calculated average mass losses in Al average -4.7g/100g and -2.4g/100g in quartz-apatite and olivine facies ores respectively. Two possible mechanisms accounting for these systematic variations include:

i) mixing between the pelitic gneiss component, and an exotic TiO_2 and Zr bearing component with very low Al_2O_3 content and, or;
ii) replacement of pre-existing chemical-clastic sediments.

It is unlikely that the variations in Al_2O_3 abundances reflect a mixing process between some exotic component and pelitic gneiss. If this was the case, the exotic component must have had essentially the same TiO_2/Zr ratio as the pelitic gneiss, and the mixing process did not affect this ratio. Alternatively, a model involving the replacement of pre-existing chemical-clastic sediments is consistent with the observed geochemical trends in quartz-apatite and olivine facies ores. In this scenario, Al_2O_3 was mobile, whilst TiO_2/Zr ratios remained unchanged, i.e. Ti and Zr immobility. This model also explains the greater calculated net mass-volume changes in quartz-apatite and olivine facies ores in comparison to biotite-garnet ores (Tables 6.9, 6.10 and 6.8 respectively). Hence, the geochemical evidence indicates that quartz-apatite and some olivine facies ores formed, in part, by sub-surface replacement of pre-existing metalliferous sediments. This interpretation provides a reasonable explanation for the observed transitional relationships between the ore facies (section 4.4) and their extreme compositional diversity and delicate compositional banding.

Overall, variations in mass gains ultimately reflect proportions of pelitic versus hydrothermal components in the graphitic ores. Large mass gains indicate higher proportions of hydrothermal components and lower mass gains more pelitic components. This aspect suggests a mixing phenomenon between hydrothermal and detrital constituents. Using the calculated mass changes it is possible to model and quantify this mixing process. The

proportions of total hydrothermal (H%) and detrital material (pelitic detritus, P%) comprising the ores can be calculated from equations (7) and (8), and the reconstructed compositions relative to pelitic gneiss from equation (1). Normalisation of the mass changes to the calculated total % hydrothermal components (H%) yields the relative percentages of the hydrothermal constituents. The remainder comprises the pelitic component. A similar approach was undertaken to model mixing between hydrothermal sediment and tuff in exhalites from the Key Tuffite in the Matagami district of Canada (Liaghat and MacLean, 1992).

The results of the mixing model calculations are presented in Figure 6.19. Ores that have undergone the least mass gains contain the highest proportion of pelitic components and vice-versa. Biotite-garnet facies ores consistently contain less total hydrothermal components compared to apatite-quartz and olivine facies ores. Percentages of major hydrothermal contributors are variable in the biotite-garnet facies, i.e. Si, Fe, Pb and Zn. Fe, Mn and Si are the most consistent major hydrothermal contributors in olivine facies ores, whereas Si is the principle contributor in quartz-apatite facies ores. Unequivocal evidence is lacking as to the cause of this variation between samples. However, abrupt fluctuations in the physicochemical conditions caused by pulses of hydrothermal discharge, combined with variable hydrothermal sediment accumulation rates and subsurface replacement are possible mechanisms consistent with the weight of evidence. A similar process was proposed for the formation of the Key Tuffite in the Matagami district of Canada (Liaghat and MacLean, 1992).

6.7.3 Host rock associations: implications for palaeoconditions during ore formation

The genetic link between pelitic gneiss and graphitic ores, coupled with their interpreted chemical-clastic sedimentary origin, suggests that ore formation occurred during a more quiescent period in the sedimentary history of the region. In fact, the Al-rich character of the gahnite-bearing schist suggests that ambient sedimentary rates were slow enough to allow the deposition of more mature Al-rich pelagic sediments in comparison to the less mature pelitic gneiss protolith. However, the Al_2O_3-TiO_2-Zr systematics indicate that the ores do not contain an Al-rich pelitic component. This suggests that concomitant deposition of the ores and the gahnite-bearing schist protolith did not occur, even though a strong spatial relationship exists between them and the gahnite-bearing schist is extremely anomalous in Zn (~3000ppm). Nevertheless, these interpretations are particularly significant with regard to regional exploration strategies.

The genetic association between pelites and the ores at Cannington differs substantially from interpreted sedimentary associations at the Broken Hill deposit, New South Wales. On the basis of gamma signatures from well logs, Haydon and McConachy (1987) argued that the Broken Hill deposit is hosted within psammites that comprise the upper members of a major upward-coarsening sedimentary sequence deposited in a shallow-water prograding deltaic environment. This model was expanded in subsequent studies (e.g. Wright et al., 1987;

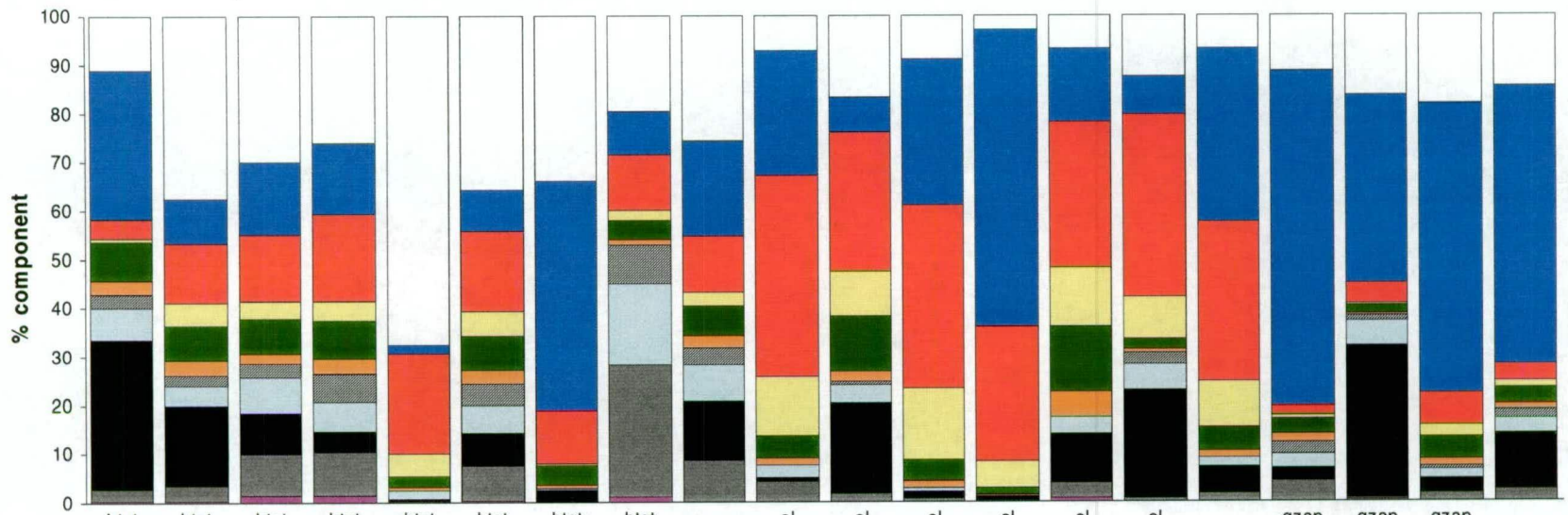

	btgt NZ016-1	btgt NZ029-8	btgt NZ033-2	btgt NZ039-3	btgt NZ047-8	btgt NZ029-13	btgt SZ157-11	btgt NZ160-31	btgt avg	ol NZ040-4a	ol NZ044-2	ol NZ044-5	ol NZ070-4	ol NZ160-20	ol NZ047-2	ol avg	qzap NZ040-4b	qzap NZ030-13	qzap NZ035-13	qzap avg
□ pelitic gneiss	11.03	37.39	29.86	25.97	67.48	35.78	33.86	19.80	25.79	7.28	16.95	8.81	2.81	6.76	12.49	6.71	11.31	16.30	18.23	14.69
■ Si	30.72	9.34	15.09	14.60	1.76	8.67	47.32	8.93	19.49	25.57	6.99	30.05	61.09	14.89	7.80	35.88	69.10	38.76	59.50	57.09
■ Fe	3.95	12.05	13.78	17.95	20.68	16.25	10.83	11.22	11.51	41.51	28.51	38.08	27.77	30.09	37.60	32.68	1.56	4.31	6.44	3.70
■ Mn	0.69	4.77	3.58	3.95	4.87	5.16	0.56	2.37	2.73	11.98	9.43	14.37	5.30	12.07	8.61	9.24	0.92	0.25	2.77	1.19
■ Ca	7.79	7.30	6.87	7.93	2.06	6.96	3.87	3.68	6.30	4.81	11.21	4.53	1.64	13.66	2.06	5.19	3.36	1.86	4.47	3.18
■ P	2.97	3.01	2.34	3.23	0.62	2.98	0.82	1.22	2.35	1.28	2.41	1.29	0.25	5.00	0.78	1.52	1.47	0.29	1.52	1.12
▨ LOI	2.85	2.07	2.84	5.55		4.24		7.86	3.64		0.60				2.45		2.69	1.18	0.74	1.70
■ S	6.46	4.21	6.96	6.32	1.98	5.57	0.31	16.82	7.29	2.40	3.67	0.56	0.14	3.58	5.33	1.79	2.76	5.02	1.86	3.23
■ Pb	30.70	16.31	8.70	4.20	0.08	7.02	2.26	0.07	12.32	0.74	18.49	1.43	0.60	10.07	22.12	5.21	2.65	31.42	2.75	11.67
■ Zn	2.64	3.32	8.65	8.89	0.35	7.01	0.13	27.03	8.46	4.31	1.59	0.80	0.36	3.25	0.64	1.66	4.06	0.42	1.66	2.29
■ others	0.19	0.22	1.34	1.39	0.12	0.34	0.04	1.01	0.10	0.10	0.17	0.08	0.05	0.62	0.12	0.12	0.13	0.20	0.06	0.13

Figure 6.19 Calculated percentage of pelitic gneiss in biotite-garnet, olivine and quartz-apatite facies ore samples, including major absolute mass gains that comprise the hydrothermal component. The biotite-garnet facies has a greater proportion of pelitic sediment than the olivine and quartz-apatite facies ores. Absent data in the table represent mass losses.

Haydon et al., 1993; Wright et al., 1993), and an "inhalative" genetic model involving replacement of coarse-grained, porous sandstone units by Pb-Zn sulphides proposed. Sandstone units within the sedimentary basin were interpreted to have facilitated regional-scale movement of basinal brines and were regarded as hydrothermal fluid reservoirs (Haydon et al., 1993; Wright et al., 1993).

Even though there appears to be an increase in psammitic and garnetiferous quartzite lithologies toward the ore at Cannington (Chapter 3), the geochemistry and close spatial association of the ores with gahnite-bearing schists, preclude a cognate relationship with psammites exclusively. Even the most siliceous ores, such as the quartz-apatite facies, contain a pelitic component, albeit small. Perhaps the local increase in psammitic lithologies adjacent to the orebody are indicative of an active period of sedimentation just before, or after ore formation. This latter aspect has direct implications for exploration.

6.7.4 Significance of REE signatures

6.7.4.1 Preservation of primary REE abundances

REE mobility during hydrothermal alteration and ore formation has been clearly demonstrated in a variety of geological settings and rock types (Campbell et al., 1984; Lottermoser, 1990; McLennan and Taylor, 1991; Wood and Williams-Jones, 1994; Banks et al., 1994; Klinkhammer et al., 1994; Bingen et al., 1996; Lewis et al., 1997; and many others). The degree of REE mobility depends on: i) the composition of the rock and therefore REE concentrations in the reacting minerals; ii) the relative stability of these minerals with regard to the physicochemical conditions during alteration and fluid composition, especially temperature, fO_2 and pH of the fluid; iii) the availability of sites within the secondary minerals to accommodate the REE; iv) pre-existing REE concentrations in the hydrothermal fluid; v) the capability of the fluid to remove REE from the environment and; vi) the fluid/rock ratio (Alderton et al., 1980; Humphries, 1984; Bau, 1991; Lottermoser, 1992).

Provided the REE remain immobile during subsequent post-depositional processes, such as metamorphism and retrogression, primary hydrothermal REE signatures will be preserved (Lottermoser, 1989, 1992; Bau, 1991; Parr, 1992; Bierlein, 1995). REE immobility during metamorphism is difficult to ascertain in regionally metamorphosed terrains because unmetamorphosed precursors either do not exist, or are extremely rare. However, Muecke et al. (1979) and Taylor et al. (1986) demonstrated that primary REE signatures are preserved during partial melting, provided the melt remains *in situ*. Lottermoser (1989), Parr (1992) and Bierlein (1995) argued that the lack of a relationship between REE abundances and mineral assemblages comprising metamorphosed exhalites located in the Olary Block and adjacent to the Broken Hill and Pinnacles BHT deposits, was unequivocal evidence that primary REE signatures had been preserved through metamorphism. At Cannington, REE abundances and chondrite normalised REE profiles are independent of metamorphic mineral assemblages in the host rocks and graphitic ores, suggesting that primary REE signatures have been

preserved. This interpretation is supported by the close similarity in chondrite normalised and hydrothermal REE profiles in the mineralogically diverse ore facies that comprise graphitic ore.

Numerous studies have shown that primary REE signatures in rocks typically remain unchanged during retrogression and/or subsequent hydrothermal events unless fluid/rock ratios are extremely high, e.g. $>10^6$ (Lesher et al., 1986; Michard and Albarède, 1986; Michard, 1989; Bau, 1991; Parr, 1992). In contrast, a number of studies have demonstrated REE mobility during retrogression and metasomatism. For example, Lottermoser (1989) proposed that REE were probably locally mobilised and redeposited by retrograde fluids in shear zones at Broken Hill. Bierlein (1995) recognised that metasomatism caused significant Eu depletion and that late-stage retrograde fluids produced strong LREE enrichments in altered rocks. At Cannington, the mass balance calculations indicate that Stage IIa metasomatism of one particular olivine facies ore sample caused HREE enrichment.

Overall, the evidence suggests primary REE abundances in the host rocks and ores have not been modified by subsequent metamorphism. REE abundances therefore reflect primary hydrothermal processes related to premetamorphic alteration and ore formation rather than later metamorphism. In contrast, Stage IIa retrograde fluids had the capacity to modify primary REE signatures.

6.7.4.2 Garnetiferous host rocks

Sillimanite-garnet and gahnite-bearing schists (i.e. the altered host rocks) at Cannington have greater variability in chondrite normalised REE patterns in comparison to the gneiss, indicating that some mobility of the REE occurred during premetamorphic hydrothermal alteration (Fig. 6.15c and d). This is supported by absolute mass change profiles for the REE, which indicate the LREE were significantly more mobile compared to HREE during hydrothermal alteration, especially La, Ce and Nd (Figs. 6.8c and 6.9c). Hydrothermal LREE profiles in the latter rocks are generally flat, with the greatest variability occurring in the HREE profiles. These relationships are exemplified by the greater range in Gd/Yb ratios compared to La/Sm ratios (Table 6.13).

The flat LREE profiles suggest that hydrothermal alteration involved systematic adjusted of LREE abundances by a near constant factor for a given sample, irrespective of associated mass changes. In contrast, positive and negative trends for the HREE profiles suggest that enrichment and depletion varied systematically during alteration for a given sample, as well as between samples. Slight positive Eu anomalies indicate Eu enrichment relative to the other REE, irrespective of mass losses or gains in the REE during hydrothermal alteration. However, the absence of a positive Eu anomaly in two gahnite-bearing schist samples, suggests that this relationship is not always consistent.

6.7.4.3 Graphitic ores and significance of Eu anomalies

Mass change REE profiles are characterised by greater mass gains in LREE compared to the HREE in graphitic ores assuming a pelitic gneiss precursor composition. The ore-forming fluid therefore deposited greater concentrations of LREE in comparison to HREE (Figs. 6.10c, 6.11c and 6.12c). However, LREE enrichment relative to HREE is not apparent in the hydrothermal REE profiles of graphitic ores. Instead, the hydrothermal REE signatures are characterised by near flat profiles (e.g. La/Sm ~1.0-2.0; Table 6.13) and strong positive Eu anomalies when normalised to the precursor pelitic gneiss composition. This suggests that the relative abundances of REE (except for Eu) in the ores and the pelitic gneiss are similar, even though calculated absolute mass changes indicate LREE enrichment. In other words, the degree of REE enrichment was essentially uniform relative to the pelitic gneiss. Such a relationship supports a genetic association between the ores and the pelitic gneiss. However, the variability in the hydrothermal HREE signatures (e.g. Gd/Yd ~0.7-7.8; Table 6.13) tends to mitigate this genetic association.

The most notable feature of the hydrothermal REE profiles is enrichment in Eu relative to the precursor pelitic gneiss. Eu anomalies are caused by fractionation of Eu^{+2} over Eu^{+3} in the source hydrothermal reservoir by fluid/rock interaction. The degree of fractionation is controlled by the fluid composition and physicochemical conditions within the hydrothermal reservoir, insomuch as the hydrothermal fluid must have the capacity to leach and transport Eu^{+2} aqueous species. Sverjensky (1984) demonstrated that fractionation of Eu^{+2} over Eu^{+3} is strongly temperature dependent and, to a lesser degree, fO_2 and pH dependent. Eu^{+2} solubility is higher in reduced, low pH, hydrothermal fluids at temperatures >250°C, whereas Eu^{+3} solubility is greater under more oxidised, higher pH conditions and temperatures <250°C (Sverjensky, 1984). Concentrations of Eu^{+2} are contained in plagioclase (especially albite), via substitution with Ba^{+2} and Sr^{+2}. Breakdown of plagioclase by reduced, hot (>250°C) slightly acid hydrothermal fluids (e.g. leaching of feldspathic volcaniclastic rocks) liberates Eu^{+2}, which is incorporated into the hydrothermal fluid and transported to the ore-forming environment (Michard and Albarède, 1986; Klinkhammer et al., 1994; Bau, 1991; Blundy and Wood, 1991; Lottermoser, 1992). The physicochemical characteristics of the scavenging fluid, abundance of plagioclase (including its composition) and degree of hydrothermal alteration (i.e. degree of plagioclase breakdown) are therefore, major controls on REE abundances in the hydrothermal fluid in the source reservoir. Temperatures >250°C and reduced conditions must be maintained to facilitate the transport Eu^{+2} to the site of ore formation. At this point, Eu^{+2} complexes must be destabilised by a sharp increase in pH, decrease in temperature, or fO_2, or more likely combinations of these, for the hydrothermal precipitates to inherit the Eu^{+2} enriched signature of the hydrothermal fluid (Sverjensky, 1984; Lottermoser, 1989, 1992).

At Cannington, positive Eu anomalies therefore suggest that plagioclase breakdown occurred in the source hydrothermal reservoir and that the ore-forming fluid was hot (>250°C), reduced and slightly acid. However, it is clear that the size of the positive Eu anomaly differs between

the ore facies that comprise graphitic ore. For example, Eu anomalies in biotite-garnet facies ores are smaller than those in quartz-apatite and olivine facies ores (Table 6.12; Fig. 6.15e to g). These features can also be seen in the hydrothermal REE signatures (Table 6.13; Fig. 6.16c to e). Variations in the intensity of the Eu anomaly may attributed to one or more of the following explanations (Bierlein, 1995):

- mineralogical control;
- dilution due to variable proportions of detrital material in the ores, i.e. simple mixing between hydrothermal and detrital REE;
- changing physicochemical conditions, i.e. temperature, oxidation state, pH of the hydrothermal fluid.

It is unlikely that the intensity of the Eu anomaly is related to a mineralogical control, because Eu anomalies in quartz-apatite and olivine facies ores are of equal intensity even though these ores consist of very different mineral assemblages (see Chapter 4). This is consistent with other studies that demonstrate a clear independence of REE systematics to mineralogy in hydrothermal environments (Baker and Hellingwerf, 1988; Lottermoser, 1989; Parr, 1992; Bierlein, 1995). It is generally accepted that this independence is indicative of adsorption of REE onto the surfaces of hydrothermal precipitates, such as clays and/or Fe-hydroxides, rather than predominantly via substitution into appropriate crystal lattice sites (Klinkhammer et al., 1994).

The intensity of the Eu anomaly could be related to the proportion of detrital material in the ores, i.e. an antipathetic relationship between the intensity of the Eu anomaly and the proportion of detrital material in the ores caused by dilution of the hydrothermal REE signature. Figure 6.20a confirms a general antipathetic relationship between the intensity of the Eu anomaly in the hydrothermal REE signatures and the calculated % detrital pelitic component in graphitic ores and the garnetiferous schists (sillimanite-garnet and gahnite-bearing schists). Garnetiferous schists contain the highest proportion of pelitic material (~75-98%) and have the least intense Eu anomalies (~1-4). Biotite-garnet facies ores generally contain ~25-45% pelitic material, but Eu anomalies are variable, ranging between ~3.5-16. Olivine facies ores contain less pelitic material, ranging between ~2-25%. The intensity of Eu anomalies in olivine facies ores containing >20% pelitic material are similar to those in the majority of biotite-garnet facies ores. However, in samples with <20% pelitic material, the intensity of the Eu anomaly increases in an exponential manner to a maximum of ~40 in samples that approach 100% hydrothermal components. Quartz-apatite facies ores display similar trends to the olivine facies ores. These relationships are supported by a similar antipathetic relationship between the calculated absolute mass changes in Eu and the % pelitic material in the ores and garnetiferous rocks (Fig. 6.20b). However, such a mixing model, as suggested by the latter relationships, does not explain the variation in intensity of the Eu anomaly in the *hydrothermal* signatures considering that the latter represents the REE signature after *'removal'* of the pelitic component. Therefore, if the intensity of the Eu anomaly is related to a mixing-type phenomenon alone, then removing the pelite component should reveal equally sized Eu

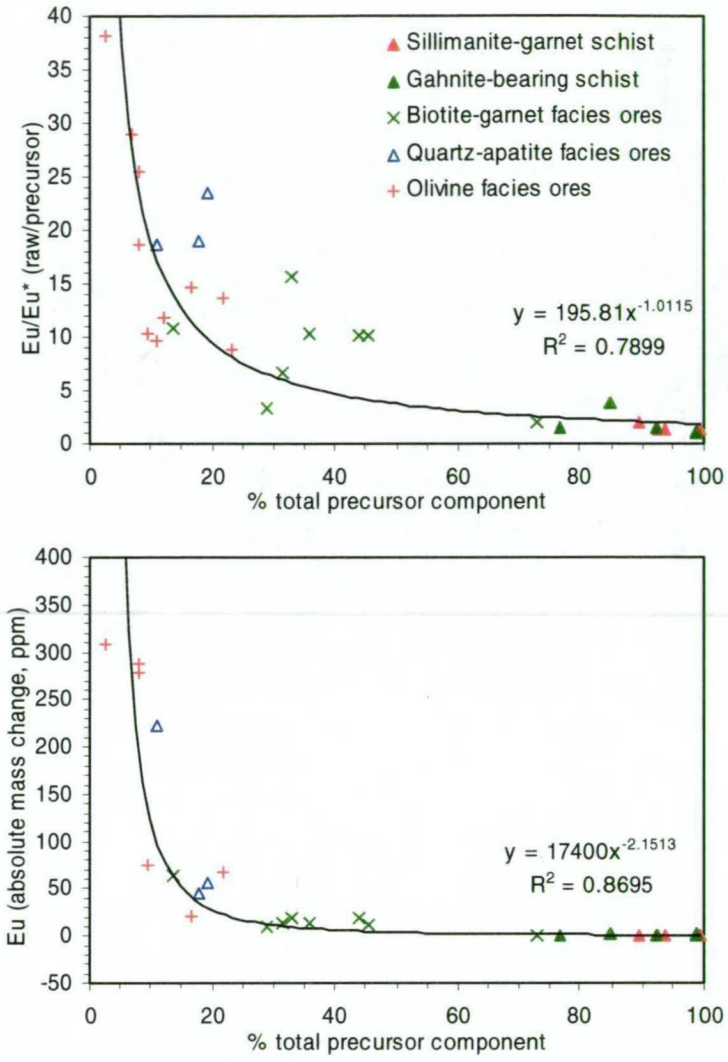

Figure 6.20 Bivariate plots of Eu versus the % precursor pelitic gneiss component in the ores and garnetiferous rocks. **A.** the Eu anomaly from the hydrothermal REE signatures. **B.** the calculated absolute mass change in Eu (ppm).

anomalies in the hydrothermal signatures, i.e. the *hydrothermal* signature is independent of the % pelitic component in the ores. This is clearly not the case in the hydrothermal signatures of graphitic ores.

Changing physicochemical conditions are likely to reflect the observed variations in the intensity of the Eu anomaly in the hydrothermal REE signatures. However, the inverse relationship between the intensity of the Eu anomaly and the % pelitic material in the ores suggests that the ratio between the hydrothermal component to the pelite (i.e. the fluid/rock ratio) has a significant effect on Eu^{+2} concentrations, and therefore the intensity of the Eu anomaly (cf. Peter and Goodfellow, 1996). Considering the latter aspect coupled with Eu^{+2} solubility, a model involving decreasing temperature, increasing fO_2 and possibly pH, with decreasing fluid/rock ratios best explains the variation in the Eu anomaly. In this scenario, it is envisaged that Eu^{+2} will be deposited in the hotter, lower pH and more reduced proximal areas of the hydrothermal system where the fluid/rock ratios are high (i.e. low proportion of pelitic material in the chemical sediments), yielding large positive Eu anomalies, e.g. olivine and quartz-apatite facies ores. Decreasing temperature and increasing fO_2 and pH associated

with decreasing fluid/rock ratios (i.e. higher proportions of pelitic material in the chemical sediments) in more distal areas will result in progressively smaller Eu anomalies due to decreasing Eu^{+2} concentration in the hydrothermal fluid, e.g. biotite-garnet facies ores. In the most distal areas, only very small Eu anomalies will be present, e.g. sillimanite-garnet schists. Similar models were proposed to explain variations in REE signatures observed in exhalites and alteration systems in the Olary Block (Bierlein, 1995), the Broken Hill and Pinnacles BHT deposits and associated distal exhalites (Lottermoser, 1989; Parr, 1992), massive sulphide deposits associated with hydrothermal sediments of the Brunswick Horizon in Canada (Peter and Goodfellow, 1996) and metalliferous sediment from the TAG Mound, Mid-Atlantic Ridge (German et al., 1990).

Negative Ce anomalies in modern-day Fe-Mn metalliferous sediments (Alt, 1988) are believed to be indicative of seawater interaction via adsorption of seawater REE predominantly after accumulation (German et al., 1990; Olivarez and Owen, 1991; Lottermoser, 1992; Mills and Elderfield, 1995b; Peter and Goodfellow, 1996). Modification of primary hydrothermal REE patterns by seawater depends on the degree of "mixing" with seawater and the period of time the precipitates are exposed to seawater interaction (German et al., 1990; Olivarez and Owen, 1991). German et al. (1990) calculated that a hydrothermal vent fluid/seawater mixing ratio of 0.01 (i.e. 99% seawater) was required before a slight negative Ce anomaly was evident in the REE profiles from suspended particulate matter within a buoyant plume above the TAG hydrothermal field. However, a positive Eu anomaly was still present in the REE profiles. The absence of negative Ce anomalies in graphitic ores and garnetiferous schists at Cannington discounts significant seawater interaction/mixing, considering that such low hydrothermal fluid/seawater ratios (e.g. 0.01; ibid.) are required to modify hydrothermal REE signatures. It also suggests that the metalliferous sediments were not exposed to seawater over an extended period of time.

6.7.4.4 Comparison to other deposits

Typical REE variations in Pb-Zn skarn deposits have not been documented. However, of the few published studies on REE systematics in skarn deposits, Fe-Cu (Abramson, 1981; Vander Auwera and Andre, 1991) and W-Mo (Baker and Hellingwerf, 1988) skarns are characterised by negative Eu anomalies and enrichment in LREE when normalised to chondrite. The host limestone to the Continental Fe-Cu(-Zn) skarn deposit in New Mexico for example, has LREE-enriched patterns and positive Eu anomalies, whereas the skarn formed in the limestone has negative Eu anomalies (Abramson, 1981). Documented REE signatures in skarns are therefore very different to those of graphitic ores at Cannington. Hence, the REE signatures are inconsistent with the post-peak metamorphic metasomatic model of Chapman and Williams (1998), unless the signatures were inherited from the protolith. The latter notion would require the protolith to have been a hydrothermal sediment (this study; cf. Chapman and Williams, 1998). However, the evidence does not fully discount a metasomatic model given that REE variations in Pb-Zn skarns are poorly documented.

Strong similarities between the REE signatures at the Broken Hill and Pinnacles BHT deposits and those of modern-day hydrothermal solutions and metalliferous sediments from the East Pacific Rise (Michard and Albarède, 1986; Alt, 1988), the Mid-Atlantic Ridge (German et al., 1990; Klinkhammer et al., 1994; Mills and Elderfield, 1995a and b), the Guaymas Basin, the Juan de Fuca Ridge and the Mariana spreading centre (Klinkhammer et al., 1994), and the Red Sea deeps (Courtois and Treuil, 1977; Calvez et al., 1988), were used as evidence to support a submarine exhalative origin for the Broken Hill and Pinnacles BHT deposits (Lottermoser, 1989; Parr, 1992). Peter and Goodfellow (1996) noted similarities between the REE signatures of the Brunswick Horizon in Canada and modern-day submarine hydrothermal vent fluids, and based on this proposed a submarine exhalative genetic model. The chondrite normalised LREE enriched signatures and distinctive positive Eu anomalies in the graphitic ores at Cannington are also very similar to those of the Broken Hill and the Pinnacles BHT deposits, as well as modern-day submarine hydrothermal vent fluids. In particular, the hydrothermal REE signatures are display a striking similarity to shale normalised REE profiles of hydrothermal precipitates from the TAG Mound, Mid-Atlantic Ridge (German et al., 1990; Mills and Elderfield, 1995a and b). The REE signatures are therefore consistent with a genetic model involving the accumulation of metalliferous sediment proximal to a major submarine hydrothermal hot spring.

6.7.5 Mass changes associated with Stage IIa metasomatism

Calculated mass changes provide evidence that Si, Fe, Mn and minor Zn were leached from the banded olivine facies ore during Stage IIa metasomatism. Mass gains in Pb and S are manifested as galena in the altered rock, and enrichment in Ca by the formation of hedenbergite and calcic almandine alteration assemblages. Concomitant loss of Fe and Mn is evidenced by knebelite breakdown. Mass loss in Si is unexpected considering that many hedenbergite veins contain appreciable quartz. It is possible that silicification in this single instance, is an apparent visual artefact caused by consumption of Fe-Mn bearing phases in the quartz-rich bands during alteration.

In particular, the calculated mass changes indicate that the metasomatic fluid not only had the capacity to transport metals (Pb, Sb, Ag) and S, but also to leach metals (e.g. mass loss in Zn, Cd and As; cf. Dong et al., 1997a and b). Moreover, the fluid possessed the potential to redistribute pre-existing metal concentrations to other areas of the orebody via solution-associated remobilisation and possibly impart a deposit-wide zone refining (cf. Bodon, 1998; Walters and Bailey, 1998). This interpretation is also supported by high concentrations of Pb (2.2-8.9 wt%) in multiphase, hypersaline fluid inclusions (30-60 wt% NaCl equiv.) from quartz in hedenbergite-garnet bearing rocks and veins (Jenkins, 1994; Dong et al., 1997b). In addition to Pb, the fluid inclusions also contain high Zn (0.12-0.73 wt%) and Mn (1.2-4.9 wt%), and have low Fe/Mn ratios (0.5-2.2; Dong et al., 1997b).

The mass changes in metals closely reflect the major metal associations in the deposit, insomuch as Zn, As and Cd are enriched in hedenbergite ores, whereas Pb, Ag and Sb are

enriched olivine-pyroxenoid ores. However, mass gains in Pb, Sb and Ag and mass losses in Zn, As and Cd indicate that gangue-metal associations in the sample studied are the opposite to typical gangue mineral associations. This area of the orebody may therefore have been a source for Zn, As, and Cd, and a site of Pb, Ag and Sb upgrading.

Mass changes in REE provide evidence for HREE enrichment during metasomatism (Fig. 6.16f). HREE are predominantly transported as carbonate complexes in hydrothermal fluids (Bau, 1991). CO_2-rich fluid inclusions in metasomatic quartz (Dong et al., 1997b) and presence of calcite in Stage IIa quartz veins, suggests that the hypersaline fluid was CO_2-bearing. Hence, HREE enrichment is consistent with the CO_2-bearing nature of the metasomatic fluid.

6.8 CARBON ISOTOPES

Graphitic ore is unique with respect to its relative enrichment in disseminated graphite compared to other ore types and host metasediments. In particular, the biotite-garnet-hornblende-apatite facies contains the highest abundances of graphite, reaching up to 5 modal% in some bands. From the preceding sections, the geochemical evidence suggests that graphitic ores consist of variably mixed, interbanded hydrothermal sediments and pelitic detritus. Textural evidence supports a premetamorphic, pre-D_1 timing for graphite, similar to the sulphides in graphitic ore (Chapter 4 and 5). The absence of later graphite generations precludes its formation as an alteration product and/or hydrothermal precipitate associated with Stage II post-peak metamorphic metasomatism or Stage III near-surface hydrothermal activity (see Chapter 4). In fact, Stage IIa hedenbergite-garnet-quartz alteration involved the consumption of pre-existing Stage I graphite. It is therefore apparent that reduced carbon, as graphite, is an additional primary component in graphitic ores, that potentially played a role in ore formation. However, the source of carbon and the processes leading to its formation remain unclear. The temporal and geochemical constraints leave only two possibilities for the origin of graphite, viz.:

- thermal maturation of pre-existing organic matter during prograde metamorphism via graphitisation (Grew, 1974; Hoefs and Frey, 1976; Bonijoly et al., 1982; Large et al., 1994), or;
- precipitation of hydrothermal graphite during ore formation and its preservation through subsequent prograde metamorphism.

The former possibility requires either: i) biogenic activity at the site of sulphide deposition, and/or; ii) settling of detrital organic matter from the water column and its accumulation in a euxinic bottom-water environment. Conversely, carbonic gases such as CO, CO_2 and CH_4, or aqueous species such as HCO_3^- or H_2CO_3 are required in the ore-forming fluid if the graphite has a hydrothermal origin. In this case, graphite precipitation would have been controlled by changes in the redox state of the fluid (Ohmoto and Kerrick, 1977; Rumble et al., 1986; Luque et al., 1998). It would be expected that hydrothermal carbon could have been derived from a

multitude of sources, or a mixture thereof, via a range of processes, such as scavenging of carbon from pre-existing carbonate or kerogen-bearing rocks by hydrothermal fluid, or magmatic volatile release, or even mixing of the ore-forming brine with an exotic hydrocarbon-bearing fluid at some stage in its evolution or at the site of sulphide deposition. In light of these hypotheses, this section aims to determine:

- the source of reduced carbon in graphite;
- the most plausible process that lead to the formation of graphite in graphitic ore, and;
- the implications for ore genesis.

6.8.1 Methods

The most appropriate technique for determining the source of carbon in graphite and ultimately the processes responsible for its formation, is measurement of the $^{13}C/^{12}C$ isotopic ratio, i.e. $\delta^{13}C$. Samples with the greatest visual abundance of graphite were collected from drillcore and comprised 11 samples of graphitic ore and 1 sample of graphite-bearing banded olivine facies ore. Locations and sample descriptions can be found in Appendix 3. All samples had no Stage IIa hedenbergite-garnet-quartz alteration except for one that had only weak hedenbergite-garnet alteration of knebelite bands (sample no. NZ034-7). Most samples contained very minor to no Stage IIc pyrosmalite veinlets and none contained Stage III assemblages.

Mineral assemblages comprising graphitic ore and characteristic ore textures have been described in Chapter 4, but are briefly reiterated here to assist the discussion and provide context. Graphite is typically concentrated in quartz-sulphide (-garnet-apatite)-rich bands and is rare to absent in knebelite (±pyroxferroite-grunerite)-rich bands. Abundances typically vary from band to band and in instances, vary across the width of a single band. The greatest concentrations are found in biotite-rich bands in biotite-garnet facies ores, where local concentrations of up to 10 modal% may occur. These bands may also be enriched in apatite (e.g. up to ~10-15 modal%). Disseminated graphite is very common in quartz-rich bands, but abundances are typically lower, e.g. ≤2 modal%. Textural features of graphite are consistent between all samples, occurring as disseminated flakes and laths up to 1mm in length aligned along grain boundaries of granoblastic quartz, and as inclusions mostly in quartz, biotite and garnet. Graphite typically defines the dominant foliation (i.e. S_1 and/or S_2) in conjunction with biotite (when present), and in instances is intergrown with the latter.

The fine-grained, disseminated habit of graphite and intergrowths with other silicates, especially quartz, precludes its physical separation with ease. Instead, an HCl digestion technique similar to that of Large et al. (1994) was used to extract any carbonate carbon in the samples. $\delta^{13}C$ determinations were then carried out on the partially digested, carbonate-free residue. Details of the method are outlined in Appendix 3. All samples were analysed for wholerock C, H and S concentrations (wt%) on a Carlo Erba EA1108 elemental analyser using standard techniques at the Central Science Laboratory, University of Tasmania.

Table 6.14 $\delta^{13}C$ values determined from graphite and corresponding wholerock C contents in graphitic to banded olivine ores. Refer Appendix 3 for additional geochemistry and sample data.

Sample No.	$\delta^{13}C$ (‰, PDB)	C (wt%)	S (wt%)	% clastic component
NZ160-1	-22.63	0.74	1.97	-
SZU134-1	-24.01	0.70	1.92	-
NZ029-8	-25.61	-	-	-
SZ157-22	-23.65	1.09	2.62	-
NZ004-6	-26.71	0.76	1.71	-
NZ029-13	-25.56	1.58	2.74	38
NZ040-8	-23.36	1.54	0.06	-
NZ035-10	-22.99	0.89	2.83	-
NZ009-3	-24.83	0.99	2.03	-
NZ042-4	-22.17	0.77	1.18	-
NZ039-3b (BAND08)	-26.02	1.71	1.88	27
NZ034-7	-23.60	1.13	1.98	12
NZ016-1a	-27.09	1.45	3.91	12
NZ160-31	-27.96	0.67	5.32	21
NZ033-2 (BAND09)	-26.57	1.12	2.33	31
MAX	*-22.17*	*1.71*	*5.32*	
MIN	*-27.96*	*0.67*	*0.06*	
AVERAGE	***-24.85***	***1.08***	***2.32***	
STDEV	*1.79*	*0.36*	*1.23*	
MEDIAN	*-24.83*	*1.04*	*2.01*	
Precision	*±0.03*	*±0.02*	*±0.1*	
Detection limit	*n/a*	*0.01*	*0.05*	

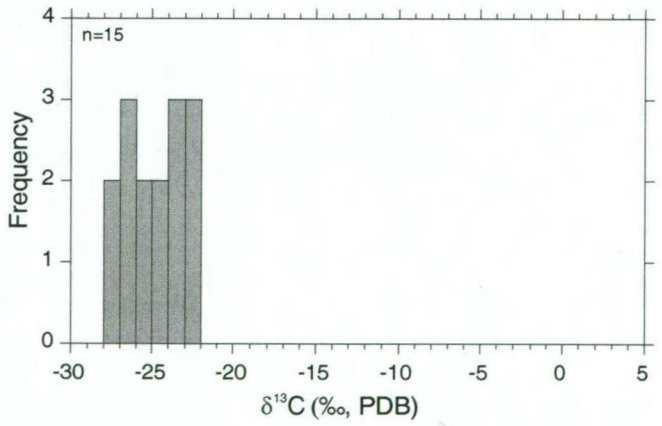

Figure 6.21 Frequency histogram illustrating the distribution in $\delta^{13}C$ values from graphite in predominantly graphitic to banded olivine ores in the Northern Zone of the deposit. All samples fall within a narrow range between approximately -22‰ to -28‰.

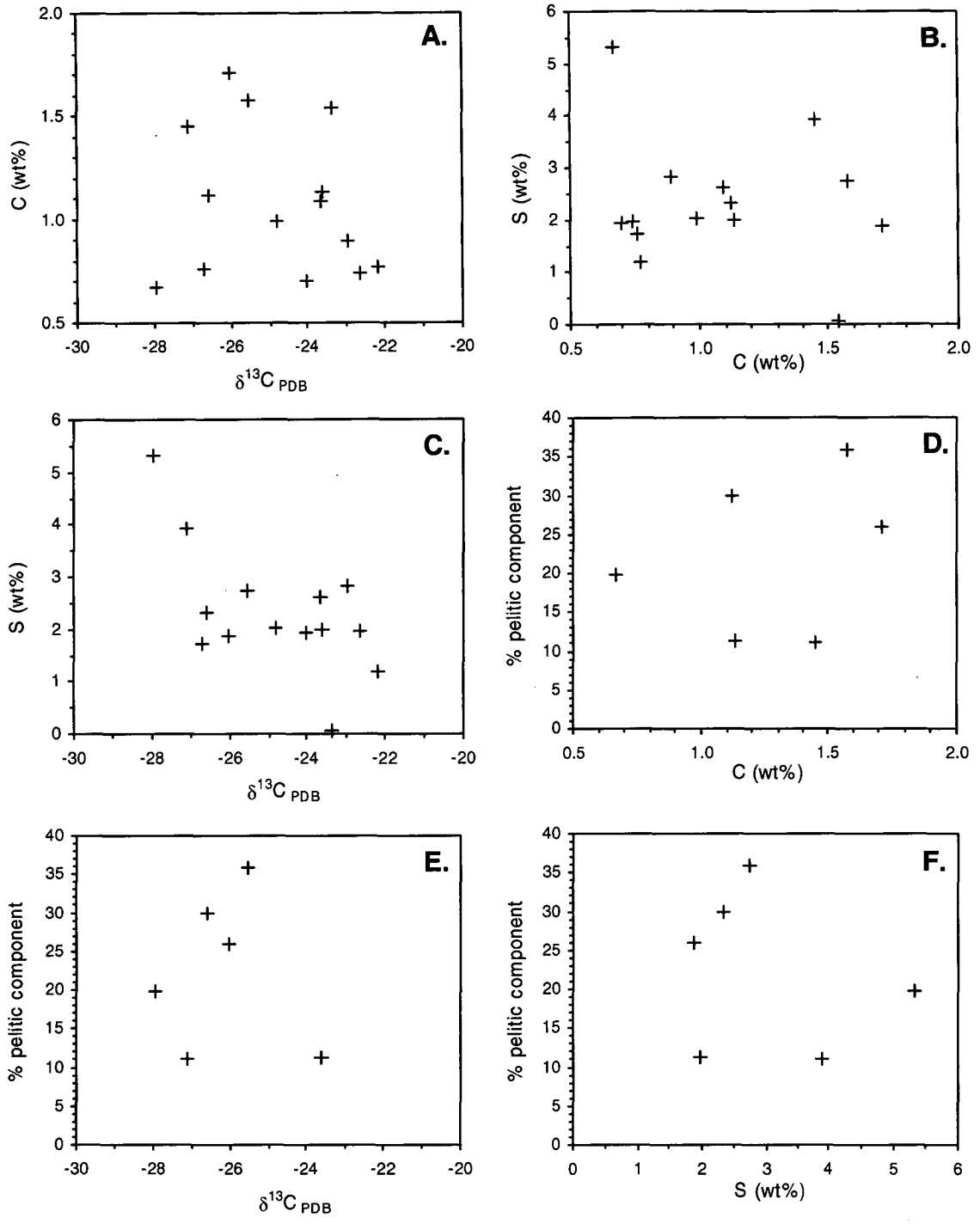

Figure 6.22 Bivariate plots depicting relationships between $\delta^{13}C$, C, S and % pelitic component.

6.8.2 Results

$\delta^{13}C$ values from graphite and wholerock C and S concentrations can be found in Table 6.14 and Appendix 3. $\delta^{13}C$ values fall within a narrow range between approximately -22 to -28‰, with an average of -25‰. The narrow range in values is supported by a small standard deviation of 1.79‰ and is clearly illustrated on a frequency histogram plot (Fig 6.21). Graphite in the banded quartz-olivine ore sample (NZ034-7) with weak Stage IIa hedenbergite-garnet alteration returned a similar value of -23.6‰. There are no clear relationships between $\delta^{13}C$, C (wt%), S (wt%) and the calculated % pelitic component in the samples (Fig. 6.22).

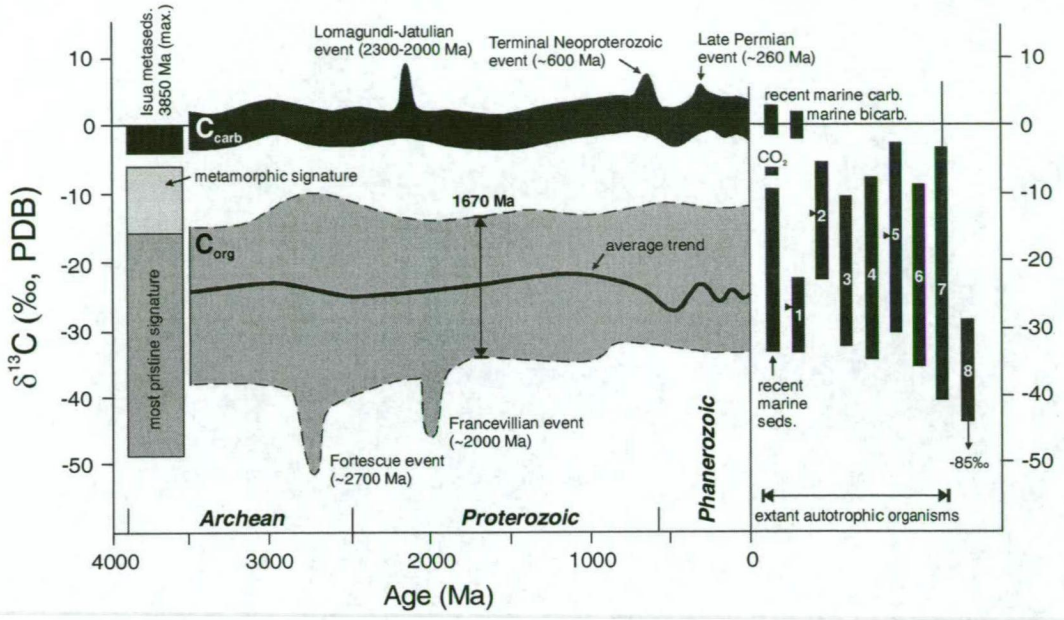

Figure 6.23 Isotopic evolution of the Earth with respect to $\delta^{13}C$ values of organic carbon (C_{org}) and carbonate carbon (C_{carb}) compared to the isotopic compositions of present-day carbon reservoirs such as marine bicarbonate and biogenic matter (modified after Schidlowski, 2001). The diagram shows that $\delta^{13}C$ values for C_{org} and C_{carb} have varied little from the oldest recognised biogenic signature preserved in ~3850 Ma old metasediments of the Isua Supracrustal Belt in western Greenland ($\delta^{13}C$ < -16‰; Mojzsis et al., 1996; Schidlowski, 2001) to the present-day. The light grey field for the Isua metasediments represents resultant partial isotopic re-equilibration of biogenic $\delta^{13}C$ values in graphite caused by amphibolite facies metamorphism. Negative perturbations along the lower organic carbon field at ~2700 Ma and ~2000 Ma provide evidence for periods of significant methane participation in the formation of precursor organisms. Expected most pristine $\delta^{13}C$ values for organic carbon (graphite) in the gneiss at Cannington should range between approximately -13‰ to -34‰ with an average close to -23‰ based on a maximum depositional age of 1670 Ma. Isotopic ranges in present-day organisms include: 1 – C3 plants; 2 – C4 plants; 3 – CAM plants; 4 – eukaryotic algae; 5 – natural and cultured cyanobacteria; 6 – photosynthetic bacteria other than cyanobacteria; 7 – methanogenic bacteria; 8 – methanotrophic bacteria. Black triangles indicate approximate averages for particular organisms.

6.8.3 Carbon sources

There are essentially 4 main carbon reservoirs on Earth. The mantle is believed to have $\delta^{13}C$ values ranging between -3 to -8‰ with an average of -6‰ (Large, et al., 1994; Schidlowski, 2001). Modern marine carbonates range between -1 to 2‰, and marine bicarbonates have similar ranges between -2 to 1‰ (Schidlowski, 2001). However, transient periods of heavier values between ~5 to 8‰ have been recorded in Earth's history (Fig. 6.23). Biogenic carbon is isotopically light, ranging between -20 to -30‰, with the terrestrial biomass averaging -26±7‰ (Schidlowski, 1987).

Biological activity is the most effective naturally occurring process that fractionates carbon isotopes (Schidlowski, 1987, 2001). The intrinsic light $\delta^{13}C$ signature of biogenic carbon is due to metabolically driven fractionation of inorganic carbon through CO_2-fixing by living organisms (op. cit.). The lighter ^{12}C isotope is strongly partitioned into organically produced carbon during anabolic and catabolic reactions necessary for life. The fractionation process that drives this is largely controlled by isotopic reaction kinetics that occur during enzymatic CO_2-fixing (Schidlowski, 2001). This is especially true for photosynthesis. The greatest fractionation between $^{13}C/^{12}C$ occurs during the production of methane by anaerobic degradation of organic matter, or thermal maturation of kerogen at temperatures >100°C. Biological methanogenesis causes extreme fractionation with residual products having $\delta^{13}C$ values of approximately -80‰, e.g. methanogenic and methanotrophic bacteria (op. cit.).

Apart from minor transient perturbations (ibid.), the average isotopic signature of biological carbon has remained essentially constant throughout the geological record (Schidlowski, 2001; Fig. 6.23). The unique range and consistency of $\delta^{13}C$ values through time provides a well defined basis for discriminating organic carbon in a wide variety of rocks of any age, including hydrothermally precipitated graphite (reduced C) and carbonate (oxidised C), i.e. recycled carbon (Rumble et al., 1986; Rumble and Hoering, 1986; Luque et al., 1998). At Cannington the average $\delta^{13}C$ signature of graphite (-25‰) in graphitic ore is very close to the average $\delta^{13}C$ value of biogenic matter in rocks of similar age to the host metasediments, i.e. 1670 Ma (Page and Sun, 1998; Giles, 2000). This is consistent with a biogenic source for graphite in the ores.

6.8.4 Metamorphic effects and preservation of graphite

To preserve graphite in carbonaceous metapelites from devolatilising into a mixture of CH_4 and CO_2 during metamorphism, local conditions must be maintained at low a_{H2O} and fO_2, i.e. graphite stable, reduced conditions and low X_{H2O} fluids (Ohmoto and Kerrich, 1977; Holloway, 1984; Burton, 1986; Rumble and Hoering, 1986; Large et al., 1994; Connolly, 1995). Numerous studies have shown that during metamorphism of carbonaceous metapelites, $\delta^{13}C$ signatures increase with increasing metamorphic grade (McKirdy and Powell, 1974; Hoefs and Frey, 1976; Valley, 1986; Horita, 2001). If there is coexisting carbonate, then the system moves toward isotopic equilibrium, and the difference in $\delta^{13}C$ values between carbonate and graphite ($\Delta_{cc\text{-}gr}$‰) decreases with increasing metamorphic grade (Fig. 6.24; op. cit.). Hence, the $\delta^{13}C$ value of organic carbon increases during metamorphism provided there is a second carbon species in the system (either a mineral, or introduced fluid) to permit isotopic exchange. Preservation of a pristine biogenic signature is therefore facilitated by the absence of other carbon-bearing phases.

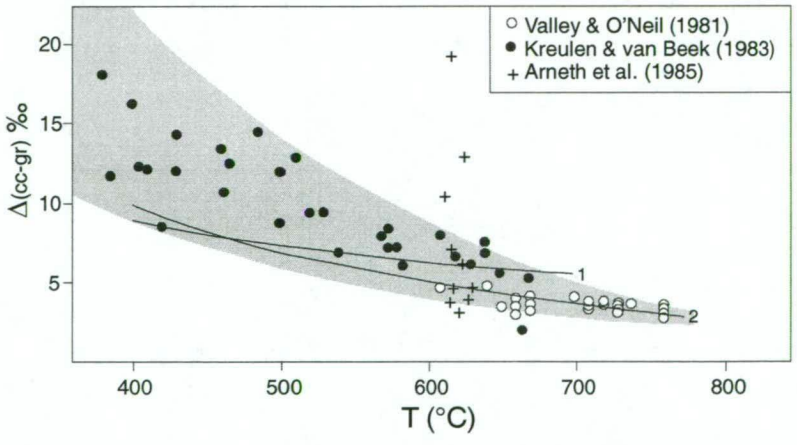

Figure 6.24 Carbon isotope fractionation between sedimentary organic carbon and carbonate carbon as a function of increasing metamorphic grade (modified after Valley, 1986; Schidlowski, 2001). Fractionation in metamorphosed rocks is expressed in terms of the difference between $\delta^{13}C$ values of coexisting calcite (cc) and graphite (gr), such that $\Delta(cc\text{-}gr) = \delta^{13}C_{cc} - \delta^{13}C_{gr}$. The grey field represents the envelope of natural data. Actual field data from various metamorphic terranes (see legend), and calculated isotope equilibria (Bottinga, 1969, curve 1) and empirically determined fractionation (Wada and Suzuki, 1983, curve 2) indicate that $\Delta(cc\text{-}gr)$ decreases with increasing metamorphic grade, i.e. the degree of re-equilibration increases proportionally with metamorphic grade. Essentially, the isotopic signature of biogenic matter will increase to heavier $\delta^{13}C$ values (Schidlowski, 2001). Departures from this trend, such as retention of high $\Delta(cc\text{-}gr)$ values at elevated temperatures are believed to be related to kinetic retardation of isotopic re-equilibration.

However, in the absence of a second carbon-bearing phase such as carbonate, isotopic fractionation will still occur during metamorphism, albeit less effectively, due to Rayleigh distillation associated with devolatilisation. For example, metamorphism of carbonaceous shale under low fO_2 (i.e. reduced) conditions produces isotopically light CH_4, leaving residual carbonaceous matter enriched in ^{13}C (Nabelek et al., 1984; Rumble and Hoering, 1986; Valley, 1986). Therefore, as reaction progress proceeds, the $\delta^{13}C$ value of remaining graphite will increase. If devolatilisation involves the release of CO_2, then ^{13}C is partitioned into the fluid phase and the residual carbon is enriched ^{12}C (Valley, 1986; Rumble and Hoering, 1986).

For graphite to have been preserved and retain a near-pristine biogenic $\delta^{13}C$ value in the graphitic ores at Cannington, graphite stable, low a_{H2O}, reduced conditions must have been maintained in the ores during metamorphism. The composition of the coexisting metamorphic fluid must also have been maintained at a low X_{H2O} (~ <0.6), and a unique balance between isotopically heavy CO_2 and isotopically light CH_4 during devolatilisation. Burton (1986) argued that unusual sector-zoned garnets in graphitic pelites were indicative of growth in the presence of graphite under reduced conditions (e.g. log fO_2 of ~ -23 at 500°C and 6.5kbar) and a fluid phase characterised by high X_{CO2} (0.48) relative to X_{CH4} (0.001). The texture of sector-zoned garnets in graphitic ores at Cannington are very similar to those described by Burton (1986), and may provide possible evidence for graphite buffered, reduced, high X_{CO2} conditions during metamorphism. A fluid with CO_2>CH_4 is therefore likely to have aided the preservation of light $\delta^{13}C$ values in the residual graphite in the ores.

6.8.5 Implications for ore genesis

Even though the $\delta^{13}C$ value of graphite in graphitic ore at Cannington is consistent with the presence of biogenic carbon, the origin of the carbon is still questionable. As previously outlined, carbon (as graphite) could either have: i) a direct biogenic origin via thermal maturation of *in situ* kerogen during metamorphism, or ii) may represent a hydrothermal precipitate from the primary ore-forming fluid.

In the first instance, biogenic carbon could have either accumulated with the detrital pelitic component in the ores, or formed by *in situ* microbial activity in the metalliferous sediments. Figure 6.22d demonstrates that there is no relationship between the % pelitic component and the concentration of C in the ores. If the calculations of the % clastic component in the ores are correct, then the lack of a positive correlation suggests that organic matter did not accumulate at the same rate as clastic sedimentation. This provides evidence that either: i) C is not of detrital origin and therefore formed microbially in response to nutrient availability within the metalliferous sediment, or; ii) that C detrital and was later partially consumed via devolatilisation during metamorphism, thereby upsetting a correlation with the proportion of pelitic detritus in the ores. Considering the lack of C in host pelitic sediments compared to graphitic ores, a chiefly detrital origin is unlikely. This implies that *in situ* biological activity may have occurred in the chemical sediments, leaving scope for biogenic sulphate reduction as a mechanism for sulphide deposition. Such a hypotheses could be further explored using

sulphur isotope determinations on sphalerite and galena within individual bands, based on the premise that syn-diagenetic C may have been available to sulphate reducing bacteria.

In the second instance, if graphite was precipitated from the ore-forming fluid, then the biogenic signature is consistent with recycled organic carbon deposited from an isotopically light, possibly CH_4-bearing, reduced hydrothermal fluid. Overall, the available evidence neither confirms nor denies either of the hypotheses.

6.9 SUMMARY AND CONCLUSIONS

Relative compositional variations between Al_2O_3, TiO_2 and Zr in the gneiss are consistent with primary sedimentary fractionation processes rather than variations in provenance. Psammitic gneiss are characterised by Zr enrichment relative to TiO_2 and Al_2O_3, in contrast to pelitic gneiss that are comparatively enriched Al_2O_3 and TiO_2 and depleted in Zr. The preservation of primary sedimentary fractionation trends suggests that the latter elements remained immobile during metamorphism.

Garnetiferous quartzites, sillimanite-garnet schists and gahnite-bearing schists represent the metamorphosed alteration halo that envelops the Cannington deposit (Chapter 3). Primary sedimentary fractionation trends in the gneiss have been preserved in these garnetiferous rocks based on Al_2O_3, TiO_2 and Zr immobility during premetamorphic hydrothermal alteration and subsequent metamorphism. Immobile element ratios provide evidence that sillimanite-garnet schists have pelitic protoliths equivalent in composition to the pelitic gneiss. In contrast, garnetiferous quartzites had psammitic precursors. Compared to pelitic gneiss and sillimanite-garnet schists, gahnite-bearing schists are enriched in Al relative to TiO_2 and Zr. Compositional features are consistent with a more mature Al-rich shale protolith; the unaltered and metamorphosed equivalent of which has not been identified in the host metasedimentary succession at Cannington. The gahnite-bearing schist is therefore interpreted as an enigmatic, more mature Al-rich sedimentary unit spatially associated with graphitic ores in the Northern Zone.

Unlike the metasedimentary host rocks, Zr displays immobile behaviour in graphitic ores along with TiO_2. Al_2O_3 displays mobile behaviour in same olivine and quartz-apatite facies ores. Similar TiO_2/Zr ratios provide evidence for a pelitic component in graphitic ore. In particular, biotite-garnet facies ores plot within the pelitic gneiss population on an Al_2O_3-TiO_2-Zr ternary diagram. The clear correlations between Al_2O_3-TiO_2-Zr systematics in graphitic ore and pelitic gneiss compositions indicate that geochemical trends are primary premetamorphic features. Hence, Al_2O_3, TiO_2 and Zr systematics were not modified during metamorphism.

Calculated mass changes using an average pelitic gneiss precursor composition for sillimanite-garnet schists, are characterised by absolute mass gains in Si, K, Al, Mn, Pb, Zn and Rb, and absolute mass losses in Fe, Mg, Na and Sr. Similar absolute mass gains and losses were determined for gahnite-bearing schist using a calculated Al-rich pelitic precursor

composition. Calculated hydrothermal REE signatures are generally characterised by flat LREE profiles and weak positive Eu anomalies. Greater variations occur in the hydrothermal HREE signatures, in spite of smaller mass losses in comparison to the larger mass changes in LREE, especially Ce and Nd. Application of the mass changes to the development of a modified BHT alteration index results in expansion of the BHT alteration field on bivariate plots when compared to the original BHT index (Walters, 1994b). This may indicate that the modified index is more sensitive to the intensity of BHT alteration than the original BHT index and therefore, may be more useful for determining vectors to ore. However, its application requires rigorous testing.

Calculated mass-volume changes for graphitic ore using an average pelitic gneiss precursor vary considerably from net mass gains of ~25g/100g for biotite-garnet facies ores that contain the highest proportion of pelitic detritus, to 1834g/100g for olivine facies ores that contain the smallest proportion of pelitic detritus. Similarly, relative net volume changes range from ~14 to 2469% respectively. Such large net mass-volume changes are unrealistic with regard to replacement of pelitic sediments alone, but are more consistent with coincident accumulation of pelitic detritus and metalliferous hydrothermal sediment. The delicate, laterally continuous mineralogical banding that is intrinsic to graphitic ore, especially biotite-garnet facies ore, may indicate that ore formation involved a complex interplay between variations in hydrothermal fluid fluxes and accumulation of pelitic detritus. Same quartz-apatite and olivine facies ores formed by replacement of pre-existing metalliferous chemical-clastic sediments very soon after their accumulation, based on evidence for Al_2O_3 mobility. However, selective replacement of favourable, possibly more permeable units in the chemical sediments cannot be resolved from the geochemistry.

Chondrite normalised REE signatures in the graphitic ore are characterised by LREE-enrichment and strong positive Eu anomalies that strongly resemble REE profiles of hydrothermal vent fluids and chemical sediments proximal to submarine hydrothermal hot springs. Enrichment in Eu suggests the hydrothermal fluid was hot (>250°C), reduced and slightly acid in order to facilitate the transport of Eu^{+2} from the source hydrothermal reservoir to the site ore deposition. Biotite-garnet facies ores have less intense Eu anomalies in comparison to olivine facies ores. A positive correlation between the intensity of the Eu anomaly in the calculated hydrothermal REE signature and the proportion of pelitic detritus is interpreted to reflect changing physicochemical conditions. It is proposed that the concentration of Eu^{+2} in the hydrothermal fluid progressively decreased in response to decreasing temperature and/or increasing fO_2 and pH with concomitant increasing proportions of pelitic detritus in the chemical sediments. Strong positive Eu anomalies and small pelitic detrital content indicate that olivine ores probably formed in a more proximal environment to the fluid source where conditions were hotter and reduced, whereas biotite-garnet ores formed in a distal, cooler and possibly more oxidised environment along with higher proportions of pelitic material.

$\delta^{13}C$ values indicate that graphite carbon has a premetamorphic biogenic origin, and formed either by *in situ* microbial activity in the metalliferous sediments, or accumulated as a detrital component. The preservation of graphite and near-pristine biogenic $\delta^{13}C$ values suggests that metamorphic mineral equilibria was buffered by graphite.

Mass changes associated with hedenbergite-garnet-quartz metasomatism of olivine facies ore are characterised by gains in Ca, S, Pb, Sb, Ag and Y, and depletion in Si, Fe, Mn, Zn, Cd, As and W. These mass changes are consistent with the breakdown of olivine to hedenbergite and garnet, deposition of argentiferous galena, and consumption of sphalerite and loellingite/ arsenopyrite. LREE and Eu remained relatively immobile during metasomatism in contrast to HREE enrichment. This is likely to be related to high a_{CO_2} in the hypersaline fluid, which increases the solubility of HREE. Mass gains in Al and Zr suggest that these commonly immobile elements were slightly mobile during high temperature metasomatism. The mass changes demonstrate that Stage IIa metasomatic fluid was capable of remobilising metals from pre-existing ores.

Chapter 7

Pb Isotope Systematics: Metal sources

7.1 INTRODUCTION

Pb isotope studies have been successfully used to resolve various ore genesis quandaries (Stanton and Russell, 1959; Zartman and Stacey, 1971; Cummings and Richards, 1975; Stacey and Kramers, 1975; Loveless, 1975; Gulson, 1986; Carr et al., 1995; Sun et al., 1994 and 1996; Carr and Sun, 1996; Roache, 1996; and many others). In particular, they have been used as a geochronological tool for determining the age of ore formation, and discriminating post-mineralisation hydrothermal and magmatic events in terrains characterised by complex geodynamic histories (Zartman and Stacey, 1971; Gulson, 1986; Carr et al., 1995). Pb isotopes have also been used for identifying potential metal-bearing source rocks from a crustal-scale perspective (e.g. crustal versus mantle reservoirs; Doe and Zartman, 1979), to a regional-scale (e.g. particular rock units within older basement, or a particular magmatic body or event; Carr et al., 1995). By integrating such Pb isotope data with a detailed understanding of geological relationships for a particular metallogenic province, it is possible to construct terrain specific Pb evolution models augmented by U-Pb_{zircon} age dating (e.g. Carr et al., 1995; Sun et al., 1994 and 1996). Such models can then be incorporated into mineral exploration strategies.

At Cannington, Pb isotopes can be used to reconcile the timing of ore formation, as well as possible Pb-bearing source rocks on a regional- to crustal-scale. The main aims of the study are to:

- characterise the isotopic variability of the ore types and host rocks from a genetic and paragenetic viewpoint and ascertain whether Pb was introduced during one or more hydrothermal events;
- determine possible Pb-bearing source rocks on a regional- and crustal-scale and substantiate if there is a genetic link between the deposit and granites of the Williams-Naraku Batholith;
- determine the source of Pb in amazonite from lode pegmatites and gahnite-bearing schists;
- determine a Pb-model age (or ages) for mineralisation using a terrain specific Pb evolution model for the Proterozoic of northern Australia (Sun et al., 1994 and 1996) and determine whether it correlates with U-Pb zircon ages from Cannington.

7.2 METHODS

7.2.1 Sampling strategy and preparation

All samples used in the Pb isotope study were collected from drillcore, the locations of which are illustrated in Figure 7.1. The complete sample dataset, including other datasets from

Cannington, are summarised in Table 7.1.

Galena samples were taken from all ore types throughout the deposit. In order to assess potential isotopic variation, 30 representative galena samples were carefully selected covering every stage of the paragenesis. Stage I galena in olivine-pyroxenoid ore was obtained from polished thin sections of least retrogressed samples. Sampling was restricted to micropickings of spheroidal galena inclusions (≥150μm in diameter) within peak metamorphic knebelite (Fig. 7.2), and was achieved using a fine stainless-steel needle to carefully gouge out the inclusion under a binocular microscope. The natural static cling of the extracted galena to the needle point facilitated direct transferral of the sample to a teflon vessel, which is used in the electro-deposition stage of sample preparation (refer Appendix 4). This high-resolution sampling technique guaranteed pristine, high quality samples with very minimal to no contamination by

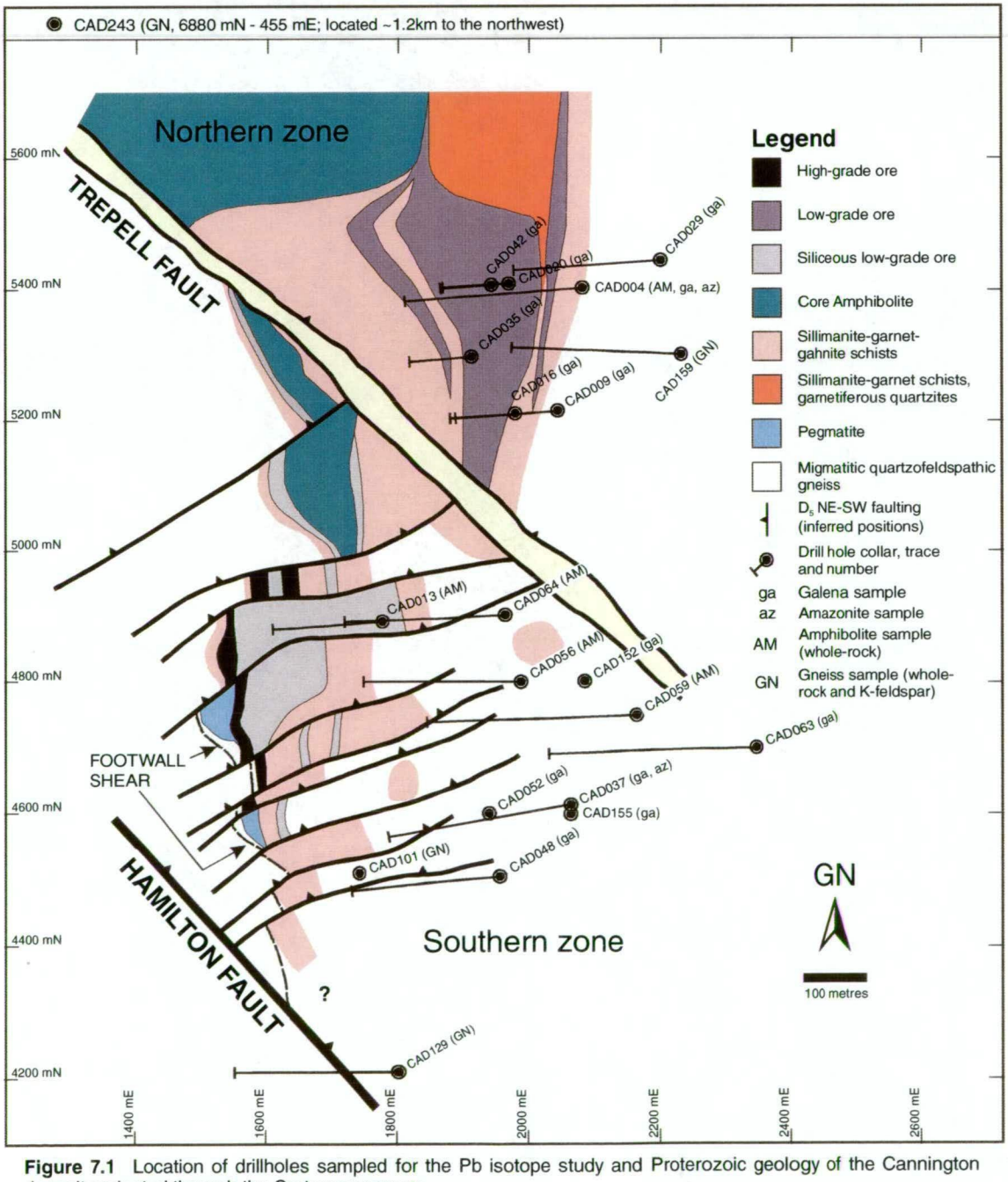

Figure 7.1 Location of drillholes sampled for the Pb isotope study and Proterozoic geology of the Cannington deposit projected through the Cretaceous cover.

Table 7.1 Summary of all Cannington Pb isotope data used in this study (actual data can be found in the relevant sources).

Source of data	Sample	Number of samples	Number of analyses and laboratory location	Comments
McCarthy (1996)	galena	5	5 (CSIRO)	paragenetically constrained samples
BHP unpubl. report (1992)	wholerock (sulphide ore)	4	4 (?)	3m composites from drill core, data corrected for CSIRO lab., sample data unavailable
McNaughton (1995) JCU/AMIRA P438 (1997)	galena	5	5 (UWA)	paragenetically unconstrained, sample data unavailable
McNaughton (1996) JCU/AMIRA P438 (1997)	orthoclase (pegmatite)	3	3 (UWA)	sample data unavailable
This study	galena	18	17 (CSIRO) 8 (RSES)	paragenetically constrained samples. 4 double-spike repeats from McCarthy (1996) samples
	K-feldspar:		11 (CSIRO)	
	orthoclase (gneiss)	5		
	amazonite (lode pegmatite)	2		
	wholerock:		11 (CSIRO)	
	amphibolite	5		
	gneiss	5		
TOTAL		52	64	

CSIRO – Conventional data from the Commonwealth Scientific and Industrial Research Organisation, Exploration and Mining, North Ryde.
RSES – Double-spike data from the Research School of Earth Sciences, Australian National University, Canberra.
UWA – Conventional data from the University of Western Australia, Perth.
? – laboratory location unknown.

later generations of galena. Stage II and III galena samples were handpicked (i.e. scratchings) from polished thin sections and drillcore samples using a stainless-steel needle. In instances, micropickings from polished thin sections were required so as to overcome contamination from other galena generations.

Host rocks were sampled from drillcore with the aim of delineating potential ore-Pb sources and characterise Pb evolution growth curves. Only least altered/retrogressed samples were used. None of the samples contained secondary feldspar associated with a regional sodic metasomatism, but did contain very weak, albeit ubiquitous, incipient sericite alteration

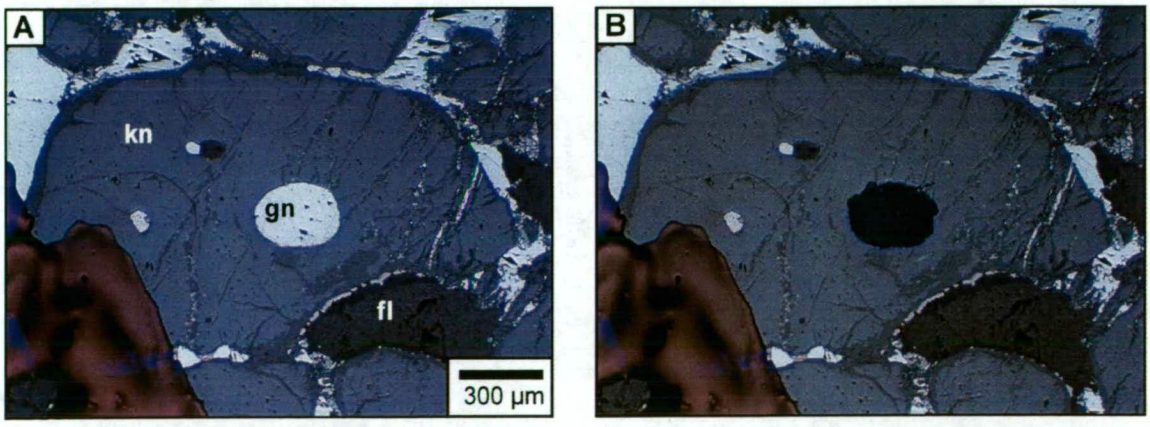

Figure 7.2 Photomicrograph of stage I spheroidal galena inclusion in knebelite. A. prior to extraction. **B.** the hole left after removal using the micropicking technique (reflected light, SZ037-13, 517.9m). Abbreviations: fl-fluorite, gn-galena, kn-knebelite.

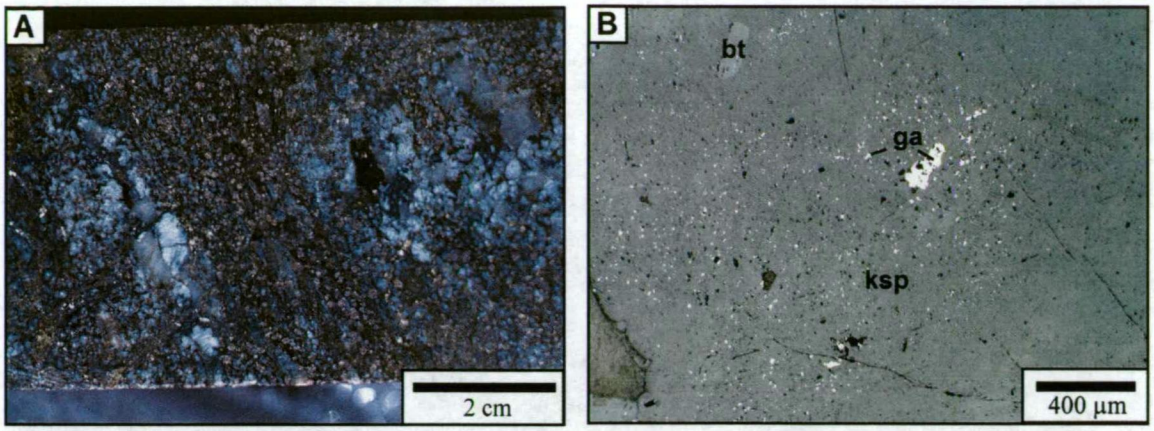

Figure 7.3 **A.** Biotite-garnet (±gahnite) schist containing grey coloured K-feldspar (partial melt fraction) that was sampled for Pb isotope determination. **B.** The grey colouration is due to fine inclusions of galena in the K-feldspar that formed by partial assimilation of pre-existing sulphide during peak metamorphism (NZ009-4, 226.9m). Abbreviations: bt-biotite, ga-galena, ksp-K-feldspar.

the Core Amphibolite were analysed for wholerock Pb isotope ratios. Four of these samples were supplied by S. Walters (BHP Minerals). Three representative samples of quartzofeldspathic gneiss (Gandry Dam Gneiss) were collected from within 100m of the deposit. One of these samples was supplied by K. McGuckin (BHP Minerals). To minimise the possibility that these samples had been contaminated by ore Pb due to close proximity to the deposit, two distal samples were also collected. One of these samples was taken from a drillhole approximately 1.2km along strike from the deposit to the north, and another from a drillhole south of the Hamilton Fault. Both samples were supplied by Dr. S. Walters (BHP Minerals).

All host rock samples were crushed and pulverised in a tungsten carbide (i.e. low-Pb) mill and then analysed for wholerock Pb. K-feldspar (orthoclase) mineral separates were also collected (212µm to 600µm sieved fraction) from the gneiss samples using a Franz isomagnetic separator set at 1.2 Amps, 30° vertical inclination and 20° lateral inclination. To separate grains that contained inclusions of garnet and/or biotite, the samples were further purified using a setting of 2.4 Amps, 30° vertical inclination and 10° lateral inclination, and lastly checked under a binocular microscope. Minor inclusion free quartz was also contained in the mineral separates.

To ascertain the source of Pb in lode pegmatites, amazonite mineral separates were collected from an intrusive lode pegmatite hosted in the Core Amphibolite (Southern Zone), and an amazonite-bearing *in situ* partial melt in gahnite-bearing schist (Northern Zone). A grey-coloured K-feldspar containing minor fine grained disseminated galena from an *in situ* partial melt in the latter rock type was also sampled using a dentistry drill (Fig. 7.3).

7.2.2 Analytical procedures

Sample preparation for conventional Pb isotope analyses was carried out in the Pb isotope facility at CSIRO Exploration and Mining in North Ryde, New South Wales. For low-Pb samples (orthoclase separates and host rocks), a sequential acid-leach technique was

employed (details are outlined in Appendix 4; see also Gulson et al., 1984, and Carr et al., 1995). The sequential acid-leach method provides a means of extracting the radiogenic Pb component — a product of *in situ* radioactive decay of U and Th since the formation of the rock — that typically occurs along grain margins and fractures in minerals. This radiogenic Pb component masks the initial Pb isotope ratios to a degree (i.e. manifest radiogenic signatures) and is therefore regarded as a contaminant. Theoretically, the first leachate will be enriched in radiogenic Pb and subsequent leachates will contain progressively less, yielding isotopic ratios closer to initial values when the mineral or rock formed. However, departures in this sequence can occur and (in cases) later leachates can be more radiogenic than initial leachates. This is probably due to variabilities in the geological history of the sample in question, as well as sample procedures in the laboratory. As a precautionary measure, a similar sequential leach method was used for the wholerock analyses on amphibolite samples to overcome any potential radiogenic Pb contamination produced by either *in situ* decay of U and Th, and/or possible post-depositional hydrothermal alteration (if present).

Wholerock U and Th concentrations in host rock samples (gneiss and amphibolite) were determined by XRF analysis to assess the possible degree of radiogenic Pb input (refer Appendix 4 for analytical results). Unfortunately, U and Th contents were not determined for:

- samples from which amazonite separates were collected, i.e. lode pegmatites; and
- amazonite and orthoclase separates.

Unlike the inherent problem of radiogenic Pb contamination in low-Pb samples, U and Th do not substitute into the galena lattice. Therefore, Pb isotope determinations from galena represent initial ratios at the time of crystallisation. Hence, the procedure employed for galena separates involved microelectrode deposition of Pb rather than acid digestion.

Determinations were carried out on a VG Isomass 54E solid source thermal ionisation mass spectrometer run in fully automatic mode at the CSIRO, North Ryde. Data were normalised to the U.S. National Bureau of Standards SRM 981 by the application of a 0.08% per atomic mass unit correction (Gulson et al., 1984; Gulson, 1985; Carr et al., 1995). Analytical precision (2σ) has been estimated at ±0.05% for $^{207}Pb/^{206}Pb$ and $^{207}Pb/^{204}Pb$, and ±0.1% for $^{208}Pb/^{206}Pb$, $^{208}Pb/^{204}Pb$ and $^{206}Pb/^{204}Pb$ (Gulson et al., 1984; Carr et al., 1995). Errors are displayed in the upper left corner of the ratio plots presented here and represent 95% confidence limits, as well as the machine fractionation trend determined from over 1,400 analyses of international Pb standards (Carr et al., 1995). These precision ellipses only apply to the CSIRO analyses undertaken in this study and that of McCarthy (1996).

The double-spike procedure was applied to seven samples comprising three new galena samples and four galena samples previously analysed using the conventional analytical technique described above. The double-spike procedure yields an order of magnitude greater precision and accuracy in comparison to the conventional technique, and is particularly useful for resolving ambiguous trends in conventional Pb isotope data, i.e. more precise

interpretations can be attained. This high precision method is achieved by the use of a $^{207}Pb/^{204}Pb$ double-spike for the correction of mass fractionation effects during conventional Pb isotope analyses (Woodhead et al., 1995), reducing the size of the error ellipse on the subsequent ratio plots by approximately $^1/_5$ (S-S. Sun, pers. comm., 1998). Sample preparation was carried out at the Research School of Earth Sciences (RSES), Australian National University, using the method outlined by Woodhead et al. (1995). Analyses were acquired using a Finnigan MAT261 multicollector mass spectrometer at the RSES by Dr S-S. Sun of the Australian Geological Survey Organisation (AGSO) working on behalf of the AMIRA P480 Pb isotope project: the data are presented here with permission from Drs G. Carr (CSIRO) and A. Goode (AMIRA). Data were normalised to the U.S. National Bureau of Standards SRM 981. Analytical precision (2σ) has been estimated at ±0.01% for $^{208}Pb/^{204}Pb$ and ±0.003% for all other ratios based on over 100 analyses of the SRM 981 standard (Woodhead et al., 1995).

With regard to mineral separate samples, Pb contents were determined by the Pb isotope dilution technique (Gulson, 1986). Such data may vary from wholerock XRF analyses and routine Pb assays of 1m drillcore samples (i.e. 1m composite samples) on mineralised rocks. For example, galena separates have Pb contents of 86.58 wt%, whereas the Pb assay of the corresponding 1m composite from which the sample was taken will be significantly lower due to dilution by other components in the rock.

7.3 ADDITIONAL Pb ISOTOPE DATA

Additional Pb isotope data from Cannington is summarised in Table 7.1. Paragenetically constrained pickings of Stage III galenas from vuggy quartz-carbonate veins associated with D_5 subvertical faults in the Southern Zone were carried out by McCarthy (1996). Analyses were conducted at the CSIRO, North Ryde. Double-spike repeats on these samples were done at the Research School of Earth Sciences (RSES, Australian National University, Canberra) by Dr. S-S. Sun (AGSO).

Four wholerock Pb isotope determinations were provided by BHP Minerals (S. Konecny, pers. comm., 1996). Each sample comprised 3m drillhole composites of mineralised rock from the Northern and Southern Zones of the deposit. To bring the BHP data into alignment with data produced at the CSIRO laboratory (and this study), a correction was applied (G. Carr, pers. comm., 1996).

Additional Pb isotope data from analyses of three orthoclase separates from pegmatite(s) in the immediate vicinity of the deposit and five galena separates from mineralised rock, were carried out at the University of Western Australia, Perth, (AMIRA P438 project, McNaughton, 1997a and b). No correction to the data was required to bring it into alignment with the CSIRO data. Unfortunately, the AMIRA P438 galena samples and BHP wholerock data (mineralised rock) are unconstrained within the paragenetic framework for the deposit, and the precise

locations of samples have not been recorded in relevant reports. Both sample datasets are therefore poorly defined.

Pb isotope data from other significant Proterozoic Pb-Zn deposits in the Mount Isa Inlier, McArthur Basin and Broken Hill Block were gathered from published and unpublished works and the CSIRO open-file dataset (Table 7.2). Care was taken when choosing data due to potential problems related to interlaboratory variability and age of the data. Hence, the compiled dataset used here is as internally consistent as possible with the majority of analyses acquired through the CSIRO.

Table 7.2 Summary of Pb isotope data used in this study from other significant Proterozoic Pb-Zn deposits (actual data can be found in the relevant sources).

Deposit	Deposit type and Location	Source of data	Sample	Number of analyses and lab.
Maronan	Broken Hill-type, Mount Isa Inlier	McNaughton (1997)	galena separates	5 (UWA)
Fairmile	Broken Hill-type affinities, Mount Isa Inlier	CSIRO open-file dataset (G. Carr, pers. comm., 1998)	wholerock (gossans and Fe-stones)	20 (CSIRO)
Pegmont	Broken Hill-type, Mount Isa Inlier	CSIRO open-file dataset (G. Carr, pers. comm., 1998)	wholerock (Fe-stones, gossans, drill core), some galena separates	37 (CSIRO)
Squirrel Hills	Broken Hill-type, Mount Isa Inlier	CSIRO open-file dataset (G. Carr, pers. comm., 1998)	wholerock (gossan)	8 (CSIRO)
Dugald River	Sediment hosted Pb-Zn, Mount Isa Inlier	CSIRO open-file dataset (G. Carr, pers. comm., 1998)	wholerock (mineralisation), some galena separates	11 (CSIRO)
		Gulson (1985)	wholerock (mineralisation)	9 (CSIRO)
McArthur River, HYC	Sediment hosted Pb-Zn, McArthur Basin	Gulson (1985)	wholerock (mineralisation – main orebody only)	12 (CSIRO)
Mount Isa	Sediment hosted Pb-Zn, Mount Isa Inlier	Gulson (1985)	wholerock (mineralisation), galena separates	14 (CSIRO)
		Richards (1975)	wholerock (mineralisation – stratiform ore only)	7 (RSES)
Hilton	Sediment hosted Pb-Zn, Mount Isa Inlier	Gulson (1985)	wholerock (mineralisation), galena separates	6 (CSIRO)
Lady Loretta	Sediment hosted Pb-Zn, Mount Isa Inlier	Gulson (1985)	wholerock (mineralisation), galena, sphalerite, pyrite separates	29 (CSIRO)
Broken Hill	Broken Hill-type, Broken Hill Block	Cooper et al. (1969)	galena separates	1 (average)
		Gulson (1984)	sphalerite and pyrrhotite separates	34 (CSIRO)
Monakoff	Broken Hill-type affinities, Mount Isa Inlier	McNaughton (1997)	galena separates	2 (UWA)
Sandy Creek	Shear zone hosted quartz-vein system, Mount Isa Inlier	Ramsden and Davidson (in prep.)	galena separates	3 (CSIRO)
Pinnacles	Broken Hill-type, Broken Hill Block	Gulson et al. (1985)	galena, magnetite, sphalerite, pyrrhotite, loellingite, chalcopyrite separates, supergene material	20 (CSIRO)

CSIRO – Commonwealth Scientific and Industrial Research Organisation.
RSES – Research School of Earth Sciences, Australian National University.
UWA – University of Western Australia.

7.4 RESULTS

A total of 39 conventional and eight double-spike Pb isotope determinations were carried out on 39 samples during the course of this study (Table 7.3). The higher number of total analyses (n=47; Table 7.3) compared to total samples was due to repeat analyses, or analyses of sequential leachates from individual samples. Sample data and ranges in Pb isotope determinations for galena and host rocks are summarised in Table 7.3. Detailed sample data including Pb isotope ratios, Pb contents of analysed mineral separates, wholerock geochemistry (U, Th, Pb) where applicable, and the McCarthy (1996) dataset are presented in Appendix 4.

Pb isotope data are presented on standard $^{207}Pb/^{204}Pb$ and $^{208}Pb/^{204}Pb$ versus $^{206}Pb/^{204}Pb$ diagrams. The double-spike data falls within the precision ellipse of the conventional data for like samples, and therefore the former data are included in plots of conventional determinations. Although the two datasets are directly comparable, there appears to be a consistent variation, albeit slight, between the double-spike and conventional data and it has been suggested that a small correction be made to bring the conventional data from the CSIRO laboratory into alignment with the double-spike data (G. Carr and S-S. Sun, pers. comm., 1998).

Table 7.3 Summary of general sample data for this study only and corresponding range in Pb isotope ratios (refer to Appendix 4 for the complete Cannington dataset).

Sample type	No. of samples	No. of analyses	$^{206}Pb/^{204}Pb$ *(range)*	$^{207}Pb/^{204}Pb$ *(range)*	$^{208}Pb/^{204}Pb$ *(range)*
galena (Stage I)	5	6	16.002-16.038 *(0.036)*	15.374-15.431 *(0.057)*	35.601-35.783 *(0.182)*
	2 DS	3 DS	16.017-16.020 *(0.003)*	15.393-15.397 *(0.004)*	35.662-35.675 *(0.013)*
galena (Stage II)	7	8	16.000-16.032 *(0.032)*	15.375-15.417 *(0.042)*	35.597-35.731 *(0.134)*
	1 DS	1 DS	16.020*	15.398*	35.675*
galena (Stage III)	2	2	16.009-16.145 *(0.136)*	15.384-15.473 *(0.089)*	35.616-35.819 *(0.203)*
	4†	4 DS	16.019-16.137 *(0.118)*	15.398-15.416 *(0.018)*	35.672-35.785 *(0.113)*
amazonite (lode pegmatite)	2	6	16.080-16.103 *(0.095)*	15.375-15.433 *(0.058)*	35.604-35.787 *(0.183)*
galena + grey orthoclase (partial melt)	1	1	16.018*	15.392*	35.660*
orthoclase (gneiss)	5	5	16.218-17.361 *(1.143)*	15.425-15.595 *(0.17)*	35.798-36.614 *(0.816)*
gneiss (wholerock)	5	5	16.371-18.964 *(2.593)*	15.417-15.701 *(0.284)*	35.744-36.917 *(1.173)*
amphibolite (wholerock)	5	6	16.037-16.068# *(0.031)*	15.377-15.408# *(0.031)*	35.598-35.731# *(0.133)*
TOTAL	39	47			

DS – double-spike analyses.
* – one analysis only, ie., no range in ratios.
# – 2 determinations not included due to poor quality analyses.
† – double-spike repeats from McCarthy (1996) Pb isotope samples.

The Pb-isotope evolution models most commonly used today for data interpretation are the Stacey and Kramers (1975), and Cumming and Richards (1975) models. All plots include the Cummings and Richard (1975) average crustal growth curve as a basis for discussion. Both models are essentially based upon the mathematical equations of the Holmes-Houtermans single-stage model (Holmes, 1946; Houtermans, 1946) with minor modifications. The Stacey and Kramers (1975) model assumes that Pb isotopes evolved in two stages rather than one, with the second stage commencing at 3700 Ma in response to crustal development resulting in higher μ ($^{238}U/^{204}Pb$) values for the crust. The Cumming and Richards (1975) model assumes a single stage model in which μ values have progressively increased over time as a response to crustal development as opposed to remaining constant. The Cumming and Richards (1975) growth curve was chosen over the Stacey and Kramers (1975) growth curve in the subsequent figures, because it reflects more accurately the possible path in which ore Pb at Cannington evolved (i.e. the evolutionary path for the source of Pb at Cannington; Fig. 7.4). This is irrespective of the greater conformity between the maximum depositional age for gneissic host rocks at Cannington (ca. 1675 Ma; Page and Sun, 1998; Giles, 2000) and the Pb model age (ca. 1580 Ma) based on the Stacey and Kramers (1975) growth curve.

7.4.1 General distribution of data

Figure 7.4 illustrates the distribution of all Pb isotope data for Cannington, independent of sample type. On the $^{207}Pb/^{204}Pb$ versus $^{206}Pb/^{204}Pb$ plot the majority of data forms an elongate-shaped population that parallels the isotope fractionation trend of the analytical instrument (i.e. the machine fractionation trend), and fall within the limits of the precision ellipse. A scatter of more radiogenic values form a "tail" subparallel to the Cumming and Richards (1975) and Stacey and Kramers (1975) average crustal growth curves, broadly falling within the expected Pb evolution trajectory from the aforementioned least radiogenic population. Approximately 90% of the data lie below the Cumming and Richards (1975) growth curve, whereas all but one sample lies above the Stacey and Kramers (1975) growth curve. The average Pb isotope signature for the McArthur River HYC deposit lies close to the most radiogenic determinations from Cannington, but has a higher $^{207}Pb/^{204}Pb$ ratio.

On the $^{208}Pb/^{204}Pb$ versus $^{206}Pb/^{204}Pb$ plot (Fig. 7.4), the data display a similar distribution with the majority defining a single least radiogenic population parallel to the machine fractionation trend, but within the limits of the precision ellipse. More radiogenic data forms a tail subparallel to the Cumming and Richards (1975) and Stacey and Kramers (1975) average crustal growth curves, and plot broadly within the expected Pb evolution trajectory from the least radiogenic population. Approximately 90% of the data plots below the Cumming and Richards (1975) growth curve, whereas the Stacey and Kramers (1975) growth curve passes through the average Pb isotope signature for galena from Cannington. The vast majority of determinations are less radiogenic than the average Pb isotope signature for the McArthur River deposit.

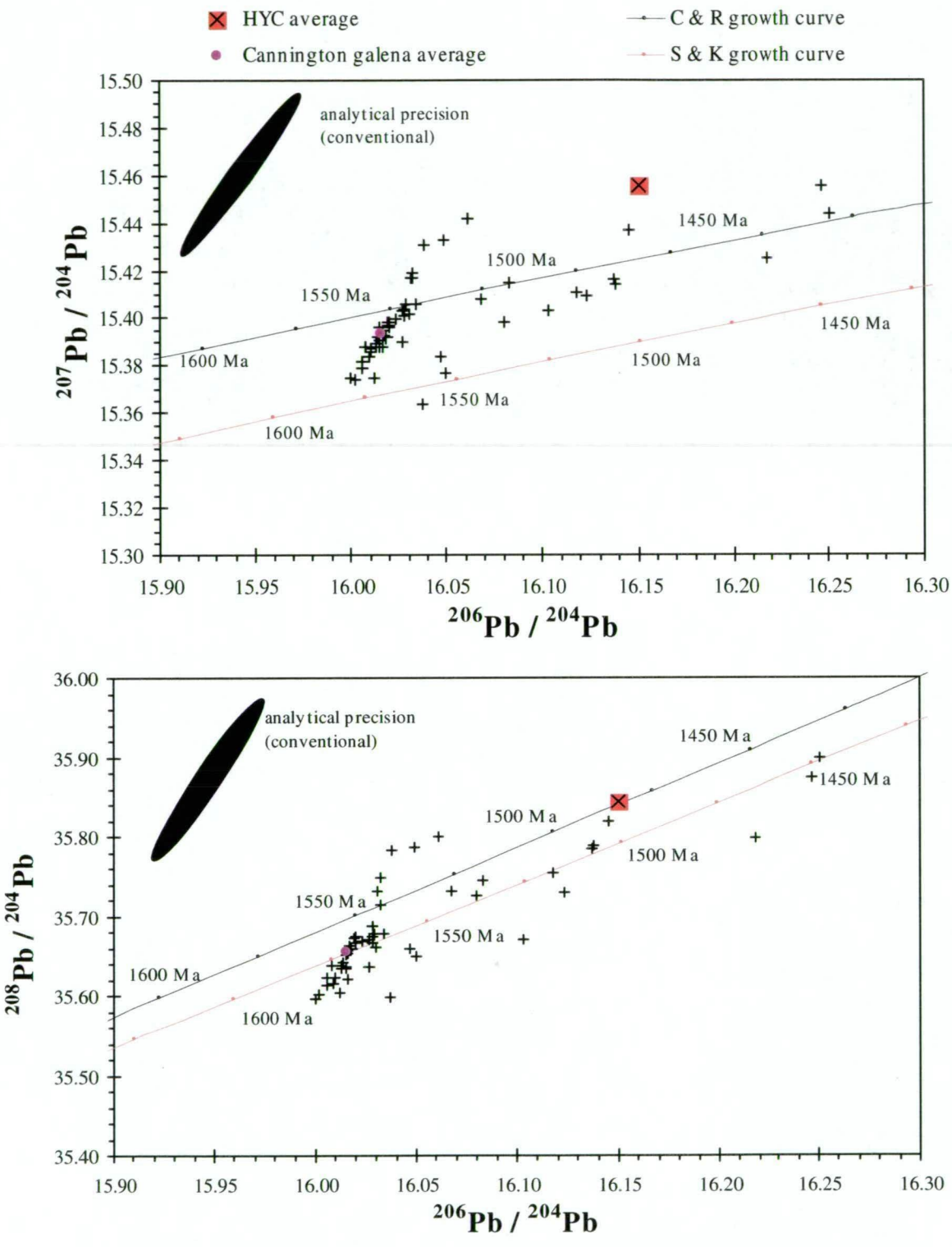

Figure 7.4 $^{207}Pb/^{204}Pb$ vs. $^{206}Pb/^{204}Pb$ and $^{208}Pb/^{204}Pb$ vs. $^{206}Pb/^{204}Pb$ plots of all K-feldspar, wholerock and galena determinations from Cannington (n=65; refer to Table 7.1 for a breakdown of number and sources of analyses). The majority of the data form a distinct linear cluster that fall within the limits of the precision ellipse for conventional analyses at the CSIRO laboratory (top left). However, a significant scattered population of more radiogenic data is apparent. Approximately 95% of the data are less radiogenic than the average Pb isotope signature of the McArthur River (HYC) Pb-Zn deposit.

To gain a more detailed understanding of the Pb isotope systematics at Cannington, the data were subdivided into two main groups:

- galena data (galena separates), and;
- host rock data (wholerock Pb, and K-feldspar separates).

This subdivision provides a convenient method for separating high-Pb samples from low-Pb samples, and therefore galena samples from silicate samples respectively. It also provides clarification of potential Pb-bearing source rocks in the Cannington region.

7.4.2 Galena

The entire Pb isotope dataset for galena (39 determinations from 32 samples) from various sources is summarised in Table 7.1, and ranges in Pb isotope ratios for galena separates from this study are summarised in Table 7.3. Plotting of all the galena datasets on a $^{207}Pb/^{204}Pb$ versus $^{206}Pb/^{204}Pb$ plot (Fig. 7.5) highlights the existence of two populations: i) a least radiogenic population (~90% of the data) defined as a linear array parallel to the machine fractionation trend and falling within the precision ellipse; and ii) a more radiogenic population (~10% of the data). The double-spike data also reflects the populations. One spurious result plots midway between the two latter populations. Three of the BHP determinations plot within the least radiogenic population, and one other in the second, more scattered radiogenic population (Fig. 7.5). Similarly, three of the determinations from McCarthy (1996) fall within the least radiogenic population, and two determinations within the more radiogenic population. All galena determinations from the JCU/AMIRA project plot as a tight cluster within the least radiogenic population.

The data have a similar distribution on a $^{208}Pb/^{204}Pb$ versus $^{206}Pb/^{204}Pb$ plot (Fig. 7.5). The most important feature of this plot is that there are no major deviations from trends illustrated in the $^{207}Pb/^{204}Pb$ plot, indicating that there has been no major addition of radiogenic Pb by the radioactive decay of Th, and/or loss of U.

7.4.2.1 Stage I galena

Ranges in Pb isotope data for various paragenetic stages of galena are summarised in Table 7.3. Six conventional and three high precision double-spike analyses were obtained from seven samples of Stage I galena in hanging wall and footwall olivine-pyroxenoid (Burnham/ Nithsdale) and banded olivine-pyroxenoid ore (Broadlands), as well as graphitic ore (Inveravon) from the Northern Zone of the deposit (Appendix 4). Approximately 90% of the Stage I data plots below the Cumming and Richards (1975) growth curve forming a distinct linear population parallel to the machine fraction trend and within the limits of the analytical precision ellipse (Fig. 7.6).

The high precision double-spike data plot as a tight group below the Cummings and Richards (1975) growth curve. From a statistical point of view, this tight distribution could be interpreted as an artefact of the small double-spike sample set, being comprised of two galena micropickings from the same thin section and a repeat analysis. Due to this, it is difficult to

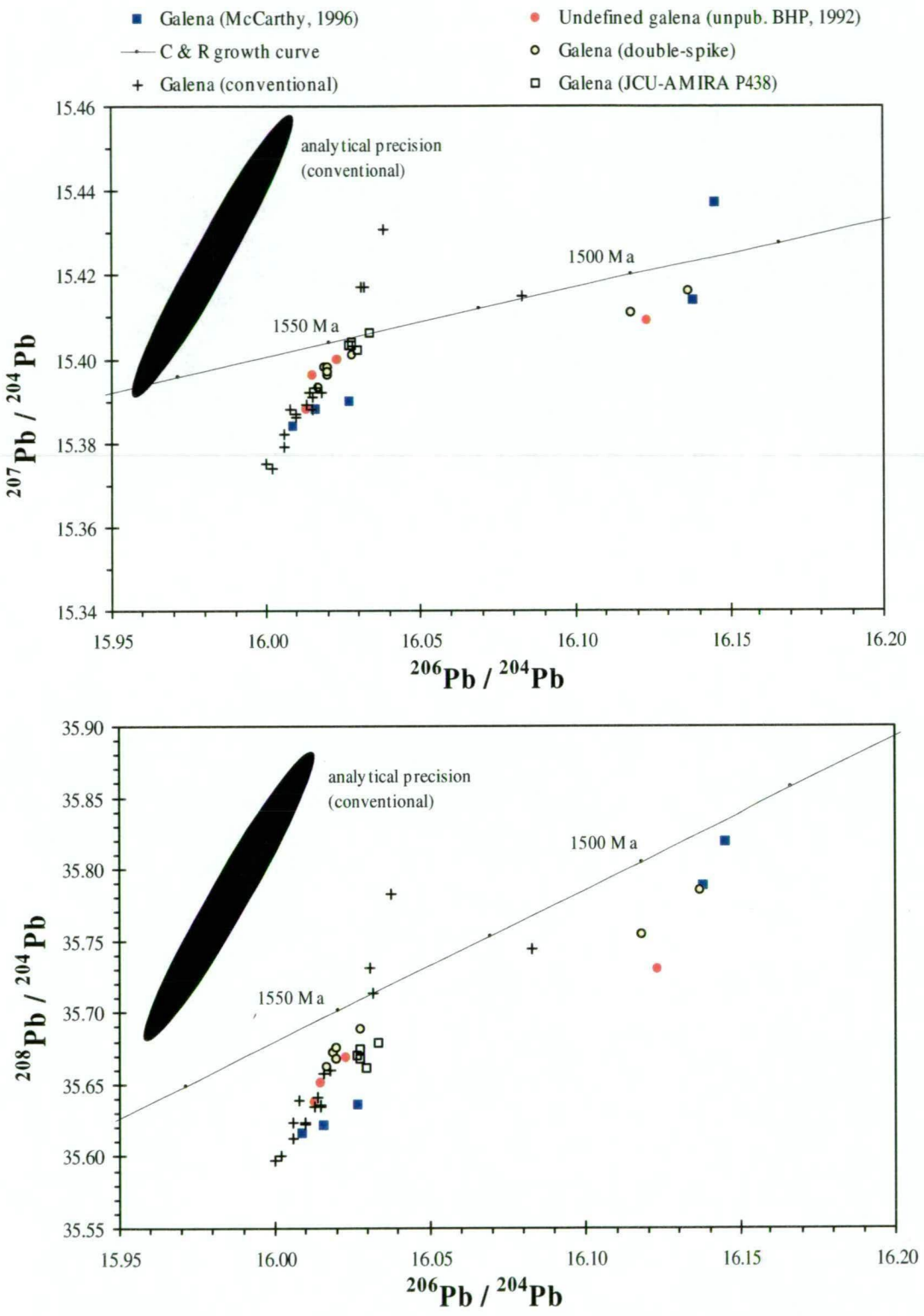

Figure 7.5 $^{207}Pb/^{204}Pb$ vs. $^{206}Pb/^{204}Pb$ and $^{208}Pb/^{204}Pb$ vs. $^{206}Pb/^{204}Pb$ plots of all Cannington galena determinations from this study (n=25), McCarthy (1996; n=5), JCU/AMIRA P438 project (1995-1997; n=5) and BHP (unpubl. report, 1992; n=4). The majority of the data form a distinct linear cluster that fall within the limits of the precision ellipse for conventional analyses at the CSIRO laboratory (top left). However, a small scattered population of more radiogenic samples is also present. Approximately 90% of the data lie below the Cumming and Richards (1975) average Pb growth curve, and all data are less radiogenic than the average Pb isotope signature of the McArthur River (HYC) Pb-Zn deposit.

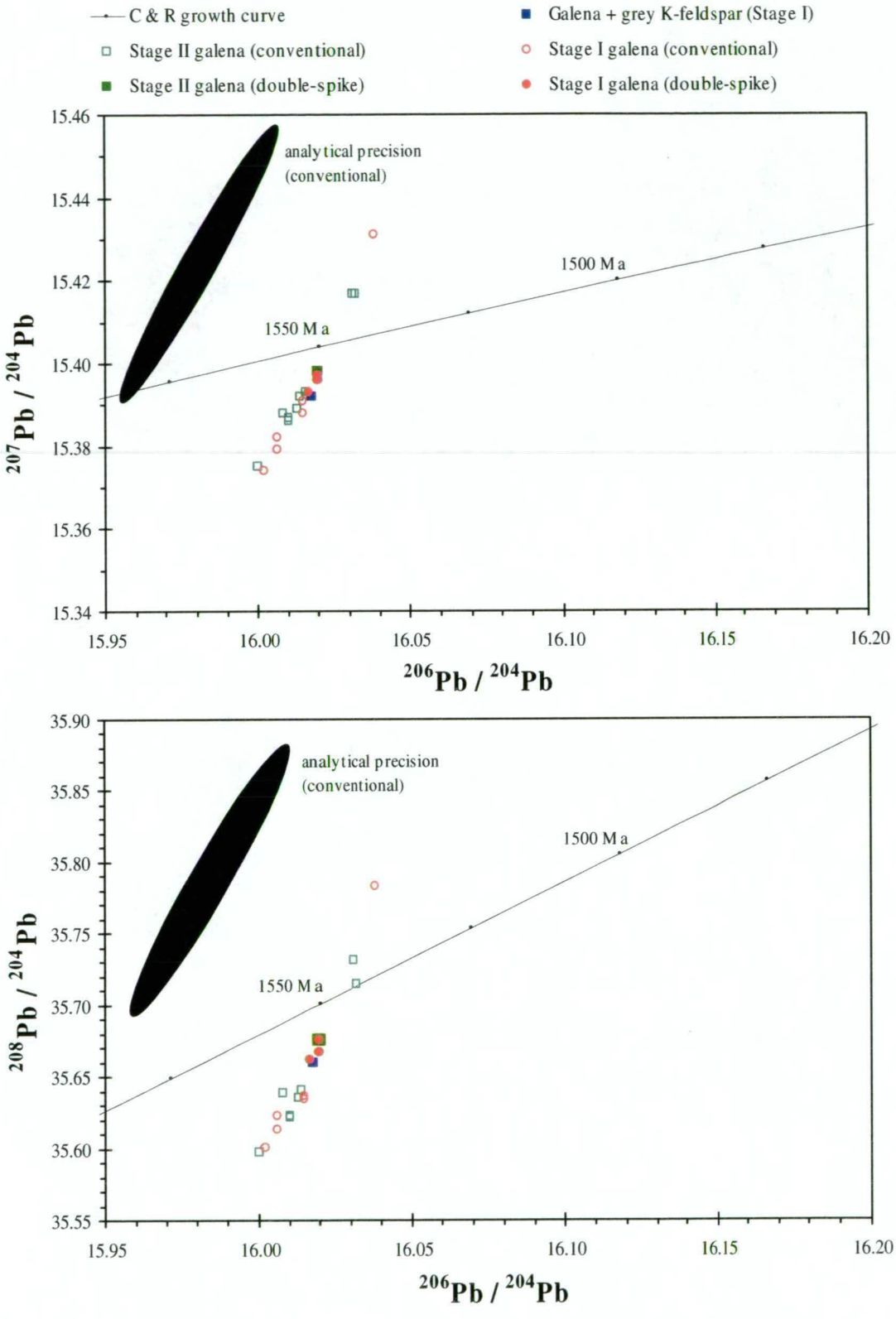

Figure 7.6 $^{207}Pb/^{204}Pb$ vs. $^{206}Pb/^{204}Pb$ and $^{208}Pb/^{204}Pb$ vs. $^{206}Pb/^{204}Pb$ plots of paragenetically constrained galena samples determined by conventional and double-spike procedures. Stage III galena data from McCarthy (1996) is also included. Isotopic data from Stage I and II galenas form a distinct least radiogenic population that fall within the limits of the precision ellipse for conventional analyses (CSIRO lab.), whereas Stage III galenas display the greatest variability and define the more radiogenic tail observed in Figure 7.5.

confidently assess any degree of heterogeneity in Stage I galenas based solely on the double-spike data. Given that both conventional and double-spike Stage I galena determinations plot as a distinct population within the boundaries of the precision ellipse and because they are linearly distributed parallel to the machine fractionation trend, it is unlikely that there is any significant isotopic heterogeneity in on a deposit-wide scale.

7.4.2.2 Stage II galena

Eight conventional and one high precision double-spike analysis were obtained from eight Stage II galenas (Table 7.3). Galena is rarely observed in Stages IIa and IIb of the paragenesis, so samples were restricted to Stage IIc galenas typically associated with pyrosmalite ± secondary magnetite. To test for any deposit-scale isotopic heterogeneity, samples were obtained from all ore types comprising the deposit (Appendix 4).

Approximately 80% of the Stage IIc galena data plots below the Cumming and Richards (1975) growth curve (Fig. 7.6). There are no significant isotopic differences between Stage I and Stage IIc galenas (Fig. 7.6), and isotopic ranges are very similar (Table 7.3). The similarity is also supported by the solitary Stage IIc galena double-spike analysis that plots within the tight cluster of Stage I double-spike analyses (Fig. 7.6). Like Stage I galenas, it is unlikely that there is any significant isotopic heterogeneity in Stage IIc galena on a deposit-wide scale.

7.4.2.3 Stage III galena

Two conventional and four high precision double-spike analyses were obtained from six Stage III galenas (Table 7.3). The 2 conventional analyses represent galena sampled from carbonate-bearing type 2 siliceous Pb-Zn-Ag ore (Glenholme Breccia; section 4.9.2) spatially associated with D_5 faulting, and galena from a vuggy quartz-carbonate-fluorite vein within a D_5 fault zone overprinting mixed banded olivine-pyroxenoid/hedenbergite ores (Broadlands). An additional five Stage III galena samples (spatially associated with D_5 faults) from the work of McCarthy (1996), brought the total number of conventional analyses to seven. Details of the McCarthy (1996) dataset can be found in Appendix 4. Double-spike determinations consisted of repeat analyses on four samples from the McCarthy (1996) sample set. Overall, the dataset represents a near complete coverage of the "environments" in which Stage III galena occurs in the deposit.

Stage III galena determinations display the greatest range in isotopic ratios in comparison to Stage I and II galenas, especially for $^{206}Pb/^{204}Pb$ ratios (Table 7.3). Approximately 45% of all the data falls within the least radiogenic population, whereas the remaining samples (McCarthy, 1996 data and double-spike repeats) define the scattered radiogenic population referred to previously (Fig. 7.7). One sample plots just outside of the least radiogenic field. Galena from carbonate-bearing type 2 siliceous Pb-Zn-Ag ore plots within the least radiogenic population, whereas galena from the quartz-carbonate-fluorite vein plots midway between the two populations. The most radiogenic samples were taken from D_5 faults (McCarthy, 1996). Double-spike repeats lie below the Cumming and Richards (1975) growth curve, forming an

obvious trend subparallel to it.

It is clear that isotopic variability is restricted to Stage III galenas, and this feature characterises syn-D_5 near-surface hydrothermal activity. It is likely that the one BHP sample that plots within the most radiogenic population consists predominantly of Stage III galena. High precision double-spike repeats reinforce this variability when compared to respective conventionally analysed samples. For example, the double-spike repeat for sample 3 in Figure 7.7 displays a significant shift, whereas sample 4 has a very slight shift. Double-spike and conventional data for the same sample should, theoretically, fall along the machine fractionation trend (within error). All samples, apart from sample 2 in Figure 7.7 display this behaviour. Overall, the data indicate inter- and some intra-sample variability in isotopic ratios for Stage III galenas.

7.4.3 Host rocks

Pb isotopes obtained from host rocks were subdivided according to rock type with the aim of characterising lithologies, assessing tectonic provenance and potential as Pb-bearing source rocks.

7.4.3.1 Amphibolite

Six conventional wholerock analyses were obtained from five Core Amphibolite samples (Table 7.3). The analytical procedure employed was atypical for low-Pb wholerock samples and was similar to K-feldspar separates, i.e. sequential acid leaches. This method provided a means of reducing the amount of radiogenic Pb contamination that would affect the final analyses. Theoretically, the method increases the likelihood of obtaining initial isotopic ratios at the time of amphibolite emplacement. Samples comprised the most typical, distal (from the ore lenses), least-altered and retrogressed examples of amphibolite from the Northern and Southern Zones of the deposit (Appendix 4). Pb content in the amphibolite samples range from 50-177ppm with an average of 112ppm (σ =46). The average U content is 0.2ppm and Th, 0.6 ppm (Table 7.4; Appendix 4).

Ranges in $^{207}Pb/^{204}Pb$ and $^{208}Pb/^{204}Pb$ ratios for the Core Amphibolite are similar to Stage I and II galenas, but $^{206}Pb/^{204}Pb$ ratios are slightly more radiogenic (Table 7.5; Fig. 7.8). Pb isotope ratios plot as a distinct near-linear array parallel to the machine fractionation trend, and within the boundaries of the precision ellipse. All data plots below the Cumming and Richards (1975) growth curve. The consistency in distribution of the data between the $^{207}Pb/^{204}Pb$ and $^{208}Pb/^{204}Pb$ plots suggests negligible thoranogenic Pb.

Table 7.4 Average wholerock Pb, Zn, U, and Th concentrations (ppm) in the Core Amphibolite at Cannington (data from this study) compared to other amphibolites in the Maronan Supergroup. Data has been collated from the AGSO geochemical database (1999) and O. Hatton (pers. comm., 1999).

	Cannington (n=11)				Maronan Supergroup (n=38)			
	Pb	Zn	U	Th	Pb	Zn	U	Th
Average	95	212	0.2	0.6	8	67	<0.5	<1.5
Standard deviation	71	51	0.03	0.02	9	46	-	-

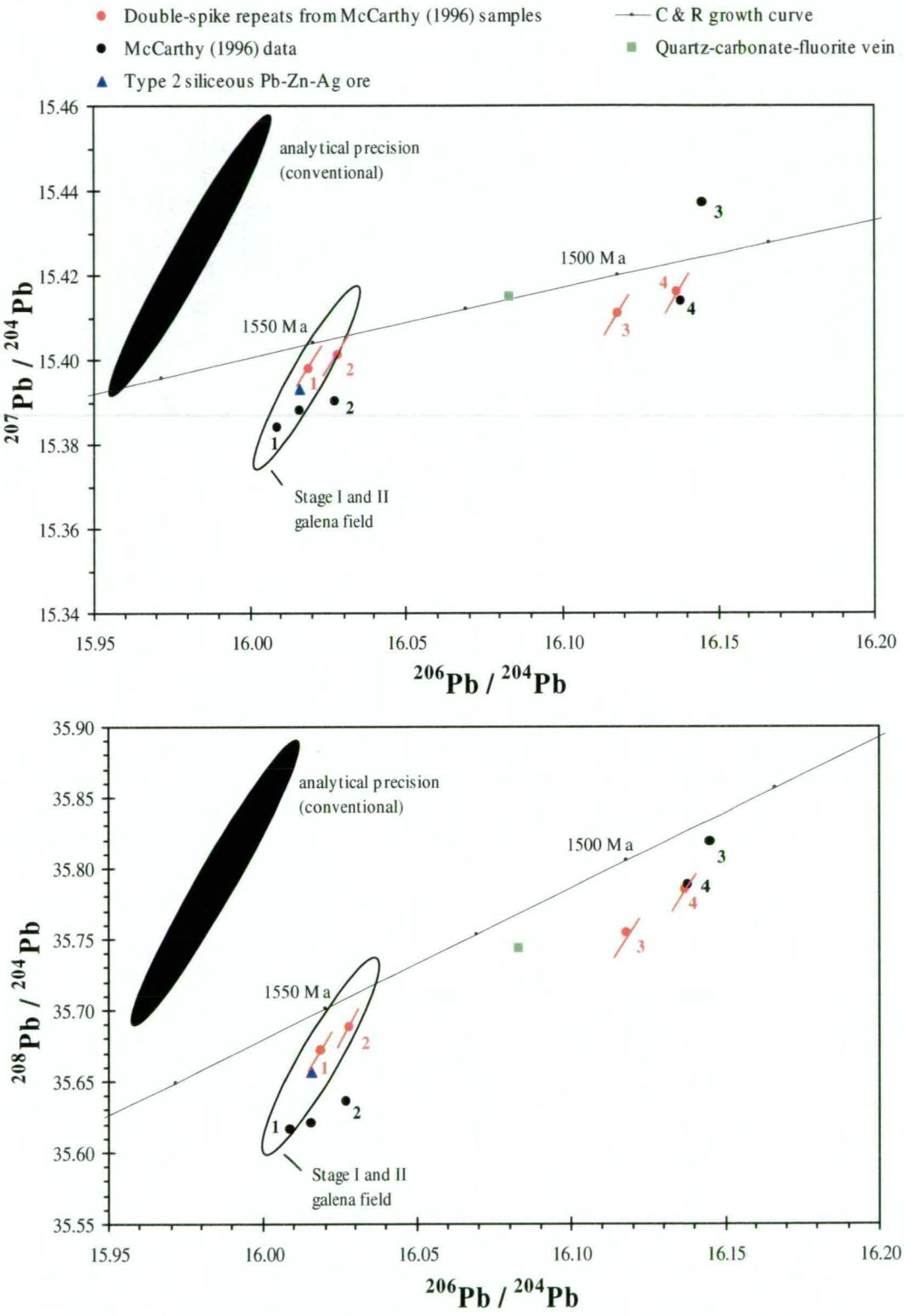

Figure 7.7 $^{207}Pb/^{204}Pb$ vs. $^{206}Pb/^{204}Pb$ and $^{208}Pb/^{204}Pb$ vs. $^{206}Pb/^{204}Pb$ plots of Stage III galena conventional data and double-spike repeats. Red lines mark the orientation of the machine fractionation trend and error for the double-spike data. Numbered points equate to samples that were analysed using both conventional and double-spike procedures; variations highlighting inter- and intra-sample heterogeneity in Pb isotope signatures for samples 1 to 3. Sample 4 displays essentially displays no variability.

Table 7.5 Average Pb isotope compositions for the Core Amphibolite compared to Stage I and II galenas combined. Standard deviations are listed in brackets.

	$^{206}Pb/^{204}Pb$	$^{207}Pb/^{204}Pb$	$^{208}Pb/^{204}Pb$
Amphibolite (n=4)	16.051 (0.013)	15.383 (0.018)	35.660 (0.055)
Stage I and II galena (n=19)	16.016 (0.010)	15.393 (0.015)	35.654 (0.047)

7.4.3.2 Pegmatite — orthoclase separates

Three analyses were carried out on orthoclase separates from pegmatites by McNaughton (1996, 1997a) for the JCU/AMIRA P438 research project (1994-1997). Two determinations plot close to the least radiogenic population defined by Stage I and II galena determinations, whereas the third is comparatively more radiogenic. A line of best fit through the pegmatite data is subparallel to the Cumming and Richards (1975) growth curve (Fig. 7.8).

7.4.3.3 Lode pegmatites – amazonite separates

Six conventional analyses were obtained from two amazonite separates collected from two lode pegmatites occurring in the Northern Zone (Table 7.3). As previously stated in Section 7.2.1, one sample was obtained from a lode pegmatite within the Core Amphibolite (sample no. NZ004-2) and the other from an *in situ* partial melt in gahnite-bearing schist (sample no. SZ037-25; Appendix 4). The excess of determinations over samples was due to analyses of sequential acid leachates from each sample. Amazonites were devoid of any late alteration, including Stage II metasomatism.

Ranges in the Pb isotope ratios are similar to Stage I and II galenas (Table 7.3). All isotopic determinations on leachates from sample NZ004-2 plot as a linear array parallel to the machine fractionation trend and within the boundaries of the precision ellipse (Fig. 7.8). In addition, the data plots either within (e.g. the HCl and final $HF/HClO_4/HNO_3$ leachates) or close to (e.g. the HCl/HNO_3 leachate) the least radiogenic population defined by Stage I and II galena, with the most significant variations being in $^{207}Pb/^{204}Pb$ ratios, i.e. the data plots along the machine fractionation trend. In comparison, data for sample SZ037-25 plots as a near linear array parallel to the Cummings and Richards (1975) growth curve and therefore, displays greater variability in $^{206}Pb/^{204}Pb$ rather than $^{207}Pb/^{204}Pb$ ratios, i.e. the HCl and HCl/HNO_3 leachates contain radiogenic Pb (Fig. 7.8). The inconsistency in distribution of the data between the $^{207}Pb/^{204}Pb$ and $^{208}Pb/^{204}Pb$ plots for sample SZ037-25 may also indicate that a component of thoranogenic Pb is present in the initial leachates. However, the final leachates ($HF/HClO_4/HNO_3$) are theoretically the best estimate of initial Pb isotope ratios at the time of amazonite crystallisation. For both samples, this data plots within the least radiogenic field defined by Stage I and II galenas (Fig. 7.8).

7.4.3.4 Gneiss – wholerock

Five conventional wholerock analyses were obtained from five least-altered and retrogressed migmatitic gneiss samples adjacent and distal to the orebody (refer section 7.2.1; Table 7.3, Appendix 4). The analytical procedure employed was typical for low-Pb wholerock samples, i.e. the sequential acid leach method (Appendix 4). Analyses were conducted on the final $HF/HClO_4/HNO_3$ residual leach only, increasing the chance of obtaining isotopic ratios closer to

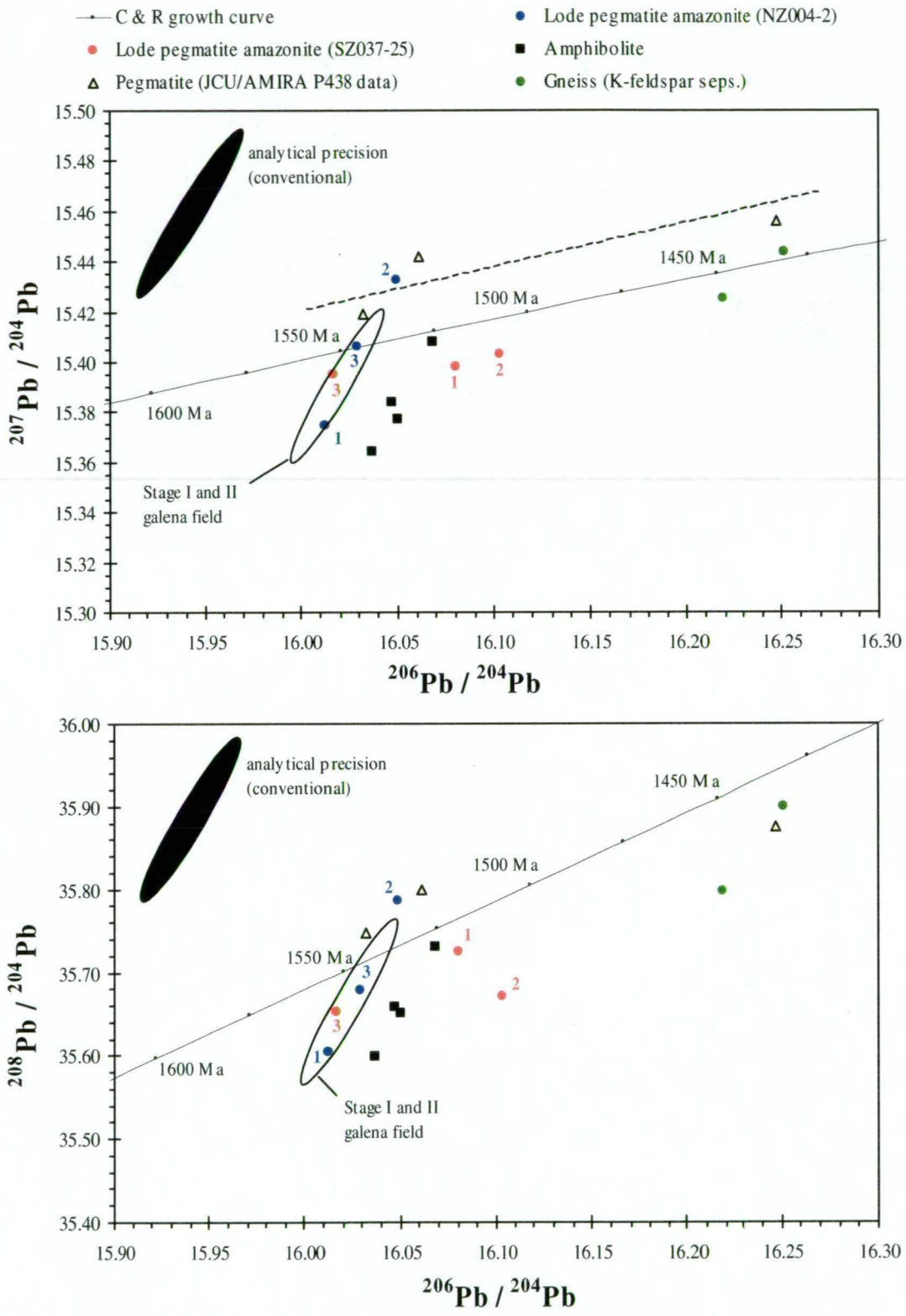

Figure 7.8 $^{207}Pb/^{204}Pb$ vs. $^{206}Pb/^{204}Pb$ and $^{208}Pb/^{204}Pb$ vs. $^{206}Pb/^{204}Pb$ plots of K-feldspar separate data from pegmatites (JCU/AMIRA P438 project, 1997), lode pegmatites and gneiss. Wholerock data from the Core Amphibolite is also plotted. The dashed line represents the interpreted linear trend of the pegmatite data, which falls above the Cumming and Richards (1975) growth curve. Amphibolite data forms a distinct linear cluster parallel to the machine fractionation trend and is characterised by slightly more radiogenic Pb isotope signatures in comparison to the Stage I and II galena field. Numbers for amazonite separate data correspond to sequential leachates (1 – initial HCl leach, 2 – HCl/HNO_3 leach, 3 – final residual $HF/HClO_4/HNO_3$ leach). Position 3 for both amazonite samples theoretically represents the most plausible initial Pb isotope signature.

initial values. It was presumed that earlier leachates would contain a higher component of radiogenic Pb and were therefore not analysed (G. Carr, pers. comm., 1999).

Ranges in the wholerock Pb isotope ratios are the largest for all rock-types and mineral separates analysed (Table 7.3). The wholerock data can be divided into two populations; i) a least radiogenic population, and, ii) a more radiogenic population (Fig. 7.9). However, determinations comprising the least radiogenic population are comparatively more radiogenic than the amphibolite samples and Stage I and II galenas (Fig. 7.9). All samples generally follow the Cumming and Richards (1975) growth curve on the $^{207}Pb/^{204}Pb$ vs. $^{206}Pb/^{204}Pb$ plot. A regression line through the data passes through the Stage I and II galena and Core Amphibolite fields (Fig. 7.9). On the $^{208}Pb/^{204}Pb$ vs. $^{206}Pb/^{204}Pb$ plot, the departure of the data from the growth curve increases with increasing $^{206}Pb/^{204}Pb$ ratios (Fig. 7.9). This direct relationship is attributed to a progressive increase in radiogenic Pb content from the decay of U and only minor input from the decay of Th, minimising the overall range in $^{208}Pb/^{204}Pb$ ratios. Because the data do not plot within a single population that varies along the machine fractionation trend and within the limits of the precision ellipse, the results are not representative of initial isotopic ratios for the gneiss. This is also supported by the inconsistency in distribution of the data between the $^{207}Pb/^{204}Pb$ and $^{208}Pb/^{204}Pb$ plots, and progressive departure from the growth curve in the $^{208}Pb/^{204}Pb$ plot.

7.4.3.5 Gneiss – orthoclase separates

In order to increase the chances of obtaining possible initial isotopic ratios for the gneiss, five K-feldspar (orthoclase + quartz) mineral separates were collected from the five gneiss samples referred to in the preceding section (Table 7.3, Appendix 4). Like the wholerock samples, the analytical procedure employed was typical for low-Pb wholerock samples, i.e. the sequential acid leach method. Analyses were conducted on the final $HF/HClO_4/HNO_3$ residual leach only, increasing the chance of obtaining isotopic ratios closer to initial values (G. Carr, pers. comm., 1999).

Ranges in isotopic ratios for the orthoclase separates are smaller than the wholerock determinations, but are greater than amazonite separates from lode pegmatites (Table 7.3). Like the wholerock determinations, the data can be divided into two populations; i) a least radiogenic population, and, ii) a more radiogenic population (Fig. 7.9). Individual samples comprising these populations are equivalent to those that comprise the most and least radiogenic populations in the wholerock data. Even though orthoclase separates contain less radiogenic Pb than their wholerock counterparts, their isotopic ratios are more radiogenic than the amphibolite and Stage I and II galena data. However, the least radiogenic population has ratios very similar to the most radiogenic pegmatite determination (Fig. 7.8).

All samples generally follow the Cumming and Richards (1975) growth curve on the $^{207}Pb/^{204}Pb$ vs. $^{206}Pb/^{204}Pb$ plot. A regression line through the data passes through the Stage I and II galena and Core Amphibolite fields (Fig. 7.9). On the $^{208}Pb/^{204}Pb$ vs. $^{206}Pb/^{204}Pb$ plot,

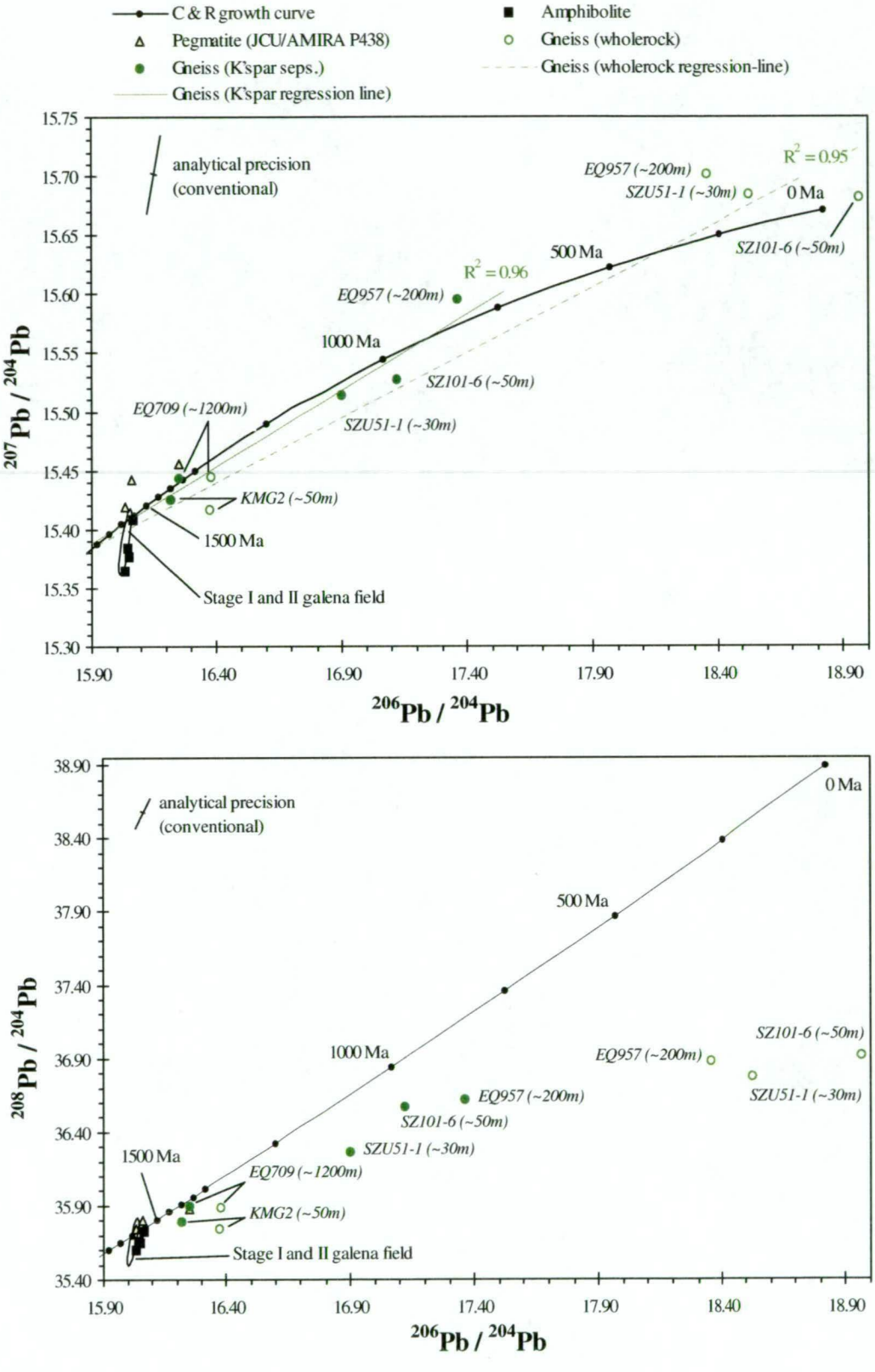

Figure 7.9 $^{207}Pb/^{204}Pb$ vs. $^{206}Pb/^{204}Pb$ and $^{208}Pb/^{204}Pb$ vs. $^{206}Pb/^{204}Pb$ plots of all Cannington host rock determinations (wholerock and K-feldspar separates). Pegmatite data (n=3) from the JCU/AMIRA P438 project (1997) is also included. Gneissic rocks (K-feldspar separates and wholerock) are characterised by a large spread in Pb isotope ratios. It is clear from both plots that significant radiogenic Pb occurs in the gneiss samples. Sample numbers and relative distance from the orebody are included for each gneiss sample.

the departure of the data from the growth curve increases in the most radiogenic population indicating a greater contribution of radiogenic Pb from the decay of U rather than Th (Fig. 7.9). This trend may indicate that the gneissic rocks have been depleted in Th due to amphibolite facies metamorphism, M_1. It is unlikely that data comprising the least radiogenic population represents initial Pb isotope ratios of the gneiss, because pegmatites formed via anatectic partial melting of the latter have less radiogenic isotopic ratios (Fig. 7.8). Furthermore, the data do not plot within a single population that varies along the machine fractionation trend and within the limits of the precision ellipse, and the most radiogenic population display a notable departure from the growth curve in the $^{208}Pb/^{204}Pb$ plot.

7.5 DISCUSSION

7.5.1 Isotopic homogeneity and heterogeneity in ore deposits

Homogeneous Pb isotope signatures typify significant Broken Hill-type Pb-Zn-Ag deposits within Australia. Good examples include the Broken Hill (Gulson, 1984) and Pinnacles (Gulson et al., 1985) deposits in New South Wales, and the Pegmont (G. Carr, pers. comm., 1998) deposit, approximately 30km west of Cannington. This is also true of large sediment-hosted Pb-Zn deposits such as Mt. Isa (Richards, 1975; Gulson et al., 1983; Gulson, 1985), Hilton-George Fisher (Gulson, 1985), McArthur River HYC (Richards, 1975; Gulson, 1975, 1985) and Century (Sun et al., 1996; Carr and Sun, 1996; Carr and Whitford, 1997). In contrast, smaller subeconomic deposits are typically characterised by heterogeneous Pb isotope signatures, such as Squirrel Hills (G. Carr, pers. comm., 1998), Fairmile (G. Carr, pers. comm., 1998), and possibly Maronan, although limited analyses have been carried out (McNaughton, 1997b). However, the subeconomic Pegmont deposit (Mount Isa Inlier) is a notable exception (ibid.). Probably the most recognised example of extreme isotopic heterogeneity in a sediment-hosted Pb-Zn deposit in the Mount Isa Inlier, is the Lady Loretta Pb-Zn deposit (Gulson, 1985 and 1986). Whether a deposit possesses homogenous or heterogeneous Pb isotope signatures is dependent on three controlling factors:

1) the isotopic composition of the Pb-bearing source rock;
2) the size and longevity of the hydrothermal system, and;
3) the effects of post-depositional processes.

7.5.1.1 Isotopic composition of the source rock

The degree of isotopic homogeneity of the source rock depends upon the geological processes involved in its formation, e.g. sedimentary (Gulson, 1985), or igneous processes (Gulson, 1986). Sedimentary rocks can be isotopically heterogeneous due to variable provenance in so much as detrital components may have been derived from rocks possessing different μ values ($\mu=^{238}U/^{204}Pb$). However, homogenisation of Pb isotope signatures in sedimentary rocks may be achieved due to mixing of detrital components in closed basins (e.g. the Black Sea; Cooper et al., 1974). Individual bodies of igneous rock tend to be more isotopically homogeneous due to melting processes (cf. Doe, 1978), i.e. melting has the ability to homogenise (isotopically and chemically) rocks of differing composition via assimilation so

that the final μ value of the magma represents a cumulative average. Such a process has been referred to as Pb recycling by Carr et al. (1995). Yet for both sedimentary and igneous rocks, the production of radiogenic Pb from the decay of *in situ* U and Th since deposition can be a complicating factor that causes isotopic heterogeneity over time (cf. Ludwig and Silver, 1977; Gulson, 1986; Godwin et al., 1988).

7.5.1.2 Size and longevity of the hydrothermal system

Large hydrothermal systems operating over extended periods of time possess the capacity to homogenise metals and isotopic characteristics (Gulson, 1985 and 1986; Carr et al., 1995). Such well-mixed hydrothermal fluid reservoirs reduce inherent primary variations in Pb isotope compositions in the source rocks via water-rock interaction (Gulson, 1985 and 1986) and essentially the isotopic signature of the fluid represents the overall average isotopic signature of the rock. In this case, primary galena precipitates are likely to have homogeneous isotopic signatures (Gulson, 1985 and 1986) that could be used to determine metal provenance and/or fluid sources (Farmer and DePaolo, 1997), especially if the deposit is located in close proximity to the metal-bearing source rock (Zartman and Stacey, 1971; Doe, 1978; Sawkins and Kowalik, 1981).

In contrast, poorly mixed fluids associated with small hydrothermal systems operating over shorter time spans lack the ability to homogenise Pb, especially if primary isotopic variations exist in the source rock (Fehn et al., 1983; Gulson, 1985 and 1986) and low water-rock ratios prevail (Roache, 1996). This aspect may be compounded if radiogenic Pb is scavenged (via water-rock interaction) during migration from the source to the depositional site (e.g. Blattner and Lassey, 1992; Farmer and DePaolo, 1997), especially if the deposit is located a significance distance from the source hydrothermal reservoir, i.e. isotopic contamination (Zartman and Stacey, 1971; Doe, 1978; Sawkins and Kowalik, 1981).

What controls isotopic variability essentially relates to the chemistry of the ore-forming fluid and its interaction with rocks over time and distance from source to depositional site. In addition to water-rock ratios, a number of other factors are involved. In particular, the concentration of Pb in the fluid versus the concentration of Pb in the rock, the reaction/diffusion rates between fluid and rock, and the relationship between advective transport and reaction flux, i.e. the Damköhler and Pélect numbers (Lassey and Blattner, 1988; Blattner and Lassey, 1989 and 1992; Farmer and DePaolo, 1997). The isotopic composition of the fluid should be retained under internally buffered conditions and high water-rock ratios during transport, if the fluid is saturated in Pb. Under externally buffered conditions and low water-rock ratios, it is likely that the isotopic signature of the fluid will progressively evolve via interaction with multiple rock types along the migratory path from source to depositional environment, especially if the fluid is undersaturated with respect to Pb. This may cause heterogeneity in isotopic signatures in short-lived small hydrothermal systems (i.e., small deposits), as well as signatures that may not reflect any single source rock within a region, but a variety of source rocks with different μ values, or may not reflect any particular source rock within a region.

From an exploration point of view, whether isotopic ratios in ore deposits can be used as source rock tracers depends on whether the hydrothermal fluid retains the isotopic signature of the source rock during transport to the depositional site.

A particularly good example of the complexities and ambiguities involved in interpreting deposits with heterogeneous Pb isotope ratios comes from work on the Lady Loretta deposit. Heterogeneity is thought to be due to mixing of metal-bearing fluids from more than one source with differing μ values via different fluid pathways at a similar time, or at slightly different times through the same fluid pathway (Carr and Gulson, 1984; Gulson, 1985). Alternatively, the data may indicate that the source rocks possessed similar μ values but have a significant age difference (Gulson, 1985), or the metals were deposited over a protracted period of time (Sun et al., 1994). Yet another alternative may involve the addition of radiogenic Pb sourced from the surrounding host rocks in distal areas of the hydrothermal system where low water-rock ratios would be expected, i.e. isotopic contamination. This may have occurred during ore formation, or may have occurred during a separate hydrothermal event that was active a substantial time after the formation of the deposit. Roache (1996) proposed a similar model to explain heterogeneity at the Menninnie Dam deposit in South Australia.

7.5.1.3 Post-depositional effects

Pb-rich deposits formed from long-lived, large hydrothermal systems will preserve isotopic homogeneity due to near zero U+Th/Pb ratios in galena, i.e. $\mu = 0$. The homogenous signature in galena will not be modified in the event of later hydrothermal activity associated with metamorphism and/or magmatism unless later fluids are enriched in Pb (Carr et al., 1995). However, some heterogeneity may arise if externally derived Pb is introduced during a separate hydrothermal event a significant time after the formation of the deposit (e.g. Roache, 1996). However, the degree to which the initial values are modified are dependent on the size and longevity of the post-depositional hydrothermal system and the concentration of Pb in the fluid. To fully understand the genetic implications of isotopic heterogeneity, paragenetically constrained samples of galena need to be analysed within the interpreted geological framework of the deposit.

7.5.1.4 Isotopic homogeneity at Cannington

Isotopic homogeneity in galenas suggest that the hydrothermal system that formed Cannington was large and operated over an extended period of time. The Pb-bearing source rocks either had little variation in isotopic composition, or the isotopic composition was homogenised by hydrothermal processes active over a protracted period of time. It is likely that the isotopic composition of the fluid was internally buffered and that the water-rock ratio was high. In addition the preservation of the isotopic composition of the fluid would be enhanced if high Pb concentrations were maintained during transport.

However, it is unlikely that the isotopic homogeneity at Cannington is a reflection of its large size because the Pegmont deposit 30km to the west, possesses a very similar homogenous signature (G. Carr, pers. comm., 1998), yet is significantly smaller in size and is a quarter of

the tonnage. Presumably the local hydrothermal system at Pegmont was smaller than that of Cannington and operated over a shorter period of time. It is likely the homogeneous signature simply indicates the Pb-rich character of the hydrothermal system rather than its size and duration of activity (cf. Gulson, 1985 and 1986). This implies that heterogeneity in Broken Hill-type deposits of the Eastern Succession may be due to post-depositional effects rather than primary ore processes (cf. Carr and Sun, 1996). The similarity in isotopic composition between Cannington and Pegmont provides evidence for a common heritage and it is possible that fluids involved in the formation of Pegmont and possibly other Broken Hill-type deposits in the region, were tapped from the same large, isotopically homogenous hydrothermal aquifer as Cannington.

7.5.2 Sources of Pb

It is difficult to ascertain possible Pb sources for the primary ore at Cannington (i.e. Stage I galena) before interpreting the genetic and temporal implications of Pb isotope data from other generations of galena, host rocks and granites of the Williams-Naraku Batholith. Essentially, integration of these latter interpretations provides a basis for developing a Pb source model for the deposit.

7.5.2.1 Stage II galena — metasomatism (syn- to post-D_2 retrogression)

Some workers propound that Cannington resembles an epigenetic skarn that formed after peak metamorphism, i.e. the metasomatic model (Chapman, 1993; Strain, 1993; Richmond, 1994; Jenkins, 1994; Richmond et al., 1996a and b; Williams et al., 1996; Chapman and Williams, 1998). Part of their supporting evidence relies on the existence of Pb-rich (2.2 to ~14 wt% Pb; Dong et al., 1997a) hypersaline fluid inclusions in quartz (Williams et al., 1996; and Chapman and Williams, 1998). However, hypersaline fluid inclusions have only been observed in quartz temporally and spatially related to Stage IIa hedenbergite-garnet-quartz metasomatism and quartz (± hedenbergite, hornblende, garnet, carbonate) veins that overprint pre-existing mineralised rocks. Pb-rich fluid inclusions could therefore, be reinterpreted as evidence for remobilisation of pre-existing metals by the introduction of externally derived hypersaline fluid during syn- to post-D_2 metasomatism (Bodon, 1996a and b, 1998; Walters and Bailey, 1998). The source of Pb is paramount when determining which model is the most plausible, i.e. was exotic Pb introduced during Stage II metasomatism, or was Pb simply leached from the pre-existing mineralised rocks?

Textural evidence indicates that Stage I galena was present prior to metamorphism and deformation, and that the bulk of Stage II galena was precipitated during the waning stages of post-peak M_1 metasomatism, i.e. the low-grade hydrous Stage IIc (refer Chapter 4). Evidence for large-scale Pb introduction during metasomatism should be manifested by obvious heterogeneity in the isotopic composition of Stage II galenas due to mixing with pre-existing Stage I Pb. However, there is no detectable difference in Pb isotope ratios between Stage I

and II galenas; the signatures are exactly the same suggesting that the metasomatic fluid:

- inherited the homogenous Pb isotope signature from pre-existing Stage I sulphides even though metasomatism occurred after M_1, syn-to post D_2; and
- did not introduce exotic Pb, or possess a sufficiently high enough concentration of exotic Pb to produce a unique isotopic signature.

Therefore, the metasomatic model proposed by Williams et al. (1996) and Chapman and Williams (1998) is inconsistent with the Pb isotope data unless all Pb was introduced during metasomatism; an unlikely scenario given the textural (Chapter 4), thermobarometric (Chapter 5) and geochemical evidence (Chapter 6). The data supports the interpretation that solution–associated remobilisation of pre-existing Pb (i.e. Stage I) occurred during metasomatism and that little or no externally derived Pb was introduced during this event. Given the high homogenisation temperatures (average 450°C) and hypersalinity (30-60 wt% NaCl equivalent) of fluid inclusions (Jenkins, 1994; Dong et al., 1997b; Dong and Pollard, 1997), it is not surprising that such a fluid would have the capacity to leach pre-existing Pb and transport it in very high concentrations. The mass balance study clearly demonstrates that this was the case (Chapter 6).

7.5.2.2 Stage III galena – near-surface hydrothermal activity (syn- to post-D_5)

Stage III galenas display the greatest variability in Pb isotope signatures, both inter- and minor intra-sample heterogeneity, albeit commonly within analytical error, and comprise the most radiogenic population at Cannington. More radiogenic compositions in veins and distal areas of deposits have been reported in a variety of deposit styles around the world (e.g. Russell and Farquhar, 1960; Zartman and Stacey, 1971; Godwin et al., 1982). Roache (1996) interpreted that more radiogenic signatures in galenas toward the periphery of the Proterozoic Menninnie Dam Pb-Zn deposit (Gawler Craton, South Australia) indicated the presence of host rock derived Pb. This Pb was deposited either at the same time as the main orebody under conditions of low water-rock ratios, or was temporally associated with a late stage alteration event a significant time after the formation of the deposit. Similarly, Thompson and Beaty (1990) observed that galena-bearing veins in the Leadville MVT district, USA, displayed a greater variation in isotopic composition than galenas in the major carbonate replacement bodies, and that this was due to a larger component of wallrock-derived radiogenic Pb distal from the orebodies.

At Cannington, some Stage III galenas possess identical isotopic compositions to that of Stage I and II galenas, suggesting inheritance of the Pb isotope signature from pre-existing ore. Other samples contain a significant component of radiogenic Pb likely to have been externally derived. As previously discussed, the double-spike procedure yields an order of magnitude greater precision than the conventional method and therefore greater emphasis can be placed on the interpretations made by this procedure. The double-spike analyses demonstrate that the majority of spread in the isotopic data for Stage III galena occurs in $^{206}Pb/^{204}Pb$ ratios rather than $^{207}Pb/^{204}Pb$ and $^{208}Pb/^{204}Pb$ ratios. The regression line for Stage III data (shown in

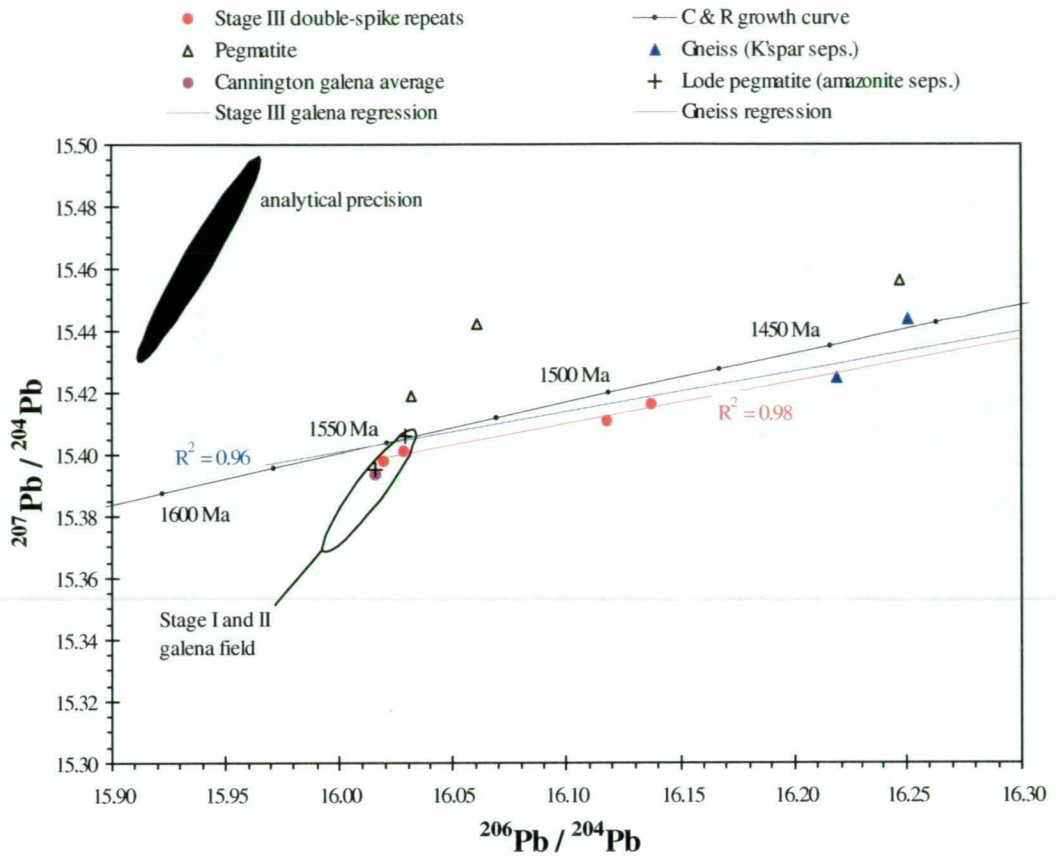

Figure 7.10 $^{207}Pb/^{204}Pb$ vs. $^{206}Pb/^{204}Pb$ plot depicting possible Pb sources for Stage III galena. The close spatial relationship between the regression line for K-feldspar separates from gneissic host rocks and the regression line for Stage III galena (double-spike data) indicates that the most likely source for Stage III Pb was local mixing between radiogenic Pb leached from the host gneiss and pre-existing Pb in the deposit syn- to post-D_5. Final $HF/HClO_4/HNO_3$ leachates from amazonite plot close to the Cannington galena average, suggesting that Pb in lode pegmatites was sourced from pre-existing Pb in the deposit.

red on Fig. 7.10) highlights a clear spatial correlation with the regression line for the K-feldspar data from the gneissic host rock (shown in blue on Fig. 7.10) with very little variation in $^{207}Pb/^{204}Pb$, i.e. clearly within analytical error. This correlation supports the interpretation that radiogenic Pb was sourced from the surrounding gneissic host rocks. The Stage III regression line therefore represents a mixing line between pre-existing Pb in the deposit and evolved, more radiogenic Pb sourced from the host gneiss at some later time (i.e. a secondary isochron).

Low-Pb rocks such as the gneissic host rocks at Cannington, are typically characterised by radiogenic Pb isotope signatures. This feature can be attributed to differences in the availability of radiogenic versus non-radiogenic Pb within host minerals that comprise the rock. Pb is strongly bound within mineral lattices (e.g. orthoclase), unlike U and Th that occur as interstitial ions in labile sites (i.e. less firmly chemically bound), especially in U/Th-bearing minerals such as monazite and zircon. Due to this, U and Th, including radiogenic Pb (^{206}Pb, ^{207}Pb, ^{208}Pb) produced by their *in situ* radioactive decay, may concentrate along mineral grain margins, and inter- and intragranular fractures. As a consequence radiogenic Pb is more susceptible to leaching by hydrothermal fluids than non-radiogenic Pb (Doe and Delevaux, 1972; Ludwig and Silver, 1977; Doe et al., 1979; Godwin et al., 1988). Godwin et al. (1988) suggested that radiation damage to minerals during radioactive decay may also assist the

accessibility of radiogenic Pb to hydrothermal fluids.

Evidence for leaching of radiogenic Pb from the host gneiss at Cannington via similar processes has been recognised by Giles (2000), who discovered that overgrowths on metamict zircon grains displayed significant Pb loss. He attributed this loss of Pb to open system U-Pb behaviour during hydrothermal interaction. U-Pb SHRIMP dating of this material yielded an imprecise discordant age of ~500 Ma for the hydrothermal event, a similar age to that of Thackaringa-type, vein-hosted mineralisation in the Broken Hill Block (op. cit.). Interestingly, the fault-hosted vein-style of Stage III sulphides at Cannington is also similar to the morphology of Thackaringa-type vein-hosted sulphides (op. cit.).

Overall, there is abundant textural evidence that Stage III galena is temporally associated with syn- to post-D_5, near-surface, hydrothermal activity (refer Chapter 4). D_5 fluids migrating through faults/joints and/or shear zones leached radiogenic Pb from the adjacent host rocks at ca. 500 Ma. This radiogenic Pb was introduced into the orebody via D_5 faults where upon the fluid interacted with the pre-existing ore. Various degrees of mixing between these two compositional end-members (i.e. host rock derived radiogenic Pb versus pre-existing ore Pb) during water-rock interaction produced the isotopic diversity observed in Stage III galenas. The least radiogenic galenas therefore represent higher degrees of D_5 fluid interaction with pre-existing ore Pb, i.e. ore dominated.

7.5.2.3 Amazonite-bearing lode pegmatites

Pb isotope ratios determined from final residual $HF/HClO_4/HNO_3$ leachates on amazonite separates plot within the least radiogenic galena population (Figs. 7.8 and 7.10). One sample (SZ037-25) possesses an isotopic ratio very similar to the average isotopic composition for Stage I and II galenas (Fig. 7.10). This similarity in isotopic composition between the final leachate data and Stage I and II galena supports the interpretation that Pb in lode pegmatites was sourced from pre-existing ore Pb. It is likely that ore Pb was assimilated into the pegmatites during their emplacement peak- to post-peak metamorphism. Hence, lode pegmatites inherited the Pb isotope signature of the ore. Geological observations consistent with these interpretations include:

- the spatial distribution of intrusive amazonite-bearing lode pegmatites is strongly controlled by proximity to pre-existing mineralised rocks. They are less typically hosted in the Core Amphibolite and the gneissic host rocks adjacent to the deposit. For example, *in situ* partial melts containing amazonite have only been observed in gahnite-bearing schists (anomalous in Pb and Zn) adjacent to the orebody in the Northern Zone;
- in some cases, lode pegmatites contain partially assimilated clasts of mineralised rock; and
- macroscopic mingling textures between lode pegmatite and ore have been observed underground.

Isotopic data from initial leachates provide evidence for an association between the isotopic composition of lode pegmatites and the type of rock in which they are hosted. Initial leachate data for amazonite from an intrusive lode pegmatite hosted in the Core Amphibolite (sample NZ004-2) highlights the absence of radiogenic Pb present in the sample, i.e. variations in the isotopic signatures are spread along the machine fractionation trend, plotting within and just above the least radiogenic population defined by Stage I and II galenas (Fig. 7.8). However, initial leachate data for lode pegmatitic material formed by *in situ* partial melting of gahnite-bearing schist (sample SZ037-25) highlights the presence of radiogenic Pb (Fig. 7.8). Similar to Stage III galenas, the distribution of the data from the *in situ* lode pegmatite falls along a linear trend subparallel to the projected evolution of the least radiogenic galena population, as well as the regression line for K-feldspar data from the host rock gneiss. Four possible models could explain this feature:

- radiogenic Pb was sourced from the host schist during partial melting, i.e. assimilation during anatexis;
- radiogenic Pb from the host schist was introduced after partial melting;
- radiogenic Pb was produced by *in situ* radioactive decay of U and Th within the partial melt; or
- various combinations of the above.

It is unlikely that radiogenic Pb was sourced from the host schist during metamorphism considering that the intrusive lode pegmatite (sample NZ004-2) contains no radiogenic Pb, even though Pb was presumably sourced from a similar quartzofeldspathic protolith. This option would only be possible if a major component of Pb in the intrusive lode pegmatite was sourced via assimilation of galena rather than Pb in the host gneiss. Radiogenic Pb produced by *in situ* decay of U and Th is unlikely for a similar reason, i.e. the intrusive lode pegmatite contains no radiogenic Pb. However, it is possible that radiogenic Pb was scavenged from the host schist and introduced into the *in situ* lode pegmatite fraction via inter- and intragranular fractures during retrogression and/or by fluids associated with a much younger hydrothermal event such as D_5. Evidence for the latter is provided by the presence of abundant retrograde muscovite (M_3 ca. 1510 Ma), minor chlorite-sericite alteration along joint surfaces, fine fractures and cleavage planes in the host gahnite-bearing schist and pegmatitic fraction. In this scenario, it would be expected that initial leachates would manifest the presence of radiogenic Pb.

Some additional salient points can be made from the *in situ* partial melt data. The isotopic signature of the partial melt should theoretically have been inherited from the host schist (op.cit.). Using this logic, the host schist must have an initial isotopic ratio similar to that of the final leachate signature for the amazonite in the *in situ* lode pegmatite and therefore, ore Pb. Hence, Pb in the host schist was possibly introduced by the same hydrothermal fluids that formed the deposit. Such an interpretation is consistent with the host gahnite-bearing schist being a metamorphosed hydrothermally altered rock (Chapters 3 and 6). Elevated wholerock Pb and Zn (average Pb=808ppm, Zn=4300ppm, n=5), presence of peak-metamorphic gahnite

porphyroblasts, rare fine (<3mm) bands of granoblastic quartz-apatite-garnet-graphite (± galena, pyrrhotite) reminiscent of graphitic ore, and rare fine-grained disseminated galena inclusions in K-feldspar-rich partial melt fractions (Fig. 7.3), provide additional evidence for this interpretation.

Due to the absence of radiogenic Pb, the intrusive lode pegmatite hosted in the Core Amphibolite (sample SZ037-25) must contain very little ~~or no~~ U and Th. It is unlikely that locally derived radiogenic Pb from the Core Amphibolite was introduced by later retrograde or D_5 fluids because the amphibolite contains negligible U and Th, and therefore very little or no radiogenic Pb (refer section 7.5.2.4 below). Furthermore, from the preceding discussion, it is possible that a large component of Pb in the lode pegmatite could have been sourced from the ore via assimilation of galena during metamorphism. Hence, all leachate data forms a population aligned to the machine fractionation trend. If radiogenic Pb was present, then it is likely that the majority of Pb would have been sourced from schists (i.e. pre-metamorphic hydrothermally altered rocks such as gahnite-bearing schist) adjacent to the orebody, during metamorphism.

7.5.2.4 Core Amphibolite

Wholerock Pb isotope data obtained from the Core Amphibolite form a population that is distributed along the machine fractionation trend, but within analytical error (Fig. 7.8 and Fig. 7.11). This feature negates the presence of appreciable radiogenic Pb in the amphibolite that if present, would be manifested by a greater range in the $^{206}Pb/^{204}Pb$ ratios, beyond the limits of the analytical precision ellipse. Due to this, the determinations are likely to represent initial isotopic ratios (G. Carr, pers. comm., 1999). Further evidence supporting this interpretation includes:

- the low U and Th content of the amphibolite (Table 7.4) suggests that negligible radiogenic Pb would have been produced over time by the decay of the latter elements;
- the lack of significant post-metamorphic alteration apart from weak, albeit pervasive sericitisation of feldspar, eliminates the possibility of externally derived radiogenic Pb associated with a subsequent hydrothermal event.

On first account, the slightly more radiogenic isotopic composition of the amphibolite compared to Stage I and II galenas indicates that the amphibolite was emplaced after the formation of the deposit, assuming a primary igneous origin for the contained Pb. This interpretation is consistent with geological relationships (section 3.7.4) and a $U\text{-}Pb_{zircon}$ age of 1578±15 Ma for the timing of emplacement, just prior to peak metamorphism (M_1) ca. 1580 Ma (Giles, 2000). Furthermore, an apparent Pb model age of ca. 1575 Ma, using the Cumming and Richards (1975) Pb evolution model, is within error of the of $U\text{-}Pb_{zircon}$ age. Nevertheless, high concentrations of Pb (and Zn) in the Core Amphibolite are enigmatic in comparison to other

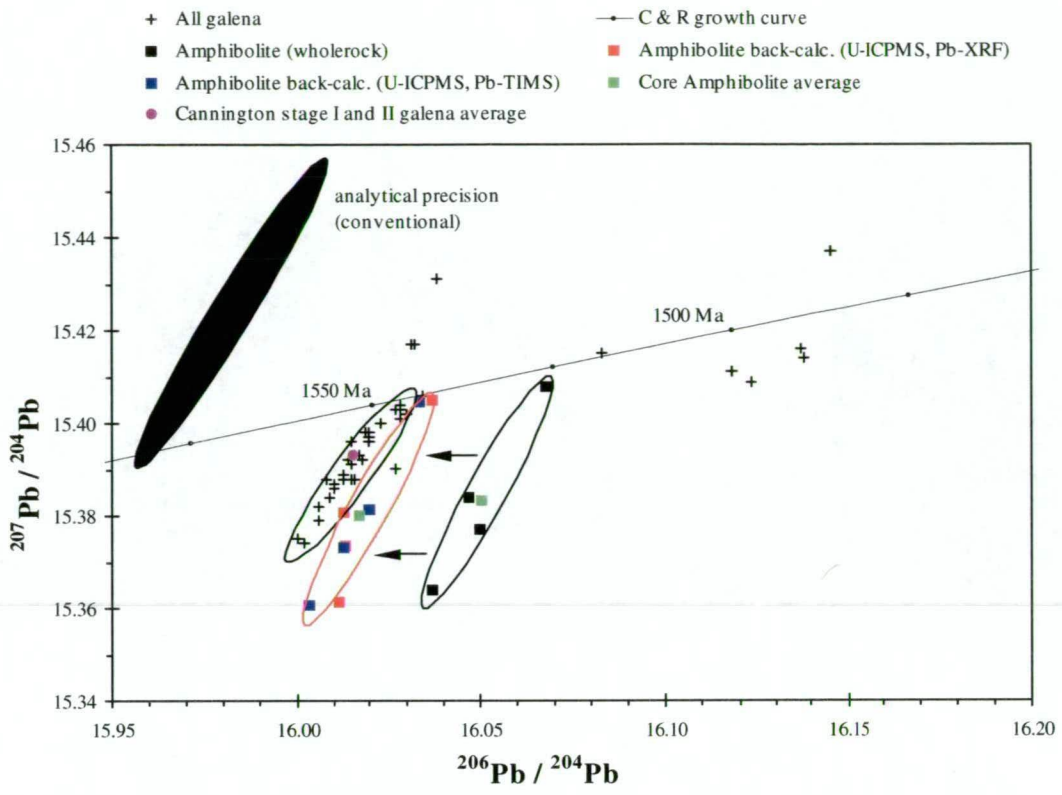

Figure 7.11 $^{207}Pb/^{204}Pb$ vs. $^{206}Pb/^{204}Pb$ plot of all galena and Core Amphibolite (wholerock) determinations. Subtraction of the calculated radiogenic Pb component in the Core Amphibolite samples places initial ratios very close to the least radiogenic galena population. The similarity of Pb isotope ratios to the least radiogenic galena population in addition to the high average Pb content of the Core Amphibolite, indicates that ore Pb was assimilated during emplacement of the amphibolite into the orebody.

amphibolites in the Maronan Supergroup that are distal to known sulphide deposits[#] (Table 7.4). On this basis, it is highly unlikely that Pb is of primary igneous origin, raising suspicions of an externally derived, secondary origin.

The Core Amphibolite is remarkably homogenous with respect to mineralogy, texture and geochemistry (section 3.7.4). However, compared to other amphibolites in the region it is anomalous in Pb and Zn (Table 7.6). Pb-enrichment in the Core Amphibolite is manifested by minor fine-grained disseminated galena inclusions in peak metamorphic minerals such as plagioclase (Fig. 7.12), indicating that Pb (and S) was introduced sometime before peak metamorphism and deformation. In instances where galena occurs interstitially to late-stage sericite, textures indicate that galena has been either locally remobilised, or that sericitic alteration has simply overprinted pre-existing silicates hosting minor inclusions of galena. Pb-enrichment was therefore unrelated to a subsequent, post-peak metamorphic hydrothermal event. Overall, the textural features imply that the Core Amphibolite has undergone some degree of alteration (or contamination) either during or sometime after emplacement, but prior to peak metamorphism and deformation, i.e. Pb was probably externally derived[†]. Isotopic ratios should therefore be viewed with some scepticism, as they may not represent the primary composition of the Core Amphibolite, but that of the exotic Pb contained within it.

[#] Published Pb concentrations in amphibolites proximal to known deposits in the Maronan Supergroup are lacking (e.g. Williams, 1998a).

[†] Some Pb was introduced during Stage IIa metasomatism as evidenced by rare galena-bearing hedenbergite-garnet-quartz veins. However, this Pb is spatially restricted and based on Pb isotope data, was sourced from the ore (refer section 7.5.2.1). In addition, Stage IIa alteration was not observed in any of the amphibolite samples used for this Pb isotope study.

Table 7.6 Average geochemical compositions of amphibolites from various localities in the Maronan Supergroup compared to the Core Amphibolite (data sources are listed in italics).

	Cannington *(this study)*	Marramungee *(Williams, 1998)*	Fairmile *(Williams, 1998)*	AGSO database	Toole Creek Volcanics *(O. Hatton, pers. comm., 1999)*
(wt%)					
SiO_2	48.04	48.89	48.56	49.35	47.50
TiO_2	1.17	2.14	1.69	1.66	0.86
Al_2O_3	14.42	13.20	13.21	13.43	13.95
Fe_2O_3		2.77	2.69	3.33	
FeO		12.62	11.04	9.97	
Total Fe_2O_3	13.53	15.12	14.71		11.87
MnO	0.24	0.29	0.43	0.25	0.20
MgO	7.99	5.73	5.79	5.48	8.52
CaO	10.47	8.07	10.72	10.86	11.56
Na_2O	2.00	1.26	2.22	2.71	2.19
K_2O	0.70	1.49	0.49	0.38	0.93
P_2O_5	0.08	0.22	0.13	0.16	0.05
(ppm)					
Zn	223	-	-	74	70
Pb	104	-	-	22	4
Nb	4.1	12	7	9	2.7
Zr	65	147	79	114	44
Sr	129	84	190	161	129
Ba	53	-	-	86	151
Y	21	41	27	32	15
Bi	<2	-	-	<2	-
W	<2	-	-	<2	-
Rb	22	108	18	9	59
U	0.20	0.46	-	<0.5	<1.5
Th	0.57	1.21	-	1	<1.5
La	5.17	10.3	-	18	-
Ce	11.06	25.8	-	34	-
Nd	8.91	-	-	21	-
Sm	2.75	5.0	-	-	-
Eu	1.07	1.7	-	-	-
Tb	0.67	1.2	-	-	-
Yb	1.97	4.0	-	-	-
Sc	37.76	45	46	48	42
Lu	0.27	0.48	-	-	-
n=	10	9	3	27	11

During intrusion of the amphibolite it is possible that pre-existing ore Pb, as well as Zn and S, was assimilated into the melt, i.e. Pb-enrichment was due to assimilation of ore Pb. In such a scenario it would be expected that the amphibolite should inherit the Pb isotope composition of the ore. However, the isotopic ratios are more radiogenic than ore Pb. This difference may be due to the addition of radiogenic Pb from the decay of *in situ* U and Th in the amphibolite since its emplacement.

To test this hypothesis, the initial isotopic ratio of each sample was back-calculated to the time of ore formation (at t_1) from present ratios (at t_2) based on the present concentration of Pb and U in each sample, and estimating a maximum Pb-model age (t_2) for the Core Amphibolite of 1640 Ma using the terrain specific Pb-model proposed for the Proterozoic of northern Australia

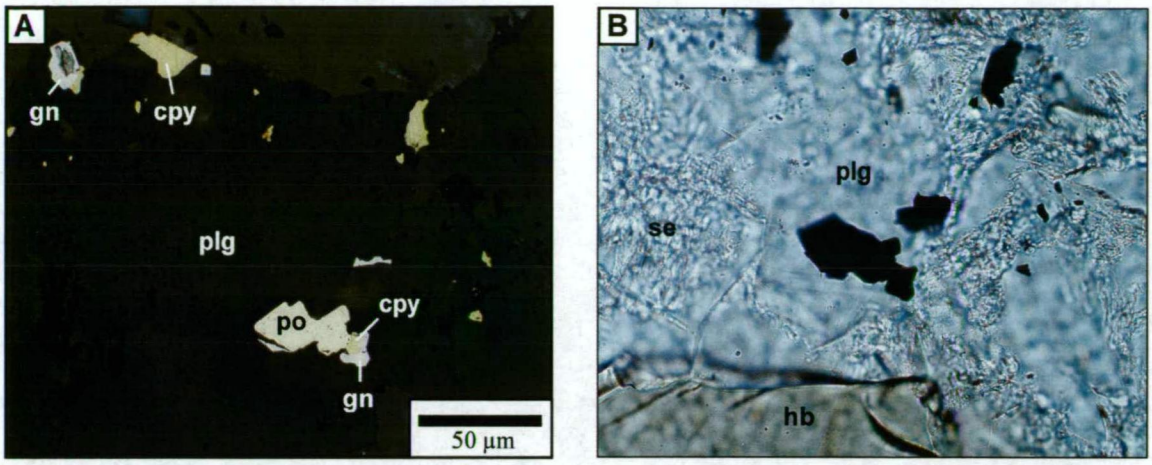

Figure 7.12 Photomicrograph of composite pyrrhotite-chalcopyrite-galena inclusion in plagioclase from the Core Amphibolite. Textures indicate that sulphides are not temporally associated with late sericite alteration of plagioclase, but rather predate peak metamorphism. **A.** reflected light. **B.** transmitted light (SZ056-1, 371.0m).

(Sun et al., 1994, 1996). In effect, this procedure removes the radiogenic Pb component in the samples (see Appendix 4 for results of the calculations). The calculation assumes that each sample has been closed to movement of U and Th since emplacement of the amphibolite at t_1. Uranium concentrations were calculated based on the Pb content (wholerock XRF data) and present Pb isotope ratios (at t_2) of respective samples, and using a maximum Pb model age for Cannington of 1670 Ma determined from the terrain specific Pb model (op. cit.). This was done to test the mathematical model, results comparing favourably with the analytical data (Appendix 4.3).

Calculated initial ratios at t_1 are very close to the isotopic composition of the ore, but are still slightly more radiogenic (Fig. 7.11). There is very little difference in the calculated t_1 ratios if a maximum age of ca. 1510 Ma is determined for t_2 using the Cummings and Richards (1975) Pb evolution model, or ca. 1580 Ma from the Stacey and Kramers (1975) model (Appendix 4.3). The results indicate that:

- the temporal constraints eliminate the possibility that ore Pb was sourced from the Core Amphibolite;
- the Pb isotope signature of the amphibolite was inherited from the ore via assimilation;
- the disparity between the ca. 1640 Ma Pb model age using the terrain specific Pb model (Sun et al., 1994, 1996) and the ca. 1580 Ma U-Pb_{zircon} age is an artefact of the inherited Pb isotope signature caused by assimilation of older ore Pb during emplacement of the amphibolite;
- the more radiogenic signature of the amphibolite in comparison to the ore Pb is a manifestation of the accumulated radiogenic Pb component produced by *in situ* radioactive decay of contained U in the amphibolite since its emplacement.

However, a limitation of the intrusive model is that it does not explain why other major elements, such as Fe, Mn and P are not enriched in comparison to other amphibolites in the region (Table 7.6), as would be expected if assimilation of the ore occurred during intrusion of the Core Amphibolite.

7.5.2.5 Gneiss

Pb isotope ratios from gneissic host rocks vary significantly and it is unlikely that any of the analyses represent initial isotopic ratios as they do not form a cohesive population aligned along the machine fractionation trend. In general, the isotopic data is notably more radiogenic than Stage I and II galenas and the Core Amphibolite. Regression lines through the wholerock and K-feldspar data pass through the Stage I and II galena and Core Amphibolite populations, possibly suggesting a common Pb source and therefore a genetic association (Fig. 7.9).

To test this hypothesis, the initial isotopic ratios of the samples were back-calculated using the same method as was performed on the Core Amphibolite data. Maximum model ages for t_2 (K-feldspar – 1575 Ma, wholerock – 1495 Ma) were determined using the terrain specific Pb model proposed by Sun et al. (1994, 1996). As a precursor, U concentrations were also calculated because:

- calculated initial isotopic ratios for the wholerock samples were unrealistic when U contents from XRF analyses were used in the equations;
- K-feldspar separates are not routinely analysed for U; and
- the data can be used as a "quality check" on the validity of the calculated initial ratios.

Calculated U contents for the wholerock gneiss samples are lower than XRF analyses by 1-5ppm suggesting that the samples were open to the movement of U and Th since their deposition, i.e. open rather than closed system (Appendix 4). It is apparent from the data that U has been added to the samples, possibly during metamorphism. The open system behaviour is also supported by the significant departure of the more radiogenic data from the Cumming and Richards (1975) growth curve on a $^{208}Pb/^{204}Pb$ versus $^{206}Pb/^{204}Pb$ plot (Fig. 7.9), i.e. either Th depletion and/or U addition during metamorphism. Overall, these discrepancies suggest that calculated initial ratios for the wholerock samples are an unreliable estimate and any ensuing interpretations are open to conjecture. With the absence of analytical data for U in the K-feldspar samples, it is difficult to assess the validity of the calculated U concentrations and ultimately, the calculated initial ratios. However, given the consistently low calculated U content between samples (Appendix 4), it is not unreasonable to assume that the calculated initial ratios are meaningful.

Plotting the isotopic evolutionary paths for individual samples can further test the applicability of the calculated initial ratios from the K-feldspar separates. This is based on the presumption that each sample will have its own unique growth curve. The starting point of each growth curve represents the initial isotopic ratio for the particular sample and should lie along a 1676 Ma isochron considering that the maximum depositional age for the gneiss is 1676 ± 5 Ma (U-Pb SHRIMP date from zircon; Page and Sun, 1996 and 1998). The isotopic evolutionary path for the gneiss from its time of formation can be estimated within maximum and minimum limits defined by two 1670 - 0 Ma isochrons. The area bounded by the isochrons can be referred to as the "host rock corridor" that defines the expected range in isotopic ratios for the gneiss from 1670 Ma to the present (Fig. 7.13). This estimation assumes that the gneiss has been closed

to the movement of U and Th since its time of deposition. Calculated initial isotopic ratios for K-feldspar separates plot within the host rock corridor very close to the 1670 Ma isochron, adding credence to their significance (Fig. 7.13).

Calculated initial isotopic ratios for the K-feldspars form a scattered population lying slightly above the amphibolite and Stage I and II galena fields on a $^{207}Pb/^{204}Pb$ versus $^{206}Pb/^{204}Pb$ diagram (Fig. 7.13). Isotopic ratios are very similar to least radiogenic determinations from the pegmatites hosted within the gneiss. Such an observation lends support to the interpretation that pegmatites formed during partial melting of the host gneiss. The K-feldspar data has a tendency to plot along the projected machine fractionation trends of the Stage I and II galena and Core Amphibolite fields, indicating that the gneissic rocks are essentially the same age as the deposit. Such a finding supports the synsedimentary model for the formation of the deposit (Chapter 6).

On the other hand, Pb sources appear to be slightly different between the gneiss and the ore with the majority of gneiss samples plotting at higher μ values in comparison to galenas, i.e. comparatively higher $^{207}Pb/^{204}Pb$ ratios. Overlap between the two populations indicates that mixing between the two Pb-sources may have occurred. Three possible mixing models explaining the distribution of the data involve:

i) isotopic mixing between hydrothermal fluids responsible for ore formation, and the sedimentary protolith of the gneiss; or,
ii) isotopic contamination of the hydrothermal fluid via leaching of Pb from the gneiss, i.e. the opposite of i); or
iii) the gneiss has a mixed Pb provenance with differing μ values. Differing isotopic ratios would therefore be controlled by the proportion of mixing between the source rocks during sedimentary processes.

It is unlikely that the gneiss samples contain Pb sourced from the same hydrothermal fluid that was involved in the formation of the deposit as this implies that they have been hydrothermally altered. Plotting MnO wt% against the Broken Hill-type alteration index (Walters, 1994b), demonstrates that they are unaltered and therefore, have not interacted with the ore-forming fluids at any stage (Fig. 7.14).

It is possible that the hydrothermal fluid scavenged some Pb from the surrounding host rocks. Such a mixing scenario would occur toward the periphery of the hydrothermal system where low water-rock ratios would persist, thereby changing the isotopic composition of the fluid toward that of the rock, i.e. isotopic contamination of the fluid. Isotopic ratios of the resultant hydrothermally altered rock and any precipitated galena would fall somewhere between the two end-member compositions. In reality this model should be regarded with caution given that the overlap between the two populations is within analytical error; the overlap could simply be an artefact of the analytical precision. Also, isotopic ratios of altered rocks have not been determined.

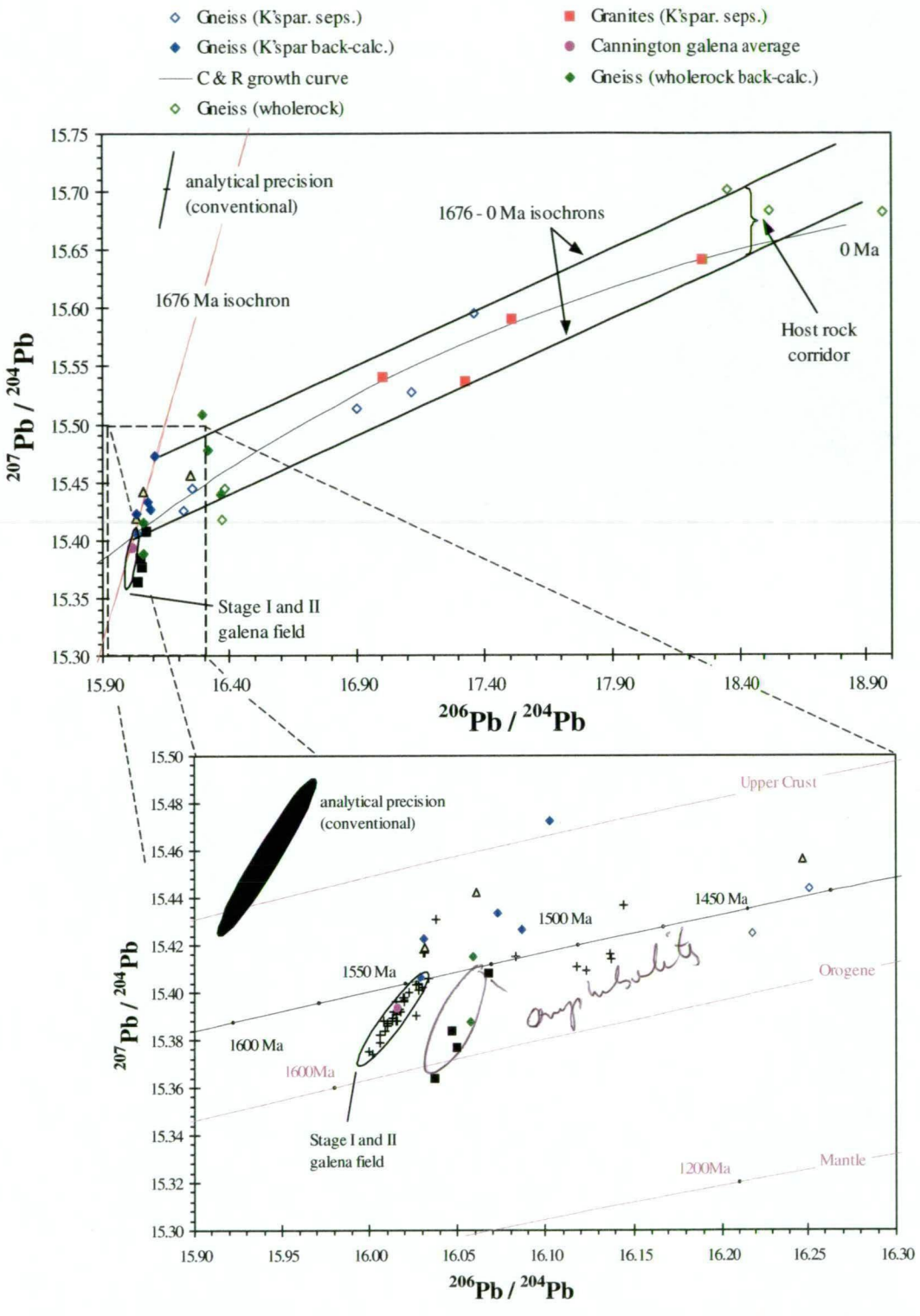

Figure 7.13 $^{207}Pb/^{204}Pb$ vs. $^{206}Pb/^{204}Pb$ plot of possible initial isotopic ratios for the gneiss (K-feldspar separates) calculated using the terrain specific, Pb evolution model of Sun et al. (1994 and 1996). The "host rock corridor" represents the theoretical evolutionary trend of Pb in the gneissic host rocks to the present and is therefore defined by two 1676–0 Ma isochrons (the approximate maximum depositional age of the gneiss). Calculated initial ratios for the gneiss plot within the host rock corridor. K-feldspars from pegmatites at Cannington, and the Mt. Angelay and Saxby granites plot within the corridor. In general, the pegmatite and back-calculated gneiss data are characterised by higher μ values than galena in the ores, indicating a more upper crustal Pb source according to the plumbotectonics model of Doe and Zartman (1979) and Zartman and Doe (1981). Granite data sourced from the JCU/AMIRA P438 project (McNaughton, 1997a and b).

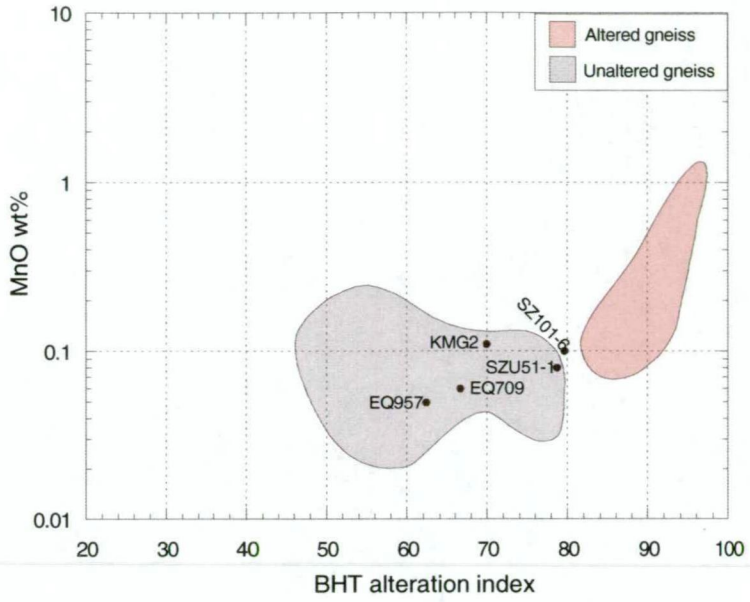

Figure 7.14 Plot of MnO wt% versus the Broken Hill-type alteration index (Walters, 1994b) for gneissic rocks of the Maronan Supergroup. All gneiss samples used in the Pb isotope study plot within the unaltered field except for sample SZ101-6 that plots just outside.

Lastly, the immobile element (Al_2O_3-TiO_2-Zr) geochemistry of the gneiss indicates that the sedimentary host succession had a single source (section 6.4.2). Therefore, a mixed Pb provenance with differing μ values can be discounted as a possible mixing model explaining the overlap between the ore Pb and calculated initial isotopic ratios for the gneiss.

7.5.2.6 Granites

Pb isotope data from K–feldspar separates collected from the Mt. Angelay and Saxby granites of the Williams Batholith plot within the gneissic host rock corridor (Fig. 7.13). This relationship indicates that both Pb in the granites and gneiss have a common heritage. U–Pb SHRIMP dates from the Mount Angelay granite (1524±4 Ma; JCU/AMIRA P438 project, 1995) are ~150 Ma younger than the gneiss at Cannington. It is therefore a distinct possibility that the Gandry Dam Gneiss (host rocks at Cannington) was the source for Pb in the granites.

7.5.3 Sources for primary ore Pb

Doe and Zartman (1979) proposed a "plumbotectonics" model that was based on a relationship that they recognised between the isotopic variability of deposits of the same age and the tectonic setting in which they were formed. As a result, they suggested that Pb was derived from three separate global tectonic reservoirs, i.e. lower crustal, mantle and upper crustal. Mixing between these reservoirs in variable proportions via crustal differentiation and recycling by subduction processes, lead to the delineation of a fourth reservoir termed "orogene". All four reservoirs possess distinct Pb evolution growth curves (Fig. 7.15) that can be used as a basis for interpreting generalised large-scale Pb sources. Their model was further refined by Zartman and Doe (1981).

The Core Amphibolite and the vast majority of Cannington galena data lie below the mid-point between the upper crust and orogene growth curves (Fig. 7.15), suggesting that Pb was

derived from a mixture of reservoirs (i.e. orogene) with a slightly higher component of upper crustal Pb. In comparison, the pegmatite data indicates a slightly greater component of Pb sourced from the upper crust, whereas the gneiss and granite data range between the orogene and upper crustal growth curves. These relationships indicate that primary ore Pb was sourced from more "primitive" rock types than the gneissic host rocks, possibly mantle derived components (cf. Carr and Sun, 1996; Page and Sun, 1998).

In the absence of regional Pb isotope data from various rock types throughout the Mt Isa Inlier, it is difficult to confidently determine possible primitive sources for primary ore Pb (i.e. pre-metamorphic Stage I galena); unequivocal genetic links are lacking at this stage. The Core Amphibolite and its parental magma can be discounted as a possible Pb source, as magmatism occurred some 100 Ma after ore formation, during compressional tectonics of the Isan Orogeny (section 7.5.2.4). Based on the spatial association between high-Fe metatholeiites similar in composition to the Core Amphibolite, and Broken Hill-type deposits in the Eastern Succession (e.g. Marramungee, Fairmile; Williams, 1998a), Georgetown Inlier (Withnall, 1985) and the Broken Hill Block (Phillips et al., 1985; James et al., 1987) a genetic association has been proposed. Based upon the unusual high-Fe, MORB-like geochemistry of these rocks, it is thought that the metatholeiites represent differentiates from high-level magma chambers that were generated by large degrees of partial melting of the mantle associated with major intracontinental rifting (Sinton et al., 1983; James et al., 1987; Page and Sun, 1998;

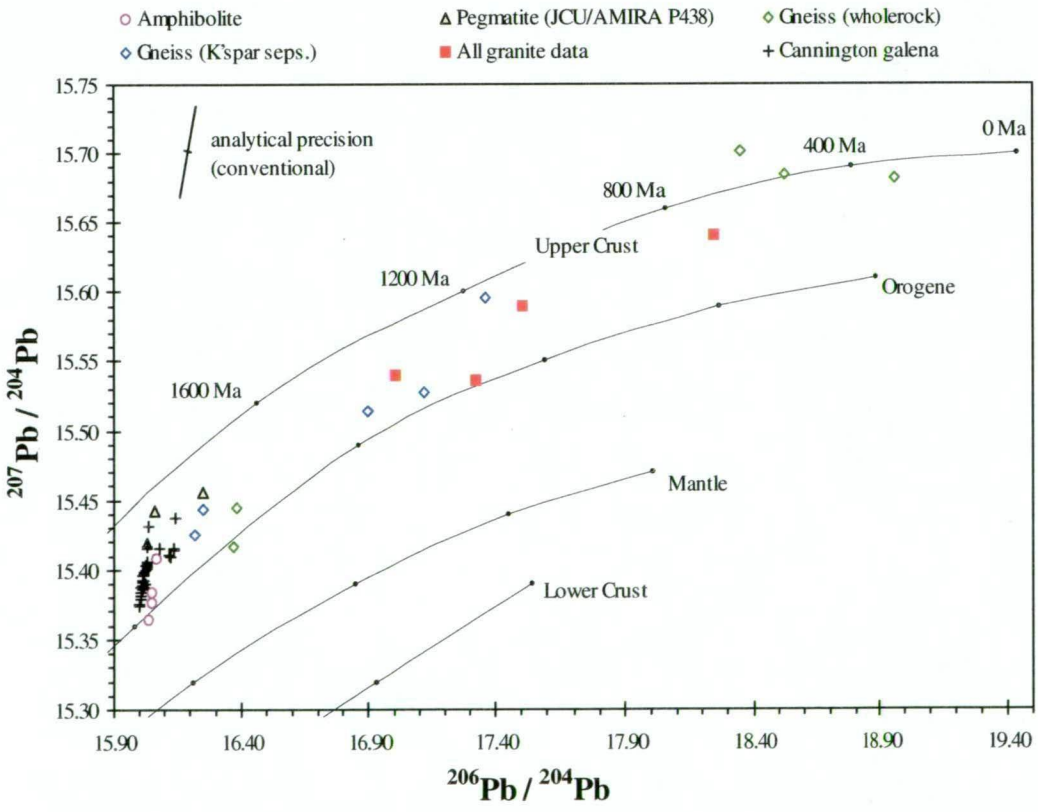

Figure 7.15 The plumbotectonics model proposed by Zartman and Doe (1981). The mantle, lower crustal and upper crustal growth curves represent evolution of three major Pb reservoirs, whereas the orogene curve represents mixing of these in various proportions. The majority of the Cannington galena data plots below the mid-point between the upper crustal and orogene curves. The amphibolite data also plots in a similar position, or just below the orogene curve. However, pegmatite data plots above the mid-point between the upper crustal and orogene curves. The gneiss and granite data plot anywhere between the latter growth curves.

Williams, 1998a). However, in the absence of Pb isotope data and U-Pb_{zircon} geochronology, a genetic link must be regarded as speculative.

εNd and Nd-depleted mantle model ages (T_{DM}) for the Mount Isa Inlier, indicate that extensional tectonics may have been induced by underplating of mantle-derived rocks in the lower crust (Page and Sun, 1998; cf. Wyborn et al., 1987; Oliver et al., 1991). The Mt. Isa seismic transect (MacCready et al., 1998; Goleby et al., 1996a and b) provides evidence for the existence of up to two bodies of mafic underplate in the Mt Isa Inlier. It is believed that underplating was driven by mantle pluming between 1780-1730 Ma (Oliver et al., 1991), and that melting of the underplate resulted in the eruption of the continental flood basalts that form the Eastern Creek Volcanics in the Western Succession (Page and Sun, 1998). Similarly, Page and Sun (1998) implied that significant mantle melting associated with underplating may have produced the high-Fe metatholeiites of the Eastern Succession circa 1670 Ma. It is therefore possible that large-scale, deep-seated hydrothermal activity existed during underplating and that primary ore Pb was sourced from the mantle derived rocks, i.e. the parental magmas of metabasic rocks in the Eastern Succession.

7.5.4 Broken Hill-type deposits versus sediment-hosted Pb-Zn deposits in the Mt Isa Inlier and McArthur Basin

Gulson (1985) recognised differences between the Pb isotopic composition of the Dugald River and BHT deposits in the Eastern Succession, and other sediment-hosted Pb-Zn deposits such as Mount Isa and Hilton in the Western Succession of the Mt. Isa Inlier. Broken Hill-type deposits in the Eastern Succession are characterised by primitive Pb isotope signatures (μ = ~10.724[†]) in comparison to large sediment-hosted Pb-Zn deposits such as Mount Isa and McArthur River (μ = ~10.834[†]; Fig. 7.16). The Broken Hill deposit in New South Wales has the most primitive Pb isotope signature of all Broken Hill-type deposits. Essentially, these deposit types can be distinguished on the basis of their Pb isotope composition (Sun et al., 1994, 1996; Carr and Sun, 1996; Carr and Whitford, 1997). Using the plumbotectonics model of Zartman and Doe (1981), the higher μ value of the sediment-hosted deposits indicates an upper crustal Pb source, such as a sedimentary succession associated with intracratonic rifting (Carr and Whitford, 1997). In comparison, Broken Hill-type deposits are characterised by a more primitive Pb source comprising a mixture of upper crustal, mantle, and lower crustal derived Pb, i.e. just above the orogene growth curve (Fig. 7.15).

The Dugald River deposit is the only "classic" sediment-hosted Pb-Zn deposit in the Eastern Succession. Isotopic ratios for Dugald River plot midway between the Broken Hill-type and sediment-hosted Pb-Zn growth curves (Fig. 7.16) suggesting that the hydrothermal fluid involved in the formation of the deposit possibly leached Pb from both BHT and sediment-hosted Pb-Zn-type source rocks. A similar scenario could be invoked for the shear zone-hosted Sandy Creek deposit, although geological evidence indicates a syn- to post-orogenic

[†] calculated using the Cumming and Richards (1975) model III.

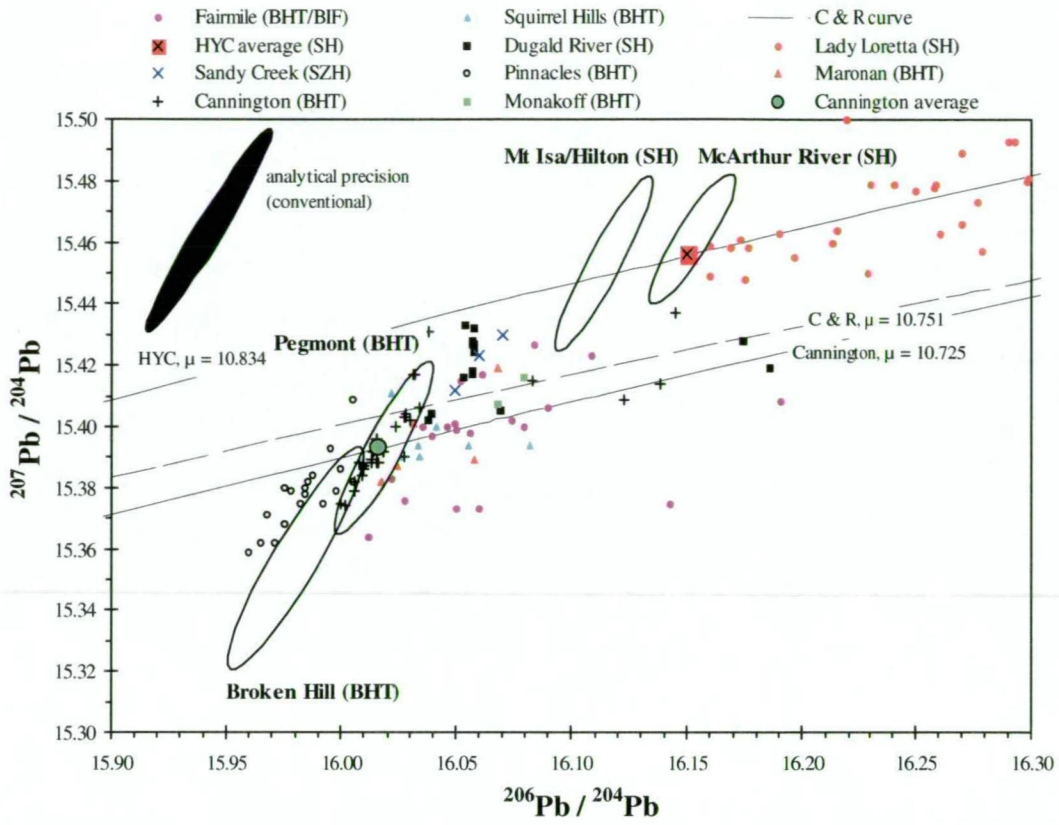

Figure 7.16 $^{207}Pb/^{204}Pb$ vs. $^{206}Pb/^{204}Pb$ plot of significant Broken Hill-type ("BHT") and sediment hosted Pb-Zn ("SH") deposits in the Mt. Isa Inlier and McArthur Basin. The Pinnacles and Broken Hill deposits located in the Broken Hill Block are also included for comparison. The Sandy Creek deposit is the only widely accepted significant shear zone hosted ("SZH") Pb-Zn deposit in the Eastern Succession of the Mt. Isa Inlier (Ramsden, 1998). Isotopic ratios from sediment hosted Pb-Zn deposits define a distinctly higher μ growth curve in comparison to the BHT growth curve. μ values calculated using the Cumming and Richards (1975) model. Sources of Pb isotope data are listed in Table 7.2.

timing for mineralisation (Ramsden, 1998). Alternatively, Pb may have been derived from crustal rocks containing a greater proportion of primitive Pb than is commonly found in the Inlier. Overall, the difference in Pb isotopic compositions between Broken Hill-type deposits and sediment-hosted Pb-Zn deposits points to basic differences in metallogenic processes and tectonic setting between the major deposit types (cf. Sun et al., 1994, 1996; Carr and Sun, 1996; Carr and Whitford, 1997), i.e. early rift-phase and input of primitive components, versus sag-phase and crustal dominated components.

It is worth mentioning that Broken Hill-type deposits in the Eastern Succession (and for that matter the Broken Hill Block and Georgetown Inlier) have extraordinarily similar Pb isotope compositions. This feature indicates a narrow period of time in which they formed, as well as similar Pb-bearing source rocks and ore-forming processes (Carr and Sun, 1996; Page and Sun, 1998).

7.5.5 Pb-model age

The most popular average crustal Pb evolution models used for determining Pb model ages are the Stacey and Kramers (1975) two-stage model and the Cumming and Richards (1975) evolving μ model. Both models attempt to reduce the difference between accepted geological ages and the calculated Pb model age of massive sulphide deposits around the world.

However, Pb model ages determined from these generalised models for deposits hosted in Proterozoic terrains in Australia are unreliable, often resulting in large discrepancies in comparison to other dating methods (Table 7.7). This makes the task of assessing synsedimentary versus epigenetic models particularly arduous. Gulson (1986) considered that the Stacey and Kramers (1975) growth curve displayed a better correlation with stratigraphic age determinations for the Proterozoic of Australia even though errors of ~100 Ma were apparent. Similarly, the Cummings and Richards (1975) model renders an age for Mt. Isa ore ~100 Ma younger than those determined from U-Pb zircon dating of the enclosing host rocks largely because the model is constrained by an age of 430 Ma for the Captains Flat Pb-Zn deposit, i.e. the model has been optimised for deposits in the Palaeozoic Lachlan Fold Belt of eastern Australia rather than the Proterozoic. Despite the low accuracies, the models can still be used for determining relative age differences between deposits in the same geological terrain.

To overcome the perennial problem of accuracy, terrain specific Pb evolution models can substantially minimise errors in absolute Pb model ages to within 10-30 Ma of ages determined by more reliable means (e.g. U-Pb SHRIMP dating of zircons). Terrain specific models are based on the premise that individual geological terrains possess a unique Pb evolution that can be modelled by using reliable, independent geological age determinations from rocks (within the particular terrain in question) as "control points". The age control points are then used as a basis for calibrating absolute Pb-model ages using either the Stacey and Kramers (1975) model or the Cumming and Richards (1975) model.

Sun et al. (1994) recognised the need to develop a terrain specific Pb evolution model for the Proterozoic of northern Australia with the aim of resolving issues related to ore genesis and as an aid to exploration strategies. They based their terrain specific Pb evolution model on an optimised Cumming and Richards (1975) model using a $U\text{-}Pb_{zircon}$ age of 1640±3 Ma for the McArthur River Pb-Zn deposit as an independent age control point. This U-Pb date was determined from zircons in tuffaceous beds adjacent to mineralised rock in the Barney Creek Formation (Page and Sweet, 1998), and was an appropriate choice due to strong evidence for

Table 7.7 Pb-model ages calculated using the terrain specific model for major Proterozoic Pb-Zn deposits in northern Australia and Broken Hill, NSW, in comparison to other Pb-model ages and U-Pb SHRIMP ages of zircons from immediate host rocks to the deposits. All ages are in millions of years (Ma).

Deposit	Zircon U-Pb SHRIMP age	Stacey and Kramers (1975) two-stage model	Cumming and Richards (1975) evolving μ model	Terrain specific model
McArthur River	1640 ± 3 Page and Sweet (1998)	~1610	~1510	1640†
Mount Isa	1652 ± 7 Page and Sweet (1998)	~1620	~1530	~1655
Broken Hill	1690 ± 5 Page and Laing (1992)	~1600	~1545	~1680
Cannington	1676 ± 5 Page and Sun (1996, 1998), Giles (2000)	~1610	~1540	~1670

† - model constrained on this U-Pb SHRIMP age.

the synsedimentary timing of ore formation at the McArthur River deposit (Hinman et al., 1994; Hinman, 1996; Large et al., 1998). Sun et al. (1996), and Carr and Sun (1996) found that Pb model ages were in close agreement with U-Pb_{zircon} ages for rocks hosting other significant Pb-Zn deposits such as Mount Isa. They also recognised that the Pb model compared favourably with U-Pb_{zircon} ages from rocks hosting Broken Hill-type deposits in the Georgetown Inlier (e.g. Railway Flat deposit), Broken Hill Block (e.g. Broken Hill) and the Eastern Succession of the Mt. Isa Inlier (e.g. Cannington). The Pb model greatly enhanced the reliability and usefulness of Pb-isotopes as a geochronological and exploration tool for Proterozoic terrains in northern Australia.

The terrain-specific model of Sun et al. (1996), and Carr and Sun (1996) was recalculated to incorporate the new analyses presented here. The recalculated model produced very similar Pb model ages for Broken Hill (1680 Ma), Mount Isa (1655 Ma) and Cannington (1670 Ma; Fig. 7.17b; Table 7.7). However, the Pb model age for Cannington using a modified Stacey and Kramers (1975) model was 1642 Ma, 28 Ma younger than the modified Cumming and Richards (1975) model, and essentially the same age as the McArthur River deposit (Fig. 7.17a; Table 7.7).

7.5.5.1 Timing of ore formation

Determination of the Pb-model age of the Cannington deposit helps to establish whether the timing of sulphide mineralisation is synsedimentary or post-peak metamorphic metasomatic. For the Pb isotope data to support a metasomatic model (e.g. Chapman and Williams, 1998), the isotopic composition of galenas should reflect a younger relative Pb-model age than the host gneiss, unless the Pb signature was inherited from a pre-existing concentration of Pb, such as an *in situ* or remobilised synsedimentary Pb-Zn deposit. However, from textural evidence and the Pb isotope data, a remobilisation model is unlikely because:

- any pre-existing Pb concentration must have been the same age as the host gneiss because the Pb isotope data falls along the same general isochron as the calculated initial ratios for the gneiss;
- the pre-existing Pb concentration must have endured the same polydeformation and high grade metamorphism as the gneiss; and
- textural evidence at Cannington indicates that sulphides are associated with peak metamorphic minerals such as knebelite, pyroxferroite and almandine.

A synsedimentary timing for ore formation best explains the correlation between the Pb isotope data and the calculated initial isotopic composition of the gneiss. The terrain specific Pb model age of 1670 Ma is very close to the 1676±5 Ma maximum depositional age for the host gneiss.

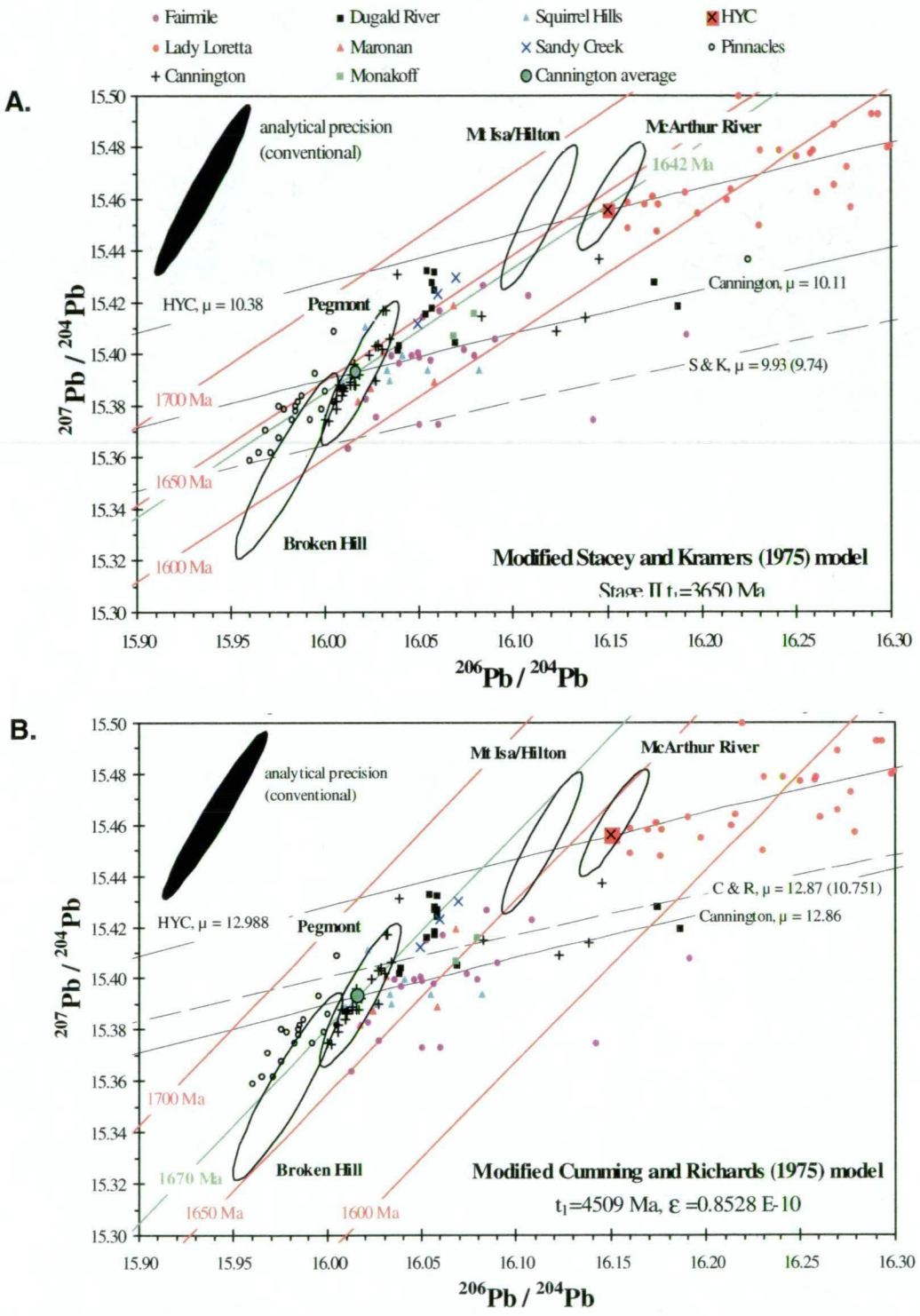

Figure 7.17 $^{207}Pb/^{204}Pb$ vs. $^{206}Pb/^{204}Pb$ plots of the terrain specific Pb evolution models for the Proterozoic Mt. Isa Inlier and McArthur Basin. Models were calculated using a U-Pb zircon age of 1640 ± 3 Ma (Page and Sweet, 1998) for the McArthur River deposit as an independent age control point. **A.** calculations based on a modified Stacey and Kramers (1975) model. **B.** calculations based on a modified Cumming and Richards (1975) model III. An age of ~1642 Ma was determined for Cannington using the Stacey and Kramers model. This is essentially the same as the McArthur River deposit, but some 34 Ma younger than the maximum depositional age for the host gneiss (1676 ± 5 Ma; Page and Sun, 1996, 1998). In contrast, an estimated age of ~1670 Ma for Cannington using the Cumming and Richards model, correlates well with the depositional age for the host gneiss.

7.6 SUMMARY AND CONCLUSIONS

Pb isotope ratios were determined for:

- paragenetically constrained galena samples (including eight double-spike analyses);
- amazonite separates from lode pegmatites;
- K-feldspar separates and wholerock samples from gneissic host rocks (Gandry Dam Gneiss); and
- wholerock samples from the Core Amphibolite.

Stage I and II galenas plot as a distinct linear cluster oriented along the machine fractionation trend but within the limits of the precision ellipse. The strong correlation between Stage I and II galenas indicates that Stage II metasomatism sourced Pb from the pre-existing Stage I ore and that little or no exotic Pb was introduced. Isotopic data from Stage III galenas plot within the Stage I and II galena field indicating that Stage III inherited the isotopic signature of the pre-existing galena. However, Stage III galenas also form a more radiogenic population forming a linear trend subparallel to the K-feldspar separate data from gneissic rocks. This correlation suggests that some radiogenic Pb was sourced from the local host rock gneiss during Stage III near-surface hydrothermal activity syn- to post-D_5. The radiogenic Pb was introduced into the orebody via D_5 faults, whereby mixing occurred with pre-existing ore Pb.

Pb isotope ratios for sequential leachates on amazonites from an intrusive lode pegmatite in the Core Amphibolite plot along the same linear machine fractionation trend as Stage I and II galenas. This relationship indicates that isotopic ratios were inherited from the pre-existing ore despite the younger age of the lode pegmatite. Initial leachates from an *in situ* lode pegmatite contain radiogenic Pb interpreted to have been sourced from the surrounding gahnite-bearing schist, possibly during metamorphism or retrogression (M_3). The data indicates that the protolith of the schist was a hydrothermally altered rock and that the alteration was spatially and temporally related to ore formation (Chapter 6).

Pb isotope ratios of gneissic host rocks vary significantly and it is unlikely that any of the analyses represent initial isotopic ratios. Calculation of initial isotopic ratios indicates that the gneiss has a similar isotopic signature to pegmatites hosted within them. This aspect supports the interpretation that pegmatites formed by anatectic partial melting of the gneiss during metamorphism. In particular, the observation that calculated initial ratios for the gneiss plot above the Stage I and II galena field (i.e. at a higher μ value) indicates that ore Pb was sourced from a more primitive protolith than the gneiss. Pb isotope data from granites of the nearby Williams Batholith plot within the "host rock corridor" suggesting a common Pb heritage to the gneissic rocks, i.e. the Gandry Dam Gneiss.

Pb isotope data from the Core Amphibolite plots as a distinct cluster aligned along the machine fractionation trend, but within the limits of the analytical precision ellipse. The distribution and lack of significant radiogenic Pb indicates that the data probably represents

initial Pb isotopic ratios. However, the presence of fine-grained pre-peak metamorphic galena suggests isotopic ratios were inherited from the pre-existing ore via assimilation during emplacement and then subsequently modified by the addition of minor radiogenic Pb from the decay of *in situ* U and Th. As a result, the Core Amphibolite is the only rock type that possesses a similar low μ value to the primary ore at Cannington. High-Fe metatholeiites similar in composition the Core Amphibolite are considered to have formed by significant partial melting of mantle-derived mafic rocks induced by underplating during the formation of the Eastern Succession crust at ca. 1670 Ma. It is a distinct possibility that large-scale, deep-seated hydrothermal activity was driven by this magmatism and that primary ore Pb at Cannington was sourced from the primitive parental magmas.

Isotopic homogeneity within a deposit is generally believed to signify that the hydrothermal system associated with ore formation was large and operated over an extended period of time. However, it is difficult to argue this point considering that the significantly smaller Pegmont deposit also possesses a homogenous Pb isotope signature. Instead, homogeneity probably indicates the Pb-rich character of the hydrothermal system rather than its size and duration of activity. Nonetheless, the similarity in Pb isotope signatures for Broken Hill-type deposits in Eastern Succession points to common Pb-bearing source rocks.

Using a terrain specific Pb-evolution model developed for the Proterozoic of northern Australia, the age of the Cannington deposit has been estimated at ~1670 Ma. This Pb-model age is in close agreement with the maximum depositional age of the host gneiss determined from detrital zircons (ca. 1680-1670 Ma; Page and Sun, 1996, 1998; Giles, 2000). In particular, calculated initial isotopic ratios of K-feldspar separates from the gneissic host rocks fall along the same general 1670 Ma isochron as the Stage I and II galena data. Overall, the isotopic evidence supports a synsedimentary timing for ore formation.

Pb-model ages estimated for other significant Proterozoic Pb-Zn deposits, such as Mount Isa and Broken Hill, using the terrain specific model correlate well with accepted ages of formation determined by U-Pb SHRIMP dating of zircons. It is interesting to note that the accuracy of relative Pb-model ages using the terrain specific model are dependent on errors in $^{206}Pb/^{204}Pb$ and $^{207}Pb/^{204}Pb$ caused by machine fractionation effects in the analytical instrument. For conventional isotopic analyses this is ~±10 Ma, whereas double-spike analyses reduce this to a mere ~±0.8 Ma (Sun et al., 1996). The implications of this with regard to exploration strategies and isotopic discrimination of particular hydrothermal events, as well as resolving contentious ore genesis issues in the Proterozoic of northern Australia are particularly significant.

Chapter 8

Geodynamic Evolution and Ore Genesis

8.1 INTRODUCTION

A concise ore genesis model requires the integration of deposit-scale paragenetic information with the orogenic history recorded in the surrounding host rocks. Such a marriage provides a sound basis for determining the chronological sequence of events and timing of ore formation. This is particularly relevant to the complex structural and metamorphic histories that characterise BHT deposits and the terrains in which they are hosted. The characterisation and subsequent removal of deformational, metamorphic and indeed, any retrograde metasomatic effects, is a necessary prerequisite when deciphering genetic models for deposits that have been subjected to these post-depositional processes. The genetic model presented here recognises the importance of the latter and in line with this, makes the distinction between two fundamental aspects:

- the geodynamic evolution as recorded from the beginning of the Isan Orogeny; and
- possible ore formation processes.

These objectives are achieved by integrating the research findings into a constrained genetic model that is consistent with:

- the interpreted paragenesis of the deposit;
- Pb isotope systematics and potential metal sources;
- wholerock and REE geochemistry;
- carbon sources from C isotope data;
- mineralogical assemblages;
- metal zonation features; and
- the structural and metamorphic history recorded in the host metasediments.

This chapter firstly reiterates the timing of ore formation and subsequent post-depositional evolution commencing from the Isan Orogeny. From this basis, characterising the effects and distribution of post-depositional processes within the deposit facilitates their removal from the pre-existing mineralised system. The remaining features of the deposit theoretically represent the principal attributes of the original hydrothermal system. The preservation of these gross characteristics provides an insight into processes of primary ore formation. Consequently, the final section of this thesis integrates the main conclusions of the study into a speculative genetic model for the Cannington deposit.

8.2 TIMING OF ORE FORMATION AND THE PROXIMAL ALTERATION HALO

The timing of ore formation can be constrained by sulphide-silicate textures and their temporal relationships to deformation and metamorphic fabrics developed in the ores (Chapter 4). The strongest textural evidence for the timing of ore formation is recorded in graphitic ores that have not been subjected to retrogression or Stage II post-peak metamorphic metasomatism. Assemblages in these rocks are entirely dominated by granoblastic Stage I, peak metamorphic fabrics. Disseminated sulphides within these rocks display classic granoblastic sulphide-silicate and spheroidation textures indicative of co-recrystallisation during prograde metamorphism. The ores also preserve an S_1 fabric defined by the preferred alignment of graphite and biotite, and grain aggregates of knebelite, pyroxferroite and hornblende. Micro- to macro-scale F_1 folds are common. Spheroidal sulphide inclusions in granoblastic, peak metamorphic (M_1) quartz, garnet and rarely knebelite are also characteristic. Similar spheroidal sulphide inclusions occur in Stage I peak metamorphic silicates, magnetite and rare calcite in olivine-pyroxenoid and hedenbergite ore, although deformation fabrics such as durchbewegt textures and mylonitic zones are difficult to correlate with particular deformation events (cf. Giles, 2000). Overall, it is evident from sulphide-silicate textures that sulphide mineralisation pre-dated M_1 and D_1, implying a minimum age of ca. 1580 Ma for ore formation.

However, ore formation can be traced back even further through time. Scant to non-existent evidence for the earliest pre-peak-metamorphic deformation event (D_i) in graphitic ores suggests that ore formation possibly occurred during the very early stages of the Isan Orogeny. Circumstantial evidence for a pre-D_i timing comes from the observed preservation of a relic S_i fabric in garnet porphyroblasts in the proximal alteration halo (Giles, 2000). If the ores and proximal alteration halo are temporally equivalent, as spatial relationships, geometries and textural evidence suggests, then the ores and proximal halo must predate D_i.

Stronger evidence for a pre-D_i timing is retained in garnets that possess unusual internal bow-tie textures in the graphitic ores. Such textures elsewhere have been interpreted to have formed by pseudomorphic replacement of possible chloritoid (cf. Stanton, 1989). If this is correct, then these texturally distinct garnets grew during prograde metamorphism and did not form during post-peak metamorphic metasomatism. The occurrence of fine sulphide inclusions in these prograde garnets provide unequivocal evidence that graphitic ores retain the same metamorphic history as that recorded in the host metasediments (e.g. Giles, 2000).

Geothermometric calculations (Chapter 5) indicate that graphitic ores were subjected to peak metamorphic temperatures similar to those calculated from the host metasediments and the Core Amphibolite, i.e. 730-750°C. Calculated temperature profiles across garnets in graphitic ores indicate that the prograde metamorphic history has been preserved, with garnet rims reflecting the highest (peak metamorphic) temperatures. Lower temperatures (by as much as ~150°C) in the cores of garnets are consistent with the presence of graphite and elevated Mn in the graphitic ores during prograde garnet growth in contrast to the flattened temperature

profiles in graphite-free garnet-bearing assemblages in the host metasediments and the Core Amphibolite. Graphite facilitates the maintenance of a low oxidation state and a reduced water activity ($a_{H_2O} \approx 0.1$) during garnet growth (Burton and O'Nions, 1991; Ohmoto and Kerrick, 1977). This affects metamorphic equilibria in two ways.

Firstly, reduced water activities allow garnet-forming dehydration reactions to occur at significantly lower temperatures (Burton and O'Nions, 1991). The presence of elevated Mn enhances this effect by also stabilising garnet at lower temperatures (Williams and Grambling, 1990). Furthermore, the net effect is exacerbated by the significantly lower Mn contents in the graphite-free assemblages of the host metasediments and Core Amphibolite, where garnet stability would have been comparatively retarded at low temperatures.

Secondly, the presence of graphite affects C-O-H fluid equilibria. This has a profound effect on garnet reaction and physical crystalline growth kinetics, resulting in the formation of unusual internal radial textures defined by fine quartz inclusions in sector-zoned garnets. These characteristic textures develop if the oxidation state is maintained below the quartz-fayalite-magnetite buffer (Burton, 1986). As a consequence, the compositions of fluids generated in graphite-bearing assemblages diverge substantially from pure H_2O, typically containing appreciable CO_2. The presence of CO_2 in the fluid phase suppresses the solubility of SiO_2. As a result, chemical equilibrium between quartz and garnet is retarded and instead of quartz being transported in the intergranular fluid phase and reprecipitated in favourable sites, thus lowering the free energy of the system and re-establishing chemical equilibrium, quartz is incorporated in garnet as fine intergrowths. This also impairs the normal coarsening in grain size of matrix minerals during typical prograde recrystallisation (Spry, 1969; Burton, 1986). Garnet textures and the fine grain size of graphitic ores are consistent with this process and implies that the ores were subjected to prograde metamorphism. The preservation of graphite, low water activity and suppressive effects of CO_2 on mineral solubilities, suggest that metamorphism of graphitic ores was essentially isochemical, apart from the loss of volatiles.

In summary, ore formation at Cannington is interpreted to have predated peak metamorphism and can be traced back through the prograde metamorphic history to before the earliest recorded deformation event in the region (D_i). A synsedimentary to pre-D_i timing for ore formation is therefore inferred. The age of D_i is not known, and the lack of timing criteria preserved in the ores before this time precludes arguments based solely on textural evidence. Any timing criteria must therefore rely on geochemical evidence and gross physical features of the hydrothermal system.

In Chapter 7, a Pb model age of ca. 1670 Ma was determined for Stage I galena inclusions in peak metamorphic knebelites from a variety of ore types. In fact, all galena data apart from Stage III galenas plot as a tight linear population parallel to the machine fractionation trend and within the limits of analytical error. This age is very similar to the ca. 1675 Ma U-Pb_{zircon}

maximum depositional age for the host sediments (Page and Sun, 1998; Giles, 2000) and closely links the timing of ore formation to a synsedimentary to syndiagenetic timing.

From Chapter 6, carbon isotope signatures of graphite from graphitic ores indicate a biogenic origin for the carbon as opposed to a metamorphic phenomena. Kerogenous matter must have been present in the rocks when they were deposited. Textural relationships between graphite and sulphides are equivocal with regard to a synsedimentary timing for ore formation owing to metamorphic recrystallisation. However, the fact that graphite and base-metal sulphides occur as co-existing inclusions in peak metamorphic garnet and quartz, provide supportive, although circumstantial evidence, that biogenic material was intimately related with ore formation. A temporal and genetic relationship may therefore be valid and a synsedimentary or syndiagenetic timing for formation implied.

Evidence for synsedimentary timing comes from geochemical mass balance calculations (Chapter 7). Graphitic ores consist of detrital pelitic material and hydrothermal components that have been mixed in variable proportions. This aspect, coupled with the millimetre- to centimetre scale laterally continuous compositional banding and variation in pelitic to hydrothermal ratios between the various facies comprising graphitic ores, is comparable to chemogenic sediment that formed via coincident accumulation of detrital pelagic material and hydrothermal precipitates. It is unlikely that graphitic ores were formed exclusively by replacement of pelagic sediment, as such an infiltration-type process should have resulted in lateral metal and mineralogical zonation from source-proximal to distal. Laterally continuous, delicate millimetre- to centimetre-scale compositional bands in graphitic ores are characterised by stark differences in mineralogy and geochemistry. These intrinsic features are accompanied by erratic metal distribution in any one drillhole intersection (Chapter 4). Coupled with the absence of lateral zonation features, the latter features are inconsistent with a replacement model. Calculated volume changes >100% are also unrealistic with regard to replacement of pelitic sediments, and are more consistent with coincident accumulation of pelitic detritus and metalliferous hydrothermal sediment (section 6.7.2).

Sharp contacts between host garnetiferous metasediments and graphitic ores, and gross concordancy of graphitic ore lenses to adjacent interpreted bedding are also consistent with a synsedimentary model. Augen in gahnite-bearing sillimanite-biotite-garnet schists that have similar mineralogies and garnet textures to graphitic ores may represent thin chemogenic horizons intercalated with clastic sedimentary material. Indeed, the laterally continuous Fe-Mn silicate units in the host metasediments of the deposit probably represent chemogenic horizons. Sharp contacts, as opposed to deformed tectonic contacts, are consistent with this interpretation.

8.3 GEODYNAMIC EVOLUTION

Integration of the paragenetic framework (Chapter 4) with the structural and metamorphic history of the host metasediments (Chapter 3) into a complete geodynamic evolutionary model for the deposit from the beginning of the Isan Orogeny is summarised in Figure 8.1. Where possible, the framework has been constrained by U-Pb zircon and monazite ages, and $^{40}Ar/^{39}Ar$ thermochronology (after Giles, 2000). The post-depositional evolution of the deposit can be subdivided into four stages on the basis of deformation and temporally related metamorphic events. These four stages are summarised in this section. Note, however, that these evolutionary stages are not equivalent to the paragenetic stages. Speculations on primary ore formation processes prior to the post-depositional geodynamic evolution of Cannington are presented in section 8.4.

8.3.1 Stage 1

The deposit originally consisted of a concordant, synsedimentary, zoned lens (Fig. 8.2). Possible early extension (D_i ?) associated with lithospheric thinning preceded the initiation of compressional tectonics related to the early stages of the Isan Orogeny. D_1/M_1-D_2/M_2 polydeformation and high grade metamorphism (upper amphibolite to transitional granulite facies) was associated with the initiation of a west-vergent fold-thrust terrain ca. 1600Ma (Giles, 2000). Metamorphism was characterised by a low pressure - high temperature prograde path, with peak metamorphic conditions attaining 730-750°C and 5-6kbars. Contemporaneous anatectic partial melting of the host sediments occurred during peak metamorphism (M_1) ca. 1580 Ma (Page and Sun, 1998; Giles, 2000), forming the migmatitic gneiss (Mark et al., 1998). It was during this period that characteristic Stage 1 peak

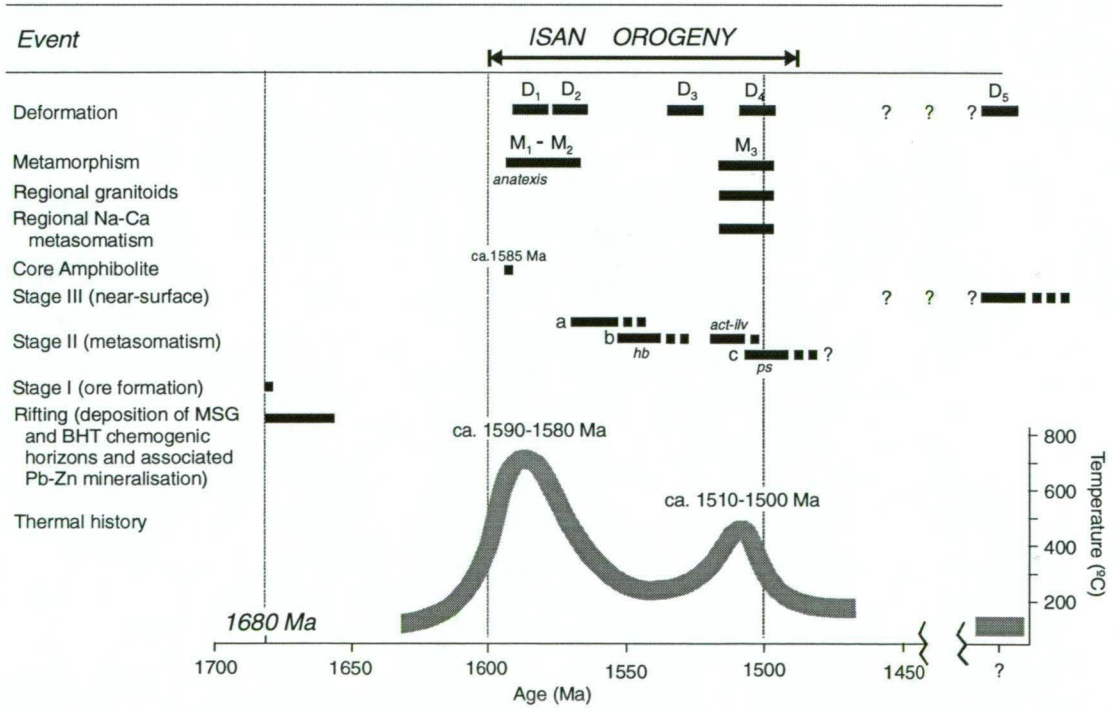

Figure 8.1 Interpretive geodynamic framework for the Cannington region. Where possible, the framework has been constrained by U-Pb zircon and monazite ages, and $^{40}Ar/^{39}Ar$ thermochronology determined from micas and amphiboles. Ages of events after 1480 Ma are unknown.

Stage 1: D_1-D_2 folding and shearing associated with the initiation of a fold-thrust terrain ca. 1600 Ma, i.e. the commencement of the Isan Orogeny. Syn- to post-D_2 Stage IIa hedenbergite-garnet-quartz and Stage IIb hornblende metasomatism.

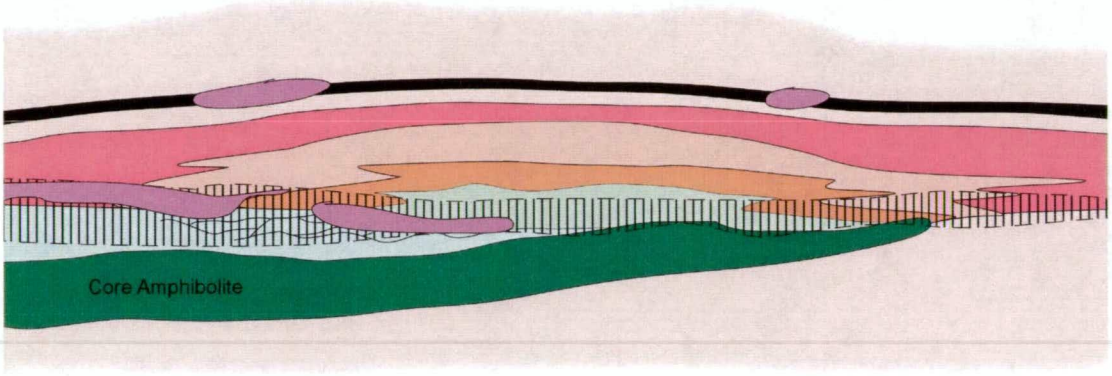

Stage 2: Focussed shearing and macroscopic recumbent folding occurred during D_3. Development of the Cannington Synform and Footwall Shear are believed to represent a fold-thrust couple. Syn- to chiefly post-D_3, Stage IIb ferro-actinolite-ilvaite alteration associated with pervasive circulation of M_3 retrograde fluids. .

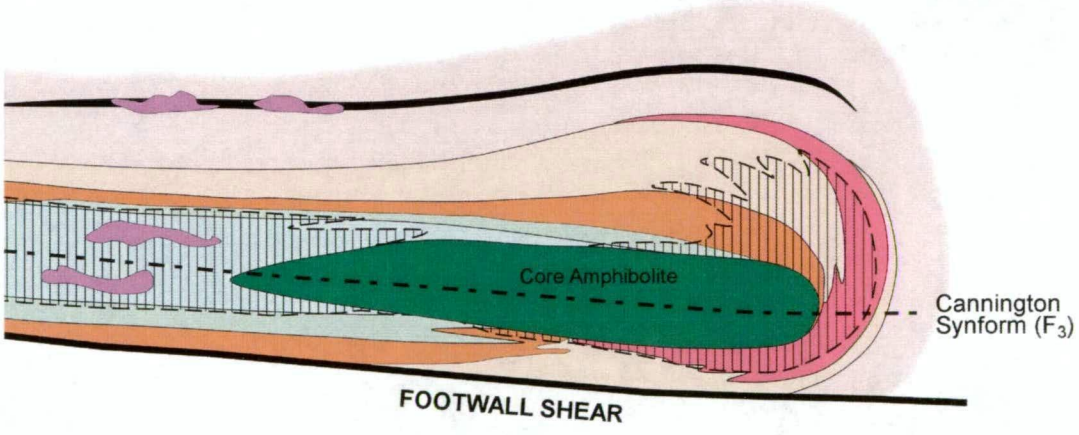

LEGEND

- Core Amphibolite
- Sillimanite-garnet schists and garnetiferous quartzites
- Silicified stringer zone (Siliceous Zn ore with quartz-gahnite-sphalerite veins)
- Hedenbergite ore (Zn)
- Olivine-pyroxenoid ore (Pb-Ag)
- Banded olivine-pyroxenoid ore (Pb-Ag)
- Fe-Mn silicate unit
- Graphitic ore (Pb-Zn-Ag)
- Stage IIa metasomatism (hedenbergite-garnet-quartz alteration, veining and breccias and tension gashes)
- Stage IIa intense silicification, quartz veining, brecciation and minor hedenbergite-garnet quartz veining
- Stage III quartz-carbonate-sulphide veining, chlorite-quartz-carbonate-pyrite/marcasite alteration

Figure 8.2 Stages 1 and 2 in the geodynamic evolution of the Cannington deposit from the beginning of the Isan Orogeny to the present day (modified after Bodon, 1998).

metamorphic assemblages and granoblastic to durchbewegt and mylonitic fabrics were developed in the ores.

D_2/M_2 was characterised by the ingress of an acid fluid phase that resulted in the development of S_2 microshears filled with secondary sillimanite in the gneiss and metamorphosed alteration halo surrounding the deposit (i.e. the garnetiferous rocks). P-T conditions of 500-650°C and 3-6kbars suggest M_2 was a retrograde event that occurred during the initial stages of cooling, following peak metamorphism.

Overall, the large-scale geometry of D_1/D_2 structures are poorly understood and difficult to resolve (cf. Giles, 2000). The development of relic small-scale isoclinal F_2 folds and characteristic sillimanite fabrics (S_2) suggests that strain rates were high (op. cit.). However, the events appear to have had little influence on the geometry of the deposit, apart from the possible transposition of the siliceous footwall stringer zone into the plane of S_1/S_2. Although local-scale remobilisation of sulphides occurred during D_1/M_1-D_2/M_2, it appears that gross primary metal zonation features within the deposit remained intact.

A U-Pb_{zircon} age of ca. 1585 Ma for the crystallisation of the Core Amphibolite suggests that it was emplaced just prior to peak metamorphism (Giles, 2000). This age provides evidence for mafic melt generation during orogenesis. The anomalous Pb-Zn character of the Core Amphibolite and Pb isotope signature suggest that pre-existing Pb and Zn was assimilated during its emplacement. This interpretation is supported by the U-Pb_{zircon} age.

Ingress of M_2 fluids into the orebody was facilitated by D_2 dilational structures and zones of brecciation and shearing that formed in response to competency contrasts between rock types, such as the Fe-Mn silicate unit in the structural hanging wall and along the margins of the Core Amphibolite respectively. These structures provided the necessary plumbing systems for the circulation of the retrograde fluid through the deposit. It is likely that the high competency of the Core Amphibolite influenced the fold geometry and hence zones of dilatancy during D_2. Fluxing of the orebody by M_2 fluids caused widespread syn- to post-D_2, high temperature (~500°C) hedenbergite-quartz-garnet metasomatism (Stage IIa) of pre-existing Fe-Mn silicate ore. Brecciation and silicification of graphitic ore resulted in the formation of siliceous Pb-Zn-Ag ore, and further silicification of the footwall stringer zone forming siliceous Zn ore (Chapter 4). Subsequent lower temperature Stage IIb hornblende alteration and deposition of minor secondary sphalerite, pyrrhotite, chalcopyrite and arsenopyrite, occurred during the waning stages of metasomatic event (Chapter 4). Mass balance calculations indicate that the hypersaline fluid was capable of redistributing pre-existing metals via solution-associated remobilisation and possibly caused widespread modification of pre-existing ores (Chapter 6).

8.3.2 Stage 2

Stage 2 was characterised by focused shearing and macroscopic recumbent, isoclinal folding during D_3. It was during this period that movement along the Footwall Shear resulted in the formation of a thrust-propagation fold (the Cannington Synform; Fig. 8.2) during east vergent back-thrusting in a dominantly west vergent fold-thrust belt (Giles, 2000). D_3 had a significant effect on the geometry of the deposit, causing repetition of ore lenses and dilation (e.g. brecciation) in the hinge and pressure shadow zones adjacent to the eastern and western margins of the Core Amphibolite respectively. Movement along the Footwall Shear resulted in attenuation of the lower limb of the Cannington Synform and progressive truncation of ore lenses to the south.

Dilatant structures and breccia zones were subsequently fluxed by syn- to chiefly post-D_3 retrograde fluids that caused localised ferro-actinolite and minor ilvaite alteration (late Stage IIb) of pre-existing hedenbergite Zn ores, and associated deposition of secondary sphalerite, pyrrhotite, chalcopyrite, arsenopyrite and minor galena. The event was synchronous with post-D_3 static biotite recrystallisation and replacement of sillimanite by coarse grained muscovite in the host rocks, the relative timing of which was broadly coincident with a transient thermal perturbation (M_3, ca. 1510 Ma) related to the intrusion of the Williams Batholith (Chapter 4; Giles, 2000). Hence, retrogression at this time was related to the ingress of M_3 retrograde fluids. Minimum P-T conditions during M_3 were ~400°C and ~3kbars based on petrogenetic and textural evidence from host metasediments (Giles, 2000).

8.3.3 Stage 3

Stage 3 was characterised by D_4 upright, open folding that had a moderate effect on the geometry of the deposit (Fig. 8.3), and subsequent Stage IIc metasomatism during the waning stages of M_3 (Fig. 8.1). Stage IIc metasomatism had a profound effect on the deposit, and involved pervasive circulation of late-stage M_3 fluids through the orebody. The event caused widespread pyrosmalite-magnetite-sulphide-sulphosalt veining and associated pyrosmalite-secondary magnetite alteration. Fluid-flow appears to have been facilitated by pre-existing D_3 structures and fabrics that resulted in pervasive alteration of strongly sheared olivine-pyroxenoid ores adjacent to the Footwall shear. The event caused widespread solution-associated remobilisation of metals and Ag-upgrading, evidenced by the deposition of abundant late-stage galena, Ag-sulphosalts and antimonides in pyrosmalite-magnetite altered rocks.

8.3.4 Stage 4

D_5 was marked by a change to brittle deformation and is considered to have been related to locking up of the fold-thrust belt, with further strain accommodated by regional-scale wrench faulting. The event is associated with the development of early north-south trending faults that form the Brolga Fault Zone (D_{5a}) in the eastern area of the deposit (Fig. 8.3). Subsequent subvertical brittle faulting (D_{5b}) involved the development of a conjugate fault set, characterised

Stage 3: D_4 open, upright folding and Stage IIc metasomatism associated with pervasive circulation of late-stage M_3 retrograde fluids.

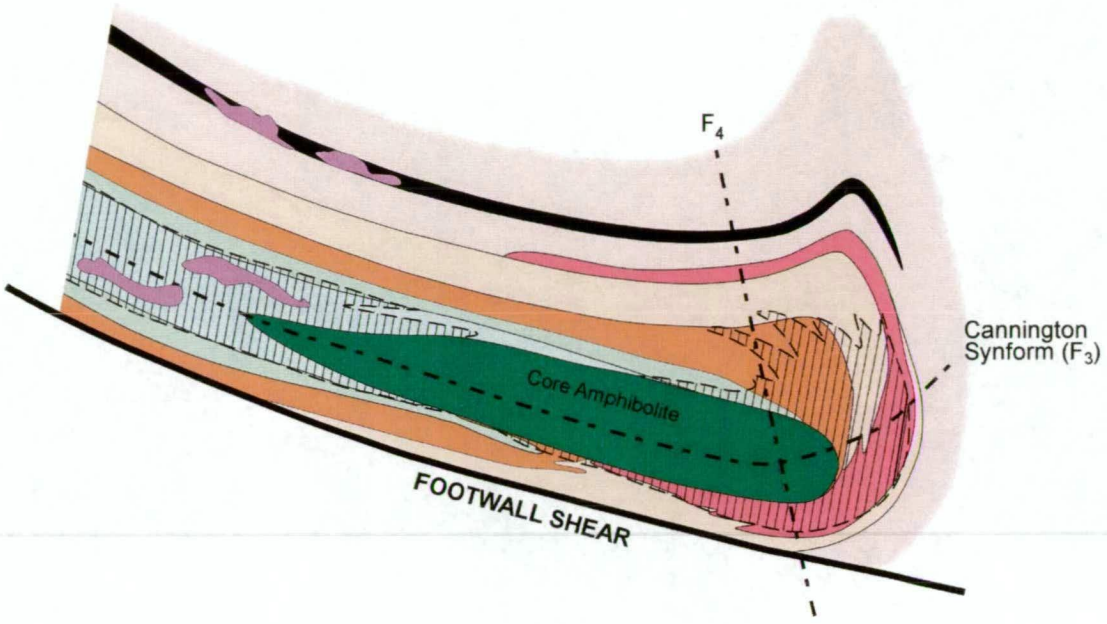

Stage 4: D_5 subvertical faulting and Stage III near-surface veining, brecciation and local hydrothermal alteration.

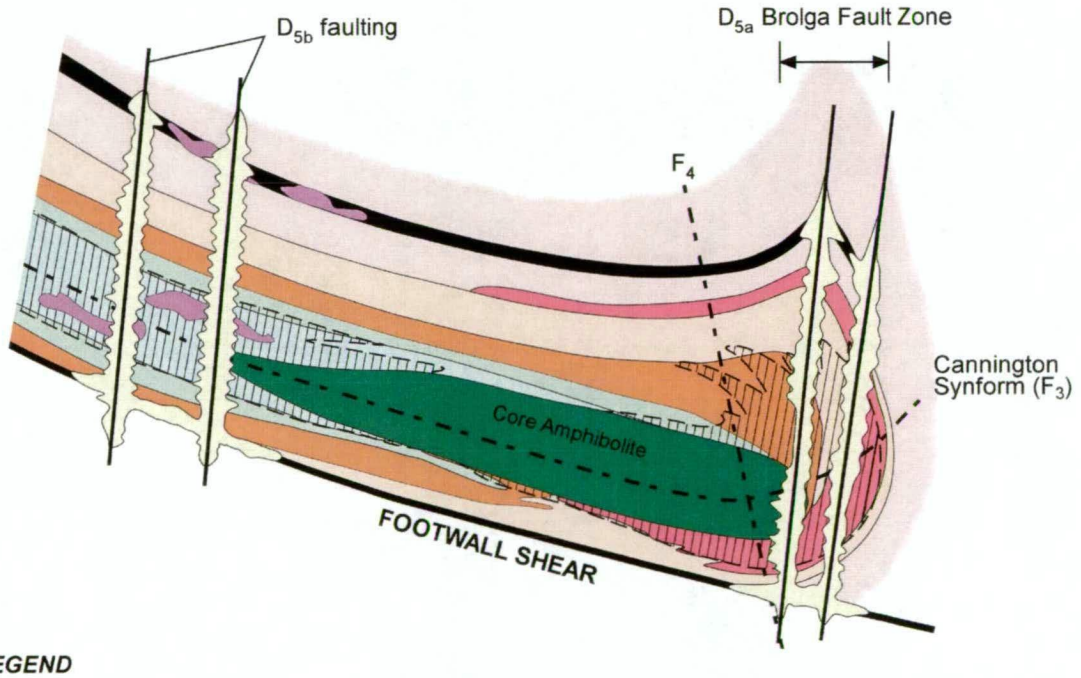

LEGEND

- Core Amphibolite
- Sillimanite-garnet schists and garnetiferous quartzites
- Silicified stringer zone (Siliceous Zn ore with quartz-gahnite-sphalerite veins)
- Hedenbergite ore (Zn)
- Olivine-pyroxenoid ore (Pb-Ag)
- Banded olivine-pyroxenoid ore (Pb-Ag)
- Fe-Mn silicate unit
- Graphitic ore (Pb-Zn-Ag)
- Stage IIa metasomatism (hedenbergite-garnet-quartz alteration, veining and breccias and tension gashes)
- Stage IIa intense silicification, quartz veining, brecciation and minor hedenbergite-garnet quartz veining
- Stage III quartz-carbonate-sulphide veining, chlorite-quartz-carbonate-pyrite/marcasite alteration

Figure 8.3 Stages 3 and 4 in the geodynamic evolution of the Cannington deposit from the beginning of the Isan Orogeny to the present day (modified after Bodon, 1998).

by the major northwest striking Trepell and Hamilton faults and smaller northeast striking faults, such as the FOY and Bustard faults. A near-surface, low temperature (marcasite stable) hydrothermal event (Stage III) was associated with D_5. Stage III is characterised by abundant vuggy, crustiform quartz-carbonate-sulphide veining and brecciation with adjacent quartz-chlorite-carbonate-pyrite/marcasite alteration selvedges. The event formed late carbonate-bearing Type II siliceous Pb-Zn-Ag ore within the D_{5a} Brolga Fault Zone. Solution-associated remobilisation of pre-existing metals and fluorine is evident from the occurrence of galena, sphalerite, Ag-sulphosalts and fluorite in Stage III veins. However, the Pb isotope evidence suggests that Stage III fluids introduced some Pb sourced from the metasediments. Overall, D_5 faulting had a minor effect on the geometry of the deposit.

8.4 ORE GENESIS

8.4.1 Hydrothermal fluid and metal sources

Hydrothermal fluids associated with the formation of BHT deposits are generally considered to have a predominantly mixed magmatic-seawater source with subsequent chemical modification by interaction with host rocks (Parr and Plimer, 1993). This is consistent with primitive signatures in lead, sulphur and strontium isotopes at Broken Hill. Abundant fluorine-, phosphorus-, calcium- and boron-bearing minerals is consistent with an ore-forming fluid with a metasomatised mantle signature rich in CO_2, F and B, that was tapped via major fractures associated with rifting (Plimer, 1985; Parr and Plimer, 1993). The advantage of this deep-seated fluid source model is its potential to produce large volumes of hydrothermal fluid, and explain the unusual geochemistry of the sulphide-bearing rocks at Broken Hill. Plimer (1985), Vaughan and Stanton (1986), Parr (1992) and Large et al. (1996) favour one sulphur source to explain the narrow spread in $\delta^{34}S$ from the Broken Hill, Pinnacles, and Pegmont deposits; either a direct magmatic parentage, or an inherited magmatic sulphur signature produced by leaching of underlying felsic volcaniclastic rocks. The latter notion is supported by Pb isotopes from the Pinnacles deposit (Parr, 1992, 1994). However, other workers suggest that $\delta^{34}S$ values indicate variable sulphur sources involving mixing of magmatic sulphur with biogenically (Both and Smith, 1975), or inorganically reduced seawater sulphate (Spry, 1987). In addition to these fluid sources, boron isotopes indicate that non-marine evaporites deeper in the stratigraphy may also have played a role in the fluid chemistry of some tourmaline-bearing horizons adjacent to the Broken Hill deposit, and that a possible evaporitic component contributed sulphur to the ore system itself (Slack et al., 1989).

At Cannington, the homogeneous Pb isotope signature of the ores is more primitive than the host rocks and granites of the region, requiring an exotic Pb source. The lack of evidence for a Pb mixing trend between the host rocks and ores suggests that the hydrothermal fluids did not leach significant Pb from the basin sediments during ascent to the depositional site. This is consistent with one or all of the following:

- rapid fluid advection during ascent, suggesting a deep-seated highly overpressured source reservoir;

- high fluid-rock ratios to maintain internal buffering; and
- high concentrations of aqueous Pb in order to counteract any potential contamination by Pb sourced from adjacent wallrocks during ascent to the depositional site.

To satisfy these aspects, the fluid pathway must have been strongly focussed and was therefore probably facilitated by a major basement piercing extensional structure capable of tapping exotic hydrothermal fluids from more primitive, deep-seated source rocks external to the basin.

Dong et al. (1997b) used a combination of fluid inclusion, $\delta^{18}O$ and δD isotopes, to advocate a magmatic-hydrothermal source for the ore-forming fluids at Cannington. However, their work was based on samples collected chiefly from dilational veins and breccia infills associated with Stage IIa metasomatic assemblages. Their results reflect characteristics of the syn- to post-D_2 metasomatic fluid, rather than the primary ore-forming fluids, and support the view that such fluids were possibly granite-derived.

8.4.2 BHT fluid compositions and depositional mechanisms – an overview

Very little is known about the compositions of hydrothermal fluids and the physicochemical processes involved in the formation of BHT deposits, mainly because primary depositional features and mineralogies have been extensively modified by metamorphism and deformation. The task is made even more difficult by the unusual geochemistry and mineralogies of the ores, and lack of primary (pre-metamorphic) fluid inclusions. The principal controls on base-metal transport in sedimentary brines are temperature, salinity, redox state, total sulphur concentrations and pH (Hanor, 1996; Cooke et al., 2000). By combining metal solubility behaviour and mineral equilibria, it is possible to overcome some of these difficulties, and constrain particular fluid parameters and depositional mechanisms.

Large and Davidson (1991) suggested that the fluid was hypersaline, but had low concentrations of ΣS, was reduced, and ranged between 150-250°C. These parameters were supported by Large et al. (1996), who used metal solubility data to argue that the lack of significant Cu in the ores, and relative abundance of Pb, Zn and Ag suggested deposition from a reduced ($\Sigma H_2S >> \Sigma SO_4^{2-}$), saline brine (~25wt% NaCl equiv.) <250°C, with chloride as the dominant metal ligand. Low ΣS was supported by the dominance of pyrrhotite over pyrite in the ores, with an inferred concentration of 0.001*m* in the fluid (Large et al., 1996). In fact, an order of magnitude lower concentration (~0.0001*m*) is not unreasonable, given that the majority of Fe is taken up in silicate phases rather than sulphides (D.Cooke, pers. comm., 2001). This is also true for Cannington, but in addition to silicates, a large proportion of the total Fe-budget is taken up in magnetite. Overall, the solubility data indicate that the total activity of metals in the hydrothermal fluid possibly far outweighed the total sulphur content, and that the concentration of dissolved metals in the fluid was high (e.g. up to 1000ppm Pb; Large et al., 1996).

Further constraints on fluid compositions and depositional mechanisms can be established from Fe and Mn solubility. The high content of Mn in BHT ore systems and associated hydrothermal alteration has been used as an indicator of redox and pH conditions in the hydrothermal fluid. Calculations conducted by Spry and Wonder (1989) on Fe and Mn solubility in hydrothermal fluids below 325°C, indicated that high solubilities are favoured by low pH and fO_2 fluids. It was proposed that garnet-rich altered rocks enveloping the Broken Hill deposit were produced by the mixing of reduced fluids with neutral, oxidised seawater (op. cit.). These results also reveal that fractionation of aqueous Fe and Mn is promoted by gradual pH increase, or gradual oxidation (Large et al., 1996). Hence, ores with high Mn/Fe ratios, typical of BHT deposits, are likely to have formed from slightly acid to neutral, reduced hydrothermal fluids that mixed with oxidised basin waters under conditions of increasing pH and oxidation (Large et al., 1996). Reduced acid fluids are consistent with the elevated Au grades at Broken Hill and Cannington, and contrast markedly with the comparatively low Au contents of sediment-hosted Pb-Zn deposits that are inferred to have formed from oxidised brines (Cooke et al., 2000).

Following this line of argument, Large et al. (1996) proposed that high Mn:Fe ratios in Pb-Ag-rich ores compared to Zn-rich ores at Cannington and Broken Hill, possibly indicated that hydrothermal fluid pulses varied in pH and oxidation state, with more reduced acidic pulses forming Zn-rich ore with low Mn:Fe ratios, and less reduced more, alkaline pulses, forming Pb-Ag-rich ore with high Mn:Fe ratios. Alternatively, this zonation may simply be due to the degree of mixing between the hydrothermal fluid and oxidised seawater, with Zn ores representing low mixing ratios proximal to hydrothermal feeders, and Pb-Ag ores representing high mixing ratios distal to fluid source sites (Large, et al., 1996). This model is supported by rare-earth element zonation patterns in exhalites proximal to the Broken Hill deposit, which exhibit reduced hydrothermal signatures, whereas distal exhalites display signatures indicative of major seawater input (Lottermoser, 1989). However, whilst this is correct for the distal environment, it may not necessarily reflect the processes that operated in the proximal ore-forming environment, as the REE zonation can also be caused by the cooling of the hydrothermal fluid. Unified cooling and increasing pH are considered to be the main depositional mechanisms in the ore-forming environment because it is these factors that fundamentally control Pb-Zn metal transport and deposition under static saline conditions.

Overall, the fluid parameters for BHT deposits (Large et al., 1996; Cooke et al., 1999 and 2000) are; 1) low ΣH_2S (~0.001 – 0.0001*m*); 2) high salinity (~15-25wt% equiv. NaCl); 3) temperatures <250°C; 4) pH ~4 to 5.5, 5) Σmetals >> ΣH_2S and 6) high ΣCO_2 (~1*m*). Depositional mechanisms appear to be principally controlled by increasing pH, decreasing temperature and increasing fO_2. Similar fluid compositions and depositional mechanisms are likely to have been responsible for ore formation at Cannington, based on mineralogical similarities and metal zonation features. However, it is possible to constrain the chemical parameters even further by determining possible primary hydrothermal mineral assemblages.

8.4.3 Primary mineral assemblages at Cannington

In order to constrain likely fluid compositions and depositional mechanisms, an indication of the likely precursor hydrothermal silicate gangue mineralogy is required. Stage I peak metamorphic silicate gangue minerals represent the end products of a series of prograde metamorphic devolatilisation reactions. However, lower temperature prograde assemblages have not been preserved in the ores. The principal elements controlling the composition of silicate phases at Cannington are solid-solutions between Fe, Mn and Ca, e.g. knebelite, hedenbergite, pyroxferroite, manganoan almandine, and manganoan grunerite. These minerals are notably Mg-depleted suggesting that the primary ore-forming fluid contained negligible Mg. Assuming that prograde metamorphism was isochemical, apart from the loss of volatiles, and accounting for the distinct lack of Mg in the ores, primary gangue mineral assemblages in the ores were likely to have been dominated by Fe-Mn-Ca carbonates (e.g. siderite, ankerite) Fe-rich chlorites (e.g. chamosite, greenalite) and quartz. During prograde metamorphism these minerals reacted to produce the characteristic silicate gangue mineral assemblages that characterise the ores at Cannington via devolatilisation reactions such as:

1. $FeCO_3 + SiO_2 \Leftrightarrow FeSiO_3 + CO_2(g)$
   siderite quartz pyroxferroite

2. $2FeCO_3 + SiO_2 \Leftrightarrow Fe_2SiO_4 + 2CO_2(g)$
   siderite quartz fayalite

3. $CaFe(CO_3)_2 + 2SiO_2 \Leftrightarrow CaFeSi_2O_6 + 2CO_2(g)$
   ankerite quartz hedenbergite

4a. $(Fe_{10}Al_2)(Si_6Al_2O_{20})(OH)_{16} + 2SiO_2 \Leftrightarrow 2Fe_3Al_2Si_3O_{12} + 2Fe_2SiO_4 + 8H_2O$
   chamosite quartz almandine fayalite

4b. $(Fe_{10}Al_2)(Si_6Al_2O_{20})(OH)_{16} + 4SiO_2 \Leftrightarrow 2Fe_3Al_2Si_3O_{12} + 4FeSiO_3 + 8H_2O$
   chamosite quartz almandine pyroxferroite

5. $Fe_6Si_4O_{10}(OH)_8 \Leftrightarrow 3Fe_2SiO_4 + SiO_2 + 4H_2O$
   greenalite fayalite quartz

6. $Fe_6Si_4O_{10}(OH)_8 + 2SiO_2 \Leftrightarrow 6FeSiO_3 + 4H_2O$
   greenalite quartz pyroxferroite

7. $Fe_6Si_4O_{10}(OH)_8 \Leftrightarrow 2FeSiO_3 + 2Fe_2SiO_4 + 4H_2O$
   greenalite pyroxferroite fayalite

On the basis of these reactions, it is possible to deduce the primary mineral assemblages for particular ore types (Table 8.1). The occurrence of mangano-siderite and pyrrhotite in all ore types (to some degree), coupled with solubility data for Pb and Zn places important constraints on the fluid chemistry and depositional mechanisms involved during ore formation. These aspects are the subject of the next section.

8.4.4 Metal transport and deposition

Figure 8.4 shows the stability of siderite-pyrrhotite-magnetite assemblage, and Pb and Zn solubilities calculated at 250°C and 10wt% equiv. NaCl. Pyrrhotite-siderite stability indicates

Table 8.1 Interpreted primary (pre-metamorphic) hydrothermal mineralogy of the principal ore types.

Ore type	Peak metamorphic gangue mineralogy	Primary hydrothermal mineralogy
Hedenbergite	Hedenbergite, calcic almandine, fluorite, magnetite, fluorapatite	Mangano-ankerite to siderite, chamosite, greenalite, magnetite, quartz, fluorite, fluorapatite
Olivine-pyroxenoid	Knebelite, pyroxferroite, magnetite, fluorite, fluorapatite, minor grunerite, rare calcite	Mangano-siderite, magnetite, greenalite, fluorite, fluorapatite, minor quartz
Graphitic	Quartz, hedenbergite, calcic to manganoan almandine, knebelite, pyroxferroite, fluorapatite, biotite, graphite, grunerite, hornblende, rare fluorite and calcite	Quartz, mangano-ankerite to siderite, chamosite, greenalite, fluorapatite, organic matter, rare fluorite,

that the fluid must have been reduced. In order to facilitate the transport of high concentrations of Pb and Zn as chloride complexes, the fluid must have had a pH of ~4.5. The composition of the hydrothermal fluid at Cannington therefore falls within the siderite-pyrrhotite field at position A (i.e. mildly acidic and reduced).

It is evident from Figure 8.4 that Pb-Zn solubilities are very sensitive to changes in pH, rather than the oxidation state of the fluid at the given conditions. For example, an increase in pH from position A to position B will result in Pb and Zn saturation in the hydrothermal fluid and precipitation of sphalerite and galena. A shift in oxidation state to position C while maintaining a constant pH will not result in Pb-Zn saturation and the deposition of sphalerite and galena.

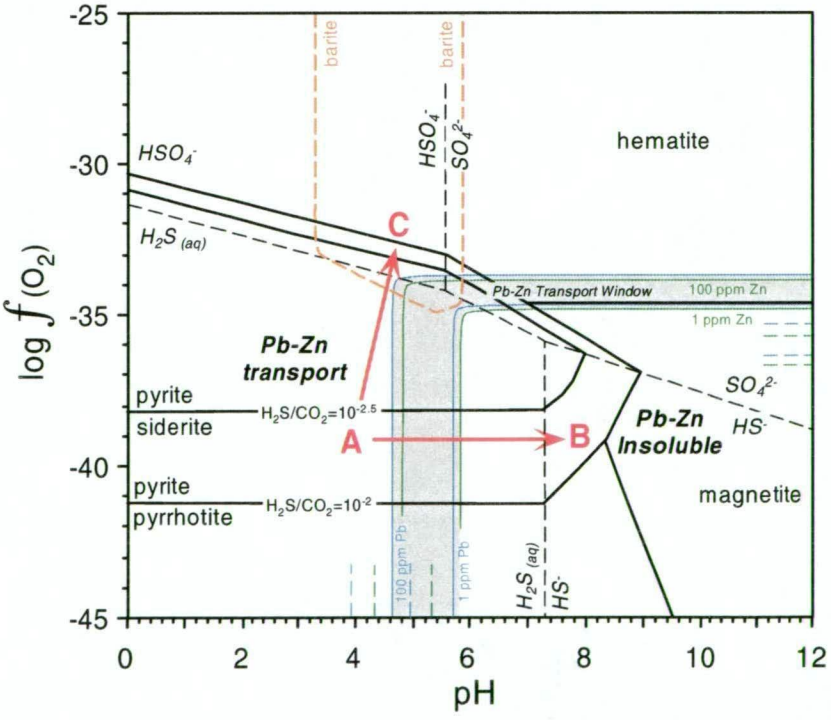

Figure 8.4 Log fO_2-pH diagram illustrating the predominance areas for the principal aqueous sulphur species and stabilities for minerals in the Fe-O-S-H system, as well as barite and siderite stability and Pb-Zn solubility contours (compiled after Cooke et al., 1998, 2000; Hannington et al., 1999). The shaded region represents the metal transport window for galena and sphalerite. The primary fluid composition is constrained by the interpreted precursor assemblage of siderite-pyrrhotite-magnetite (position A). Arrow A-B depicts the most efficient precipitation trajectory for sphalerite and galena deposition from a reduced, mildly acidic fluid under isothermal conditions. Arrow A-C indicates that isothermal oxidation of the fluid is an inefficient mechanism for the deposition of sphalerite and galena. The 'oxidized' trajectory reflects mineral reactions that are characteristic of distal chemogenic sediments, i.e. the precipitation of sulphates (e.g. barite, anhydrite), Fe-Mn oxides (e.g. hematite) and minor pyrite. The diagram is calculated for T=250°C, $\Sigma S=10^{-3}$m and ΣCO_2=1m (~4wt%).

Oxidation of a reduced fluid is therefore a poor mechanism for the deposition of Pb and Zn under isothermal conditions. A shift in oxidation state in this manner would result in the precipitation of oxidised assemblages such as barite and/or anhydrite and minor pyrite. Such assemblages are inconsistent with interpreted precursor mineral assemblages at Cannington. A decrease in temperature shifts the metal solubilities toward lower pH in the reduced, H_2S field. Cooling of the hydrothermal fluid is therefore also an effective mechanism for the precipitation of sphalerite and galena. Overall, Pb-Zn transport is favoured by mildly acid to acid conditions in reduced fluids (i.e. $H_2S > SO_4^{2-}$). The primary metal-bearing fluid at Cannington was therefore mildly acid and reduced. Mixing of this fluid-type with more neutral, cooler fluid would be the most efficient mechanism for the deposition of sphalerite and galena.

Metal zonation features at Cannington and other BHT deposits such as Broken Hill, are characterised by an inner Zn-As(-Cu) zone that grades outward to a Pb-Ag-Sb zone. This metal zonation can be explained by cooling of a reduced, acidic hydrothermal fluid. Solubilities of common base metal sulphides and argentite as a function of temperature are depicted in Figure 8.5. Cooling of a 250°C fluid with an a_{H_2S} and fO_2 fixed by the pyrite-pyrrhotite-magnetite buffer will initially deposit sphalerite and arsenopyrite upon cooling forming a proximal Zn-As zone. Galena and argentite will precipitate as cooling continues, forming a more distal Pb-Ag zone, whereas chalcopyrite saturation occurs at significantly higher temperatures than sphalerite and galena, and will therefore be deposited proximal to the fluid source. Cooling of the hydrothermal fluid at Cannington therefore, appears to be a particularly important depositional mechanism. From the preceding discussion, coincident cooling, increasing pH (and possible addition of H_2S?) are the most effective mechanisms for rapid

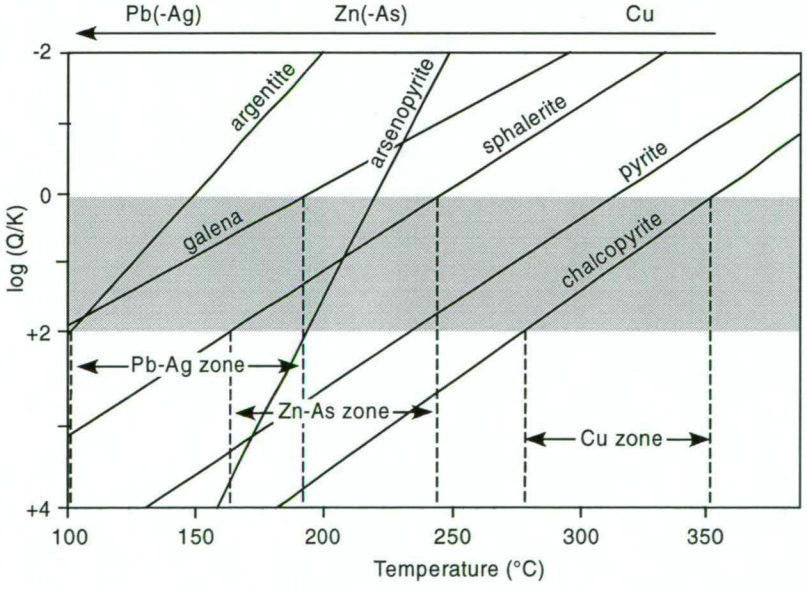

Figure 8.5 Calculated solubilities of common sulphide minerals and argentite as a function of temperature and $\log_{(Q/K)}$ (modified after Hannington et al., 1999). Solubilities are based on the assumption that metals are transported as chloride complexes in a fluid similar in composition to that of modern-day MOR vent fluids. The a_{H_2S} and fO_2 is fixed by the pyrite-pyrrhotite-magnetite buffer. Fluids are undersaturated when $\log_{(Q/K)}$ is <0 and are supersaturated at $\log_{(Q/K)}$ is >0. Mineral saturation occurs to the left of the solubility lines. The shaded region represents the most reasonable depositional temperatures based on the solubility data. The diagram indicates that cooling of the hydrothermal fluid could produce the characteristic Zn(-As) → Pb-Ag metal zonation at Cannington and other BHT deposits such as Broken Hill, Australia. Sphalerite, galena and argentite precipitate below 250°C, whereas chalcopyrite saturation occurs at significantly higher temperatures (>250°C).

metal deposition, and are capable of producing the observed metal zonation from an inner zone of hedenbergite Zn ore to an outer olivine-pyroxenoid Pb-Ag zone.

8.4.5 Ore formation – the brine pool model

The genetic model must be able to account for the previously described fluid composition and physicochemical controls on ore deposition. In particular, a synsedimentary reduced environment for ore deposition must be maintained within an otherwise oxidised basin. The other important factor that the model must account for is the absence of barite and anhydrite, which suggests that mixing with oxidised seawater did not occur. This is consistent with the lack of negative Ce anomalies in calculated hydrothermal REE signatures for graphitic ores and garnetiferous metasediments that comprise the metamorphosed alteration halo enveloping the deposit (section 6.7.4.3). The environment of ore deposition and the physicochemical processes involved in ore formation must have had the capacity to develop large (≥50Mt) deposits that consisted of at least in part, delicately banded, stratiform, metalliferous, chemogenic sediment that was not zoned laterally. Reduced, moderate temperature fluids (250-300°C) with low a_{H_2S}, such as proposed here for Cannington, must be highly saline (~10-25 wt% equiv. NaCl) in order to possess the capacity to transport significant concentrations of aqueous metals within geologically reasonable pH ranges (Large et al., 1996).

An exhalative seafloor environment must be invoked for the deposition of chemogenic sediment. However, ocean-floor discharge of a reduced high salinity fluid into seawater will result in a negatively buoyant hydrothermal plume, that will settle upon cooling into a dense "bottom-hugging" brine (Sato, 1972; McDougall, 1984; Sangster, 2002). The dense brine will eventually collect as a pool in a local topographic depression adjacent to, or even on top of, the discharge site (Sangster, 2002). The brine pool environment behaves as a closed system with regard to the external oxidised (seawater) environment (op. cit.). Its insulation from seawater is facilitated by the development of a transitional layer of intermediate salinity and oxidation state (Zierenberg, 1990; Sangster, 2002). In this way a reduced environment can be maintained in which finely banded sulphide-bearing chemogenic sediment can accumulate within an oxidised external environment.

An added advantage of a brine pool model is the capacity for the development of large base metal deposits and regionally extensive chemogenic horizons. The most appropriate modern day analogue is the Atlantis II Deep located in the Red Sea (Pottorf and Barnes, 1983; Zierenberg and Shanks, 1988; Zierenberg, 1990; Anschutz and Blanc, 1995; Anschutz et al., 2000). The Atlantis II Deep is one of 17 brine pools that occur along a ~300km linear belt within a medial intracontinental rift valley (Pottorf and Barnes, 1983). An estimated 200Mt of metalliferous sediment up to 30m thick has accumulated on the floor of the pool since its formation ~10,000 years ago. The dimensions of the pool are staggering (14km x 5km and up to 200m deep), holding some 5km^3 of brine. Two main hydrothermal fluid types are believed to be operating in the environment. The first is an oxidised, shallow-level high salinity,

moderate temperature (250°C) fluid that has leached metals from adjacent evaporate-bearing shales. The second is a hot (>300°C), high salinity reduced BHT-like fluid with low ΣS ($0.001m$) that is comparatively minor in volume and has been sourced from a deeper level hydrothermal system that has leached metals from a basalt-peridotite source. These fluids mix in the subsurface environment and the resultant hybrid fluid is expelled into the anoxic brine pool at a temperature of 200-250°C (op. cit.). The brine forms a buoyant plume that rises and cools depositing out sulphide particulate in addition to anhydrite, amorphous silica and smectite proximal to the discharge site. The plume rises to a less saline upper brine layer, representing a transitional dysoxic zone between the main brine pool and overlying seawater. During a pulse of fluid discharge, the plume migrates along this interface and interacts with the latter causing precipitation of Fe-Mn oxyhydroxides and mangano-siderite (Pottorf and Barnes, 1983; Zierenberg, 1990).

It is envisaged that Cannington formed by similar physicochemical brine pool dynamics, except that the ore-forming fluid was enriched in Pb, Ag, Fe, Mn, Ca, P and F. Given these inferences, it is now possible to integrate the pertinent findings of this study into a constrained genetic model. The proposed model is summarised in Figures 8.6 and 8.7.

8.4.5.1 Regional-scale perspective

Ore formation occurred during a period of intracontinental rifting ca. 1680-1650 Ma (Giles, 2000). It is possible that extension was caused by underplating in the lower to middle crust by mantle-derived mafic melts (MacCready et al., 1997, 1998). Alternatively, underplating may have been related to delamination of the lithosphere (MacCready et al., 1998). Deep-seated circulating hydrothermal fluids generated during partial melting related to underplating, scavenged metals from the mafic underplate (position 1, Fig. 8.6). A possible minor metal contribution was made by fluids that scavenged metals from the supracrustal metasediments in the adjacent hanging wall to the underplate (position 2, Fig. 8.6). Tapping of the hydrothermal source reservoir was facilitated by a major extensional fault that pierced the hot, metasomatised underplate (position 3, Fig. 8.6). Advection of fluid up this structure was rapid due to overpressuring of the source reservoir in the middle crust, with little wallrock interaction before being expelled into a topographic depression on the ocean floor (position 4, Fig. 8.6). Due to the high salinity of the fluid, it formed a dense, bottom-hugging brine pool that was thermally and chemically insulated from the overlying oxidised seawater (position 5, Fig. 8.6). The brine pool was possibly regionally extensive and was potentially one of several submarine brine "lakes" at the time. Metalliferous sediment slowly accumulated in an adiabatic environment on the floor of the pool (position 6, Fig. 8.6). Descending pelagic detrital material penetrated the pool and accumulated within the hydrothermal sediments (position 7, Fig. 8.6). The brine pool was essentially the surface manifestation of a larger hydrothermal system located in the middle crust.

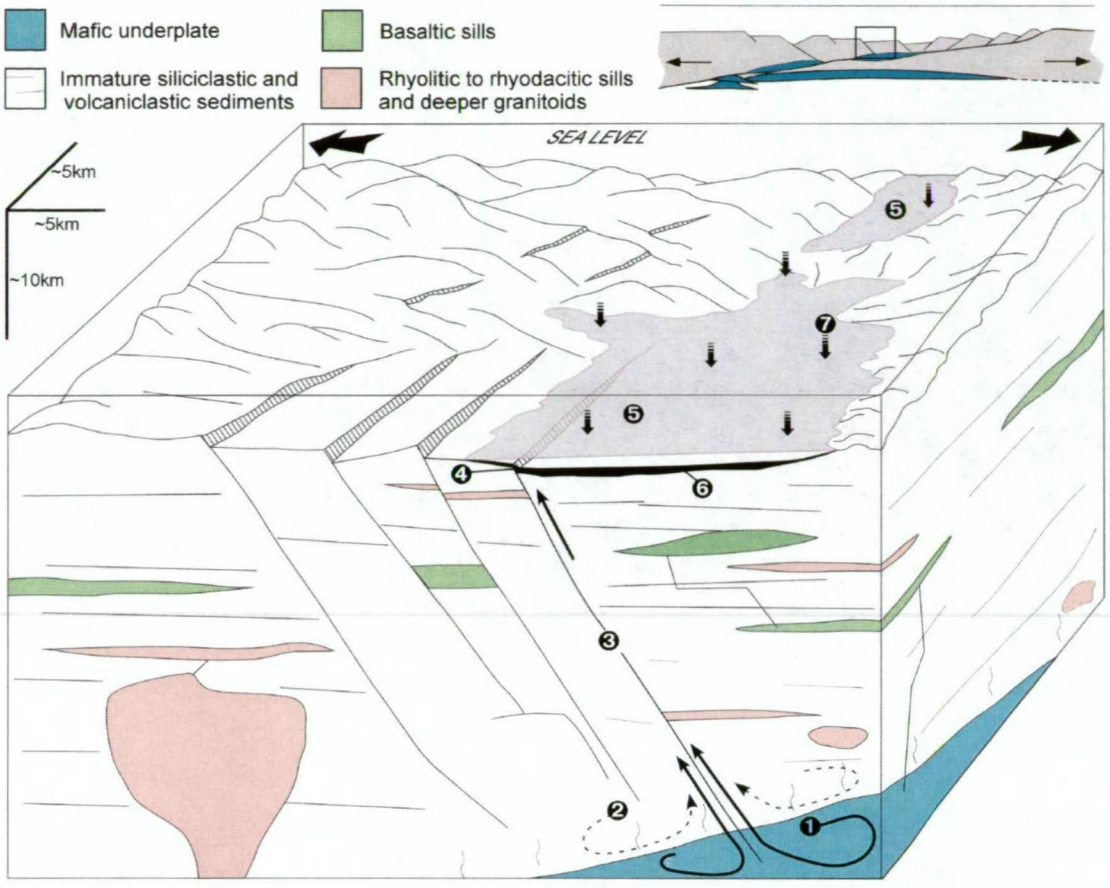

Figure 8.6 Block diagram illustrating the pertinent features of the proposed brine pool model for ore formation. The small inset shows the large-scale extensional environment and lower crustal mantle derived mafics that were emplacement along a crustal-scale detachment (MacCready et al., 1997, 1998).

8.4.5.2 Physicochemical dynamics of ore deposition

The principal zonation features and physicochemical dynamics of the brine pool model are illustrated in Figure 8.7. Reduced, mildly acid brine originating from a syn-extensional fault (position 1, Fig. 8.7) was discharged into seawater. The highly saline, negatively buoyant fluid ponded in a seafloor topographic depression that continued to fill with time, during a quiescent period of clastic sedimentation. Density stratification of the brine pool developed as the dynamics of the brine pool matured, forming an upper dysoxic and lower, more dense anoxic layer. Ambient deposition of chemogenic sediment on the floor of the brine pool (position 2, Fig. 8.7) was facilitated by simple cooling of the hydrothermal plume column and along the interface between the upper and lower brine layer (position 3, Fig. 8.7). Low total sulphur was a limiting factor in sulphide production resulting in the deposition of Fe monosulphide, magnetite, mangano-siderite, greenalite, amorphous silica, fluorapatite and minor fluorite. Turbulence (position 4, Fig. 8.7) driven by tectonic activity and pulses of hydrothermal discharge (position 5, Fig. 8.7) produced abrupt, short-lived disruptions in the chemical equilibrium resulting in the deposition of delicately layered metalliferous chemogenic sediment (position 2, Fig. 8.7). Variations in the detrital clastic input (position 6, Fig. 8.7) also contributed to the formation of banding. The availability of nutrients from the hydrothermal fluid possibly fostered enhanced biological activity at the brine interface, and over time, organic matter accumulated in the metalliferous muds.

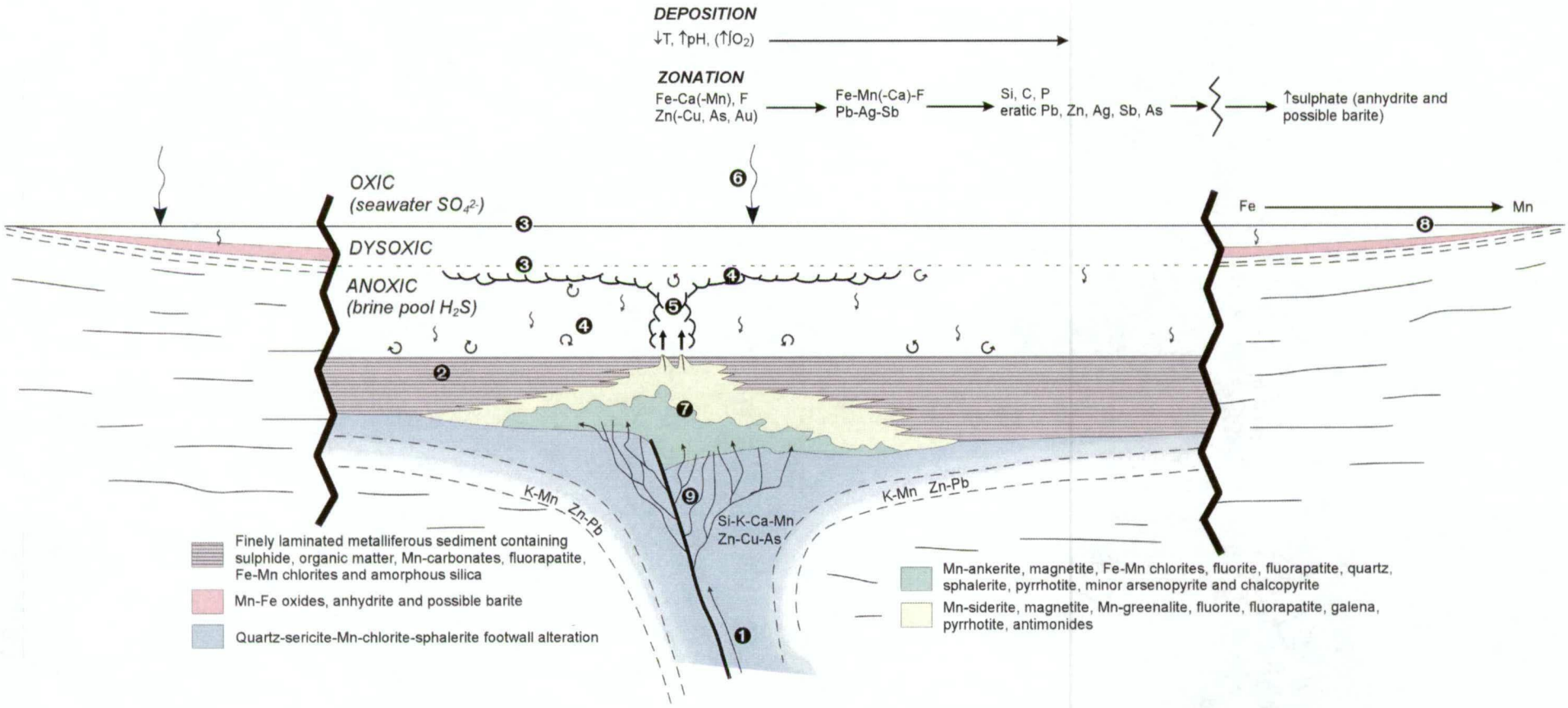

Figure 8.7 Schematic illustration depicting the principal zonation features and physicochemical dynamics of the brine pool model.

Hotter fluids channelled through the unconsolidated metalliferous sediment draped over the vent site, interacted with pre-existing precipitates resulting in veining, alteration, replacement and reworking of the proximal metalliferous sediment. Previously accumulated sediments were replaced by progressively higher temperature alteration assemblages proximal to the vent site as fluids migrated through the pile to the brine pool floor. A telescoped alteration system was established. This was possibly characterised by an outer Fe-Mn siderite-chlorite, magnetite, fluorite, Pb-Ag-Sb zone (i.e. olivine facies graphitic ore grading inward to olivine-pyroxenoid Pb-Ag ore protoliths), and an inner proximal, hotter Fe-Ca-Mn carbonate (ankerite to siderite), chamosite, greenalite, magnetite, fluorite, Zn-As(-Cu) zone (hedenbergite-Zn protoliths; position 7, Fig. 8.7).

At the same time, in the more distal, shallower, dysoxic perimeter of the brine pool, sediments comprising Fe and Mn oxyhydroxides, Mn-siderite and anhydrite were deposited (position 8, Fig. 8.7). Amorphous silica, phosphatic hydrothermal precipitates and organic matter were deposited throughout the pool. The footwall stringer zone was characterised by a stockwork of quartz-sphalerite(-chalcopyrite) veins and spatially associated quartz-sericite-Mn-chlorite altered siliciclastic sediments (position 9, Fig. 8.7).

At some stage after accumulation of metalliferous sediments and sub-surface replacement, tectonism closed the supply of hydrothermal fluid to the brine pool. Turbidity currents activated by this tectonism deposited immature siliciclastic sediments into the brine pool, effectively filling it. The unusual geochemistry of the brine pool may have imparted its hydrothermal signature into clastic sediments that accumulated within it, until such time that it was completely filled with sediment. Smaller brine-pools developed in the immediate hanging wall during short-lived quiescent periods in clastic sedimentation. Over time, the system waned and the rift basin evolved into a period of sag-phase sedimentation during which the remaining stratigraphy of the Maronan Supergroup was deposited. 70 Ma later, the deposit underwent polydeformation, high grade metamorphism, and retrograde metasomatism that spanned a ca. 120 Ma period of compressional tectonics related to the Isan Orogeny (section 8.3).

Chapter 9
References

Abramson, B. S., 1981, The mineralizing fluids responsible for skarn and ore formation at the Continental Mine, Fierro, New Mexico, in light of REE analyses and fluid inclusion studies: Unpublished Masters thesis, New Mexico Institute of Mining and Technology, 143 p.

Ahmad, R. and Wilson, C. J. L., 1982, Microstructural relationships of sillimanite and "fibrolite" at Broken Hill, Australia: Lithos, v. 15, p. 49-58.

Alcock, P., Camilleri, A., and Poole, J. R., 1973, Placer prospecting projects 72, 74 Fairmile final report, Queensland Department of Mines open file company report, p. 95.

Alderton, D. H. M., Pearce, J. A., and Potts, P. J., 1980, Rare earth element mobility during granite alteration: evidence from southeast England: Earth and Planetary Science Letters, v. 49, p. 149-165.

Alt, J. C., 1988, Hydrothermal oxide and nontronite deposits on seamounts in the eastern Pacific: Marine Geology, v. 81, p. 227-239.

AMOCO, 1976, 1975 Annual Report, Squirrel Hills Project: Queensland Department of Mines; Open File.

Andrews, E. C., 1922, Geology of the Broken Hill District: New South Wales Geological Survey, Memoir 8, 432 p.

Andrews, S. J., 1998, Stratigraphy and depositional setting of the upper McNamara Group, Lawn Hills region, northwest Queensland: Economic Geology, v. 93, p. 1450-1462.

Anschutz, P., and Blanc, G., 1995, Geochemical dynamics of the Atlantis II Deep (Red Sea); silica behavior: Marine Geology, v. 128, p. 25-36.

Anschutz, P., Blanc, G., Monnin, C., and Boulegue, J., 2000, Geochemical dynamics of the Atlantis II Deep (Red Sea); II, Composition of metalliferous sediment pore waters: Geochimica et Cosmochimica Acta, v. 64, p. 3995-4006.

Argast, S., and Donnelly, T. W., 1987, The chemical discrimination of clastic sedimentary components: Journal of Sedimentary Petrology, v. 57, p. 813-823.

Arneth, J. D., Schidlowski, M., Sarbas, B., Goerg, U., and Amstutz, G. C., 1985, Graphite content and isotopic fractionation between calcite-graphite pairs in metasediments from Mgama Hills, southern Kenya: Geochimica et Cosmochimica Acta, v. 49, p. 1553-1560.

Bailey, A., 1998, Cannington silver-lead-zinc deposit, *in* Berkman, D. A., and Mackenzie, D. H., eds., Geology of Australian and Papua New Guinean Mineral Deposits: Melbourne, Victoria, Australasian Institute of Mining and Metallurgy, p. 783-792.

Baker, J. H. and Hellingwerf, R. H., 1988, Rare earth element geochemistry of W-Mo-(Au) skarns and granites from western Berslagen, central Sweden: Mineralogy and Petrology, v. 39, p. 231-244.

Baker, T., 1996, Ore fluid chemistry and conditions at the Eloise Cu-Au deposit, NW Queensland: James Cook University, Economic Geology Research Unit, Contribution 55, p. 10-13.

Baker, T., 1998, Alteration, mineralization and fluid evolution at the Eloise Cu-Au deposit, Cloncurry district, northwest Queensland, Australia: Economic Geology, v. 93, p. 1213-1236.

Baker, T., and Laing, W. P., 1998, Eloise Cu-Au deposit, East Mt Isa Block - structural environment and structural controls on ore: Australian Journal of Earth Sciences, v. 45, p. 429-444.

Banks, D. A., Yardley, B. W. D., Campbell, A. R., and Jarvis, K. E., 1994, REE composition of an aqueous magmatic fluid: a fluid inclusion study from the Capitan pluton, New Mexico: Chemical Geology, v. 113, p. 259-272.

Barnes, R. G., Stroud, W. J., Brown, R. E., Willis, I. L. and Bradley, G. M., 1983, Zinc, manganese, and iron-rich rocks and various minor rock types: Geological Survey of New South Wales Records, v. 21, p. 289-323.

Barrett, T. J. and MacLean, W. H., 1991, Chemical, mass, and oxygen isotope changes during extreme hydrothermal alteration of an Archean Rhyolite, Noranda, Quebec: Economic Geology, v. 86, p. 406-414.

Barrett, T. J. and MacLean, W. H., 1994a, Mass changes in hydrothermal alteration zones associated with VMS Deposits of the Noranda Area: Exploration Mining Geology, v. 3, p. 131-160.

Barrett, T. J., and MacLean, W. H., 1994b, Chemostratigraphy and hydrothermal alteration in exploration for VHMS deposits in greenstones and younger volcanic rocks, *in* Lentz, D. R., ed., Alteration and Alteration Processes Associated with Ore-forming Systems: Geological Association of Canada Short Course Notes, 11, p. 433-465.

Bartley, J. M., 1986, Evaluation of REE mobility in low-grade metabasalts using mass-balance calculations: Norsk Geologisk Tidsskrift, v. 66, p. 145-152.

Bau, M., 1991, Rare-earth element mobility during hydrothermal and metamorphic fluid-rock interaction and the significance of the oxidation state of europium: Chemical Geology, v. 93, p. 219-230.

Beardsmore, T. J., 1992, Petrogenesis of Mount Dore-style breccia-hosted copper±gold mineralization in the Kuridala-Selwyn region of northwestern Queensland: Unpublished PhD thesis, James Cook University, Townsville, Queensland.

Beardsmore, T. J., Newbery, S. P., and Laing, W. P., 1988, The Maronan Supergroup: an inferred volcanosedimentary rift sequence in the Mount Isa Inlier, and it's implications for ensialic rifting in the Middle Proterozoic of northwest Queensland: Precambrian Research, v. 40-41, p. 487-507.

Beeson, R., 1990, Broken Hill-type lead-zinc deposits - An overview of their occurrence and geological setting: Institute of Mining and Metallurgy Transactions, Section B, v. 99, p. B163-B175.

Bence, A. E. and Taylor, B. E., 1985, Rare-earth element systematics of West Shasta metavolcanic rocks: petrogenesis and hydrothermal alteration: Economic Geology, v. 80, p. 2164-2176.

Berman, R. G., 1990, Mixing properties of Ca-Mg-Fe-Mn garnets: American Mineralogist, v. 75, p. 328-344.

Berman, R. G., and Koziol, A. M., 1991, Ternary excess properties of grossular-pyrope-almandine garnet and their influence in geothermobarometry: American Mineralogist, v. 76, p. 1223-1231.

Betts, P. G., 1999, Palaeoproterozoic mid-basin inversion in the northern Mt Isa terrane, Queensland: Australian Journal of Earth Sciences, v. 46, p. 735-748.

Betts, P. G., Aillères, L., and Lister, G. S., 1997a, Geological overview of the Mount Isa terrane, *in* Aillères, L., and Betts, P. G., eds., Structural Elements of the Eastern Successions - a field guide illustrating the structural geology of the eastern Mount Isa terrane, Australia, Australian Crustal Research Centre, Technical Publication 63, p. 1-16.

Betts, P. G., Aillères, L., O'Dea, M., and MacCready, T., 1997b, Poly-phase thrust-related deformation of the Mitakoodi Culmination: evidence along the eastern limb of the Duck Creek Anticline, *in* Aillères, L., and Betts, P. G., eds., Structural Elements of the Eastern Successions - a field guide illustrating the structural geology of the eastern Mount Isa terrane, Australia, Australian Crustal Research Centre, Technical Publication 63, p. 17-36.

Betts, P. G., Aillères, L., and Hough, M., 1997c, Structural elements in the hanging wall of the Overhang Shear: evidence from the Marimo-Staveley Block and the Kuridala region, *in* Aillères, L., and Betts, P. G., eds., Structural Elements of the Eastern Successions - a field guide illustrating the structural geology of the eastern Mount Isa terrane, Australia, Australian Crustal Research Centre, Technical Publication 63, p. 37-60.

Betts, P. G., Aillères, L., Giles, D., and Hough, M., 2000, Deformation history of the Hampden Synform in the Eastern Fold Belt of the Mt Isa terrane: Australian Journal of Earth Sciences, v. 47, p. 1113-1125.

Betts, P. G., and Lister, G. S., 2001, Comparison of the 'strike-slip' versus the 'episodic rift-sag' models for the origin of the Isa Superbasin: Australian Journal of Earth Sciences, v. 48, p. 265-280.

Betts, P. G., Lister, G. S., and O'Dea, M. G., 1998, Asymmetric extension of the Middle Proterozoic lithosphere, Mount Isa terrane, Queensland, Australia: Tectonophysics, v. 296, p. 293-316.

Betts, P. G., Lister, G. S., and Pound, K. S., 1999, Architecture of a Palaeoproterozoic rift system: evidence from the Fiery Creek Dome region, Mt Isa terrane: Australian Journal of Earth Sciences, v. 46, p. 533-554.

Bierlein, F. P., 1995, Rare-earth element geochemistry of clastic and chemical metasedimentary rocks associated with hydrothermal sulphide mineralisation in the Olary Block, South Australia: Chemical Geology, v. 122, p. 77-98.

Billington, L. G., 1976, Geochemistry and origin of garnet-rich rocks around the lead-lode, N.B.H.C. mine, Broken Hill, N.S.W.: Unpublished MSc thesis, University of New South Wales.

Bingen, B., Demaiffe, D., and Hertogen, J., 1996, Redistribution of rare earth elements, thorium, uranium over accessory minerals in the course of amphibolite to granulite facies metamorphism: The role of apatite and monazite in orthogneisses from southwestern Norway: Geochimica et Cosmochimica Acta, v. 60, p. 1341-1354.

Birch, W. D., 1983, Summary of mineral data: *in* Worner, H. K. and Mitchell, R. W., eds., Minerals of Broken Hill, Australian Mining and Smelting Limited, Griffin Press, Australia, p. 196-222.

Birch, W. D., Chapman, A., and Pecover, S. R., 1983, The minerals, *in* Worner, H. K., and Mitchell, R. W., eds., Minerals of Broken Hill, Australian Mining and Smelting Limited, Griffin Press Ltd., Australia, p. 68-195.

Black, L. P., and Withnall, I. W., 1993, The ages of Proterozoic granites in the Georgetown Inlier of northeastern Australia, and their relevance to the dating of tectonothermal events: Australian Geological Survey Organisation, Journal of Australian Geology and Geophysics, v. 14, p. 331-341.

Black, L. P., Gregory, P., Withnall, I. W., and Bain, J. H. C., 1998, U-Pb zircon age for the Etheridge Group, Georgetown region, north Queensland: implications for relationship with the Broken Hill and Mt Isa sequences: Australian Journal of Earth Sciences, v. 45, p. 925-935.

Blake, D. H., 1982, A review of the Corella Formation, Mount Isa Inlier: Bureau of Mineral Resources Journal of Australian Geology and Geophysics, v. 7, p. 113-118.

Blake, D. H., 1987, Geology of the Mount Isa Inlier and environs, Queensland and Northern Territory: Bureau of Mineral Resources Bulletin 225, 83 p.

Blake, D. H., and Page, R. W., 1988, Early Proterozoic migmatitic basement in the Kalkadoon-Leichhardt Belt of the Mount Isa Inlier, northwestern Queensland: Bureau of Mineral Resources, Journal of Australian Geology and Geophysics, v. 10, p. 323-328.

Blake, D. H., and Stewart, A. J., 1992, Stratigraphic and tectonic framework, Mount Isa Inlier, *in* Stewart, A. J. and Blake, D. H., eds., Detailed Studies of the Mount Isa Inlier, Bureau of Mineral Resources Bulletin 243, p. 1-11.

Blake, D. H., Etheridge, M. A., Page, R. W., Stewart, A. J., Williams, P. R., and Wyborn, L. A. I., 1990, Mount Isa Inlier - regional geology and mineralisation, *in* Hughes, F. E., ed., Geology of the Mineral Deposits of Australia and Papua New Guinea, Australasian Institute of Mining and Metallurgy, Monograph 14, p. 915-925.

Blake, D. H., Jaques, A. L., and Donchak, P. J. T., 1983, Geology of the Selwyn region: 1:100,000 geological map commentary: Bureau of Mineral Resources, Canberra, Australia.

Blattner, P., and Lassey, K. R., 1989, Stable-isotope exchange fronts, Damköhler numbers, and fluid to rock ratios: Chemical Geology, v. 78, p. 381-392.

Blattner, P., and Lassey, K. R., 1992, The natural evolution of geothermal systems in light of infiltration fronts and a look back at fluid-to-rock ratios, *in* Kharaka, Y. K., and Maest, A. S., eds., Proceedings of the 7th International Symposium on Water-rock Interaction, Volume 2, Moderate and High Temperature Environments: Edmonton, AB, Canada, International Association of Geochemistry and Cosmochemistry and Alberta Research Council, p. 1039-1042.

Blundy, J. D., and Wood, B. J., 1991, Crystal-chemical controls on the partitioning of Sr and Ba between plagioclase feldspar, silicate melts, and hydrothermal solutions: Geochimica et Cosmochimica Acta, v. 55, p. 193-209.

Bodon, S. B., 1994, Annual PhD report on the Cannington Ag-Pb-Zn deposit, Mt. Isa Inlier, Northwest Queensland, Unpublished report, Centre for Ore Deposit and Exploration Studies, University of Tasmania, p. 48.

Bodon, S. B., 1995, Annual PhD report on the Cannington Ag-Pb-Zn deposit, Mt. Isa Inlier, Northwest Queensland, Unpublished report, Centre for Ore Deposit and Exploration Studies, University of Tasmania, p. 48.

Bodon, S. B., 1996a, Paragenetic relationships at the Cannington Ag-Pb-Zn deposit, Mount Isa Inlier, northwest Queensland: James Cook University, Economic Geology Research Unit, Contribution 55, p. 15-19.

Bodon, S. B., 1996b, Genetic implications of the paragenesis and rare-earth element geochemistry at the Cannington Ag-Pb-Zn deposit, Mt. Isa Inlier, northwest Queensland, *in* Pongratz, J., and Davidson, G., eds., New Developments in Broken Hill Type Deposits, University of Tasmania, Centre for Ore Deposit and Exploration Studies, Special Publication No. 1, p. 133-144.

Bodon, S. B., 1998, Paragenetic relationships and their implications for ore genesis at the Cannington Ag-Pb-Zn deposit, Mount Isa Inlier, Queensland, Australia: Economic Geology, v. 93, p. 1463-1488.

Bodon, S. B., and Valenta, R. K., 1995, Primary and tectonic features of the Currawong Zn-Cu-Pb(-Au) massive sulfide deposit, Benambra, Victoria - implications for ore genesis: Economic Geology, v. 90, p. 1694-1721.

Bonijoly, M., Oberlin, M. and Oberlin, A., 1982, A possible mechanism for natural graphite formation: International Journal of Coal Geology, v. 1, p. 283-312.

Both, R.A. and Smith, J.W., 1975, A sulfur isotope study of base-metal mineralization in the Willyama Complex, western New South Wales: Economic Geology, v. 70, p. 308-318.

Bottinga, Y., 1969, Calculated fractionation factors for carbon and hydrogen isotope exchange in the system calcite-carbon dioxide-graphite-methane-hydrogen-water vapor: Geochimica et Cosmochimica Acta, v. 33, p. 49-64.

Brett, R., and Kullerud, G., 1967, The Fe-Pb-S system: Economic Geology, v. 62, p. 354-369.

Brown, P. E., Essene, E. J., and Peacor, D. R., 1980, Phase relations inferred from field data for Mn pyroxenes and pyroxenoids: Contributions Mineralogy and Petrology, v. 74, p. 417-425.

Burton, K. W., 1986, Garnet-quartz intergrowths in graphitic pelites: the role of the fluid phase: Mineralogical Magazine, v. 50, p. 611-620.

Burton, K. W., and O'Nions, R. K., 1991, High-resolution garnet chronometry and the rates of metamorphic processes: Earth and Planetary Science Letters, v. 107, p. 649-671.

Calvez, J. Y., Cochiere, A., and Oudin, E., 1988, Sr-Nd isotopes and REE signatures of the hydrothermal activity in the Red Sea: Chemical Geology, v. 70, p. 133.

Campbell, I. H., Lesher, C. M., Coad, P., Franklin, J. M., Gorton, M. P. and Thurston, P. C., 1984, Rare-earth element mobility in alteration pipes below massive Cu-Zn-sulfide deposits: Chemical Geology, v. 45, p. 181-202.

Carr, G. R., and Gulson, B. L., 1984, Multiple lead sources in the stratiform Lady Loretta Zn-Pb-Ag deposit, northwest Queensland: Abstracts, 7th Australian Geological Convention, Geological Society of Australia, v. 12, p. 90-92.

Carr, G. R., and Sun, S.-s., 1996, Lead isotope models applied to Broken Hill style terrains - syngenetic vs. epigenetic metallogenesis, *in* Pongratz, J., and Davidson, G., eds., New Developments in Broken Hill Type Deposits, University of Tasmania, Centre for Ore Deposit and Exploration Studies, Special Publication No. 1, p. 77-87.

Carr, G. R., and Whitford, D. J., 1997, The role of the mantle in large scale hydrothermal processes - evidence from radiogenic isotope systems: 3rd National Conference of the Specialist Group in Economic Geology, Geological Society of Australia, Abstracts no. 44, p. 19.

Carr, G. R., Dean, J. A., Suppel, D. W., and Heithersay, P. S., 1995, Precise lead isotope fingerprinting of hydrothermal activity associated with Ordovician to Carboniferous metallogenic events in the Lachlan fold belt of New South Wales: Economic Geology, v. 90, p. 1467-1505.

Carter, E. K., Brooks, J. H., and Walker, K. R., 1961, The Precambrian Mineral Belt of northwestern Queensland: Bureau of Mineral Resources Bulletin 51, p. 344 p.

Chapman, L. H., 1993, The nature and origin of pyroxene-pyroxenoid-garnet alteration, Cannington Ag-Pb-Zn deposit, Cloncurry District, Mt. Isa Inlier, NW Queensland: Unpublished Honours thesis, James Cook University, Townsville, 94 p.

Chapman, L. H., and Williams, P. J., 1998, Evolution of pyroxene-pyroxenoid-garnet alteration at the Cannington Ag-Pb-Zn deposit, Cloncurry District, Queensland, Australia: Economic Geology, v. 93, p. 1390-1405.

Chappell, B. W., and Stephens, W. E., 1988, Origin of infracrustal (I-type) granite magmas: Transactions of the Royal Society of Edinburgh, Earth Sciences, v. 79, p. 71-86.

Chatterjee, N. D., and Johannes, W., 1974, Thermal stability and standard thermodynamic properties of synthetic2M_1-muscovite $KAl_2(AlSi_3O_{10}(OH)_2)$: Contributions Mineralogy and Petrology, v. 48, p. 89-114.

Connolly, J. A. D., 1995, Phase diagram methods for graphitic rocks and application to the system C-O-H-FeO-TiO_2-SiO_2: Contributions to Mineralogy and Petrology, v. 119, p. 94-116.

Connors, K. A., and Page, R. W., 1995, Relationships between magmatism, metamorphism and deformation in the western Mount Isa Inlier, Australia: Precambrian Research, v. 71, p. 131-153.

Cooke, D. R., and Large, R. R., 1996, Manganese transport in sedimentary brines - chemical controls on McArthur-type and Broken Hill-type sediment-hosted Pb-Zn deposits: Centre for Deposit Research, University of Tasmania, AMIRA/ARC P384A, 1996 Annual report, p. 33-40.

Cooke, D. J.; Bodon, S. B., and Bull, S. W., 1998, Element associations and depositional processes for McArthur-type and Selwyn-type sediment-hosted Pb-Zn deposits: AMIRA P384A Final Report, Centre for Ore Deposit Research, v. 2, p. 145-182.

Cooke, D. R., Bull, S. W., Large, R. R., and McGoldrick, P. J., 2000, The importance of oxidized brines for the formation of Australian Proterozoic stratiform sediment-hosted Pb-Zn (sedex) deposits: Economic Geology, v. 95, p. 1-17.

Cooke, D. R., Large, R. R., Bull, S. W., and McGoldrick, P. J., 1999, Brine chemistry and the spectrum of stratiform sediment-hosted Pb-Zn deposits, *in* Stanley, C. J., ed., Mineral Deposits: Processes to Processing: London, Proceeding of the 5th biennial SGA meeting, p. 829-832.

Cooper, J. A., Dasch, E. J., and Kaye, M., 1974, Isotopic and elemental geochemistry of Black Sea sediments, in The Black Sea: Geology, Chemistry, and Biology; Geochemistry: American Association of Petroleum Geologists, Memoir 20, p. 554-565.

Cooper, J. A., Reynolds, P. H., and Richards, J. R., 1969, Double-spike calibration of the Broken Hill standard lead: Earth and Planetary Science Letters, v. 6, p. 467-478.

Costa, M. D., Barrett, T. J. and Kerrich, R., 1983, The Mattagami Lake Mine Archean Zn-Cu sulfide deposit, Quebec: hydrothermal coprecipitation of talc and sulfides in a sea-floor brine pool - evidence from geochemistry, $^{18}O/^{16}O$, and mineral chemistry: Economic Geology, v. 78, p. 1144-1203.

Courtois, C., and Treuil, M., 1977, Distribution des terres rares et de quelques éléments en trace dans les sédiments récents des fosses de la mer rouge: Chemical Geology, v. 20, p. 57-72.

Craig, J. R., and Vaughan, D. J., 1981, Ore microscopy and ore petrography: New York, Wiley, 406 p.

Cumming, G. L., and Richards, J. R., 1975, Ore lead isotope ratios in a continuously changing Earth: Earth and Planetary Science Letters, v. 28, p. 155-171.

de Jong, G., and Williams, P. J., 1995, Giant metasomatic system formed during exhumation of mid-crustal Proterozoic rocks in the vicinity of the Cloncurry Fault, northwest Queensland: Australian Journal of Earth Sciences, v. 42, p. 281-290.

de Jong, G., Rotherham, J., Phillips, G. N., and Williams, P. J., 1998, Mobility of rare-earth elements and copper during shear-zone-related retrograde metamorphism: Geologie en Mijnbouw, v. 76, p. 311-319.

Deer, W. A., Howie, R. A. and Zussman, J., 1992, An introduction to the rock-forming minerals: London, Longman.

Derrick, G. M., 1980, Marabba, Queensland: 1:100,000 geological map commentary: Bureau of Mineral Resources, Canberra, Australia, 33 p.

Derrick, G. M., 1982, A Proterozoic rift zone at Mount Isa, Queensland, and implications for mineralisation: Bureau of Mineral Resources, Journal of Australian Geology and Geophysics, v. 7, p. 81-92.

Derrick, G. M., 1993, Mt. Isa Inlier Field Course: Geological Development and Exploration Strategies: Australian Mineral Foundation, Excursion Guide, Course 832/93, p. 206.

Derrick, G. M., Wilson, I. H., and Hill, R. M., 1976, Revision of stratigraphic nomenclature in the Precambrian of northwestern Queensland. V: Soldiers Cap Group: Queensland Government Mining Journal, v. 77, p. 600-604.

Derrick, G. M., Wilson, I. H., and Hill, R. M., 1977, Revision of stratigraphic nomenclature in the Precambrian of northwestern Queensland. VI: Mary Kathleen Group: Queensland Government Mining Journal, v. 78, p. 15-23.

Dickinson, W. R., 1985, Interpreting provenance relations from detrital modes of sandstones, *in* Zuffa, G. G., ed., Provenance of Arenites: Dordrecht-Boston, International, Reidel Publishing Company, p. 333-361.

Doe, B. R., 1978, The application of lead isotopes to mineral prospect evaluation of Cretaceous-Tertiary magmatothermal ore deposits in the western United States: Proceedings, 7th International Geochemical Exploration Symposium, Golden, Colorado, p. 227-232.

Doe, B. R., and Delevaux, M. H., 1972, Source of lead in southeast Missouri galena ores: Economic Geology, v. 67, p. 409-425.

Doe, B. R., and Zartman, R. E., 1979, Plumbotectonics, the Phanerozoic, *in* Barnes, H. L., ed., Geochemistry of hydrothermal ore deposits: New York, U.S.A, John Wiley & Sons, p. 22-70.

Doe, B. R., Steven, T. A., Delevaux, M. H., Stacey, J. S., Lipman, P. W., and Fisher, F. S., 1979, Genesis of ore deposits in the San Juan volcanic field, southwestern Colorado - lead isotope evidence: Economic Geology, v. 74, p. 1-26.

Donchak, P. J. T., Blake, D. H., Noon, T. A., and Jaques, A. L., 1983, Kuridala region, Queensland: 1:100,000 map commentary: Bureau of Mineral Resources, Canberra, Australia, 32 p.

Dong, G., and Pollard, P. J., 1997, Identification of ferropyrosmalite by laser Raman microprobe in fluid inclusions from metalliferous deposits in the Cloncurry District, NW Queensland, Australia: Mineralogical Magazine, v. 61, p. 291-293.

Dong, G., Ryan, C. G., Pollard, P. J. and Williams, P. J., 1997a, PIXE microanalysis of hypersaline fluid inclusions from Cloncurry ore systems: James Cook University, Economic Geology Research Unit Newsletter, September issue, p. 7-9.

Dong, G., Blake, K. L. and Pollard, P. J., 1997b, The Cannington Ag-Pb-Zn deposit, Cloncurry district, northwest Queensland: fluid inclusion and stable isotope evidence for a magmatic-hydrothermal fluid source: Economic Geology Research Unit, James Cook University, AMIRA P438 Final Report; v. 2, p. 12-1 - 12-37.

Drummond, B. J., Goleby, B. R., Goncharov, A. G., Wyborn, L. A. I., Collins, C. D. N., and MacCready, T., 1998, Crustal-scale structures in the Proterozoic Mount Isa Inlier of north Australia: their seismic response and influence on mineralisation: Tectonophysics, v. 288, p. 43-56.

Dugmore, M. A., 1998, Silver mineralisation in the Footwall Lead Lode, Cannington Ag-Pb-Zn deposit, Queensland: unpublished MSc thesis, James Cook University, 138 p.

Dzevanshir, R. D., Buryakovskiy, L. A., and Chilingarian, G. V., 1986, Simple quantitative evaluation of porosity of argillaceous sediments at various depths of burial: Sedimentary Geology, v. 46, p. 169-175.

Elliot, S. M., 1979, Geochemistry of the rocks enclosing Broken Hill type deposits in the Broken Hill Block, Australia: Unpublished PhD thesis, University of New South Wales.

Elliot-Meadows, S. R. and Appleyard, E. C., 1991, The alteration geochemistry and petrology of the Lar Cu-Zn deposit, Lynn Lake area, Manitoba: Economic Geology; v. 86, p. 486-505.

Ellis, D. J., 1980, Osumilite-sapphirine-quartz granulites from Enderby Land, Antarctica; P-T conditions of metamorphism, implications form garnet-cordierite equilibria and the evolution of the deep crust: Contributions to Mineralogy and Petrology; v. 74, p. 201-210.

Essene, E. J., 1982, Geologic thermometry and barometry, *in* Ferry John, M., ed., Characterization of metamorphism through mineral equilibria, 10. Reviews in Mineralogy: Washington, DC, United States, Mineralogical Society of America, p. 153-206.

Essene, E. J., 1989, The current status of thermobarometry in metamorphic rocks, *in* Daly, J. S., Cliff, R. A., and Yardley, B. W. D., eds., Evolution of metamorphic belts; proceedings of the 1987 joint meeting of the Metamorphic Studies Group and IGCP project 235., 43. Geological Society Special Publications: London, United Kingdom, Geological Society of London, p. 1-44.

Etheridge, M. A., Rutland, R. W. R., and Wyborn, L. A. I., 1987, Orogenesis and tectonic process in the early to middle Proterozoic of northern Australia, *in* Kroener, A., ed., Proterozoic lithospheric evolution, American Geophysical Union, 17, p. 131-147.

Etheridge, M., and Wall, V. J., 1994, Tectonic and structural evolution of the Australian Proterozoic, *in* Freeman, M. J., ed., Geoscience Australia; 1994 and beyond, Geological Society of Australia Abstracts 37, p. 102-103.

Farmer, G. L., and De Paolo, D. J., 1997, Sources of hydrothermal components - heavy isotopes, *in* Barnes, H. L., ed., Geochemistry of hydrothermal ore deposits: New York, U.S.A., John Wiley & Sons, p. 31-61.

Fehn, U., Doe, B. R., and Delevaux, M. H., 1983, The distribution of lead isotopes and the origin of Kuroko ore deposits in the Hokuroku District, Japan: Economic Geology, Monograph 5, p. 488-506.

Ferry, J. M., and Spear, F. S., 1978, Experimental calibration of the partitioning of Fe and Mg between biotite and garnet: Contributions to Mineralogy and Petrology, v. 66, p. 113-117.

Finlow-Bates, T. and Stumpfl, E. F., 1981, The behaviour of so-called immobile elements in hydrothermally altered rocks associated with volcanogenic submarine-exhalative ore deposits: Mineralium Deposita, v. 16, p. 319-328.

Floyd, P. A. and Winchester, J. A., 1978, Identification of altered and metamorphosed volcanic rocks using immobile elements: Earth and Planetary Science Letters; v. 27, p. 211-218.

French, D., Ramsden, A. R., and Walters, S. G., 1994, Mineralogical characterisation of the southern portion (line 4800N) of the Cannington lead-zinc-silver deposit, Queensland: CSIRO Division of Exploration and Mining, Restricted Investigation Report for BHP Minerals 253R, p. 117.

Frost, B. R., and Tracy, R. J., 1991, P-T paths from zoned garnets; some minimum criteria: American Journal of Science, v. 291, p. 917-939.

Ganguly, J., and Saxena, S. K., 1984, Mixing properties of aluminosilicate garnets; constraints from natural and experimental data, and applications to geothermo-barometry: American Mineralogist, v. 69, p. 88-97.

Garcia, D., Coelho, J., and Perrin, M., 1991, Fractionation between TiO_2 and Zr as a measure of sorting within shale and sandstone series (northern Portugal): European Journal of Mineralogy, v. 3, p. 401-414.

Garcia, D., Fonteilles, M., and Moutte, J., 1994, Sedimentary fractionations between Al, Ti, and Zr and the genesis of strongly peraluminous granites: Journal of Geology, v. 102, p. 411-422.

German, C. R., Klinkhammer, G. P., Edmond, J. M., Mitra, A., and Elderfield, H., 1990, Hydrothermal scavenging of rare-earth elements in the ocean: Nature, v. 345, p. 516-518.

Giles, D., 2000, Tectonic setting of Broken Hill-type mineralisation: the Cannington perspective: Unpublished PhD thesis, Monash University, Melbourne, Victoria.

Giles, D., and MacCready, T., 1997, The structural and stratigraphic position of the Soldiers Cap Group in the Mount Isa Inlier, *in* Aillères, L., and Betts, P. G., eds., Structural Elements of the Eastern Successions - a field guide illustrating the structural geology of the eastern Mount Isa terrane, Australia, Australian Crustal Research Centre, Technical Publication 63, p. 61-73.

Gilligan, L. B., and Marshall, B., 1987, Textural evidence for remobilization in metamorphic environments: Ore Geology Reviews, v. 2, p. 205-229.

Glikson, A. Y., and Derrick, G. M., 1970, The Proterozoic metamorphic rocks of the Cloncurry 1:100,000 sheet area, (Soldiers Cap Belt) northwestern Queensland: Bureau of Mineral Resources, Australia.

Godwin, C. I., Gabites, J. E., and Andrew, A., 1988, Lead table: a galena lead isotope data base for the Canadian Cordillera, with a guide to its use by explorationists: British Columbia, Ministry of Energy, Mines and Petroleum Resources Paper, v. 1988-4, p. 188.

Godwin, C. I., Sinclair, A. J., and Ryan, B. D., 1982, Lead isotope models for the genesis of carbonate-hosted Zn-Pb, shale-hosted Ba-Zn-Pb, and silver-rich deposits in the northern Canadian Cordillera: Economic Geology, v. 77, p. 82-94.

Goleby, B. R., Drummond, B. J., MacCready, T., and Goncharov, A., 1996a, The Mount Isa deep seismic transect: James Cook University, Economic Geology Research Unit, Contribution 55, p. 51-55.

Goleby, B. R., Drummond, B. J., and MacCready, T., 1996b, The Mount Isa geodynamic transect - the deep seismic reflection profile south of Mount Isa and Cloncurry: Australian Geological Survey Organisation, Research Newsletter, v. 24, p. 6-8.

Graham, C. M. and Powell, R., 1984, A garnet-hornblende geothermometer: calibration, testing, and application to the Pelona Schist, Southern California: Journal of Metamorphic Petrology; v. 3, p. 13-21.

Grant, J. A., 1986, The Isocon diagram - A simple solution to Gresens' Equation for metasomatic alteration: Economic Geology; v. 81, p. 1976-1982.

Gray, D. R., 1993, Structural report on the Cannington Pb-Zn-Ag deposit, Mt. Isa Inlier: Unpublished report to BHP Minerals.

Gray, D. R., 1994, Structural geology of the Cannington Ag-Pb-Zn deposit, Mt. Isa Inlier: Unpublished report to BHP Cannington Project, p. 15 p.

Gresens, R. L., 1967, Composition-volume relationships of metasomatism: Chemical Geology; v. 2, p. 47-65.

Grew, E. S., 1974, Carbonaceous material in some metamorphic rocks of New England and other areas: Journal of Geology, v. 82, p. 50-73.

Gromet, L. P., Dymek, R. F., Haskin, L. A. and Korotev, R. L., 1984, The "North American shale composite"; its compilation, major and trace element characteristics: Geochimica et Cosmochimica Acta, v. 48, p. 2469-2482.

Gulson, B. L., 1975, Differences in lead isotope composition in the stratiform McArthur zinc-lead-silver deposit: Mineralium Deposita, v. 10, p. 277-286.

Gulson, B. L., 1984, Uranium-lead and lead-lead investigations of minerals from the Broken Hill lodes and mine sequence rocks: Economic Geology, v. 79, p. 476-490.

Gulson, B. L., 1985, Shale-hosted lead-zinc deposits in northern Australia; lead isotope variations: Economic Geology, v. 80, p. 2001-2012.

Gulson, B. L., 1986, Lead isotopes in mineral exploration: Amsterdam, Netherlands, Elsevier, 245 p.

Gulson, B. L., Korsch, M. J., Cameron, M., Vaasjoki, M., Mizon, K. J., Porritt, P. M., Carr, G. R., Kamper, C., Dean, J. A., and Calvez, J.-Y., 1984, Lead isotope ratio measurements using the Isomass 54E in fully automated mode: International Journal of Mass Spectrometry and Ion Processes, v. 59, p. 125-142.

Gulson, B. L., Perkins, W. G., and Mizon, K. J., 1983, Lead isotope studies bearing on the genesis of copper orebodies at Mount Isa, Queensland: Economic Geology, v. 78, p. 1466-1504.

Gulson, B. L., Porritt, P. M., Mizon, K. J., and Barnes, R. G., 1985, Lead isotope signatures of stratiform and strata-bound mineralization in the Broken Hill Block, New South Wales, Australia: Economic Geology, v. 80, p. 488-496.

Hamilton, L. H., 1965, Concepts of ore genesis to the Broken Hill Lode, N.S.W: Journal of the University of New South Wales, Mining and Geological Society, v. 3, p. 43-66.

Hannington, M. D., Bleeker, W., and Kjarsgaard, I., 1999, Sulfide mineralogy, geochemistry, and ore genesis of the Kidd Creek deposit: part I. North, central, and south orebodies: Economic Geology, Monograph 10, p. 163-224.

Hanor, J. S., 1996, Controls on the solubilization of lead and zinc in basinal brines, *in* Sangster, D. F., ed., Carbonate-hosted lead-zinc deposits, 4, Economic Geology Special Publication, p. 483-500.

Haydon, R. C. and McConachy, G. W., 1987, The stratigraphic setting of Pb-Zn-Ag mineralization at Broken Hill: Economic Geology, v. 82, p. 826-856.

Haydon, R. C., McConachy, G. W. and Wright, J. V., 1993, Broken Hill ore environment - examples of critical guides to ore location: International Symposium - World Zinc, 1993, Hobart, Australia, p. 131-149.

Hellman, P. L., Smith, R. E. and Henderson, P., 1979, The mobility of the rare-earth elements: evidence and implications from selected terrains affected by burial metamorphism: Contribution Mineralogy and Petrology, v. 71, p. 23-44.

Herron, M. M., 1988, Geochemical classification of terrigenous sands and shales from core or log data: Journal of Sedimentary Petrology, v. 58, p. 820-829.

Hill, E. J., Loosveld, R. J. H., and Page, R. W., 1992, Structure and geochronology of the Tommy Creek Block, Mount Isa Inlier, *in* Stewart, A. J., and Blake, D. H., eds., Detailed Studies of the Mount Isa Inlier, Australian Geological Survey Bulletin 243, p. 329-348.

Hinman, M. C., Wall, V. J., and Heinrich, C., 1994, The interplay between sedimentation, deformation and mineralization at the McArthur Pb-Zn(-Cu) deposit: Geological Society of Australia, Abstracts No. 37, p. 176-177.

Hinman, M., 1996, Constraints, timing and processes of stratiform base metal mineralization at the HYC Ag-Pb-Zn deposit, McArthur River: James Cook University, Economic Geology Research Unit, Contribution 55, p. 56-59.

Hodges, K. V., and Spear, F. S., 1982, Geothermometry, geobarometry and the Al_2SiO_5 triple point at Mt. Moosilauke, New Hampshire: American Mineralogist, v. 67, p. 1118-1134.

Hodgson, 1975, The geology and geological development of the Broken Hill Lode, in the New Broken Hill Consolidated Mine Australia, Part II: Mineralogy: Journal of the Geological Society of Australia, v. 22, p. 33-50.

Hoefs, J. and Frey, M., 1976, The isotopic composition of carbonaceous matter in a metamorphic profile from the Swiss Alps: Geochimica et Cosmochimica Acta, v. 40, p. 945-951.

Hoisch, T. D., 1990, Empirical calibration of six geobarometers for the mineral assemblage quartz+muscovite+biotite+plagioclase+garnet: Contributions to Mineralogy and Petrology, v. 104, p. 225-234.

Holcombe, R. J., Pearson, P. J., and Oliver, N. H. S., 1991, Geometry of a middle Proterozoic extensional décollement in northeastern Australia: Tectonophysics, v. 191, p. 255-274.

Holdaway, M. J., 1971, Stability of andalusite and the aluminum silicate phase diagram: American Journal of Science, v. 271, p. 97-131.

Holdaway, M. J., Mukhopadhyay, B., Dyar, M. D., Guidotti, C. V., and Dutrow, B. L., 1997, Garnet-biotite geothermometry revised; new Margules parameters and a natural specimen data set from Maine: American Mineralogist, v. 82, p. 582-595.

Holland, T., and Blundy, J., 1994, Non-ideal interactions in calcic amphiboles and their bearing on amphibole-plagioclase thermometry: Contributions to Mineralogy and Petrology, v. 116, p. 433-447.

Höller, W., Touret, J. L. R., and Stumpfl, E. F., 1996, Retrograde fluid evolution at the Rampura Agucha Ph-Zn-(Ag) deposit, Rajasthan, India: Mineralium Deposita, v. 31, p. 163-171.

Hollister, L. S., Garnet zoning: an interpretation based on the Rayleigh fractionation model: Science, v. 154, p. 1647-1651.

Holloway, J. R., 1984, Graphite-CH_4-H_2O-CO_2 equilibria at low-grade metamorphic conditions: Geology, v. 12, p. 455-458.

Holmes, A., 1946, An estimate of the age of the Earth: Nature, v. 157, p. 680-684.

Holtzclaw, H.F., Robinson, W.R., and Nebergall, W.H., 1984, General Chemistry: D.C. Heath and Company, USA, 932 p.

Horita, J., 2001, Carbon isotope exchange in the system CO_2-CH_4 at elevated temperatures: Geochimica et Cosmochimica Acta, v. 65, p. 1907-1919.

Houtermans, F. G., 1946, Die Isotopenhäufigkeiten im natürlichen Blei und das Alter des Urans: Naturwissenschaften, v. 33, p. 185-186, 219.

Huang, W., 1995, Overview of fold interference patterns in the Eastern Successions: a key step towards regional structural correlations: Australian Crustal Research Centre, Technical Publication 9.

Humphries, S. E., 1984, The mobility of rare earth elements in the crust, *in* Henderson, P., ed., Rare Earth Element Geochemistry. Developments in Geochemistry, 2: Amsterdam, Elsevier, p. 317-342.

Huston, D. L., 1993, The effect of alteration and metamorphism on wall rocks to the Balcooma and Dry River South volcanic-hosted massive sulphide deposits, Queensland, Australia: Journal of Geochemical Exploration, v. 48, p. 277-307.

Ishikawa, Y., Sawaguchi, T., Iwaya, S., and Horiuchi, M., 1976, Delineation of prospecting targets for Kuroko deposits based on modes of volcanism of underlying dacite and alteration halos: Mining Geology, v. 26, p. 105-117.

James, S. D., Pearce, J. A., and Oliver, R. A., 1987, The geochemistry of the lower Proterozoic Willyama Complex volcanics, Broken Hill Block, New South Wales, *in* Pharaoh, T. C., Beckinsale, R. D., and Rickard, D. T., eds., Geochemistry and Mineralization of Proterozoic Volcanic Suites: London, United Kingdom, Geological Society of London Special Publications, 33, p. 395-408.

Jaques, A. L., Blake, D. H., and Donchak, P. J. T., 1982, Regional metamorphism in the Selwyn Range area, northwest Queensland: Bureau of Mineral Resources Journal of Australian Geology and Geophysics, v. 7, p. 181-196.

Jenkins, M. K., 1994, The origin and evolution of the Glenholme Breccia, Cannington Ag-Pb-Zn deposit, Mount Isa Inlier, northwest Queensland: Unpublished Honours thesis, James Cook University, Townsville, 75 p.

Johnson, I. R., and Klingner, G. D., 1975, Broken Hill ore deposit and its environment: Australasian Institute of Mining and Metallurgy, Monograph 5, p. 476-491.

Kerr, T. L., 1994, Magnetic characteristics of Broken Hill type deposits and their host provinces: Unpublished MEconGeol thesis, University of Tasmania, 185 p.

Kerrich, R. and Fryer, B. J., 1979, Archean precious-metal hydrothermal systems, Dome Mine, Abitibi Greenstone Belt. II: REE and oxygen isotope relations: Canadian Journal of Earth Science, v. 16, p. 440-458.

Kleemann, U. and Reinhardt, J., 1994, Garnet-biotite thermometry revisited: The effect of Al^{VI} and Ti in biotite: European Journal of Mineralogy; v. 6, p. 925-941.

Klinkhammer, G. P., Elderfield, H., Edmond, J. M. and Mitra, A., 1994, Geochemical implications of rare earth element patterns in hydrothermal fluids from mid-ocean ridges: Geochimica et Cosmochimica Acta, v. 58, p. 5105-5113.

Kohn, M. J., and Spear, F. S., 1989, Empirical calibration of geobarometers for the assemblage garnet + plagioclase + quartz: American Mineralogist, v. 74, p. 77-84.

Kozoil, A. M., 1989, Recalibration of the garnet-plagioclase-Al_2SiO_5-quartz (GASP) geobarometer and application to natural parageneses: EOS Transactions of the American Geophysical Union, v. 70, p. 493.

Kranidiotis, P. and MacLean, W. H., 1987, Systematics of chlorite alteration at the Phelps Dodge massive sulfide deposit, Matagami, Quecbec: Economic Geology, v. 82, p. 1898-1911.

Krassay, A. A., Bradshaw, B. E., Domagala, J., and Jackson, M. J., 2000a, Siliciclastic shoreline to growth-faulted, turbiditic sub-basin; the Proterozoic River Supersequence of the upper McNamara Group on the Lawn Hill Platform, northern Australia: Australian Journal of Earth Sciences, v. 47, p. 533-562.

Krassay, A. A., Domagala, J., Bradshaw, B. E., and Southgate, P. N., 2000b, Lowstand ramps, fans and deep-water Palaeoproterozoic and Mesoproterozoic facies of the Lawn Hill Platform; the Term, Lawn, Wide and Doom supersequences of the Isa Superbasin, northern Australia: Australian Journal of Earth Sciences, v. 47, p. 563-597.

Kreulen, R., and van Beek, P. C. J. M., 1983, The calcite-graphite isotope thermometer; data on graphite bearing marbles from Naxos, Greece: Geochimica et Cosmochimica Acta, v. 47, p. 1527-1530.

Laing, W. P., 1990, The Cloncurry Terrane: An allochthon of the Diamantina Orogen rafted onto the Mount Isa Orogen, with its own distinctive metallogenic signature: in Mount Isa Inlier Geology Conference, Abstracts, Victorian Institute of Earth and Planetary Sciences, Monash University, p. 19-22.

Laing, W. P., 1996, The Diamantina Orogen linking the Willyama and Cloncurry terranes, eastern Australia, *in* Pongratz, J., and Davidson, G. J., eds., New Developments in Broken Hill-type Deposits, Centre for Ore Deposit Research Special Publication 1, p. 67-72.

Laing, W. P., 1998, Structural-metasomatic environment of the East Mt Isa Block base-metal-gold province: Australian Journal of Earth Sciences, v. 45, p. 413-428.

Laing, W. P., Marjoribanks, R. W. and Rutland, R. W. R., 1978, Structure of the Broken Hill mine area and its significance for the genesis of the orebodies: Economic Geology; v. 73, p. 1112-1136.

Large, D. J., Christy, A. G. and Fallick, A. E., 1994, Poorly crystalline carbonaceous matter in high grade metasediments: implications for graphitisation and metamorphic fluid compositions: Contributions to Mineralogy & Petrology, v. 116, p. 108-116.

Large, R. R. and McGoldrick, P. J., 1998, Lithogeochemical halos and geochemical vectors to stratiform sediment hosted Zn-Pb-Ag deposits, 1. Lady Loretta Deposit, Queensland: Journal of Geochemical Exploration; v. 63, p. 37-56.

Large, R. R., and Davidson, G. J., 1991, Controls of brine chemistry on the spectrum of Proterozoic sediment-hosted base metal deposits: Ore Fluids Conference, Canberra, Australia, 1991, p. 50-51.

Large, R. R., Bodon, S., Davidson, G. J., and Cooke, D., 1996, The chemistry of BHT ore formation - one of the keys to understanding the differences between SEDEX and BHT deposits, *in* Pongratz, J., and Davidson, G., eds., New Developments in Broken Hill Type Deposits: Hobart, Centre for Ore Deposit Research, University of Tasmania, p. 105-111.

Large, R. R., Bull, S. W., Cooke, D. R., and McGoldrick, P. J., 1998, A genetic model for the HYC deposit, Australia: Based on regional sedimentology, geochemistry, and sulfide-sediment relationships: Economic Geology, v. 93, p. 1345-1368.

Large, R. R., Gemmell, J. B., Paulick, H., and Huston, D. L., 2001, The alteration box plot: a simple approach to understanding the relationship between alteration mineralogy and lithogeochemistry associated with volcanic-hosted massive sulfide deposits: Economic Geology, v. 96, p. 957-971.

Lassey, K. R., and Blattner, P., 1988, Kinetically controlled oxygen isotope exchange between fluid and rock in one-dimensional advective flow: Geochimica et Cosmochimica Acta, v. 52, p. 2169-2175.

Lawrence, L. J., 1967, Sulphide neomagmas and highly metamorphosed sulphide deposits: Mineralium Deposita, v. 2, p. 5-10.

Lawrence, L. J., 1968, The minerals of the Broken Hill district: Australasian Institute of Mining and Metallurgy, Monograph 3, p. 103-136.

Lawrence, L. J., 1973, Polymetamorphism of the sulphide ores of Broken Hill, N.S.W., Australia: Mineralium Deposita, v. 8, p. 211-236.

Leake, B. E., Woolley, A. R., Arps, C. E. S., Birch, W. D., Gilbert, M. C., Grice, J. D., Hawthorne, F. C., Kato, A., Kisch, H. J., Krivovichev, V. G., Linthout, K., Laird, J., Mandarino, J. A., Maresch, W. V., Nickel, E. H., Rock, N. M. S., Schumacher, J. C., Smith, D. C., Stephenson, N. C. N., Ungaretti, L., Whittaker, E. J. W., and Guo, Y., 1997, Nomenclature of amphiboles; report of the subcommittee on amphiboles of the International Mineralogical Association, Commission on New Minerals and Mineral Names: The Canadian Mineralogist, v. 35, p. 219-246.

Leitch, C. H. B., and Lentz, D. R., 1994, The Gresens approach to mass balance constraints of alteration systems: methods, pitfalls, examples, *in* Lentz, D. R., ed., Alteration and Alteration Processes Associated with Ore-forming Systems: Geological Association of Canada Short Course Notes, 11, p. 161-192.

Lentz, D. R. and Goodfellow, W. D., 1993, Petrology and mass balance constraints on the origin of quartz-augen schist associated with the Brunswick massive sulphide deposits, Bathurst, New Brunswick: The Canadian Mineralogist, v. 31, p. 877-903.

Lesher, C. M., Goodwin, A. M., Campbell, I. H. and Gorton, M. P., 1986, Trace-element geochemistry of ore-associated and barren, felsic metavolcanic rocks in the Superior Province, Canada: Canadian Journal of Earth Science, v. 23, p. 222-237.

Lewis, A. J., Palmer, M. R., Sturchio, N. C., and Kemp, A. J., 1997, The rare earth element geochemistry of acid-sulphate and acid-sulphate-chloride geothermal systems from Yellowstone National Park, Wyoming, USA: Geochimica et Cosmochimica Acta, v. 61, p. 695-706.

Liaghat, S. and MacLean, W. H., 1992, The Ket Tuffite, Matagami mining deposit: Origin of the tuff components and mass changes: Exploration Mining Geology; v. 1, p. 197-207.

Lister, G. S., 1997, Day 3 - Selwyn Shear, *in* Aillères, L., and Betts, P. G., eds., Structural Elements of the Eastern Successions - a field guide illustrating the structural geology of the eastern Mount Isa terrane, Australia, Australian Crustal Research Centre, Technical Publication 63, p. 144-145.

Lister, G. S., Betts, P. G., Giles, D., and MacCready, T., 1997, The active tectonic environment of ore deposition in the Mount Isa terrane, *in* Aillères, L., and Betts, P. G., eds., Structural Elements of the Eastern Successions - a field guide illustrating the structural geology of the eastern Mount Isa terrane, Australia, Australian Crustal Research Centre, Technical Publication 63, p. 117-130.

Lister, G. S., Thomas, A., and Dunn, J., 1986, Tectonic processes in the Mount Isa Inlier; the significance of transpressional strike-slip faulting, *in* Branch, C. D., ed., Proceedings of the Eighth Australian geological convention; Geological Society of Australia; Earth resources in time and space, Geological Society of Australia Abstracts 15, p. 127-128.

Locsei, J., 1977, Pegmont: a stratiform lead-zinc deposit in the Precambrian of northwest Queensland: Proceedings - Australasian Institute of Mining and Metallurgy, v. 262, p. 25-27.

Loomis, T. P., 1983, Compositional zoning of crystals: a record of growth and reaction history, *in* Saxena, S. K., ed., Kinetics and Equilibrium in Mineral Reactions, Vol. 3., Springer-Verlag, New York, p. 1-60.

Loosveld, R. J. H., 1988, Structure and tectono-thermal history of the eastern Mount Isa Inlier, Australia: Unpublished PhD thesis, Australian National University, Canberra, Australian Capital Territory.

Loosveld, R. J. H., 1989a, The intra-cratonic evolution of the central eastern Mount Isa Inlier, northwest Queensland, Australia: Precambrian Research, v. 44, p. 243-276.

Loosveld, R. J. H., 1989b, The synchronism of crustal thickening and high T/ low P metamorphism in the Mount Isa Inlier, Australia; 1, An example, the central Soldiers Cap Belt: Tectonophysics, v. 158, p. 173-190.

Loosveld, R. J. H., 1989c, The synchronism of crustal thickening and low-pressure facies metamorphism in the Mount Isa Inlier, Australia; 2, Fast convective thinning of mantle lithosphere during crustal thickening: Tectonophysics, v. 165, p. 191-218.

Loosveld, R. J. H., 1992, Structural geology of the central Soldiers Cap Belt, Mount Isa Inlier, Australia, *in* Stewart, A. J., and Blake, D. H., eds., Detailed Studies of the Mount Isa Inlier, Australian Geological Survey Bulletin 243, p. 349-359.

Lottermoser, B. G., 1988, Rare earth element composition of garnets from the Broken Hill Pb-Zn-Ag orebodies, Australia: Neues Jahrbuch fuer Mineralogie, Monatshefte, v. 9, p. 423-431.

Lottermoser, B. G., 1989, Rare earth element study of exhalites within the Willyama Supergroup, Broken Hill Block, Australia: Mineralium Deposita, v. 24, p. 92-99.

Lottermoser, B. G., 1990, Rare-earth element and heavy-metal behavior associated with the epithermal gold deposit on Lihir Island, Papua New Guinea: Journal of Volcanological and Geothermal Research, v. 40, p. 269-289.

Lottermoser, B. G., 1992, Rare earth elements and hydrothermal ore formation processes: Ore Geology Reviews, v. 7, p. 25-41.

Loveless, A. J., 1975, Lead isotopes - a guide to major mineral deposits: Geoexploration, v. 13, p. 13-27.

Ludden, J. N. and Thompson, G., 1979, An evaluation of the behaviour of the rare-earth elements during the weathering of sea-floor basalt: Earth and Planetary Science Letters, v. 43, p. 85-92.

Ludden, J. N., Gelinas, L. and Trudel, P., 1982, Archean metavolcanics from the Rouyn-Noranda district, Abitibi Greenstone Belt, Quebec. 2: mobility of trace element and petrogenetic constraints: Canadian Journal of Earth Science, v. 19, p. 2276-2287.

Ludwig, K. R., and Silver, L. T., 1977, Lead-isotope inhomogeneity in Precambrian igneous K-feldspars: Geochimica et Cosmochimica Acta, v. 41, p. 1457-1471.

Luque, F. J., Pasteris, J. D., Wopenka, B., Rodas, M. and Barrenechea, J. F., 1998, Natural fluid-deposited graphite: mineralogical characteristics and mechanisms of formation: American Journal of Science, v. 298, p. 471-498.

Luth, W. D., Jahns, R. H., and Tuttle, O. F., 1964, The granite system at pressures of 4 to 10 kilobars: Journal of Geophysical Research, v. 69, p. 659-773.

Lydon, J. W., 1988, Volcanogenic massive sulphide deposits, Part 2: Genetic models: Geoscience Canada Reprint Series 3, p. 155-182.

MacCready, T., Goleby, B. R., Goncharov, A., Drummond, B. J., and Lister, G. S., 1998, A framework of overprinting orogens based on interpretation of the Mount Isa deep seismic transect: Economic Geology, v. 93, p. 1422-1434.

MacCready, T., Goleby, B. R., Goncharov, A., Lister, G. S., and Drummond, B. J., 1997, An evolutionary framework for the Isan Orogeny: Geodynamics and Ore Deposits Conference, Abstracts, Australian Geodynamics Cooperative Research Centre, Ballarat, Victoria, p. 42-45.

MacLean, W. H. and Barrett, T. J., 1993, Lithogeochemical methods using immobile elements: Journal of Exploration Geochemistry; v. 48, p. 109-133.

MacLean, W. H., 1988, Rare earth element mobility at constant inter-REE ratios in the alteration zone at the Phelps Dodge massive sulphide deposit, Matagami, Quebec: Mineralium Deposita; v. 23, p. 231-238.

MacLean, W. H., 1990, Mass changes calculations in altered rocks series: Mineralium Deposita; v. 25, p. 44-49.

MacLean, W. H., and Kranidiotis, P., 1987, Immobile elements as monitors of mass transfer in hydrothermal alteration: Phelps Dodge Massive Sulphide Deposit, Matagami, Quebec: Economic Geology, v. 82, p. 951-962.

Main, J. V., Mason, D. O. and Tuckwell, K. D., 1983, The characteristics and interpretation of whole rock geochemical data, Willyama Supergroup, New South Wales - trends towards ore: The AUSIMM Conference, Broken Hill, p. 115-131.

Mares, V. M., 1998, Structural development of the Soldiers Cap Group in the Eastern Fold Belt of the Mt Isa Inlier - a succession of horizontal and vertical deformation events and large-scale shearing: Australian Journal of Earth Sciences, v. 45, p. 373-387.

Mark, G., 1993, Pegmatites and partial melting at the Cannington Ag-Pb-Zn deposit: Unpublished Honours thesis, James Cook University, Townsville, Queensland, 94 p.

Mark, G., 1998, Albite formation by selective pervasive sodic alteration of tonalite plutons in the Cloncurry district, Queensland: Australian Journal of Earth Sciences, v. 45, p. 765-774.

Mark, G., 2001, Nd isotope and petrogenetic constraints for the origin of the Mount Angelay igneous complex: implications for the origin of intrusions in the Cloncurry district, NE Australia: Precambrian Research, v. 105, p. 17-35.

Mark, G., and de Jong, G., 1996, Synchronous granitoid emplacement and episodic sodic-calcic alteration in the Cloncurry district: styles, timing and metallogenic significance: James Cook University, Economic Geology Research Unit, Contribution 55, p. 77-80.

Mark, G., and Foster, D. R. W., 2000, Magmatic-hydrothermal albite-actinolite-apatite-rich rocks from the Cloncurry district, NW Queensland, Australia: Lithos, v. 51, p. 223-245.

Mark, G., Phillips, G. N., and Pollard, P. J., 1998, Highly selective partial melting of pelitic gneiss at Cannington, Cloncurry district, Queensland: Australian Journal of Earth Sciences, v. 45, p. 169-176.

Marshall, B., and Gilligan, L. B., 1987, An introduction to remobilization: information from orebody geometry and experimental considerations: Ore Geology Reviews, v. 2, p. 87-131.

Marshall, B., and Gilligan, L. B., 1989, Durchbewegung structure, piercement cusps, and piercement veins in massive sulfide deposits; formation and interpretation: Economic Geology, v. 84, p. 2311-2319.

Marshall, B., and Spry, P. G., 2000, Discriminating between regional metamorphic remobilization and syntectonic emplacement in the genesis of massive sulfide ores, *in* Spry, P. G., Marshall, B., and Vokes, F. M., eds., Metamorphosed and metamorphogenic ore deposits., Reviews in Economic Geology, v. 11, p. 39-80.

Marshall, B., Vokes, F. M., and Larocque, A. C. L., 2000, Regional metamorphic remobilization: upgrading and formation of ore deposits, *in* Spry, P. G., Marshall, B., and Vokes, F. M., eds., Metamorphosed and metamorphogenic ore deposits., Reviews in Economic Geology, v. 11, p. 19-38.

Mavrogenes, J. A., MacIntosh, I. W., and Ellis, D. J., 2001, Partial melting of the Broken Hill galena-sphalerite ore: Experimental studies in the system PbS-FeS-ZnS-(Ag2S): Economic Geology, v. 96, p. 205-210.

McCarthy, C., 1996, Alteration associated with late (D4) brittle faults, Cannington, NW Queensland: Unpublished Honours thesis, University of Tasmania, Hobart, 107 p.

McDougall, T. J., 1984, Fluid dynamic implications for massive sulfide deposits of hot saline fluid flowing into a submarine depression from below: Deep Sea Research, v. 31, p. 145-170.

McKirdy, D. M. and Powell, T. G., 1974, Metamorphic Alteration of Carbon Isotopic Composition in Ancient Sedimentary Organic Matter: New Evidence from Australia and South Africa: Geology, v. 2, p. 591-595.

McLaren, S., Sandiford, M., and Hand, M., 1999, High radiogenic heat-producing granites and metamorphism - An example from the western Mount Isa Inlier, Australia: Geology, v. 27, p. 679-682.

McLennan, S. M., and Taylor, S. R., 1991, Sedimentary rocks and crustal evolution: tectonic setting and secular trends: Journal of Geology, v. 99, p. 1-21.

McNaughton, N., 1995, Cloncurry lead isotope data, *in* Pollard, P., ed., Cloncurry Base Metals and Gold P438: Australian Mineral Industries Research Association, P438 1995 annual report, p. 7-1 - 7-11.

McNaughton, N., 1996, Lead isotope studies: wholerocks and feldspars, *in* Pollard, P., ed., Cloncurry Base Metals and Gold P438: Australian Mineral Industries Research Association, P438 1996 annual report, p. 7-1 - 7-11.

McNaughton, N., 1997a, Lead isotope characteristics of Proterozoic rocks and minerals in the Cloncurry District, Mount isa Inlier, Australia, *in* Pollard, P., ed., Cloncurry Base Metals and Gold, 1, Australian Mineral Industries Research Association (AMIRA), P438 final report, p. 5-1 - 5-11.

McNaughton, N., 1997b, Lead isotope characteristics of ore deposits in the Cloncurry District, Mount Isa Inlier, Australia, *in* Pollard, P., ed., Cloncurry Base Metals and Gold, 1, Australian Mineral Industries Research Association (AMIRA), P438 final report, p. 5a-1 - 5a-18.

Meinert, L. D., 1992, Skarns and skarn deposits: Geoscience Canada, v. 19, p. 145-162.

Meinert, L. D., 1993, Skarns and skarn deposits, *in* Sheahan, P. A., and Cherry, M. E., eds., Ore deposit models II, Geoscience Canada Reprint Series 6: Stittsville, Geological Association of Canada, p. 117-134.

Meinert, L. D., 1995, Report of observations: BHP Cannington deposit; unpublished report to BHP Minerals, Department of Geology, Washington State University, USA, 6p.

Meinert, L. D., 1998, Application of skarn deposit zonation models to mineral exploration: Exploration Mining Geology, v. 6, p. 185-208.Michard, A. and Albarède, F., 1986, The REE content of some hydrothermal fluids: Chemical Geology, v. 55, p. 51-60.

Michard, A., 1989, Rare earth element systematics in hydrothermal fluids: Geochimica et Cosmochimica Acta, v. 53, p. 745-750.

Michard, A., and Albarède, F., 1986, The REE content of some hydrothermal fluids: Chemical Geology, v. 55, p. 51-60.

Mills, R. A. and Elderfield, H., 1995a, Rare earth element geochemistry of hydrothermal deposits from the active TAG Mound, 26°N Mid-Atlantic Ridge: Geochimica et Cosmochimica Acta, v. 59, p. 3511-3524.

Mills, R. A. and Elderfield, H., 1995b, Hydrothermal activity and the geochemistry of metalliferous sediment: American Geophysical Union, Geophysical Monograph 91, p. 392-407.

Mojzsis, S. J., Arrhenius, G., McKeegan, K. D., Harrison, T. M., Nutman, A. P., and Friend, R. L., 1996, Evidence for life on Earth before 3800 million years ago: Nature, v. 384, p. 55-59.

Mookherjee, A., 1976, Ores and metamorphism: temporal and genetic relationships, *in* Wolf, K. H., ed., Handbook of Strata-bound and Stratiform Ore Deposits, 4: Amsterdam, Elsevier, p. 203-260.

Muecke, G. K., Pride, C., and Sarkar, P., 1979, Rare earth element geochemistry of regional metamorphic rocks, *in* Ahrens, L. H., ed., Origin and Distribution of Elements: Oxford, Pergamon, p. 449-464.

Munoz, J. L., 1984. F-OH and Cl-OH exchange in micas with applications to hydrothermal ore deposits, *in* Bailey, S. W., ed., Micas, 13. Reviews in Mineralogy: Chelsea, Michigan, Mineralogical Society of America, p. 469-494.

Nabelek, P. I., Labotka, T. C., O Neil, J. R. and Papike, J. J., 1984, Contrasting fluid/rock interaction between the Notch Peak granitic intrusion and argillites and limestones in western Utah: evidence from stable isotopes and phase assemblages: Contributions to Mineralogy and Petrology, v. 86, p. 25-34.

Newbery, S. P., 1990, The Middle Proterozoic Maronan Supergroup, Soldiers Cap Belt, eastern Mount Isa Inlier: a rationalisation of the geology and mineralisation of a complexly deformed and metamorphosed terrane: Unpublished PhD thesis, James Cook University, Townsville, Queensland.

Newbery, S., 1991, Iron formation hosted base metal mineralisation in the Cloncurry Terrane, Mount Isa Inlier: James Cook University, Economic Geology Research Unit Contribution 38, p. 89-99.

Nutman, A. P., and Ehlers, K., 1998, Evidence for multiple Palaeoproterozoic thermal events and magmatism adjacent to the Broken Hill Pb-Zn-Ag orebody, Australia: Precambrian Research, v. 90, p. 203-238.

O'Dea, M. G., Lister, G., MacCready, T., Betts, P. G., Oliver, N. H. S., Pound, K. S., Huang, W., and Valenta, R. K., 1997a, Geodynamic evolution of the Proterozoic Mount Isa terrain, *in* Burg, J. P., and Ford, M., eds., Orogeny Through Time, Geological Society of London, Special Publications 121, p. 99-122.

O'Dea, M. G., Lister, G. S., Betts, P. G., and Pound, K. S., 1997b, A shortened intraplate rift system in the Proterozoic Mount Isa terrane, NW Queensland, Australia: Tectonics, v. 16, p. 425-441.

O'Dea, M. G., Betts, P. G., MacCready, T., and Aillères, L., in press, Sequential development of a mid-crustal fold-thrust complex in the Mount Isa Inlier, Australia: Precambrian Research.

Ohmoto, H. and Kerrick, D. M., 1977, Devolatilization equilibria in graphitic systems: American Journal of Science, v. 277, p. 1013-1044.

Olivarez, A. M., and Owen, R. M., 1991, The europium anomaly of seawater: implications for fluvial versus hydrothermal REE inputs to the oceans: Chemical Geology, v. 92, p. 317-328.

Oliver, N. H. S., 1995, Hydrothermal history of the Mary Kathleen Fold Belt, Mt Isa Block, Queensland: Australian Journal of Earth Sciences, v. 42, p. 267-279.

Oliver, N. H. S., and Wall, V. J., 1987, Metamorphic plumbing system in Proterozoic calc-silicates, Queensland, Australia: Geology, v. 15, p. 793-796.

Oliver, N. H. S., Cartwright, I., and Rubenach, M. J., 1995, Mid- to lower-crustal metamorphism and fluid-rock interaction, with reference to the Mt Isa Inlier: Australian Journal of Earth Sciences, v. 42, p. 231-232.

Oliver, N. H. S., Cartwright, I., Wall, V. J., and Golding, S. D., 1993, The stable isotope signature of kilometre-scale fracture-dominated metamorphic fluid pathways, Mary Kathleen, Australia: Journal of Metamorphic Geology, v. 11, p. 705-720.

Oliver, N. H. S., Holcombe, R. J., Hill, E. J., and Pearson, P. J., 1991, Tectono-metamorphic evolution of the Mary Kathleen fold belt, northwest Queensland: a reflection of mantle plume processes?: Australian Journal of Earth Sciences, v. 38, p. 425-455.

Page, R. W., 1983, Timing of superposed volcanism in the Proterozoic Mount Isa Inlier, Australia: Precambrian Research, v. 21, p. 223-245.

Page, R. W., 1988, Geochronology of early to middle Proterozoic fold belts in northern Australia: a review: Precambrian Research, 40-41, p. 1-19.

Page, R. W., 1993, Geochronological results from the Eastern Fold Belt, Mount Isa Inlier: Australian Geological Survey Organisation Research Newsletter 19, p. 4-5.

Page, R. W., 1994, Mount Isa geochronology: Australian Geological Survey Organisation 1993 Yearbook, p. 60.

Page, R. W., 1998, Links between eastern and western fold belts in the Mount Isa Inlier, based on SHRIMP U-Pb studies: Geological Society of Australia Abstracts, v. 49, p. 349.

Page, R. W., and Bell, T. H., 1986, Isotopic and structural responses of granite to successive deformation and metamorphism: Journal of Geology, v. 94, p. 365-379.

Page, R. W., and Laing, W. P., 1992, Felsic metavolcanic rocks related to the Broken Hill Pb-Zn-Ag orebody, Australia: geology, depositional age, and timing of high-grade metamorphism: Economic Geology, v. 87, p. 2138-2168.

Page, R. W., and Sun, S.-s., 1996, Age and provenance of granitic rocks and host sequences in the Mount Isa Eastern Succession: James Cook University, Economic Geology Research Unit, Contribution 55, p. 95-98.

Page, R. W., and Sun, S.-s., 1998, Aspects of geochronology and crustal evolution in the Eastern Fold Belt, Mt Isa Inlier: Australian Journal of Earth Sciences, v. 45, p. 343-361.

Page, R. W., and Sweet, I. P., 1998, Geochronology of basin phases in the western Mt Isa Inlier, and correlation with the McArthur Basin: Australian Journal of Earth Sciences, v. 45, p. 219-232.

Page, R. W., and Williams, I. S., 1988, Age of the Barramundi Orogeny in northern Australia by means of ion microprobe and conventional U-Pb zircon studies: Precambrian Research, v. 40-41, p. 21-36.

Page, R. W., Sun, S.-s., and MacCready, T., 1997, New geochronological results in the central and eastern Mount Isa Inlier and implications for mineral exploration: Abstracts, Geodynamics and Ore Deposits Conference, Australian Geodynamics Cooperative Research Centre, Ballarat, Victoria, p. 9-12.

Parr, J. M., 1992, Rare-earth element distribution in exhalites associated with Broken Hill-type mineralisation at the Pinnacles deposit, New South Wales, Australia: Chemical Geology, v. 100, p. 73-91.

Parr, J. M., 1994, The geology of the Broken Hill-type Pinnacles Pb-Zn-Ag deposit, Western New-South-Wales, Australia: Economic Geology, v. 89, p. 778-790.

Parr, J. M., and Plimer, I. R., 1993, Models for Broken Hill-type lead-zinc-silver deposits, *in* Kirkham, R. V., Sinclair, W. D., Thorpe, R. I., and Duke, J. M., eds., Mineral Deposit Modeling, Geological Association of Canada, Special Paper 40, p. 253-288.

Passchier, C. W., 1986, Evidence for early extensional tectonics in the Proterozoic Mount Isa Inlier, Australia: Geology, v. 14, p. 1008-1011.

Passchier, C. W., and Williams, P. R., 1989, Proterozoic extensional deformation in the Mount Isa Inlier, Queensland, Australia: Geological Magazine, v. 126, p. 43-53.

Pearce, J. A. and Cann, J. R., 1973, Tectonic setting of basic volcanic rocks determined using trace element analysis: Earth and Planetary Science Letters; v. 19, p. 290-300.

Pearce, T. H., 1968, A contribution to the theory of variation diagrams.: Contribution Mineralogy and Petrology; v. 19, p. 142-157.

Pearson, P. J., Holcombe, R. J., and Oliver, N. H. S., 1987, The Mary Kathleen Fold Belt, northwest Queensland: D1, a product of crustal extension?: Abstracts, Geological Society of Australia, International Conference on Deformation of Crustal Rocks 19, p. 37-38.

Pearson, P. J., Holcombe, R. J., and Page, R. W., 1992, Synkinematic emplacement of the Middle Proterozoic Wonga Batholith into a mid-crustal shear zone, Mount Isa Inlier, Queensland, Australia: Australian Geological Survey Organisation Bulletin 243, p. 289-328.

Perchuk, L. L. and Aranovich, L. Y., 1984, Improvement in biotite-granitic geothermometry; correction for amount of fluorine in biotite (in Russian): Doklady Akademii Nauk SSSR; v. 277, p. 471-475.

Perkins, C., and Wyborn, L. A. I., 1998, Age of Cu-Au Mineralisation, Cloncurry district, eastern Mt Isa Inlier, Queensland, as determined by 40Ar/39Ar Dating: Australian Journal of Earth Sciences, v. 45, p. 233-246.

Perring, C. S., Pollard, P. J., and Nunn, A. J., 2001, Petrogenesis of the Squirrel Hills granite and associated magnetite-rich sill and vein complex: Lightning creek prospect, Cloncurry district, Northwest Queensland: Precambrian Research, v. 106, p. 213-238.

Perring, C. S., Pollard, P. J., Dong, G., Nunn, A. J., and Blake, K. L., 2000, The Lightning Creek sill complex, Cloncurry district, northwest Queensland: a source of fluids for Fe oxide Cu-Au mineralization and sodic-calcic alteration: Economic Geology, v. 95, p. 1067-1089.

Peter, J. M., and Goodfellow, W. D., 1996, Mineralogy, bulk and rare earth element geochemistry of massive sulphide-associated hydrothermal sediments of the Brunswick horizon, Bathurst mining camp, New Brunswick: Canadian Journal of Earth Sciences, v. 33, p. 252-283.

Phillips, G. N., Archibald, N. J., and Wall, V. J., 1985, Metamorphosed high-Fe tholeiites: their alteration and relationship to sulphide mineralization, Broken Hill, Australia: Transactions of the Geological Society of South Africa, v. 88, p. 49-59.

Phillips, G. N., Williams, P. J., and de Jong, G., 1994, The nature of metamorphic fluids and significance for metal exploration, *in* Parnell, J., ed., Geofluids: Origin, Migration and Evolution of Fluids in Sedimentary Basins, Geological Society of London Special Publication No. 78, p. 55-68.

Plimer, I. R., 1979, Sulphide rock zonation and hydrothermal alteration at Broken Hill, Australia: Institution of Mining and Metallurgy, Transactions, v. 88, p. B161-B176.

Plimer, I. R., 1980, Hydrothermal mobilization of silver during retrograde metamorphism at Broken Hill, Australia: Neues Jahrbuch fuer Mineralogie, Monatshefte, v. 10, p. 433-439.

Plimer, I. R., 1984, The mineralogical history of the Broken Hill Lode, NSW: Australian Journal of Earth Sciences, v. 31, p. 379-402.

Plimer, I. R., 1985, Broken Hill Pb-Zn-Ag deposit - a product of mantle metasomatism: Mineralium Deposita, v. 20, p. 147-153.

Plimer, I. R., 1986, Sediment-hosted exhalative Pb-Zn deposits - products of contrasting ensialic rifting: Geological Society of South Africa, Transactions, v. 89, p. 57-73.

Plimer, I. R., 1987, Remobilization in high-grade metamorphic environments: Ore Geology Reviews, v. 2, p. 231-245.

Plimer, I. R., 1991, Broken Hill type deposits: James Cook University, Economic Geology Research Unit, Contribution 38, p. 60-76.

Plumb, K. A., Derrick, G. M., and Wilson, I. H., 1980, Precambrian geology of the McArthur River-Mount Isa region, northern Australia, *in* Henderson, R. A., and Stephenson, P. J., eds., The Geology and Geophysics of Northeastern Australia: Geological Society of Australia, Queensland Division, p. 71-88.

Pollard, P. J., 1997, AMIRA P438 Cloncurry base metals and gold: executive summary: Economic Geology Research Unit, James Cook University, AMIRA P438 Final Report, v. 1, p. 1-2.

Pollard, P. J., 2001, Sodic(-calcic) alteration in Fe-oxide-Cu-Au districts: an origin via unmixing of magmatic H2O-CO2-NaCl ± CaCl2-KCl fluids: Mineralium Deposita, v. 36, p. 93-100.

Pollard, P. J., and Perkins, C., 1997, 40Ar/39Ar geochronology of alteration and Cu-Au-Co mineralization in the Cloncurry district, Mount Isa Inlier, Australia: Economic Geology Research Unit, AMIRA P438 Final Report, v. 1, p. 3-1 - 3-40.

Pollard, P. J., Blake, K. L., and Dong, G., 1997, Proterozoic Cu-Au-Co and Pb-Zn-Ag mineralization in the Cloncurry district, eastern Mount Isa Inlier, Australia: constraints on fluid sources from mineralogical, fluid inclusion and stable isotope data: Economic Geology Research Unit, James Cook University, AMIRA P438 Final Report, v. 1, p. 7-1 - 7-50.

Pollard, P. J., Mark, G., and Mitchell, L. C., 1998, Geochemistry of post-1540 Ma granites in the Cloncurry district, northwest Queensland: Economic Geology, v. 93, p. 1330-1344.

Potma, W. A., and Betts, P. G., 1997, The role of basin inversion in the evolution of the Mitakoodi Culmination, *in* Aillères, L., and Betts, P. G., eds., Structural Elements of the Eastern Successions - a field guide illustrating the structural geology of the eastern Mount Isa terrane, Australia, Australian Crustal Research Centre, Technical Publication 63, p. 75-90.

Pottorf, R. J., and Barnes, H. L., 1983, Mineralogy, geochemistry, and ore genesis of hydrothermal sediments from the Atlantis II Deep, Red Sea: Economic Geology, v. Monograph 5, p. 198-223.

Pringle, V. E-J., 1999, The nature, distribution and paragenesis of the Inveravon Lode, Northern Zone, Cannington Ag-Pb-Zn deposit, NW Queensland - a geological framework: Unpublished Honours thesis, James Cook University, 140 p.

Ramdohr, P., 1950, The ore deposits of Broken Hill in N.S.W. in the light of new geological knowledge and ore microscope investigations: Heidelberger Beitrage zur Mineralogie und Petrographie, v. 2.

Ramsden, A. R., 1998, The structure, alteration and mineralisation of the Sandy Creek Cu-Au deposit: Unpublished BSc (Hons) thesis, University of Tasmania, Hobart, 90 p.

Randell, J., 1993, Maronan Cu-Pb-Zn-Ag-Au prospect, *in* Derrick, G., ed., Core Shack Explanatory Notes, AMF Course 832/93, Australian Mineral Foundation, Glenside, South Australia, p. 24-28.

Richards, J. R., 1975, Lead isotope data on three North Australian galena localities: Mineralium Deposita, v. 10, p. 287-301.

Richmond, J. M., 1994, The garnet-quartz-sillimanite rich envelope at the Cannington Ag-Pb-Zn deposit, NW Queensland: Unpublished B.Sc. Honours thesis, Queensland, James Cook University, 80 p.

Richmond, J. M., Chapman, L. H., and Williams, P. J., 1996a, Two phases of garnet alteration at the Cannington Ag-Pb-Zn deposit, NW Queensland: James Cook University, Economic Geology Research Unit, Contribution 55, p. 113-117.

Richmond, J. M., Chapman, L. H., and Williams, P. J., 1996b, Post-peak metamorphic metasomatism in Broken Hill-type Pb-Zn-Ag deposits: evidence from Cannington, NW Queensland, Australia: 28th Annual Meeting, Geological Society of America, Abstracts, v. 28, p. 474.

Roache, M. W., 1996, The geology, timing of mineralisation, and genesis of the Menninnie Dam Zn-Pb-Ag deposit, Eyre Peninsula, South Australia: Unpublished PhD thesis, University of Tasmania, Hobart.

Robinson, P., Higgins, N. C. and Jenner-George, A., 1986, Determination of rare-earth elements, yttrium and scandium in rocks by an ion exchange-X-ray fluorescence technique: Chemical Geology, v. 55, p. 121-137.

Roche, M. T., 1994, The Cannington silver lead zinc deposit - at feasibility: Australasian Institute of Mining and Metallurgy (AusIMM) Annual Conference, Publication Series No. 5/94, p. 193-197.

Rubenach, M. J., and Barker, A. J., 1998, Metamorphic and metasomatic evolution of the Snake Creek Anticline, Eastern Succession, Mt Isa Inlier: Australian Journal of Earth Sciences, v. 45, p. 363-372.

Rubenach, M. J., and Foster, D. R. W., 1996, Interrelationships between multiple metamorphic episodes, high strain zones, granulites and metasomatism, Mount Isa Inlier, *in* Buick, I. S., and Cartwright, I., eds., Evolution of Metamorphic Belts, Geological Society of Australia, Abstracts 42, p. 40-41.

Rubenach, M. J., and Foster, D. R. W., 1997, Metamorphism and metasomatism in the Mount Isa Inlier, *in* Aillères, L., and Betts, P. G., eds., Structural Elements of the Eastern Successions - a field guide illustrating the structural geology of the eastern Mount Isa terrane, Australia, Australian Crustal Research Centre, Technical Publication 63, p. 91-94.

Rumble, D. and Hoering, T. C., 1986, Carbon isotope geochemistry of graphite vein deposits from New Hampshire, USA: Geochimica et Cosmochimica Acta, v. 50, p. 1239-1247.
Rumble, D., Duke, E. F. and Hoering, T. L., 1986, Hydrothermal graphite in New Hampshire: evidence of carbon mobility during regional metamorphism: Geology, v. 14, p. 452-455.
Russell, R. D., and Farquhar, R. M., 1960, Lead isotopes in geology: New York, U.S.A., Interscience, 243 p.
Ryburn, R. J., Wilson, I. H., Grimes, K. G., and Hill, R. M., 1988, Cloncurry, Queensland: 1:100,000 Geological Map Commentary: Bureau of Mineral Resources, Australia, 30 p.
Sangster, D. F., 2002, The role of dense brines in the formation of vent-distal sedimentary-exhalative (SEDEX) lead-zinc deposits: field and laboratory evidence: Mineralium Deposita, v. 37, p. 149-157.
Sato, T., 1972, Behaviours of ore-forming solutions in seawater: Mining Geology, v. 22, p. 31-42.
Sawkins, F. J., and Kowalik, J., 1981, The source of ore metals at Buchans: magmatic versus leaching models, *in* Swanson, E. A., Strong, D. F., and Thurlow, J. G., eds., The Buchans Orebodies: Fifty Years of Geology and Mining: Toronto, Canada, Geological Association of Canada Special Paper, 22, p. 255-267.
Schidlowski, M., 1987, Application of stable carbon isotopes to early biochemical evolution on Earth: Annual Review of Earth and Planetary Sciences, v. 15, p. 47-72.
Schidlowski, M., 2001, Carbon isotopes as biogeochemical recorders of life over 3.8 Ga of Earth history: evolution of a concept: Precambrian Research, v. 106, p. 117-134.
Schwandt, C. S., Papike, J. J., Shearer, C. K. and Brearley, A. J., 1993, A SIMS investigation of REE chemistry of garnet in garnetite associated with the Broken Hill Pb-Zn-Ag orebodies, Australia: Canadian Mineralogist; v. 31, p. 371-379.
Sheehan, P., 1994, The structural geology of the host rocks to Ag-Pb-Zn mineralisation at BHP's Cannington deposit, Eastern Fold Belt, north west Queensland: Unpublished Honours thesis, Monash University, 96 p.
Shriver, N. A. and MacLean, W. H., 1993, Mass, volume and chemical changes in the alteration zone at the Norbec mine, Noranda, Quebec: Mineralium Deposita, v. 28, p. 157-166.
Sinton, J. M., Wilson, D. S., Christie, D. M., Hey, R. N., and Delaney, J. R., 1983, Petrologic consequences of rift propagation on oceanic spreading ridges: Earth and Planetary Science Letters, v. 62, p. 193-207.
Skrzeczynski, R. H., 1993, From concept to Cannington: a decade of exploration in the Eastern Succession: Symposium on Recent Advances in the Mount Isa Block, Australian Institute of Geoscientists, Bulletin 13, p. 35-38.
Slack, J. F., Herriman, N., Barnes, R. G. and Plimer, I. R., 1984, Stratiform tourmalinites in metamorphic terranes and their geologic significance: Geology, v. 12, p. 713-716.
Slack, J.F., Palmer, M.R. and Stevens, B.P.J., 1989, Boron isotope evidence for the involvement of non-marine evaporites in the origin of the Broken Hill ore deposits: Nature, v. 342, p. 913-916.
Smith, M. J., 1999, Geochemical and paragenetic characterisation of the "Core Amphibolite", Cannington Ag, Pb, Zn Mine, northwestern Queensland: Unpublished Honours thesis, James Cook University, 91 p.
Southgate, P. N., Bradshaw, B. E., Domagala, J., Jackson, M. J., Idnurm, M., Krassay, A. A., Page, R. W., Sami, T. T., Scott, D. L., Lindsay, J. F., McConachie, B. A., and Tarlowski, C. Z., 2000, Chronostratigraphic basin framework for Palaeoproterozoic rocks (1730-1575 Ma) in northern Australia and implications for base-metal mineralisation: Australian Journal of Earth Sciences, v. 47, p. 461-483.
Southgate, P. N., Bradshaw, B. E., Domagala, J., Jackson, M. J., Idnurm, M., Krassay, A. A., Page, R. W., Sami, T. T., Scott, D. L., Lindsay, J. F., McConachie, B. A., and Tarlowski, C. Z., 2000, Chronostratigraphic basin framework for Palaeoproterozoic rocks (1730-1575 Ma) in northern Australia and implications for base-metal mineralisation: Australian Journal of Earth Sciences, v. 47, p. 461-483.
Southgate, P. N., Bradshaw, B. E., Domagala, J., Jackson, M. J., Idnurm, M., Krassay, A. A., Page, R. W., Sami, T. T., Scott, D. L., Lindsay, J. F., McConachie, B. A., and Tarlowski, C. Z., 2000, Chronostratigraphic basin framework for Palaeoproterozoic rocks (1730-1575 Ma) in northern Australia and implications for base-metal mineralisation: Australian Journal of Earth Sciences, v. 47, p. 461-483.
Spear, F. S., 1980, NaSi - CaAl exchange equilibrium between plagioclase and amphibole: Contributions to Mineralogy and Petrology; v. 72, p. 33-41.
Spear, F. S., 1981, An experimental study of hornblende stability and compositional variability in amphibolite: American Journal of Science, v. 281, p. 697-734.

Spear, F. S., 1993, Metamorphic phase equilibria and pressure-temperature-time paths: Mineralogical Society of America Monograph, Washington D.C., U.S.A., p. 799.
Spear, F. S., Kohn, M. J., and Cheney, J. T., 1999, P-T paths from anatectic pelites: Contributions to Mineralogy and Petrology, v. 134, p. 17-32.
Spear, F. S., Peacock, S. M., Kohn, M. J., Florence, F. P. and Menard, T., 1991, Computer programs for petrologic P-T-t path calculations: American Mineralogist, v. 76, p. 2009-2012.
Spikings, R., 1999, Thermochronology and tectonics of the Mount Isa, Murphy and Georgetown Inliers, northeastern Australia: Unpublished PhD thesis, La Trobe University, Melbourne, Victoria.
Spry, A., 1969, Metamorphic textures: Oxford, Pergamon Press.
Spry, P. G., 1987, The chemistry and origin of zincian spinel associated with the Aggeneys Cu-Pb-Zn-Ag deposits, Namaqualand, South Africa: Mineralium Deposita, v. 22, p. 262-268.
Spry, P. G., 2000, Sulfidation and oxidation haloes as guides in the exploration for metamorphosed massive sulfide ores, *in* Spry, P. G., Marshall, B., and Vokes, F. M., eds., Metamorphosed and metamorphogenic ore deposits., Reviews in Economic Geology, v. 11, p. 149-162.
Spry, P. G., and Wonder, J. D., 1989, Manganese-rich garnet rocks associated with the Broken Hill lead-zinc-silver deposit, New South Wales, Australia: Canadian Mineralogist, v. 27, p. 275-292.
Stacey, J. S., and Kramers, J. D., 1975, Approximation of terrestrial lead isotope evolution by a two-stage model: Earth and Planetary Science Letters, v. 26, p. 207-221.
Stanton, R. L., 1965, Mineral interfaces in stratiform ores: Transactions of the Institution of Mining and Metallurgy, v. 74, part 2, p. 45-79.
Stanton, R. L., 1967, Composition and textures of conformable ores as guides to their formation: Proceedings Commonwealth Mining and Metallurgical Congress, 6, p. 1263-1268.
Stanton, R. L., 1976, Petrochemical studies of the ore environment at Broken Hill, New South Wales, 2: regional metamorphism of banded iron formations and their immediate associates: Institution of Mining and Metallurgy, Transactions, Section B, Applied Earth Science, v. 85, p. B118-B131.
Stanton, R. L., 1989, The precursor principle and the possible significance of stratiform ores and related chemical sediments in the elucidation of processes of regional metamorphic mineral formation: Philosophical Transactions of the Royal Society of London, v. A 328, p. 529-646.
Stanton, R. L., and Gorman, H., 1968, A phenomenological study of grain boundary migration in some common sulfides: Economic Geology, v. 63, p. 907-923.
Stanton, R. L., and Russell, R. D., 1959, Anomalous leads and the emplacement of lead sulfide ores: Economic Geology, v. 54, p. 588-607.
Strain, H. L., 1993, Gold mineralisation in the Cannington Ag-Pb-Zn deposit, northwest Queensland: Unpublished Honours thesis, James Cook University, Townsville, 118 p.
Sun, S.-s., Carr, G. R., and Page, R. W., 1996, A continued effort to improve lead-isotope model ages: Australian Geological Survey Organisation Research Newsletter, v. 24, p. 19-20.
Sun, S.-s., Page, R., and Carr, G., 1994, Lead-isotope-based stratigraphic correlations and ages of Proterozoic sediment-hosted Pb-Zn deposits in the Mount Isa Inlier: Australian Geological Survey Organisation Research Newsletter, v. 20, p. 1-2.
Sverjensky, D. A., 1984, Europium redox equilibria in aqueous solution: Earth and Planetary Science Letters, v. 67, p. 70-78.
Taylor, S. R., and McLennan, S. M., 1985, The Continental Crust: Its Composition and Evolution: Oxford, Blackwell, 312 p.
Taylor, S. R., Rudnick, R. L., McLennan, S. M., and Erikson, K. A., 1986, Rare earth element patterns in Archean high-grade metasediments and their tectonic significance: Geochimica et Cosmochimica Acta, v. 50, p. 2267-2279.
Thompson, T. B., and Beaty, D. W., 1990, Geology and the origin of ore deposits in the Leadville District, Colorado: Part II, Oxygen, hydrogen, carbon, sulfur, and lead isotope data and the development of a genetic model: Economic Geology, Monograph 7, p. 156-179.
Turner, F. J., 1981, Metamorphic petrology; mineralogical, field, and tectonic aspects. 2 ed: Washington, DC, United States | McGraw-Hill Book Co. New York, NY, United States, Hemisphere Pub. Corp., 524 p.

Valley, J. W., 1986, Stable isotope geochemistry of metamorphic rocks, *in* Valley, J. W., Taylor-Hugh, P. J., and O Neil, J. R., eds., Stable isotopes in high temperature geological processes, 16. Reviews in Mineralogy: Washington DC, Mineralogical Society of America, p. 445-489.

Valley, J. W., and O'Neil, J. R., 1981, $^{13}C/^{12}C$ exchange between calcite and graphite: a possible thermometer in Grenvilee marbles: Geochimica et Cosmochimica Acta, v. 45, p. 411-419.

Valley, J. W., Bohlen, S. R., Essene, E. J. and Lamb, W., 1990, Metamorphism in the Adirondacks; II, The role of fluids: Journal of Petrology; v. 31, p. 555-596.

van der Pluijm, B. A. and Marshak, S., 1997, Earth structure: an introduction to structural geology and tectonics: McGraw-Hill, U.S.A., p. 495.

Vander Auwera, J. and Andre, L., 1991, Trace elements (REE) and isotopes (O, C, Sr) to characterize the metasomatic fluid sources: evidence from the skarn deposit (Fe, W, Cu) of Traversella (Ivrea, Italy): Contributions to Mineralogy and Petrology, v. 106, p. 325-339.

Vaughan, J. P. and Stanton, R. L., 1986, Sedimentary and metamorphic factors in the development of the Pegmont stratiform Pb-Zn deposit, Queensland, Australia: Institution of Mining and Metallurgy, Transactions, Section B; v. 95, p. B94-B121.

Vernon, R. H., 1979, Formation of late sillimanite by hydrogen metasomatism (base-leaching) in some high-grade gneisses: Lithos, v. 12, p. 143-152.

Vernon, R. H., 1987, Growth and concentration of fibrous sillimanite related to heterogeneous deformation in K-feldspar-sillimanite metapelites: Journal of Metamorphic Petrology; v. 5, p. 51-68.

Vernon, R. H., Flood, R. H. D. and Arcy, W. F., 1987, Sillimanite and andalusite produced by base-cation leaching and contact metamorphism of felsic igneous rocks: Journal of Metamorphic Petrology; v. 5, p. 439-450.

Vokes, F. M., 1969, A review of the metamorphism of sulphide deposits: Earth Science Reviews, v. 5, p. 99-143.

Wada, H., and Suzuki, K., 1983, Carbon isotopic thermometry calibrated by dolomite-calcite solvus temperatures: Geochimica et Cosmochimica Acta, v. 47, p. 697-706.

Walters, S. and Bailey, A., 1998, Geology and mineralization of the Cannington Ag-Pb-Zn deposit: An example of Broken Hill-type mineralization in the Eastern succession, Mount Isa Inlier, Australia: Economic Geology; v. 93, p. 1307-1329.

Walters, S. G., 1994a, Geology and lode characterisation: Cannington Southern Zone: Brisbane, BHP Minerals, p. 367.

Walters, S. G., 1994b, Lithogeochemical alteration haloes associated with Broken Hill Type Pb-Zn-Ag deposits: new geochemical tools for exploration: Brisbane, Unpublished BHP Minerals report, p. 157.

Walters, S. G., 1996, Broken Hill Type Pb-Zn-Ag deposits: geological characteristics and exploration models: *in* New Developments *in* Broken Hill Type Deposits, J. Pongratz and G. Davidson, eds., Centre for Ore Deposit and Exploration Studies, supplement to Special Publication No. 1, University of Tasmania.

Walters, S. G., 1998, Broken Hill-type deposits: Australian Geological Survey Organisation (AGSO) Journal of Australian Geology & Geophysics, v. 17(4), p. 229-237.

Walters, S. G., 2000, Broken Hill Type Pb-Zn-Ag deposits, Broken Hill type Pb-Zn-Ag deposits and Proterozoic Cu-Au deposits: Hobart, Tasmania, Ore Deposit Models and Exploration Strategies Short Course Manual, Centre for Ore Deposit Research, University of Tasmania, p. 1.1-1.11.

Walters, S. G., and Bailey, A., 1996, Geology and mineralisation of the Cannington Ag-Pb-Zn deposit - an example of Broken Hill Type mineralisation in the eastern succession of the Mount Isa Inlier, NW Queensland: MIC'96 Conference, extended Abstracts, Economic Geology Research Unit, James Cook University, contribution Series No. 55, p. 137-138.

Wang, S. Q., and Williams, P. J., 2001, Geochemistry and origin of Proterozoic skarns at the Mount Elliott Cu-Au(-Co-Ni) deposit, Cloncurry district, NW Queensland, Australia: Mineralium Deposita, v. 36, p. 109-124.

Webster, A. E., 1994, The structure and stratification of Lead Lode, Southern Operations, Broken Hill, NSW, Australia: Unpublished MSc thesis, James Cook University, 255 p.

Webster, A. E., 1996, A detailed description of the Broken Hill deposit - lessons from the ore fabrics: University of Tasmania, Centre for Ore Deposit and Exploration Studies, Special Publication 1, p. 95-103.

Wellman, P., 1992, Structure of the Mount Isa region inferred from gravity and magnetic anomalies: *in* Stewart, A.J. and Blake, D.H., eds., Detailed Studies of the Mount Isa Inlier, Australian Geological Survey Organisation Bulletin 243, p. 15-27.

Williams, M. L., and Grambling, J. A., 1990, Manganese, ferric iron, and the equilibrium between garnet and biotite: American Mineralogist, v. 75, p. 886-908.
Williams, P. J., 1995a, Metalliferous deposits in the Proterozoic rocks of the Cloncurry District, NW Queensland: a review of the deposits and their geological context based on published works and theses: Economic Geology Research Unit, James Cook University, AMIRA P438 1995 Annual Report, p. 2-1 - 2-70.
Williams, P. J., 1995b, Paragenesis and paragenetic sequence of Cloncurry ore systems: Economic Geology Research Unit, James Cook University, AMIRA P438 1995 Annual Report, p. 3-1 - 3-35.
Williams, P. J., 1998a, Magmatic iron enrichment in high-iron metatholeiites associated with 'Broken Hill-type' Pb-Zn-Ag deposits, Mt Isa Eastern Succession: Australian Journal of Earth Sciences, v. 45, p. 389-396.
Williams, P. J., 1998b, Metalliferous economic geology of the Mt Isa Eastern Succession, Queensland: Australian Journal of Earth Sciences, v. 45, p. 329-341.
Williams, P. J., 1998c, An introduction to the metallogeny of the McArthur River-Mount Isa-Cloncurry minerals province: Economic Geology, v. 93, p. 1120-1131.
Williams, P. J., and Baker, T., 1995, A regional-scale association of skarn alteration and base metal deposits in the Cloncurry district, Mount Isa Inlier, Queensland, Australia: Transactions of the Institution of Mining and Metallurgy, v. 104, p. B187-196.
Williams, P. J., and Blake, K. L., 1993, Alteration in the Cloncurry District: James Cook University, Economic Geology Research Unit Contribution 49, p. 75 p.
Williams, P. J., and Heinemann, M., 1993, Maramungee: a Proterozoic Zn skarn in the Cloncurry district, Mount Isa Inlier, Queensland, Australia: Economic Geology, v. 88, p. 1114-1134.
Williams, P. J., and Pendergast, W. J., 1996, Post metamorphic K-silicate-garnet alteration in the wall rocks of the Pegmont Pb-Zn deposit, Cloncurry district: James Cook University, Economic Geology Research Unit, Contribution 55, p. 146-148.
Williams, P. J., and Phillips, G. N., 1992, Cloncurry Mapping Project 1990: Geology of the Selwyn Range (McKinlay River and Maramungee Creek areas): James Cook University, Economic Geology Research Unit Contribution 40, 21 p.
Williams, P. J., Chapman, L. H., and Richmond, J., 1997, Alteration in Broken Hill-type deposits: evidence from Cannington: New developments in research for ore deposit exploration - 3rd national conference of the Specialist Group in Economic Geology, Geological Society of Australia, Abstracts 44, p. 74.
Williams, P. J., Chapman, M. H., Richmond, J., Baker, T., Heinemann, M., and Pendergast, W. J., 1996, Significance of late orogenic metasomatism in the Broken Hill-type deposits of the Cloncurry district, NW Queensland, *in* Pongratz, J., and Davidson, G., eds., New Developments in Broken Hill Type Deposits, University of Tasmania, Centre for Ore Deposit and Exploration Studies, Special Publication No. 1, p. 119-132.
Williams, P. J., Dong, G., Pollard, P. J., Ryan, C. G., Chapman, L. H., and Pendergast, K., 1998b, Two-stage, dual source origin of Broken Hill-type Pb-Zn-Ag deposits: Geoscience for the New Millennium, Geological Society of Australia, Abstracts 49, p. 470.
Williams, P. J., Pendergast, W. J., and Dong, G. Y., 1998, Late orogenic alteration in the wall rocks of the Pegmont Pb-Zn deposit, Cloncurry District, Queensland, Australia: Economic Geology, v. 93, p. 1180-1189.
Williams, P. R., 1989, Nature and timing of early extensional structures in the Mitakoodi Quartzite, Mount Isa Inlier, northwest Queensland: Australian Journal of Earth Sciences, v. 36, p. 283-296.
Wilson, J. C., and McBride, E. F., 1988, Compaction and porosity evolution of Pliocene sandstones, Ventura Basin, California: American Association of Petroleum Geologists Bulletin, v. 72, p. 664-681.
Wintsch, R. P. and Andrews, M. S., 1988, Deformation induced growth of sillimanite; "stress" minerals revisited: Journal of Geology; v. 96, p. 143-161.
Withnall, I. W., 1985, Geochemistry and tectonic significance of Proterozoic mafic rocks from the Georgetown Inlier, north Queensland: Bureau of Mineral Resources, Journal of Australian Geology and Geophysics, v. 9, p. 339-351.
Wood, S. A., and Williams-Jones, A. E., 1994, The aqueous geochemistry of the rare-earth elements and yttrium 4. Monazite solubility and REE mobility in exhalative massive sulfide-depositing environments: Chemical Geology, v. 115, p. 47-60.
Woodhead, J. D., Volker, F., and McCulloch, M. T., 1995, Routine lead isotope determinations using a lead-207-lead-204 double spike: a long term assessment of analytical precision and accuracy: Analyst, v. 120, p. 35-39.

Worner, H. K., and Mitchell, R. W., 1983, Minerals of Broken Hill: Melbourne, Australian Mining and Smelting Limited, Griffin Press Limited, 259 p.

Wright, J. V., Haydon, R. C., and McConachy, G. W., 1987, Sedimentary model for the giant Broken Hill Pb-Zn deposit, Australia: Geology, v. 15, p. 598-602.

Wright, J. V., Haydon, R. C., and McConachy, G. W., 1993, Sedimentary analysis and implications for Pb-Zn mineralisation at Broken Hill, Australia: James Cook University, Economic Geology Research Unit, Contribution 48, 91 p.

Wyborn, L. A. I., 1988, Petrology, geochemistry and origin of a major Australian 1880-1840 Ma felsic volcano-plutonic suite: a model for intracontinental felsic magma generation: Precambrian Research, v. 40-41, p. 37-60.

Wyborn, L. A. I., 1992, The Williams and Naraku batholiths, Mt. Isa Inlier: an analogue of the Olympic Dam granites?: Bureau of Mineral Resources Research Newsletter 16, p. 13-14.

Wyborn, L. A. I., and Page, R. W., 1983, The Proterozoic Kalkadoon and Ewen batholiths, Mount Isa Inlier, Queensland; source, chemistry, age, and metamorphism: Bureau of Mineral Resources, Journal of Australian Geology and Geophysics, v. 8, p. 53-69.

Wyborn, L. A. I., Page, R. W., and McCulloch, M. T., 1988, Petrology, geochronology and isotope geochemistry of the post-1820 Ma granites of the Mount Isa Inlier: mechanisms for the generation of Proterozoic anorogenic granites: Precambrian Research, v. 40-41, p. 509-541.

Wyborn, L. A. I., Page, R. W., and Parker, A. J., 1987, Geochemical and geochronological signatures in Australian Proterozoic igneous rocks, *in* Pharaoh, T. C., Beckinsale, R. D., and Rickard, D. T., eds., Geochemistry and Mineralization of Proterozoic Volcanic Suites: Geological Society Special Publications: London, United Kingdom, Geological Society of London Special Publications, 33, p. 377-394.

Wyborn, L. A. I., Wyborn, D., Warren, R. G., and Drummond, B. J., 1992, Proterozoic granite types in Australia: implications for lower crust composition, structure and evolution, *in* Brown, P. E., and Chappell, B. W., eds., The second Hutton Symposium on the Origin of Granites and Related Rocks, proceedings, Geological Society of America, Special Paper 272, p. 201-209.

Wyborn, L., 1998, Younger ca 1500 Ma granites of the Williams and Naraku Batholiths, Cloncurry district, eastern Mt Isa Inlier: geochemistry, origin, metallogenic significance and exploration indicators: Australian Journal of Earth Sciences, v. 45, p. 397-411.

Xu, G. and Pollard, P. J., 1999, Origin of CO_2-rich fluid inclusions in synorogenic veins from the Eastern Mount Isa Fold Belt, NW Queensland, and their implications for mineralization: Mineralium Deposita; v. 34, p. 395-404.

Yardley, B. W. D., 1981, A note on the composition and stability of Fe-staurolite: Nueus Jahrbuch für Mineralogie Monatschafte 1981, p. 127-132.

Yardley, B. W. D., 1989. An introduction to metamorphic petrology: New York, John Wiley and Sons, 248 p.

Zartman, R. E., and Doe, B. R., 1981, Plumbotectonics - the model: Tectonophysics, v. 75, p. 135-162.

Zartman, R. E., and Stacey, J. S., 1971, Lead isotopes and mineralization ages in Belt Supergroup rocks, northwestern Montana and northern Idaho: Economic Geology, v. 66, p. 849-860.

Zhu, C., and Sverjensky, D. A., 1991, Partitioning of F-Cl-OH between minerals and hydrothermal fluids: Geochimica et Cosmochimica Acta, v. 55, p. 1837-1858.

Zhu, C., and Sverjensky, D. A., 1992, F-Cl-OH partitioning between biotite and apatite: Geochimica et Cosmochimica Acta, v. 56, p. 3435-3467.

Zierenberg, R. A., 1990, Deposition of metalliferous sediment beneath a brine pool in the Altantis II Deep, Red Sea, *in* McMurry, G. R., ed., Gorda Ridge: a seafloor spreading center in the United States' exclusive economic zone: New York, Springer-Verlag, p. 131-142.

Zierenberg, R. A., and Shanks, W. C. I., 1988, Isotopic studies of epigenetic features in metalliferous sediment, Atlantis II Deep, Red Sea: Canadian Mineralogist, v. 26, p. 737-753.

Appendix 1
Electron microprobe analytical data

ANALYTICAL PROCEDURES

All quantitative analyses were conducted on a Cameca SX50 electron microprobe located in the Central Science Laboratory, University of Tasmania under the guidance of Dr David Steele. A beam current of 25nA and acceleration voltage of 15kV was used for all minerals. A beam spot size of 3μm was used for all minerals except for amphibole and plagioclase where a spot size of 7-8μm was employed.

Actinolite

Cations calculated on the basis of 23 (O) and 2 (OH, F, Cl)
All Fe as FeO

	Hedenbergite ore, fluorite-rich (Colwell)					
Wt %	sz037-23a 1_actinol1	sz037-23a 1_actinol2	sz037-23a 1_actinol3	sz037-23a 2_actinol1	sz037-23a 3_actinol1	sz037-23a 3_actinol2
SiO2	49.02	45.98	48.1	48.81	48.94	49.01
TiO2	0.02	0	0.03	0	0.02	0
Al2O3	0.03	0.02	0.01	0.04	0.01	0
Cr2O3	0.03	0	0	0.03	0.01	0.03
Fe2O3(c)	1.25	31.6	22.52	2.11	3.55	2.25
FeO(c)	33.35	9.08	16.54	32.25	31.19	31.53
MnO	3.09	5.58	5.04	3.09	3.44	3.69
MgO	0.1	0.35	0.26	0.19	0.2	0.2
CaO	11.7	4.95	7.13	11.32	11.14	11.25
Na2O	0.01	0.01	0.03	0.03	0.05	0.03
K2O	0.01	0.02	0	0	0.01	0
BaO	0	0	0	0	0.1	0.04
SrO	0.03	0	0	0	0	0
SO3	0	0.38	0.01	0	0.01	0
F	0.01	0	0	0	0	0
Cl	0.02	0.13	0.03	0.01	0.01	0.02
H2O(c)	1.85	1.88	1.92	1.85	1.87	1.85
O=F	0	0	0	0	0	0
O=Cl	0	0.03	0.01	0	0	0.01
Sum Ox%	100.52	99.96	101.61	99.74	100.53	99.91
Cations						
Si	7.896	7.21	7.481	7.898	7.856	7.911
Ti	0.002	0	0.004	0	0.003	0
Al/Al IV	0.006	0.005	0.002	0.007	0.001	0
Al VI	0	0	0	0	0	0
Cr	0.003	0	0	0.004	0.001	0.004
Fe3+	0.152	3.728	2.636	0.257	0.429	0.273
Fe2+	4.492	1.191	2.152	4.364	4.187	4.256
Mn2+	0.422	0.741	0.664	0.424	0.468	0.505
Mg	0.025	0.081	0.06	0.046	0.049	0.048
Ca	2.02	0.832	1.188	1.962	1.916	1.945
Na	0.002	0.003	0.01	0.01	0.015	0.008
K	0.002	0.003	0	0	0.003	0.001
Ba	0	0	0	0	0.006	0.002
Sr	0.003	0	0	0	0	0
S	0	0.045	0.002	0	0.001	0
F	0.004	0	0	0	0	0
Cl	0.006	0.034	0.009	0.004	0.002	0.007
OH	1.99	1.966	1.991	1.996	1.998	1.993
Sum Cat#	17.024	15.838	16.198	16.972	16.933	16.954
XMg	0.005	0.064	0.027	0.01	0.011	0.011

Actinolite

Cations calculated on the basis of 23 (O) and 2 (OH, F, Cl)
All Fe as FeO

	Hedenbergite ore, minor fluorite (Kheri)							
Wt %	sz028-6 3_bladed acti-nol1	sz028-6 3_bladed acti-nol2	sz028-6 5_coarse bladed actinol1	sz028-6 5_coarse bladed actinol2	sz028-6 5_fine bladed actinol1	sz028-6 5_fine bladed actinol2	sz028-6 4_ps1	sz028-6 4_ps2
SiO2	48.77	48.75	48.51	48.76	48.45	47.87	49.3	48.96
TiO2	0	0	0	0.02	0.01	0	0.01	0
Al2O3	0.02	0.03	0.14	0.26	0.26	0.61	0.49	0.43
Cr2O3	0	0	0	0.03	0	0.07	0	0.01
Fe2O3(c)	0.13	0.15	0	0.39	0.01	0.63	0	0
FeO(c)	35.49	35.73	35.78	34.28	35.75	34.99	34.32	34.26
MnO	0.85	0.76	0.78	1.6	0.71	0.77	0.83	0.84
MgO	0.3	0.3	0.2	0.48	0.24	0.24	0.88	0.9
CaO	11.61	11.74	11.88	11.58	11.74	11.63	11.81	11.83
Na2O	0.06	0.04	0.05	0.03	0.03	0.07	0.06	0.08
K2O	0.01	0	0.03	0.17	0.07	0.07	0.06	0.06
BaO	0	0	0.08	0	0.01	0	0.03	0
SrO	0	0	0	0	0	0	0	0
SO3	0	0	0	0.02	0	0	0	0
F	0.08	0.06	0.07	0.06	0.05	0.08	0.06	0.05
Cl	0.13	0.16	0.2	0.42	0.23	0.28	0.22	0.22
H2O(c)	1.77	1.77	1.75	1.72	1.75	1.72	1.78	1.77
O=F	0.03	0.03	0.03	0.02	0.02	0.03	0.03	0.02
O=Cl	0.03	0.04	0.05	0.09	0.05	0.06	0.05	0.05
Sum Ox%	99.16	99.42	99.41	99.69	99.24	98.95	99.77	99.35
Cations								
Si	7.951	7.935	7.913	7.908	7.909	7.838	7.932	7.919
Ti	0	0	0	0.002	0.002	0.001	0.001	0
Al/Al IV	0.004	0.005	0.027	0.05	0.051	0.118	0.068	0.081
Al VI	0	0	0	0	0	0	0.025	0.002
Cr	0	0	0	0.003	0	0.009	0	0.001
Fe3+	0.017	0.019	0	0.047	0.001	0.078	0	0
Fe2+	4.839	4.863	4.882	4.649	4.88	4.791	4.617	4.635
Mn2+	0.117	0.104	0.108	0.22	0.098	0.107	0.113	0.115
Mg	0.072	0.073	0.049	0.117	0.059	0.059	0.211	0.217
Ca	2.028	2.047	2.076	2.011	2.053	2.041	2.036	2.05
Na	0.019	0.012	0.016	0.008	0.009	0.022	0.017	0.024
K	0.002	0	0.007	0.036	0.014	0.014	0.013	0.013
Ba	0	0	0.005	0	0.001	0	0.002	0
Sr	0	0	0	0	0	0	0	0
S	0	0	0	0.003	0	0	0	0
F	0.039	0.033	0.036	0.029	0.027	0.042	0.031	0.028
Cl	0.036	0.043	0.057	0.115	0.064	0.079	0.06	0.059
OH	1.925	1.923	1.907	1.856	1.908	1.879	1.909	1.913
Sum Cat#	17.049	17.058	17.084	17.055	17.075	17.077	17.036	17.057
XMg	0.015	0.015	0.01	0.025	0.012	0.012	0.044	0.045

Apatite

Cations calculated on the basis of 25 (O) and 2 (OH, F, Cl)

	Graphitic ore (Inveravon)						Graphitic ore, biotite-garnet (Inveravon)		
Wt%	nz016-1b 2_apat1	nz016-1b 2_apat2	nz016-1b 2_apat3	nz016-1b 2_apat1	nz016-1b 2_apat2	nz016-1b 2_apat3	nz047-5 1_apat1	nz047-5 1_apat2	nz047-5 1_apat3
SiO2	0.01	0.05	0.03	0.03	0.02	0.06	0.1	0.01	0.01
Fe2O3	0.16	0.04	0.05	0.1	0.08	0.09	0.41	0.03	0.1
MnO	0.04	0.09	0.08	0.14	0.11	0.1	0.29	0.21	0.18
MgO	0	0	0	0	0	0	0	0	0
CaO	50.3	51.11	57.75	58.7	50.75	44.7	57.25	57.37	57.42
Na2O	0	0	0	0	0	0	0.01	0	0.02
P2O5	42.15	42.21	42.08	37.73	34.45	33.44	41.61	42.67	42.02
SO3	0.01	0	0.02	0	0	0	0	0.02	0
La2O3	0	0	0	0.01	0	0	0	0.03	0.02
Ce2O3	0	0	0.09	0.04	0	0.04	0.02	0	0.02
Nd2O3	-	-	-	-	-	-	-	-	-
Sm2O3	-	-	-	-	-	-	-	-	-
Gd2O3	-	-	-	-	-	-	-	-	-
Y2O3	0	0	0	0	0	0	0	0	0
SrO	0.02	0.06	0.07	0	0.1	0.02	0.15	0.04	0.05
BaO	0.08	0	0.04	0	0.03	0.05	0.09	0.1	0.11
K2O	0	0.02	0.02	0	0	0.01	0	0	0
F	4.42	4.66	4.82	3.81	3.35	3.2	4.59	4.62	4.82
Cl	0.02	0.01	0	0.02	0.02	0.01	0.01	0	0
H2O(c)	0	0	0	0	0	0	0	0	0
O=F	1.86	1.96	2.03	1.6	1.41	1.35	1.93	1.94	2.03
O=Cl	0	0	0	0	0	0	0	0	0
Sum Ox%	95.35	96.29	103.02	98.98	87.49	80.38	102.6	103.16	102.75
Cations									
Si	0.002	0.009	0.005	0.005	0.003	0.013	0.016	0.002	0.002
Fe3+	0.02	0.006	0.006	0.014	0.012	0.014	0.052	0.004	0.013
Mn2+	0.006	0.013	0.011	0.021	0.019	0.018	0.041	0.029	0.026
Mg	0	0	0	0	0	0	0	0	0
Ca	9.394	9.483	10.226	10.989	10.655	10.057	10.192	10.1	10.194
Na	0	0	0	0	0	0	0.005	0	0.007
P	6.221	6.188	5.887	5.582	5.715	5.945	5.853	5.935	5.895
S	0.001	0	0.002	0	0	0.001	0	0.003	0
La	0	0	0	0.001	0	0	0	0.002	0.001
Ce	0	0	0.005	0.003	0	0.003	0.001	0	0.001
Nd	-	-	-	-	-	-	-	-	-
Sm	-	-	-	-	-	-	-	-	-
Gd	-	-	-	-	-	-	-	-	-
Y	0	0	0	0	0	0	0	0	0
Sr	0.002	0.006	0.006	0	0.011	0.002	0.014	0.004	0.005
Ba	0.006	0	0.003	0	0.003	0.004	0.006	0.007	0.007
K	0	0.003	0.003	0	0	0.003	0.001	0	0
F	2.436	2.553	2.518	2.105	2.076	2.122	2.413	2.4	2.528
Cl	0.006	0.004	0.001	0.006	0.006	0.005	0.003	0	0.001
OH	0	0	0	0	0	0	0	0	0
Sum Cat#	18.095	18.265	18.674	18.725	18.5	18.189	18.596	18.487	18.68
Me	9.408	9.506	10.255	11.014	10.688	10.089	10.26	10.142	10.241
X	6.244	6.202	5.898	5.6	5.73	5.972	5.92	5.941	5.91
Z	2.442	2.557	2.518	2.111	2.081	2.127	2.416	2.4	2.529

Biotite

Cations calculated on the basis of 22 (O) and 4 (OH, F, Cl)
All Fe as FeO

	Amphibolite				Migmatitic pelitic gneiss				Gahnite-bearing schist			
wt%	sz068-14 pos3.3	sz068-14 pos3.4	sz068-14 pos4.1	sz068-14 pos4.2	szu51-1 pos1.1	szu51-1 pos1.2	szu51-1 pos1.1	szu51-1 pos1.2	nz160-33 pos4.1	nz160-33 pos4.2	nz160-33 pos5.1	nz160-33 pos5.2
SiO2	31.65	31.65	33.99	34.06	34.09	33.7	35.02	34.69	34.3	34.17	34.47	34.39
TiO2	3.31	2.69	3.64	3.56	1.89	2.15	1.77	2.01	3.14	3.29	2.88	2.81
Al2O3	15.11	15.71	15.53	15.4	19.86	19.63	21.29	21.69	19	18.83	19.18	19.11
Cr2O3	0	0	0	0.01	0.07	0.03	0.08	0.05	0.08	0.06	0.14	0.04
FeO	28.35	28.62	26.26	25.58	23.27	23.44	21.32	21.66	22.79	23.17	22.7	22.77
V2O3	0	0	0	0	0	0	0	0	0	0.01	0	0
ZnO	0.02	0.02	0.04	0	0	0.05	0.08	0.05	0.18	0.08	0.07	0.26
MnO	0.11	0.15	0.1	0.1	0.03	0.05	0.09	0.09	0.12	0.17	0.24	0.22
MgO	7.58	7.95	7.31	7.26	7.06	7.03	6.67	6.18	6.05	6.05	6.03	6.13
CaO	0.54	0	0.11	0.01	0	0	0	0.01	0.01	0.01	0.01	0.03
Na2O	0.11	0.12	0.11	0.13	0.21	0.23	0.08	0.16	0.1	0.1	0.12	0.12
K2O	5.93	5.9	9.07	9.43	9.74	9.66	7.41	8.19	9.81	9.7	9.94	10.01
BaO	0	0.01	0.13	0.06	0	0	0	0	0	0	0	0
Rb2O	-	-	-	-	-	-	-	-	-	-	-	-
Cs2O	-	-	-	-	-	-	-	-	-	-	-	-
SrO	0	0	0	0	0	0	0	0	0	0	0	0
NiO	0	0	0	0.01	0.04	0.05	0.04	0.01	0.01	0.09	0.08	0.05
F	0.22	0.19	0.27	0.24	0.41	0.4	0	0	1.27	1.46	1.3	1.32
Cl	0.21	0.22	0.2	0.3	0.36	0.37	0.21	0.3	0.29	0.27	0.39	0.42
H2O(c)	3.51	3.53	3.63	3.6	3.6	3.58	3.85	3.84	3.19	3.1	3.16	3.14
O=F	0.09	0.08	0.12	0.1	0.17	0.17	0	0	0.53	0.61	0.55	0.56
O=Cl	0.05	0.05	0.04	0.07	0.08	0.08	0.05	0.07	0.07	0.06	0.09	0.09
Sum Ox%	96.51	96.63	100.23	99.59	100.35	100.13	97.85	98.88	99.74	99.89	100.07	100.17
Cations												
Si	5.174	5.16	5.343	5.384	5.257	5.223	5.381	5.312	5.326	5.308	5.336	5.329
Ti	0.406	0.33	0.43	0.423	0.219	0.251	0.205	0.232	0.366	0.385	0.335	0.328
Al/Al IV	2.826	2.84	2.657	2.616	2.743	2.777	2.619	2.688	2.674	2.692	2.664	2.671
Al VI	0.085	0.179	0.221	0.253	0.867	0.808	1.236	1.227	0.802	0.755	0.836	0.819
Cr	0	0	0	0.002	0.008	0.004	0.01	0.006	0.01	0.007	0.017	0.005
Fe2+	3.876	3.902	3.452	3.38	3.001	3.038	2.74	2.774	2.96	3.01	2.94	2.951
V	0	0	0	0	0	0	0.001	0	0	0.001	0	0
Zn	0.002	0.002	0.005	0	0	0.006	0.009	0.006	0.021	0.009	0.008	0.03
Mn2+	0.015	0.021	0.014	0.014	0.004	0.006	0.012	0.012	0.016	0.022	0.031	0.029
Mg	1.848	1.933	1.713	1.71	1.623	1.623	1.528	1.411	1.4	1.402	1.391	1.416
Ca	0.095	0	0.019	0.001	0	0	0	0.002	0.002	0.001	0.002	0.005
Na	0.034	0.039	0.032	0.041	0.062	0.068	0.023	0.047	0.03	0.031	0.036	0.036
K	1.237	1.227	1.818	1.9	1.916	1.909	1.452	1.599	1.942	1.923	1.963	1.979
Ba	0	0	0.008	0.004	0	0	0	0	0	0	0	0
Rb	-	-	-	-	-	-	-	-	-	-	-	-
Cs	-	-	-	-	-	-	-	-	-	-	-	-
Sr	0	0	0	0	0	0	0	0	0	0	0	0
Ni	0	0	0	0.002	0.004	0.006	0.005	0.001	0.001	0.011	0.01	0.006
F	0.116	0.1	0.137	0.122	0.199	0.198	0	0	0.623	0.717	0.634	0.649
Cl	0.059	0.059	0.052	0.081	0.093	0.098	0.054	0.078	0.077	0.072	0.103	0.11
OH	3.825	3.84	3.811	3.797	3.708	3.704	3.946	3.922	3.3	3.211	3.263	3.241
Sum Cat#	19.6	19.634	19.713	19.729	19.704	19.72	19.219	19.318	19.551	19.557	19.569	19.603
XMg	0.323	0.331	0.332	0.336	0.351	0.348	0.358	0.337	0.321	0.318	0.321	0.324
Oct	6.233	6.367	5.835	5.783	5.726	5.743	5.744	5.67	5.577	5.601	5.569	5.583
Int	1.367	1.267	1.878	1.946	1.978	1.977	1.474	1.648	1.975	1.955	2.001	2.02

Biotite cont.

Cations calculated on the basis of 22 (O) and 4 (OH, F, Cl)
All Fe as FeO

	Graphitic ore (Inveravon)		Graphitic ore, biotite-garnet schist (Inveravon)				Banded olivine-pyroxenoid ore (Broadlands)				
wt%	nz042-4 1_biot1	nz042-4 1_biot2	nz047-5 1_biot1	nz047-5 1_biot2	nz047-5 1_biot1	nz047-5 1_biot2	sz032-8 1_biot	sz032-8 1_biot1	sz032-8 1_ biot2	sz032-8 2_biot1	sz032-8 2_biot2
SiO2	33.22	33.28	32.26	32.33	32.84	32.75	32.57	29.64	32.01	31.67	32.52
TiO2	1.89	1.78	1.25	1.24	1.26	1.32	0.65	0.68	0.6	1.19	1.48
Al2O3	12.98	12.8	13.42	13.26	13.51	13.47	15.88	16.44	15.59	14.87	15.45
Cr2O3	0	0.03	0.07	0	0.02	0.02	0.05	0	0	0.02	0.01
FeO	36.44	35.51	37.08	36.39	36.41	36.96	35.45	38.21	36.67	35.45	35.83
V2O3	0	0	0	0	0	0	0.02	0.04	0.02	0	0
ZnO	0.08	0.12	0.2	0.36	0.16	0.21	0.45	0.39	0.4	0.3	0.3
MnO	0.62	0.51	0.92	0.97	0.97	0.89	0.17	0.76	0.17	0.41	0.16
MgO	1.88	1.95	1.18	1.13	1.01	1.03	1.18	1.2	1.27	1.47	1.38
CaO	0	0	0.15	0.15	0.02	0	0	0.02	0.02	0.19	0.01
Na2O	0.02	0.04	0.04	0.06	0.06	0.08	0.11	0.08	0.13	0.08	0.09
K2O	9.18	9.34	8.48	8.76	9.38	9.32	9.19	6.01	9.01	7.68	8.94
BaO	0	0.05	0.06	0	0.02	0.05	0	0.05	0.21	0.06	0
Rb2O	-	-	-	-	-	-	-	-	-	-	-
Cs2O	-	-	-	-	-	-	-	-	-	-	-
SrO	0	0	0	0	0	0	0	0	0	0	0
NiO	0	0	0.01	0	0.02	0.01	0	0.01	0.03	0.01	0.06
F	0.19	0.31	0.32	0.46	0.79	0.22	0.56	0.4	0.61	0.21	0.48
Cl	1.94	1.8	0.91	0.88	0.93	0.92	0.53	0.43	0.52	0.44	0.48
H2O(c)	3.01	2.96	3.15	3.07	2.95	3.22	3.2	3.19	3.16	3.31	3.27
O=F	0.08	0.13	0.13	0.2	0.33	0.09	0.23	0.17	0.26	0.09	0.2
O=Cl	0.44	0.41	0.21	0.2	0.21	0.21	0.12	0.1	0.12	0.1	0.11
Sum Ox%	100.94	99.96	99.15	98.68	99.83	100.17	99.64	97.28	100.04	97.19	100.15
Cations											
Si	5.537	5.587	5.479	5.514	5.537	5.511	5.423	5.093	5.355	5.398	5.386
Ti	0.237	0.225	0.159	0.159	0.16	0.167	0.081	0.088	0.075	0.153	0.184
Al/Al IV	2.463	2.413	2.521	2.486	2.463	2.489	2.577	2.907	2.645	2.602	2.614
Al VI	0.088	0.119	0.164	0.18	0.222	0.184	0.54	0.421	0.429	0.386	0.403
Cr	0	0.004	0.01	0	0.003	0.002	0.006	0	0	0.003	0.001
Fe2+	5.081	4.986	5.267	5.19	5.133	5.202	4.936	5.491	5.131	5.052	4.964
V	0	0	0	0	0	0	0.003	0.005	0.003	0	0
Zn	0.01	0.015	0.025	0.046	0.02	0.026	0.055	0.05	0.05	0.038	0.036
Mn2+	0.087	0.073	0.132	0.14	0.139	0.126	0.024	0.111	0.023	0.059	0.022
Mg	0.468	0.487	0.299	0.288	0.255	0.259	0.293	0.307	0.317	0.374	0.341
Ca	0	0.001	0.027	0.027	0.004	0	0	0.003	0.003	0.035	0.002
Na	0.006	0.014	0.014	0.018	0.02	0.026	0.036	0.026	0.044	0.028	0.028
K	1.951	2	1.838	1.907	2.018	2.001	1.952	1.318	1.922	1.671	1.888
Ba	0	0.003	0.004	0	0.001	0.004	0	0.004	0.014	0.004	0
Rb	-	-	-	-	-	-	-	-	-	-	-
Cs	-	-	-	-	-	-	-	-	-	-	-
Sr	0	0	0	0	0	0	0	0	0	0	0
Ni	0	0	0.002	0	0.003	0.001	0	0.001	0.004	0.001	0.009
F	0.103	0.167	0.172	0.25	0.419	0.118	0.293	0.216	0.325	0.112	0.252
Cl	0.548	0.513	0.262	0.254	0.265	0.262	0.149	0.126	0.148	0.127	0.135
OH	3.35	3.32	3.566	3.495	3.316	3.62	3.559	3.658	3.527	3.761	3.613
Sum Cat#	19.929	19.928	19.941	19.956	19.978	19.998	19.927	19.824	20.014	19.803	19.879
XMg	0.084	0.089	0.054	0.053	0.047	0.047	0.056	0.053	0.058	0.069	0.064
Oct	5.971	5.909	6.058	6.004	5.935	5.967	5.936	6.469	6.029	6.066	5.96
Int	1.957	2.019	1.883	1.952	2.043	2.031	1.988	1.351	1.982	1.737	1.919

Biotite cont.

Cations calculated on the basis of 22 (O) and 4 (OH, F, Cl)
All Fe as FeO

	Graphitic ore (Inveravon)		Graphitic ore, olivine facies (Inveravon)			
wt%	nz040-8 1_biot1	nz040-8 1_biot2	nz039-2 2_biot1	nz039-2 2_biot2	nz039-2 3_biot1	nz039-2 3_biot2
SiO2	32.4	32.23	32.8	33.09	32.94	32.8
TiO2	1.46	1.44	0.73	0.78	1.5	1.42
Al2O3	15.28	15.62	13.54	13.37	12.13	12.12
Cr2O3	0.04	0.04	0	0	0	0
FeO	32.97	33.15	34.8	33.91	35.21	35.87
V2O3	0	0	0	0	0	0.05
ZnO	0.52	0.51	0	0.14	0.26	0.21
MnO	0.14	0.26	0.77	0.78	0.59	0.64
MgO	1.82	1.72	3.08	3.1	1.83	1.88
CaO	0.01	0.01	0.03	0	0	0.01
Na2O	0.06	0.04	0.05	0.04	0.05	0.06
K2O	9.37	9.1	9.12	9.11	9.16	9.29
BaO	0	0	0.48	0.35	0.19	0.28
Rb2O	-	-	-	-	-	-
Cs2O	-	-	-	-	-	-
SrO	0	0	0	0	0	0
NiO	0	0.04	0	0	0	0.11
F	0.35	0.3	0.61	0.62	0.86	0.86
Cl	1.48	1.36	2.04	2.1	2.36	2.66
H2O(c)	3.03	3.08	2.77	2.73	2.49	2.43
O=F	0.15	0.13	0.26	0.26	0.36	0.36
O=Cl	0.33	0.31	0.46	0.47	0.53	0.6
Sum Ox%	98.45	98.47	100.09	99.4	98.67	99.74
Cations						
Si	5.446	5.41	5.506	5.569	5.644	5.597
Ti	0.185	0.182	0.092	0.099	0.193	0.183
Al/Al IV	2.554	2.59	2.494	2.431	2.356	2.403
Al VI	0.473	0.5	0.186	0.22	0.093	0.035
Cr	0.005	0.005	0	0	0.001	0
Fe2+	4.634	4.654	4.885	4.773	5.045	5.118
V	0	0	0	0	0	0.007
Zn	0.064	0.063	0.001	0.017	0.033	0.026
Mn2+	0.02	0.037	0.109	0.112	0.086	0.093
Mg	0.456	0.43	0.771	0.778	0.466	0.477
Ca	0.002	0.002	0.005	0	0	0.001
Na	0.02	0.014	0.015	0.013	0.015	0.021
K	2.01	1.949	1.952	1.956	2.001	2.023
Ba	0	0	0.031	0.023	0.013	0.019
Rb	-	-	-	-	-	-
Cs	-	-	-	-	-	-
Sr	0	0	0	0	0	0
Ni	0	0.005	0	0	0	0.016
F	0.186	0.159	0.324	0.333	0.467	0.465
Cl	0.421	0.387	0.579	0.6	0.684	0.77
OH	3.392	3.453	3.097	3.067	2.848	2.764
Sum Cat#	19.868	19.841	20.046	19.991	19.946	20.019
XMg	0.09	0.085	0.136	0.14	0.085	0.085
Oct	5.837	5.877	6.043	5.999	5.917	5.949
Int	2.031	1.964	2.004	1.992	2.029	2.063

Clinopyroxene (hedenbergite)

Cations calculated on the basis of 6 (O)

	Banded olivine-pyroxenoid with stage IIa alteration overprint (Broadlands/ Inveravon, olivine facies)						Olivine-pyroxenoid ore, hedenbergite-bearing, (Nithsdale)			
Wt%	sz061-11a 1-1	sz061-11a 1-2	sz061-11a 1-6	sz061-11a 3-2	sz061-11a 5-3	sz061-11a 5-4	sz113-2 3_hd1	sz113-2 3_hd2	sz113-2 3_pf1	sz113-2 3_pf2
SiO2	46.28	46.64	46.36	46.24	46.14	45.06	47.2	47.29	47.28	47.18
TiO2	0.09	0.03	0.07	0.1	0.08	0.18	0	0.03	0	0
Al2O3	0.3	0.22	0.35	0.33	0.28	1.8	0.09	0.11	0.11	0.1
Cr2O3	0.01	0	0.04	0.03	0	0.03	0.07	0	0	0
Fe2O3(c)	2.72	2.64	2.76	2.51	2.87	4.57	2.19	1.72	1.86	1.43
FeO(c)	24.54	24.89	24.79	24.64	24.36	25.51	25.86	25.96	26	25.97
MnO	5.35	4.42	5.23	5.76	4.67	4.36	3.54	3.3	3.51	3.49
MgO	0.16	0.23	0.19	0.17	0.25	0.23	0.66	0.65	0.6	0.65
CaO	19.01	19.93	18.92	18.54	19.52	16.66	19.74	19.93	19.78	19.75
Na2O	0.18	0.1	0.18	0.17	0.14	0.46	0.12	0.13	0.12	0.1
K2O	0	0	0	0.02	0.01	0.08	0	0	0	0
Sum Ox%	98.65	99.11	98.91	98.53	98.33	98.93	99.47	99.11	99.28	98.66
Cations										
Si	1.953	1.956	1.952	1.956	1.951	1.898	1.967	1.974	1.973	1.979
Ti	0.003	0.001	0.002	0.003	0.003	0.006	0	0.001	0	0
Al/Al IV	0.015	0.011	0.018	0.016	0.014	0.089	0.005	0.005	0.006	0.005
Al VI	0	0	0	0	0	0	0	0	0	0
Cr	0	0	0.001	0.001	0	0.001	0.002	0	0	0
Fe3+	0.086	0.083	0.087	0.08	0.091	0.145	0.069	0.054	0.059	0.045
Fe2+	0.866	0.873	0.873	0.871	0.861	0.898	0.901	0.906	0.907	0.911
Mn2+	0.191	0.157	0.187	0.206	0.167	0.155	0.125	0.117	0.124	0.124
Mg	0.01	0.014	0.012	0.011	0.016	0.015	0.041	0.04	0.037	0.04
Ca	0.86	0.896	0.854	0.84	0.884	0.752	0.881	0.892	0.884	0.888
Na	0.014	0.009	0.014	0.014	0.011	0.038	0.009	0.01	0.01	0.008
K	0	0	0	0.001	0.001	0.004	0	0	0	0
Sum Cat#	4	4	4	4	4	4	4	4	4	4
Wo(Ca)	49.52	50.23	49.10	48.78	50.19	45.17	48.33	48.50	48.35	48.27
En(Mg)	0.59	0.81	0.70	0.63	0.91	0.87	2.24	2.19	2.05	2.20
Fs(Fe2+)	49.89	48.96	50.20	50.59	48.90	53.96	49.43	49.31	49.60	49.53
XMg	0.01	0.02	0.01	0.01	0.02	0.02	0.04	0.04	0.04	0.04

Clinopyroxene

Cations calculated on the basis of 6 (O)

	Hedenbergite ore, fluorite-rich (Colwell)									
Wt%	sz058-6b 1_hd1	sz058-6b 1_hd2	sz058-6b 2_hd1	sz058-6b 2_hd2	sz037-23a 1_hd1	sz037-23a 1_hd2	sz037-23a 2_hd1	sz037-23a 2_hd2	sz037-23a 3_hd1	sz037-23a 3_hd2
SiO2	47.07	47.42	47.3	46.96	47.64	47.84	47.9	47.69	47.41	47.47
TiO2	0	0	0.01	0.01	0	0	0.01	0	0.02	0
Al2O3	0.26	0.21	0.24	0.23	0.09	0.07	0.14	0.1	0.13	0.12
Cr2O3	0	0.05	0	0	0	0.02	0	0.02	0	0
Fe2O3(c)	1.22	2.35	2.69	2.24	2.48	1.3	1.14	2	1.74	1.97
FeO(c)	27	27.07	26.71	26.63	24.46	25.89	25.73	25.16	25.6	25.34
MnO	1.96	2.34	2.18	2.05	4.3	3.83	3.71	3.85	3.96	3.98
MgO	0.32	0.39	0.36	0.35	1.13	1.09	1.07	1.02	1.06	1.1
CaO	20.33	20.3	20.64	20.53	19.94	19.59	20.05	20.16	19.49	19.56
Na2O	0.14	0.12	0.12	0.11	0.13	0.09	0.04	0.07	0.05	0.08
K2O	0.02	0	0.01	0	0	0	0	0	0	0
Sum Ox%	98.32	100.24	100.24	99.11	100.17	99.71	99.81	100.07	99.46	99.63
Cations										
Si	1.98	1.963	1.957	1.964	1.964	1.981	1.98	1.969	1.971	1.969
Ti	0	0	0	0	0	0	0	0	0.001	0
Al/Al IV	0.013	0.01	0.012	0.012	0.004	0.003	0.007	0.005	0.006	0.006
Al VI	0	0	0	0	0	0	0	0	0	0
Cr	0	0.002	0	0	0	0.001	0	0	0	0
Fe3+	0.039	0.073	0.084	0.07	0.077	0.041	0.036	0.062	0.054	0.062
Fe2+	0.95	0.937	0.924	0.931	0.844	0.896	0.89	0.869	0.89	0.879
Mn2+	0.07	0.082	0.076	0.073	0.15	0.134	0.13	0.134	0.139	0.14
Mg	0.02	0.024	0.022	0.022	0.069	0.067	0.066	0.063	0.066	0.068
Ca	0.916	0.9	0.915	0.92	0.881	0.869	0.888	0.892	0.868	0.869
Na	0.011	0.01	0.009	0.009	0.01	0.007	0.004	0.006	0.004	0.006
K	0.001	0	0	0	0	0	0	0	0	0
Sum Cat#	4	4	4	4	4	4	4	4	4	4
Wo(Ca)	48.58	48.37	49.16	49.11	49.11	47.42	48.17	48.90	47.60	47.85
En(Mg)	1.06	1.28	1.19	1.15	3.86	3.67	3.58	3.45	3.60	3.75
Fs(Fe2+)	50.36	50.35	49.65	49.74	47.03	48.91	48.25	47.65	48.80	48.40
XMg	0.02	0.03	0.02	0.02	0.08	0.07	0.07	0.07	0.07	0.07

Clinopyroxene

Cations calculated on the basis of 6 (O)

	Banded hedenbergite ore (Kheri)						Hedenbergite ore, minor fluorite (Kheri)	
Wt%	sz153-25 1_hd1	sz153-25 1_hd2	sz153-25 2_hd1	sz153-25 2_hd2	sz153-25 3_hd1	sz153-25 3_hd2	sz028-6 3_hd1	sz028-6 3_hd2
SiO2	46.82	47.23	47.37	46.78	47.16	47.01	47.08	47.23
TiO2	0.05	0	0.02	0.02	0.04	0.04	0.01	0
Al2O3	0.68	0.62	0.38	0.86	0.85	0.79	0.37	0.45
Cr2O3	0.06	0	0.02	0.01	0.04	0.04	0.02	0
Fe2O3(c)	2.79	3.07	2.56	2.81	2.15	2.58	2.53	2.22
FeO(c)	25.59	25.4	25.92	25.46	25.97	25.71	26.43	26.6
MnO	2.05	2.07	2.02	1.95	2.16	2.21	2.42	2.44
MgO	0.29	0.26	0.27	0.25	0.27	0.26	0.47	0.43
CaO	20.8	21.22	21.36	20.77	20.75	20.66	20.38	20.42
Na2O	0.24	0.26	0.18	0.27	0.23	0.26	0.1	0.1
K2O	0.03	0.04	0	0.07	0.04	0.05	0	0
Sum Ox%	99.39	100.16	100.11	99.26	99.66	99.61	99.82	99.89
Cations								
Si	1.948	1.949	1.957	1.947	1.954	1.95	1.955	1.959
Ti	0.001	0	0.001	0.001	0.001	0.001	0	0
Al/Al IV	0.034	0.03	0.019	0.042	0.042	0.039	0.018	0.022
Al VI	0	0	0	0	0	0	0	0
Cr	0.002	0	0.001	0	0.001	0.001	0.001	0
Fe3+	0.087	0.095	0.08	0.088	0.067	0.081	0.079	0.069
Fe2+	0.89	0.876	0.896	0.886	0.9	0.892	0.918	0.922
Mn2+	0.072	0.072	0.071	0.069	0.076	0.077	0.085	0.086
Mg	0.018	0.016	0.017	0.015	0.017	0.016	0.029	0.027
Ca	0.927	0.938	0.945	0.926	0.921	0.918	0.907	0.907
Na	0.019	0.021	0.015	0.021	0.019	0.021	0.008	0.008
K	0.002	0.002	0	0.004	0.002	0.003	0	0
Sum Cat#	4	4	4	4	4	4	4	4
Wo(Ca)	50.52	51.25	50.89	50.67	50.13	50.27	48.92	48.87
En(Mg)	0.96	0.86	0.91	0.85	0.90	0.89	1.57	1.44
Fs(Fe2+)	48.52	47.89	48.21	48.48	48.97	48.83	49.51	49.69
XMg	0.02	0.02	0.02	0.02	0.02	0.02	0.03	0.03

Feldspar

Cations calculated on the basis of 8 (O)

	Core Amphibolite (An_{42}, labradorite)				Gahnite-bearing schist (orthoclase)
Wt%	sz068-14 pos6	sz068-14 pos6.2	sz068-14 pos5.1	sz068-14 pos5.2	nz160-33
SiO2	57.07	57.13	57.26	57.47	63.77
TiO2	0.04	0.02	0.01	0	0
Al2O3	27.55	27.75	27.67	27.6	18.91
Fe2O3	0.06	0.11	0.06	0.01	0.09
MnO	0	0	0	0.01	0
MgO	0	0	0	0	0
CaO	9.09	8.95	8.93	8.83	0.02
SrO	0.03	0	0	0.05	0
BaO	0.01	0	0.08	0.08	0
Na2O	6.84	6.82	6.79	6.88	1.4
K2O	0.14	0.16	0.15	0.15	14.49
Rb2O	-	-	-	-	-
P2O5	0	0.03	0.01	0.01	0.06
Sum Ox%	100.81	100.98	100.97	101.09	98.74
Cations					
Si	2.544	2.541	2.547	2.553	2.969
Ti	0.001	0.001	0	0	0
Al/Al IV	1.448	1.455	1.451	1.445	1.038
Al VI	0	0	0	0	0
Fe3+	0.002	0.004	0.002	0	0.003
Mn2+	0	0	0	0	0
Mg	0	0	0	0	0
Ca	0.434	0.427	0.425	0.42	0.001
Sr	0.001	0	0	0.001	0
Ba	0	0	0.001	0.001	0
Na	0.591	0.588	0.585	0.592	0.126
K	0.008	0.009	0.009	0.009	0.861
Rb	-	-	-	-	-
P	0	0.001	0	0.001	0.002
Sum Cat#	5.029	5.025	5.022	5.024	5
Ab	57.159	57.442	57.334	57.844	12.78
An	41.991	41.697	41.672	41.045	0.079
Or	0.756	0.86	0.847	0.855	87.14
Celsian	0.014	0	0.136	0.13	0
Rb-Feld	0	0	0	0	0
Sr-Feld	0.079	0	0.012	0.126	0

Gahnite

Cations calculated on the basis of 4 (O)

	Gahnite-bearing schist			
Wt%	nz160-33 pos5.4	nz160-33 pos5.5	nz160-33 pos5.6	nz160-33 pos5.7
SiO2	0.01	0	0.02	0.03
TiO2	0.01	0.04	0.02	0
Al2O3	56.27	56.52	56.33	56.09
Cr2O3	0.29	0.29	0.26	0.46
Fe2O3(c)	1.33	0.44	0.87	0.74
FeO	12.84	13.27	12.78	13.44
V2O3	0.09	0.1	0.11	0.08
MnO	0.22	0.15	0.19	0.19
MgO	0.99	0.87	0.89	0.84
ZnO	28.87	28.65	29.12	28.37
NiO	0.16	0.02	0.06	0.02
CoO	-	-	-	-
GeO2	-	-	-	-
CuO	-	-	-	-
Sum Ox%	101.06	100.35	100.65	100.25
Cations				
Si	0	0	0.001	0.001
Ti	0	0.001	0	0
Al/Al IV	0	0	0	0
Al VI	1.961	1.979	1.97	1.969
Cr	0.007	0.007	0.006	0.011
Fe3+	0.03	0.01	0.019	0.017
Fe2+	0.317	0.33	0.317	0.335
V	0.002	0.002	0.003	0.002
Mn2+	0.005	0.004	0.005	0.005
Mg	0.044	0.039	0.04	0.037
Zn	0.63	0.628	0.638	0.624
Ni	0.004	0	0.001	0
Co	-	-	-	-
Ge	-	-	-	-
Cu	-	-	-	-
Sum Cat#	3	3	3	3
XCr	0.342	0.346	0.31	0.544
XFe2+	87.927	89.53	88.925	90.02
YFe3+	1.482	0.488	0.974	0.833

Garnet

Cations calculated on the basis of 12 (O)

	Banded olivine-pyroxenoid with stage IIa alteration overprint (Broadlands/Inveravon, olivine facies)										
Wt%	sz061-11a 1-3	sz061-11a 1-4	sz061-11a 1-5	sz061-11a 3-1	sz061-11a 3-6	sz061-11a 5-1	sz061-11a 5-2	sz061-11a 6-1	sz061-11a 7-4	sz061-11a 7-5	sz061-11a 7-6
SiO2	35.79	35.69	36.17	35.83	35.96	35.88	35.63	35.33	35.95	35.77	35.74
TiO2	0.03	0.01	0.03	0.04	0.06	0.04	0.01	0.05	0.02	0.04	0.05
Al2O3	19.78	19.96	19.82	19.79	19.36	19.63	19.35	19.32	19.66	19.73	19.39
Cr2O3	0	0	0.06	0.02	0.1	0.03	0.04	0.05	0	0.05	0
Fe2O3(c)	2.57	2.54	2.44	3.31	3.61	3.33	3.35	2.6	2.59	3.3	3.12
FeO	16.1	15.85	17.07	16.35	16.07	16.26	16.35	16.73	17.19	16.71	16.47
MnO	16.43	16.76	15.83	16.23	16.62	16.27	16.92	15.81	15.67	16.11	16.12
MgO	0.01	0.02	0	0.03	0.02	0.05	0.01	0.01	0.03	0.04	0.02
CaO	7.86	7.68	7.94	7.83	7.89	7.89	7.11	7.44	7.72	7.58	7.77
ZrO2	-	-	-	-	-	-	-	-	-	-	-
Y2O3	-	-	-	-	-	-	-	-	-	-	-
V2O3	-	-	-	-	-	-	-	-	-	-	-
Sum Ox%	98.56	98.51	99.37	99.43	99.7	99.38	98.78	97.33	98.83	99.33	98.68
Cations											
Si	2.956	2.948	2.963	2.938	2.947	2.944	2.95	2.96	2.963	2.938	2.955
Ti	0.002	0.001	0.002	0.002	0.004	0.003	0.001	0.003	0.001	0.003	0.003
Al/Al IV	0.044	0.052	0.037	0.062	0.053	0.056	0.05	0.04	0.037	0.062	0.045
Al VI	1.881	1.892	1.878	1.852	1.816	1.843	1.837	1.867	1.873	1.849	1.844
Cr	0	0	0.004	0.001	0.007	0.002	0.003	0.003	0	0.003	0
Fe3+	0.16	0.158	0.151	0.204	0.223	0.205	0.209	0.164	0.161	0.204	0.194
Fe2+	1.112	1.095	1.17	1.121	1.101	1.116	1.132	1.172	1.185	1.148	1.138
Mn2+	1.149	1.172	1.099	1.127	1.154	1.131	1.186	1.122	1.094	1.121	1.128
Mg	0.001	0.002	0.001	0.003	0.003	0.006	0.002	0.001	0.004	0.005	0.003
Ca	0.695	0.679	0.697	0.688	0.693	0.694	0.631	0.668	0.681	0.667	0.688
Zr	-	-	-	-	-	-	-	-	-	-	-
Y	-	-	-	-	-	-	-	-	-	-	-
V	-	-	-	-	-	-	-	-	-	-	-
Sum Cat#	8	8	8	8	8	8	8	8	8	8	8
Pyrope	0.035	0.073	0.02	0.113	0.095	0.216	0.058	0.034	0.14	0.158	0.093
Almandine	37.594	37.133	39.44	38.138	37.313	37.865	38.362	39.556	39.973	39.033	38.485
Spessartine	38.854	39.756	37.046	38.339	39.103	38.386	40.21	37.875	36.901	38.12	38.15
Andradite	7.824	7.713	7.41	9.921	10.858	10.006	10.183	8.036	7.905	9.914	9.509
Uvarovite	0.001	0.001	0.196	0.064	0.323	0.097	0.141	0.166	0.001	0.161	0.001
Grossularite	15.692	15.325	15.888	13.425	12.309	13.431	11.045	14.334	15.08	12.612	13.763
XMg	0.001	0.002	0.001	0.003	0.003	0.006	0.002	0.001	0.003	0.004	0.002

Garnet

Cations calculated on the basis of 12 (O)

	Banded olivine-pyroxenoid with stage IIa alteration overprint (Broadlands/Inveravon, olivine facies)										
Wt%	sz061-11b 2-2	sz061-11b 2-3	sz061-11b 2-4	sz061-11b 4-2	sz061-11b 4-3	sz061-11b 7-1	sz061-11b 7-2-1	sz061-11b 7-2-2	sz061-11b 7-2-3	sz061-11b 7-2-4	sz061-11b 7-2-5
SiO2	35.58	35.59	35.46	35.73	35.83	35.86	35.5	35.85	35.65	35.42	35.77
TiO2	0.07	0.03	0.07	0	0.03	0.08	0.08	0.09	0.06	0.02	0.04
Al2O3	19.3	19.22	19.21	19.6	19.68	19.49	19.03	18.84	19.04	19.22	19.25
Cr2O3	0.04	0.08	0.02	0.02	0	0.02	0.08	0.06	0.04	0.04	0.04
Fe2O3(c)	3.36	2.9	3.28	3.15	3.01	3.29	3.57	2.93	3.14	4.27	3.36
FeO	16.48	16.29	15.99	16.35	17.03	16.81	15.69	16.85	16.35	16.25	15.7
MnO	15.83	16.28	16.64	16.79	16.61	15.83	16.71	15.58	15.92	16	17.02
MgO	0.04	0.01	0.03	0.05	0.06	0.05	0.03	0.04	0.08	0.04	0.06
CaO	7.82	7.65	7.46	7.25	6.94	7.81	7.69	8	7.87	7.68	7.62
ZrO2	-	-	-	-	-	-	-	-	-	-	-
Y2O3	-	-	-	-	-	-	-	-	-	-	-
V2O3	-	-	-	-	-	-	-	-	-	-	-
Sum Ox%	98.5	98.04	98.16	98.94	99.2	99.24	98.37	98.25	98.14	98.95	98.85
Cations											
Si	2.948	2.962	2.951	2.949	2.95	2.949	2.949	2.978	2.964	2.928	2.955
Ti	0.004	0.002	0.004	0	0.002	0.005	0.005	0.006	0.004	0.001	0.002
Al/Al IV	0.052	0.038	0.049	0.051	0.05	0.051	0.051	0.022	0.036	0.072	0.045
Al VI	1.832	1.847	1.834	1.855	1.86	1.837	1.813	1.823	1.83	1.801	1.829
Cr	0.003	0.005	0.002	0.002	0	0.001	0.005	0.004	0.003	0.003	0.002
Fe3+	0.209	0.182	0.205	0.195	0.186	0.204	0.223	0.183	0.196	0.266	0.209
Fe2+	1.142	1.134	1.112	1.128	1.173	1.156	1.09	1.171	1.136	1.124	1.085
Mn2+	1.111	1.147	1.173	1.174	1.159	1.103	1.176	1.096	1.121	1.121	1.191
Mg	0.005	0.001	0.004	0.006	0.008	0.006	0.004	0.005	0.009	0.005	0.007
Ca	0.694	0.682	0.665	0.641	0.612	0.688	0.684	0.712	0.701	0.68	0.675
Zr	-	-	-	-	-	-	-	-	-	-	-
Y	-	-	-	-	-	-	-	-	-	-	-
V	-	-	-	-	-	-	-	-	-	-	-
Sum Cat#	8	8	8	8	8	8	8	8	8	8	8
Pyrope	0.157	0.03	0.142	0.207	0.27	0.219	0.132	0.166	0.313	0.182	0.242
Almandine	38.685	38.245	37.651	38.259	39.733	39.141	36.893	39.238	38.298	38.352	36.68
Spessartine	37.647	38.71	39.687	39.806	39.258	37.335	39.807	36.727	37.775	38.251	40.26
Andradite	10.214	8.931	10.034	9.521	9.103	9.955	10.914	9.092	9.659	12.824	10.227
Uvarovite	0.131	0.243	0.077	0.076	0.001	0.065	0.253	0.19	0.133	0.14	0.12
Grossularite	13.166	13.841	12.409	12.132	11.635	13.285	12.002	14.588	13.821	10.251	12.47
XMg	0.004	0.001	0.004	0.005	0.007	0.006	0.004	0.004	0.008	0.005	0.007

Garnet

Cations calculated on the basis of 12 (O)

	Banded olivine-pyroxenoid with stage IIa alteration overprint (Broadlands/Inveravon, olivine facies)				Migmatitic gneiss						
Wt%	sz061-11b 8-3	sz061-11b 8-4	sz061-11b 8-5	sz061-11b 8-6	szu51-1 1-1	szu51-1 1-2	szu51-1 1-3	szu51-1 1-4	szu51-1 1-5	szu51-1 1-6	szu51-1 1-7
SiO2	35.46	35.32	35.03	35.73	36.09	36.57	36.36	36.26	36.33	36.62	36.59
TiO2	0.06	0.02	0.07	0.03	0	0.02	0	0.01	0.01	0.01	0
Al2O3	19.69	16.57	18.24	19.75	20.95	21.15	21.21	20.92	21.21	21.27	21.4
Cr2O3	0	0.03	0.01	0.03	0	0	0.03	0.01	0	0.04	0
Fe2O3(c)	2.98	3.9	4.15	2.91	1.4	1.33	1.52	0.45	1.66	0.81	1.16
FeO	16.7	19.91	18.21	18	35.75	35.69	34.97	34.9	34.55	34.97	35
MnO	16.9	14.88	15.95	17.06	2.88	2.08	2.12	2.26	2.51	2.46	2.45
MgO	0.04	0.11	0.09	0.07	2.23	3.02	3.34	3.24	3.3	3.33	3.3
CaO	6.69	5.52	5.8	5.74	0.4	0.44	0.32	0.31	0.38	0.32	0.32
ZrO2	-	-	-	-	-	-	-	-	-	-	-
Y2O3	-	-	-	-	-	-	-	-	-	-	-
V2O3	-	-	-	-	-	-	-	-	-	-	-
Sum Ox%	98.52	96.26	97.53	99.33	99.7	100.29	99.87	98.37	99.93	99.83	100.2
Cations											
Si	2.941	3.033	2.956	2.947	2.948	2.952	2.942	2.974	2.938	2.96	2.949
Ti	0.004	0.001	0.004	0.002	0	0.001	0	0.001	0.001	0	0
Al/Al IV	0.059	0	0.044	0.053	0.052	0.048	0.058	0.026	0.062	0.04	0.051
Al VI	1.866	1.677	1.771	1.867	1.965	1.964	1.964	1.996	1.96	1.987	1.981
Cr	0	0.002	0	0.002	0	0	0.002	0.001	0	0.003	0
Fe3+	0.186	0.252	0.264	0.181	0.086	0.081	0.092	0.028	0.101	0.049	0.07
Fe2+	1.158	1.43	1.285	1.241	2.443	2.41	2.366	2.394	2.337	2.364	2.358
Mn2+	1.187	1.082	1.14	1.192	0.199	0.142	0.145	0.157	0.172	0.168	0.167
Mg	0.005	0.014	0.011	0.009	0.272	0.364	0.403	0.396	0.397	0.401	0.396
Ca	0.594	0.508	0.524	0.507	0.035	0.038	0.028	0.027	0.033	0.027	0.027
Zr	-	-	-	-	-	-	-	-	-	-	-
Y	-	-	-	-	-	-	-	-	-	-	-
V	-	-	-	-	-	-	-	-	-	-	-
Sum Cat#	8	8	8	8	8	8	8	8	8	8	8
Pyrope	0.186	0.469	0.381	0.293	9.221	12.324	13.698	13.327	13.517	13.56	13.43
Almandine	39.323	47.125	43.405	42.096	82.85	81.593	80.421	80.467	79.515	79.833	79.979
Spessartine	40.308	35.665	38.51	40.412	6.754	4.806	4.926	5.288	5.841	5.681	5.662
Andradite	9.04	13.033	12.929	8.809	1.174	1.277	0.955	0.917	1.127	0.925	0.929
Uvarovite	0.001	0.106	0.022	0.108	0	0	0.083	0.032	0	0.127	0
Grossularite	11.142	3.601	4.753	8.282	0	0	0	0	0	0	0
XMg	0.005	0.01	0.009	0.007	0.1	0.131	0.146	0.142	0.145	0.145	0.144

Garnet

Cations calculated on the basis of 12 (O)

	Banded olivine-pyroxenoid with stage IIa alteration overprint (Broadlands/ Inveravon, olivine facies)		Core Amphibolite								
Wt%	SZU51-1 1-8	SZU51-1 1-9	SZ068-14 1-1	SZ068-14 1-2	SZ068-14 1-3	SZ068-14 1-4	SZ068-14 2-1	SZ068-14 2-2	SZ068-14 2-3	SZ068-14 2-4	SZ068-14 2-5
SiO2	35.93	35.66	36.55	36.76	36.85	36.62	36.59	36.62	36.8	36.75	36.39
TiO2	0.01	0.02	0.14	0.15	0.02	0.16	0.01	0.04	0.04	0.06	0.04
Al2O3	20.85	20.88	20.88	20.77	20.94	20.8	20.81	20.68	20.96	21.01	20.79
Cr2O3	0.08	0.03	0	0.01	0	0.03	0.03	0.01	0.06	0.03	0
Fe2O3(c)	1.56	1.53	2.15	1.51	0.93	1.76	2.31	2.96	1.52	1.6	2.74
FeO	34.7	35	27.11	27.72	28.51	28.08	28.41	27.65	28.53	28.63	27.89
MnO	2.1	3.41	4.59	4.09	3.54	3.64	3.04	3.06	3.26	3.09	2.87
MgO	3.13	1.98	1.73	1.78	1.87	1.88	1.95	1.93	1.89	1.97	1.95
CaO	0.44	0.53	7.02	7.08	6.75	6.89	6.86	7.51	6.91	6.82	7.23
ZrO2	-	-	-	-	-	-	-	-	-	-	-
Y2O3	-	-	-	-	-	-	-	-	-	-	-
V2O3	-	-	-	-	-	-	-	-	-	-	-
Sum Ox%	98.78	99.03	100.17	99.86	99.41	99.85	100.02	100.45	99.97	99.96	99.91
Cations											
Si	2.943	2.937	2.937	2.96	2.974	2.949	2.942	2.933	2.957	2.952	2.929
Ti	0	0.001	0.009	0.009	0.001	0.01	0.001	0.002	0.002	0.004	0.002
Al/Al IV	0.057	0.063	0.063	0.04	0.026	0.051	0.058	0.067	0.043	0.048	0.071
Al VI	1.955	1.964	1.915	1.93	1.966	1.923	1.914	1.884	1.942	1.941	1.901
Cr	0.005	0.002	0	0	0	0.002	0.002	0.001	0.004	0.002	0
Fe3+	0.096	0.095	0.13	0.092	0.056	0.106	0.14	0.178	0.092	0.097	0.166
Fe2+	2.377	2.411	1.822	1.866	1.924	1.891	1.911	1.852	1.917	1.923	1.877
Mn2+	0.146	0.238	0.312	0.279	0.242	0.248	0.207	0.208	0.222	0.21	0.196
Mg	0.382	0.243	0.207	0.214	0.225	0.226	0.234	0.23	0.226	0.236	0.234
Ca	0.038	0.046	0.604	0.61	0.584	0.594	0.591	0.645	0.594	0.587	0.624
Zr	-	-	-	-	-	-	-	-	-	-	-
Y	-	-	-	-	-	-	-	-	-	-	-
V	-	-	-	-	-	-	-	-	-	-	-
Sum Cat#	8	8	8	8	8	8	8	8	8	8	8
Pyrope	12.99	8.274	7.035	7.192	7.57	7.622	7.946	7.852	7.648	7.991	8
Almandine	80.756	82.051	61.857	62.86	64.664	63.902	64.922	63.105	64.772	65.059	64.036
Spessartine	4.946	8.096	10.6	9.391	8.139	8.385	7.035	7.075	7.493	7.105	6.685
Andradite	1.308	1.579	6.325	4.518	2.791	5.215	6.803	8.629	4.493	4.743	8.018
Uvarovite	0.243	0.084	0.011	0.022	0.011	0.087	0.096	0.032	0.195	0.108	0
Grossularite	0	0	14.173	16.017	16.825	14.789	13.199	13.307	15.398	14.995	13.26
XMg	0.139	0.092	0.102	0.103	0.105	0.107	0.109	0.111	0.106	0.109	0.111

Garnet

Cations calculated on the basis of 12 (O)

	Core Amphibolite										
Wt%	sz068-14 grt trav_1	sz068-14 grt trav_2	sz068-14 grt trav_3	sz068-14 grt trav_4	sz068-14 grt trav_5	sz068-14 grt trav_6	sz068-14 grt trav_7	sz068-14 grt trav_8	sz068-14 grt trav_9	sz068-14 grt trav_10	sz068-14 grt trav_11
SiO2	36.78	37.03	37.18	36.91	36.38	37.09	36.81	37	36.76	37.12	36.93
TiO2	0.01	0.06	0.03	0.03	0.09	0.15	0.14	0.02	0.02	0.01	0.11
Al2O3	21.42	21.31	21.36	21.19	20.86	20.97	21.1	21.38	21.04	21.46	21.43
Cr2O3	0	0.04	0	0	0	0.02	0.01	0	0	0	0.01
Fe2O3(c)	1.39	1.74	0.63	1.92	2.82	1.53	2.06	1.47	2.07	1.73	1.52
FeO	28.71	28.71	29.05	28.4	27.28	28.04	27.71	28.96	28.33	28.79	28.7
MnO	3.03	3.1	3.2	3.61	4.11	4.58	4.52	3.34	3.49	3.16	3.08
MgO	1.83	2.01	1.72	1.83	1.98	1.68	1.71	1.78	1.82	2.05	1.97
CaO	6.99	6.96	7.15	6.92	6.72	6.9	6.88	6.85	6.94	6.85	6.99
ZrO2	0.01	0.02	0.04	0.06	0	0.08	0.03	0.04	0.07	0.05	0.06
Y2O3	0.06	0.03	0	0.01	0	0.07	0	0.04	0.01	0	0
V2O3	0	0.05	0.03	0.04	0.05	0.03	0.05	0	0.03	0	0.01
Sum Ox%	100.23	101.07	100.38	100.93	100.3	101.14	101.03	100.86	100.59	101.23	100.8
Cations											
Si	2.945	2.942	2.971	2.942	2.921	2.955	2.935	2.949	2.94	2.943	2.94
Ti	0.001	0.004	0.002	0.002	0.006	0.009	0.008	0.001	0.001	0.001	0.006
Al/Al IV	0.055	0.058	0.029	0.058	0.079	0.045	0.065	0.051	0.06	0.057	0.06
Al VI	1.966	1.937	1.982	1.933	1.894	1.924	1.918	1.956	1.925	1.948	1.95
Cr	0	0.002	0	0	0	0.001	0.001	0	0	0	0
Fe3+	0.084	0.104	0.038	0.115	0.17	0.092	0.124	0.088	0.125	0.103	0.091
Fe2+	1.923	1.907	1.941	1.893	1.831	1.868	1.848	1.93	1.895	1.909	1.911
Mn2+	0.206	0.209	0.216	0.244	0.279	0.309	0.305	0.225	0.237	0.212	0.208
Mg	0.218	0.238	0.205	0.218	0.237	0.2	0.203	0.211	0.217	0.242	0.234
Ca	0.6	0.592	0.612	0.591	0.578	0.589	0.588	0.585	0.595	0.582	0.596
Zr	0	0.001	0.002	0.002	0	0.003	0.001	0.002	0.003	0.002	0.002
Y	0.003	0.001	0	0.001	0	0.003	0	0.002	0	0	0
V	0	0.003	0.002	0.002	0.003	0.002	0.003	0	0.002	0	0.001
Sum Cat#	8	8	8	8	8	8	8	8	8	8	8
Pyrope	7.403	8.079	6.881	7.399	8.114	6.743	6.905	7.156	7.384	8.217	7.93
Almandine	65.265	64.731	65.269	64.264	62.582	62.977	62.767	65.395	64.375	64.809	64.803
Spessartine	6.98	7.087	7.271	8.273	9.549	10.426	10.366	7.63	8.034	7.213	7.04
Andradite	4.092	5.079	1.875	5.605	8.214	4.512	6.022	4.293	6.072	5.034	4.428
Uvarovite	0	0.115	0.001	0	0	0.07	0.039	0	0	0	0.021
Grossularite	16.26	14.909	18.704	14.457	11.54	15.272	13.9	15.526	14.135	14.727	15.778
XMg	0.102	0.111	0.095	0.103	0.115	0.097	0.099	0.099	0.103	0.113	0.109

Garnet

Cations calculated on the basis of 12 (O)

	Core Amphibolite		Gahnite-bearing sillimanite-biotite-garnet schist								
Wt%	sz068-14 grt trav_12	sz068-14 grt trav_13	NZ160-33 1-1	NZ160-33 1-2	NZ160-33 1-3	NZ160-33 1-4	NZ160-33 1-5	NZ160-33 1-6	NZ160-33 2-1	NZ160-33 2-2	NZ160-33 2-3
SiO2	37.13	37.25	36.17	35.99	35.95	35.97	36.12	35.9	35.7	36.06	35.89
TiO2	0.06	0.04	0	0.01	0	0.05	0.02	0.02	0.03	0	0.06
Al2O3	21.1	21.35	20.78	20.72	20.48	20.65	20.78	20.86	20.64	20.78	20.59
Cr2O3	0	0	0	0.01	0.08	0	0.01	0.04	0.04	0.01	0.04
Fe2O3(c)	1.99	1.68	0.37	1.02	1.63	1.25	2.12	1.51	1.29	1.27	1.18
FeO	28.82	29.11	31.43	31.02	30.71	31.2	31.26	31.04	30.43	30.99	30.67
MnO	3.09	2.85	7.31	6.82	7.01	6.82	6.91	7.39	7.7	7.4	7.35
MgO	1.97	1.78	1.05	1.3	1.32	1.28	1.3	1.07	1.12	1.17	1.21
CaO	7.02	7.35	1.98	2.19	2.19	2.08	2.06	1.96	1.94	1.98	2.1
ZrO2	0.03	0.01	-	-	-	-	-	-	-	-	-
Y2O3	0	0	-	-	-	-	-	-	-	-	-
V2O3	0.01	0.02	-	-	-	-	-	-	-	-	-
Sum Ox%	101.22	101.42	99.09	99.07	99.38	99.31	100.58	99.8	98.89	99.67	99.09
Cations											
Si	2.948	2.95	2.98	2.963	2.955	2.958	2.938	2.943	2.951	2.957	2.958
Ti	0.004	0.002	0	0	0	0.003	0.001	0.001	0.002	0	0.004
Al/Al IV	0.052	0.05	0.02	0.037	0.045	0.042	0.062	0.057	0.049	0.043	0.042
Al VI	1.923	1.943	1.998	1.973	1.939	1.959	1.93	1.959	1.962	1.964	1.959
Cr	0	0	0	0	0.005	0	0	0.003	0.003	0	0.003
Fe3+	0.119	0.1	0.023	0.063	0.101	0.077	0.129	0.093	0.08	0.078	0.073
Fe2+	1.914	1.928	2.166	2.135	2.111	2.145	2.126	2.128	2.104	2.125	2.114
Mn2+	0.208	0.191	0.51	0.475	0.488	0.475	0.476	0.513	0.539	0.514	0.513
Mg	0.234	0.21	0.129	0.159	0.162	0.157	0.158	0.131	0.138	0.144	0.149
Ca	0.597	0.623	0.174	0.193	0.193	0.183	0.18	0.172	0.172	0.174	0.185
Zr	0.001	0	-	-	-	-	-	-	-	-	-
Y	0	0	-	-	-	-	-	-	-	-	-
V	0	0.001	-	-	-	-	-	-	-	-	-
Sum Cat#	8	8	8	8	8	8	8	8	8	8	8
Pyrope	7.915	7.127	4.345	5.375	5.486	5.311	5.36	4.445	4.677	4.854	5.034
Almandine	64.819	65.291	72.678	72.064	71.456	72.46	72.325	72.279	71.244	71.869	71.386
Spessartine	7.043	6.468	17.123	16.037	16.515	16.034	16.201	17.431	18.258	17.381	17.328
Andradite	5.795	4.885	1.128	3.113	4.936	3.8	6.114	4.546	3.915	3.823	3.584
Uvarovite	0	0	0.001	0.022	0.248	0.001	0.021	0.128	0.13	0.021	0.13
Grossularite	14.428	16.228	4.726	3.389	1.359	2.395	0	1.172	1.777	2.052	2.537
XMg	0.109	0.098	0.056	0.069	0.071	0.068	0.069	0.058	0.062	0.063	0.066

Garnet

Cations calculated on the basis of 12 (O)

	Gahnite-bearing sillimanite-biotite-garnet schist										
Wt%	NZ160-33 2-4	NZ160-33 2-5	NZ160-33 2-6	NZ160-33 3-1	NZ160-33 3-2	NZ160-33 3-3	NZ160-33 3-4	NZ160-33 3-5	NZ160-33 3-6	NZ160-33 4-1	NZ160-33 4-2
SiO2	35.82	36.04	35.73	35.79	35.93	36.05	35.86	35.99	35.78	35.29	35.88
TiO2	0.1	0.07	0	0.01	0.03	0.08	0.03	0.02	0	0.04	0
Al2O3	20.69	20.39	20.84	20.71	20.71	20.46	20.62	20.86	20.62	20.59	20.68
Cr2O3	0	0.04	0	0.03	0.06	0.06	0	0	0.05	0.07	0.01
Fe2O3(c)	1.19	1.87	1.4	1.04	1.58	1.09	1.49	1.62	1.81	1.7	1.45
FeO	30.71	30.96	30.62	30.9	31.18	31.18	30.64	31.29	31	30.81	31.44
MnO	7.31	7.16	7.42	7.56	6.85	6.81	6.99	6.92	7.42	7.03	6.82
MgO	1.2	1.26	1.23	0.97	1.23	1.3	1.27	1.3	1.08	1.06	1.22
CaO	2.09	2.09	1.88	1.97	2.1	2.17	2.28	1.91	1.82	1.88	1.86
ZrO2	-	-	-	-	-	-	-	-	-	-	-
Y2O3	-	-	-	-	-	-	-	-	-	-	-
V2O3	-	-	-	-	-	-	-	-	-	-	-
Sum Ox%	99.1	99.88	99.12	98.98	99.66	99.2	99.18	99.91	99.58	98.48	99.35
Cations											
Si	2.952	2.953	2.945	2.958	2.947	2.967	2.952	2.944	2.943	2.933	2.952
Ti	0.006	0.004	0	0	0.002	0.005	0.002	0.001	0	0.003	0
Al/Al IV	0.048	0.047	0.055	0.042	0.053	0.033	0.048	0.056	0.057	0.067	0.048
Al VI	1.962	1.922	1.968	1.975	1.948	1.951	1.952	1.954	1.942	1.951	1.957
Cr	0	0.002	0	0.002	0.004	0.004	0	0	0.003	0.005	0.001
Fe3+	0.074	0.115	0.087	0.065	0.097	0.067	0.093	0.1	0.112	0.106	0.09
Fe2+	2.116	2.122	2.11	2.135	2.139	2.146	2.109	2.14	2.133	2.142	2.163
Mn2+	0.51	0.497	0.518	0.529	0.476	0.475	0.487	0.479	0.517	0.495	0.475
Mg	0.147	0.154	0.151	0.12	0.15	0.16	0.156	0.159	0.132	0.131	0.15
Ca	0.185	0.184	0.166	0.174	0.184	0.191	0.201	0.167	0.161	0.168	0.164
Zr	-	-	-	-	-	-	-	-	-	-	-
Y	-	-	-	-	-	-	-	-	-	-	-
V	-	-	-	-	-	-	-	-	-	-	-
Sum Cat#	8	8	8	8	8	8	8	8	8	8	8
Pyrope	4.966	5.217	5.139	4.046	5.081	5.377	5.291	5.383	4.501	4.474	5.073
Almandine	71.544	71.754	71.643	72.189	72.533	72.217	71.41	72.663	72.472	72.947	73.278
Spessartine	17.249	16.817	17.578	17.884	16.135	15.978	16.496	16.273	17.57	16.862	16.096
Andradite	3.622	5.629	4.228	3.178	4.749	3.32	4.522	4.864	5.447	5.141	4.377
Uvarovite	0.001	0.118	0	0.087	0.203	0.206	0	0	0.15	0.237	0.043
Grossularite	2.618	0.465	1.411	2.617	1.299	2.901	2.28	0.816	0	0.34	1.133
XMg	0.065	0.068	0.067	0.053	0.065	0.069	0.069	0.069	0.058	0.058	0.065

Garnet

Cations calculated on the basis of 12 (O)

Wt%	Gahnite-bearing sillimanite-biotite-garnet schist					Olivine-pyroxenoid ore (Burnham)		Graphitic ore, quartz-apatite facies (Inveravon)			
	nz160-33 4-2	nz160-33 4-3	nz160-33 4-4	nz160-33 4-5	nz160-33 4-6	nz033-6 2_gt1	nz033-6 2_gt2	nz042-4 1_gt1	nz042-4 1_gt2	nz042-4 grt_trav_a-1	nz042-4 grt_trav_a-2
SiO2	35.88	35.26	35.64	35.75	35.59	36.64	36.32	36.66	36.9	36.79	36.55
TiO2	0	0.05	0	0.02	0	0.04	0	0.01	0.04	0	0.07
Al2O3	20.68	20.17	20.39	20.64	20.52	19.89	19.94	21.03	20.84	20.56	21.08
Cr2O3	0.01	0.01	0	0.02	0.03	0.01	0.02	0.02	0.01	0	0.03
Fe2O3(c)	1.45	1.6	2.15	1.21	1.23	2.61	3.03	1.86	1.38	1.93	2.12
FeO	31.44	30.58	30.82	31.06	31.23	18.64	18.27	21.97	21.95	22.55	22.91
MnO	6.82	6.86	6.91	7.13	7.08	15.21	15.29	11.06	10.45	11.88	11.05
MgO	1.22	1.23	1.25	1.2	0.97	0.11	0.08	0.15	0.16	0.14	0.18
CaO	1.86	1.94	2.02	1.82	1.9	7.5	7.49	8.12	8.89	7.18	7.33
ZrO2	-	-	-	-	-	0	0.09	0.02	0.06	0.06	0.07
Y2O3	-	-	-	-	-	0.24	0.17	0	0.03	0.02	0
V2O3	-	-	-	-	-	0.09	0	0.05	0	0.05	0.02
Sum Ox%	99.35	97.7	99.18	98.85	98.54	101.01	100.69	100.96	100.7	101.16	101.4
Cations											
Si	2.952	2.951	2.941	2.955	2.956	2.962	2.946	2.945	2.965	2.962	2.931
Ti	0	0.003	0	0.001	0	0.003	0	0	0.003	0	0.004
Al/Al IV	0.048	0.049	0.059	0.045	0.044	0.038	0.054	0.055	0.035	0.038	0.069
Al VI	1.957	1.941	1.925	1.966	1.965	1.857	1.853	1.936	1.939	1.912	1.924
Cr	0.001	0	0	0.002	0.002	0.001	0.001	0.001	0	0	0.002
Fe3+	0.09	0.101	0.134	0.075	0.077	0.159	0.185	0.112	0.083	0.117	0.128
Fe2+	2.163	2.14	2.127	2.147	2.169	1.26	1.24	1.476	1.475	1.518	1.537
Mn2+	0.475	0.487	0.483	0.5	0.498	1.042	1.05	0.753	0.711	0.81	0.75
Mg	0.15	0.154	0.153	0.148	0.12	0.014	0.009	0.018	0.019	0.017	0.021
Ca	0.164	0.174	0.178	0.161	0.169	0.649	0.651	0.699	0.765	0.619	0.63
Zr	-	-	-	-	-	0	0.004	0.001	0.002	0.002	0.003
Y	-	-	-	-	-	0.01	0.007	0	0.001	0.001	0
V	-	-	-	-	-	0.006	0	0.003	0	0.003	0.001
Sum Cat#	8	8	8	8	8	8	8	8	8	8	8
Pyrope	5.073	5.209	5.207	5.022	4.052	0.461	0.314	0.621	0.626	0.582	0.724
Almandine	73.278	72.439	72.303	72.639	73.385	42.5	42.025	50.106	49.657	51.206	52.303
Spessartine	16.096	16.467	16.422	16.898	16.85	35.136	35.606	25.544	23.947	27.331	25.54
Andradite	4.377	4.939	6.068	3.675	3.766	7.806	9.034	5.468	4.108	5.732	6.207
Uvarovite	0.043	0.022	0	0.076	0.098	0.047	0.064	0.051	0.023	0.001	0.09
Grossularite	1.133	0.924	0	1.691	1.85	14.051	12.957	18.21	21.639	15.15	15.137
XMg	0.065	0.067	0.067	0.065	0.052	0.011	0.007	0.012	0.012	0.011	0.014

Garnet

Cations calculated on the basis of 12 (O)

	Graphitic ore, quartz-apatite facies (Inveravon)								Biotite-garnet schist (Inveravon)	
Wt%	nz042-4 grt_trav a-3	nz042-4 grt_trav a-4	nz042-4 grt_trav a-5	nz042-4 grt_trav b-1	nz042-4 grt_trav b-2	nz042-4 grt_trav b-3	nz042-4 grt_trav b-4	nz042-4 grt_trav b-5	nz047-5 1_gt1	nz047-5 1_gt2
SiO2	36.47	36.3	36.43	36.01	35.89	36.22	36.64	36.61	36.3	36.1
TiO2	0.04	0.07	0.04	0.08	0.08	0.08	0.05	0	0.02	0.02
Al2O3	20.9	21.11	20.4	21.07	20.9	20.84	21.04	20.7	20.77	20.82
Cr2O3	0	0.01	0	0.03	0	0.02	0	0.03	0	0.02
Fe2O3(c)	1.29	1.9	2.61	1.81	2.22	2.34	1.53	2.17	0.74	0.95
FeO	22.54	21.71	21.43	21.33	21.43	21.9	23.09	21.79	24.81	25.05
MnO	12.05	13.38	13.21	13.38	13.5	12.11	11.08	11.54	14.77	14.58
MgO	0.11	0.1	0.07	0.07	0.07	0.11	0.12	0.17	0.1	0.11
CaO	6.81	6.28	6.78	6.35	6.08	7.07	7.3	7.82	2.72	2.49
ZrO2	0.03	0.03	0.04	0.01	0.06	0.07	0.04	0.04	0.03	0.04
Y2O3	0	0.08	0.08	0.26	0.24	0.04	0	0.01	0	0
V2O3	0.13	0.06	0.01	0.07	0.08	0.08	0.08	0.03	0.04	0.06
Sum Ox%	100.37	101.03	101.1	100.48	100.54	100.89	100.96	100.91	100.31	100.24
Cations										
Si	2.955	2.93	2.943	2.923	2.917	2.925	2.949	2.948	2.971	2.96
Ti	0.003	0.004	0.002	0.005	0.005	0.005	0.003	0	0.001	0.001
Al/Al IV	0.045	0.07	0.057	0.077	0.083	0.075	0.051	0.052	0.029	0.04
Al VI	1.951	1.937	1.886	1.938	1.918	1.909	1.945	1.913	1.975	1.971
Cr	0	0	0	0.002	0	0.001	0	0.002	0	0.002
Fe3+	0.079	0.115	0.158	0.111	0.136	0.142	0.092	0.132	0.046	0.059
Fe2+	1.527	1.465	1.448	1.447	1.457	1.479	1.554	1.468	1.698	1.717
Mn2+	0.827	0.915	0.904	0.92	0.929	0.828	0.755	0.787	1.024	1.013
Mg	0.013	0.011	0.008	0.008	0.009	0.014	0.015	0.02	0.012	0.014
Ca	0.591	0.543	0.586	0.552	0.529	0.611	0.629	0.675	0.239	0.219
Zr	0.001	0.001	0.002	0.001	0.002	0.003	0.002	0.001	0.001	0.002
Y	0	0.003	0.004	0.011	0.01	0.002	0	0.001	0	0
V	0.008	0.004	0.001	0.005	0.005	0.005	0.005	0.002	0.003	0.004
Sum Cat#	8	8	8	8	8	8	8	8	8	8
Pyrope	0.443	0.391	0.288	0.287	0.299	0.468	0.506	0.675	0.418	0.458
Almandine	51.617	49.927	49.13	49.436	49.816	50.432	52.617	49.763	57.109	57.971
Spessartine	27.957	31.171	30.683	31.407	31.776	28.25	25.573	26.684	34.443	34.19
Andradite	3.856	5.578	7.72	5.342	6.529	6.875	4.513	6.414	2.265	2.883
Uvarovite	0.001	0.017	0.001	0.099	0	0.063	0.001	0.089	0.005	0.074
Grossularite	16.126	12.916	12.18	13.429	11.58	13.911	16.791	16.376	5.761	4.424
XMg	0.009	0.008	0.006	0.006	0.006	0.009	0.01	0.013	0.007	0.008

Garnet

Cations calculated on the basis of 12 (O)

	Biotite-garnet schist (Inveravon)									Banded olivine-pyroxenoid (Warenda)	
Wt%	nz047-5 grt_trav a-1	nz047-5 grt_trav a-2	nz047-5 grt_trav a-3	nz047-5 grt_trav a-4	nz047-5 grt_trav a-5	nz047-5 grt_trav a-6	nz047-5 grt_trav a-7	nz047-5 grt_trav a-8	nz047-5 grt_trav a-9	sz032-8 1_gt1	sz032-8 1_gt2
SiO2	36.46	36.22	36.43	36.33	36.22	36.23	36.13	36.34	36.33	36.94	36.77
TiO2	0.02	0	0.04	0.03	0.01	0.06	0.04	0.04	0	0	0
Al2O3	20.78	20.81	20.54	20.45	20.55	20.53	20.56	20.69	20.96	21.11	21.09
Cr2O3	0	0.04	0.02	0.01	0.04	0	0	0.06	0	0	0
Fe2O3(c)	1.6	2.37	1.39	1.49	1.86	2.1	1.74	1.83	1.2	0.6	1.11
FeO	23.73	24.08	25.26	25.33	24.62	25.03	24.89	25.06	23.7	34.03	33.52
MnO	14.98	14.3	14.52	14.37	14.66	14.98	14.87	14.51	15.21	1.44	1.51
MgO	0.07	0.09	0.09	0.08	0.08	0.09	0.08	0.09	0.05	0.15	0.15
CaO	3.58	3.6	2.72	2.69	2.91	2.37	2.46	2.8	3.31	6.6	6.76
ZrO2	0.01	0.03	0.03	0.01	0.04	0.05	0.01	0.02	0	0.07	0.02
Y2O3	0	0.05	0	0	0.01	0	0	0.02	0	0.18	0.01
V2O3	0.03	0.03	0	0.07	0.03	0	0.01	0.01	0.01	0.02	0
Sum Ox%	101.26	101.6	101.05	100.87	101.05	101.45	100.78	101.47	100.77	101.14	100.94
Cations											
Si	2.956	2.931	2.967	2.966	2.951	2.946	2.953	2.949	2.957	2.973	2.963
Ti	0.001	0	0.002	0.002	0	0.003	0.002	0.002	0	0	0
Al/Al IV	0.044	0.069	0.033	0.034	0.049	0.054	0.047	0.051	0.043	0.027	0.037
Al VI	1.941	1.916	1.939	1.933	1.925	1.914	1.934	1.927	1.969	1.976	1.967
Cr	0	0.002	0.002	0.001	0.003	0	0	0.004	0	0	0
Fe3+	0.097	0.144	0.085	0.091	0.114	0.129	0.107	0.112	0.074	0.036	0.068
Fe2+	1.609	1.63	1.72	1.729	1.678	1.702	1.701	1.701	1.613	2.291	2.259
Mn2+	1.029	0.98	1.002	0.994	1.011	1.032	1.03	0.997	1.049	0.098	0.103
Mg	0.009	0.011	0.011	0.01	0.01	0.011	0.01	0.011	0.007	0.018	0.018
Ca	0.311	0.312	0.237	0.235	0.254	0.207	0.215	0.243	0.288	0.569	0.584
Zr	0.001	0.001	0.001	0	0.002	0.002	0	0.001	0	0.003	0.001
Y	0	0.002	0	0	0.001	0	0	0.001	0	0.008	0
V	0.002	0.002	0	0.005	0.002	0	0.001	0.001	0.001	0.001	0
Sum Cat#	8	8	8	8	8	8	8	8	8	8	8
Pyrope	0.298	0.366	0.377	0.331	0.334	0.37	0.348	0.358	0.222	0.589	0.605
Almandine	54.397	55.573	57.914	58.255	56.809	57.68	57.546	57.617	54.553	76.976	76.221
Spessartine	34.785	33.426	33.724	33.484	34.246	34.95	34.831	33.779	35.473	3.297	3.485
Andradite	4.767	6.971	4.203	4.501	5.577	6.28	5.24	5.461	3.6	1.784	3.321
Uvarovite	0.001	0.116	0.077	0.044	0.139	0	0.001	0.192	0.001	0	0
Grossularite	5.753	3.549	3.705	3.386	2.896	0.72	2.035	2.593	6.152	17.353	16.367
XMg	0.005	0.007	0.006	0.006	0.006	0.006	0.006	0.006	0.004	0.008	0.008

Garnet

Cations calculated on the basis of 12 (O)

	Banded olivine-pyroxenoid (Warenda)		Biotite-garnet schist (Inveravon)								
Wt%	sz032-8 2_gt1	sz032-8 2_gt2	nz040-8 1_gt trav_1	nz040-8 1_gt trav_2	nz040-8 1_gt trav_3	nz040-8 1_gt trav_4	nz040-8 1_gt trav_5	nz040-8 1_gt trav_6	nz040-8 1_gt trav_7	nz040-8 1_gt trav_8	nz040-8 1_gt trav_9
SiO2	36.86	36.6	36.48	36.46	36.48	36.56	36.42	36.61	36.12	36.3	36.58
TiO2	0	0	0.02	0.03	0	0.04	0	0.04	0.03	0.03	0.03
Al2O3	21.34	21.13	21.41	21.43	21.42	21.37	21.42	21.19	21.42	21.27	21.35
Cr2O3	0.02	0.01	0	0.01	0	0.01	0.03	0.02	0	0	0.01
Fe2O3(c)	1.48	2.16	1.56	0.74	0.95	0.56	1.98	1.36	1.78	1.51	0.92
FeO	31.71	31.08	32.62	33.87	31.87	29.46	25.87	24.64	23.98	24.28	24.71
MnO	2	1.96	2.4	3.63	5.63	7.1	9.63	11.2	11.38	11.45	11.39
MgO	0.13	0.19	0.36	0.35	0.32	0.22	0.15	0.16	0.14	0.13	0.13
CaO	7.9	8.09	6.2	4.3	4.29	5.25	6.01	5.89	5.83	5.74	5.7
ZrO2	0.02	0.01	0	0.07	0.02	0.03	0.06	0	0.01	0.06	0
Y2O3	0.04	0	0	0.03	0	0	0	0.13	0	0.2	0
V2O3	0	0	0.03	0.04	0	0.04	0	0.01	0	0.04	0.05
Sum Ox%	101.5	101.24	101.09	100.96	100.98	100.64	101.56	101.24	100.68	101	100.87
Cations											
Si	2.948	2.935	2.935	2.949	2.95	2.959	2.923	2.948	2.922	2.932	2.953
Ti	0	0	0.001	0.002	0	0.003	0	0.002	0.002	0.002	0.002
Al/Al IV	0.052	0.065	0.065	0.051	0.05	0.041	0.077	0.052	0.078	0.068	0.047
Al VI	1.959	1.933	1.966	1.992	1.991	1.997	1.95	1.958	1.965	1.957	1.983
Cr	0.001	0.001	0	0.001	0	0.001	0.002	0.001	0	0	0.001
Fe3+	0.089	0.13	0.094	0.045	0.057	0.034	0.12	0.082	0.108	0.092	0.056
Fe2+	2.121	2.084	2.195	2.291	2.155	1.994	1.736	1.659	1.622	1.64	1.668
Mn2+	0.135	0.133	0.164	0.248	0.386	0.487	0.655	0.764	0.78	0.784	0.779
Mg	0.016	0.023	0.043	0.042	0.039	0.027	0.018	0.019	0.017	0.015	0.015
Ca	0.677	0.695	0.535	0.373	0.371	0.455	0.517	0.508	0.506	0.497	0.493
Zr	0.001	0	0	0.003	0.001	0.001	0.002	0	0.001	0.002	0
Y	0.002	0	0	0.001	0	0	0	0.006	0	0.009	0
V	0	0	0.002	0.003	0	0.002	0	0.001	0	0.002	0.003
Sum Cat#	8	8	8	8	8	8	8	8	8	8	8
Pyrope	0.532	0.783	1.465	1.425	1.312	0.902	0.603	0.65	0.565	0.515	0.516
Almandine	71.93	70.995	74.748	77.549	73.027	67.314	59.352	56.243	55.476	55.865	56.456
Spessartine	4.583	4.543	5.579	8.412	13.077	16.426	22.381	25.891	26.665	26.689	26.353
Andradite	4.339	6.303	4.578	2.204	2.806	1.661	5.771	4.01	5.213	4.44	2.721
Uvarovite	0.059	0.04	0	0.038	0	0.038	0.091	0.066	0	0	0.039
Grossularite	18.557	17.336	13.629	10.372	9.778	13.66	11.801	13.14	12.08	12.491	13.915
XMg	0.007	0.011	0.019	0.018	0.018	0.013	0.01	0.011	0.01	0.009	0.009

Garnet

Cations calculated on the basis of 12 (O)

	Biotite-garnet schist (Inveravon)						Graphitic ore, biotite-garnet facies (Inveravon)				
Wt%	nz040-8 1_gt trav_10	nz040-8 1_gt trav_11	nz040-8 1_gt trav_12	nz040-8 1_gt trav_13	nz040-8 1_gt trav_14	nz040-8 1_gt trav_15	nz016-1b 1_gt trav_1	nz016-1b 1_gt trav_2	nz016-1b 1_gt trav_3	nz016-1b 1_gt trav_4	nz016-1b 1_gt trav_5
SiO2	36.58	36.66	52.24	36.62	36.6	36.55	36.64	36.88	36.44	36.46	36.36
TiO2	0.05	0.01	0	0	0	0.01	0.04	0.05	0.06	0.08	0.07
Al2O3	21.26	21.12	15.87	21.63	21.26	21.29	21.06	21.33	21.06	21.06	20.96
Cr2O3	0.02	0	0	0.03	0.02	0.03	0.02	0.01	0.05	0	0.06
Fe2O3(c)	0.77	1.02	0	1.22	0.46	1.26	2.33	1.4	1.36	1.74	2.55
FeO	25.48	27.8	21.93	32.8	33.99	32.98	24.64	25.28	24.17	24.57	23.51
MnO	10.66	8.56	3.78	4.6	2.8	2.33	9.8	9.87	10.19	10.26	11.53
MgO	0.15	0.18	0.34	0.27	0.4	0.34	0.09	0.11	0.09	0.11	0.09
CaO	5.66	5.51	3.63	4.59	4.87	6.07	7.14	6.76	7	6.66	6.41
ZrO2	0.03	0.01	0	0.04	0	0	0.07	0	0.01	0	0.04
Y2O3	0	0	0	0	0	0.08	0.07	0	0.14	0	0
V2O3	0	0.04	0.04	0.02	0	0	0	0.01	0.02	0.04	0.04
Sum Ox%	100.66	100.91	97.83	101.82	100.39	100.92	101.9	101.7	100.61	100.97	101.63
Cations											
Si	2.958	2.961	3.955	2.938	2.969	2.947	2.93	2.949	2.946	2.94	2.921
Ti	0.003	0.001	0	0	0	0.001	0.002	0.003	0.004	0.005	0.004
Al/Al IV	0.042	0.039	0	0.062	0.031	0.053	0.07	0.051	0.054	0.06	0.079
Al VI	1.985	1.972	1.416	1.982	2.002	1.97	1.916	1.959	1.952	1.942	1.906
Cr	0.001	0	0	0.002	0.001	0.002	0.001	0	0.003	0	0.004
Fe3+	0.047	0.062	0	0.074	0.028	0.076	0.14	0.084	0.083	0.105	0.154
Fe2+	1.723	1.878	1.388	2.2	2.306	2.224	1.648	1.691	1.634	1.657	1.58
Mn2+	0.731	0.586	0.242	0.312	0.192	0.159	0.664	0.669	0.698	0.701	0.785
Mg	0.019	0.022	0.039	0.032	0.049	0.04	0.011	0.013	0.011	0.013	0.011
Ca	0.49	0.477	0.294	0.395	0.423	0.524	0.612	0.58	0.606	0.575	0.552
Zr	0.001	0	0	0.001	0	0	0.003	0	0	0	0.001
Y	0	0	0	0	0	0.003	0.003	0	0.006	0	0
V	0	0.002	0.002	0.001	0	0	0	0	0.002	0.003	0.003
Sum Cat#	8	8	7.336	8	8	8	8	8	8	8	8
Pyrope	0.63	0.748	1.981	1.095	1.634	1.369	0.376	0.448	0.387	0.429	0.369
Almandine	58.168	63.395	70.704	74.855	77.647	75.439	56.151	57.271	55.396	56.254	53.969
Spessartine	24.657	19.771	12.336	10.624	6.476	5.41	22.623	22.65	23.659	23.79	26.803
Andradite	2.3	3.045	0	3.58	1.385	3.721	6.788	4.106	4.045	5.132	7.444
Uvarovite	0.047	0.002	0.001	0.104	0.049	0.078	0.065	0.019	0.163	0	0.184
Grossularite	14.197	13.04	14.978	9.742	12.809	13.983	13.998	15.506	16.35	14.395	11.23
XMg	0.011	0.012	0.027	0.014	0.021	0.018	0.007	0.008	0.007	0.008	0.007

Garnet

Cations calculated on the basis of 12 (O)

	Graphitic ore, biotite-garnet facies (Inveravon)										
Wt%	nz016-1b 1_gt trav_6	nz016-1b 1_gt trav_7	nz016-1b 1_gt trav_8	nz016-1b 1_gt trav_9	nz016-1b 1_gt trav_10	nz016-1b 1_gt trav_11	nz016-1b 2_gt trav_1	nz016-1b 2_gt trav_2	nz016-1b 2_gt trav_3	nz016-1b 2_gt trav_4	nz016-1b 2_gt trav_5
SiO2	36.53	36.24	36.31	36.4	36.49	36.67	36.67	36.69	34.01	36.06	36.3
TiO2	0	0.04	0.08	0.06	0.02	0	0.03	0.02	0.04	0.03	0.04
Al2O3	21.25	21.15	20.97	21.02	21.17	20.76	21.27	20.91	19.35	21.09	21.02
Cr2O3	0.02	0.01	0.03	0.02	0.03	0.06	0.02	0.02	0.03	0.05	0.03
Fe2O3(c)	1.24	1.93	1.59	1.38	1.77	1.96	1.36	1.29	4.49	2.13	1.71
FeO	23.72	23.19	24.19	24.32	25.12	24.95	25.12	24.42	22.29	23.89	23.86
MnO	11.43	11.25	10.85	9.96	10.07	9.72	9.62	10.39	9.72	10.86	11.45
MgO	0.12	0.11	0.12	0.11	0.13	0.1	0.14	0.11	0.09	0.12	0.14
CaO	6.42	6.72	6.38	7.02	6.35	6.94	6.86	6.85	6.58	6.28	6.08
ZrO2	0.07	0.05	0.1	0.05	0.05	0.03	0.05	0.02	0.03	0.02	0.1
Y2O3	0	0.07	0.05	0	0	0.02	0	0	0	0.1	0.08
V2O3	0.03	0.06	0.08	0.08	0.06	0.12	0.08	0.09	0.02	0.12	0.04
Sum Ox%	100.83	100.83	100.75	100.42	101.27	101.34	101.22	100.83	96.63	100.76	100.84
Cations											
Si	2.947	2.927	2.938	2.947	2.936	2.949	2.945	2.961	2.884	2.919	2.936
Ti	0	0.003	0.005	0.003	0.001	0	0.002	0.001	0.003	0.002	0.002
Al/Al IV	0.053	0.073	0.062	0.053	0.064	0.051	0.055	0.039	0.116	0.081	0.064
Al VI	1.968	1.94	1.938	1.952	1.944	1.917	1.958	1.949	1.818	1.931	1.94
Cr	0.001	0.001	0.002	0.001	0.002	0.004	0.001	0.001	0.002	0.003	0.002
Fe3+	0.075	0.117	0.097	0.084	0.107	0.119	0.082	0.078	0.287	0.13	0.104
Fe2+	1.601	1.566	1.636	1.646	1.691	1.678	1.687	1.648	1.581	1.617	1.614
Mn2+	0.781	0.77	0.743	0.683	0.686	0.662	0.655	0.71	0.698	0.745	0.785
Mg	0.014	0.014	0.014	0.013	0.016	0.012	0.017	0.013	0.011	0.015	0.017
Ca	0.555	0.582	0.553	0.609	0.548	0.598	0.591	0.592	0.598	0.545	0.527
Zr	0.003	0.002	0.004	0.002	0.002	0.001	0.002	0.001	0.001	0.001	0.004
Y	0	0.003	0.002	0	0	0.001	0	0	0	0.004	0.003
V	0.002	0.004	0.005	0.005	0.004	0.008	0.005	0.006	0.001	0.008	0.003
Sum Cat#	8	8	8	8	8	8	8	8	8	8	8
Pyrope	0.479	0.467	0.484	0.455	0.527	0.396	0.565	0.441	0.382	0.514	0.576
Almandine	54.249	53.435	55.529	55.771	57.506	56.877	57.21	55.619	54.734	55.359	54.843
Spessartine	26.473	26.257	25.222	23.141	23.34	22.448	22.196	23.969	24.166	25.486	26.666
Andradite	3.664	5.672	4.728	4.101	5.203	5.797	4.005	3.852	13.577	6.248	5.059
Uvarovite	0.059	0.025	0.082	0.07	0.081	0.191	0.065	0.064	0.08	0.167	0.084
Grossularite	15.076	14.144	13.955	16.461	13.343	14.292	15.958	16.055	7.061	12.226	12.772
XMg	0.009	0.009	0.009	0.008	0.009	0.007	0.01	0.008	0.007	0.009	0.01

Garnet

Cations calculated on the basis of 12 (O)

	Graphitic ore, biotite-garnet facies (Inveravon)									
Wt%	nz016-1b 2_gt trav_6	nz016-1b 2_gt trav_7	nz016-1b 2 gt trav_8	nz016-1b 2_gt trav_9	nz016-1b 2_gt trav_10	nz016-1b 2_gt trav_11	nz016-1b 2_gt trav_12	nz016-1b 2_gt trav_13	nz016-1b 2_gt trav_14	nz016-1b 2_gt trav_15
SiO2	36.23	36.06	36.16	36.2	36.11	36.37	36.32	36.42	36.44	36.55
TiO2	0.05	0.06	0.06	0.04	0.05	0.06	0.04	0.06	0.05	0.03
Al2O3	20.98	20.94	21.06	21.15	20.97	21.15	21.1	21.15	21.15	20.85
Cr2O3	0	0	0.01	0	0.05	0.01	0	0.02	0.07	0.04
Fe2O3(c)	1.75	2.19	1.2	2.13	2.2	1.5	1.66	1.82	1.95	1.97
FeO	23.51	23.15	23.51	22.97	23.3	24.08	23.59	24.03	24.36	24.67
MnO	11.85	11.93	11.95	11.88	11.9	11.77	11.05	10.76	10.08	9.54
MgO	0.15	0.16	0.14	0.16	0.18	0.17	0.16	0.16	0.18	0.13
CaO	5.95	5.99	5.82	6.29	5.9	5.7	6.56	6.57	6.81	7.17
ZrO2	0.05	0.06	0.05	0.03	0	0.1	0.04	0.04	0.02	0.06
Y2O3	0.15	0.04	0.07	0.17	0.12	0	0	0.02	0.12	0
V2O3	0.03	0.03	0.03	0.11	0.04	0.1	0.07	0	0.07	0.05
Sum Ox%	100.7	100.63	100.05	101.14	100.82	100.99	100.6	101.05	101.29	101.08
Cations										
Si	2.936	2.924	2.945	2.919	2.924	2.937	2.937	2.934	2.929	2.944
Ti	0.003	0.004	0.004	0.003	0.003	0.003	0.002	0.004	0.003	0.002
Al/Al IV	0.064	0.076	0.055	0.081	0.076	0.063	0.063	0.066	0.071	0.056
Al VI	1.939	1.926	1.966	1.929	1.925	1.95	1.949	1.942	1.932	1.923
Cr	0	0	0	0	0.003	0	0	0.001	0.005	0.002
Fe3+	0.107	0.134	0.074	0.129	0.134	0.091	0.101	0.111	0.118	0.12
Fe2+	1.593	1.57	1.601	1.549	1.577	1.627	1.596	1.619	1.638	1.662
Mn2+	0.813	0.82	0.824	0.811	0.816	0.805	0.757	0.734	0.686	0.651
Mg	0.018	0.02	0.017	0.019	0.021	0.02	0.02	0.019	0.022	0.016
Ca	0.517	0.521	0.508	0.544	0.512	0.493	0.569	0.567	0.586	0.619
Zr	0.002	0.002	0.002	0.001	0	0.004	0.002	0.002	0.001	0.002
Y	0.007	0.002	0.003	0.007	0.005	0	0	0.001	0.005	0
V	0.002	0.002	0.002	0.007	0.002	0.006	0.004	0	0.004	0.003
Sum Cat#	8	8	8	8	8	8	8	8	8	8
Pyrope	0.598	0.673	0.586	0.666	0.725	0.681	0.669	0.636	0.755	0.545
Almandine	54.175	53.587	54.274	52.98	53.897	55.24	54.253	55.085	55.852	56.375
Spessartine	27.655	27.971	27.93	27.759	27.883	27.336	25.743	24.977	23.407	22.084
Andradite	5.177	6.463	3.599	6.215	6.472	4.421	4.914	5.368	5.701	5.826
Uvarovite	0.001	0	0.02	0.014	0.159	0.024	0.013	0.068	0.225	0.109
Grossularite	12.395	11.306	13.591	12.366	10.865	12.297	14.408	13.866	14.06	15.061
XMg	0.011	0.012	0.011	0.012	0.013	0.012	0.012	0.011	0.013	0.01

Garnet

Cations calculated on the basis of 12 (O)

	Graphitic ore, olivine facies (Inveravon/Broadlands)								
Wt%	nz039-2 1_gt1	nz039-2 1_gt2	nz039-2 2_gt rim	nz039-2 2_gt int1	nz039-2 2_gt int2	nz039-2 2_gt int3	nz039-2 2_gt core	nz039-2 3_gt1	nz039-2 3_gt2
SiO2	35.97	36.34	36.27	35.92	36.02	36.37	36.56	31.53	31.93
TiO2	0.04	0	0	0	0.04	0	0.01	0.03	0
Al2O3	20.38	20.51	20.83	20.99	20.5	20.63	20.99	0	0
Cr2O3	0.01	0.04	0.03	0	0	0	0.01	0	0
Fe2O3(c)	2.16	1.12	1.1	1.96	2.44	1.54	1.44	1.1	0
FeO	24.35	24.3	24.25	20.99	18.52	19.27	24.92	28.69	29.61
MnO	15.57	15.68	16.1	18.1	20.8	20.66	15.09	8.95	8.24
MgO	0.17	0.14	0.13	0.21	0.17	0.14	0.32	0.01	0.02
CaO	2.06	2.39	2.01	2.55	2.51	2.39	2.3	0.01	0.01
ZrO2	0.03	0.05	0	0	0	0.01	0	0.07	0
Y2O3	0.06	0	0	0	0	0	0	0	0.04
V2O3	0	0	0.04	0	0.04	0.04	0	0.03	0.04
Sum Ox%	100.81	100.57	100.75	100.72	101.06	101.05	101.65	70.41	69.9
Cations									
Si	2.944	2.973	2.962	2.931	2.936	2.961	2.956	3.939	4.003
Ti	0.002	0	0	0	0.003	0	0.001	0.003	0
Al/Al IV	0.056	0.027	0.038	0.069	0.064	0.039	0.044	0	0
Al VI	1.911	1.95	1.966	1.949	1.906	1.941	1.955	0	0
Cr	0.001	0.003	0.002	0	0	0	0	0	0
Fe3+	0.133	0.069	0.067	0.121	0.15	0.094	0.087	0.103	0
Fe2+	1.667	1.662	1.656	1.432	1.262	1.312	1.685	2.998	3.104
Mn2+	1.079	1.086	1.113	1.251	1.436	1.424	1.033	0.947	0.875
Mg	0.021	0.018	0.016	0.026	0.021	0.018	0.039	0.001	0.004
Ca	0.181	0.209	0.176	0.223	0.219	0.208	0.199	0.001	0.002
Zr	0.001	0.002	0	0	0	0	0	0.004	0
Y	0.003	0	0	0	0	0	0	0	0.003
V	0	0	0.003	0	0.003	0.003	0	0.003	0.004
Sum Cat#	8	8	8	8	8	8	8	8	7.994
Pyrope	0.701	0.589	0.544	0.876	0.71	0.591	1.318	0.025	0.093
Almandine	56.554	55.866	55.919	48.856	42.951	44.29	56.995	75.969	77.904
Spessartine	36.612	36.514	37.591	42.673	48.877	48.094	34.952	23.989	21.958
Andradite	6.132	3.411	3.31	5.826	7.266	4.62	4.273	0.017	0
Uvarovite	0.045	0.136	0.086	0	0.012	0.001	0.024	0.013	0.217
Grossularite	0	3.484	2.55	1.768	0.183	2.405	2.437	0	0
XMg	0.012	0.01	0.01	0.018	0.016	0.013	0.023	0	0.001

Garnet

Cations calculated on the basis of 12 (O)

	Banded hedenbergite ore (Kheri)				Siliceous Zn ore (Cukadoo) data from French et al. (1994)						
Wt%	sz153-25 1_garnet1	sz153-25 1_garnet2	sz153-25 3 gamet1	sz153-25 3_garnet2	cad32, 403.9m	cad58, 151.3m	cad58, 151.3m	cad58, 243.1m	cad58, 243.1m	cad58, 243.1m	cad58, 243.1m
SiO2	36.2	36.55	36.63	36.71	38.09	38.56	38.21	38.63	38.46	38.70	38.65
TiO2	0.02	0.02	0	0.02	0.04	0.02	0.05	0.08	0.15	0.07	0.10
Al2O3	19.47	19.83	19.53	19.39	21.07	21.72	21.55	20.51	20.91	20.50	19.74
Cr2O3	0.02	0.01	0	0	0.05	0.01	0.00	0.00	0.07	0.00	0.00
Fe2O3(c)	4.66	3.71	3.61	4.16	0.33	0.00	0.00	1.63	1.68	1.04	2.76
FeO	21.25	21.73	21.26	21.15	21.44	29.44	28.58	11.52	10.76	12.15	14.70
MnO	6.71	6.81	7.19	7.08	7.09	2.31	2.13	6.16	7.38	5.87	3.37
MgO	0.04	0.03	0	0.04	0.18	0.32	0.37	0.05	0.07	0.06	0.00
CaO	11.86	11.75	11.94	12.16	12.93	10.40	10.42	22.18	21.64	21.93	21.85
ZrO2	0.01	0.02	0.07	0.07							
Y2O3	0.17	0.21	0.15	0.19	0.02	0.02	0.00	0.00	0.00	0.00	0.03
V2O3	0	0	0	0	0.05	0.01	0.02	0.10	0.09	0.02	0.05
Sum Ox%	100.42	100.67	100.38	100.97	101.30	102.84	101.44	100.99	101.37	100.50	101.51
Cations											
Si	2.925	2.941	2.956	2.948							
Ti	0.001	0.001	0	0.001							
Al/Al IV	0.075	0.059	0.044	0.052							
Al VI	1.779	1.821	1.813	1.784							
Cr	0.001	0.001	0	0							
Fe3+	0.284	0.225	0.219	0.251							
Fe2+	1.436	1.462	1.435	1.42							
Mn2+	0.459	0.464	0.491	0.481							
Mg	0.005	0.003	0	0.004							
Ca	1.027	1.013	1.033	1.046							
Zr	0	0.001	0.003	0.003							
Y	0.007	0.009	0.006	0.008							
V	0	0	0	0							
Sum Cat#	8	8	8	8							
Pyrope	0.171	0.11	0.007	0.151	0.705	1.249	1.474	0.193	0.271	0.231	0
Almandine	49.071	49.682	48.489	48.11	47.113	64.456	63.870	24.900	23.348	26.242	31.882
Spessartine	15.682	15.782	16.604	16.307	15.780	5.122	4.821	13.485	16.219	12.841	7.403
Andradite	13.676	10.929	10.73	12.265	0.985	0	0	4.812	4.906	3.101	8.149
Uvarovite	0.06	0.029	0.005	0.001	0.157	0.031	0	0	0.215	0	0
Grossularite	21.339	23.469	24.165	23.166	35.261	29.142	29.835	56.610	55.041	57.584	52.567
XMg	0.003	0.002	0	0.003							

Grunerite

Cations calculated on the basis of 23 (O) and 2 (OH, F, Cl)

	Olivine-pyroxenoid ore (Burnham)				Graphitic ore, olivine facies (Inveravon/Broadlands)		Hedenbergite ore, minor fluorite (Kheri)	
Wt%	nz033-6 1_grun1	nz033-6 1_grun2	nz033-6 1_grun3	nz033-6 1_grun4	nz039-2 1a_grun1	nz039-2 1a_grun2	sz028-6 1_grun1	sz028-6 1_grun2
SiO2	47.69	47.48	47.8	47.6	47.74	47.69	46.58	47.31
TiO2	0	0	0.04	0.01	0.03	0	0.01	0
Al2O3	0.06	0.11	0.12	0.06	0.33	0.28	0.17	0.19
Cr2O3	0.02	0	0.06	0	0	0	0	0
Fe2O3(c)	45.45	44.66	45.46	45.48	46.08	46.48	48.62	48.52
FeO(c)	0	0	0	0	0	0	0	0
MnO	5.99	6.37	6.04	5.82	3.86	3.83	2.52	2.66
MgO	1.28	1.25	1.28	1.37	2	2.04	0.65	0.75
CaO	0.87	1.31	0.89	0.85	0.17	0.15	0.84	0.76
Na2O	0.04	0.07	0.04	0.04	0.12	0.14	0.09	0.1
K2O	0.01	0	0	0	0	0.01	0.01	0
BaO	0.02	0	0	0.13	0.01	0	0	0
SrO	0	0	0	0	0	0	0.06	0
SO3	0.02	0	0	0	0	0	0	0.01
F	0.01	0	0.02	0.03	0.09	0.09	0.12	0.1
Cl	0.09	0.1	0.1	0.1	0.23	0.28	0.08	0.07
H2O(c)	1.99	1.99	1.99	1.98	1.91	1.91	1.91	1.94
O=F	0	0	0.01	0.01	0.04	0.04	0.05	0.04
O=Cl	0.02	0.02	0.02	0.02	0.05	0.06	0.02	0.02
Sum Ox%	103.5	103.32	103.81	103.43	102.48	102.8	101.6	102.35
Cations								
Si	7.086	7.077	7.08	7.081	7.099	7.081	7.026	7.064
Ti	0	0	0.005	0.001	0.003	0	0.001	0
Al/Al IV	0.011	0.02	0.021	0.01	0.059	0.048	0.031	0.033
Al VI	0	0	0	0	0	0	0	0
Cr	0.002	0	0.007	0	0	0	0	0
Fe3+	5.081	5.009	5.067	5.091	5.156	5.193	5.519	5.452
Fe2+	0	0	0	0	0	0	0	0
Mn2+	0.753	0.804	0.758	0.733	0.486	0.481	0.322	0.337
Mg	0.283	0.278	0.283	0.304	0.443	0.451	0.145	0.167
Ca	0.138	0.209	0.14	0.135	0.027	0.024	0.136	0.121
Na	0.011	0.02	0.011	0.012	0.033	0.04	0.027	0.028
K	0.001	0	0	0	0.001	0.003	0.002	0
Ba	0.001	0	0	0.008	0	0	0	0
Sr	0	0	0	0	0	0	0.005	0
S	0.002	0	0	0	0	0	0	0.002
F	0.003	0	0.01	0.013	0.043	0.042	0.058	0.047
Cl	0.023	0.025	0.025	0.024	0.058	0.071	0.021	0.017
OH	1.973	1.975	1.965	1.963	1.899	1.887	1.921	1.935
Sum Cat#	15.369	15.418	15.373	15.374	15.307	15.32	15.213	15.204
XMg	1	1	1	1	1	1	1	1

Hornblende

Cations calculated on the basis of 23 (O) and 2 (OH, F, Cl)

	Core Amphibolite								Olivine-pyroxenoid ore (Nithsdale)	
Wt%	sz68-14 pos3.1	sz68-14 pos3.2	sz68-14 pos4.3	sz68-14 pos4.4	sz68-14 pos5.3	sz68-14 pos5.4	sz68-14 pos6.3	sz68-14 pos6.4	sz113-2 3_amph1	sz113-2 3_amph2
SiO2	40.03	40.19	39.61	39.94	39.91	39.83	39.98	39.85	36.71	36.21
TiO2	1.31	1.25	1.36	1.36	1.35	1.32	1.38	1.36	0.03	0
Al2O3	13.59	13.56	13.7	13.8	13.7	13.69	13.67	13.98	9.25	9.56
Cr2O3	0	0.02	0.02	0	0.02	0	0	0.02	0	0
Fe2O3(c)	4.45	4.78	4.86	5.18	4.21	4.05	5.13	4.94	8.35	8.81
FeO(c)	18.69	18.71	18.56	18.22	19.21	19.08	18.56	18.54	25.17	24.92
MnO	0.19	0.27	0.22	0.27	0.33	0.33	0.22	0.24	1.93	1.72
MgO	5.5	5.45	5.55	5.64	5.5	5.68	5.62	5.56	0.54	0.5
CaO	11.2	11.24	11.45	11.27	11.51	11.73	11.39	11.48	10.82	10.69
Na2O	1.51	1.49	1.42	1.56	1.53	1.44	1.5	1.43	1.5	1.53
K2O	1.15	1.15	1.18	1.15	1.21	1.21	1.17	1.19	1.82	1.94
BaO	0	0	0	0	0	0	0.02	0.01	0	0.07
SrO	0	0	0	0	0	0	0	0	0	0
SO3	0.01	0.02	0.01	0.02	0.05	0	0.05	0.03	0.01	0.04
F	0.15	0.16	0.15	0.16	0.12	0.16	0.15	0.16	0.35	0.34
Cl	0.19	0.21	0.18	0.16	0.16	0.21	0.16	0.18	2.95	3.11
H2O(c)	1.83	1.83	1.83	1.84	1.86	1.82	1.85	1.84	0.87	0.83
O=F	0.06	0.07	0.06	0.07	0.05	0.07	0.06	0.07	0.15	0.14
O=Cl	0.04	0.05	0.04	0.04	0.04	0.05	0.04	0.04	0.66	0.7
Sum Ox%	99.68	100.21	100.01	100.49	100.58	100.43	100.77	100.68	99.49	99.44
Cations										
Si	6.168	6.166	6.097	6.106	6.116	6.114	6.105	6.088	6.165	6.096
Ti	0.152	0.145	0.158	0.157	0.156	0.152	0.159	0.157	0.004	0
Al/Al IV	1.832	1.834	1.903	1.894	1.884	1.886	1.895	1.912	1.831	1.897
Al VI	0.636	0.617	0.582	0.592	0.591	0.59	0.565	0.605	0	0
Cr	0	0.002	0.003	0	0.002	0.001	0	0.002	0	0
Fe3+	0.516	0.551	0.563	0.596	0.485	0.468	0.589	0.567	1.055	1.117
Fe2+	2.408	2.401	2.39	2.33	2.462	2.449	2.371	2.368	3.534	3.509
Mn2+	0.025	0.036	0.029	0.035	0.043	0.042	0.029	0.031	0.274	0.246
Mg	1.263	1.246	1.274	1.286	1.256	1.299	1.28	1.266	0.135	0.126
Ca	1.849	1.848	1.889	1.847	1.891	1.93	1.863	1.879	1.946	1.928
Na	0.45	0.443	0.425	0.461	0.454	0.429	0.444	0.425	0.489	0.499
K	0.226	0.226	0.232	0.225	0.237	0.236	0.229	0.231	0.389	0.416
Ba	0	0	0	0	0	0	0.001	0.001	0	0.004
Sr	0	0	0	0	0	0	0	0	0	0
S	0.001	0.002	0.002	0.003	0.006	0	0.006	0.003	0.002	0.006
F	0.073	0.077	0.074	0.078	0.06	0.079	0.071	0.077	0.184	0.179
Cl	0.049	0.055	0.046	0.042	0.042	0.056	0.042	0.046	0.839	0.888
OH	1.878	1.868	1.88	1.88	1.897	1.865	1.887	1.876	0.977	0.933
Sum Cat#	17.525	17.516	17.545	17.533	17.581	17.595	17.536	17.534	17.824	17.844
XMg	0.344	0.342	0.348	0.356	0.338	0.347	0.351	0.348	0.037	0.035

Hornblende

Cations calculated on the basis of 23 (O) and 2 (OH, F, Cl)

	Graphitic ore, quartz-apatite facies (Inveravon)		Banded olivine-pyroxenoid ore (Warenda)		Graphitic ore, biotite-garnet facies (Inveravon)		Hedenbergite ore, fluorite-rich (Colwell)			
Wt %	nz042-4 1_amph1	nz042-4 1_amph2	sz032-8 2_amph1	sz032-8 2_amph2	nz016-1b 1_amph1	nz016-1b 1_amph2	sz058-6b 1_amph1	sz058-6b 1_amph2	sz058-6b 2_amph1	sz058-6b 2_amph2
SiO2	35.7	36.14	37.12	37.25	37.54	37.34	38.28	39.18	39.08	39.22
TiO2	0.24	0.31	0.42	0.4	0.91	0.95	0	0	0	0
Al2O3	11.53	11.12	13.74	13.1	9.78	9.72	10.09	8.9	9.26	9.71
Cr2O3	0.02	0.01	0.01	0	0.01	0.04	0	0	0	0
Fe2O3(c)	6.6	5.09	4.7	3.89	4.24	4.11	7.4	7.35	6.68	8.67
FeO(c)	26.13	27.33	26.36	27.17	27.62	27.95	26.45	26.82	26.77	25.6
MnO	1.07	0.72	0.19	0.25	1.02	1.01	1.05	1.4	1.39	1.24
MgO	0.74	0.7	0.7	0.73	0.65	0.71	0.28	0.32	0.36	0.38
CaO	11.4	11.33	11.35	11.49	10.95	11.14	11.03	11.16	11.19	11
Na2O	0.54	0.55	1.08	1	0.83	0.81	1.28	1.2	1.1	1.32
K2O	3.66	3.67	2.11	2.28	2.76	2.93	1.26	1.11	1.18	0.67
BaO	0.01	0	0.03	0	0	0.07	0.02	0.11	0	0.02
SrO	0	0	0	0	0	0	0	0	0	0
SO3	0	0.02	0.02	0.04	0.02	0.03	0.04	0.02	0.01	0
F	0.36	0.27	0.56	0.58	0.56	0.55	0.34	0.27	0.27	0.29
Cl	2.62	2.57	0.52	0.55	1.17	1.24	1.27	1.13	1.07	0.73
H2O(c)	0.97	1.02	1.46	1.43	1.24	1.22	1.34	1.42	1.43	1.53
O=F	0.15	0.11	0.24	0.24	0.23	0.23	0.14	0.11	0.11	0.12
O=Cl	0.59	0.58	0.12	0.12	0.26	0.28	0.29	0.25	0.24	0.17
Sum Ox%	100.86	100.16	100	99.78	98.78	99.3	99.7	100.03	99.43	100.1
Cations										
Si	5.925	6.035	5.999	6.056	6.266	6.225	6.283	6.418	6.42	6.355
Ti	0.03	0.04	0.051	0.049	0.114	0.119	0	0	0	0
Al/Al IV	2.075	1.965	2.001	1.944	1.734	1.775	1.717	1.582	1.58	1.645
Al VI	0.18	0.224	0.615	0.565	0.189	0.135	0.234	0.136	0.212	0.21
Cr	0.003	0.001	0.001	0	0.001	0.005	0	0	0	0
Fe3+	0.825	0.64	0.571	0.476	0.532	0.515	0.913	0.906	0.826	1.057
Fe2+	3.627	3.817	3.562	3.694	3.856	3.898	3.63	3.674	3.677	3.47
Mn2+	0.15	0.101	0.026	0.034	0.144	0.143	0.146	0.195	0.194	0.17
Mg	0.184	0.175	0.169	0.178	0.161	0.176	0.069	0.079	0.089	0.092
Ca	2.028	2.026	1.965	2.001	1.959	1.99	1.939	1.958	1.969	1.911
Na	0.174	0.177	0.338	0.316	0.268	0.261	0.406	0.381	0.352	0.415
K	0.775	0.781	0.434	0.472	0.588	0.623	0.264	0.232	0.246	0.139
Ba	0.001	0	0.002	0	0	0.005	0.002	0.007	0	0.001
Sr	0	0	0	0	0	0	0	0	0	0
S	0	0.003	0.002	0.004	0.003	0.004	0.005	0.003	0.002	0.001
F	0.19	0.142	0.288	0.297	0.293	0.289	0.176	0.138	0.141	0.15
Cl	0.737	0.727	0.143	0.151	0.331	0.351	0.353	0.313	0.297	0.201
OH	1.073	1.131	1.569	1.551	1.376	1.36	1.471	1.548	1.562	1.649
Sum Cat#	17.977	17.984	17.737	17.788	17.815	17.875	17.609	17.571	17.567	17.465
XMg	0.048	0.044	0.045	0.046	0.04	0.043	0.019	0.021	0.024	0.026

Hornblende

Cations calculated on the basis of 23 (O) and 2 (OH, F, Cl)

	Banded hedenbergite ore (Kheri)						Hedenbergite ore, minor fluorite (Kheri)					
Wt %	sz153-25 1_amphib 1	sz153-25 1_amphib 2	sz153-25 2_amphib 1	sz153-25 2_amphib 2	sz153-25 3_amphib 1	sz153-25 3_amphib 2	sz028-6 1_amphib 1	sz028-6 1_amphib 2	sz028-6 2_amphib 1	sz028-6 2_amphib 2	sz028-6 3_amphib 1	sz028-6 3_amphi b2
SiO2	38.2	38.99	37.58	38.87	37.11	37.49	37.1	37.52	37.12	37.26	37.87	37.7
TiO2	0.24	0.24	0.14	0.14	0.1	0.09	0.04	0.07	0.07	0.05	0.04	0.03
Al2O3	10.14	9.12	10.54	9.35	10.75	10.36	9.28	9.56	9.66	9.15	9.2	9.48
Cr2O3	0.02	0	0.01	0	0	0	0	0.01	0.02	0.01	0	0
Fe2O3(c)	6.57	6.49	6.82	6.41	6	6.15	6.01	7.35	6.43	8.56	6.93	6.8
FeO(c)	26.91	27.67	27.2	27.76	27.39	27.42	27.72	27.03	27.51	26.47	27.52	27.46
MnO	1.19	1.27	1.07	0.98	1.1	1.1	0.86	0.87	0.9	1.03	0.99	0.94
MgO	0.21	0.19	0.15	0.18	0.14	0.14	0.36	0.32	0.35	0.37	0.31	0.31
CaO	10.99	11.09	11.13	11.07	11.16	11.15	11.13	11.01	11.16	10.99	11.17	11.13
Na2O	1.28	1.21	1.29	1.24	1.16	1.23	0.6	0.59	0.55	0.49	0.63	0.58
K2O	1.53	1.42	1.81	1.38	2.15	1.79	3	2.81	3.09	2.92	2.68	2.8
BaO	0	0	0	0	0	0	0.16	0.07	0.06	0	0	0.03
SrO	0	0	0.04	0	0	0	0	0	0	0	0	0
SO3	0.04	0.06	0.09	0.03	0.09	0.1	0.04	0.04	0.05	0.04	0	0.05
F	0.23	0.17	0.22	0.19	0.22	0.18	0.45	0.52	0.56	0.5	0.51	0.51
Cl	0.35	0.43	0.61	0.43	0.58	0.55	1.54	1.38	1.36	1.4	1.24	1.27
H2O(c)	1.63	1.64	1.57	1.63	1.56	1.59	1.17	1.21	1.18	1.21	1.25	1.24
O=F	0.09	0.07	0.09	0.08	0.09	0.08	0.19	0.22	0.23	0.21	0.21	0.21
O=Cl	0.08	0.1	0.14	0.1	0.13	0.12	0.35	0.31	0.31	0.31	0.28	0.29
Sum Ox%	99.35	99.84	100.05	99.5	99.29	99.13	98.93	99.82	99.54	99.92	99.83	99.83
Cations												
Si	6.274	6.388	6.167	6.383	6.147	6.206	6.252	6.233	6.204	6.2	6.29	6.261
Ti	0.03	0.03	0.018	0.018	0.012	0.011	0.005	0.009	0.009	0.006	0.005	0.003
Al/Al IV	1.726	1.612	1.833	1.617	1.853	1.794	1.748	1.767	1.796	1.794	1.71	1.739
Al VI	0.237	0.148	0.205	0.193	0.245	0.227	0.096	0.105	0.107	0	0.091	0.116
Cr	0.003	0	0.001	0	0	0	0	0.001	0.003	0.001	0	0.001
Fe3+	0.812	0.8	0.843	0.793	0.748	0.766	0.762	0.918	0.809	1.072	0.866	0.849
Fe2+	3.696	3.791	3.732	3.812	3.794	3.796	3.908	3.755	3.845	3.684	3.822	3.814
Mn2+	0.165	0.176	0.149	0.137	0.155	0.155	0.123	0.122	0.128	0.145	0.139	0.132
Mg	0.052	0.048	0.038	0.043	0.034	0.034	0.091	0.08	0.088	0.093	0.077	0.077
Ca	1.933	1.947	1.957	1.948	1.981	1.978	2.011	1.959	1.998	1.96	1.987	1.981
Na	0.406	0.385	0.412	0.395	0.373	0.396	0.195	0.191	0.178	0.158	0.201	0.187
K	0.322	0.297	0.378	0.289	0.455	0.378	0.645	0.596	0.658	0.621	0.567	0.593
Ba	0	0	0	0	0	0	0.011	0.005	0.004	0	0	0.002
Sr	0	0	0.004	0	0	0	0	0	0	0	0	0
S	0.005	0.007	0.011	0.004	0.012	0.012	0.005	0.005	0.006	0.005	0	0.006
F	0.117	0.089	0.114	0.1	0.118	0.095	0.242	0.271	0.294	0.262	0.267	0.267
Cl	0.097	0.12	0.169	0.12	0.164	0.155	0.44	0.387	0.386	0.394	0.348	0.357
OH	1.786	1.791	1.717	1.78	1.718	1.751	1.318	1.341	1.32	1.344	1.384	1.376
Sum Cat#	17.661	17.629	17.747	17.631	17.809	17.753	17.851	17.746	17.834	17.739	17.755	17.761
XMg	0.014	0.012	0.01	0.011	0.009	0.009	0.023	0.021	0.022	0.025	0.02	0.02

Olivine

Cations calculated on the basis of 4 (O)

	Olivine-pyroxenoid ore (Burnham)									
Wt %	NZ024-23A 1-1	NZ024-23A 1-3	NZ024-23A 1-4	NZ024-23A 2-1	NZ024-23A 2-2	NZ024-23A 3-3	NZ024-23A 3-4	NZ024-23A 5-2	NZ024-23A 5-3	NZ024-23A 5-4
SiO2	28.7	28.73	28.63	28.91	28.8	29.18	28.94	29.03	29.12	28.64
TiO2	0	0	0	0	0	0	0.03	0.02	0.01	0.01
Al2O3	0	0	0	0.01	0.01	0.02	0	0.01	0	0.02
Cr2O3	0	0.01	0	0	0.02	0	0.08	0	0	0
FeO	48.19	49.11	49.66	50.35	50.47	49.95	50.29	50.6	47.26	50.24
MnO	19.87	19.68	18.96	18.27	17.93	18.87	18.62	17.98	19.21	18.51
MgO	0.37	0.3	0.44	0.47	0.51	0.46	0.43	0.52	0.41	0.53
CaO	0.16	0.05	0.05	0.11	0.09	0.09	0.07	0.04	0.03	0.08
NiO	0	0	0.09	0	0.04	0	0.04	0	0.02	0
Sum Ox%	97.29	97.88	97.82	98.12	97.87	98.58	98.51	98.19	96.06	98.03
Cations										
Si	0.996	0.993	0.99	0.995	0.994	0.998	0.993	0.997	1.015	0.989
Ti	0	0	0	0	0	0	0.001	0	0	0
Al/Al IV	0	0	0	0	0	0.001	0	0	0	0.001
Al VI	0	0	0	0	0	0	0	0	0	0
Cr	0	0	0	0	0.001	0	0.002	0	0	0
Fe2+	1.399	1.42	1.437	1.449	1.456	1.429	1.443	1.453	1.378	1.45
Mn2+	0.584	0.576	0.556	0.533	0.524	0.547	0.541	0.523	0.567	0.541
Mg	0.019	0.015	0.023	0.024	0.026	0.023	0.022	0.027	0.022	0.027
Ca	0.006	0.002	0.002	0.004	0.003	0.003	0.003	0.002	0.001	0.003
Ni	0	0	0.002	0	0.001	0	0.001	0	0.001	0
Sum Cat#	3.004	3.007	3.01	3.005	3.006	3.001	3.005	3.002	2.984	3.011
Fa	0.987	0.989	0.985	0.984	0.982	0.984	0.985	0.982	0.985	0.981
Fo	0.013	0.011	0.015	0.016	0.018	0.016	0.015	0.018	0.015	0.019

	Banded olivine-pyroxenoid ore (Broadlands)										
Wt %	SZ061-11A 7-1	SZ061-11A 7-2	SZ061-11B 1-2	SZ061-11B 4-5	SZ061-11B 4-6	SZ061-11B 5-1	SZ061-11B 6-1	SZ061-11B 6-2	SZ061-11B 6-3	SZ061-11B 6-4	SZ061-11B 6-5
SiO2	28.87	28.78	28.51	28.64	28.51	28.43	28.59	28.52	28.6	28.23	28.28
TiO2	0	0	0	0	0	0	0.02	0.01	0	0	0
Al2O3	0	0.01	0.01	0.32	0	0	0.01	0	0.02	0	0.01
Cr2O3	0.01	0	0.04	0.01	0.01	0.01	0.04	0	0.05	0.02	0
FeO	56.53	57.82	58.2	57.39	56.87	57.54	57.94	57.22	57.87	57.71	58.5
MnO	11.72	11.33	11.49	12.02	11.8	11.94	11.62	11.69	11.44	11.7	11.74
MgO	0.11	0.15	0.17	0.2	0.23	0.22	0.28	0.22	0.26	0.23	0.28
CaO	0.06	0.03	0.07	0.03	0.03	0.03	0.03	0.06	0.07	0.06	0.04
NiO	0.02	0.05	0.01	0.04	0	0	0	0	0	0	0
Sum Ox%	97.32	98.18	98.5	98.65	97.45	98.19	98.52	97.73	98.31	97.96	98.85
Cations											
Si	1.002	0.994	0.985	0.984	0.992	0.985	0.986	0.99	0.987	0.981	0.976
Ti	0	0	0	0	0	0	0	0	0	0	0
Al/Al IV	0	0	0	0.013	0	0	0	0	0.001	0	0.001
Al VI	0	0	0	0	0	0	0	0	0	0	0
Cr	0	0	0.001	0	0	0	0.001	0	0.001	0.001	0
Fe2+	1.641	1.67	1.681	1.649	1.655	1.667	1.671	1.661	1.671	1.678	1.688
Mn2+	0.345	0.331	0.336	0.35	0.348	0.35	0.339	0.344	0.334	0.344	0.343
Mg	0.006	0.008	0.009	0.01	0.012	0.012	0.015	0.011	0.013	0.012	0.014
Ca	0.002	0.001	0.003	0.001	0.001	0.001	0.001	0.002	0.003	0.002	0.001
Ni	0	0.001	0	0.001	0	0	0	0	0	0	0
Sum Cat#	2.997	3.006	3.015	3.009	3.008	3.015	3.013	3.01	3.011	3.018	3.024
Fa	0.996	0.995	0.995	0.994	0.993	0.993	0.991	0.993	0.992	0.993	0.992
Fo	0.004	0.005	0.005	0.006	0.007	0.007	0.009	0.007	0.008	0.007	0.008

Olivine

Cations calculated on the basis of 4 (O)

	Banded olivine-pyroxenoid ore (Broadlands)				Olivine-pyroxenoid ore (Nithsdale)							
Wt %	SZ061-11B 7-3	SZ061-11B 7-4	SZ061-11B 8-1	SZ061-11B 8-2	sz037-13 1_oli1	sz037-13 1_oli2	sz037-13 2_oli1	sz037-13 2_oli2	sz113-2 2_oli1	sz113-2 2_oli2	sz113-2 3_oli1	sz113-2 3_oli2
SiO2	28.68	28.79	28.75	28.82	29.23	29.06	29.56	29.01	29.05	29.2	29.26	28.93
TiO2	0	0	0.02	0	0	0	0.01	0	0.04	0	0	0
Al2O3	0.02	0	0.03	0.01	0.01	0.01	0	0	0	0.01	0	0.01
Cr2O3	0.06	0.03	0	0	0.03	0	0.01	0	0.03	0	0	0.03
FeO	58.45	57.65	57.5	57.08	51.89	51.23	52.03	50.74	57.82	56.83	57.23	57.21
MnO	11.56	11.81	11.67	11.74	18.36	18.29	18.2	18.32	11.57	11.77	12.14	12.35
MgO	0.25	0.29	0.28	0.27	0.28	0.26	0.26	0.28	0.3	0.28	0.28	0.29
CaO	0.07	0.05	0.06	0.07	0.07	0.08	0.11	0.06	0.04	0.03	0.04	0.06
NiO	0.04	0.06	0	0	0	0	0.02	0	0.04	0.05	0	0.01
Sum Ox%	99.13	98.69	98.32	97.98	99.87	98.93	100.19	98.42	98.89	98.18	98.95	98.89
Cations												
Si	0.984	0.99	0.991	0.995	0.991	0.994	0.997	0.996	0.994	1.003	0.999	0.991
Ti	0	0	0.001	0	0	0	0	0	0.001	0	0	0
Al/Al IV	0.001	0	0.001	0	0	0	0	0	0	0	0	0
Al VI	0	0	0	0	0	0	0	0	0	0	0	0
Cr	0.002	0.001	0	0	0.001	0	0	0	0.001	0	0	0.001
Fe2+	1.676	1.657	1.657	1.649	1.472	1.465	1.468	1.457	1.655	1.633	1.634	1.64
Mn2+	0.336	0.344	0.341	0.344	0.527	0.53	0.52	0.533	0.336	0.343	0.351	0.358
Mg	0.013	0.015	0.014	0.014	0.014	0.013	0.013	0.014	0.015	0.014	0.014	0.015
Ca	0.003	0.002	0.002	0.002	0.003	0.003	0.004	0.002	0.001	0.001	0.001	0.002
Ni	0.001	0.002	0	0	0	0	0	0	0.001	0.001	0	0
Sum Cat#	3.015	3.01	3.008	3.004	3.008	3.006	3.003	3.004	3.004	2.996	3.001	3.008
Fa	0.993	0.991	0.991	0.992	0.991	0.991	0.991	0.99	0.991	0.991	0.991	0.991
Fo	0.007	0.009	0.009	0.008	0.009	0.009	0.009	0.01	0.009	0.009	0.009	0.009

	Olivine-pyroxenoid ore (Burnham)								Graphitic ore, olivine facies (Inveravon)	
Wt %	sz043-3 1_oli1	sz043-3 1_oli2	nz033-6 2_oli1	nz033-6 2_oli2	nz033-6 3_oli1	nz033-6 3_oli2	sz037-21 1_oli1	sz037-21 1_oli2	nz039-2 1_oli1	nz039-2 1_oli2
SiO2	29.51	29.32	29.22	29.4	29.06	29.33	29.27	29.05	29.27	29.33
TiO2	0	0.03	0.01	0	0	0	0	0	0.01	0
Al2O3	0	0.01	0	0.01	0.03	0.02	0	0.01	0	0
Cr2O3	0	0	0.03	0.03	0.01	0.02	0	0.04	0.02	0.01
FeO	50.66	51.11	56.71	56.9	57.82	57.73	55.31	55.42	62.02	61.71
MnO	18.43	18.69	13.06	13.01	12.09	11.96	15.06	14.65	8.03	8.14
MgO	0.58	0.56	0.27	0.23	0.27	0.29	0.19	0.21	0.43	0.38
CaO	0.06	0.06	0.06	0.06	0.08	0.08	0.08	0.09	0	0
NiO	0.04	0	0.06	0	0	0	0	0	0	0.03
Sum Ox%	99.28	99.78	99.42	99.65	99.36	99.43	99.91	99.46	99.78	99.61
Cations										
Si	1.001	0.992	0.995	0.998	0.991	0.997	0.993	0.99	0.993	0.996
Ti	0	0.001	0	0	0	0	0	0	0	0
Al/Al IV	0	0.001	0	0.001	0.001	0.001	0	0	0	0
Al VI	0	0	0	0	0	0	0	0	0	0
Cr	0	0	0.001	0.001	0	0.001	0	0.001	0.001	0
Fe2+	1.437	1.447	1.614	1.615	1.649	1.642	1.569	1.58	1.76	1.753
Mn2+	0.529	0.536	0.377	0.374	0.349	0.344	0.433	0.423	0.231	0.234
Mg	0.029	0.028	0.014	0.012	0.014	0.015	0.01	0.01	0.022	0.019
Ca	0.002	0.002	0.002	0.002	0.003	0.003	0.003	0.003	0	0
Ni	0.001	0	0.002	0	0	0	0	0	0	0.001
Sum Cat#	2.999	3.007	3.004	3.002	3.008	3.002	3.007	3.009	3.006	3.004
Fa	0.98	0.981	0.992	0.993	0.992	0.991	0.994	0.993	0.988	0.989
Fo	0.02	0.019	0.008	0.007	0.008	0.009	0.006	0.007	0.012	0.011

Olivine

Cations calculated on the basis of 4 (O)

	Graphitic ore, olivine facies (Inveravon)		Hedenbergite ore, minor fluorite (Kheri)			
Wt %	nz039-2 3_oli1	nz039-2 3_oli2	sz028-6 1_oliv1	sz028-6 1_oliv2	sz028-6 2_oliv1	sz028-6 2_oliv2
SiO2	29.32	29.52	29.11	28.87	29.02	29.21
TiO2	0	0	0	0.02	0.01	0.04
Al2O3	0	0.01	0.01	0	0	0
Cr2O3	0.01	0	0.01	0	0	0
FeO	61.66	61.12	63.31	63.35	65.17	64.15
MnO	8.13	8.19	5.42	5.69	5.57	5.52
MgO	0.47	0.49	0.19	0.18	0.14	0.17
CaO	0	0	0.04	0.03	0.04	0.02
NiO	0	0.06	0.01	0	0	0
Sum Ox%	99.61	99.39	98.11	98.14	99.96	99.12
Cations						
Si	0.996	1.002	1.003	0.997	0.988	0.998
Ti	0	0	0	0	0	0.001
Al/Al IV	0	0	0.001	0	0	0
Al VI	0	0	0	0	0	0
Cr	0	0	0	0	0	0
Fe2+	1.751	1.734	1.824	1.829	1.855	1.833
Mn2+	0.234	0.235	0.158	0.166	0.16	0.16
Mg	0.024	0.025	0.01	0.009	0.007	0.009
Ca	0	0	0.001	0.001	0.002	0.001
Ni	0	0.002	0	0	0	0
Sum Cat#	3.004	2.998	2.997	3.003	3.012	3.001
Fa	0.987	0.986	0.995	0.995	0.996	0.995
Fo	0.013	0.014	0.005	0.005	0.004	0.005

Pyrosmalite

Cations calculated on the basis of 20 (O) and 10 (OH, F, Cl)

	Hedenbergite ore, fluorite-rich (Colwell)							Hedenbergite ore, minor fluorite (Kheri)			
Wt %	sz037-23a 1_ps1	sz037-23a 1_ps2	sz037-23a 2_actinol2	sz037-23a 3_ps1	sz037-23a 3_ps2	sz037-23a 3_ps3	sz037-23a 3_ps4	sz028-6 1_actinol1	sz028-6 1_actinol2	sz028-6 4_coarse actinol1	sz028-6 4_coarse actinol2
SiO2	35.69	37.41	35.1	36.4	36.27	35.8	36.29	33.26	33.13	33.7	33.63
TiO2	0.02	0	0	0	0	0.01	0.03	0	0	0	0
Al2O3	0.02	0.05	0.09	0.06	0.04	0.07	0.11	0	0.03	0	0.04
Cr2O3	0	0.02	0.02	0	0	0	0.02	0.04	0.02	0.04	0
FeO	46.3	44.79	44.1	44.89	45.53	45.76	44.79	45.53	46.07	47.2	47.6
V2O3	0.03	0	0	0.01	0	0	0	0	0	0	0
ZnO	0.07	0	0	0	0.04	0.06	0.13	0	0	0	0
MnO	6.03	5.52	8.4	5.53	5.29	5.34	5.13	5.94	5.98	5.35	5.58
MgO	0.35	0.42	0.08	0.69	0.74	0.71	0.72	0.21	0.11	0.07	0.06
CaO	0.1	1.3	0.14	0.45	0.6	0.31	0.35	0.11	0.05	0.23	0.22
Na2O	0	0.01	0	0.03	0.03	0.03	0.05	0	0.03	0	0.01
K2O	0.01	0	0.01	0	0.02	0.01	0	0	0.01	0	0
BaO	0	0	0	0.01	0.04	0.06	0	0	0	0	0.04
P2O5	0	0	0	0	0	0	0	0	0	0	0
Rb2O	-	-	-	-	-	-	-	-	-	-	-
Cs2O	-	-	-	-	-	-	-	-	-	-	-
SrO	0	0	0	0	0	0	0	0.01	0	0.07	0
NiO	0	0	0	0.01	0	0.01	0	0	0	0	0
Y2O3	0	0	0	0	0	0	0	0	0	0	0
ZrO2	0	0	0	0	0	0	0	0	0	0	0
La2O3	0	0	0	0	0	0	0	0	0	0	0
Ce2O3	0	0	0	0	0	0	0	0	0	0	0
SO3	0	0	0.05	0	0	0	0	0	0	0	0.02
F	0	0	0	0	0	0	0	0	0	0	0
Cl	0.34	0.25	1.22	0.22	0.21	0.22	0.22	4.33	4.09	4.07	3.89
H2O(c)	8.61	8.86	8.29	8.69	8.72	8.64	8.66	7.15	7.22	7.35	7.43
O=F	0	0	0	0	0	0	0	0	0	0	0
O=Cl	0.08	0.06	0.28	0.05	0.05	0.05	0.05	0.98	0.92	0.92	0.88
Sum Ox%	97.5	98.58	97.23	96.93	97.49	97.01	96.46	95.61	95.81	97.17	97.64
Cations											
Si	6.153	6.283	6.117	6.238	6.2	6.17	6.244	6.041	6.014	6.026	5.991
Ti	0.002	0	0	0	0	0.001	0.004	0	0	0	0
Al/Al IV	0.005	0.009	0.019	0.013	0.007	0.015	0.022	0	0.006	0	0.008
Al VI	0	0	0	0	0	0	0	0	0	0	0
Cr	0	0.003	0.003	0	0	0	0.003	0.005	0.003	0.005	0
Fe2+	6.675	6.289	6.428	6.434	6.509	6.595	6.445	6.916	6.993	7.057	7.092
V	0.004	0.001	0	0.001	0.001	0	0	0	0	0	0
Zn	0.009	0	0	0	0.005	0.008	0.017	0	0	0	0
Mn2+	0.881	0.785	1.24	0.803	0.766	0.779	0.747	0.914	0.919	0.81	0.842
Mg	0.09	0.106	0.021	0.176	0.188	0.182	0.186	0.057	0.029	0.019	0.016
Ca	0.019	0.233	0.027	0.082	0.11	0.058	0.065	0.021	0.011	0.045	0.043
Na	0	0.004	0	0.009	0.009	0.011	0.016	0.002	0.011	0	0.002
K	0.001	0	0.001	0	0.005	0.002	0.001	0	0.001	0	0
Ba	0	0	0	0.001	0.003	0.004	0	0	0	0	0.003
P	0	0	0	0	0	0	0	0	0	0	0
Rb	-	-	-	-	-	-	-	-	-	-	-
Cs	-	-	-	-	-	-	-	-	-	-	-
Sr	0	0	0	0	0	0	0	0.001	0	0.007	0
Ni	0	0	0	0.001	0	0.002	0	0	0	0	0
Y	0	0	0	0	0	0	0	0	0	0	0
Zr	0	0	0	0	0	0	0	0	0	0	0
La	0	0	0	0	0	0	0	0	0	0	0
Ce	0	0	0	0	0	0	0	0	0	0	0
S	0	0	0.006	0	0	0	0	0	0	0	0.002
F	0	0	0	0	0	0	0	0	0	0	0
Cl	0.101	0.07	0.361	0.064	0.062	0.063	0.063	1.333	1.258	1.233	1.173
OH	9.899	9.93	9.639	9.936	9.938	9.937	9.937	8.667	8.742	8.766	8.827
Sum Cat#	23.84	23.713	23.861	23.759	23.803	23.828	23.748	23.957	23.987	23.971	24
XMg	0.013	0.017	0.003	0.027	0.028	0.027	0.028	0.008	0.004	0.003	0.002

Pyrosmalite

Cations calculated on the basis of 20 (O) and 10 (OH, F, Cl)

	Hedenbergite ore, minor fluorite (Kheri)		Olivine-pyroxenoid ore (Nithsdale)								
Wt %	sz028-6 4_bladed actinol1	sz028-6 4_bladed actinol2	sz045-31a 2_ps1	sz045-31a 2_ps2	sz045-31a 2_ps3	sz045-31a 2_ps4	sz045-31a 2_ps5	sz045-31a 2_ps6	sz045-31a 2_ps1	sz045-31a 2_ps2	sz045-31a 3_ps1
SiO2	34.39	33.33	32.84	33.05	34.65	35.24	33.89	26.2	32.58	32.84	33.25
TiO2	0	0	0	0.01	0.01	0	0.03	0	0.03	0.01	0
Al2O3	0	0	0.14	0.13	0.12	0.11	0.07	0.08	0.11	0.1	0.02
Cr2O3	0.01	0	0	0	0	0.02	0.04	0	0	0	0
FeO	46.49	47.46	39.6	40.04	35.79	34.82	38.33	22.55	40.01	40	38.42
V2O3	0	0	0.03	0	0	0.05	0	0.05	0.03	0	0
ZnO	0	0	0.02	0	0.13	0.09	0	0.14	0	0	0
MnO	4.88	5.21	14.13	14.42	16.17	17.68	14.84	17.07	14.05	14.33	14.92
MgO	0.07	0.06	0.39	0.43	0.38	0.34	0.37	0	0.39	0.39	0.36
CaO	0.88	0.16	0.05	0.01	0.05	0.06	0.02	0.04	0.04	0.02	0.01
Na2O	0.01	0.01	0.01	0.02	0	0.01	0.01	0.03	0.02	0	0
K2O	0.01	0.02	0	0.01	0	0	0.01	0	0.01	0.01	0
BaO	0	0	0	0.03	0	0	0.08	0.09	0.06	0.02	0
P2O5	0	0	0	0	0	0	0	0	0	0	0
Rb2O	-	-	-	-	-	-	-	-	-	-	-
Cs2O	-	-	-	-	-	-	-	-	-	-	-
SrO	0	0	0	0	0.02	0	0	0	0	0	0
NiO	0	0	0	0.05	0	0	0.07	0.04	0	0	0
Y2O3	0	0	0	0	0	0	0	0	0	0	0
ZrO2	0	0	0	0	0	0	0	0	0	0	0
La2O3	0	0	0	0	0	0	0	0	0	0	0
Ce2O3	0	0	0	0	0	0	0	0	0	0	0
SO3	0	0	0	0	0	0	0	0	0	0	0
F	0	0	0	0	0	0	0	0	0	0	0
Cl	3.38	3.88	0.8	0.79	0.74	0.91	1.23	1.92	0.84	0.83	0.92
H2O(c)	7.6	7.34	8.17	8.25	8.35	8.43	8.18	5.97	8.14	8.19	8.15
O=F	0	0	0	0	0	0	0	0	0	0	0
O=Cl	0.76	0.88	0.18	0.18	0.17	0.21	0.28	0.43	0.19	0.19	0.21
Sum Ox%	96.95	96.59	96	97.06	96.24	97.57	96.88	73.73	96.11	96.55	95.84
Cations											
Si	6.094	6.002	5.88	5.861	6.086	6.102	5.983	6.083	5.845	5.86	5.945
Ti	0	0	0	0.001	0.001	0	0.004	0	0.004	0.001	0
Al/Al IV	0	0	0.029	0.028	0.024	0.023	0.014	0.022	0.024	0.022	0.004
Al VI	0	0	0	0	0	0	0	0	0	0	0
Cr	0.001	0	0	0	0	0.003	0.005	0	0	0	0
Fe2+	6.89	7.148	5.929	5.938	5.257	5.042	5.659	4.378	6.004	5.97	5.745
V	0	0	0.005	0	0	0.006	0	0.009	0.005	0	0
Zn	0	0	0.003	0	0.017	0.012	0	0.023	0	0	0
Mn2+	0.732	0.796	2.143	2.166	2.406	2.593	2.219	3.356	2.135	2.165	2.26
Mg	0.019	0.015	0.103	0.113	0.1	0.087	0.097	0	0.104	0.103	0.096
Ca	0.167	0.032	0.009	0.002	0.008	0.012	0.004	0.009	0.008	0.004	0.002
Na	0.002	0.002	0.002	0.006	0	0.004	0.003	0.012	0.008	0	0.001
K	0.002	0.005	0	0.002	0	0	0.002	0	0.002	0.003	0
Ba	0	0	0	0.002	0	0	0.006	0.008	0.004	0.001	0
P	0	0	0	0	0	0	0	0	0	0	0
Rb	-	-	-	-	-	-	-	-	-	-	-
Cs	-	-	-	-	-	-	-	-	-	-	-
Sr	0	0	0	0	0.002	0	0	0	0	0	0
Ni	0	0	0	0.007	0	0	0.009	0.007	0	0	0
Y	0	0	0	0	0	0	0	0	0	0	0
Zr	0	0	0	0	0	0	0	0	0	0	0
La	0	0	0	0	0	0	0	0	0	0	0
Ce	0	0	0	0	0	0	0	0	0	0	0
S	0	0	0	0	0	0	0	0	0	0	0
F	0	0	0	0	0	0	0	0	0	0	0
Cl	1.015	1.184	0.241	0.236	0.221	0.268	0.368	0.755	0.255	0.252	0.278
OH	8.985	8.815	9.759	9.763	9.779	9.732	9.632	9.245	9.744	9.748	9.722
Sum Cat#	23.908	24	24.104	24.127	23.901	23.884	24.006	23.907	24.142	24.129	24.054
XMg	0.003	0.002	0.017	0.019	0.019	0.017	0.017	0	0.017	0.017	0.016

Pyrosmalite

Cations calculated on the basis of 20 (O) and 10 (OH, F, Cl)

	Olivine-pyroxenoid ore (Nithsdale)										
Wt %	sz045-31a 3_ps2	sz045-31a 3_ps3	sz045-31a 3_ps4	sz045-31a 3_ps5	sz045-31a 3_ps6	sz037-13 1_ps1	sz037-13 1_ps2	sz037-13 2_ps1	sz037-13 2_ps2	sz113-2 2_ps1	sz113-2 2_ps2
SiO2	32.31	34.68	34.62	33.76	33.7	34.95	34.65	34.32	34.81	35.54	34.91
TiO2	0	0	0	0	0	0.03	0.01	0	0	0	0.01
Al2O3	0	0.05	0.02	0	0.01	0	0	0.01	0	0.01	0.03
Cr2O3	0	0	0.02	0	0.02	0.04	0.02	0	0	0.02	0.04
FeO	39.25	35.2	35.01	27.75	28.24	33.03	33.93	35.06	33.24	41.88	42.42
V2O3	0.01	0.05	0	0.06	0	0.03	0	0	0.05	0	0
ZnO	0	0.08	0	0.04	0.05	0.01	0	0	0	0.07	0.02
MnO	14.56	16.71	16.17	23.91	23.41	18.57	18.98	18.05	19.53	9.18	9.52
MgO	0.22	0.39	0.34	0.13	0.1	0.36	0.34	0.31	0.28	0.4	0.37
CaO	0	0.02	0.05	0.31	0.03	0.05	0.04	0.1	0.17	0.11	0.07
Na2O	0.03	0.01	0.02	0	0.03	0.05	0.05	0.01	0.02	0	0
K2O	0.01	0	0	0.01	0	0	0.02	0.01	0.01	0.01	0.01
BaO	0.03	0	0.14	0.03	0.01	0	0	0.13	0	0.07	0
P2O5	0	0	0	0	0	0	0	0	0	0	0
Rb2O	-	-	-	-	-	-	-	-	-	-	-
Cs2O	-	-	-	-	-	-	-	-	-	-	-
SrO	0	0	0	0	0	0	0	0	0	0	0
NiO	0.05	0	0	0	0.04	0	0	0	0	0.01	0
Y2O3	0	0	0	0	0	0	0	0	0	0	0
ZrO2	0	0	0	0	0	0	0	0	0	0	0
La2O3	0	0	0	0	0	0	0	0	0	0	0
Ce2O3	0	0	0	0	0	0	0	0	0	0	0
SO3	0	0	0	0	0	0	0	0	0	0	0
F	0	0	0	0	0	0	0	0	0	0	0
Cl	1.13	0.68	0.75	2.95	2.79	0.76	0.85	0.92	0.94	0.41	0.5
H2O(c)	7.97	8.35	8.27	7.62	7.62	8.35	8.36	8.3	8.35	8.5	8.43
O=F	0	0	0	0	0	0	0	0	0	0	0
O=Cl	0.26	0.15	0.17	0.66	0.63	0.17	0.19	0.21	0.21	0.09	0.11
Sum Ox%	95.32	96.06	95.24	95.91	95.41	96.07	97.05	97.02	97.18	96.12	96.21
Cations											
Si	5.863	6.097	6.132	6.048	6.063	6.129	6.059	6.026	6.073	6.195	6.119
Ti	0	0	0.001	0	0	0.005	0.001	0	0.001	0	0.002
Al/Al IV	0.001	0.01	0.004	0.001	0.002	0	0	0.002	0	0.002	0.006
Al VI	0	0	0	0	0	0	0	0	0	0	0
Cr	0	0	0.003	0	0.003	0.005	0.003	0	0	0.003	0.005
Fe2+	5.958	5.176	5.186	4.158	4.25	4.845	4.961	5.148	4.849	6.105	6.217
V	0.001	0.006	0	0.009	0	0.004	0	0	0.006	0	0
Zn	0	0.01	0.001	0.006	0.006	0.001	0	0	0	0.01	0.003
Mn2+	2.237	2.489	2.426	3.628	3.568	2.759	2.81	2.684	2.886	1.356	1.414
Mg	0.059	0.102	0.09	0.034	0.026	0.095	0.088	0.081	0.072	0.104	0.095
Ca	0.001	0.004	0.009	0.06	0.005	0.009	0.007	0.018	0.031	0.02	0.013
Na	0.009	0.004	0.007	0	0.01	0.019	0.017	0.004	0.008	0	0.001
K	0.001	0	0	0.002	0	0	0.004	0.003	0.003	0.003	0.001
Ba	0.002	0	0.01	0.002	0.001	0	0	0.009	0	0.005	0
P	0	0	0	0	0	0	0	0	0	0	0
Rb	-	-	-	-	-	-	-	-	-	-	-
Cs	-	-	-	-	-	-	-	-	-	-	-
Sr	0	0	0	0	0	0	0	0	0	0	0
Ni	0.008	0	0	0	0.005	0	0	0	0	0.001	0
Y	0	0	0	0	0	0	0	0	0	0	0
Zr	0	0	0	0	0	0	0	0	0	0	0
La	0	0	0	0	0	0	0	0	0	0	0
Ce	0	0	0	0	0	0	0	0	0	0	0
S	0	0	0	0	0	0	0	0	0	0	0
F	0	0	0	0	0	0	0	0	0	0	0
Cl	0.348	0.202	0.226	0.894	0.852	0.225	0.252	0.274	0.278	0.12	0.147
OH	9.652	9.797	9.773	9.105	9.148	9.775	9.748	9.726	9.722	9.88	9.852
Sum Cat#	24.141	23.897	23.867	23.947	23.939	23.871	23.95	23.976	23.929	23.804	23.875
XMg	0.01	0.019	0.017	0.008	0.006	0.019	0.017	0.016	0.015	0.017	0.015

Pyrosmalite

Cations calculated on the basis of 20 (O) and 10 (OH, F, Cl)

	Olivine-pyroxenoid ore (Burnham) (probed 13/12/1999)				Graphitic ore, olivine facies (Inveravon)			
Wt %	sz043-3 1_ps1	sz043-3 1_ps2	sz037-21 2_ps1	sz037-21 2_ps2	nz039-2 2_ps1	nz039-2 2_ps2	nz039-2 2_ps-clear1	nz039-2 2_ps-clear2
SiO2	35.21	34.52	35.05	35.18	35.04	33.64	33.48	33.12
TiO2	0.01	0.01	0	0.04	0	0.04	0.01	0.01
Al2O3	0	0.02	0.02	0.03	0.29	0.03	0	0.03
Cr2O3	0.01	0	0	0	0.04	0.01	0.02	0.01
FeO	31.92	33.25	35.74	35.44	44.49	45.91	42.62	43.11
V2O3	0	0	0.02	0.04	0.03	0	0	0
ZnO	0	0	0	0.02	0.14	0.07	0.1	0
MnO	19.84	19.37	17.49	17.33	7.22	7.37	9.68	9.28
MgO	0.66	0.73	0.18	0.16	0.85	0.85	0.3	0.31
CaO	0.01	0.08	0.05	0.02	0.05	0	0.02	0.02
Na2O	0.02	0.02	0.01	0	0.05	0	0.01	0
K2O	0.01	0	0	0	0.03	0.02	0.01	0
BaO	0	0.07	0.04	0	0	0	0	0
P2O5	0	0	0	0	0	0	0	0
Rb2O	-	-	-	-	-	-	-	-
Cs2O	-	-	-	-	-	-	-	-
SrO	0	0	0	0	0	0	0.02	0
NiO	0.02	0.02	0.03	0.05	0.08	0	0.07	0.01
Y2O3	0	0	0	0	0	0	0	0
ZrO2	0	0	0	0	0	0	0	0
La2O3	0	0	0	0	0	0	0	0
Ce2O3	0	0	0	0	0	0	0	0
SO3	0	0	0	0	0	0	0	0
F	0	0	0	0	0	0	0	0
Cl	0.96	1.17	0.51	0.54	0.69	1.07	5.42	4.11
H2O(c)	8.37	8.29	8.51	8.49	8.49	8.23	6.98	7.25
O=F	0	0	0	0	0	0	0	0
O=Cl	0.22	0.26	0.11	0.12	0.16	0.24	1.22	0.93
Sum Ox%	96.82	97.3	97.52	97.23	97.33	97	97.51	96.34
Cations								
Si	6.125	6.027	6.084	6.11	6.065	5.933	6.007	5.983
Ti	0.002	0.002	0	0.005	0	0.006	0.001	0.001
Al/Al IV	0	0.003	0.004	0.007	0.06	0.007	0	0.006
Al VI	0	0	0	0	0	0	0	0
Cr	0.001	0	0	0	0.006	0.001	0.002	0.001
Fe2+	4.643	4.854	5.188	5.148	6.439	6.773	6.396	6.514
V	0	0	0.002	0.006	0.004	0	0	0
Zn	0	0	0	0.003	0.018	0.009	0.014	0
Mn2+	2.923	2.865	2.572	2.549	1.059	1.102	1.471	1.421
Mg	0.171	0.19	0.046	0.04	0.219	0.223	0.081	0.082
Ca	0.002	0.016	0.008	0.004	0.008	0	0.003	0.003
Na	0.008	0.008	0.003	0	0.015	0	0.004	0
K	0.001	0	0	0.001	0.006	0.004	0.001	0
Ba	0	0.005	0.003	0	0	0	0	0
P	0	0	0	0	0	0	0	0
Rb	-	-	-	-	-	-	-	-
Cs	-	-	-	-	-	-	-	-
Sr	0	0	0	0	0	0	0.002	0
Ni	0.002	0.003	0.004	0.007	0.011	0	0.01	0.002
Y	0	0	0	0	0	0	0	0
Zr	0	0	0	0	0	0	0	0
La	0	0	0	0	0	0	0	0
Ce	0	0	0	0	0	0	0	0
S	0	0	0	0	0	0	0	0
F	0	0	0	0	0	0	0	0
Cl	0.283	0.347	0.15	0.159	0.202	0.321	1.647	1.26
OH	9.717	9.653	9.85	9.84	9.797	9.679	8.353	8.74
Sum Cat#	23.878	23.973	23.914	23.879	23.91	24.058	23.993	24.013
XMg	0.035	0.038	0.009	0.008	0.033	0.032	0.013	0.012

Pyroxenoid

Cations calculated on the basis of 6 (O)

	Olivine-pyroxenoid ore (Burnham)									
Wt %	NZ024-23A 1-2	NZ024-23A 1-5	NZ024-23A 1-6	NZ024-23A 3-1	NZ024-23A 3-2	NZ024-23A 4-1	NZ024-23A 4-3	NZ024-23A 5-1	NZ024-23A 6-1	NZ024-23A 6-2
SiO2	45.43	45.18	45.47	45.24	45.1	45.68	45.39	44.99	45.69	45.07
TiO2	0	0.03	0	0	0	0	0.02	0	0.02	0
Al2O3	0.01	0.01	0.01	0.02	0.01	0.01	0	0.01	0	0.01
Cr2O3	0.01	0	0.02	0.02	0	0	0.02	0	0.05	0.01
Fe2O3(c)	0.87	0.97	0.66	0.66	1.21	0.13	0.74	0.79	0.83	0.85
FeO(c)	24	24.57	24.92	25.07	24.88	22.06	21.47	21.25	21.79	21.44
MnO	21.25	20.86	19.83	19.94	20.27	22.15	22.35	22.35	22.53	22.17
MgO	0.59	0.65	0.66	0.62	0.7	0.53	0.51	0.49	0.53	0.54
CaO	5.94	5.55	6.26	6.01	5.59	7.1	7.14	7.02	7.08	7.04
Na2O	0.02	0.02	0.04	0.01	0.03	0.02	0.03	0.01	0.01	0
K2O	0.01	0	0.01	0	0	0	0	0	0	0
Sum Ox%	98.13	97.84	97.87	97.58	97.77	97.68	97.66	96.91	98.51	97.14
Cations										
Si	1.987	1.983	1.99	1.989	1.981	1.998	1.988	1.987	1.985	1.985
Ti	0	0.001	0	0	0	0	0.001	0	0.001	0
Al/Al IV	0	0.001	0	0.001	0	0.001	0	0	0	0
Al VI	0	0	0	0	0	0	0	0	0	0
Cr	0	0	0.001	0.001	0	0	0.001	0	0.002	0
Fe3+	0.029	0.032	0.022	0.022	0.04	0.004	0.025	0.026	0.027	0.028
Fe2+	0.878	0.902	0.912	0.921	0.914	0.807	0.786	0.785	0.792	0.79
Mn2+	0.787	0.776	0.735	0.742	0.754	0.821	0.829	0.836	0.829	0.827
Mg	0.038	0.043	0.043	0.041	0.046	0.034	0.033	0.033	0.034	0.036
Ca	0.278	0.261	0.293	0.283	0.263	0.333	0.335	0.332	0.33	0.332
Na	0.002	0.002	0.003	0.001	0.002	0.002	0.003	0.001	0.001	0
K	0.001	0	0	0	0	0	0	0	0	0
Sum Cat#	4	4	4	4	4	4	4	4	4	4
Wo(Ca)	23.29	21.64	23.50	22.72	21.51	28.33	29.02	28.89	28.53	28.71
En(Mg)	3.22	3.53	3.43	3.28	3.72	2.93	2.86	2.83	2.95	3.07
Fs(Fe2+)	73.49	74.83	73.07	74.00	74.76	68.74	68.13	68.28	68.52	68.22
XMg	0.042	0.045	0.045	0.042	0.047	0.041	0.04	0.04	0.041	0.043

Pyroxenoid

Cations calculated on the basis of 6 (O)

	Olivine-pyroxenoid ore (Burnham)		Banded olivine-pyroxenoid with stage IIa alteration overprint (Broadlands/Inveravon, olivine facies)								
Wt %	NZ024-23A 7-1	NZ024-23A 7-2	SZ061-11A 1-7	SZ061-11A 3-3	SZ061-11A 3-4	SZ061-11A 3-5	SZ061-11A 6-2	SZ061-11A 7-3	SZ061-11A 7-7	SZ061-11B 1-1	SZ061-11B 2-1
SiO2	45.66	45.71	44.67	47.17	45.47	45.19	45.15	45.24	45.29	45.09	44.97
TiO2	0	0	0.02	0.04	0.04	0.02	0.01	0	0.01	0.01	0.02
Al2O3	0	0	0.01	0.14	0.02	0	0.01	0.04	0.02	0.03	0.01
Cr2O3	0.01	0	0.01	0	0	0.05	0	0	0	0.03	0.02
Fe2O3(c)	0.33	0.23	1.11	0	0.62	1.31	0.86	0.7	0.85	0.86	0.47
FeO(c)	22.43	22.2	32.23	39.37	32.93	32.13	32.46	32.74	32.26	32.81	32.26
MnO	21.39	22.27	14.2	5.82	14.19	14.56	14.14	14.34	14.81	14.37	14.66
MgO	0.54	0.5	0.11	0.3	0.1	0.13	0.17	0.21	0.2	0.24	0.25
CaO	7.38	7.01	5.03	3.41	5.32	5.3	5.33	4.95	5.09	4.67	4.71
Na2O	0.02	0.01	0.04	0.08	0.02	0.03	0.02	0.02	0	0.03	0.04
K2O	0.01	0	0.01	0.01	0	0	0	0	0	0	0
Sum Ox%	97.77	97.93	97.43	96.33	98.7	98.73	98.15	98.26	98.54	98.14	97.41
Cations											
Si	1.995	1.996	1.982	2.071	1.989	1.978	1.986	1.988	1.985	1.986	1.993
Ti	0	0	0.001	0.001	0.001	0.001	0	0	0	0	0.001
Al/Al IV	0	0	0	0	0.001	0	0	0.002	0.001	0.001	0.001
Al VI	0	0	0	0.007	0	0	0	0	0	0	0
Cr	0	0	0	0	0	0.002	0	0	0	0.001	0.001
Fe3+	0.011	0.007	0.037	0	0.02	0.043	0.028	0.023	0.028	0.029	0.016
Fe2+	0.82	0.811	1.196	1.446	1.205	1.176	1.194	1.203	1.183	1.208	1.195
Mn2+	0.792	0.824	0.534	0.216	0.526	0.54	0.527	0.534	0.55	0.536	0.55
Mg	0.035	0.032	0.007	0.019	0.007	0.009	0.011	0.014	0.013	0.016	0.016
Ca	0.346	0.328	0.239	0.16	0.249	0.248	0.251	0.233	0.239	0.22	0.223
Na	0.001	0	0.003	0.007	0.002	0.003	0.001	0.002	0	0.003	0.004
K	0	0	0	0.001	0	0	0	0	0	0	0
Sum Cat#	4	4	4	3.928	4	4	4	4	4	4	4
Wo(Ca)	28.79	28.01	16.58	9.86	17.06	17.33	17.25	16.08	16.67	15.25	15.57
En(Mg)	2.91	2.77	0.50	1.19	0.45	0.61	0.75	0.95	0.91	1.09	1.15
Fs(Fe2+)	68.30	69.23	82.92	88.95	82.49	82.07	82.01	82.97	82.43	83.65	83.28
XMg	0.041	0.038	0.006	0.013	0.005	0.007	0.009	0.011	0.011	0.013	0.014

Pyroxenoid

Cations calculated on the basis of 6 (O)

	Banded olivine-pyroxenoid with stage IIa alteration overprint (Broadlands/Inveravon, olivine facies)										
Wt %	SZ061-11B 3-1	SZ061-11B 3-2	SZ061-11B 3-3	SZ061-11B 4-1	SZ061-11B 4-4	SZ061-11B 5-2	SZ061-11B 5-3	SZ061-11B 5-4	SZ061-11B 6-6	SZ061-11B 6-7	SZ061-11B 6-8
SiO2	44.5	44.71	44.63	45.06	44.54	44.73	45.37	44.53	43.83	44.8	44.61
TiO2	0.06	0	0.02	0	0	0.04	0.02	0	0	0	0.04
Al2O3	0.1	0.02	0	0.03	0.39	0.05	0.01	0.02	0.01	0.02	0.02
Cr2O3	0	0	0	0.04	0	0.02	0.05	0	0	0.02	0.02
Fe2O3(c)	1.59	1.26	0.85	1.17	1.31	1.47	0.64	1.11	2.56	1.02	1.18
FeO(c)	32.19	32.22	32.08	31.64	31.61	32.39	32.82	31.93	30.04	32.11	32.13
MnO	13.89	14.53	14.55	15.15	14.45	14.54	14.68	14.77	14.38	14.56	14.77
MgO	0.31	0.3	0.27	0.34	0.35	0.32	0.35	0.33	0.36	0.38	0.36
CaO	4.52	4.66	4.67	4.79	4.87	4.52	4.6	4.38	5.56	4.64	4.34
Na2O	0.13	0	0.02	0.03	0.03	0	0.01	0.03	0.01	0.01	0.01
K2O	0.01	0	0	0	0.01	0.01	0	0	0	0.01	0.02
Sum Ox%	97.3	97.71	97.11	98.24	97.56	98.08	98.55	97.11	96.76	97.58	97.49
Cations											
Si	1.975	1.979	1.986	1.981	1.969	1.973	1.988	1.982	1.957	1.983	1.979
Ti	0.002	0	0.001	0	0	0.001	0.001	0	0	0	0.001
Al/Al IV	0.005	0.001	0	0.001	0.021	0.002	0.001	0.001	0.001	0.001	0.001
Al VI	0	0	0	0	0	0	0	0	0	0	0
Cr	0	0	0	0.001	0	0.001	0.002	0	0	0.001	0.001
Fe3+	0.053	0.042	0.029	0.039	0.044	0.049	0.021	0.037	0.086	0.034	0.04
Fe2+	1.195	1.193	1.194	1.163	1.169	1.195	1.203	1.189	1.122	1.189	1.192
Mn2+	0.522	0.545	0.548	0.564	0.541	0.543	0.545	0.557	0.544	0.546	0.555
Mg	0.021	0.02	0.018	0.022	0.023	0.021	0.023	0.022	0.024	0.025	0.024
Ca	0.215	0.221	0.223	0.225	0.231	0.214	0.216	0.209	0.266	0.22	0.206
Na	0.012	0	0.002	0.003	0.002	0	0.001	0.003	0.001	0.001	0.001
K	0	0	0	0	0.001	0	0	0	0	0	0.001
Sum Cat#	4	4	4	4	4	4	4	4	4	4	4
Wo(Ca)	15.03	15.43	15.52	15.98	16.21	14.94	14.99	14.72	18.83	15.36	14.50
En(Mg)	1.44	1.36	1.27	1.59	1.64	1.49	1.58	1.55	1.71	1.75	1.65
Fs(Fe2+)	83.53	83.21	83.21	82.43	82.15	83.56	83.43	83.74	79.46	82.89	83.84
XMg	0.017	0.016	0.015	0.019	0.02	0.018	0.019	0.018	0.021	0.021	0.019

Pyroxenoid

Cations calculated on the basis of 6 (O)

	Olivine-pyroxenoid ore (Burnham)								Hedenbergite ore, minor fluorite (Kheri)	
Wt %	nz033-6 1_oli1	nz033-6 1_oli2	nz033-6 2_pf1	nz033-6 2_pf2	sz037-21 2_oli1	sz037-21 2_oli2	sz037-21 1_pf1	sz037-21 1_pf2	sz028-6 2_hd1	sz028-6 2_hd2
SiO2	45.88	47.9	45.79	45.91	45.77	46.05	45.83	45.83	47.38	47.56
TiO2	0	0	0	0.02	0.02	0	0.01	0.02	0	0
Al2O3	0.04	0.13	0.03	0.02	0.02	0.03	0.05	0.04	0.22	0.24
Cr2O3	0	0.01	0.02	0.01	0	0.02	0	0	0	0
Fe2O3(c)	0.11	0	0.02	0	0.83	0.03	0.41	0.89	0	0
FeO(c)	32.95	40.97	31.66	30.92	28.64	29.14	29.21	28.68	44.87	44.89
MnO	15.35	6.04	16.08	16.18	17.62	17.44	16.86	17.69	2.81	2.8
MgO	0.41	1.15	0.37	0.32	0.27	0.24	0.29	0.27	0.83	0.75
CaO	4.41	0.86	4.69	4.97	6.06	6.11	6.12	6	0.51	0.8
Na2O	0	0	0.02	0.01	0	0	0.03	0.01	0.08	0.1
K2O	0	0	0.01	0	0	0	0.01	0	0	0
Sum Ox%	99.14	97.08	98.69	98.37	99.24	99.07	98.82	99.43	96.71	97.15
Cations										
Si	1.997	2.081	2	2.007	1.985	1.998	1.993	1.984	2.076	2.075
Ti	0	0	0	0.001	0.001	0	0	0.001	0	0
Al/Al IV	0.002	0	0	0	0.001	0.002	0.003	0.002	0	0
Al VI	0	0.007	0.001	0.001	0	0	0	0	0.011	0.012
Cr	0	0	0.001	0	0	0.001	0	0	0	0
Fe3+	0.004	0	0.001	0	0.027	0.001	0.013	0.029	0	0
Fe2+	1.199	1.489	1.157	1.13	1.039	1.058	1.062	1.038	1.644	1.638
Mn2+	0.566	0.222	0.595	0.599	0.648	0.641	0.621	0.649	0.104	0.104
Mg	0.026	0.075	0.024	0.021	0.018	0.015	0.019	0.017	0.054	0.049
Ca	0.205	0.04	0.219	0.233	0.282	0.284	0.285	0.278	0.024	0.037
Na	0	0	0.002	0.001	0	0	0.003	0.001	0.007	0.009
K	0	0	0.001	0	0	0	0	0	0	0
Sum Cat#	4	3.915	4	3.992	4	4	4	4	3.921	3.923
Wo(Ca)	14.36	2.51	15.67	16.82	21.05	20.94	20.88	20.85	1.40	2.16
En(Mg)	1.84	4.66	1.70	1.52	1.31	1.13	1.37	1.31	3.15	2.85
Fs(Fe2+)	83.81	92.83	82.63	81.66	77.64	77.94	77.75	77.84	95.45	94.99
XMg	0.021	0.048	0.02	0.018	0.017	0.014	0.017	0.017	0.032	0.029

Appendix 2

Wholerock Major and Trace Element Geochemistry

2.1 Phillips PW1480 XRF detection limits, School of Earth Sciences, University of Tasmania

(Phil Robinson, Analyst, School of Earth Sciences, University of Tasmania)

Fusion beads (major elements)

(normal silicate method)

oxide	wt %	calculated ppm
SiO2	0.002	9
TiO2	0.006	36
Al2O3	0.008	42
Fe2O3	0.0041	29
MnO	0.0035	27
MgO	0.011	66
CaO	0.009	64
Na2O	0.024	178
K2O	0.0004	3
P2O5	0.0026	11
S	0.01	40*
CuO	0.01	80
ZnO	0.01	80
PbO	0.01	93

* — if analysed as SO3

Pressed powder pellets (trace elements)

Element	ppm	Element	ppm	Element	ppm
Li	—	Zn	1	Nd	2 / 0.26*
Be	—	Ga	1.5	Sm	0.23*
B	—	As	3	Eu	0.22*
Na	180	Se	1	Gd	0.20*
Mg	70	Rb	1	Tb	0.20*
Al	40	Sr	1	Dy	0.19*
Si	10	Y	1 / 0.5*	Ho	0.18*
P	11	Zr	1	Er	0.17*
S	20	Nb	0.5	Tm	0.17*
K	3	Mo	1	Yb	0.17*
Ca	6	Ag	2	Lu	0.15*
Sc	2 / 0.17*	Cd	1	Hf	—
Ti	40	Sn	1.5	Ta	—
V	1.5	Sb	2	W	2
Cr	1	Te	3	Au	3
Mn	1	Cs	—	Tl	1
Fe	2	Ba	4	Pb	1.5
Co	2	La	2 / 0.35*	Bi	2
Ni	1	Ce	4 / 0.33*	Th	1.5
Cu	2	Pr	0.31*	U	1

* — ionic exchange XRF method (Robinson et al., 1986)

2.2 Wholerock Major and Trace Element Data

All major and trace elements determined by XRF unless otherwise stated.
REE determined by ionic exchange XRF method (Robinson et al., 1986) unless otherwise stated.

Amphibolite (Core Amphibolite)

Sample No.	SZ056-1	SGW4-274	SGW4-287	SGW13-186	SGW13-210	SGW13-229	SGW59-517	SGW59-529	SGW64-342	SGW64-370
(wt%)										
SiO2	48.27	48.82	49.14	48.10	47.88	49.05	47.48	48.32	48.64	44.73
TiO2	1.16	1.05	1.27	1.11	1.20	1.15	1.18	1.16	1.17	1.25
Al2O3	13.79	15.39	15.11	13.64	14.12	14.10	14.46	14.28	14.15	15.20
Fe2O3	13.51	12.02	13.15	13.06	13.99	13.37	13.68	13.38	13.18	15.98
MnO	0.26	0.21	0.23	0.23	0.24	0.23	0.25	0.25	0.25	0.24
MgO	8.24	6.86	6.45	8.40	8.17	7.78	8.53	8.50	7.64	9.31
CaO	10.41	12.67	11.85	11.16	9.25	10.77	10.52	10.11	10.72	7.21
Na2O	2.09	2.02	1.92	1.70	2.40	2.04	2.03	1.94	1.90	1.94
K2O	0.84	0.30	0.46	1.10	0.82	0.60	0.54	0.69	1.02	0.63
P2O5	0.08	0.07	0.07	0.08	0.08	0.08	0.08	0.08	0.08	0.09
ZnO	-	-	-	-	-	-	-	-	-	-
PbO	-	-	-	-	-	-	-	-	-	-
LOI (incl. S)	1.11	0.34	0.42	1.35	1.47	1.00	1.49	1.39	1.19	3.57
TOTAL	99.76	99.75	100.07	99.93	99.62	100.17	100.24	100.10	99.94	100.15
S	0.05	0.13	0.06	0.05	0.02	0.16	0.02	0.08	0.12	0.03
(ppm)										
Pb	177	126	40	98	70	254	107	90	50	29
Zn	252	170	200	271	199	220	291	232	219	173
Cu	-	-	-	-	-	-	-	-	-	-
Ni	-	-	-	-	-	-	-	-	-	-
Sb	3	<2	<2	2	2	6	<2	3	3	3
Cd	<1	<1	<1	<1	<1	1	<1	<1	<1	<1
Ag	<2	4	<2	<2	<2	3	<2	<2	<2	<2
Nb	3.3	3.6	3.9	4.4	3.7	4.5	4.6	4.4	4.2	4.2
Zr	65	63	68	60	68	64	66	63	66	64
Sr	115	159	150	119	127	126	121	116	128	128
Ba	74	30	50	55	73	54	34	42	55	59
Y	21	19	21	19	21	21	21	21	22	20
As	36	4	6	7	112	179	12	6	7	3
Bi	<2	2	<2	2	<2	2	<2	<2	<2	<2
W	3	3	2	<2	<2	<2	<2	<2	<2	3
Rb	24	6	17	25	32	21	18	24	25	30
U	<1.5	<1.5	<1.5	<1.5	<1.5	<1.5	<1.5	<1.5	1.5	<1.5
Th	<1.5	<1.5	<1.5	2	<1.5	<1.5	<1.5	<1.5	<1.5	<1.5
La	*4.46*	7	5	*4.32*	10	4	3	5	*4.89*	4
Ce	*10.88*	-	-	*10.72*	-	-	-	-	*11.60*	-
Pr	*1.69*	-	-	*1.65*	-	-	-	-	*1.79*	-
Nd	*8.73*	-	-	*8.41*	-	-	-	-	*9.60*	-
Sm	*2.67*	-	-	*2.57*	-	-	-	-	*3.00*	-
Eu	*1.11*	-	-	*0.95*	-	-	-	-	*1.14*	-
Gd	*3.51*	-	-	*3.32*	-	-	-	-	*3.84*	-
Tb	*0.68*	-	-	*0.64*	-	-	-	-	*0.70*	-
Dy	*3.88*	-	-	*3.63*	-	-	-	-	*4.06*	-
Ho	*0.84*	-	-	*0.77*	-	-	-	-	*0.85*	-
Er	*2.27*	-	-	*2.07*	-	-	-	-	*2.28*	-
Tm	*0.32*	-	-	*0.29*	-	-	-	-	*0.32*	-
Yb	*2.03*	-	-	*1.88*	-	-	-	-	*1.99*	-
Lu	*0.29*	-	-	*0.25*	-	-	-	-	*0.28*	-
Sc	*37.61*	-	-	*37.77*	-	-	-	-	*37.91*	-
Th	*0.59*	-	-	*0.54*	-	-	-	-	*0.58*	-
U	*0.23*	-	-	*0.17*	-	-	-	-	*0.21*	-
Y	*21.34*	-	-	*19.88*	-	-	-	-	*22.37*	-

Italicised data determined by ICP-MS, School of Earth Sciences, University of Tasmania. Samples digested using Na_2O_2 sinter method (Z. Yu and P. Robinson, pers. comm., 1999).

Migmatitic gneiss (Gandry Dam Gneiss)

Sample No.	KMG2	NZ027-6	SZU51-1	SZ101-6	EQ557	EQ657	EQ668	EQ676	EQ689	EQ700	EQ709	EQ862	EQ876	EQ957
(wt%)					BHP	BHP	BHP	BHP	BHP	BHP	BHP	BHP	BHP	BHP
SiO2	71.78	60.06	60.90	52.46	69.69	69.44	81.50	63.31	55.90	53.99	76.08	78.55	74.98	59.97
TiO2	0.46	0.75	0.69	0.67	0.51	0.56	0.32	0.92	0.84	1.00	0.43	0.41	0.34	0.68
Al2O3	13.94	17.56	16.74	17.83	15.01	14.45	8.13	16.39	20.44	20.87	11.13	9.27	11.77	18.55
Fe2O3	4.01	10.57	10.04	16.34	4.56	4.98	2.52	6.39	6.91	8.62	3.44	4.17	3.46	7.44
MnO	0.11	0.20	0.08	0.10	0.18	0.08	0.03	0.05	0.10	0.07	0.06	0.02	0.06	0.05
MgO	1.33	3.01	2.53	3.79	1.33	1.64	0.81	2.78	2.23	2.50	1.18	1.27	1.37	2.47
CaO	0.74	0.28	0.26	0.31	0.66	0.87	0.82	0.76	0.64	0.55	0.61	0.67	0.40	0.94
Na2O	1.56	0.89	1.14	1.17	2.06	2.85	1.89	3.17	1.42	0.53	1.72	2.84	1.58	3.30
K2O	3.36	4.44	3.69	3.30	3.79	4.01	0.97	2.52	6.35	5.45	2.97	1.38	4.05	3.21
P2O5	0.12	0.06	0.08	0.08	0.08	0.09	0.09	0.08	0.15	0.08	0.07	0.13	0.11	0.15
ZnO	-	-	0.01	0.01	-	-	-	-	-	-	-	-	-	-
PbO	-	-	0.01	0.02	-	-	-	-	-	-	-	-	-	-
LOI (incl. S)	2.08	2.08	3.36	2.81	-	-	-	-	-	-	-	-	-	-
TOTAL	99.49	99.90	99.54	98.89	97.87	98.97	97.08	96.37	94.98	93.66	97.69	98.71	98.12	96.76
S	0.01	0.13	0.17	0.25	0.01	0.01	0.01	0.01	0.01	0.01	0.01	0.01	0.01	0.01
(ppm)														
Pb	31	50	10	16	144	38	8	13	51	25	34	18	23	15
Zn	86	58	35	46	99	69	22	48	117	130	49	22	64	28
Cu	-	-	53	20	-	-	-	-	-	-	-	-	-	-
Ni	-	-	48	55	-	-	-	-	-	-	-	-	-	-
Sb	<2	<2	<2	<2	-	-	-	-	-	-	-	-	-	-
Cd	<1	<1	<2	<2	-	-	-	-	-	-	-	-	-	-
Ag	<2	<2	<2	<2	-	-	-	-	-	-	-	-	-	-
Nb	13.3	24.1	17.1	16.4	8	13	8	19	20	21	8	10	8	15
Zr	220	226	169	139.7	197	235	205	227	185	246	198	280	233	168
Sr	87	49	48.9	44.2	90	123	37	61	118	57	100	74	58	111
Ba	584	491	561.4	351.2	829	689	54	182	1198	787	479	264	791	362
Y	25	27	22.94	24.93	33	29	21	29	44	39	30	21	31	34
As	<3	<3	3	9	-	-	-	-	-	-	-	-	-	-
Bi	<2	<2	0.3	1.1	-	-	-	-	-	-	-	-	-	-
W	-	3	4.2	23.4	-	-	-	-	-	-	-	-	-	-
Rb	168	255	177	196	166	162	48	155	302	302	133	62	134	179
U	3.5	22.1	6.2	3.9	-	-	-	-	-	-	2.7	-	-	5.1
Th	17.5	15	15.4	15.7	-	-	-	-	-	-	18	-	-	17.7
La	*47.98*	32.00	49.31	39.49	-	-	-	-	-	-	*48.78*	-	-	*45.71*
Ce	*78.15*	-	103.63	82.10	-	-	-	-	-	-	*77.37*	-	-	*71.34*
Pr	*10.46*	-	11.58	9.61	-	-	-	-	-	-	*10.71*	-	-	*10.30*
Nd	*38.55*	-	45.84	36.72	-	-	-	-	-	-	*39.65*	-	-	*38.43*
Sm	*7.01*	-	8.07	6.47	-	-	-	-	-	-	*7.13*	-	-	*6.99*
Eu	*1.04*	-	1.14	0.94	-	-	-	-	-	-	*1.17*	-	-	*0.96*
Gd	*5.42*	-	5.60	4.37	-	-	-	-	-	-	*5.55*	-	-	*5.39*
Tb	*0.83*	-	0.96	0.81	-	-	-	-	-	-	*0.93*	-	-	*0.83*
Dy	*4.68*	-	4.08	3.89	-	-	-	-	-	-	*5.09*	-	-	*5.06*
Ho	*0.92*	-	-	-	-	-	-	-	-	-	*1.05*	-	-	*1.06*
Er	*2.69*	-	2.39	2.67	-	-	-	-	-	-	*2.97*	-	-	*3.07*
Tm	*0.41*	-	-	-	-	-	-	-	-	-	*0.46*	-	-	*0.46*
Yb	*2.81*	-	2.16	2.68	-	-	-	-	-	-	*2.81*	-	-	*3.07*
Lu	*0.40*	-	-	-	-	-	-	-	-	-	*0.40*	-	-	*0.43*
Sc	*11.23*	-	-	-	-	-	-	-	-	-	*9.91*	-	-	*17.29*
Th	*19.63*	-	-	-	-	-	-	-	-	-	*16.52*	-	-	*16.64*
U	*4.03*	-	-	-	-	-	-	-	-	-	*3.24*	-	-	*4.27*
Y	*25.84*	-	-	-	-	-	-	-	-	-	*29.44*	-	-	*29.48*

Italicised data determined by ICP-MS, School of Earth Sciences, University of Tasmania. Samples digested using Na_2O_2 sinter method (Z. Yu and P. Robinson, pers. comm., 1999).

BHP — BHP Minerals data.

Sillimanite-garnet schist and garnet quartzite

Sample No.	NZ009-1	NZ009-2	NZ047-1	SZ048-6	SZ048-27
(wt%)					
SiO2	72.84	65.37	63.29	58.96	59.22
TiO2	0.36	0.65	0.68	0.67	0.72
Al2O3	11.66	18.70	18.76	19.04	18.95
Fe2O3	8.15	3.02	4.61	11.18	9.34
MnO	1.48	0.17	0.47	1.37	0.36
MgO	0.42	0.54	0.60	0.70	0.81
CaO	0.33	0.18	0.32	0.82	0.55
Na2O	0.39	0.44	0.34	0.18	0.32
K2O	4.66	8.12	7.81	4.84	6.23
P2O5	0.11	0.14	0.14	0.19	0.15
ZnO	-	-	0.02	0.01	0.02
PbO	-	-	0.09	0.04	0.06
LOI (incl. S)	-0.51	2.51	2.25	1.62	2.20
TOTAL	99.89	99.84	99.38	99.62	98.96
S	<0.01	0.01	0.01	0.01	0.16
(ppm)					
Pb	108	2169	644	273	500
Zn	121	123	166	81	153
Cu	-	-	6	7	50
Ni	-	-	26	28	34
Sb	<2	<2	<2	<2	6.2
Cd	<1	<1	<2	<2	<2
Ag	<2	<2	<2	<2	<2
Nb	8.4	15.5	17	16	16.7
Zr	212	164	201.7	175.7	189.3
Sr	39	51	57.1	26.4	33.2
Ba	577	606	723.5	467.6	473.7
Y	21	9	21.8	36.74	35.49
As	8	<3	4	9	9
Bi	<2	<2	0.2	1.9	0.2
W	5	2	10.6	22.9	7.5
Rb	181	374	320	188	298
U	2	3.9	-	-	-
Th	13	22	21	19	19
La	*32.15*	*50.11*	52.81	52.43	52.54
Ce	*52.24*	*77.12*	104.65	91.35	101.76
Pr	*6.62*	*10.61*	12.64	11.70	12.03
Nd	*25.10*	*39.98*	53.45	45.41	47.99
Sm	*4.46*	*6.72*	12.35	8.44	8.54
Eu	*1.04*	*1.74*	2.15	1.66	1.57
Gd	*3.79*	*4.34*	7.61	6.64	6.14
Tb	*0.76*	*0.44*	1.03	1.13	1.03
Dy	*4.48*	*1.89*	3.93	5.80	5.71
Ho	*0.84*	*0.29*	-	-	-
Er	*2.24*	*0.74*	2.39	3.61	3.54
Tm	*0.32*	*0.11*	-	-	-
Yb	*2.12*	*0.77*	2.33	3.55	3.54
Lu	*0.30*	*0.12*	-	-	-
Sc	*10.29*	*9.32*	-	-	-
Th	*14.06*	*14.06*	-	-	-
U	*1.81*	*3.86*	-	-	-
Y	*24.35*	*7.41*	-	-	-

Italicised data determined by ICP-MS, School of Earth Sciences, University of Tasmania. Samples digested using Na_2O_2 sinter method (Z. Yu and P. Robinson, pers. comm., 1999).

Gahnite-bearing sillimanite-biotite-garnet schist

Sample No.	NZ027-4	NZ004-10	NZ047-7	SZ061-50	NZ160-33
(wt%)					
SiO2	58.10	57.23	58.40	61.87	53.18
TiO2	0.92	0.86	0.71	0.79	0.94
Al2O3	21.96	23.84	19.46	20.13	24.20
Fe2O3	7.09	7.10	8.06	6.45	8.25
MnO	0.34	0.35	0.47	0.15	0.94
MgO	1.11	0.76	0.96	0.90	0.79
CaO	0.33	0.47	0.41	0.45	0.51
Na2O	0.36	0.18	0.75	0.27	0.27
K2O	4.94	4.68	6.06	4.86	7.26
P2O5	0.14	0.18	0.13	0.18	0.23
ZnO	0.58	-	1.48	-	0.37
PbO	0.06	-	0.12	-	0.13
LOI (ind. S)	3.84	4.22	3.09	3.74	3.83
TOTAL	99.76	99.87	100.12	99.79	100.91
S	0.05	0.02	0.05	0.01	0.22
(ppm)					
Pb	488	765	921	401	1040
Zn	3838	1675	11057	301	2639
Cu	15	-	16	-	93
Ni	41	-	26	-	91
Sb	7.1	3	6.1	3	24.9
Cd	4	4	4.1	<1	7.4
Ag	<2	<2	<2	<2	2.8
Nb	18.5	19	14.2	18.8	19.3
Zr	167	136	137.3	155	167.6
Sr	37.3	29	42.4	30	45.6
Ba	483.7	340	583.6	230	660.1
Y	30.17	27	37.32	17	54.62
As	8	12	19	4	45
Bi	0.4	<2	0.2	<2	0.7
W	5.6	7	19.6	8	24.5
Rb	233	224	238	234	291
U	-	11.5	-	3.6	-
Th	22	18	13	14	40
La	65.82	*20.05*	28.13	*24.96*	133.59
Ce	128.31	*31.38*	55.47	*38.64*	232.08
Pr	14.17	*4.16*	6.41	*5.09*	29.92
Nd	51.87	*16.36*	23.32	*19.95*	111.21
Sm	8.37	*3.22*	4.16	*3.80*	18.46
Eu	1.35	*0.79*	0.99	*2.20*	2.54
Gd	5.99	*3.34*	3.74	*3.00*	11.17
Tb	1.16	*0.71*	0.88	*0.51*	1.89
Dy	5.09	*4.64*	5.41	*2.92*	8.90
Ho	-	*1.02*	-	*0.64*	-
Er	3.33	*2.87*	4.05	*1.90*	5.63
Tm	-	*0.41*	-	*0.29*	-
Yb	3.45	*2.73*	3.64	*1.95*	5.17
Lu	-	*0.37*	-	*0.29*	-
Sc	-	*17.67*	-	*15.87*	-
Th	-	*16.29*	-	*12.47*	-
U	-	*9.90*	-	*2.66*	-
Y	-	*28.74*	-	*16.02*	-

Italicised data determined by ICP-MS, School of Earth Sciences, University of Tasmania. Samples digested using Na_2O_2 sinter method (Z. Yu and P. Robinson, pers. comm., 1999).

Graphitic ore — biotite-garnet facies

Sample No.	NZ016-1	NZ029-8	NZ033-2	NZ039-3	NZ047-8	NZ029-13	SZ157-11	NZ160-31
(wt%)								
SiO2	53.10	39.65	41.51	39.34	45.40	36.23	75.22	31.42
TiO2	0.10	0.33	0.26	0.23	0.53	0.32	0.24	0.21
Al2O3	2.02	7.41	7.36	5.66	12.71	7.45	5.70	6.36
Fe2O3	5.32	16.38	16.66	20.13	28.29	20.48	12.00	15.89
MnO	0.62	4.25	3.11	3.37	4.48	4.74	0.43	2.52
MgO	0.28	0.56	0.64	1.60	0.97	1.02	0.56	0.72
CaO	7.50	7.19	6.56	7.41	2.38	7.06	3.11	4.33
Na2O	<0.05	0.25	<0.1	0.55	0.06	0.13	<0.05	<0.1
K2O	0.18	1.63	1.71	1.80	1.61	1.88	0.22	0.07
P2O5	4.66	4.76	3.61	4.88	1.08	4.86	1.06	2.31
ZnO	2.24	2.83	7.17	7.24	0.31	6.15	0.09	27.45
PbO	22.54	12.00	6.24	2.96	0.06	5.33	1.32	0.06
LOI (ind. S)	2.34	2.65	2.84	4.53	0.89	4.09	0.96	7.16
TOTAL	100.90	99.89	97.67	99.70	98.77	99.74	100.91	98.50
S	4.42	2.93	4.67	4.17	1.47	3.97	0.21	13.75
C	**1.45**	-	**1.12**	**1.71**	-	-	-	**0.67**
S	**3.91**	-	**2.33**	**1.88**	-	-	-	**5.32**
H	**0.00**	-	**0.10**	**0.13**	-	-	-	**0.09**
(ppm)								
Pb	-	-	-	-	-	-	-	-
Zn	-	-	-	-	-	-	-	-
Cu	-	-	-	-	-	-	-	-
Ni	-	-	-	-	-	-	-	-
Sb	357.9	67.7	288.1	93.1	4.8	44.2	52.6	43.4
Cd	72.1	80.3	165.6	149.6	7.4	156.9	<1	677.9
Ag	311.9	407.5	333.8	161.3	<3	89.9	29.7	20.2
Nb	<1	3.4	2.6	3.5	13.3	4	5.6	1.8
Zr	26.7	79	59.6	60.1	133.1	65.2	66.3	46.2
Sr	49.9	69.3	48.4	70.8	16.6	84	19.2	9.7
Ba	41.2	301.8	123.3	284	118.5	258.2	14.8	14.1
Y	22.8	19.5	29.27	17.6	48.1	17.6	-	20.11
As	*9*	*72*	*237*	*32*	*11*	*24*	*85*	*29*
Bi	*0.5*	*0.5*	*2.9*	*0.4*	*0.1*	*0.3*	*0.2*	*1.1*
W	*382*	*639*	*18*	*489*	*746*	*4.8*	*11.6*	*48.3*
Rb	*6.99*	*184*	*192*	*155*	*196*	*203*	*12.5*	*8.39*
U	*7.4*	-	*9.95*	*11.5*	-	*8.93*	-	*6.05*
Th	*3.07*	-	*3.74*	*4.87*	-	*6.81*	-	*5.59*
La	34.70	37.10	31.33	29.50	6.30	37.00	*18.10*	41.86
Ce	57.00	65.90	35.73	44.10	14.20	59.10	*30.70*	67.48
Pr	6.05	7.14	4.31	5.55	2.27	7.11	*3.85*	7.73
Nd	23.10	24.90	15.31	21.50	10.00	27.50	*14.80*	30.68
Sm	5.30	4.04	3.21	4.43	3.47	5.09	*2.80*	5.20
Eu	9.34	6.07	5.24	4.48	1.34	7.87	*7.05*	2.72
Gd	5.09	3.20	2.84	3.73	4.78	4.27	*2.60*	4.40
Tb	0.85	0.61	0.54	0.59	0.93	0.59	*0.36*	0.74
Dy	3.86	3.13	3.05	2.58	7.15	2.73	*1.60*	3.32
Ho	-	-	-	-	-	-	-	-
Er	1.82	1.94	2.45	1.57	4.50	1.18	*0.70*	1.54
Tm	-	-	-	-	-	-	-	-
Yb	1.05	1.64	2.14	1.26	3.27	1.04	*0.60*	1.19
Lu	-	-	-	-	-	-	-	-
Sc	-	-	-	-	-	-	-	-
Th	-	-	-	-	-	-	-	-
U	-	-	-	-	-	-	-	-
Y	-	-	-	-	-	-	-	-

Italicised data determined by ICP-MS, Analabs (Perth, Western Australia). Samples digested using aqua regia/ perchloric acid/hydrofluoric acid digestion technique (Analabs code 201).

Bold data determined on a Carlo Erba IA 1108 elemental analyser by G. Rowbottom (Central Science Laboratory, University of Tasmania).

Graphitic ore — quartz-apatite facies

Sample No.	NZ040-4b	NZ030-13	NZ035-13
(wt%)			
SiO2	86.48	65.40	79.90
TiO2	0.08	0.14	0.13
Al2O3	0.53	2.02	2.39
Fe2O3	2.40	6.00	6.93
MnO	0.65	0.23	1.96
MgO	0.05	0.29	0.19
CaO	2.59	1.80	3.48
Na2O	0.09	<0.05	0.05
K2O	0.01	0.69	0.20
P2O5	1.83	0.46	1.91
ZnO	2.73	0.34	1.12
PbO	1.54	22.17	1.61
LOI (incl. S)	1.77	1.30	0.92
TOTAL	100.75	100.84	100.79
S	1.5	3.31	1.03
(ppm)			
Pb	-	-	-
Zn	-	-	-
Cu	-	-	-
Ni	-	-	-
Sb	65.3	245.6	63.4
Cd	104.3	22.5	34.2
Ag	33.1	230.2	22.1
Nb	2.2	<1	2.6
Zr	21.9	33.9	35.5
Sr	24.9	11.9	25.4
Ba	11.1	125.4	76.8
Y	15.9	7.6	8.25
As	*127*	*97*	*110*
Bi	*0.1*	*32.1*	*<0.1*
W	*20.8*	*520*	*7.3*
Rb	*2.81*	*66.7*	*26.2*
U	*3.69*	-	*5.09*
Th	*1.92*	-	*4.26*
La	83.60	39.50	24.26
Ce	127.40	51.10	36.92
Pr	14.05	4.82	4.09
Nd	53.10	15.90	14.72
Sm	9.70	3.23	2.85
Eu	26.00	10.90	8.64
Gd	7.18	2.38	2.60
Tb	0.90	0.41	0.42
Dy	3.08	1.51	1.41
Ho	-	-	-
Er	0.95	0.72	0.74
Tm	-	-	-
Yb	0.48	0.61	0.41
Lu	-	-	-
Sc	-	-	-
Th	-	-	-
U	-	-	-
Y	-	-	-

Italicised data determined by ICP-MS, Analabs (Perth, Western Australia). Samples digested using aqua regia/ perchloric acid/hydrofluoric acid digestion technique (Analabs code 201).

Graphitic ore — olivine facies

Sample No.	NZ016-2	NZ039-2	NZ040-4a	NZ044-2	NZ044-5	NZ047-2	NZ047-4	SZ051-4	NZ070-4	NZ160-20
(wt%)										
SiO2	71.26	17.18	40.11	23.38	45.65	22.25	24.62	35.99	73.93	26.56
TiO2	0.08	0.17	0.06	0.16	0.07	0.12	0.09	0.05	0.02	0.06
Al2O3	1.22	4.46	0.83	3.28	1.69	1.87	3.02	0.56	0.26	1.64
Fe2O3	20.56	49.58	39.41	31.54	34.85	40.19	40.88	37.54	22.25	30.20
MnO	5.38	4.54	10.07	8.78	11.54	7.95	9.93	8.21	3.79	10.64
MgO	0.12	0.77	0.26	0.60	0.32	0.41	0.62	0.19	0.09	0.58
CaO	3.82	11.82	4.42	11.38	3.99	2.14	6.31	4.17	1.28	13.08
Na2O	<0.05	<0.1	<0.05	0.20	<0.05	<0.1	<0.1	<0.05	0.06	0.20
K2O	0.02	0.01	0.00	0.02	0.00	1.25	0.03	0.07	0.04	0.05
P2O5	0.94	8.50	1.92	4.00	1.85	1.29	4.35	1.02	0.32	7.82
ZnO	0.49	0.22	3.49	1.42	0.62	0.57	1.36	0.73	0.25	2.76
PbO	0.25	0.42	0.52	14.32	0.96	17.00	4.56	12.60	0.36	7.40
LOI (incl. S)	-1.36	0.73	-2.33	1.03	-2.06	2.24	3.97	-1.54	-1.95	-1.59
TOTAL	102.77	98.40	98.76	100.11	99.48	97.28	99.73	99.59	100.69	99.40
S	0.24	1.71	1.57	2.66	0.36	3.82	1.09	2.18	0.08	2.45
(ppm)										
Pb	-	-	-	-	-	-	-	-	-	-
Zn	-	-	-	-	-	-	-	-	-	-
Cu	-	-	-	-	-	-	-	-	-	-
Ni	-	-	-	-	-	-	-	-	-	-
Sb	25	12.8	41.7	286.4	48.6	290	133.2	510.9	10.6	238.2
Cd	6.9	<2	113.5	40.5	9.8	8.7	27.9	44	2.8	75.9
Ag	5.2	14	12.5	294.8	49	242.4	234.9	305.4	5.1	160.9
Nb	3.4	5.7	1.7	1.2	2.3	1	1.4	<1	1.8	1.4
Zr	14.3	63.4	13.2	38.5	17.9	34.6	35.4	16.4	5.1	15
Sr	16.4	78.8	33.1	42.5	21.8	17.7	49.5	12.8	5.9	118.4
Ba	7.8	9.9	9.6	5.9	9.3	206.1	16.9	15.4	12.8	8
Y	32.6	60.4	22.6	34.3	14.69	4.33	11	17.67	2.1	14.7
As	*67*	*10*	*13*	*35*	*4*	*57*	*12*	*306*	*5*	*196*
Bi	*<0.1*	*1.4*	*<0.1*	*1.7*	*0.3*	*1.8*	*0.4*	*0.8*	*<0.1*	*0.1*
W	*28.8*	*38.2*	*16.7*	*282*	*6*	*43.8*	*39.5*	*75.5*	*9.1*	*11.8*
Rb	*2.55*	*2.25*	*1.98*	*3.14*	*0.83*	*120*	*4.26*	*2.74*	*5.4*	*2.17*
U	-	-	*1.59*	-	*3.97*	-	-	-	-	-
Th	-	-	*0.85*	-	*2.34*	-	-	-	-	-
La	6.99	176.46	35.50	62.20	20.25	20.27	29.52	24.97	15.70	51.90
Ce	9.74	231.13	57.80	104.90	33.20	27.71	45.80	41.93	20.80	73.70
Pr	1.33	25.74	7.10	11.07	4.16	3.08	5.32	5.15	2.30	7.82
Nd	5.83	98.76	30.50	39.50	17.75	10.41	18.39	20.78	8.63	27.90
Sm	1.69	21.96	7.34	7.43	4.59	2.00	3.89	5.58	1.57	5.40
Eu	3.05	30.53	22.63	15.13	7.49	3.86	6.22	27.48	8.69	23.38
Gd	2.08	19.15	7.18	5.92	4.12	1.23	2.54	5.79	1.18	5.54
Tb	0.43	2.44	0.99	1.03	0.61	0.17	0.51	0.85	<0.20	0.83
Dy	2.65	9.03	4.30	4.66	2.66	0.68	1.63	3.02	0.39	2.81
Ho	-	-	-	-	-	-	-	-	-	-
Er	1.56	4.18	1.70	2.68	1.11	0.32	1.25	1.07	0.25	0.97
Tm	-	-	-	-	-	-	-	-	-	-
Yb	1.22	2.55	1.10	2.14	0.78	0.24	1.01	0.41	<0.17	0.52
Lu	-	-	-	-	-	-	-	-	-	-
Sc	-	-	-	-	-	-	-	-	-	-
Th	-	-	-	-	-	-	-	-	-	-
U	-	-	-	-	-	-	-	-	-	-
Y	-	-	-	-	-	-	-	-	-	-

Italicised data determined by ICP-MS, Analabs (Perth, Western Australia). Samples digested using aqua regia/ perchloric acid/hydrofluoric acid digestion technique (Analabs code 201).

Olivine-pyroxenoid Pb-Ag ore — olivine-fluorite ore

Sample No.	NZ033-6	NZ034-12	NZ035-32
(wt%)			
SiO2	24.04	13.30	18.06
TiO2	0.04	0.05	0.04
Al2O3	0.47	0.13	0.04
Fe2O3	40.07	35.70	39.25
MnO	8.04	4.03	8.68
MgO	0.43	0.45	0.35
CaO	5.89	15.75	5.06
Na2O	<0.1	<0.1	<0.1
K2O	<0.01	<0.01	<0.01
P2O5	0.04	0.17	0.95
ZnO	0.57	1.42	3.94
PbO	19.61	17.58	17.24
LOI (ind. S)	-1.46	0.28	5.65
TOTAL	97.74	88.86	99.24
S	3.66	5.63	4.39
(ppm)			
Pb	-	-	-
Zn	-	-	-
Cu	-	-	-
Ni	-	-	-
Sb	234.1	342.6	650.3
Cd	28.2	52.4	122.9
Ag	714.6	794.7	821.8
Nb	<1	<1	1
Zr	9.3	15	17.6
Sr	2.8	8.4	12.8
Ba	8.4	<4	9.6
Y	95.47	114.8	18.38
As	*438*	*999*	*13*
Bi	*22.3*	*6*	*0.3*
W	*25.8*	*15.5*	*27.2*
Rb	*2.96*	*0.36*	*0.69*
U	-	-	-
Th	-	-	-
La	25.58	274.19	26.48
Ce	43.28	396.70	50.90
Pr	5.23	40.84	6.61
Nd	22.32	146.53	29.04
Sm	8.20	27.95	7.65
Eu	10.03	20.48	15.16
Gd	13.48	24.55	8.92
Tb	2.65	4.44	1.02
Dy	17.10	16.37	3.50
Ho	-	-	-
Er	8.78	5.69	1.01
Tm	-	-	-
Yb	4.19	2.78	0.44
Lu	-	-	-
Sc	-	-	-
Th	-	-	-
U	-	-	-
Y	-	-	-

Italicised data determined by ICP-MS, Analabs (Perth, Western Australia). Samples digested using aqua regia/ perchloric acid/hydrofluoric acid digestion technique (Analabs code 201).

Metasomatised graphitic ore — olivine facies

Sample No.	NZ016-2 3ALT	NZ016-2 3UNALT
(wt%)		
SiO2	70.25	71.26
TiO2	0.09	0.08
Al2O3	2.57	1.22
Fe2O3	11.55	20.56
MnO	3.06	5.38
MgO	0.17	0.12
CaO	5.77	3.82
Na2O	0.08	<0.05
K2O	0.03	0.02
P2O5	0.81	0.94
ZnO	0.14	0.49
PbO	6.19	0.25
LOI (ind. S)	0.32	-1.36
TOTAL	101.03	102.77
S	0.91	0.24
(ppm)		
Pb	-	-
Zn	-	-
Cu	-	-
Ni	-	-
Sb	62.1	25
Cd	5.1	6.9
Ag	64	5.2
Nb	2	3.4
Zr	27.8	14.3
Sr	15	16.4
Ba	7.1	7.8
Y	67.2	32.6
As	*41*	*67*
Bi	*0.3*	*<0.1*
W	*23.7*	*28.8*
Rb	*2.56*	*2.55*
U	-	-
Th	-	-
La	6.85	6.99
Ce	10.2	9.74
Pr	1.32	1.33
Nd	5.78	5.83
Sm	1.53	1.69
Eu	2.72	3.05
Gd	2.24	2.08
Tb	0.49	0.43
Dy	4.36	2.65
Ho	-	-
Er	3.94	1.56
Tm	-	-
Yb	3.59	1.22
Lu	-	-
Sc	-	-
Th	-	-
U	-	-
Y	-	-

Italicised data determined by ICP-MS, Analabs (Perth, Western Australia). Samples digested using aqua regia/ perchloric acid/hydrofluoric acid digestion technique (Analabs code 201).

2.3 Wholerock Major and Trace Element Sample Data

Sample no.	Sample no. suffix	Drill hole	Depth (m)	Section (mN)	Rock code	Minz. name	Facies	Name/Mine name	Comments
SZ056-1		CAD056	371.0	4800	AMPH			Core amphibolite	good clean sample
SGW64-370		CAD064	370.0	4900	AMPH			Core amphibolite	minor qz-ab veinlet
SGW64-342		CAD064	342.0	4900	AMPH			Core amphibolite	minor veining and coarse grained
SGW59-529		CAD059	529.0	4750	AMPH			Core amphibolite	good clean sample
SGW59-517		CAD059	517.0	4750	AMPH			Core amphibolite	very fine veinlet of ??
SGW4-287		CAD004	287.0	5400	AMPH			Core amphibolite	minor qz-ab veinlets
SGW4-274		CAD004	274.0	5400	AMPH			Core amphibolite	minor qz veinlet but otherwise clean
SGW13-229		CAD013	229.5	4900	AMPH			Core amphibolite	qz-chl veining and assoc. alt.
SGW13-210		CAD013	210.0	4900	AMPH			Core amphibolite	good clean sample
SGW13-186		CAD013	186.0	4900	AMPH			Core amphibolite	coarse grained, minor sericitic alt.
KMG2		CAD159	109.9	5300	GNES			Gandry Dam Gneiss	psammitic, good clean
NZ027-6		CAD027	340.8	5600	GNES			Gandry Dam Gneiss	pelitic
SZU51-1		CUD051	112.8	4850	GNES			Gandry Dam Gneiss	pelitic
EQ557		CAD159	357.3	5300	GNES			Gandry Dam Gneiss	strong partial melting, moderate red-rock alt.
EQ657		CAD276	92.4	5650	GNES			Gandry Dam Gneiss	pelitic, significant red-rock alt., incip. white k'spar(?) alt.
EQ668		CAD257	94.1	6000	GNES			Gandry Dam Gneiss	psammitic, minor red-rock alt.
EQ676		CAD269	107.2	6150	GNES			Gandry Dam Gneiss	pelitic, significant red-rock alt., minor chl-se alt.
EQ689		CAD240	100.2	6875	GNES			Gandry Dam Gneiss	pelitic, moderate red-rock alt., incip. se alt. & vnlets
EQ700		CAD242	96.4	6875	GNES			Gandry Dam Gneiss	pelitic, minor red-rock alt.
EQ709		CAD243	97.7	6875	GNES			Gandry Dam Gneiss	psammitic
EQ862		CAD154	258.3	4500	GNES			Gandry Dam Gneiss	psammitic, minor K'spar(?) vnlets
EQ876		CAD154	359.9	4500	GNES			Gandry Dam Gneiss	minor gt spotting in bands, weak incip. se alt.
EQ957		CAD129	167.2	4200	GNES			Gandry Dam Gneiss	pelitic
SZ101-6		CAD101	230.6	4500	GNES			Gandry Dam Gneiss	pelitic
SZ048-6		CAD048	332.6	4500	SHMU			sl-gt schist	
SZ048-27		CAD048	311.0	4500	SHMU			sl-gt schist	
NZ047-1		CAD047	246.8	5300	SHMU			sl-gt schist	
NZ009-2		CAD009	108.1	5200	SHMU			sl-gt schist	
NZ009-1		CAD009	101.9	5200	GTQZ			gt quartzite	sl porphs.
SZ061-50		CAD061	491.8	4500	SHGH			sl-bt-gt-gh schist	
NZ160-33		CAD160	368.4	5625	SHGH			sl-bt-gt-gh schist	
NZ047-7		CAD047	328.6	5300	SHGH			sl-bt-gt-gh schist	
NZ027-4		CAD027	254.1	5600	SHGH			sl-bt-gt-gh schist	
NZ004-10		CAD004	129.4	5400	SHGH			sl-bt-gt-gh schist	

Continued over page

Sample no.	Sample no. suffix	Drill hole	Depth (m)	Section (mN)	Rock code	Minz. name	Facies	Name/Mine name	Comments
SZ157-11	BAND06	CAD157	311.8	4800	INBB	Graphitic	bt-gt	Inveravon	REE analyses by Analabs
NZ160-31		CAD160	354.3	5625	INBB	Graphitic	bt-gt	Inveravon	abundant graphite
NZ047-8		CAD047	394.2	5300	BTGT	Graphitic	bt-gt	Inveravon	close to contact with altered metaseds.
NZ039-3	BAND08	CAD039	134.7	5300	INBB/BTGT	Graphitic	bt-gt	Inveravon	similar to NZ047-8
NZ033-2	BAND09	CAD033	57.6	5300	INBB	Graphitic	bt-gt	Inveravon	
NZ029-8		CAD029	391.3	5450	INBB/INGB	Graphitic	bt-gt	Inveravon	
NZ029-13	BAND07	CAD029	402.4	5450	INBB	Graphitic	bt-gt	Inveravon	
NZ016-1		CAD016	75.3	5200	INGB	Graphitic	bt-gt/qz-ap	Inveravon	
NZ040-4b	BAND04	CAD040	141.2	5200	QZGA/INPM	Graphitic	qz-ap	Inveravon	minor hb, bt
NZ035-13	BAND05	CAD035	117.15	5300	QZGA	Graphitic	qz-ap	Inveravon	minor gt, kn, hb
NZ030-13		CAD030	118.95	5500	INGB/QZGA	Graphitic	qz-ap	Inveravon	minor gt, hb
NZ016-2	3UNALT	CAD016	81.3	5200	QZOL	Olivine-pyroxenoid/Graphitic	ol	Broadlands	
SZ051-4	BAND03	CAD051	576	4725	QZOL	Olivine-pyroxenoid/Graphitic	ol	Inveravon/Warenda	interbanded kn and qz-ap
NZ160-20	2UNALT	CAD160	332.6	5625	QZOL	Olivine-pyroxenoid/Graphitic	ol	Broadlands	minor fine bands of qz-ap and gt
NZ070-4	1UNALT	CAD070	106.6	5400	QZOL	Olivine-pyroxenoid/Graphitic	ol	Broadlands	massive texture
NZ047-4		CAD047	287.9	5300	INOL	Olivine-pyroxenoid/Graphitic	ol	Inveravon/Broadlands	fine of qz-ap-gt ± gr, also contains mt
NZ047-2		CAD047	256.4	5300	QZOL	Olivine-pyroxenoid/Graphitic	ol	Broadlands/Burnham	abundant bt-gr and minor fl-mt
NZ044-5	BAND02	CAD044	415.8	5225	QZOL	Olivine-pyroxenoid/Graphitic	ol	Broadlands/Inveravon	abundant dissem. gt, minor ap bands
NZ044-2		CAD044	355.4	5225	INOL	Olivine-pyroxenoid/Graphitic	ol/bt-gt	Inveravon/Broadlands	minor gr
NZ040-4a	BAND01	CAD040	141.2	5200	QZOL	Olivine-pyroxenoid/Graphitic	ol	Inveravon/Broadlands	minor fine ap bands
NZ039-2		CAD039	108.4	5300	QZOL	Olivine-pyroxenoid/Graphitic	ol	Broadlands/Inveravon	gt rich, minor gu and bands of qz-ap-gt
NZ035-32		CAD035	182.3	5300	OLMT	Olivine-pyroxenoid		Burnham	ps altered
NZ034-12		CAD034	229.1	5300	OLMT	Olivine-pyroxenoid		Burnham	minor cpy, incip. ps alt.
NZ033-6		CAD033	208.4	5300	OLMT	Olivine-pyroxenoid		Burnham	fl-rich, minor mt, gu, gt
NZ016-2 UNALT		CAD016	81.3	5200	QZOL	Graphitic	ol	Broadlands/Inveravon	Banded ol facies
NZ016-2 ALT		CAD016	81.3	5200	QZHD	Graphitic	ol	Broadlands/Inveravon	As above but overprinted by hd vein and assoc. hd-gt-qz alt.

Appendix 3

Carbon Isotope and Carlo Erba Wholerock C, H and S Geochemistry

3.1 Sample preparation for $\delta^{13}C$ analysis

Samples were crushed and pulverised, and 20g of each soaked in concentrated HCl for 24 hours at 25°C to extract potential carbonate carbon as CO_2; considered a contaminant in this instance. The only carbon remaining in the samples was that of graphite. The samples were then thoroughly washed in distilled water and dried. The technique is similar to that outlined by Large et al. (1994) except that the initial HF digestion step was omitted.

25mg of sample was then collected for $\delta^{13}C$ analysis using a conventional carbon isotope line at the Central Science Laboratory, University of Tasmania. An additional pentane step was included in the carbon isotope line to sequester excessive SO_2 generated by devolatilisation of sulphides. $\delta^{13}C$ ratios in CO_2 generated by devolatilisation of graphite, were determined on a Micromass 602D stable isotope mass spectrometer relative to the NBS-21 PDB (Peedee belemnite) international standard. Analytical precision averaged ±0.03‰.

3.2 $\delta^{13}C$ and Carlo Erba C-H-S Wholerock Analyses for Selected Graphitic Ores.

Sample No.	$\delta^{13}C_{PDB}$	C wt%	H wt%	S wt%
NZ160-1	-22.63	0.74	0.11	1.97
SZU134-1	-24.01	0.70	0.17	1.92
NZ029-8	-25.61	n/a	n/a	n/a
SZ157-22	-23.65	1.09	0.27	2.62
NZ004-6	-26.71	0.76	0.18	1.71
NZ029-13	-25.56	1.58	0.15	2.74
NZ040-8	-23.36	1.54	0.15	0.06
NZ035-10	-22.99	0.89	0.05	2.83
NZ009-3	-24.83	0.99	0.02	2.03
NZ042-4	-22.17	0.77	0.00	1.18
NZ039-3b (BAND08)	-26.02	1.71	0.13	1.88
NZ034-7	-23.60	1.13	0.03	1.98
NZ016-1a	-27.09	1.45	0.00	3.91
NZ160-31	-27.96	0.67	0.09	5.32
NZ033-2 (BAND09)	-26.57	1.12	0.10	2.33
MAX	*-22.17*	*1.71*	*0.27*	*5.32*
MIN	*-27.96*	*0.67*	*0.00*	*0.06*
AVERAGE	***-24.85***	***1.08***	***0.10***	***2.32***
STDEV	*1.79*	*0.36*	*0.08*	*1.23*
MEDIAN	*-24.83*	*1.04*	*0.11*	*2.01*
Precision	*±0.03*	*±0.02*	*±0.02*	*±0.1*
Detection limit	*n/a*	*0.01*	*0.01*	*0.05*

N.B. No C-H-S analyses were carried out on NZ029-8 due to total consumption of the sample for $\delta^{13}C$ analysis

3.3 $\delta^{13}C$ Sample Data.

Sample no.	Sample no. suffix	Drill hole	Depth (m)	Section (mN)	Rock code	Minz. name	Facies	Name/Mine name	Comments
NZ160-1		CAD160	184.45	5625	INGB	Graphitic	qz-ap	Inveravon	
SZU134-1		CUD134	265	?	INBB/INGB	Graphitic	bt-gt/qz-ap	Inveravon	
NZ029-8		CAD029	391.3	5450	INBB/INGB	Graphitic	bt-gt/qz-ap	Inveravon	
SZ157-22		CAD157	389	4800	INBB/INGB	Graphitic	bt-gt/qz-ap	Inveravon	
NZ004-6		CAD004	115.8	5400	INBB/INGB	Graphitic	bt-gt/qz-ap	Inveravon	
NZ029-13	BAND07	CAD029	402.4	5450	INBB	Graphitic	bt-gt	Inveravon	minor INGB
NZ040-8		CAD040	168.2	5200	INGB	Graphitic	qz-ap	Inveravon	
NZ035-10		CAD035	102.25	5300	INQZ/INGB	Graphitic	qz-ap	Inveravon	
NZ009-3		CAD009	161.8	5200	INGB	Graphitic	qz-ap	Inveravon	
NZ042-4		CAD042	92.3	5400	INGB	Graphitic	qz-ap	Inveravon	
NZ039-3b	BAND08	CAD039	134.7	5300	INBB/BTGT	Graphitic	bt-gt	Inveravon	repeat of other part of sample
NZ034-7		CAD034	119.5	5300	INOL/INGB	Olivine-pyroxenoid/Graphitic	ol/qz-ap	Inveravon/Broadlands	slight hd alt. of ol along some bands
NZ016-1a		CAD016	75.3	5200	INGB	Graphitic	bt-gt/qz-ap	Inveravon	
NZ160-31		CAD160	354.3	5625	INBB	Graphitic	bt-gt	Inveravon	abundant graphite
NZ033-2	BAND09	CAD033	57.6	5300	INBB	Graphitic	bt-gt	Inveravon	

Appendix 4
Pb isotopes

A-4.1 Sample preparation and analytical procedures at the CSIRO, Division of Exploration and Mining, North Ryde, New South Wales

The following information regarding sample preparation and analytical procedures has been kindly provided by Barbara Gardner (analytical technician, Pb isotope facility, CSIRO Division of Exploration and Mining, North Ryde).

N.B. *i) the procedure employed for wholerock Pb isotope analyses on amphibolite samples was similar to the K-feldspar/amazonite method.*
ii) after completion of sample preparation approximately ½ µg of Pb was loaded onto a single Re filament with silica gel and phosphoric acid.

K-feldspar (including amazonite)

HCl Leach

1. Crush K-feldspar in agate mortar and pestle;
2. Leach 130mg with cold 7M HCl for 2 hours then centrifuge;
3. Spike leachate with ^{202}Pb concentrate and dry down in teflon beakers;
4. Add 2 drops concentrated HBr and dry down;
5. Add 2ml of 1M HBr and run through anion exchange columns and finally elute into electro-deposition (ED) vessels;
6. ED sample and load† for mass spectrometer analysis.

HCl + HNO_3 leach

1. Crush sample in agate mortar and pestle;
2. Weigh 50mg into savillex beaker;
3. Leach sample in 5ml of warm 7M HCl + 7M HNO_3 for 2 hours then centrifuge;
4. Syringe leachate, transfer to clean savillex beaker, spike with ^{202}Pb, dilute and dry down;
5. Add 2 drops of concentrated HBr, dry down;
6. Take up in 3ml of 1M HBr;
7. Extract Pb in two sequential mini ion exchange columns;
8. Load for mass spectrometer analysis.

HF + HNO_3 leach

1. Take residue from HCl/HNO_3 leach and dry down.
2. Spike residue with ^{202}Pb, dilute then dry down;
3. Add 0.5ml of HF and 3 drops $HClO_4$ (perchloric acid) and evaporate to dryness;
4. Add 1 drop $HClO_4$, evaporate to dryness;
5. Add 1 drop HNO_3, evaporate to dryness;
6. Repeat HNO_3 twice;
7. Add 1 drop of concentrated HBr, dry down;
8. Take up in 3ml of 1M HBr;
9. Extract Pb in two sequential mini ion exchange columns;
10. Load for mass spectrometer analysis.

Low Pb wholerock HF/HNO_3 (host rocks)

1. Weigh out ~50mg sample in a savillex beaker;
2. Add 3ml clean 7M HCl;
3. Reflux for 2hrs at ~170°C;
4. Centrifuge beakers and decant into clean centrifuge tubes (Soln A analysed only if required);
5. Wash residue in savillex with 1ml millipore water;
6. Centrifuge-discard water;

† the loading procedure involves placing approximately ½mg of Pb sample onto a single Re filament using a silica gel-phosphoric acid technique. The sample is then placed in the mass spectrometer for analysis.

7. Repeat wash etc;
8. Dry down;
9. Add 2ml HF and 3 drops clean conc. HNO_3;
10. Reflux for 3hrs at ~170°C;
11. Centrifuge and decant into new savillex beakers (Soln B);
12. Evaporate down;
13. Add 2 drops of $HClO_4$ and evaporate down;
14. Add 2 drops of millipore water and evaporate down;
15. Repeat;
16. Add 2 drops clean conc. HNO_3 and evaporate down;
17. Repeat;
18. Add 1drop conc. HBr and evaporate down;
19. Take up in 1-2ml 1M HBr and load onto large econ. columns followed by mini columns;
20. Continue Soln A if required;
21. Transfer to clean savillex beakers and evaporate down;
22. Add 2 drops conc. HBr and evaporate down;
23. Take up in 1-2ml 1M HBr;
24. Spike with "202" dilute;
25. Load onto columns as for Soln B.

Galena

1. Hand-pick galena under binocular microscope using a clean, fine needle or pin;
2. Deposit galena sample into a clean ED vessel;
3. Add 10 drops of clean concentrated HNO_3 (2x distilled) and evaporate to dryness;
4. When cool take up in 3 drops 0.1M HNO_3 and 27 drops of millipore water.
5. Add small clean magnet with clean tweezers;
6. Place clean electrodes into ED vessel and ED for 15 minutes;
7. If there is a large amount of zinc present, transfer Pb electrode to a new pre-prepared ED vessel;
8. Continue to ED until the Pb has been "cleaned up", using clean electrodes each time;
9. Elute approximately 300-400ng of Pb from the electrode into a 1ml teflon beaker using 1-2 drops of clean 3M HCl (approx. 100ng is required for the mass spectrometer analysis[#]);
10. Dry down;
11. Add 2 drops of clean concentrated HNO_3 (as above) and dry down again, marking on outside of beaker the position of the Pb for loading purposes;
12. Sample is now ready for loading.

A-4.2 Pb isotope dataset

Legend

- Q quality of analysis (0=high, 9=low).
- † – Pb concentration in galena is 86.58 wt%.
- ppm concentrations in bold are from wholerock XRF analyses.
- ppm concentrations in italics are from wholerock ICPMS analyses.
- ppm concentrations in plain text are from wholerock TIMS analyses.
- %Pb assays listed in italics represent wholerock XRF analyses on the sample rather than a 1m composite sample interval.

[#] - 5mm of dark brown colour on Pb electrode yields ~4000ng Pb
- 5mm of brown yields ~1600ng Pb
- 5mm of gold yields ~800ng Pb
- 5mm of very light brown yields ~400ng Pb

Table A4.2.1 Mineral separate Pb isotope dataset

Sample no.	Drillhole no. (depth, m)	Lab sample no.	Sample type and method	Mineralisation type/rock type	Para-genetic stage	Comments	Analysis method and lab location	U (ppm)	Th (ppm)	Pb (ppm)	% Pb assay (inter-val)	$^{206}Pb/^{204}Pb$	$^{207}Pb/^{204}Pb$	$^{208}Pb/^{204}Pb$	Q
SZ037-21	CAD037 (441.7)	S01	galena separate, micropicking	h/w olivine-pyroxenoid (Burnham)	I	ga inclusion in kn, slightly flazered texture with il and ps	conventional (CSIRO)	-	-	†	16 (441-442)	16.015	15.388	35.636	2
		S02	galena separate, scratching from thin section		IIc	coarse grained ga	not analysed								
		S03	galena separate, micropicking		I	ga inclusion in kn, slightly flazered with il	not analysed								
		S04	galena separate, scratching from thin section		IIc	coarse grained ga	conventional (CSIRO)	-	-	†		16.000	15.375	35.597	2
SZ037-13	CAD037 (517.9)	S05	galena separate, micropicking	f/w olivine-pyroxenoid (Nithsdale)	I	ga inclusion kn, clean inclusion	conventional (CSIRO)	-	-	†	4.69 (517-518)	16.006	15.379	35.613	0
		S06	galena separate, micropicking		I	as above	not analysed								
NZ033-6	CAD033 (208.4)	S07	galena separate, micropicking	h/w olivine-pyroxenoid (Burnham)	I	ga inclusion in kn, clean inclusion	not analysed								
		S08	galena separate, micropicking		I	ga inclusion in kn, clean inclusion	not analysed								
		S09	galena separate, micropicking		I	ga inclusion in pf, slightly flazered	not analysed								
SZ052-24	CAD052 (400.6)	S10	galena separate, micropicking	h/w banded olivine-pyroxenoid (Broadlands)	I	ga inclusion in kn, ps alteration	double-spike (AGSO/RSES)	-	-	†	28.1 (400-401)	16.020	15.396	35.667	n/a
		S11	galena separate, micropicking		I	ga inclusion in kn, slightly flazer-textured associated with ps	double-spike (AGSO/RSES)	-	-	†		16.020	15.397	35.675	n/a
		S11				repeat analysis of above	double-spike (AGSO/RSES)	-	-	†		16.017	15.393	35.662	n/a

Sample no.	Drillhole no. (depth, m)	Lab sample no.	Sample type and method	Mineralisation type/rock type	Para-genetic stage	Comments	Analysis method and lab location	U (ppm)	Th (ppm)	Pb (ppm)	% Pb assay (inter-val)	$^{206}Pb/^{204}Pb$	$^{207}Pb/^{204}Pb$	$^{208}Pb/^{204}Pb$	Q
NZ016-1b	CAD016 (75.3)	S12	galena separate, micropicking	graphitic - qz-ap to qz-ap-gt-hb facies (Inveravon)	I	ga along triple junctions qz-ap-gr(-gt) bands	not analysed	6.04	2.11		4.88 *20.92* (75-76)				
		S13	galena separate, micropicking		I	as above	not analysed								
		S14	galena separate, micropicking		I	as above	conventional (CSIRO)	-	-	†		16.006	15.382	35.623	0
NZ029-8	CAD029 (391.3)	S15	galena separate, micropicking	graphitic - qz-ap to qz-ap-gt-hb facies (Inveravon)	I	ps-ga-fr ± allargentum vein	not analysed				8.22 *11.14* (391-392)				
		S16	galena separate, micropicking		I	ps-ga-fr ± allargentum vein	not analysed								
		S17	galena separate, micropicking		IIc	ps-ga-fr ± allargentum vein	conventional (CSIRO)	-	-	†		16.013	15.389	35.635	0
		S18	galena separate, micropicking		I	ga along qz triple juctions	conventional (CSIRO)	-	-	†		16.038	15.431	35.783	3
		S19	galena separate, micropicking		I	as above	not analysed								
		S20	galena separate, micropicking		I	as above	not analysed								
SZ155-11	CAD155 (350.7)	S21	galena separate, scratching from thin section	graphitic - qz-ap facies (Inveravon)	IIc	remobilised ga in partially silicified graphitic mineralisation	double-spike (AGSO/RSES)	-	-	†	-	16.020	15.398	35.675	n/a
NZ035-32	CAD035 (182.3)	S22	galena separate, scratching from thin section	h/w olivine-pyroxenoid (Burnham)	IIc	remobilised ga	conventional (CSIRO)	-	-	†	6.3 *16.00* (182-183)	16.032	15.417	35.714	4
NZ020-12	CAD020 (108.1)	S23	galena separate, scratching from drillcore	siliceous Pb-Zn-Ag (Glenholme Breccia Type 1)	IIc	coarse remobilised ga	conventional (CSIRO)	-	-	†	40.4 (108-109)	16.031	15.417	35.731	8
		S23				repeat analysis of above	conventional (CSIRO)	-	-	†		16.010	15.386	35.623	9

Sample no.	Drillhole no. (depth, m)	Lab sample no.	Sample type and method	Mineralisation type/rock type	Para-genetic stage	Comments	Analysis method and lab location	U (ppm)	Th (ppm)	Pb (ppm)	% Pb assay (inter-val)	$^{206}Pb/^{204}Pb$	$^{207}Pb/^{204}Pb$	$^{208}Pb/^{204}Pb$	Q
SZ063-2b	CAD063 (618.5)	S24	galena separate, scratching from drillcore	siliceous Pb-Zn-Ag (Glenholme Breccia Type 2)	III	as above but with cb and slightly vuggy	conventional (CSIRO)	-	-	†	48.6 (618-619)	16.016	15.393	35.657	2
NZ004-1	CAD004 (219.5)	S25	galena separate, scratching from drillcore	siliceous Pb-Zn-Ag (Glenholme Type 2)	III	remobilised ga lining vug in D_4 qz-cb-fl vein	conventional (CSIRO)	-	-	†	19.3 (219-220)	16.083	15.415	35.744	2
SZ152-49	CAD152 (449.7)	S26	galena separate, scratching from drillcore	mixed h/w and f/w hedenbergite (Kheri/Colwell)	IIc	remobilised ga in hd, ie. ga-rich hedenbergite mineralisation	conventional (CSIRO)	-	-	†	22.2 (449-450)	16.014	15.392	35.641	4
NZ042-8	CAD042 (137.8)	S27	galena separate, scratching from drillcore	graphitic (Inveravon)	I	disseminated ga in qz-ga ore (QZGA)	conventional (CSIRO)	-	-	†	21.6 (137-138)	16.015	15.391	35.634	1
		S27				repeat analysis of above	conventional (CSIRO)	-	-	†		16.002	15.374	35.601	1
NZ035-21	CAD035 (141.7)	S28	galena separate, scratching from drillcore	graphitic - qz-ap facies (Inveravon)	IIc	remobilised ga vein	conventional (CSIRO)	-	-	†	9.55 (141-142)	16.008	15.388	35.639	2
SZ048-3	CAD048 (421.1)	S29	galena separate, scratching from drillcore	h/w olivine-pyroxenoid (Broadlands/ Burnham)	IIc	coarse grained ga	conventional (CSIRO)	-	-	†	-	16.010	15.387	35.622	0
NZ027-5	CAD027 (256.3)	S30	gahnite separate, drilling from drillcore	gahnite-bearing sillimanite-garnet-biotite schist (SHGH)	I	gahnite porphyroblasts	not analysed								
NZ004-2	CAD004 (267.3)	S31	amazonite separate, low-Pb crusher and pickings	lode pegmatite (LPEG)	-	from lode pegmatite within the Core Amphibolite	conventional (CSIRO) $HF-HNO_3$ leach	-	-	-	-	16.029	15.406	35.678	1
		S31				as above	conventional (CSIRO) HCl leach	-	-	489		16.012	15.375	35.604	1
		S31				as above	conventional (CSIRO) $HCl-HNO_3$ leach	-	-	370		16.049	15.433	35.787	6

Sample no.	Drillhole no. (depth, m)	Lab sample no.	Sample type and method	Mineralisation type/rock type	Para-genetic stage	Comments	Analysis method and lab location	U (ppm)	Th (ppm)	Pb (ppm)	% Pb assay (inter-val)	$^{206}Pb/^{204}Pb$	$^{207}Pb/^{204}Pb$	$^{208}Pb/^{204}Pb$	Q
SZ037-25	CAD037 (394.2)	S32	amazonite separate, low-Pb crusher and pickings	lode pegmatite (LPEG)	-	from insitu partial melt in gahnite-bearing sillimanite-garnet-biotite schist (SHGH)	conventional (CSIRO) HF-HNO_3 leach	-	-	-	-	16.016	15.395	35.653	0
		S32				as above	conventional (CSIRO) HCl leach	-	-	153		16.080	15.398	35.726	3
		S32				as above	conventional (CSIRO) HCl-HNO_3 leach	-	-	149		16.103	15.403	35.671	6
NZ009-4	CAD009 (226.9)	S33	galena-Kfeldspar separate, drilling from drillcore	lode pegmatite (LPEG) to pegmatite (PEGM)	II?	partially resorbed ga in grey-coloured kf from an insitu pegmatitic melt in possible sillimanite-garnet-biotite schist (SHGH)	conventional (CSIRO)	-	-	†	-	16.018	15.392	35.660	1
KMG2	CAD159 (109.4-109.9)	-	Kfeldspar-quartz separate, crush (W-carbide), isomag. separator	quartzofeldspathic gneiss (GNES)	-	212-300 µm sieved fraction. Sample located ~50m east of orebody on the 5300mN section.	conventional (CSIRO) HF-HNO_3 leach	**3.5** ***4.03***	**17.5** ***19.63***	**31** 9.04	-	16.218	15.425	35.798	6
SZU51-1	CUD051 (112.8)	-	Kfeldspar-quartz separate, crush (W-carbide), isomag. separator	quartzofeldspathic gneiss (GNES)	-	212-300 µm sieved fraction. Sample located ~30m from orebody in footwall ~4850mN.	conventional (CSIRO) HF-HNO_3 leach	**6.2**	**15.4**	**10** 2.52	-	16.900	15.514	36.260	2
SZ101-6	CAD101 (230.6)	-	Kfeldspar-quartz separate, crush (W-carbide), hand pickings	quartzofeldspathic gneiss (GNES)	-	>600 µm sieved fraction. Sample located ~50m from orebody below Footwall Shear on the 4500mN section.	conventional (CSIRO) HF-HNO_3 leach	**3.9**	**15.7**	**16** 4.25	-	17.119	15.527	36.571	2
EQ709	CAD243 (97.4-97.7)	-	Kfeldspar-quartz separate, crush (W-carbide), isomag. separator	quartzofeldspathic gneiss (GNES)	-	212-300 µm sieved fraction. Sample located ~1.2km northwest of the orebody, 6880mN 455mE.	conventional (CSIRO) HF-HNO_3 leach	**2.7** ***3.24***	**18** ***16.52***	**34** 1.40	-	16.251	15.444	35.900	6

Sample no.	Drillhole no. (depth, m)	Lab sample no.	Sample type and method	Mineralisation type/rock type	Para-genetic stage	Comments	Analysis method and lab location	U (ppm)	Th (ppm)	Pb (ppm)	% Pb assay (inter-val)	$^{206}Pb/^{204}Pb$	$^{207}Pb/^{204}Pb$	$^{208}Pb/^{204}Pb$	Q
EQ957	CAD129 (166.9-167.2)	-	Kfeldspar-quartz separate, crush (W-carbide), isomag. separator	quartzofeldspathic gneiss (GNES)	-	212-300 µm sieved fraction. Sample located ~200m from orebody in the hanging wall adjacent to the Hamilton Fault, 4200mN section.	conventional (CSIRO) $HF-HNO_3$ leach	**5.1** ***4.27***	**17.7** ***16.64***	**15** 2.24	-	17.361	15.595	36.614	2

Table A4.2.2 Wholerock Pb isotope dataset

Sample no.	Drillhole no. (depth, m)	Lab sample no.	Sample method	Mineralisation type/rock type	Para-genetic stage	Comments	Analysis method and lab location	U (ppm)	Th (ppm)	Pb (ppm)	% Pb assay (inter-val)	$^{206}Pb/^{204}Pb$	$^{207}Pb/^{204}Pb$	$^{208}Pb/^{204}Pb$	Q
SZ056-1	CAD056 (371.0)	-	crush/mill (W-carbide) drillcore	amphibolite (AMPH)	-	Core Amphibolite	conventional (CSIRO) $HF-HNO_3$ leach	**<1.5** ***0.23***	**<1.5** ***0.59***	34 or 134(?) **177**	-	16.037	15.364	35.598	5
		-		amphibolite (AMPH)	-	as above	conventional (CSIRO) $HF-HNO_3$ leach	-	-	-		15.662	15.073	34.643	9
SGW4-274	CAD004 (274.0)	-	crush/mill (W-carbide) drillcore	amphibolite (AMPH)	-	Core Amphibolite	conventional (CSIRO) $HF-HNO_3$ leach	**<1.5**	**<1.5**	114 **126**	-	16.068	15.408	35.731	6
SGW13-186	CAD013 (186.0)	-	crush/mill (W-carbide) drillcore	amphibolite (AMPH)	-	Core Amphibolite	conventional (CSIRO) $HF-HNO_3$ leach	**<1.5** ***0.17***	**2** ***0.54***	123 **98**	-	16.047	15.384	35.659	2
SGW59-517	CAD059 (517.0)	-	crush/mill (W-carbide) drillcore	amphibolite (AMPH)	-	Core Amphibolite	conventional (CSIRO) $HF-HNO_3$ leach	**<1.5**	**<1.5**	106 **107**	-	16.050	15.377	35.650	5
SGW64-342	CAD064 (342.0)	-	crush/mill (W-carbide) drillcore	amphibolite (AMPH)	-	Core Amphibolite	conventional (CSIRO) $HF-HNO_3$ leach	**1.5** ***0.21***	**<1.5** ***0.58***	55 **50**	-	15.265	15.377	33.727	9
KMG2	CAD159 (109.4-109.9)	-	crush/mill (W-carbide) drillcore	quartzofeldspathic gneiss (GNES)	-	Sample located ~150m east of orebody on the 5300mN section.	conventional (CSIRO) $HF-HNO_3$ leach	**3.5** ***4.03***	**17.5** ***19.63***	**31** 8.37	-	16.371	15.417	35.744	4
SZU51-1	CUL051 (112.8)	-	crush/mill (W-carbide) drillcore	quartzofeldspathic gneiss (GNES)	-	Sample located ~30m from orebody in footwall ~4850mN.	conventional (CSIRO) $HF-HNO_3$ leach	**6.2**	**15.4**	**10** 2.06	-	18.527	15.684	36.774	2
SZ101-6	CAD101 (230.6)	-	crush/mill (W-carbide) drillcore	quartzofeldspathic gneiss (GNES)	-	Sample located ~50m from orebody below Footwall Shear on the 4500mN section	conventional (CSIRO) $HF-HNO_3$ leach	**3.9**	**15.7**	**16** 0.96	-	18.964	15.682	36.917	4
EQ709	CAD243 (97.4-97.7)	-	crush/mill (W-carbide) drillcore	quartzofeldspathic gneiss (GNES)	-	Sample located ~1.2km northwest of the orebody, 6880mN 455mE	conventional (CSIRO) $HF-HNO_3$ leach	**2.7** ***3.24***	**18** ***16.52***	**34** 12.2	-	16.380	15.445	35.889	4
EQ957	CAD129 (166.9-167.2)	-	crush/mill (W-carbide) drillcore	quartzofeldspathic gneiss (GNES)	-	Sample located ~200m from orebody in the hanging wall adjacent to the Hamilton Fault, 4200mN section	conventional (CSIRO) $HF-HNO_3$ leach	**5.1** ***4.27***	**17.7** ***16.64***	**15** 0.764	-	18.350	15.701	36.880	0

Table A4.2.3 McCarthy (1996) Pb isotope dataset including 1998 double-spike repeats

Sample no.	Drillhole no. (depth, m)	Lab sample no.	Sampling method	Mineralisation type/rock type	Para-genetic stage	Comments	Analysis method and lab location	U (ppm)	Th (ppm)	Pb (ppm)	% Pb assay (inter-val)	$^{206}Pb/^{204}Pb$	$^{207}Pb/^{204}Pb$	$^{208}Pb/^{204}Pb$	Q
Ua71ND	u/ground grab sample (156.5)	C1	galena separate, hand picking from grab sample	D_4 vein	III	D_4 vein from fault	conventional (CSIRO)	-	-	†	-	16.009	15.384	35.616	0
		C1					double-spike (AGSO/RSES)	-	-	†		16.019	15.398	35.672	n/a
Uc88SD	u/ground grab sample (161.2)	C2	galena separate, hand picking from grab sample	D_4 vein	III	D_4 vein from fault	conventional (CSIRO)	-	-	†	-	16.027	15.390	35.636	1
		C2					double-spike (AGSO/RSES)	-	-	†		16.028	15.401	35.688	n/a
CUD095	CUD095 (224.9)	C3	galena separate, hand picking from drillcore	D_4 vein	III	D_4 vein from fault	conventional (CSIRO)	-	-	†	-	16.016	15.388	35.621	3
CUD120-12	CUD120 (58.25)	C4	galena separate, hand picking from drillcore	D_4 vein	III	D_4 vein from fault, cb-marcasite breccia in quartzite (Bustard Fault)	conventional (CSIRO)	-	-	†	-	16.145	15.437	35.819	2
		C4					double-spike (AGSO/RSES)	-	-	†		16.118	15.411	35.754	n/a
CUD135	CUD135 (131.7)	C5	galena separate, hand picking from drillcore	D_4 vein	III	D_4 vein from fault, cb vein with ga selvage in a cherty quartzite (Puffin Fault)	conventional (CSIRO)	-	-	†	-	16.130	15.403	35.761	9
		C5					double-spike (AGSO/RSES)	-	-	†		16.137	15.416	35.785	n/a

A4.3 Initial Pb isotope calculations

Calculation of possible initial Pb isotope ratios for the gneissic host rock and the Core Amphibolite based on the terrain specific model (Sun et al., 1994 and 1996) and the Cummings and Richards (1975) global Pb evolution model III.

Rock type	Sample no.	U (ppm) Analysis	U (ppm) Calculated TSM=1670Ma	U (ppm) Calculated C&R=1540Ma	Pb (ppm)	Maximum model age (t_2) TSM	Maximum model age (t_2) C&R	Present ratios (at t_2) 206/204	Present ratios (at t_2) 207/204	Calculated initial ratios (at t_1) TSM 206/204	Calculated initial ratios (at t_1) TSM 207/204	Calculated initial ratios (at t_1) C&R 206/204	Calculated initial ratios (at t_1) C&R 207/204
Gneiss													
(K-feldspar)	KMG2	-	0.09	0.10	9.04‡	1575	1440	16.22	15.43	16.03	15.41	16.03	15.41
	SZU51-1	-	0.11	0.12	2.52‡	1575	1440	16.90	15.51	16.07	15.43	16.08	15.44
	SZ101-1	-	0.23	0.25	4.25‡	1575	1440	17.12	15.53	16.09	15.43	16.10	15.43
	EQ709	-	0.02	0.02	1.40‡	1575	1440	16.25	15.44	16.03	15.42	16.03	15.42
	EQ957	-	0.14	0.16	2.24‡	1575	1440	17.36	15.60	16.10	15.47	16.11	15.48
Gneiss													
(wholerock)	KMG2	3.50	0.54	0.60	31†	1495	1350	16.37	15.42	16.06	15.39	16.09	15.39
	SZU51-1	6.20	1.18	1.29	10†	1495	1350	18.53	15.68	16.31	15.48	16.55	15.51
	SZ101-6	3.90	2.20	2.41	16†	1495	1350	18.96	15.68	16.36	15.44	16.64	15.48
	EQ709	2.70	0.61	0.67	34†	1495	1350	16.38	15.45	16.06	15.42	16.09	15.42
	EQ957	5.10	1.65	1.80	15†	1495	1350	18.35	15.70	16.29	15.51	16.51	15.54
Core Amphibolite													
(wholerock)	SZ056-1	0.23Δ	0.18	0.20	177†	1640	1510	16.04	15.36	16.00	15.36	16.01	15.36
	SGW4-274	0.20§	0.32	0.36	126†	1640	1510	16.07	15.41	16.03	15.40	16.04	15.41
	SGW13-186	0.17Δ	0.15	0.17	98†	1640	1510	16.05	15.38	16.02	15.38	16.02	15.38
	SGW59-517	0.20§	0.18	0.20	107†	1640	1510	16.05	15.38	16.01	15.37	16.02	15.37

† - XRF analysis Δ - ICP-MS analysis TSM – terrain specific model (this study; Sun et al., 1994 and 1996)

§ - calculated average content ‡ - TIMS analysis C&R – Cummings and Richards (1975) model III

Appendix 5

Refereed Publication

Bodon, S. B., 1998, Paragenetic relationships and their implications for ore genesis at the Cannington Ag-Pb-Zn deposit, Mount Isa Inlier, Queensland, Australia: Economic Geology, v. 93, p. 1463-1488.